Universidad Autónoma de Madrid

Doctoral Thesis

Planetary systems across different niches

Synergies between *Kepler* and Calar Alto observatories

Author:
Jorge Lillo Box

Supervisor:
Dr. David Barrado Navascués

A thesis submitted in fulfillment of the requirements
for the degree of Doctor in Astrophysics

in the

Centro de Astrobiología (CSIC-INTA)
Departamento de Astrofísica

Madrid, May 2015

Declaración de autoría

Yo, **Jorge Lillo Box**, declaro que esta tesis titulada "Sistemas planetarios en diferentes nichos: Sinergias entre la misión espacial Kepler y el observatorio de Calar Alto" y el trabajo incluído en ella son propios y confirmo que:

- Este trabajo ha sido realizado en mi candidatura al grado de Doctor en esta universidad.
- Donde se haya consultado otros trabajos publicados, esto está siempre explicitado y atribuído.
- Donde se cita el trabajo de otros, siempre se proporciona la fuente. Con excepción de dichas citas, el trabajo es enteramente mío.
- He agradecido apropiadamente a las fuentes de ayuda.
- Donde esta tesis haya sido fruto del trabajo conjunto con otros investigadores, queda explícitamente indicado qué partes han sido realizadas por otros y cuáles por mí mismo.

En Madrid, a 8 de Mayo de 2015

Jorge Lillo Box

Por su parte, **David Barrado Navascués**, Doctor en Ciencias Físicas y Científico titular del Centro de Astrobiología (INTA-CSIC) y **Eva Gloria Villaver Sobrino**, Doctora en Ciencias Físicas y Profesora Contratada Doctor por la Universidad Autónoma de Madrid

CERTIFICAN que la presente memoria

Sistemas planetarios en diferentes nichos:
Sinergias entre la misión espacial Kepler y el observatorio de Calar Alto

ha sido realizada por **Jorge Lillo Box** bajo nuestra dirección y tutela, respectivamente. Así, consideramos que esta memoria contiene aportaciones suficientes para constituir la Tesis Doctoral del interesado.

En Madrid, a 8 de Mayo de 2015

David Barrado Navascués

Eva Gloria Villaver Sobrino

Universidad Autónoma de Madrid
Departamento de Física Teórica

Tesis Doctoral

Sistemas planetarios en diferentes nichos

Sinergias entre la misión espacial *Kepler* y el observatorio de Calar Alto

Autor:
Jorge Lillo Box

Director:
Dr. David Barrado Navascués

Tesis depositada en cumplimiento de los requerimientos para la obtención del grado de Doctor en Astrofísica

en el

Centro de Astrobiología (CSIC-INTA)
Departamento de Astrofísica

Madrid, Mayo de 2015

A todos aquellos que me han guiado, apoyado e inspirado en estos 27 años de vida.
A mis padres, a mi hermana y a Alba.

Agradecimientos

Esto va a ser complicado. Sentado delante de la pantalla de mi ordenador que tanto he mirado en estos últimos cuatro años de tesis, me encuentro ante la difícil tarea de hacer un compendio de las personas que más me han ayudado a llegar a este momento. No las he contado, pero podrían ser cientas las personas que han influido en mí de alguna forma y me han dado fuerza para terminar este trabajo. Así que voy a intentar resumir.

Quiero empezar con un agradecimiento muy especial. Y es que este viaje que ahora termina, lo hace sin una de las pasajeras que me acompañaron a subir al barco y que durante los primeros años se preocuparon porque estuviese cómodo. Tía, han sido muchos los momentos en los que has estado ahí, y cuando tuve que salir de casa nunca dejaste de llamar para preguntar por tu sobrino, el *astrofísico*. Aunque ya no estés, aunque te bajaras de este barco sin quererlo, siempre estarás con nosotros. Gracias tía.

Un lugar privilegiado en estos agradecimientos lo han de ocupar mis padres. Mamá, papá, vosotros me lo habéis dado todo, siempre a mi lado sin faltar un segundo, sin dudar ni un ápice de mis capacidades y otorgándome una libertad de pensamiento que me ha permitido tener siempre la mente abierta, algo crucial en esta profesión. Nunca habéis dicho "no" a mis decisiones. Aún recuerdo cuando allá por 2005 os dije que quería estudiar esa cosa tan rara que es la Astrofísica. Si bien es cierto que nunca dudé de que me permitiríais hacerlo, vuestra respuesta en forma de total apoyo y confianza (aunque eso supusiera distanciarnos) me hizo sentirme arropado en esa nueva etapa. Mamá, tu tesón y exigencia, combinados con altas dosis de cariño y ánimo han sido los pilares de mi formación tanto personal como académica. Tus "Pero hijo, ¿sólo un 9.5 en Matemáticas? ¿qué ha pasado?" me mantenían siempre alerta y con los pies en el suelo. Tu valentía y entereza en momentos muy duros me hicieron comprender el valor de la vida, y cambiaron para siempre mi forma de vivirla. Papá, tu capacidad de esfuerzo, tu preocupación por los demás, tu humildad y tu dedicación como padre han sido claves en mi formación personal. Siempre has sido un referente para mí, un ejemplo de serenidad, de trabajo duro y de éxito profesional, pero sin olvidar tus raíces. Y todo ello siempre con una sonrisa. En fin, vuestra dedicación, cariño y esfuerzo durante tantos años ha sido el motor de este barco. Os lo debo todo. Gracias.

La otra componente de los Lillo-Box es mi hermana. Claudia, cada vez que pienso en ti se me dibuja una sonrisa en la cara. Eres la alegría y el carácter combinados en una sola persona. No recuerdo la cara que puse cuando te vi por primera vez en aquella habitación de hospital, en los brazos de la mamá, pero recuerdo que me acerqué y comprendí que ibas a ser alguien importante en mi vida. Hemos vivido juntos doce años de nuestras vidas en los que hemos aprendido mucho el uno del otro. Cuando me fui, sin embargo, supe que me perdería una parte muy importante de la tuya, una parte en la que necesitarías mi apoyo. Lo hice persiguiendo mi sueño, ya lo sabes,

pero siempre estaré en deuda contigo por ello. Me has enseñado a ser feliz y a entender muchas otras partes de la vida. Eres una luchadora que no se da por vencida. Y eso te hace ser muy, muy grande. Gracias enana.

Hace ya unos poco años me trasladé a La Laguna (Tenerife) para terminar la licenciatura. Allí entró de lleno en mi vida una chica de nombre astronómico que vino para quedarse, Alba. En estos últimos seis años has sido mi compañera de viaje (tanto literalmente como en sentido figurado) y la persona en la que he confiado sin dudar. Tu respuesta siempre ha sido una sonrisa. Has sido mi apoyo, mi ánimo y mi guía, el timón del barco. Has sabido animarme y sacarme del agobio en los momentos difíciles. Tu inteligencia y tu capacidad crítica me han hecho ver las cosas de otro modo. Sin ti, todo esto hubiese sido mucho más difícil. Por todo esto, muchas, muchas gracias Alba. También a la familia Aller-Egea, que me acogió como uno más desde el primer momento.

Quiero agradecer también a mis tíos, Juan y Mari Carmen, por tratarme siempre como a otro hijo más. A Clara por su interminable sonrisa y alegría. Y a mi primo Juan Alberto porque sé que siempre está ahí cuando le necesito y me ha acompañado durante toda mi vida. A mi abuela Hortensia, porque me ha querido siempre con locura y porque es un ejemplo de superación personal y capacidad de sacar adelante una familia con trabajo y esfuerzo. A mis tías Pepita y Carmen, porque siempre habéis estado y estaréis ahí.

En esta lista no pueden faltar Mari y Diego, porque siempre me han tratado como a un hijo y han estado para lo que hiciera falta. Mari con sus anéctodas y Diego con sus bromas, gracias a los dos. Gracias también a mis tíos Pedro y Elena, por esos veranos en el campo y esas cenas de Navidad tan divertidas. A mi prima Andrea, por todos los momentos de diversión y locura que vivimos juntos en el campo. Y a mi abuela Margarita, porque fueron pocos los años que pudimos pasar juntos pero los recuerdo con gran cariño y alegría.

Esta tesis que aquí presento no hubiera podido realizarla sin David, mi director. Gracias David por confiar en mí. Porque cuando después de aquél *trainee* en ESAC te escribí para preguntarte si estarías interesado en que hiciera la tesis contigo, tu respuesta fue un conciso pero alentador “Perfecto, vayamos adelante. D.” (e-mail del 22 de Febrero de 2010). Esa corta pero decisiva frase puso ante mí el reto de realizar una tesis doctoral. Desde el minuto uno has creído en mis capacidades y te has esforzado por enseñarme una forma de trabajar, organizarse y, sobre todo, de razonar, que han sido claves en mi formación. Has sabido guiarme, pero dándome libertad, permitiendo que fuese yo quien caminase solo y tropezase con los diferentes obstáculos, para después levantarme y volver a marcarme el camino correcto. Porque es así como realmente se aprende a hacer ciencia. En definitiva, gracias David por estos años de aprendizaje, por esas conversaciones y consejos en muchos casos incluso paternales, por esas tardes de elucubraciones locas sobre sistemas planetarios, por esos intercambios de mail algunas mañanas de domingo y por transmitirme tu pasión por la ciencia. Gracias por ser director y compañero.

El LAEFF (o LAEX o CAB-Villafranca) ha sido siempre una familia. Cuando llegué aquí como *trainee* en 2009 me encontré con un ambiente de trabajo excepcional. El buen ambiente y la complicidad entre la gente del centro lo hacen un lugar ideal para el desarrollo de una tesis o cualquier investigación, con personas siempre dispuestas a echar una mano. Por ello, mi agradecimiento a todos los "inquilinos" del LAEFF, que han hecho mucho más fácil este trabajo. Mención especial requieren varias personas. Benja, porque su humildad y su dedicación a los demás lo hacen grande. Porque siempre tiene palabras de aliento para todos, sin excepción, en los momentos difíciles; y porque es una fuente inagotable de bondad. Nuria, porque ha sido un apoyo en todo momento y porque su buen hacer es digno de admiración. Hervé, porque su forma de trabajar y tomarse la vida son un ejemplo tanto profesional como personal y porque me ha ayudado mucho en estos años. Amelia, porque desde que la conocí ha sido un referente para mí y porque siempre está disponible para ayudar no sólo en el plano profesional sino también en el personal. María, por acogerme tan amablemente en mi paso por Caltech, siempre disponible para atenderme y enseñarme muchísimos conceptos nuevos para mí. Y todo ello, siempre con una sonrisa. Pablo, porque además de nuestra pasión por la ciencia, nos unen muchas otras cosas que nos han hecho convertirnos en grandes amigos (aunque seas del Atleti). Porque me has enseñado mucho durante estos años y has sabido ejercer de "hermano mayor" a la perfección.

Particular mención también a Sergio y Antonio por su profesionalidad y simpatía inagotable, sois unos genios; a Natalia por transmitir el valor de la divulgación y ayudarme a mejorar en cada entrada del blog; a Carmen Morales porque fue ella quien me abrió las puertas a este mundo de la ciencia permitiéndome hacer el *trainee* con ella; a Nacho, Pilar, Jose y Pablo por aguantarme durante algún año como compañero de despacho (o de aquélla "celda" en Guantánamo); a Margie, por ser la madre de todos, por hacer que este centro funcione y por su paciencia con nuestros continuos despistes *burrocráticos*; y a Álvaro, por nuestras conversaciones locas y surrealistas sobre "cosas Bayesianas". Por supuesto, gracias a Albert, Miguel, Carmen Sánchez, Juan Ángel, Luis, Julia, Miriam, Manolo, Almudena, Raúl, Fran, Belén, Jesús, Irene, Mario, Bea, Iñaki, Mauro, Enrique, Rafa, Giovanni, Jorge, Jose, Johannes, Paco, Hristo, Patricia, Santi, Andy, David Cabezas, María Arévalo, Carlos, Ignacio y Héctor, porque entre todos habéis hecho mi estancia aquí mucho más agradable con vuestras bromas, debates y discusiones; cada uno con vuestras particularidades que os hacen únicos. Gracias también a Carlos y Eva que desde la UAM me han ayudado cada vez que lo he necesitado.

Mi paso por Caltech no hubiese sido posible sin la ayuda de John Stauffer. Thanks John for giving me the unique opportunity of working at Caltech, an unforgettable experience from both a personal and a professional point of view. You and María provided me with an important scientific background crucial before starting my PhD. It was an honor to work with you in such a scientifically rich environment. Mi estancia en Caltech me permitió también conocer a Alessio, un gran amigo entonces y ahora. Thanks Ale.

Gracias también a Nuno, por acceder a mi estancia en el CAUP (Oporto) aprendiendo de sus conocimientos y experiencia sobre velocidad radial, que me han permitido realizar este trabajo. Allí conocí a otra familia, también muy unida y que me acogió desde el primer día. Sobre todo, gracias a Elisa, Antonio, María, Pedro, Mahmoud, Ahmed, Gerasim, Vardan y Mercedes. Muito obrigado. Also thanks to Thomas, Luigi and Simona from the MPIA for the close collaboration during these years.

Un agradecimiento con mayúsculas a todo el personal del Observatorio de Calar Alto. Porque esas largas campañas de observación se hicieron tremendamente entretenidas gracias a vuestra compañía. Vuestra calidad profesional no tiene límites. Conocéis al detalle todas y cada una de las particularidades de los telescopios e instrumentos. Trabajáis siempre con enorme esfuerzo y dedicación para que cuando uno se disponga a observar todo esté en su sitio. Me habéis tratado como uno más desde mi primera noche de observación. Gracias Manolo por esa primera noche. Gracias Luzma, Ana, Gilles, Jesús, Santos, Alberto, Flori, Damián y Felipe por compartir esas noches, comidas y cenas conmigo en las que la risa era la nota predominante. Gracias Enrique, Nacho, José Luís, Elvira, David, Ángel y María Jesús. Y a todos, porque vuestro trabajo merece la pena. No es pues casualidad que vuestro observatorio aparezca en la portada de esta tesis. Calar Alto se defiende.

En el plano personal, quiero agradecer a todos mis profesores y compañeros de la Aneja porque su esfuerzo y dedicación, a pesar de todas las trabas a la educación pública, es más que meritorio. Y en especial a Maribel, Pedro, Teo y Julia por inculcar no solo conocimientos sino, aún más importante, valores de trabajo en equipo, esfuerzo personal, amistad y superación. En esta etapa crucial, fueron ellos los que supieron guiarnos y educarnos en unos valores de respeto y cariño. Fue allí también donde conocí a amigos que hoy mantengo. Gracias Ricardo por ser un amigo inmejorable durante tantos y tantos años, y por hacerme sentir como en casa cada vez que vuelvo a la *terreta*. Gracias Fran por tu amistad y por estar siempre ahí; porque cuando quedamos parece que no hubiera pasado el tiempo y, sin embargo, son ya más de 20 años que nos conocemos.

Si hay una época que marcó la dirección de mi carrera profesional, esa fue mi paso por el IES Miguel Hernández. La impresionante calidad de su profesorado y la inmensa suerte que tuve con mis compañeros de clase fue sin duda determinante. Sin embargo, hay una persona, un profesor, que destaca sobre todos. Sanz, tú me enseñaste a amar la Física con mayúsculas. Tu pasión por esta ciencia y tu impresionante capacidad para transmitirla fueron, sin duda alguna, los que me empujaron a escoger este camino. Tu opinión siempre ha sido clave en mis decisiones, y las conversaciones de bar hablando de Física y Astrofísica son siempre inspiradoras y enriquecedoras. Si hoy estoy presentando esta tesis es, en buena medida, por ti. Gracias Sanz.

Mi paso por el instituto dejo también dos amigas de las que no me puedo olvidar, Paula y Sandra. Gracias a ambas por vuestra amistad y por mantener un difícil contacto en la distancia. Gracias

por la felicidad contagiosa que transmitís, porque un café con vosotras alarga la vida. Gracias por ser geniales. Por otro lado, mi paso por la Complutense y, en particular, por el colegio mayor Guadalupe, me dejaron un gran amigo. Pablo, gracias por esas conversaciones eternas en la habitación del colegio, por las locas elucubraciones en la pizarra vileda de mi habitación, por todas las historias y anécdotas que hemos vivido juntos y porque has sido y eres el mejor amigo que se puede tener. Mi paso por el Guadalupe no hubiera sido igual si no hubieses estado tú. Por todo ello, gracias *tío*. Allí conocí también a Esther, una gran persona y una gran amiga a la que le debo muchas risas y la preciosa portada de esta tesis.

Realizar la especialidad de Astrofísica en La Laguna me permitió conocer a un grupo de personas increíble. Todos llegamos ese año a una isla en la que no conocíamos a nadie. Y sin embargo, enseguida hicimos piña y vivimos unos años inolvidables. Esas tardes en el "7 islas", esas noches en el "o'Clock", esas largas horas en el CCA haciendo las prácticas de TAI, y esas historias que, seguro, serán difíciles de olvidar. Por ello, gracias Parda, Carol, Jorge, Bea, Alba, Eneko, Rubén, Zaira, Lore, Itzi, Andrea, Irene, Pablo y David. Especial mención merece Rubén, por la confianza que tuvimos desde el primer momento y porque nunca debimos perderla.

Por último, gracias a los que torpedean e intentan reducir al mínimo la ciencia (mal llamada básica) en este país. A los que ningunean nuestro trabajo porque, dicen, no reporta ningún rédito económico. A vosotros, gracias por hacer que cada día disfrute haciendo mi trabajo con más y más entusiasmo para demostrar lo que es obvio, que la ciencia es imprescindible en nuestra vida. Espero que en este particular agradecimiento se entienda la ironía, "no vaya a ser" que me hagan ministro de Investigación y Ciencia por estas palabras de apoyo.

Espero no haber agotado la mente del lector que haya decidido zambullirse entre tanto "gracias". Si al acabar de leer no te has encontrado en ninguno de los agradecimientos ni siquiera de forma implícita, lo siento. Seguro que tengo muchas razones para darte las gracias. Así que gracias a ti también por perdonar mi olvido en esta lista.

Jorge Lillo Box

En Madrid, a 6 de Mayo de 2015.

Resumen de la tesis en castellano

Hace apenas veinte años, Michel Mayor y su estudiante de doctorado Didier Queloz abrieron definitivamente la era de la exploración exoplanetaria. Durante el congreso *Cool Stars, Stellar Systems and the Sun 9* en Florencia (Italia) en 1995, se anunció el descubrimiento de 51 Peg b, un planeta similar a Júpiter y el primero conocido en orbitar alrededor de una estrella de la secuencia principal. Este hallazgo fue posteriormente apoyado una semana más tarde por Geoff Marcy y David Butler con el análisis de observaciones independientes. Pocos años antes del descubrimiento de 51 Peg b, ya se habían detectado otros objetos de masa planetaria. Sin embargo, dichos objetos bien orbitaban alrededor de sistemas peculiares como γ Cephei A b (un planeta en un sistema binario) y PSR B1257+12 b (un sistema planetario alrededor de un púlsar) o bien fueron confirmados con posterioridad, como es el caso de HD 114762 b.

Antes de estos hallazgos, nuestro conocimiento sobre la formación, evolución y propiedades de los planetas se limitaba al del Sistema Solar. Sin embargo, la segregación básica entre planetas rocosos en órbitas cercanas a su estrella y los gaseosos más alejados de la misma quedó obsoleta tras el anuncio de los primeros exoplanetas. Los subsecuentes descubrimientos anticiparon la gran diversidad de mundos fuera del Sistema Solar. Durante los primeros cinco años de exploración exoplanetaria se encontraron planetas en sistemas binarios, planetas gigantes muy próximos a su estrella, sistemas multi-planetarios, o planetas muy masivos en órbitas muy alejadas de su estrella. Además de proporcionarnos indicios sobre la formación del Sistema Solar, estos descubrimientos han planteado muchas otras cuestiones y han desafiado nuestro conocimiento (hasta entonces teórico) sobre el desarrollo de los sistemas planetarios. Las implicaciones que esta diversidad tiene sobre la formación y evolución de estos sistemas están comenzando a ser comprendidas, pero todavía quedan muchas preguntas por responder. Paso a paso, estamos proporcionando pruebas observacionales para responderlas.

En particular, la misión espacial *Kepler* ha detectado una extraordinaria cantidad de candidatos planetarios de muy variadas propiedades que han podido ser caracterizados gracias a la técnica empleada, el método de los tránsitos, consistente en la detección de un descenso en la luminosidad de la estrella debida al paso de un planeta por delante de la misma. *Kepler* ha dedicado sus cuatro años de actividad a observar una misma región del cielo, monitorizando más de 150,000 estrellas con una cadencia temporal de unos 30 minutos para la mayoría de ellas. La impresionante precisión fotométrica alcanzada ha permitido la detección de miles de candidatos planetarios con una gran variedad de propiedades, incluyendo planetas más pequeños que la Tierra y con tamaños similares a Mercurio (como el caso de Kepler-37 b) o planetas rocosos en la zona habitable de sus estrellas (como el caso de Kepler-186 b). Sin embargo, debido a las características técnicas de la misión (necesarias para alcanzar la mencionada precisión fotométrica), la detección de un eclipse no nos permite confirmar la naturaleza planetaria del objeto transitante. Esto es debido a que existen diversas configuraciones estelares que pueden mimetizar un

tránsito planetario. Un buen ejemplo es el caso de estrellas binarias de fondo, ocultadas por la luz de una estrella más cercana que podría diluir la profundidad del eclipse, asemejándolo al de un tránsito planetario. Por ello, es clara la necesidad de un seguimiento posterior de los candidatos detectados por *Kepler* con el objetivo, no solo de confirmar su naturaleza planetaria, sino también de caracterizar las propiedades del sistema. Esta completa caracterización es crucial para analizar el origen y la historia evolutiva de estos mundos extrasolares. Una de las técnicas de confirmación más importantes por su efectividad es la llamada velocidad radial, consistente en la detección, mediante el efecto Doppler, de variaciones en la componente radial de la velocidad de la estrella alrededor del centro de masas del sistema, inducidas por la presencia del planeta.

En esta tesis, presentamos nuestra contribución al campo de la caracterización de sistemas planetarios, contribuyendo a la tarea de arrojar más luz sobre la evolución exoplanetaria. En esta memoria, describimos el seguimiento exahustivo que hemos realizado de los candidatos planetarios de la misión *Kepler* empleando instrumentación del Observatorio de Calar Alto (Almería, España). A continuación resumimos los objetivos, el desarrollo y las conclusiones derivadas de dicho seguimiento.

Objetivos y planteamiento de la tesis

El objetivo principal de este trabajo es el de aprovechar la precisión fotométrica sin precedentes proporcionada por la misión espacial *Kepler* para caracterizar nuevos sistemas extrasolares en nichos aún inexplorados. Así, en este proyecto hemos combinado el uso de los datos de dicha misión espacial con nuevas observaciones realizadas en tierra desde el Observatorio de Calar Alto, con el objetivo de confirmar los candidatos planetarios de la misión y analizar sus propiedades.

Parte de nuestro trabajo se ha centrado en una muestra de planetas con características particulares como son los planetas gigantes gaseosos alrededor de estrellas evolucionadas en la fase de gigante roja. La no detección de dichos planetas hasta la fecha parecía indicar que la evolución de la estrella en los primeros instantes tras la salida de la secuencia principal conllevaba la destrucción de los planetas en órbitas de corto periodo, engulléndolos o destruyéndolos por efectos de marea al expandirse sus capas externas. El descubrimiento de planetas que desafíen dichas teorías puede proporcionar valiosa información sobre estos procesos.

Por otro lado, los planetas más pequeños, tipo terrestre, detectados por *Kepler* no pueden ser confirmados con observaciones desde tierra por razones tecnológicas (la instrumentación actual no permite la verificación de dichos objetos mediante la caracterización de su masa). Es por ello necesaria una validación estadística, que nos permita descartar cualquier otra configuración que pudiera mimetizar un tránsito planetario de estas características. Además, la confirmación

definitiva de cualquier candidato requiere un seguimiento desde tierra con la técnica de la velocidad radial, la cual requiere un uso extensivo de tiempo de observación. Es por tanto evidente la necesidad de establecer prioridades entre la amplia diversidad de candidatos encontrados. Ambas necesidades (la imposibilidad de detectar planetas rocosos y la necesidad de establecer prioridades entre los miles de candidatos proporcionados por la misión) hacen imprescindible la observación de las estrellas candidatas a albergar planetas con imagen de alta resolución. Dichas observaciones nos permitirán descartar importantes configuraciones estelares (o falsos positivos) que podrían mimetizar un tránsito planetario, proporcionando importantes restricciones en la validación de estos sistemas. Por otro lado, la no detección de estrellas compañeras cercanas con dichas imágenes permite priorizar unos candidatos sobre otros a la hora de realizar un seguimiento más exahustivo con la técnica (más costosa en cuanto a tiempo de observación requerido) de la velocidad radial.

Metodología y desarrollo

Ante los objetivos planteados anteriormente, este proyecto se dividió en dos fases:

Fase I: Imagen de alta resolución espacial.- En esta primera fase, obtuvimos imágenes de alta resolución espacial para una amplia muestra de candidatos planetarios de la misión *Kepler*. En particular, 233 estrellas con 392 posibles planetas orbitando a su alrededor fueron observadas con el instrumento AstraLux del observatorio de Calar Alto. Dicho instrumento nos permite alcanzar resoluciones de hasta $0.1''$ y detectar estrellas alrededor de 6 magnitudes más débiles a $1''$. El objetivo principal es detectar compañeras cercanas y establecer qué candidatos están aislados (es decir, sin estrellas cercanas que puedan contaminar la curva de luz) para poder realizar un posterior análisis con otras técnicas en la siguiente fase.

Fase II: Monitorización de la velocidad radial y análisis de la curva de luz.- En esta segunda fase, una selección de los candidatos aislados en la Fase I fueron observados con el espectrógrafo de alta resolución de Calar Alto, CAFE. La obtención de espectros de alta resolución en diferentes fases del planeta a lo largo de su órbita nos permiten monitorizar las variaciones del movimiento de la estrella en la dirección radial, lo cual nos proporciona importantes parámetros del planeta como su masa. Además, estas observaciones nos permiten caracterizar su órbita, determinando su eccentricidad, orientación espcial y distancia a la estrella central. Por otro lado, el análisis exhaustivo de las curvas de luz de algunos planetas en órbitas muy cercanas a su estrella nos permite la detección de diversos efectos que pueden producir una modulación de la curva de luz en las regiones fuera de tránsito. La caracterización de dichas variaciones permite la confirmación de la naturaleza planetaria del objeto transitante a partir de la medición de su masa y sus parámetros orbitales sin la necesidad de un seguimiento con velocidad radial. Sin embargo, esto es solo aplicable en ciertos casos.

El uso intensivo de diferentes instrumentos y tipos de datos en ambas fases ha implicado el uso de diferentes técnicas de análisis y observación. Para comprender y describir correctamente dichas técnicas así como para ponerlas en contexto de los instrumentos empleados (*Kepler*, AstraLux y CAFE) y analizar los resultados obtenidos en cada una de las fases, esta tesis se ha dividido en dos partes:

En la primera parte, describimos la formulación de los principales efectos analizados en los diferentes sistemas, haciendo hincapié en las particularidades de los instrumentos empleados. En particular, el Capítulo 2 describe los datos de la misión *Kepler* y las diferentes técnicas de análisis aplicadas a la fotometría de alta precisión obtenida por dicho telescopio. En el Capítulo 3 describimos la técnica de imagen de alta resolución espacial, poniendo el foco en el instrumento AstraLux y en la formulación de un nuevo parámetro que hemos desarrollado con el fin de establecer una comparación directa de la calidad este tipo de imágenes aún habiendo sido obtenidas mediante diferentes técnicas. En el Capítulo 4 detallamos el método de la velocidad radial y describimos a fondo las particularidades del nuevo instrumento CAFE a partir de nuestra larga experiencia observacional con el mismo y la gran cantidad de datos obtenidos. Dicha experiencia nos ha permitido proponer mejoras técnicas que han proporcionado una sustancial mejora de la calidad de las observaciones y de la reducción de los datos, estando disponibles para toda la comunidad de usuarios.

En la segunda parte de la tesis, nos hemos centrado en los resultados científicos obtenidos mediante la explotación de los datos adquiridos con la intrumentación mencionada. En particular, en el Capítulo 5 se exponen los resultados de la anteriormente descrita Fase I del proyecto, relativa a la observación de un alto número de candidatos mediante imagen de alta resolución espacial. En el Capítulo 6 se describe el análisis y los resultados de la monitorización con la técnica de velocidad radial de una submuestra de los candidatos observados en la primera fase (Fase II), con el objetivo de confirmar su naturaleza planetaria y carcaterizar sus propiedades. Finalmente, en el Capítulo 7 los planetas confirmados y caracterizados en esta tesis son puestos en contexto con la muestra de planetas conocidos, exponiendo los diferentes nichos explorados y la información que estos planetas aportan en nuestra comprensión del proceso de formación y evolución planetaria.

Resultados

El desarrollo del proyecto anteriormente descrito ha proporcionado los siguientes resultados científicos:

Fase I:

- Publicación de un amplio catálogo (en términos de número de objetos observados y profundidad de las observaciones) de imagen de alta resolución en la muestra de candidatos

de *Kepler*. Entre los 233 candidatos observados, encontramos 78 de ellos (33,5,%) con binarias visuales más cerca de $6''$, mientras que 155 (66,5,%) se encontraban aisladas dentro de nuestros límites de detección. Entre la muestra de objetos con compañeras, detectamos al menos un compañero más cerca de $3''$ en 42 casos (18,0,%), mientras que al menos un compañero en el rango de $3 - 6''$ se encontró en 46 casos (19,7 %).

- Para caracterizar las observaciones en alta resolución definimos un nuevo parámetro que mide la probabilidad de que un objeto esté realmente aislado dadas las observaciones realizadas (BSC, por sus siglas en inglés). Dicho parámetro es empleado para asegurar que las estrellas aisladas lo estén realmente. Además, este parámetro nos permite comparar nuestro catálogo con otros realizados en muestras análogas extraídas de la lista de *Kepler*. Los resultados indican que nuestras imágenes reducen la probabilidad de que el tránsito esté producido por una binaria eclipsante de fondo en más de un 50% para el 62% de la muestra, mejorando los resultados de otros catálogos realizados con técnicas similares.

- Nuestro análisis sugiere que en 10 de los casos con compañeras cercanas, dichas compañeras podrían estar físicamente asociadas a la estrella central en la que se detectó el tránsito, siendo pues posibles sistemas binarios con planetas orbitando alrededor de una de las componentes. En particular, sugerimos la posible asociación de la compañera de Kepler-444 (KOI-3851), que alberga un sistema de cuatro planetas de tamaño terrestre validados por otros trabajos. Dicha compañera estaría situada a unas 65 unidades astronómicas, mucho más cerca de lo esperado por la teoría para este tipo de sistemas.

- Los parámetros de los planetas detectados por *Kepler* alrededor de estrellas con compañeras cercanas detectadas con AstraLux han de ser corregidos teniendo en cuenta la luz proveniente de la compañera. En este trabajo proporcionamos la dilución producida por la compañera en la curva de luz, un parámetro clave para realizar dicha corrección. En particular, proporcionamos la corrección al radio del planeta.

Fase II:

- Hemos confirmado y caracterizado el exoplaneta Kepler-91 b por dos técnicas completamente independientes: velocidad radial y modulaciones de la curva de luz. Ambas técnicas, unidas a la detección del tránsito primario, nos han permitido conocer las propiedades de este planeta y establecer que se encuentra orbitando alrededor de una estrella gigante, en un estado evolutivo avanzado. El planeta se encuentra en una órbita muy cercana a la estrella, a tan solo 2.4 radios estelares. Nuestro análisis indica que el límite superior a la vida de este planeta es de unos 55 millones de años, habiendo vivido ya el 99% de su vida. Además, es el primer planeta confirmado que transita una estrella de este tipo, lo cual nos ha permitido conocer su densidad, de un tercio de la de Júpiter, lo cual indica que se encuentra inflado, probablemente debido a su cercanía a su estrella.

- Hemos confirmado la naturaleza planetaria de Kepler-432 b, otro planeta gaseoso alrededor de una estrella en la fase de gigante roja. Gracias a los datos de velocidad radial obtenidos hemos podido caracterizar su órbita excéntrica y determinar su masa, de unas 5 veces la masa de Júpiter. Tras Kepler-91 b, este es el segundo planeta confirmado que transita a una gigante roja.

- La confirmación de Kepler-447 b también se pudo realizar gracias a la intensa monitorización de la velocidad radial de su estrella anfitriona. Además, este planeta tiene el tránsito más rasante conocido hasta la fecha, con un parámetro de impacto superior a 1.

- Nuestros resultados preliminares también indican la posible confirmación de otros planetas en la muestra como son KOI-372.01 (con un posible tercer planeta detectado por variaciones en los tiempos de tránsito), KOI-375.01 (un planeta gigante con un largo periodo que podría encontrarse en la zona habitable de su estrella), KOI-1032.10 (un posible planeta masivo), KOI-5684 (un posible sistema de dos planeta en resonancia 3:1), KOI-2481 (un posible sistema planetario muy compacto con una estrella compañera cercana), KOI-684.01 (un posible planeta tipo Neptuno) y KOI-3919 (un posible "falso" falso positivo), algunos con periodos orbitales muy largos.

- Además, hemos podido descartar la naturaleza planetaria de seis candidatos y establecido límites superiores a la masa de otros siete candidatos que no pudieron ser analizados con velocidad radial debido a la alta velocidad de rotación de sus estrellas.

- Finalmente, un análisis detallado de la curva de luz de una muestra de candidatos nos ha permitido detectar modulaciones en el intervalo fuera de tránsito de la curva de luz. Los resultados preliminares de dicho análisis sugieren que los objetos transitantes en cinco casos corresponden a objetos subestelares (enanas marrones) mientras que en un sexto caso determinamos una masa compatible con un planeta. Todos ellos se encuentran a una distancia de sus estrellas anfitrionas inferior a 12 veces el radio estelar, suponiendo una gran fuente de información para la calibración de modelos de interiores estelares y formación de enanas marrones.

Además de estos resultados científicos, se han desarrollado diferentes utilidades y estudios técnicos que se describen a continuación:

- Desarrollo del parámetro BSC (por sus siglas en inglés), que proporciona la seguridad de que un objeto esté realmente aislado dada una imagen de alta resolución espacial en la que no se detecta ninguna estrella cercana. Además de proporcionar una medida de la calidad y profundida de la imagen obtenida, permite una comparación directa con otras técnicas de imagen de alta resolución.

- Creación de una herramienta de ajuste (*GAbox*) basada en los algoritmos genéticos. Esta herramienta permite el ajuste de modelos con un elevado número de parámetros libres en escalas de tiempo relativamente cortas en comparación con otros métodos y que evita de forma eficiente los mínimos locales. *GAbox* ya ha sido usado con diferentes objetivos como el ajuste de distribuciones espectrales de energía, o el modelado de curvas de luz y de velocidad radial.

- Caracterización en profundidad del instrumento CAFE y desarrollo de herramientas de análisis en tiempo real de las observaciones, así como mejora de diversos aspectos del software de reducción proporcionado por el observatorio. En particular, hemos seleccionado una muestra mayor de líneas de Thorio-Argon para la calibración en longitud de onda, sugerimos la necesidad de la instalación de un obturador y un control pasivo de la cámara en la que se encuentra el instrumento (que fueron posteriormente instalados) y hemos proporcionado un seguimiento de la calidad de las observaciones mediante el estudio de nuestros propios datos a lo largo de varios años de operación desde su puesta en marcha. Todos estos estudios han resultado en una mejora de la calidad de las observaciones y de la precisión del instrumento.

Conclusiones

A lo largo de esta tesis hemos descrito detalladamente las técnicas de observación y análisis empleadas, incluyendo fotometría de alta precisión, imagen de alta resolución espacial y espectroscopía de alta resolución espectral. La combinación de estas técnicas nos ha permitido realizar un seguimiento exhaustivo de los planetas candidatos de la misión espacial *Kepler* mediante observaciones desde tierra en el observatorio de Calar Alto.

Los resultados de este trabajo nos han permitido explorar nichos planetarios en los que no se habían detectados planetas hasta la fecha. Por ejemplo, la confirmación de planetas en órbitas muy cercanas a estrellas en la fase de gigante roja, como es el caso de Kepler-91 b y Kepler-432 b. Estos hallazgos demuestran la existencia de planetas alrededor de estrellas de masa intermedia. Dadas las cortas escalas de tiempo en las que el disco protoplanetario es disipado en la formación de estos objetos, nuestros resultados podrían sugerir que el principal mecanismo de migración de planetas gigantes para alcanzar órbitas de corto periodo parece no ser debido a interacciones con el disco (planetas tan masivos aún no habrían tenido tiempo de formarse). Por el contrario, la interacción gravitatoria entre el planeta y la estrella podría ser la causante de la migración de estos gigantes gaseosos en estrellas de masa intermedia (en sistemas con más de un planeta, la interacción planeta-planeta también podría jugar un papel importante). Una menor eficiencia de este mecanismo o la posterior destrucción o ingestión del planeta por parte de la estrella anfitriona podría explicar la escasez de estos planetas en órbitas cercanas alrededor de estrellas evolucionadas.

Además, Kepler-91 b y Kepler-432 b son los primeros planetas confirmados en transitar una estrella gigante roja. Ambos casos nos pueden ayudar a entender la evolución física de los gigantes gaseosos cuando sus estrellas anfitrionas evolucionan fuera de la secuencia principal. Con estos hallazgos podemos empezar a pensar en cómo dicha evolución de las estrella anfitriona afecta a las propiedades físicas de los planetas que la orbitan. Sin embargo, aún se necesitan más detecciones para poder empezar a responder a esta pregunta desde un punto de vista observacional.

Por otro lado, hemos confirmado la existencia de planetas gigantes (además de enanas marrones en resultados preliminares) en órbitas muy cercanas a sus estrellas anfitrionas. La presencia de estos objetos masivos tan cercanos no puede ser explicada por ninguna de las dos teorías de formación planetaria (acrecimiento del núcleo o inestabilidad gravitatoria). Esto indica la necesidad de procesos de migración planetaria en los primeros estadios de la vida de los planetas. Los casos estudiados en este trabajo aumentan la muestra de estos tipos de objetos, permitiendo arrojar más luz sobre estos procesos.

Finalmente, algunos de los planetas gigantes estudiados se encuentran en la zona de habitabilidad de sus estrellas anfitrionas (KOI-246.10, KOI-375.01 y KOI-372.02). Aunque estos objetos no pueden ser habitables debido a su naturaleza gaseosa, sin embargo, pueden albergar objetos menores (rocosos) como lunas o troyanos que serían habitables dada su distancia a la estrella primaria. La existencia de lunas de tipo rocoso en el Sistema Solar o de troyanos en la órbita de Júpiter indican que este tipo de objetos son un subproducto de la formación planetaria. Su existencia en sistemas exoplanetarios, aunque aún por demostrar, es por tanto posible. Por ello, la detección de gigantes gaseosos en la zona de habitabilidad de sus estrellas como los que mostramos en este trabajo (además de verdaderos planetas rocosos) es importante en nuestra búsqueda de planetas habitables.

Para terminar, este trabajo muestra las importantes sinergias entre observatorios espaciales y terrestres, subrayando la necesidad de telescopios de la clase 2-4m (además de telescopios mayores) para complementar las misiones espaciales y, en particular en este campo, para completar la caracterización de sistemas planetarios. En nuestro caso, el desarrollo y mantenimiento de instrumentación en el Observatorio de Calar Alto, conjuntamente con la valiosa experiencia de su personal, ha supuesto un importante empuje a este proyecto, permitiendo su desarrollo y correcta ejecución en un tiempo aceptable. El uso intensivo de la instrumentación del observatorio a lo largo de este tiempo nos ha permitido sugerir mejoras técnicas (como la introducción de un obturador en CAFE o una mejorada selección de las líneas de Thorio-Argon para la calibración en longitud de onda) que han sido posteriormente implementadas con resultados excelentes, beneficiando a toda la comunidad de usuarios.

Universidad Autónoma de Madrid

Doctoral Thesis

Planetary systems across different niches

Synergies between *Kepler* and Calar Alto observatories

A thesis submitted by

Jorge Lillo Box

in fulfillment of the requirements for the degree of
Doctor in Astrophysics

with the supervision of
Dr. David Barrado Navascués

Madrid, May 2015

Abstract

Since the discovery of the first extrasolar planets around two decades ago, more than a thousand of these worlds have been confirmed and characterized. The wide and unexpected diversity of properties shown by these planetary systems suggest the complexity of the planet formation and evolution processes. Apart from providing indications on the formation of the Solar System, these discoveries have opened many others. Step-by-step, we are providing observational hints to answer them. In particular, the *Kepler* mission has provided an impressive sample of planet candidates of any kind that can be fully characterized thanks to the technique used and the subsequent ground-based follow-up. This full characterization is important in order to analyze their origin and evolution history.

In this thesis, we present our contribution to complete the picture of the evolution of planetary systems. We have performed a comprehensive follow-up of the *Kepler* candidates by making use of ground-based instrumentation at Calar Alto Observatory. Due to the characteristics of the *Kepler* mission, the detected transits (due to the pass of an object in front of a star) could be due to other blended configurations mimicking a planetary-like transit. Our work has been centered on ruling out these configurations, confirming the planetary-nature of the transiting objects, and analyzing their properties. To that end, we have carried out a two-phases project making use of different datasets and techniques. The two phases consisted on i) obtaining high-spatial resolution images of a large sample of *Kepler* candidates owing to unveil possible companions and ii) obtaining high-resolution spectroscopy of a smaller carefully selected sub-sample to monitor the radial velocity of the host star and characterize the physical and orbital properties of the planet. In addition, we have analyzed the *Kepler* light curve looking for modulations induced by the presence of a planetary-mass or substellar object.

The results of this follow-up have yielded to the confirmation of five planets in four host stars. Among them, we have found the closest-in planet orbiting a giant star (Kepler-91 b), being the first confirmed planet known to transit one of these evolved stars. Additionally, we confirmed other close-in giant planet around another giant star (Kepler-432 b), the planet having the most grazing transit known to date (Kepler-447 b), and a two-planet system revolving around a young solar-analog (KOI-372). Besides, our high-resolution images of more than 170 planet host candidates have improved the candidacy of tens of planets and have reported close blended companions in around 18% of the sample. In this dissertation we present the observations and analysis that lead to these results and discuss their relevance in the exoplanetary field.

Contents

List of Figures

List of Tables

Acronyms & Abbreviations

ADU	**A**nalog **D**igital **U**nits
AO	**A**daptive **O**ptics
BERV	**B**arycentric **E**arth **R**adial **V**elocity
BIC	**B**ayesian **I**nference **C**riterion
BIS	**BIS**ector
BSC	**B**ackground **S**ource **C**confidence
CAB	**C**entro de **A**stro**B**iología
CAFE	**C**alar **A**lto **F**iber-fed **É**chelle spectrograph
CAHA	**C**entro **A**astronómico **H**ispano-**A**lemán
CCD	**C**harge **C**ouple **D**evice
CCF	**C**ross **C**orrelation **F**unction
CC	**C**lose de **C**ompanions
CFOP	**C**ommunity **F**ollow-up **O**bserving **P**rogram
DL	**C**ore **A**ccretion
DL	**D**iffraction **L**imited
EPF	**E**levation **P**rofile of **F**itness
FWHM	**F**ull-**W**idth **H**alf-**M**aximum
GA	**G**enetic **A**lgorithm
GI	**G**avitational **I**nstability
HZ	**H**abitable **Z**one
IDL	**I**nteractive **D**ata **L**anguage
KIC	***Kepler* I**nput **C**atalog
KOI	***Kepler* O**bject of **I**nterest
LC	**L**ight **C**urve
MCMC	**M**onte **C**arlos **M**arkov **C**hain
MPG	**M**ax-**P**lanck **G**esellschaft
MPIA	**M**ax-**P**lanck **I**nstitut für **A**stronomie
OHP	**O**bservatoire de **H**aute-**P**rovence
PG	**P**hysical **G**ain
PSF	**P**oint **S**pread **F**uction
REB	**R**eflection **E**llipsoidal **B**eaming
RGB	**R**ed **G**iant **B**ranch
RV	**R**adial **V**elocity
SDSS	**S**loan **D**igital **S**ky **S**urvey
SED	**S**pectral **E**nergy **D**istribution
SG	**S**oftware **G**ain
SL	**S**eeing **L**imited
SR	**S**trehl **R**atio
TNG	**T**elecopio **N**ationale di **G**alileo
VLT	**V**ery **L**arge **T**elescope

Symbols

Main symbols used in this dissertation:

Symbol	Description	Units
P	Orbital period	W (Js^{-1})
i	Inclination of the orbital plane	radians
a	Semi-major axis of the orbit	m
e	Eccentricity of the orbit	m
r	Star-planet distance	m
E	Eccentric anomaly	radians
T_0	Time of mid-transit	days
M	Mean anomaly	radians
$M_p,\ R_p,\ \rho_p$	Planetary mass, radius, and density	I.S.
$M_\star,\ R_\star,\ \rho_\star$	Stellar mass, radius, and density	I.S.
$\log g$	Surface gravity	dex (c.g.s.)
$T_{\rm eq}$	Equilibrium temperature	K
$T_{\rm eff}$	Effective temperature	K
[Fe/H]	Iron abundance (aka metallicity)	dex
$v \sin i$	Projected rotational velocity	km/s
K	Radial velocity semi-amplitude	km/s
$V_{\rm sys}$	Systemic radial velocity	km/s
Ω	Longitude of the ascending node	rad.
ω	Argument of the periastron	rad.
ν	True anomaly of the planet	rad.
ν_c	True anomaly of the planet at conjunction	rad.
θ	Orbital phase of the planet	rad.
ϕ	Temporal phase of the planet measured from conjunction	
$\phi_{\rm peri}$	Temporal phase of the planet measured from periastron	

Physical Constants

Speed of Light	c	=	$2.997\ 924\ 58 \times 10^8$ m/s
Gravitational constant	G	=	$6.6742799 \times 10^{-11}\ m^3\ kg^{-1}\ s^{-2}$
Solar radius	$R_\odot$	=	6.9634202×10^8 m
Solar mass	$M_\odot$	=	1.9891001×10^{30} kg
Solar mean density	$\rho_\odot$	=	1408 kg/m^3
Jupiter radius	R_{Jup}	=	7.14920×10^7 m
Jupiter mass	M_{Jup}	=	1.8990001×10^{27} kg
Jupiter mean density	ρ_{Jup}	=	1240.692 kg/m^3
Earth radius	$R_\oplus$	=	6.37840×10^6 m
Earth mass	$M_\oplus$	=	5.9735999×10^{24} kg
Earth mean density	$\rho_\oplus$	=	5495.564 kg/m^3

Chapter 1

Introduction

Contents

"There are more things in heaven and earth, Horatio, Than are dreamt of in your philosophy."

HAMLET (1.5.167-8), Hamlet to Horatio

William Shakespeare

1.1 The age of exoplanet exploration

1.1.1 Just twenty years ago...

Just twenty years ago Michel Mayor and his PhD student at that moment, Didier Queloz, definitively opened the era of exoplanet exploration. During the *Cool Stars, Stellar Systems and the Sun 9* meeting in Florence (Italy) in 1995 they announced the discovery of 51 Peg b, a close-in Jupiter-like planet, the first known to orbit around a main-sequence star (Mayor & Queloz, 1995). This discovery was subsequently supported one week later by Geoff Marcy and David Butler, who published independent radial velocity data (Marcy & Butler, 1995). Prior to 51 Peg b, other planetary-mass objects had been found orbiting peculiar systems like γ Cephei A b (a planet in a binary system Campbell et al., 1988), HD 114762 b (firstly identified as a brown dwarf by Latham et al., 1989, and later confirmed as a planet), and PSR B1257+12 b (a terrestrial planetary system around a millisecond pulsar, Wolszczan & Frail, 1992).

Prior to these discoveries, our knowledge about planet properties was restricted to the Solar System.[1] The basic distinction between rocky/inner and gaseous/outer planets, however, became obsolete after the first exoplanets were announced. Different discoveries anticipated the great diversity of worlds outside the Solar System. During the first five years of exoplanet exploration, we found planets in binary systems, close-in giant planets, multi-planet systems, or really massive planets in wide orbits. The implications of this diversity on planet formation and evolution theories is currently starting to be understood, but many questions still remain open.

In the search for an answer to the question about how life was formed, the different branches of science must provide the pieces to construct this jigsaw puzzle. The role of Astronomy is multiple in this game. We are in charge of numerous pieces that we have built over the last centuries, perfecting their shapes along many years. The recent discovery of exoplanets is probably the last piece built by Astronomy and we are in charge of giving it the correct shape.

In February 1990, prior to the confirmation of the first extrasolar planets, Carl Sagan suggested NASA to turn the camera of the Voyager 1 spacecraft around and observe the Earth beyond the orbit of Neptune. The image showed the Earth as a "pale blue dot" at just 40 AU (see Fig. 1.1), and highlighted the difficulties of finding other worlds around much more distant stars. In this regard, the detection techniques that were previously applied to other fields and the instruments that allow their applicability have been improved and adapted. Both ground- and space-based observatories are being our tools to shape the piece of extrasolar planets.

[1] Although the International Astronomical Union (IAU) has not yet provided a definition for extrasolar planet, in the 2006 IAU Meeting, the new definition of planet was approved and reads: "a *planet* is defined as a celestial body that (a) is in orbit around the Sun, (b) has sufficient mass for its self-gravity to overcome rigid body forces so that it assumes a hydrostatic equilibrium (nearly round) shape, and (c) has cleared the neighbourhood around its orbit." (www.iau.org/news/pressreleases/detail/iau0603/).

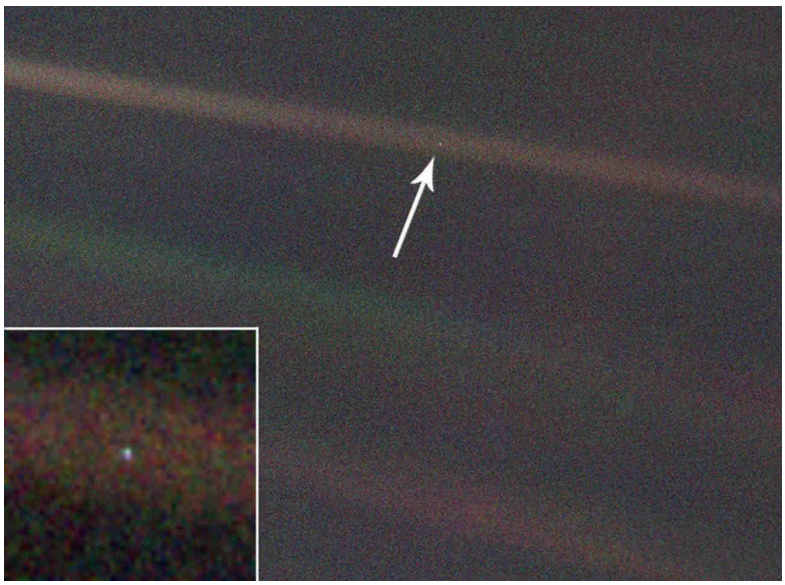

FIGURE 1.1: The pale blue dot. The Earth as seen by the Voyager 1 spacecraft from the edge of the Solar System, at 6200 million kilometers (41.3 AU). Credit: NASA.

1.1.2 Detection methods and parameter dependencies

Unlike stars, planets do not emit light (at least at a perceivable level[2]) to allow their direct detection. Thus, indirect techniques need to be used to uncover the imprints of planets revolving around their hosts. To date, different techniques have been applied, each of which make use of different effects, allowing the determination of the orbital and physical properties of the planet. These techniques had been previously applied to eclipsing and visual binaries, and their precision was subsequently improved to detect extrasolar planets. Here, we briefly summarize those techniques that succeeded in detecting at least one planet as of today[3] (in Fig. 1.2 we summarize the number of planets detected by each technique):

- **Radial velocity.-** The orbital motion of a planet around its host star provokes the star to wobble around the center of masses of the system with the same period (action-reaction Newton's law). If the orbital plane of the planet is not face-on respect to our line-of-sight, this wobble can be detected by measuring the variations of the radial component of the stellar motion (i.e., the radial velocity) at different positions of the planet in the orbit. Since this action-reaction law depends on the masses of both bodies, it allows us to determine the relation between the mass of the planet (M_p) and the mass of its host ($M_\star$). Actually, due to projection reasons, only a minimum mass for the planet can be derived ($M_p \sin i$). As a reference, the amplitude of the radial velocity variation induced by Jupiter

[2]It is known that giant planets have their own thermal emission but their proximity to their host star masquerades this brightness.

[3]For a complete review of all families of techniques used to detect extrasolar planets see the last update of the diagram by Perryman (2014).

to the Sun is of the order of 12 m/s while the Earth provokes a RV amplitude of few tens of cm/s. The first planets were detected by this technique and 597 have been currently confirmed (according to The Extrasolar Planets Encyclopaedia, exoplanet.eu).

- **Primary transit.-** Similar to the detection of stellar binary eclipses, in this method we detect the pass of the planet in front of the star as seen from Earth. Hence, by measuring the relative brightness of a star during a planetary eclipse (that we will call *transit*), we can infer the presence of this body. Since planets do not have (at least a relevant) intrinsic brightness, the depth of this transit directly provides the relative size between the transiting body and its host (i.e., $R_p/R_\star$). However, in order to transit, the orbital plane of the planet must be nearly edge on ($i \sim 90°$) with respect to our line-of-sight. This makes this method inefficient for small searches, although really powerful for massive photometric surveys like *Kepler* (Borucki et al., 2009) or CoRoT (Schneider et al., 1998). As an example, the transit of Jupiter on the Sun would induce a light drop of $\sim 1\%$, while the Earth transit would be of 0.0084%, or equivalently, 84 parts per million (hereafter ppm). This is thus the required precision to detect Earth-like planets orbiting Sun-like stars. The first planet detected by this method was HD 209458 b (Charbonneau et al., 2000). In total, 420 planets have been detected by this technique and subsequently confirmed by using other techniques to measure their masses. Additionally, another 715 planets detected by this method were statistically validated, although their masses still remain unknown (Lissauer et al., 2014, Rowe et al., 2014). Also, several thousands of planet candidates have been found by *Kepler*, but they are still awaiting for confirmation.

- **Direct imaging.-** Direct detection of extrasolar planets is difficult. First, planets do not have an intrinsic brightness (at least not at a detectable level) so that all the light they can emit mainly comes from the reflected light of their hosts. This light is dimmer as compared to that emitted by the host star, thus making almost impossible to distinguish the planet. Second, the short orbital separations and the large distances to those systems prevent us from spatially resolving them. Thus, trying to directly observe a planet is like pretending to detect a candle right beside a lighthouse from many kilometers of distance. However, different groups have already been able to confirm 53 planets with this technique by applying coronography and extreme high-contrast and high-resolution techniques.

- **Microlensing.-** By taking profit of general relativity, the gravitational microlensing technique detects the slightly different curvature of the light when a planetary system occults a background star. The need of chance-aligned events, and its short duration make this technique relatively inefficient. Moreover, due to their characteristics, the detected planets cannot usually be followed-up with other techniques, so further characterization is not possible. To date 34 planets have been discovered by this method.

- **Pulsar timing.-** Anomalies in the extremely periodic radio waves emitted by pulsars can be interpreted as the motion of the neutron star around its center of mass due to the presence of planets in the system. Although this method is capable of detecting sub-Earth mass planets, the nature of the host stars (and the few pulsars known) makes it not very popular in the quest for planetary systems similar to our own. To date, 16 planets have been confirmed by using this method.

- **Transit timing variations (TTV).-** This technique has been used to detect additional planets in known planetary systems in which at least one of the planets transits its star. In case of the presence of additional bodies in the system, small gravitational perturbations can induce the transit to happen earlier or later than expected, depending on the relative position of both planets at the time of transit. The TTVs can be very large in resonant planetary systems, thus becoming more easily detectable. To date, only a handful number of planets have been detected by this technique (e.g., Kepler-19c, Ballard et al., 2011). But the increasing number of high-accurate and high-cadence photometers can increase this number in the forthcoming years.

- **Astrometry.-** As in the case of the radial velocity, the orbital motion of a planet around a star provokes an orbital motion of the latter around the center of masses of the system. If the star is sufficiently close to us, we can directly measure the wobbling movement by precisely measuring its position on the plane of the sky. The difficulties of this method are mainly technological since precisions of sub-milli-arcsec are needed to detect the stellar orbital oscillation induced by a planetary-mass object. Some low-mass companions (e.g., Sahlmann et al., 2015a) and one planetary detection (HD 176051 Muterspaugh et al., 2010) have been detected by this method.

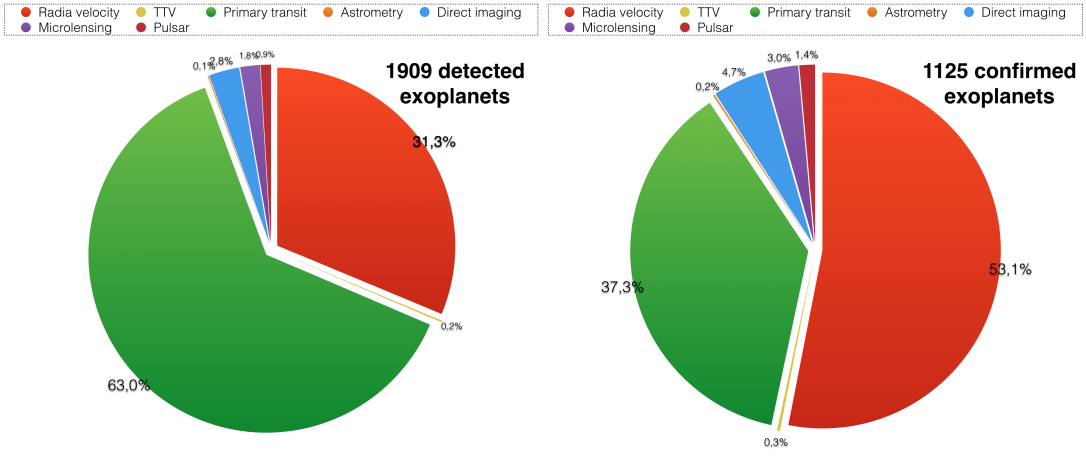

FIGURE 1.2: Number of established (left, including confirmed and validated) and confirmed (right, with derived masses) extrasolar planets by different techniques. Source: exoplanet.eu.

In total, more than 1900 planets have been confirmed or validated so far. Among them, we have characterized the masses of 1125 (the rest being statistically validated). In Fig. 1.3, we show the

number of detected planets per year, showing the increasing interest in this field in the last two decades.

Apart from these methods, there are other techniques that, despite not having yet detected any planet by themselves, are useful for confirming or characterizing the properties of known or candidate planetary systems, and their atmospheres. In this group we find the detection of secondary eclipses of hot-Jupiter planets, transmission spectroscopy, the detection of light curve modulations due to the reflection of the stellar light by the atmosphere of the planet, tidal variations in close-in planets, or the photometric imprint of the radial velocity induced by the planet on the star (the Doppler beaming).

Although none of these techniques can completely characterize the orbital and physical properties of a planetary system by itself, their combination is needed to complete the picture for every system. In particular, the application of the two most common and efficient techniques (the radial velocity and the detection of the primary transit) provides the mass and size of the planets, which in turn describes their bulk composition by providing its density. Figure 1.4 shows a scheme about the different orbital and physical parameters that can be derived by using the different techniques.

In Part I of this dissertation (Chapters 2, 3, and 4), we will describe in depth the techniques entensively used in this work, involving light curve analysis (transit, secondary eclipse, light curve modulations, and asteroseismology), high-spatial resolution imaging of the host stars, and radial velocity.

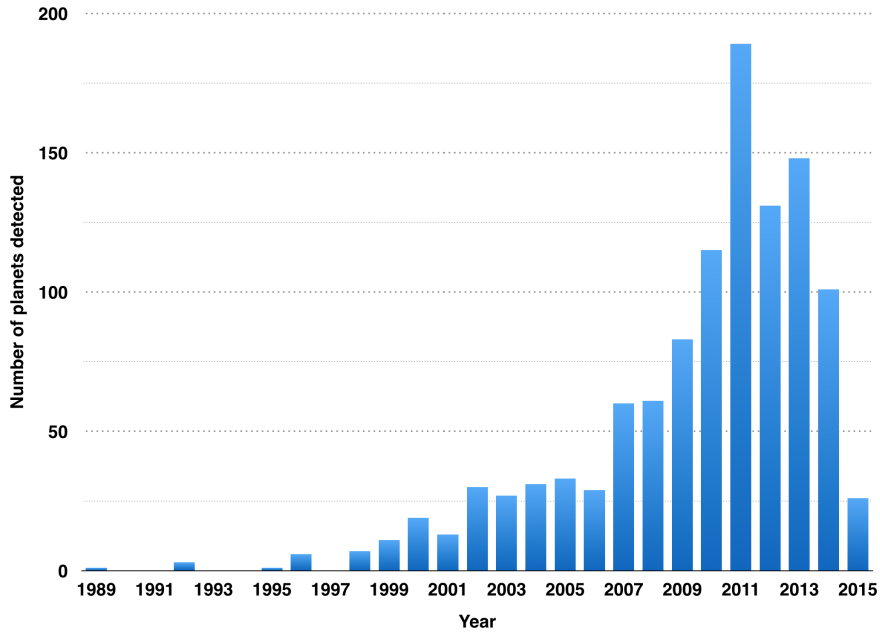

FIGURE 1.3: Number of planets with confirmed masses per year of detection as of April 2015. Source: exoplanet.eu.

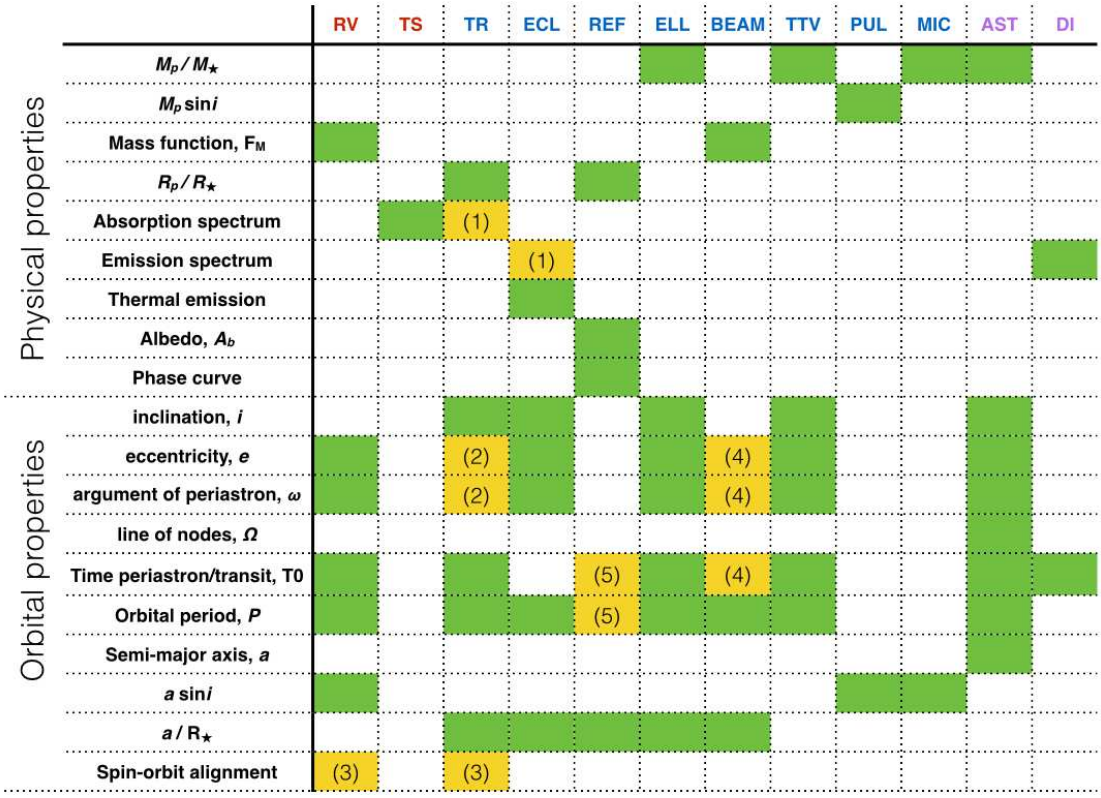

FIGURE 1.4: Orbital and physical parameters derivable with different techniques (green squares) based on spectra (red title), photometry (blue title), and imaging (purple title).
Abbreviations: RV (radial velocity), TS (transmission spectroscopy), TR (transit), ECL (secondary eclipse), REF (planet reflection), ELL (ellipsoidal variations), BEAM (Doppler beaming), TTV (transit timing variations), PUL (pulsar timing), MIC (microlensing), AST (astrometry), DI (direct imaging). Mass function is defined as: $F_M = M_p^3 \sin^3 i/(M_p + M_\star)^2$.
Notes on yellow squares: (1) Characterizing this property requires observations of this effect at different wavelength ranges; (2) High-cadence and high-accurate photometry is needed to determine the eccentricity and argument of the periastron from duration differences between the ingress and egress of the transit; (3) The determination of the angle between the stellar spin axis and the perpendicular to the plane of the orbit (spin-orbit angle) requires detecting the Rossiter-McLaughlin effect, which in turn requires observing the perturbation of the radial velocity curve during the planet transit; (4) Determining these parameters with the beaming effect requires photometric precision better than 1 ppm, which is unfeasible with current instrumentation, but theoretically possible; (5) High-cadence and high-accurate photometry is needed.

1.1.3 Instrumentation: breaking our frontiers

All the techniques previously described had already been applied to stellar binary systems before being used in exoplanet detection. However, the precision of previous instruments did not allowed the detection of these small, obscure, and low-mass objects. The greatest change that has allowed the impressive development of the exoplanetary exploration has been the instrumental advances. We have seen that tens of m/s of precision in RV is required to detect the most massive planets, and photometric contrast of few parts per thousand are demanded to detect the largest

planets (while rocky planets request few ppm). Also, sub-milliarcsec precision is necessary for detecting planets by astrometry and high-contrast ratios to directly image them.

These numbers illustrate the challenge that detecting planets represents for instrument builders. Achieving such precisions involves not only a really good knowledge of the physics taking place in the instrument but also an extremely accurate control of enviromental conditions, and the hardware and software involved. For instance, regarding radial velocity, we are achieving sub-m/s precisions with HARPS/MPG and HARPS-N/TNG as well as few m/s with some other instruments like SOPHIE/OHP, HIRES/Keck, FIES/NOT, or CAFE/CAHA. The forthcoming instruments ESPRESSO/VLT and CODEX/E-ELT will provide very-high-resolution spectra (R = 220 000 and R = 135 000, respectively) and will be located in large telescopes, what will allow us to reach cm/s precisions for fainter stars.

In the case of high-accurate photometry, the space-based *Kepler* mission has broken the frontiers of photometric precision by reaching few tens of ppm and detecting sub-Mercury size planets (Barclay et al., 2013, Campante et al., 2015). Also, the CoRoT mission played an important role prior to *Kepler*, achieving less than 100 ppm precision. From the ground, much worse precisions can be obtained due to atmospheric contamination in terms of stability and variable conditions. To date, just several hundreds of parts per million precision can be derived by applying defocusing techniques (see, for instance, Southworth et al., 2009). The new generation of forthcoming missions *TESS* (Ricker et al., 2014), *CHEOPS* (Broeg et al., 2013), and *PLATO* (Rauer et al., 2014) will provide similar precisions than *Kepler* and will focus on larger regions of the sky, also providing higher-cadence photometry. In addition, the *Gaia* mission (Perryman et al., 2001) will be able to detect planets via astrometry (see, e.g., Sahlmann et al., 2015b).

In the case of direct imaging, the adaptive optics systems of NACO/VLT, PHARO/Palomar, ARIES/MMT, or Robo-AO, together with speckle-imaging (e.g., DSSI/WYIN) and lucky-imaging (e.g., AstraLux North/CAHA and AstraLux South/La Silla) are able to detect relatively faint sources with spatial resolutions of few tenths of arcsec (as a reference, 0.1 arcsec at 10 pc correspond to 1 AU). The new high-contrast and high-resolution instruments like GPI/Gemini South or SPHERE/VLT provide diffraction limited resolution ($\sim$ 0.1 arcsec) and contrasts of $>$ 12 mag, able to directly image and characterize faint giant planets at closer orbital separations.

In summary the exponential increase in the number of detected planets in the last two decades has gone hand in hand with the development of state-of-the-art instrumentation, adapting and improving the techniques and allowing the detection of planet effects that were previously thought to be unaccessible.

1.2 The planet plethora

The techniques and instruments described in the previous section have allowed the detection of a large crop of planetary systems. Among the numerous diagrams compiling their properties, there are two that briefly describe and summarize the current population. These are the mass vs. radius and the semi-major axis (or period) vs. planet mass diagrams. We show both diagrams in Figs. 1.5 and 1.6. In the former, we can easily distinguish the physical properties of the discovered planets in terms of bulk composition. Gaseous giant planets stand out in this diagram in the upper right region, while the detection of rocky planets is currently populating the bottom left region of the diagram. Icy giants connect both regimes but this region is still poorly populated and the few well-characterized Neptune-like planets have a very wide range of densities, suggesting different compositions and thus formation histories. Gas giants also show a wide diversity of densities, from Jupiter-like to $\sim 0.3\ \rho_{\rm Jup}$. The lower density for the gas giants is associated to those with smaller orbital separations (the hot-Jupiters), suggesting that they could be inflated. Different mechanisms have been proposed to explain this inflation (e.g., tidal heating, Bodenheimer et al. 2001; or dissipation of the stellar irradiation in the planet's atmosphere, Guillot & Showman 2002) but none is able to exhaustively explain the wide diversity.

From Fig. 1.6, we can see that transit and radial velocity searches are not sensitive to the farther out planets (beyond Jupiter's orbital separation). Instead, other techniques like direct imaging, pulse timing or microlensing are sensitive to these regimes. As we will see in the next section, detecting those farther out planets is important to constrain the different proposed planet formation mechanisms. Also in this figure, we see a deficit of close-in planets between the Jupiter- and the Earth-mass domain (at $\sim 40\ M_{\oplus}$), which could be a consequence of the formation process rather than just an observational bias (Mordasini et al., 2012).

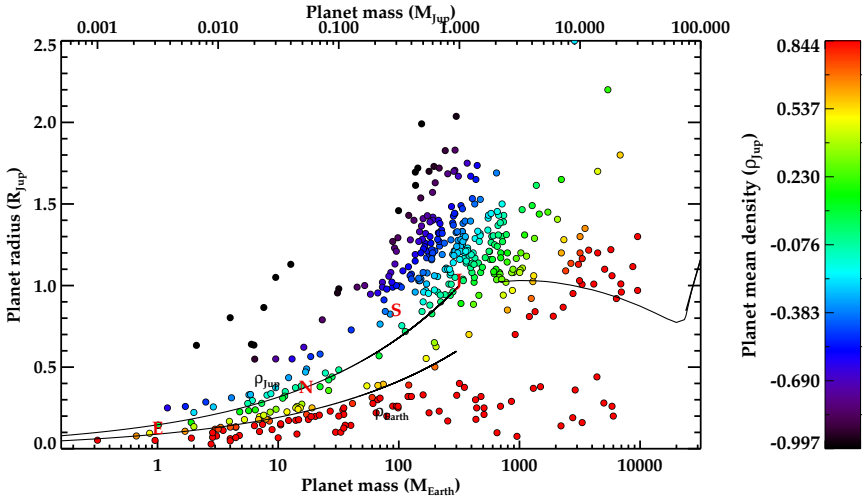

FIGURE 1.5: Mass-Radius diagram for known extrasolar planets (from exoplanet.eu). The location of some Solar System planets is also indicated by their first capital letters.

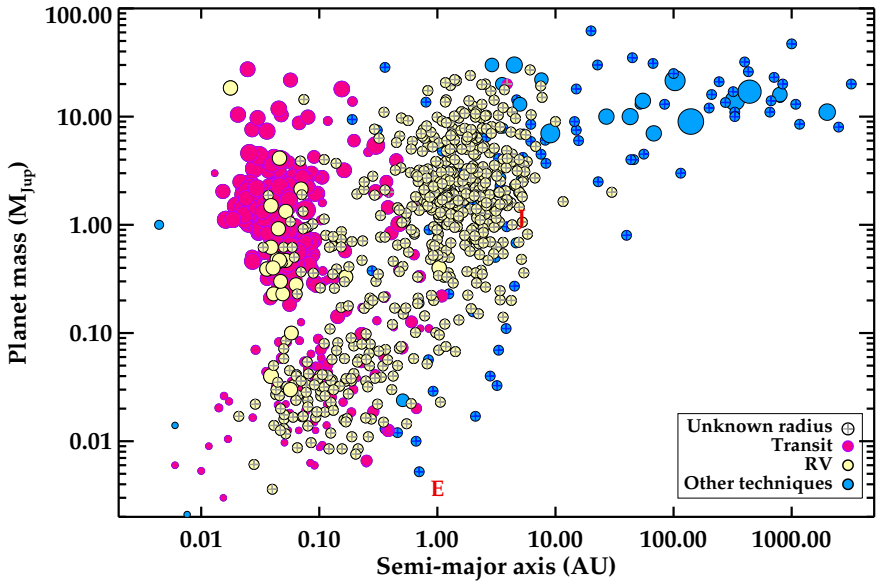

FIGURE 1.6: Mass (or $M_p \sin i$ in the case of the radial velocity detected planets) versus semi-major axis for known extrasolar planets (from exoplanet.eu). The size of the symbols correspond to the size of the planets for those detected (or also detected) by transit. Those without determination of the radius are marked by a "plus" symbol. The location of Jupiter and Earth is also indicated by their capital letters.

1.3 The formation an evolution of planetary systems

The formation and evolution of planetary systems is intimately linked to that of their parent star. The properties of their host will not only determine the properties of the planet but also its evolution and possibilities of harboring life. It is thus crucial to understand the whole process of stellar and planet formation from a comprehensive perspective in order to explain the characteristics of the large crop of exoplanets known to date, their trends, and the apparent deserts in the parameter space of some properties. In this section, we summarize the current paradigm of stellar and planet formation, including the most popular theories.

From molecular clouds to protostars

It is now widely accepted that stellar formation starts with the fragmentation of molecular clouds (accumulations of gas and dust) into smaller and denser cores that yield to gravitational instabilities provoking the collapse of the surrounding material into these denser aggregates (see Fig.1.7). The origin of this fragmentation has been a matter of debate for several decades and different (not mutually exclusive) mechanisms have been proposed, namely collision of molecular clouds, or nearby supernova explosions causing shock waves increasing the density of some regions of the molecular cloud and triggering stellar formation. For instance, observational hints were provided for the latter mechanism in λ Orionis star forming region by Dolan & Mathieu (2002) but were subsequently contested by Bayo et al. (2012, 2011), who studied a lower-mass population of stars in this region.

Regardless of the actual mechanism for starting the cloud collapse, these denser cores break the initial equilibrium of the cloud, previously supported against gravitational collapse by a combination of thermal, magnetic, and turbulent pressures (Mouschovias, 1991, Shu et al., 1987). We can consider this as the initial stage of star formation ($t = 0$). The surrounding material then starts to fall into the denser core, forming an envelope of material gravitationally attracted by the protostellar core.

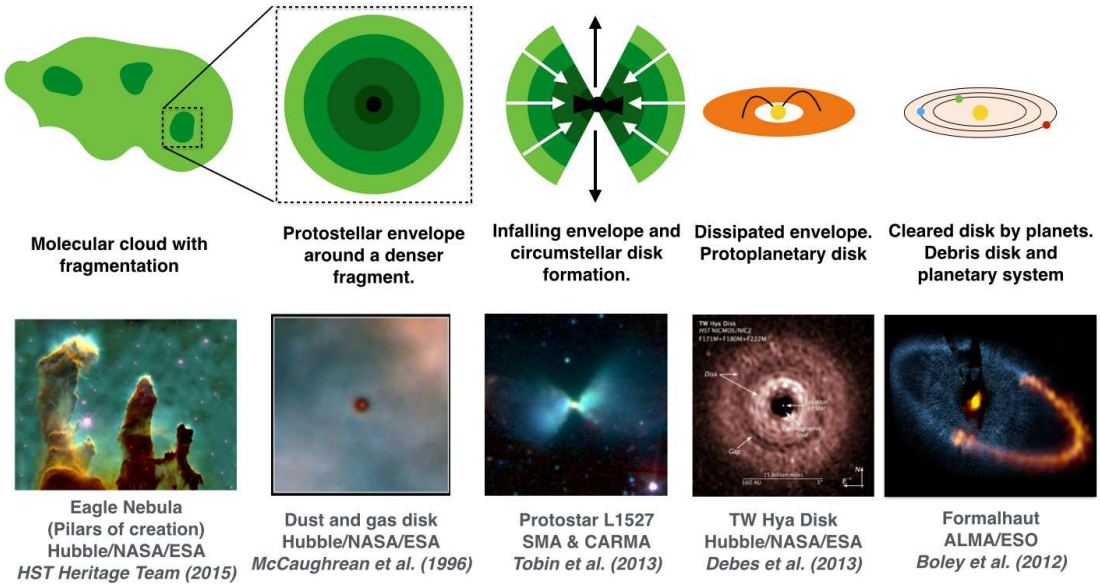

FIGURE 1.7: Stellar formation scheme (upper panels, inspired in Shu et al. 1987) and corresponding real images of the different stages (bottom panels). In the upper panels, we have illustrated denser regions with darker colors.

From protostars to protoplanetary disks

Although the subsequent processes are likely to depend on the mass of the system, the commonly accepted mechanism is as follows. In order to conserve the primordial angular momentum of the cloud, the in-falling material starts to become deposited on a plane perpendicular to the angular momentum vector, forming the so-called protostellar disk (Goodman, 1993). This disk revolves around the accreting protostar, which is still embedded in a fewer dense envelope of in-falling gas and dust. Once the envelope has been exhausted or dissipated, the protoplanetary disk is definitely formed. Numerical models of collapsing molecular cores show that disks are formed within the first 10^4 years (Yorke et al., 1993), and this is a key phase in the subsequent formation of planetary systems. The total mass accumulated by the disk will determine its final properties.

From protoplanetary disks to planetary systems

Once the protoplanetary disk is configured, the process of planet formation starts. The exact mechanism on how this process is triggered is still a matter of debate. There are two main proposed scenarios (see Mordasini et al., 2010, for a complete review):

- **Core accretion (CA).-** In the core accretion model (also called the *bottom-up* model), planets are formed in the disk through the aggregation of dust particles into larger bodies until they clear their orbits around the central host. While the underlying physics on how small dust particles grow to become meter-size bodies is relatively well understood (Brauer et al., 2008), how these bodies end up forming kilometer-size planetesimals (the so-called *meter-size barrier*) is still controversial. Meter-size bodies reach high velocities, colliding and destructing each other with high probability. They also drift rapidly to the star, being thus destroyed (Nakagawa et al., 1986, Weidenschilling, 1977). Alternative mechanisms to this "classical coagulation" have been proposed to address this barrier (see Mordasini et al., 2010, and references therein for a complete review). Similarly, the kilometer to thousands of kilometer growth process is still poorly understood due to different difficulties in simulating the process. But regardless of the actual aggregation mechanism, the larger presence of heavier elements in the inner regions of the disk (that can condensate at high temperatures) can lead the growth of rocky planets. By contrast, beyond the *snow line*,[4] more massive cores ($\sim 10\ M_{\oplus}$) can be formed and have the sufficient gravitational pull to accrete gaseous hydrogen and helium, forming the giant massive planets. Although these processes were thought to last several tens of Myr (Safronov & Zvjagina, 1969), recent simulations show that they can take place during the first 10 Myr (e.g., Pollack et al., 1996, Rafikov, 2004), with the solid core formation in the case of gas giants lasting around 1 Myr at 5.2 AU (Pollack et al., 1996). In summary, the CA mechanism could thus grow planets in a wide range of masses (from rocky to gas giants) having enhanced metallicity due to dust accretion, to be formed in orbits > 4 AU in a relatively large period of time of around 10 Myr.

- **Gravitational instability (GI).-** In this model, giant planets are formed by the direct collapse of part of the protoplanetary disk into a clump due to gravitation instabilities. As deduced from the Toomre parameter (Q, Toomre et al., 1981), disks become unstable when they are cold and massive. These two requirements put important constraints in both the orbital separations in which the disk can be unstable and the properties of the forming star, respectively. Because of the first requirement (that the disk must be cold), one can infer that fragmentation in a massive disk cannot occur close to the star. It is clear that disks massive enough to be gravitationally unstable are not cool at small orbital separations. Rafikov (2005) analyzed different configurations of disk properties and orbital separations in terms of thermodynamical conditions. They concluded that gravitational instability cannot form planets closer than ~ 10 AU. Indeed, even at larger separations (~ 100 AU) the resulting planets from disk fragmentation would be very massive ($M_p \sim 10\ M_{\rm Jup}$) as compared to the masses of the large majority of detected exoplanets. Additionally, GI would require a massive disk of $\sim 10\%$ of the stellar mass, while

[4]The snow line (Hayashi, 1981) is the distance beyond which volatiles can condensate into solid grains.

observational constraints point to a disk mass of $\sim$ 1% of the stellar mass (Andrews & Williams, 2005, 2007). Instead, GI can grow giant planets extremely fast ($\sim$ 0.01 Myr), in contrast to the core accretion scenario ($\sim$ 10 Myr). In summary, planets formed by the GI mechanism are expected to be massive (even in the brown dwarf and low-mass domain), to revolve at wide orbits, to have metallicities similar to the original nebula (and thus to their host), and to be formed extremely fast.

Early evolution of recently formed planets: migration theories

Interestingly, some types of detected extrasolar planets shown in section § 1.2 seem to contradict the expected population of planets according to both planet formation theories. For instance, the large crop of massive gas giants revolving in close-in orbits ($<$ 1 AU) to their hosts (also called hot-Jupiters) represents a challenge for both theories, since they predict their formation in outer orbits. In order to solve this dichotomy and based on our knowledge of the Solar System history, several migration processes have been proposed to explain this niche of hot-Jupiters. These processes are supposed to take place during the first hundreds of million years after the formation of the planetary system. The proposed mechanisms producing this migration are: i) planet-disk interactions, ii) planet-planet scattering, and iii) planet-star tidal interactions.

In the first case, the formed planet that has cleared its orbit from material in the surrounding disk of the star continues accreting mass, forcing the planet to move towards the star to conserve the angular momentum (e.g., Lin et al., 1996). By definition, this mechanism needs the circumstellar disk ($\sim$ 10 Myr, e.g., Carpenter et al., 2006, Lada et al., 2006, Ribas et al., 2015), putting a strong constraint for its temporal range. The planet-planet scattering mechanism is based on gravitational interactions between the formed planets (Adams & Laughlin, 2003). Thus, this mechanism can be active during several hundreds of Myr. Finally, tidal interactions between the star and the planet, for instance due to the evolution of the star across the Herztsprung-Russell diagram, can provoke the inward migration of planets in timescales of the order of Gyr. From this summary it seems to be clear that unveiling the planet occurrence at different stellar ages (and evolutionary stages) is crucial to disentangle which of these planet migration mechanisms (if any) predominates.

Death and revival

Once the planetary system has reached a dynamically stable stage, the evolution of the star dominates the evolution of the whole system. During the main-sequence stage, the luminosity of the star varies significantly, affecting, for instance, the orbital regions in which liquid water can be maintained in the surface of rocky planets (usually called the habitable zone). As an example, the luminosity of the Sun when it reached the main-sequence was 75% of the current luminosity (according to evolutionary models by Baraffe et al., 2003). This evolution has moved

out the habitable zone of the Solar System, what has excluded Venus from this region in the last 2 Gyr (e.g., Leconte et al., 2013).

Another critical step is the evolution of the star off the main-sequence, when it has exhausted the hydrogen and its core contracts expanding its external layers and asymptotically increasing its luminosity. The implications of this phase on planet formation are starting to be understood and several theoretical studies have been proposed to explain the apparent paucity of close-in planets around sub-giant and giant stars ascending the red giant branch (e.g., Burkert & Ida, 2007, Villaver & Livio, 2009, Villaver et al., 2014), including planet-engulfment and/or evaporation. The detection of dust tails in the light curves of close-in planets around evolved stars (e.g. Adamów et al., 2012, Sanchis-Ojeda et al., 2015) could be an empirical proof for this scenario. The survivability of planets in these agitated stages depends on many factors. Observationally, planets have been detected revolving stars in the horizontal branch (e.g., Silvotti et al., 2007), what may indicate that they have survived the He-flash. But some studies indicate that the strong ionizing fluxes at the extreme horizontal branch could also evaporate close-in planets (Bear & Soker, 2011).

All these processes dominate the evolution of planets, being threatened on every stage of the evolution of their parents. However, planets have also been found in highly evolved (dead) stars, including pulsars (e.g., Wolszczan & Frail, 1992). But whether these planets actually formed in those systems or they were subsequently captured or even formed in debris disk as a consequence of the disruption of stellar companions (Yan et al., 2013) is still a matter of debate.

From theory to observations

The recent ALMA observations of HL Tau (see left panel of Fig. 1.8, ALMA Partnership et al., 2015), with seven detected gaps in an extremely young protoplanetary disk (1-2 Myr, Briceño et al., 2002) shows characteristics that seem to favor and contradict both mechanisms of planet formation (CA and GI) at the same time: i) the fast planet formation in HL Tau is allowed by GI but is difficult to explain with the classical CA mechanism (at least for the close-in gaps); ii) the close orbital separations of $\sim 13 - 90$ AU are thermodynamically difficult to explain by GI but theoretically possible with CA (although not at these timescales).

Additionally, the detection of streams of flowing material in the ALMA image of HD 142527 (Casassus et al., 2013, see middle panel of Fig. 1.8) has also provided more hints and questions to the formation of planetary systems. This detection would indicate the possible formation of giant planets inside the wide gap (10-100 AU) splitting the planetary disk into an inner and an outer disk. Those planets would have cleared their orbits, forming the detected gap. A denser concentration of material at around 90 AU could indicate the position of the forming planet.

These recent detections with state-of-the-art technology shed more light to our understanding of the planet formation process. However, some of their properties also represent a challenge for the described theories, none of which is able to reproduce the high-resolution and high-contrast observations of protoplanetary disks and the current population of extrasolar planets. Finally, we are also detecting planets in the last stages of their lives, starting to be disrupted by their parents (see Fig. 1.8, right panel).

It is thus clear that in order to have a complete picture of planet formation and evolution, more work is needed from both theoretical and observational points of view.

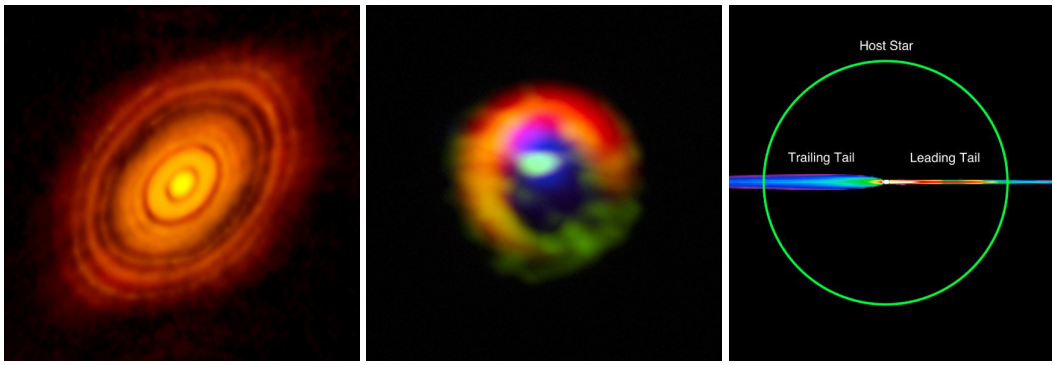

FIGURE 1.8: **Left:** Signs of planet formation in HL Tau as seen by ALMA (ALMA Partnership et al., 2015). The image shows seven detectable dark rings, probable gaps cleared by forming planets in a multi-planet system. The inner gap is at ~ 13.1 AU while the farther out gap is calculated to be at 91 AU. **Middle:** High-resolution image of HD 142527 take with ALMA (ESO/NAOJ/NRAO) by Casassus et al. (2013). The image shows a clear outer disk with possible streams connecting an accumulation of material in the disk gap at ~ 90 AU (light green region in the center of the image). **Right:** Simulation of the disrupted planet EPIC 201637175 b from Sanchis-Ojeda et al. (2015).

1.4 Orbital mechanics

Calculating the location of a celestial body revolving around a star at a particular time is an old problem. The solution was proposed by Johannes Kepler in his book about *Epitome Astronomiae Copernicanae* (1621). Some years before (in 1609), Kepler published *Astronomia Nova*, containing the first and second laws of motion that he proposed for Mars but which are currently applied to all celestial bodies. The third law was subsequently stated in *Harmonices Mundi* (1619). Here we present their current and original formulation in latin:

1. **The orbit of every planet is an ellipse with the Sun at one of the two foci.**
   "Ellipsin fieri orbitam planetae [...] Sole (Foco altero huius ellipsis) [...]", Kepler (1609)

2. **A line joining a planet and the Sun sweeps out equal areas during equal intervals of time.**

"Dictum quidem est in superioribus, divisa orbita in particulas minutissimas aequales: accrescete iis moras planetae per eas, in proportione intervallorum inter eas & Solem.", Kepler (1609)

3. **The square of the orbital period of a planet is directly proportional to the cube of the semi-major axis of its orbit.**
   "Sed res est certissima exactissimaque quod proportio qua est inter binorum quorumcunque Planetarum tempora periodica, sit praecise sesquialtera proportionis mediarum distantiarum, id est Orbitum ipsorum ...", Kepler (1619).

The third Kepler law is of key importance when studying orbital motions and, in particular, in the exoplanetary field. Its current mathematical shape is

$$\frac{P^2}{a^3} = \frac{4\pi^2}{GM_\star}, \tag{1.1}$$

where G is the gravitational constant, $M_\star$ is the mass of the central object (the star), P is the orbital period, and a is the semi-major axis of the orbital ellipse. Since the term at the right hand of this equation depends just on the stellar mass, the left-hand quantity remains constant for all planets orbiting the central star in Keplerian orbits.

In this formulation, Kepler established the equation of motion, relating the **eccentric** and **mean anomalies** (**E** and **M**, respectively) with the **eccentricity** (**e**) of the orbit as

$$M = E - e \sin E. \tag{1.2}$$

The eccentric anomaly, E, is defined as the angle in the plane of the orbit between the periastron and the projected position of the planet into a circle of radius equal to the semi-major axis of the orbit (see Fig. 1.9). The mean anomaly, M, instead, is not a physical angle. It describes the position of the object along the orbit

$$\begin{aligned} M &= \frac{2\pi}{P} t_{\rm peri} = 2\pi\phi_{\rm peri} \\ &= \frac{2\pi}{P} t_{\rm ref} + M_{\rm ref} = 2\pi\phi_{\rm ref} + M_{\rm ref}, \end{aligned} \tag{1.3}$$

where $\mathbf{t_{peri}}$ and $\phi_{\mathbf{peri}} = t_{\rm peri}/P$ are the **time** and **phase** (respectively) **since the periastron passage**. To refer the time reference from another orbital location (e.g., time of planet-star conjunction in transiting planets), we must include $M_{\rm ref}$, the mean anomaly difference between the periapsis and the reference location.

The eccentric anomaly is then related to a more comprehensive orbital angle, the **true anomaly**, $\boldsymbol{\nu(t)}$, defined as the angle measured from the star between the periastron passage and the position of the planet (see Fig. 1.9). This relation is given by

$$\tan\frac{\nu}{2} = \sqrt{\frac{1+e}{1-e}}\tan\frac{E}{2}. \tag{1.4}$$

The Kepler's equation of motion (Eq. 1.2) has no analytical solution. Thus, numerical methods are needed to accurately solve the problem. We normally measure observable quantities (e.g., radial velocity) at a particular time t and need to translate this time t, to a position of the planet in its orbit. To answer this question, we must first select a frame of reference. Along this work, we will use the line of sight (Z) as the reference axis. Hence, we can set $t = 0$ to the time of conjunction (i.e., **time of mid-transit**, $\boldsymbol{T_c}$). Following the scheme in Kallrath & Milone (2009), we can start by calculating the **true anomaly at conjunction** ($\boldsymbol{\nu_c}$). From Fig. 1.9, it is clear that $\nu_c = 90° - \omega$, with $\boldsymbol{\omega}$ being the **argument of the periastron**. By using Eq. 1.4, we can get the eccentric anomaly at the moment of conjunction (E_c) and directly obtain the mean anomaly at conjunction ($M_{\rm ref} \equiv M_c$) by applying Eq. 1.2. Once $M_{\rm ref}$ is known, we can obtain the mean anomaly at any time (also known as **orbital phase**) from conjunction and calculate the eccentric anomaly by using numerical methods on Eq. 1.2.[5] The eccentric anomaly is then used to compute $\nu(t)$ by using Eq. 1.4. For visualization purposes, it is convenient to also define the **geometrical phase**, $\boldsymbol{\theta}$, defined as the angle between conjunction and the position of the planet along its orbit. With this definition the mid-transit of a transiting planet would occur at $\theta = 0$ while the secondary eclipse would occur at $\theta = \pi$. The geometrical phase is directly given by

$$\theta(t) = \nu(t) + \omega - \pi/2 \tag{1.5}$$

In Fig. 1.10, we show the relation between the orbital phase (θ) and the temporal phase from conjunction (ϕ_c) for different orbital configurations (i.e., different eccentricities and arguments of the periastron). From the bottom panels of this figure, in the case of eccentric orbits not aligned with the line of sight ($\omega \neq \pi/2$ and $\omega \neq 3\pi/2$), we can see that the mid temporal phase ($\phi = 0.5$) does not corresponds to $\theta = 180°$.

Once the true anomaly is known, the position of the planet in the plane of the orbit can be determined at any time. Let's call this two dimensional reference frame as $\hat{x} - \hat{y}$, with the origin

[5] The solutions of this equation along this dissertation are obtained by using a Newton-Raphson method with a tolerance of 10^{-5} (i.e., $E - E_{\rm old} < 10^{-5}$).

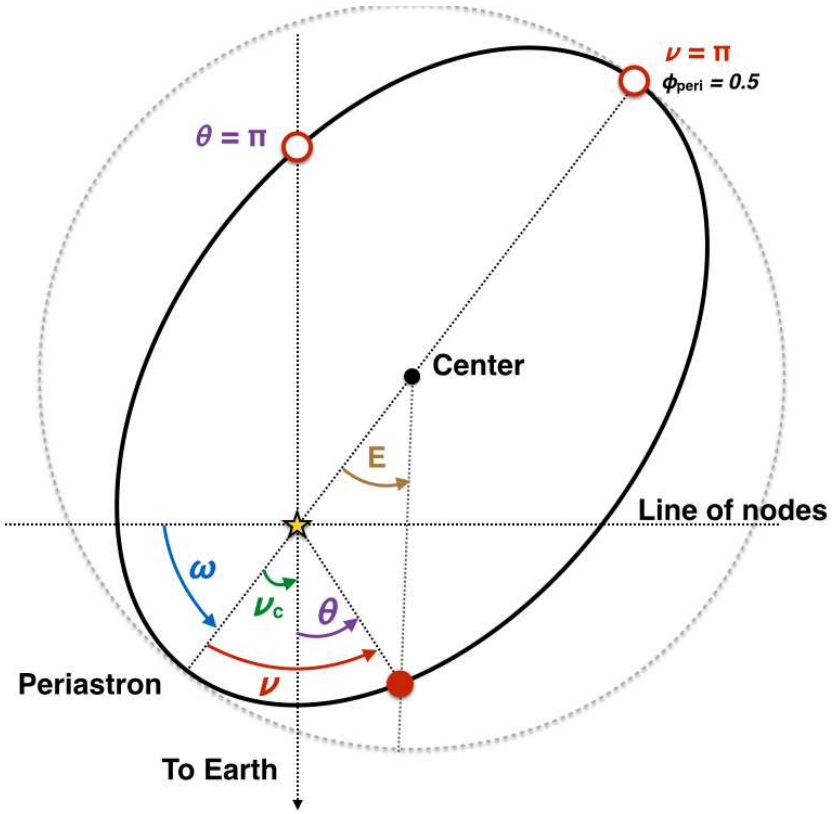

FIGURE 1.9: Description of the conventions for the orbital elements used in this thesis for an object orbiting around a star in a eccentric orbit not aligned with the line of sight.

being at the location of the star (at one of the foci of the ellipse). In this frame, the positive $\hat{x}$ is defined in the direction of the periapsis. The cartesian coordinates of the planet in this reference frame can be written as

$$x = r\cos\nu \tag{1.6}$$

$$y = r\sin\nu \tag{1.7}$$

$$z = 0 \tag{1.8}$$

where $\boldsymbol{r}$ represents the **star-planet distance** at each particular time

$$r = a\frac{1-e^2}{1+e\cos\nu} \tag{1.9}$$

For circular orbits, this equation reduces to $r = a$. This simple reference frame serves as a first understanding of the complicated problem of locating objects in 3D motions. However, a more complete (3D) formulation is needed to study the orbital motion of planets around other stars. As demonstrated by Euler (1776)

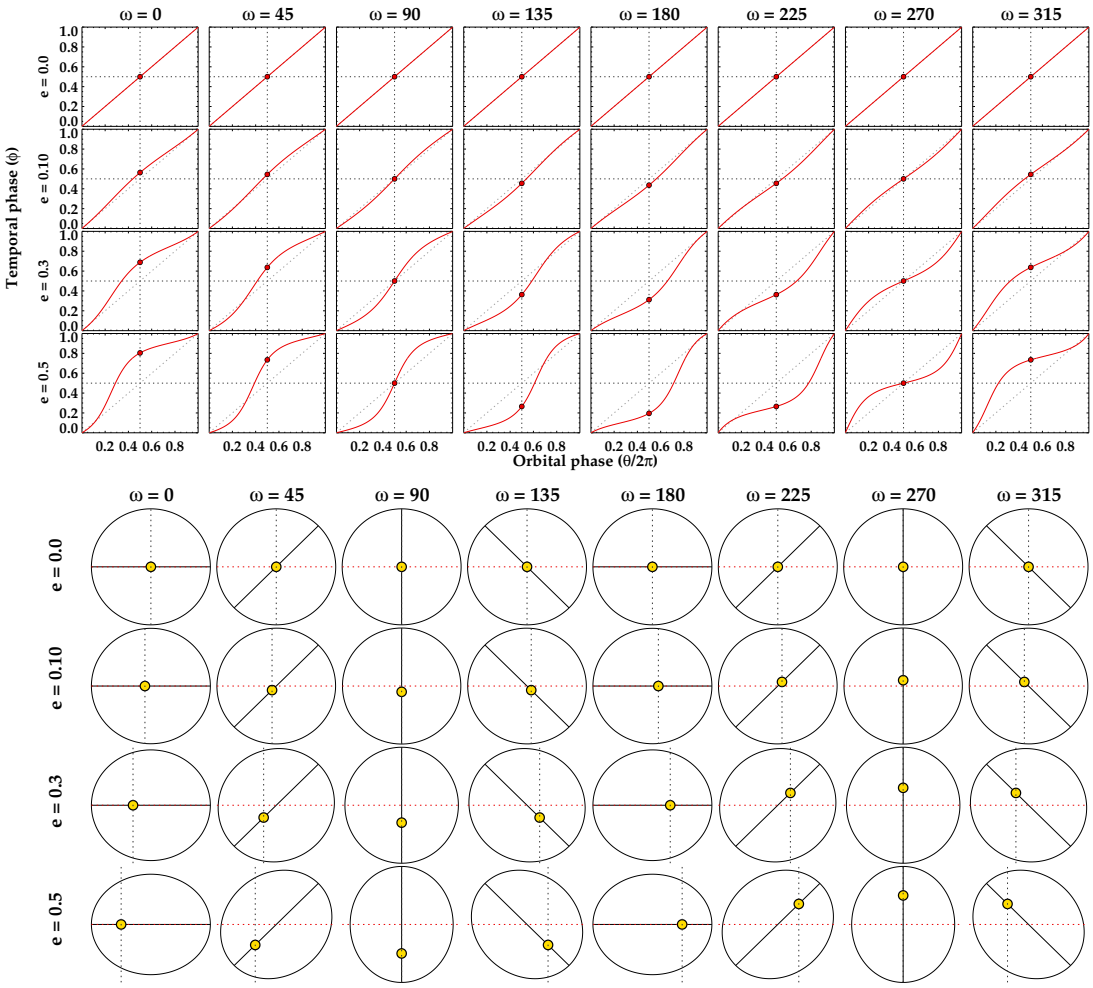

FIGURE 1.10: Representation of the solution to Kepler's equation (Eq. 1.2) for different eccentricities and arguments of the periastron. In the upper panel, I show the difference between the orbital (geometrical) phase, θ, and the temporal phase, ϕ for the different configurations. The physical representation of the orbits is shown in the lower panel, being the observer located below the figure.

"Theorem. When a sphere is moved around its centre it is always possible to find a diameter whose direction in the displaced position is the same as in the initial position."
"Theorema. Quomodocunque sphaera circa centrum suum conuertatur, semper assignari potest diameter, cuius directio in situ translato conueniat cum situ initiali." [6]

In other words, we can describe any movement around a fixed point in three dimensions by using three rotations. These rotations are described by three angles (see Fig. 1.11). In the case of orbital motion, the orientation of the orbit in the three dimensional space (XYZ) can be described by the **longitude of the ascending node Ω**, representing the angle subtended from the reference direction (X) to the ascending node of the orbit (i.e., the point at which the planet crosses the reference plane or plane of the sky); the **argument of the periastron** (ω), defined in

[6] Novi Commentarii academiae scientiarum Petropolitanae 20, 1776, pp. 189-207 (E478).

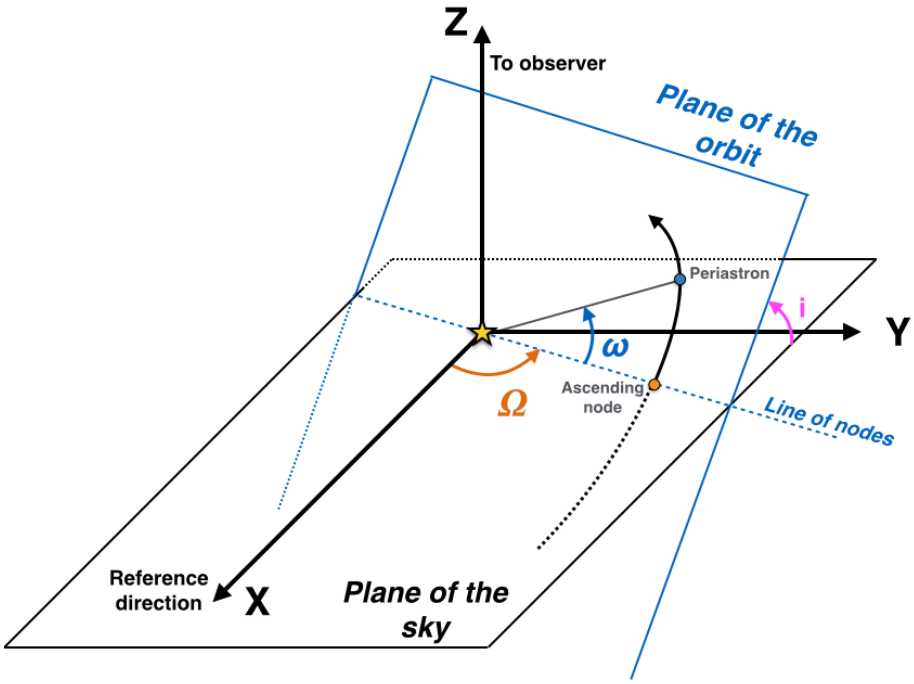

FIGURE 1.11: Description of the three dimensional orbital elements used to describe the orientation between the plane of the orbit and the plane of the sky.

the orbital plane from the ascending node to the periapsis of the orbit; and the **inclination** of the orbit (***i***), being the angle between the reference plane and the orbital plane. Along this thesis I will name the reference frame as the **plane of the sky**. These angles are represented in Fig. 1.11.

Assuming that the observer is located at $\{X, Y, Z\} = \{0, 0, +\infty\}$ and applying the appropriate rotation matrices to the cartesian coordinates in the $\hat{x} - \hat{y}$ reference frame, we can obtain

$$X = r[\cos\Omega\cos(\omega + \nu) - \sin\Omega\sin(\omega + \nu)\cos i] \tag{1.10}$$

$$Y = r[\sin\Omega\cos(\omega + \nu) + \cos\Omega\sin(\omega + \nu)\cos i] \tag{1.11}$$

$$Z = r\sin(\omega + \nu)\sin i \tag{1.12}$$

The projected position of the planet in the plane of the sky is then just given by the $\{X, Y\}$ coordinates.

In Fig. 1.4, we summarized the observation and detection techniques that can be used to determine the different orbital and physical parameters of a planetary system.

1.5 Motivations and purposes of this thesis

Since ancient times, different questions about our own existence are recurrent. The adverb "how" predominates in those questions. We have wondered how life appeared on Earth, how

Earth was formed, how the Solar System was built, how stars are born, and how galaxies and the whole universe grew. All these questions are indeed related to each other so that a complete answer must come from the interplay and results of different science branches. The role of this thesis in this huge quest is to focus in a small part of a small piece of the puzzle, that can be summarized in one question using the "how" adverb: how do planets form and evolve?

Unveiling the whole process of planet formation and evolution requires the combination of theoretical analysis supported by observations. The latter implies the detection and characterization of extrasolar planets, as well as a deep study of the Solar System. Several ground- and space-based surveys have been dedicated to it and a large effort is being spent in finding new worlds to explain our own. In this context, the *Kepler* mission has provided the largest crop of exoplanet candidates known to date by using the transit method, looking for planetary transits in more than 150 000 stars. The detection of these planetary transits must be followed by subsequent confirmation and characterization by other techniques.

In this dissertation we aim to take advantage of the unprecedented photometric precision provided by the *Kepler* mission to characterize new extrasolar planets in unexplored niches. We intend to fill some gaps in the wide diversity of exoplanets owing to provide hints of the formation and evolution process. In this regard, ground-based instrumentation (from the Calar Alto observatory in Almería, Spain) is used to study the *Kepler* candidates and analyze their properties. This is done in a two-phase project. In the first phase, we have collected high-spatial resolution images of a large sample of *Kepler* candidates with the AstraLux instrument, aiming at unveiling possible blended companions and to validate the planets in case of their absence (i.e., if the host is isolated within our sensitivity limits). In the second phase, some of these isolated candidates were followed-up with the high-resolution spectrograph CAFE owing to monitor the radial velocity reflex motion of the host star, whose periodicity could confirm the presence of planetary-mass bodies and characterize their physical and orbital properties.

This thesis has been divided in two parts. In *Part I*, we carefully describe the three sets of observations extensively used in this work and the corresponding techniques applicable to these data. This part is necessary in order to explain in detail the observing techniques used in this mainly observational dissertation: In Chapter 2, we describe the unprecedented accurate light curves obtained by the *Kepler* mission and the different techniques that we have used to characterize different effects detectable on them (transits, eclipses, modulations, and asteroseismology). In Chapter 3, we present the need for high-spatial resolution observations in exoplanetary searches and describe the technique used in this dissertation, the lucky-imaging. In Chapter 4, we briefly explain the radial velocity technique and describe the capabilities of the new Calar Alto instrument CAFE as a planet hunter. On the other hand, *Part II*, we present and analyze our scientific results based on the observations and techniques described in the first part: Chapter 5 focusses

on the high-resolution observations of more than 170 candidates. In Chapter 6, the radial velocity results of a selected sample of the isolated candidates is presented, confirming the planetary nature of some of them and characterizing their properties. In Chapter 7 we put in context our results with the known sample of extrasolar planets, providing an analysis of its impact on the formation and evolution processes. Finally, in Chapter 8, we summarize the results of this dissertation.

Part I

Techniques and methodologies: the hunt for extrasolar planets

In this first part of the dissertation, we revise the three techniques that we have extensively used in the present work. In particular, we inspect their mathematical formulation and analyze the dependency of the different parameters on the shape of the orbits and planet properties. We focus on the instrumentation used to obtain our data and review the forthcoming instruments and telescopes as well as their impact in the future of the exoplanetary field. The final goal is to understand how these techniques influence the observations and affect the conclusions derived by the analysis of our data.

In particular, in Chapter 2 we analyze the different effects detectable by means of high-accurate photometry (planetary transits and occultations, lightcurve modulations, and asteroseismology). The *Kepler* mission is also briefly described. In Chapter 3, we describe the high-spatial resolution technique with particular focus on the lucky-imaging and the AstraLux instrument in Calar Alto Observatory. In Chapter 4, we revisit the radial velocity technique and summarize the different technical aspects involving long-term programs, with particular focus to the CAFE instrument in Calar Alto.

Chapter 2

High-precision photometry in the *Kepler* era

Contents

"I demonstrate by means of philosophy that the Earth is round, and is inhabited on all sides; that it is insignificantly small, and is borne through the stars."[1]

Astronomia Nova (1609)

Johannes Kepler (1571-1630)

[1]Translation by Frederic P. Miller, Agnes F. Vandome, McBrewster John in Astronomia Nova (VDM Publishing, 2011).

2.1 The *Kepler* mission in a nutshell

Several works dealing with the possibility of finding planets with precise photometry by the transits method (e.g. Rosenblatt, 1971), Borucki & Summers (1984) demonstrated that only Jovian planets could be accessible from the ground. The search for Earth analogs was then focused on space-based observations. After three rejected proposals in the late nineties, in 2001 the *Kepler* mission was selected by NASA as Discovery Mission #10. Eight years later, on March 6th 2009, the spacecraft was successfully launched from Cape Cañaveral Air Force Station (US).

The main goal of the *Kepler* mission was to detect Earth-like planets around Sun-like stars, looking for potentially habitable worlds with the transits method. As seen from outside of the Solar System, the Earth would produce a transit depth of $\sim$ 84 ppm (parts per million, 10^{-6}), while Mars and Mercury would induce $\sim$ 24 ppm and $\sim$ 12 ppm, respectively. To achieve this extraordinary precision requirements, *Kepler* was a 0.95m Schmidt telescope with a 105 deg^2 field of view, equipped with a photometer composed of 42 CCDs (charge coupled devices) of 2200×1024 pixels. The pixel size was 27×27 μm, corresponding to an image scale of 3.98 arcsec/pixel. It provides full-width at half-maximum (FWHM) point-spread functions (PSF) of 3.1-7.5 arcsec.

The mission observed a single field of view centered at right ascension RA =19h 22m 40s and declination DEC =+44° 30' 00' (see Fig. 3.8), monitoring more than 150 000 stars. These stars received an identification number called *Kepler* Input Catalog (KIC). The images were defocused to 10 arcsec in order to improve the photometric precision and were obtained in a single bandpass (see the response function as compared to other bandpasses in the online *Kepler* manual[2]). The exposure time of the images was fixed to 6.02 seconds, with a 0.52 seconds of readout. The pixels of the CCDs containing stars with magnitudes brighter than $V < 14$ mag were then read every 6.54 seconds. Only few of the targets (512 in total) were stacked in 1 minute images (short cadence data) while the remaining targets were stacked in 30 minutes sets (long cadence data). The telemetry of the data from the spacecraft to the ground was carried out about once a month. The spacecraft rolled by 90 degrees about its optical axis every three months (i.e., four times per year) to optimize solar panel efficiency, thus dividing the mission into the so-called Quarters (Q). Even though the field of view was fixed, due to this rotation, a given star was located in up to four different parts of the focal plane, depending on the Quarter.

The *Kepler* Science Operations Center applies the developed Science Processing Pipeline to the received images from the spacecraft. The pipeline includes several modules to process the images, obtains the aperture photometry, and searches for transit signatures. The aperture size and shape is individually optimized for each star according to its magnitude and the presence of nearby objects. The typical aperture sizes range from 6-10 arcsec. The transit detection is

[2] http://keplergo.arc.nasa.gov/CalibrationResponse.shtml

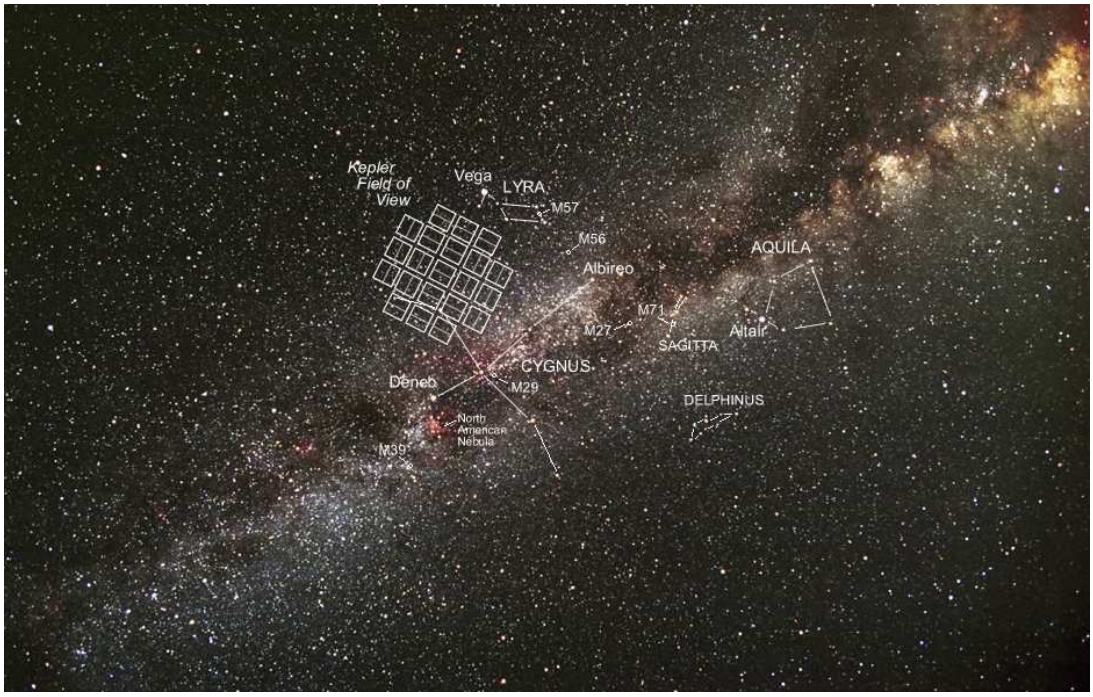

FIGURE 2.1: Location of the *Kepler* field over-imposed to an image of the Milky Way. Image credit: NASA

done through the Transit Planet Search (TPS, Jenkins et al., 2010). Based on different filters involving duration, period, and epoch of the transit, they compute the Multiple Event Statistics (MES). Targets showing a MES above 7.1 (Jenkins, 2002) are selected as Threshold Crossing Events (TCEs). Then, the LCs of these TCEs are modeled and those returning objects with radius below $2R_{\rm Jup}$ are selected as *Kepler* Objects of Interest (KOI).

In total, *Kepler* carried out 18 quarters (Q0-Q17), ending its operations on August 15th, 2013 due to the failure of two out of its four reaction wheels. This technical issue made impossible to maintain the spacecraft in a fixed position for a long period of time, preventing the normal use of the telescope and obtaining the necessary photometric precision. As for today, the *Kepler* mission has provided 8716 KOIs around 7470 stars.[3] Among these KOIs, 279 have been identified as true planets by measuring their mass using different techniques. The application of statistical techniques and the development of dedicated softwares such as BLENDER (Torres et al., 2011) or PASTIS (Díaz et al., 2014a), has led to the statistical validation of 715 planets. A planet candidate is considered as validated if the posterior probability of the planetary hypothesis is sufficiently larger than the sum of the probabilities of all false positive scenarios. This technique has been very efficient in validating multiple-planetary systems (e.g., Lissauer et al., 2014, Rowe et al., 2014). Currently, 3613 KOIs remain as planet candidates and 4109 KOIs have been established as false positives.

[3] Numbers as of May 1st, 2015

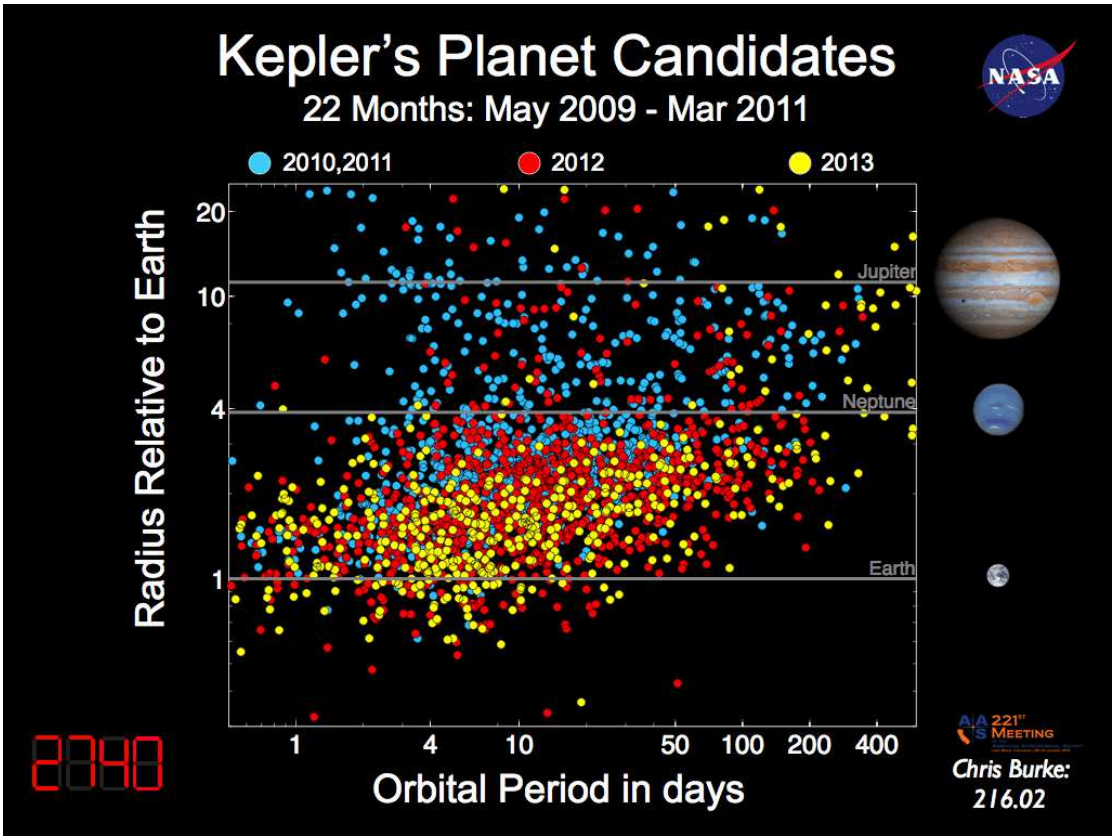

FIGURE 2.2: Evolution of the detected planet candidates in the size vs. orbital period diagram. Diagram made by C. Burke, presented in the American Astronomical Society (AAS) in 2013.

The sample of planet candidates provided by the *Kepler* mission has began to populate the region of Earth-analogs, i.e., Earth-size planets in the habitable zones of their parent stars. In Fig. 2.2, we show the evolution of the delivered candidates along the different releases provided by the *Kepler* team. It is not only the number of detected candidate and confirmed planets what make the *Kepler* mission the most important in the exoplanet exploration but also the wide diversity of these new worlds. For instance, it has discovered the smallest planets known to date, having sub-Mercury sizes like Kepler-37 b (Barclay et al., 2013) or Kepler-444 (Campante et al., 2015). It has also found disrupting planets like KIC 12557548 (Brogi et al., 2012) or the newly discovered EPIC 201637175 b (Sanchis-Ojeda et al., 2015) with the second phase of the mission, and planets at the very end of their life like Kepler-91 b (Lillo-Box et al., 2014a,c). Besides, it has found numerous multi-planet system, including Kepler-11 with up to 6 planets confirmed (Lissauer et al., 2011), and rocky planets potentially hosting liquid water on their surfaces like Kepler-22 (Borucki et al., 2012) or Kepler-186f, an Earth-analog in the habitable zone of its red dwarf star (Quintana et al., 2014).

The extremely precise photometry provided by the *Kepler* mission has allowed the exploitation of different effects. In the subsequent sections, we summarize those that have been crucial for the results presented in this dissertation and we describe their mathematical formulations.

2.2 Planetary eclipses: transits and occultations

Transits and eclipses are just geometrical effects, dependent on the relative position of the observer and the target. We call transit or conjunction to the time interval when the planet is located between the observer and the star, blocking the light coming from its host. Analogously, we call occultation or eclipse to the time interval when the planet is located behind the star.

We can start by the simple case of an spherical planet of **radius $\mathbf{R_p}$** orbiting around its host star of radius $\mathbf{R_\star}$ in a Keplerian orbit of semi-major axis $\boldsymbol{a}$, and inclination $\boldsymbol{i}$ with respect to the plane of the sky, eccentricity $\boldsymbol{e}$, and argument of the periastron $\boldsymbol{\omega}$. The detectability of a transit/eclipse depends on the projected separation between the central star and the orbiting companion in the plane of the sky and the relative sizes of both objects. The former is given by $S_{p,\star} = \sqrt{X^2 + Y^2}$, where X and Y are the projected separation of the planet in cartesian coordinates, defined in Eq. 1.10, formulated in units of the stellar radius as

$$\begin{aligned} S_{p,\star} &= \frac{r}{R_\star}\left[1 - \sin^2(\omega + \nu)\ \sin^2 i\right]^{1/2} \\ &= \frac{a}{R_\star}\frac{1 - e^2}{1 + e\cos\nu}\left[1 - \sin^2(\omega + \nu)\ \sin^2 i\right]^{1/2}, \end{aligned} \tag{2.1}$$

where in the second identity we have used the definition of planet-to-star separation in the plane of the orbit (see Eq. 1.9). This equation completely defines the shape of the transit. Interestingly, it does not depend on the longitude of the ascending node (Ω) and so this parameter cannot be determined by the transit analysis. This is clear since the observer would see the same transit shape regardless of the orientation of its path across the stellar projected disk. When the planet is located just between the observer and the star (at conjunction), we showed that $\omega + \nu = \pi/2$. By substituting this in Eq. 2.1, we obtain the projected separation at conjunction, which is known as the **impact parameter** of the orbit

$$\begin{aligned} b \equiv S_{p,\star}(\omega + \nu = \pi/2) &= \frac{r_c}{R_\star}\cos i \\ &= \frac{a}{R_\star}\cos i\frac{1 - e^2}{1 + e\sin\omega} \end{aligned} \tag{2.2}$$

The condition for a transit to be detected becomes clear with this definition and its representation in Fig. 2.3:

- If $b > 1 + R_p/R_\star$ there will be **no transit**.

- If $b < 1 - R_p/R_\star$ there will be a **complete transit**. The whole projected planet would occult part of the projected stellar disk.
- If $1 - R_p/R_\star < b < 1 + R_p/R_\star$ only part of the planet would occult the stellar disk and so the transit will be **grazing**.

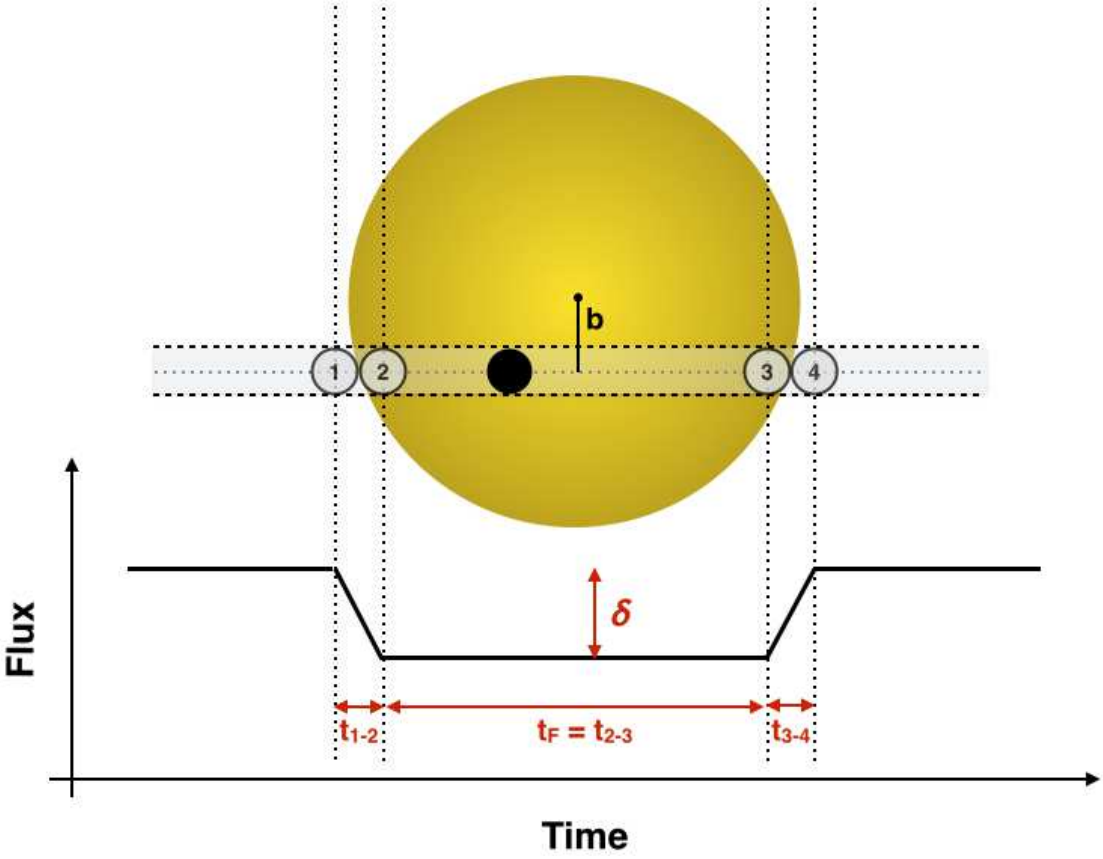

FIGURE 2.3: Definition of transit times, depth, and impact parameter.

When the planet passes behind the star, it is occulted by its host. The condition for this to happen is similar to that for the transit explained above. In this case, $\omega + \nu = -\pi/2$. By including this condition in Eq. 2.1, we obtain the impact parameter at opposition

$$b_{\rm opp} \equiv S_{p,\star}(\omega + \nu = -\pi/2) \; = \; \frac{a}{R_\star} \cos i \frac{1 - e^2}{1 - e \sin \omega} \tag{2.3}$$

In the next subsections, we will show the formalisms used to model the transits and occultations of planets around their host stars. Note that depending on the planet eccentricity and the three-dimensional orbit, the detection of a primary transit does not imply the occurrence of a secondary eclipse (even if the signal is not detectable) and vice-versa.

2.2.1 Planetary transits

For practical purposes, we will show the modeling of a planetary transit over a uniform source. Then we will intruduce the limb-darkening concept and its effect on the transit shape.

Uniform source star

The simplest case is to assume homogeneous luminosity of the star across the whole disk (i.e., no limb-darkening) and neglect the contribution of the night-side of the planet. Under these assumptions, the depth of the transit (δ) is given by

$$\delta = \frac{L_{\star,nt} - L_{\star,tr}}{L_{\star,nt}}, \tag{2.4}$$

where $L_{\star,nt} = \pi R_\star^2 F_\star$ is the flux of the star when the planet is not transiting and $L_{\star,nt} = \pi R_\star^2 F_\star - \pi R_p^2 F_\star = \pi (R_\star - R_p)^2 F_\star$ is the received flux at mid-transit, where the planet is completely inside the projected stellar disk. Thus

$$\delta = \left(\frac{R_p}{R_\star}\right)^2 \tag{2.5}$$

Consequently, by measuring the depth of the transit (and under the described assumptions), we can obtain the planet-to-star radius ratio ($R_p/R_\star$). In the specific cases in which the ingress and egress duration of the transit (t_{1-2} and t_{3-4}, respectively) can be measured, several other parameters can be derived. In Seager & Mallén-Ornelas (2003), the authors provide analytical formulae for the different orbital parameters under the assumptions of i) circular orbit, ii) $M_p << M_\star$, iii) $F_p << F_\star$, and iv) that the light comes from a single star. They define the time from second to third contact as t_F, and the total duration from the first to the fourth contact as $t_T \equiv t_{1-4} = t_{1-2} + t_F + t_{3-4}$ (see Fig. 2.3). Note that in the case of an eccentric orbit $t_{1-2} \neq t_{3-4}$ while for circular orbits $t_{1-2} = t_{3-4}$. Given these definitions, the radius of the circular orbit in units of the stellar radius is given by

$$\frac{a}{R_\star} = \left\{ \frac{\left(1 + \sqrt{\delta}\right)^2 - b^2 \left[1 - \sin^2(\pi t_T / P)\right]}{\sin^2(\pi t_T / P)} \right\}^{1/2}. \tag{2.6}$$

Additionally, the impact parameter can be derived as

$$b \equiv \frac{a}{R_\star}\cos i = \left\{\frac{\left(1-\sqrt{\delta}\right)^2 - \left[\sin^2(\pi t_F/P)/\sin^2(\pi t_T/P)\right]\left(1+\sqrt{\delta}\right)^2}{1-\left[\sin^2(\pi t_F/P)/\sin^2(\pi t_T/P)\right]}\right\}^{1/2} \tag{2.7}$$

From Eq. 2.6 and Eq. 2.7, we can obtain the inclination of the orbit (i) with respect to the plane of the sky.

For eccentric orbits, the analytical equations are slightly more complicated since the linear velocity of the planet changes at every phase, while it remains constant in the circular case. However, the modeling of the transit signal remains simple. The relative observed flux is given by

$$F_{\rm obs}(t) = \begin{cases} 1 & S_{p,\star}(t) > 1 + R_p/R_\star \\ A_{cc}[R_p/R_\star, S_{p,\star}(t)] & 1 - R_p/R_\star < S_{p,\star}(t) < 1 + R_p/R_\star \\ 1-\delta & S_{p,\star}(t) < 1 - R_p/R_\star \end{cases} \tag{2.8}$$

where, $A_{cc}[R_p/R_\star, S_{p,\star}(t)]$ is the intersected area between two circles of radius R_p and $R_\star$ separated by a distance $S_{p,\star}(t)$. This area is given by a well-known analytical solution:

$$\begin{aligned} A_{cc}(\rho, d) \;=\; & \rho^2 \cos^{-1}\left(\frac{d^2+\rho^2-1}{2d\rho}\right) + \cos^{-1}\left(\frac{d^2+1-\rho^2}{2d}\right) - \\ & - \frac{1}{2}\sqrt{(-d+\rho+1)(d+\rho-1)(d-\rho+1)(d+\rho+1)} \end{aligned} \tag{2.9}$$

where, for clarity, we have defined $d \equiv S_{p,\star}(t)$, in units of the stellar radius, and $\rho \equiv R_p/R_\star$. Thus, the parameters to be fitted are e, ω, and $a/R_\star$ to compute $S_{p,\star}(t)$, and the planet-to-star radius ratio to compute A_{cc} and δ. The effect of the different parameters on the shape of the transit is as follows (see Fig. 2.4):

- $\boldsymbol{R_p/R_\star}$.- The larger this ratio, the deepest the transit. It also affects the range of inclinations that produce a transit. The larger $R_p/R_\star$, the larger could be the impact parameters to produce a transit. With short-cadence data, differences in the ingress and egress duration can also become detectable.

- $\boldsymbol{e, \omega}$.- These parameters determine the configuration of the orbit with respect to the line of sight. They affect the ingress and egress duration (t_{1-2} and t_{3-4}). Unless in specific configurations, a non-zero eccentricity implies different ingress and egress durations. Hence, with the sufficient cadence and precision, the eccentricity and argument of the periastron can be measured from the transit signal. They also affect the duration of the transit.

- $\boldsymbol{a/R_\star}$.- The main parameter affected by $a/R_\star$ is the duration of the transit. Note that the depth is logically not affected.

- $\boldsymbol{i}$.- The inclination affects the total duration, the ingress and egress durations, and the depth of the transit. The latter parameter is just affected if the orbit is so inclined that the transit becomes grazing.

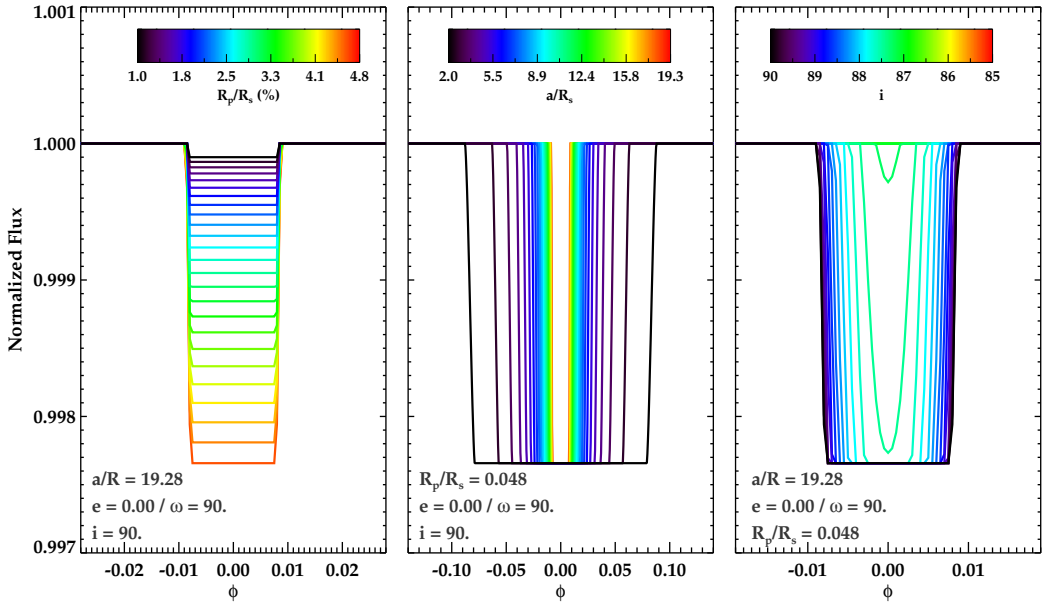

FIGURE 2.4: Dependencies of the transit shape with the different parameters in the case of a uniform source star and a planet in a circular orbit.

Non-uniform emission: the effect of limb darkening

From the observers point of view, the projected disk of a star does not emit homogeneously, being darker at the limb of the disk and brighter at the center. This is known as the limb darkening (LD) and has been theoretical formulated by several authors using different models. These models provide the luminosity of each region of the disk referred to that in the center, i.e., $I(\mu)/I(1)$, where $\mu = \cos\theta$, and θ is the angle between the normal vector to the stellar surface and the line of sight. The several formalisms are described, for instance, in Claret & Bloemen (2011). It is important to note that this intensity depends on the photometric band in which the observations are performed. The mostly used parametrization are:

$$\frac{I(\mu)}{I(1)} = 1 - u(1-\mu) \qquad \text{Linear law} \qquad (2.10)$$

$$\frac{I(\mu)}{I(1)} = 1 - a(1-\mu) - b(1-\mu)^2 \qquad \text{Quadratic law} \qquad (2.11)$$

$$\frac{I(\mu)}{I(1)} = 1 - \sum_{k=1}^{4} a_k(1-\mu^{k/2}) \qquad \text{Non-linear four-terms law} \qquad (2.12)$$

The different LD coefficients (u, a, b, and $a_1 - a_4$) were calculated and tabulated by Claret & Bloemen (2011) for different photometric bandpasses, including the *Kepler* band. These coefficients depend on the physical properties of the star ($T_{\rm eff}$, $\log g$, and $[Fe/H]$). Thus, we need to perform a trilinear interpolation of the tabulated values at the actual properties of each given star. According to Claret (2000), the non-linear four-terms LD reproduces the observations much better than any of the other laws. Hence, we will use this law for the transit fitting along this dissertation.

Thus, the LD must be introduced in the transit model (Eqs. 2.8). Mandel & Agol (2002) provided the complete formalism and the equations can be found in that work. We will use that formulation along this thesis by making use of an IDL implementation kindly implemented by Eric Agol.[4]

The shape of the transit is then modified by this differential intensity occulted by the planet along its path across the stellar disk. The effect is clearly detectable since the bottom of the transit signal is not flat anymore. Instead, it becomes round, with the minimum located at mid-transit. Additionally, the depth of the transit is modified. This is explained because the out-of-transit intensity for a limb darkened source is an average of the whole projected stellar disk, $< I(\mu) >$. This value corresponds to a particular iso-intensity radius ($r_{\rm mean}$) of the stellar disk, so that $I[\mu(r_{\rm mean})] =< I(\mu) >$. Thus, if the planet crosses the disk with an impact parameter $b < r_{\rm mean}$, the depth of the transit would be larger than in the case of a uniform source. On the contrary, if the impact parameter is $b > r_{\rm mean}$, the planet would occult darker areas of the stellar disk and so the transit would be shallower than in the case of a uniform source. This is clear in Fig. 2.5. In this figure, we show the transit shape for a Jupiter-size planet around a Solar-like star at $a/R_\star = 10$ and with different inclinations (i.e., different impact parameters) for a circular orbit assuming a uniform source and a limb-darkened source. In this case $r_{\rm mean} \sim 0.77$.

[4] http://www.astro.washington.edu/users/agol/transit.html. Please note the correction highlighted for the *transit.pro* routine.

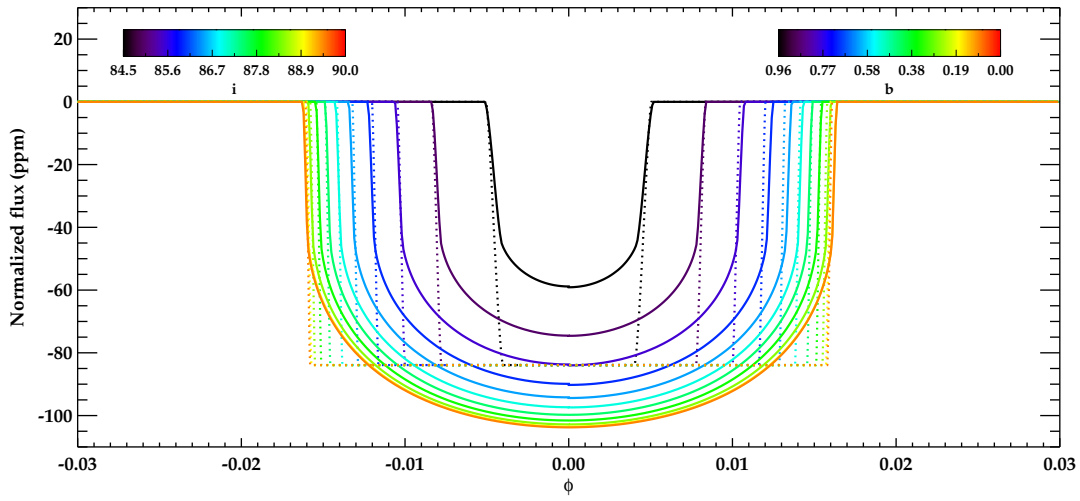

FIGURE 2.5: Dependencies of the transit shape with the inclination for a non-uniform source with the non-linear limb darkening model (solid lines). Dotted lines show the corresponding uniform source model for comparison.

2.2.2 Planetary occultations

When the planet passes behind the star, the light coming from the planet due to the reflection of stellar light and to the thermal emission of the planet (see § 2.3.1) is occulted by the stellar disk. This is reflected in the LC as an additional dip, whose depth depends on the amount of light reflected by the planet (i.e., on the albedo and the size of the planet), and the self-emission of the planet, which depends on its temperature and size. We will see in § 2.3.1 the equations describing this effect along the whole orbital phase of the planet.

The location of the secondary eclipse in the phase-folded LC provides information about the orbital configuration, i.e., the eccentricity, argument of the periastron, and inclination. The expected phase difference between the mid-transit phase (ϕ_c) and the mid-eclipse phase (ϕ_{occ}), $\Delta\phi_{occ}$, is known to be given by Wallenquist (1950)

$$\Delta\phi_{occ} = 0.5 + e\ \cos\omega\ \frac{1 + (1/\sin i)^2}{\pi} \tag{2.13}$$

In the case of circular orbit, $e = 0$ and so the mid-eclipse occurs at $\phi = \theta = 0.5$. For eccentric orbits, if the argument of the periastron is in the range $\omega \in [-\pi/2, \pi/2]$, then the eclipse occurs at $\phi_{ecl} > 0.5$. On the contrary, if $\omega \in [\pi/2, 3\pi/2]$, then $\phi_{ecl} < 0.5$. We leave to § 2.3.1 the analysis of the parameters that describe the shape of a planetary eclipse.

TABLE 2.1: Extrasolar planets with detected light-curve modulations in the out-of-transit time interval. The reference shows the firs reported detection of any of the three effects.

Object	Other name	Reflection	Ellipsoidal ($l = 2$)	Beaming	Ellipsoidal ($l > 2$)	RV	Reference
TrES-2b	KOI-0001.01	✓	✓	✓	✗	✓	Kipping & Bakos (2011)
HAT-P-7b	KOI-0002.01	✓	✓	✓	✗	✗	Mislis et al. (2012), Welsh et al. (2010)
Kepler-8b	KOI-0010.01	✓	✗	✗	✗	✓	Esteves et al. (2013)
KOI-13b	KOI-0013.01	✓	✓	✓	✓	✗	Shporer et al. (2011)
Kepler-12b	KOI-0020.01	✓	✗	✗	✗	✓	Esteves et al. (2014)
Kepler-10b	KOI-0072.01	✓	✗	✗	✗	✓	Esteves et al. (2014)
Kepler-7b	KOI-0097.01	✓	✗	✗	✗	✓	Esteves et al. (2014)
Kepler-43b	KOI-0135.01	✓	✓	✗	✗	✗	Angerhausen et al. (2014)
Kepler-41b	KOI-0196.01	✓	✓	✓	✗	✓	Esteves et al. (2014)
Kepler-412b	KOI-0202.01	✓	✓	✓	✗	✓	Deleuil et al. (2014)
Kepler-76b	KOI-1658.01	✓	✓	✓	✗	✓	Faigler & Mazeh (2011)
Kepler-91b	KOI-2133.01	✓	✓	✓	✗	✓	Lillo-Box et al. (2014a)
Kepler-17b	KOI-0203.01	✗	✓	✓	✗	✗	Angerhausen et al. (2014)
Kepler-40b	KOI-0428.01	✗	✓	✓	✗	✗	Angerhausen et al. (2014)

2.3 Light curve modulations (REBs): the Reflection, Ellipsoidal, and Beaming effects

The study of variability in binary systems has provided the formalism for different effects causing LC modulations. This formulation is now being adapted and applied to the exoplanetary field. In this section, we will study the three most relevant sources of light curve modulation in a planet-star system, the dependency of these variations with the orbital and physical parameters, and their implications in the exoplanetary field.

The high-precision photometers launched to space and installed in ground-based facilities have provided the necessary precision to detect small changes in the brightness of stars. We will study three imprints in the LC of a star hosting a planet: the reflection of stellar light by the planet and its own thermal emission, the photometric effect of the reflex motion of the star due to the presence of a planet orbiting around it (Doppler beaming), and a tidal effect that molds the stellar outer layers (ellipsoidal modulation). In Table 2.1, we summarize several planets in which some or all of these effects have been measured to date.

2.3.1 Planetary light reflection and thermal emission

A critical point when studying the planetary contribution to the light curve modulations is the so-called **phase function**, $\mathbf{\Phi(z)}$, which defines the fraction of the projected disk of the planet

illuminated by the star and visible from the observer's direction. This phase function depends on the so-called z **angle**, defined as the angle between the star and the observer as seen by the planet (i.e., the star-planet-observer angle). There are mainly two definitions of the phase function. The most simple one is to describe this dependency as the cosine of the geometrical angle between the line of sight and the position of the planet on its orbit. This formulation assumes that the received flux is proportional to the projected area of the planet on the plane of the sky. In this case, it is called the **geometrical phase function** and is given by

$$\mathbf{\Phi_{geo}}(z) = \cos z = -\sin i \cos\theta \tag{2.14}$$

The other common formulation assumes that the planet surface is an ideal isotropic reflector, reflecting the light equally to all directions in the half-sphere facing the surface (also known as Lambert sphere, Lambert, 1759, Russell, 1916). This assumption is the most common in the analysis of the LC modulations of extrasolar planets and is called the **Lambertian reflection phase function**

$$\mathbf{\Phi_{Lam}}(z) = 2\frac{(sin|z| + (\pi - |z|)cos|z|)}{\pi} \tag{2.15}$$

with $-\pi \leq z \leq \pi$. As demonstrated by Faigler & Mazeh (2014), expanding $\Phi_{\rm Lam}(z)$ in a Fourier series we find

$$\Phi_{\rm Lam}(z) = -\sin i\ \mathbf{cos\,\theta} + 0.18\sin^2 i\ \mathbf{cos\,(2\theta)} + \text{conts.} + \text{smaller terms} \tag{2.16}$$

Interestingly, the first harmonic is the geometric phase function defined in Eq. 2.14 and the second harmonic has a $\cos(2\theta)$ dependency. This dependency will be discussed in § 2.3.4. For now it is important to highlight that the maximum contribution of the second harmonic will just be as much as 18% larger than just considering the geometric (for inclined orbits this will be even smaller). However, the $\cos(2\theta)$ will be relevant when trying to derive the mass of the perturber.

Once the phase function is defined, we can analyze the direct contribution of the planet to the modulation of the out-of-transit region of the LC. This contribution is due to two main effects:

i.- **Reflected light.** The flux emitted by the host star and reaching the planet is scattered off in part by its day side. The ratio between the incident and the reflected light depends on the observed wavelength and is known as the geometric albedo of the planet, $A_g(\lambda)$. If F_0 is the incident light on the planet, the relative reflected light would be $(F_0 A_g \pi R_p^2)/(4\pi a^2)\Phi(z)$,

where $\Phi(z)$ is the phase function. Hence, the contribution to the LC modulation of the reflected light is:

$$\left(\frac{\Delta F}{F}\right)_{\rm ref} = A_g \left(\frac{R_p}{r}\right)^2 \Phi(z) \equiv A_{\rm ref}\Phi(z) \tag{2.17}$$

The calculation of the geometric albedo is complicated and there is no general simple analytic function describing it. Several authors have worked on this and have demonstrated the dependence of A_g with the wavelength, host metallicity, and star-planet separation (see, for example, Cahoy et al., 2010, Sudarsky et al., 2005). Madhusudhan & Burrows (2012) provided a clear (although complex) scheme to calculate the geometric albedo and phase function, depending on the different forms of scattering in the planetary atmospheres (isotropic, asymmetric, Lambert, or Rayleigh scattering). Kane & Gelino (2010) provided a simple formulation for giant extrasolar planets just depending on the planet-star separation based on the theoretical models of Sudarsky et al. (2005):

$$A_g = \frac{e^{r-1} - e^{-(r-1)}}{5(e^{r-1} + e^{-(r-1)})} + \frac{3}{10}, \tag{2.18}$$

where r is the planet-star separation in astronomical units (AU). We will assume this formulation along this thesis since it has been demonstrated to work with several planets, although it could just be an upper limit to the real value for short-period hot-Jupiter planets since its lower value is $A_g = 0.147$, while many planets have been found to have lower geometric albedos.[5] Note from Eq. 2.17 that if the planet transits the star, the only unknown parameter in this equation is A_g so that one can derive this value by leaving it as a free parameter. Also, if the secondary eclipse of the planet is detected with a depth $\Delta F_{\rm ecl}$ at $z = \pi$, the geometric albedo can be determined from Eq. 2.17, since $\Phi(z = \pi) = 1$ and thus $\Delta F_{\rm ecl} = A_g(R_p/r)^2$ (neglecting the thermal contribution of the planet).

ii.- **Thermal emission.** Since the planet has an effective temperature, it also emits light. The contribution to the total flux of the system from both the day- and night-sides was described by Cowan & Agol (2011) and can be formulated as

$$\left(\frac{\Delta F}{F}\right)_{\rm Th,day} = \Phi(z)\left(\frac{R_p}{R_\star}\right)^2 \frac{e^{hc/\lambda kT_{\rm eff}} - 1}{e^{hc/\lambda kT_{\rm day}} - 1} \tag{2.19}$$

and

$$\left(\frac{\Delta F}{F}\right)_{\rm Th,night} = [1 - \Phi(z)] \left(\frac{R_p}{R_\star}\right)^2 \frac{e^{hc/\lambda kT_{\rm eff}} - 1}{e^{hc/\lambda kT_{\rm night}} - 1} \tag{2.20}$$

[5] In some cases, we will leave the albedo as a free parameter.

where λ is the effective wavelength of the bandpass (e.g., 5750 Å in the case of *Kepler*, see *Kepler* Handbook[6]), and the day and night temperatures are defined by

$$T_{\rm day} = T_0(1-\alpha_{\rm bol})^{1/4}\left(\frac{2}{3}-\frac{5}{12}\epsilon\right)^{1/4} \tag{2.21}$$

and

$$T_{\rm night} = T_0(1-\alpha_{\rm bol})^{1/4}\left(\frac{\epsilon}{4}\right)^{1/4} \tag{2.22}$$

In these equations, T_0 is defined as $T_0 = T_{\rm eff}(r/R_\star)^{-1/2}$, ϵ is the energy circulation across the exoplanet atmosphere (where $\epsilon = 0$ corresponds to the maximum thermal emission), and $\alpha_{\rm bol}$ is the bolometric albedo of the planet. As stated by Mislis et al. (2012), the contribution of the thermal emission for hot-Jupiters at optical wavelengths is much smaller than the reflection component of the modulation, being smaller than 1% for orbits at periods larger than 2 days around stars with $T_{\rm eff} < 6500$ K (see Figs. 3 and 4 in the aforementioned paper).

2.3.2 Ellipsoidal variations

The ellipsoidal variations are tidal effects caused by the gravitational interaction between the companion and the star. In this case, the companion acts as a gravitational perturber to the stellar surface, inducing changes in the spherical shape of the star. In the simplest model, the stellar surface adopts a prolate ellipsoidal shape co-moving with the companion, with the major axis in the direction connecting both objects. During this motion, different amounts of light reach the observer due to the different projected area of the star in the plane of the sky, producing a detectable variability in the received stellar flux.

These changes were theoretically studied by Pfahl et al. (2008), who determined the flux variations due to the stellar oscillations induced by substellar companions. The equations provided in that work assumed Keplerian orbits, slow stellar rotation (so that only perturbations in the radial direction are relevant), spin-orbit alignment (i.e., the orbital plane is perpendicular to the stellar rotation axis), and neglect the flux variation from Doppler shifts arising from wave motions on the stellar surface. Under such assumptions, the fractional variability in the bolometric stellar flux received from the star is given by

$$\frac{\delta J}{J} = \epsilon\sum_{l=2}^{+\infty}\left(\frac{R_\star}{a}\right)^{l-2}\left(\frac{1+e\cos\nu}{1-e^2}\right)^{l+1} f_l P_l(\cos\psi_0) \tag{2.23}$$

[6] https://archive.stsci.edu/kepler/manuals/KSCI-19033-001.pdf

where

$$\epsilon = \frac{M_p}{M_\star}\left(\frac{R_\star}{a}\right)^3, \tag{2.24}$$

and

$$f_l = (2 - \lambda_l)b_l - c_l \tag{2.25}$$

The terms b_l and c_l are functions of the linear LD coefficients (see Eqs. 9 in Pfahl et al., 2008), and $\lambda_l = l+2$ is a good approximation for radiative stars. For $l = 2$ and $l = 3$, the limb darkening parameters can be written as:

$$b_2 = \frac{1+\gamma}{20(3-\gamma)} \qquad b_3 = \frac{\gamma}{4(3-\gamma)} \tag{2.26}$$

$$c_2 = \frac{3(1+3\gamma)}{10(3-\gamma)} \qquad c_3 = \frac{3\gamma}{3-\gamma} \tag{2.27}$$

where γ is the linear limb darkening coefficient, tabulated by, e.g., Claret & Bloemen (2011) for different bands. In Eq. 2.23, $P_l(\cos\psi_0)$ are the well-known Legendre polynomials that can be written for the second ($l = 2$) and third ($l = 3$) harmonics as

$$\begin{aligned} P_2 &= \frac{1}{4}\left[-(3\cos^2 i - 1) + 3\sin^2 i\,\mathbf{cos\,2\theta}\right] \\ P_3 &= \frac{1}{8}\sin i\left[-3(5\cos^2 i - 1)\mathbf{cos\,\theta} + 5\sin^2 i\,\mathbf{cos\,3\theta}\right] \end{aligned} \tag{2.28}$$

To illustrate these equations, we plot in Fig. 2.6 the contributions of the second and third harmonics for several orbital configurations $\{e, \omega\}$ (the same as in Fig. 1.11). In this example, we assume a Jupiter-mass planet around a solar-mass star with $a/R_\star = 15$, assuming $\gamma = 3/5$, and an edge-on orbit (i.e., $i = \pi/2$). Also, in Fig. 2.7 we show the equipotential surface filled by the external layers of the star as the companion moves along the orbit.

Several interesting conclusions about the importance of the different harmonics can be extracted:

- The predominant harmonic is $l = 2$ since $R_\star/a < 1$ and the exponent increases as $l - 2$. According to the corresponding Legendre polynomial, this harmonic goes as $\cos 2\theta$. In the circular case, this implies a modulation of the stellar flux with a periodicity of $P_{\rm orb}/2$

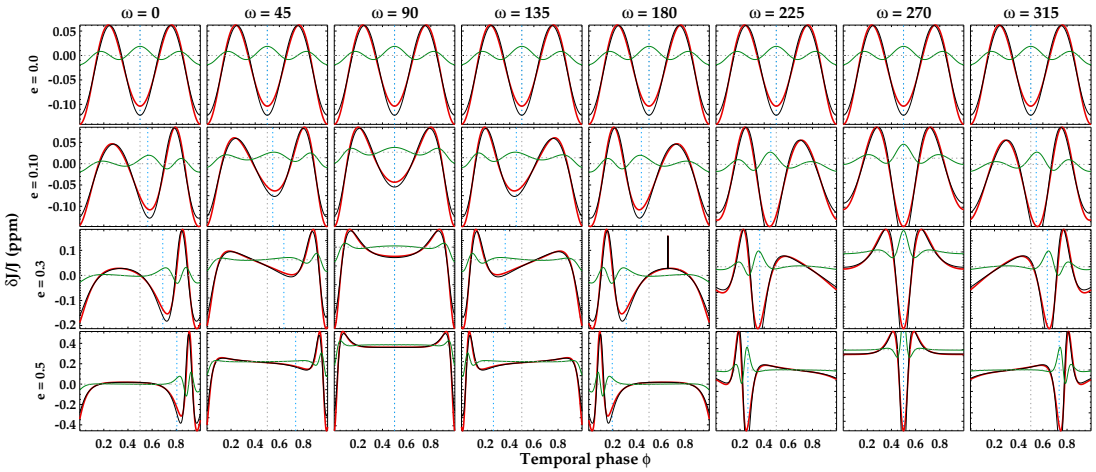

FIGURE 2.6: Ellipsoidal variations for different orbital configurations $\{e, \omega\}$ (the same as in Fig. 1.11) of a Jupiter-mass planet around a solar-mass star with $a/R_\star = 5$, assuming $\gamma = 3/5$, and an edge-on orbit (i.e., $i = \pi/2$). The red thick line represents the total contribution of the second (black) and third (green) harmonics. The blue vertical line marks the location of the planet in opposition, while the vertical gray line marks the mid-period.

and having its maxima at $\theta = \phi = 0.25$ and $\theta = \phi = 0.75$ (see Fig. 2.6). For non-circular orbits, the modulation will be asymmetric in the phase-folded light curve.

- The third harmonic ($l = 3$) includes dependencies with the geometrical phase of the companion as $\cos\theta$ and $\cos 3\theta$. This harmonic becomes more important as $a/R_\star$ decreases (i.e., as the planet is closer to the star). As stated by Pfahl et al. (2008), the third harmonic also becomes relevant in non-circular orbits.

- In the particular case of circular orbits, the third harmonic increases the flux at $\theta = \phi = 0.5$, while decreasing at $\theta = \phi = 0.0$ (i.e., during the primary eclipse). Added to this, the two maxima are slightly shifted in phase towards $\phi < 0.25$ and $\phi > 0.75$.

- Interestingly, the ellipsoidal variations can be detected at any orbital inclination (even in face-on orbits) as far as the orbit is eccentric. This can be useful to detect non-transiting companions in near face-on orbits ($i \sim 0°$).

- Asymmetries from the prolate ellipsoid appear when the third harmonic is included (see Fig, 2.7). They are clearly visible at $\theta = 90°$ and $\theta = 270°$, where the region of the star facing the companion is more inflated than the opposite side (like a water drop in free falling).

Based on this theoretical formulation, different formalisms have been proposed to model the observed variability of candidate host stars with different properties. In Table 2.2 we summarize the most used and the assumptions in each case. From this table, it is somehow clear the difference in both amplitude and phase dependency proposed by the different authors.

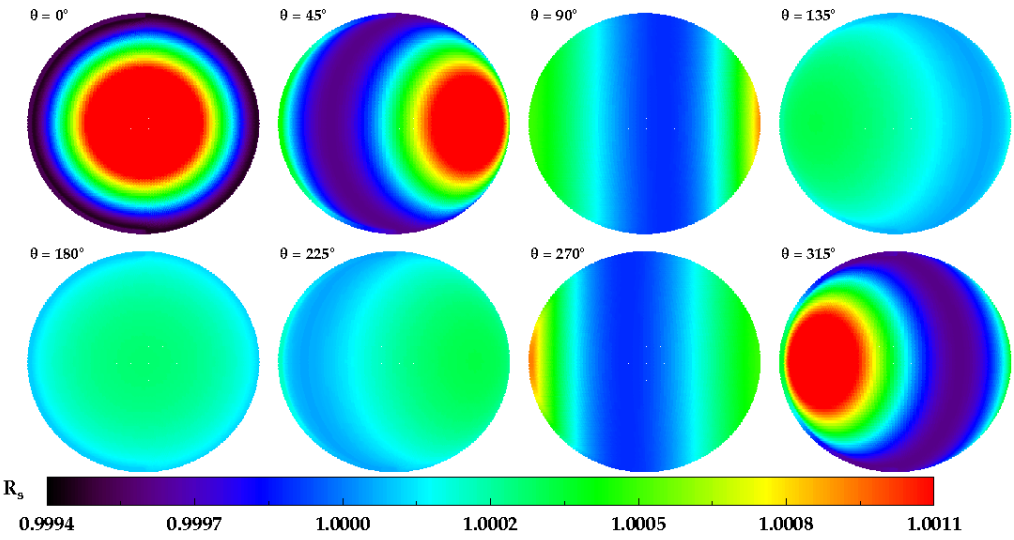

FIGURE 2.7: Ellipsoidal shape of the stellar outer layers at different positions of the companion along its eccentric orbit ($e = 0.3$, $\omega = 90°$, $i = \pi/2$), including second and third harmonics. The color-code represents the radius of the star at the different latitudes and longitudes, being $R_\star = 1$ the radius if there was no companion in the system.

TABLE 2.2: Ellipsoidal equivalences between the different formalisms

Author	Amplitude ($\Delta F_{\rm ellip}/F$)	Phase dependency	Other Factors
Faigler & Mazeh (2011)	$-\alpha_e \frac{M_p}{M_\star}\left(\frac{R_\star}{a}\right)^3 \sin^2(i)$	$\cos(2\cdot 2\pi\phi)$	
Mislis et al. (2012)	$\beta \frac{M_p}{M_\star}\left(\frac{R_\star}{d}\right)^3 \sin^3(i)$	$\lvert\sin\theta\rvert$	$\beta = \frac{\log(GM_\star/R_\star^2)}{\log T_{\rm eff}}$
Barclay et al. (2012)	$-\alpha_e \frac{M_p}{M_\star}\left(\frac{R_\star}{a}\right)^3 \sin^2(i)$	$\cos(2\cdot 2\pi\phi - l)$	$l \equiv$ time lag
Kane & Gelino (2012)	$\beta \frac{M_p}{M_\star}\left(\frac{R_\star}{r}\right)^3$	$[\cos^2(\omega+f) + sin^2(\omega+f)\cos^2 i]^{1/2}$	β = gravity darkening
Esteves et al. (2013)	$\alpha_e \frac{M_p}{M_\star}\left(\frac{R_\star}{a}\right)^3 \sin^2(i)$	$[\cos(2\cdot 2\pi\phi) + f_1\cos(2\pi\phi) + f_2\cos(3\cdot 2\pi\phi)]$	f_1,f_2 constants (Eq.9,10)
Quintana et al. (2013)	$\alpha_e \frac{M_p}{M_\star}\left(\frac{R_\star}{a}\right)^3 \sin^2(i)$	$\cos(2\cdot 2\pi\phi)$	**For circular orbit
Lillo-Box et al. (2014a)	$-\alpha_e \frac{M_p}{M_\star}\left(\frac{R_\star}{d}\right)^3 \sin^2(i)$	$\cos 2\theta$	$\alpha_e = 0.15\frac{(15+u)(1+g)}{3-u}$

According to the general formulation explained above and derived by Pfahl et al. (2008) with the corresponding assumptions, the ellipsoidal variations should be modeled as

$$\left(\frac{\Delta F}{F}\right)_{\rm ellip} = \frac{M_p}{M_\star}\left(\frac{R_\star}{d}\right)^3 \overbrace{\left(\frac{1}{4}f_2\left[-(3\cos^2 i - 1) + 3\sin^2 i\ \boldsymbol{cos2\theta}\right] + \right.}^{l=2} \underbrace{\left. + \frac{1}{8}\left(\frac{R_\star}{d}\right) f_3 \sin i\left[-3(5\cos^2 i - 1)\boldsymbol{\cos\theta} + 5\sin^2 i\ \boldsymbol{\cos 3\theta}\right]\right)}_{l=3} \tag{2.29}$$

By neglecting third order terms (which can be highly inaccurate for specific cases such as KOI-13.01, see discussion above) and expanding the remaining equation, we find

$$\left(\frac{\Delta F}{F}\right)_{\rm ellip} \approx \left[\frac{3f_2}{4}\frac{M_p}{M_\star}\left(\frac{R_\star}{d}\right)^3 \sin^2 i\ \boldsymbol{\cos 2\theta}\right] - \left[\frac{M_p}{M_\star}\left(\frac{R_\star}{d}\right)^3 \frac{f_2}{8}(3\cos^2 i - 1)\right] \tag{2.30}$$

In the case of near circular orbits $d \approx a$ and so the second term of this equation is just constant along the orbit of the companion, being thus negligible for this problem. However, we must warn that **this term should be taken into account in non-circular orbits**. The simple approximation for small eccentricity orbits can then be written as

$$\left(\frac{\Delta F}{F}\right)_{\rm ellip} \approx \alpha_e \frac{M_p}{M_\star}\left(\frac{R_\star}{d}\right)^3 \sin^2 i\ \boldsymbol{\cos 2\theta} \equiv A_{\rm ellip}\ \boldsymbol{\cos 2\theta} \tag{2.31}$$

where the term α_e includes the dependency with the limb darkening and other constants. This value is usually written in the form proposed by Morris & Naftilan (1993)

$$\alpha_e = 0.15\frac{(15+u)(1+g)}{3-u} \tag{2.32}$$

where u is the linear limb darkening coefficient and g is the gravity darkening coefficient. Both values can be calculated for the *Kepler* band from a trilinear interpolation of the effective temperature, surface gravity, and metallicity in the tabulated values by Claret & Bloemen (2011).

As shown in Table 2.2, most of the authors use this definition to model the ellipsoidal term (some of them use other definitions of the gravity and limb darkening[7]). The phase dependence, however, is more controversial, with some of the authors assuming circular orbits ($\phi = \theta$) and others using more complicated dependencies (e.g., Kane & Gelino, 2012, Mislis et al., 2012).

[7]Also, Mislis et al. (2012) used a $\sin^3 i$ dependence which is intriguing and could just be a mistake in their formula.

We could not find neither theoretical demonstrations for these dependencies nor references in these works explaining them. On the other hand, Barclay et al. (2012) introduced a time lag in the phase dependence which includes the possibility of a misalignment between the planet-star direction and the center of the tidal bulge.

According to the demonstrations provided in this section, we use along this dissertation Eq. 2.31 for systems with small eccentricities and Eq. 2.30 for blind surveys or known highly eccentric orbits. Note that in cases where additional harmonics are relevant, they will show up in the residuals of the model fit as a clear modulation (see, for instance the case of KOI-13.01 in Mazeh et al., 2012).

2.3.3 Doppler beaming

The reflex motion of the star around the center of masses of a planetary (or multiple) system produces a small shift of its spectrum towards longer wavelengths when the star moves away from the observer and towards the blue when it approaches the observer. This is the so-called Doppler effect, widely used to measure the radial velocity (and thus the mass) of planetary and multiple systems (see Chapter 4 andsection § 1.1.2). Its photometrical imprints rises when we observe a star at a particular wavelength range (photometric band). The spectral energy distribution of the star is thus bluer or redder according to the position of the companion along its orbit. As a consequence, the amount of energy falling inside the bandpass is different depending on the position of the companion.

Loeb & Gaudi (2003) studied this effect and provided the formulation for non-relativistic motions of the central star. Following this work, a star moving with a radial velocity v_r relative to the observer obtains a Doppler shift to its bolometric flux equal to $F = F_0(1 + 4 \cdot v_r/c)$, being F_0 the flux emitted in the absence of motion. Assuming a power law dependency of the emitted light with the frequency as $F_{\nu,0} \propto \nu^{\Gamma}$, the emitted flux at a particular frequency ν is described by

$$F_\nu = F_{\nu,0}\left[1 + (3 - \Gamma)\frac{\mathrm{v}_r}{c}\right] \implies \left(\frac{\Delta F}{F}\right)_{\mathrm{beam}} = (3 - \Gamma)\,\frac{\mathrm{v}_r}{c} \tag{2.33}$$

The radial velocity of a star around the center of masses of the planet-star system is given by:

$$\mathrm{v}_r(t) = V_{\mathrm{sys}} + K\,[\cos(\nu(t) + \omega) + e\ \cos\omega] \tag{2.34}$$

where V_{sys} is the systemic velocity of the system and K is the radial velocity semi-amplitude, given by

$$K = 28.4\frac{m}{s} \times \left(\frac{P}{1yr}\right)^{-\frac{1}{3}} \frac{M_p \sin i}{M_{\rm Jup}} \left(\frac{M_\star}{M_\odot}\right)^{-\frac{2}{3}} \frac{1}{\sqrt{1-e^2}} \tag{2.35}$$

Since $\nu(t) + \omega - \pi/2 = \theta(t)$ and the factor $K\, e\, \cos\omega$ in Eq. 2.33 is constant under the assumption that the orbit is neither precessing nor being circularized (i.e., ω and e are constants), the radial velocity of the star as a function of time can then be re-written as

$$\mathrm{v}_r(t) = \text{const.} + K \sin\theta \tag{2.36}$$

Thus, the beaming effect, neglecting constant terms, is described as

$$\left(\frac{\Delta F}{F}\right)_{\rm beam} = (3-\Gamma)\frac{K}{c}\sin\theta \tag{2.37}$$

The coefficient Γ can be approximated as $\Gamma = d\mathrm{Ln}F_{\nu 0}/d\nu_0$. If we assume a blackbody of temperature $T_{\rm eff}$ for the star, this coefficient can be approximated by

$$\Gamma(\nu) \approx \frac{e^x(3-x)-3}{e^x-1} \tag{2.38}$$

where $x = h_P\nu/k_{\rm boltz}T_{\rm eff}$.

A similar but more general expression was provided by Bloemen et al. (2011), who formulated a complete expression to accurately calculate the beaming effect

$$F_\lambda = F_{\lambda,0}\left[1 + B\frac{v_r}{c}\right] \longrightarrow \left(\frac{\Delta F}{F}\right)_{\rm beam} = B\,\frac{K}{c}\sin\theta \;\equiv\; A_{\rm beam}\;\sin\theta \tag{2.39}$$

with B being the beaming factor defined as $B = 5 + d\mathrm{Ln}F_\lambda/d\mathrm{Ln}\lambda$. In the case of the *Kepler* observations, they use a photon weighted bandpass-integrated beaming factor, defined as

$$< B >= \frac{\int \epsilon_\lambda \lambda F_\lambda B d\lambda}{\int \epsilon_\lambda \lambda F_\lambda d\lambda} \tag{2.40}$$

where ϵ_λ is the response function of the observing bandpass.

By comparing Eq. 2.37 and Eq. 2.39, and defining $B_\Gamma \equiv (3-\Gamma)$, we can identify that $B_\Gamma = B$. At this point, it is interesting to compare the beaming factors obtained by the different approaches, so that we can test the different validity ranges of the different approximations and extract some conclusions:

- First, if we assume black body (BB) emission from the host (i.e., $F_\lambda = F_\lambda^{BB}$), the obtained beaming factor from Eq. 2.40 (B_{BB}) should be similar than B_Γ. The red line in Fig. 2.8 represents this comparison in a range of effective temperatures from 3000-10000 K. As expected, the hotter the star, the better is the blackbody approximation (i.e., $B_\Gamma/B_{BB} \approx 1$). However, it is important to note that differences of 5-10% in the beaming factor can arise from using B_Γ or B_{BB}, even though both of them assume black body energy distribution.

- The more correct and complete way of calculating the beaming factor turns out to be Eq. 2.40 and assuming synthetic models of the host star (F_λ, according to its physical parameters). This would take the effect of spectral lines and molecular bands into account. In order to compare the three formulations for the beaming factor (i.e., B_Γ, B_{BB}, and $< B >$), we have computed B_Γ and B_{BB} for the planets studied in Esteves et al. (2014) for which the authors provided the $< B >$ values (see their Table 3), and the effective temperatures. The results are presented in Fig. 2.8. Interestingly, we get in all 13 cases analyzed with $T_{\rm eff} < 7000$ K that the factor B_Γ is 17% larger than $< B >$ (gray filled circles). The blackbody approximation of Eq. 2.40 also overestimates the value of the beaming factor by $\gtrsim$10% for this range of temperatures.

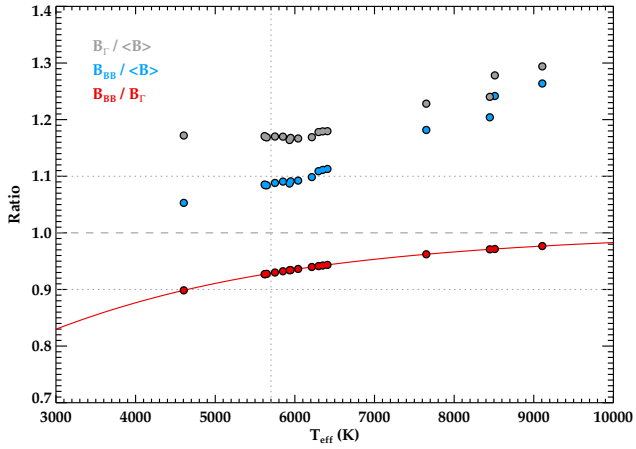

FIGURE 2.8: Comparison of the different approximations of the beaming factor.

We thus conclude that blackbody assumption in the range $T_{\rm eff} = 3000 - 10000$ K overestimates the beaming factor by more than 17%. The use of B_{BB} (Eq. 2.40) provides results closer to $< B >$ than B_Γ (Eq. 2.38). We thus hardly recommend to calculate the beaming factor as $< B >$. Other approximations can affect the determination of the planetary mass by more than 10%.

In Table. 2.3, we present the different formulations used by different authors (apart from those defined above). As shown, most of the works agree in both the amplitude and the phase dependency. In the case of Mislis et al. (2012), the additional term in the phase dependency is just a constant that is irrelevant in this problem, since we work with normalized (rather than absolute) photometry.

TABLE 2.3: Beaming effect. Equivalences between the different formalisms

Reference	Amplitude $(\Delta F_{\rm ellip}/F)$	Phase dependency	Other Factors
Faigler & Mazeh (2011)	$\alpha_{beam} 4\frac{K}{c}$	$\sin(2\pi\phi)$	α_{beam} = [0.8, 1.2], calculated from bandpass
Mislis et al. (2012)	$(3-\Gamma)\frac{K}{c}$	$\sin\theta + e\sin(\pi/2-\omega)$	Γ = Eq.2.38 ; K =Eq.2.35
Barclay et al. (2012)	$\alpha_b \frac{K}{c}$	$\sin(2\pi\phi)$	α_b = Eq.2.40 ; $K = \left(\frac{2\pi G}{P}\right)^{1/3} \frac{M_p \sin i}{M_\star^{2/3}}$
Kane & Gelino (2012)	$(3-\Gamma)\frac{K}{c}$		
Esteves et al. (2013)	$\alpha_b \frac{K}{c}$	$\sin(2\pi\phi)$	α_b = Eq.2.40
Quintana et al. (2013)	$-\alpha_{dop} 4\frac{K}{c}$	$\sin(2\pi\phi)$	$K = \left(\frac{2\pi G}{P}\right)^{1/3} \frac{M_p \sin i}{M_\star^{2/3}}$; α_{dop} from Loeb et al. (2003)
Lillo-Box et al. (2014a)	$(3-\Gamma)\frac{K}{c}$	$\sin\theta$	Γ = Eq.2.38; K =Eq.2.35

2.3.4 Interdependencies and relative contributions

When modeling the out-of-transit LC taking into account all these effects, important interdependencies come out if their amplitudes are similar. Thus, the selection of the formalisms used for each different case can be of key importance when deriving the properties of the companion. In the following, we describe the most important interdependencies between the three effects:

- **Reflection vs. ellipsoidal: Lambertian versus geometrical phase function.-** Both the ellipsoidal and the second-order term of the Lambertian phase function in the reflection effect (see Eq. 2.16) share a $\cos(2\theta)$ dependency. Neglecting this second-order term (or similarly, using the geometrical phase function, $\Phi_{\rm geo}$, in a Lambertian sphere) when the amplitudes of both effects are similar, would **overestimate** the mass of the companion from the ellipsoidal contribution. In this case, one would attribute all $\cos(2\theta)$ dependency to ellipsoidal variations, while part of them are due to the reflection effect. Mislis et al. (2012) demonstrated that the mass of HAT-P-7b is 0.67 $M_{\rm Jup}$ smaller (larger) than the true mass if one uses the geometrical (Lambertian) phase function. The residuals between the Lambertian and the geometrical phase functions are represented in panel (a) of Fig. 2.9. The residuals have the same shape as the ellipsoidal effect.

- **Reflection vs. ellipsoidal: the third harmonic of the ellipsoidal effect.-** Similarly to the previous interdependency, the third harmonic of the ellipsoidal variation ($l = 3$) has a $\cos\theta$ dependency, as it does the reflection effect. In cases where this is important as compared to the reflection amplitude, neglecting the third harmonic could underestimate the effect of the planetary reflection.

- **Reflection vs. beaming: Super-rotation.-** In the few cases where the beaming and ellipsoidal modulations have been measured (see Table. 2.1), there is a clear discrepancy between the mass of the companion derived by each of the two effects. The comparison between the RV semi-amplitude (K) derived by the beaming modulation and the one spectroscopically measured suggests an inflation of the beaming value (thus overestimating the mass of the companion). Faigler & Mazeh (2014) proposed that this effect could be due to a phase shift of the reflection/emission modulations (Eq. 2.17 and Eq. 2.19-2.20), due to equatorial super-rotation (SR) of the hot-Jupiter companion. The super-rotating model was proposed by Showman & Guillot (2002) and confirmed by Knutson et al. (2007, 2009) with Spitzer observations. They showed that tidally locked planets can develop a fast eastward jet stream from the equator to latitudes of typically $20° - 60°$, producing a phase shift of the thermal emission phase curve of the planet. The simplest way of accounting for this effect is to assume an angle shift $\delta_{\rm SR}$ and substitute $\theta \rightarrow \theta + \delta_{\rm SR}$. In practice, since $\cos(\theta + \delta_{\rm SR}) = \cos\delta_{\rm SR}\ \mathbf{\cos\theta} + \sin\delta_{\rm SR}\ \mathbf{\sin\theta}$, this angle shift includes a new term with the same dependency as the Doppler beaming effect. Thus, if present and not accounted for, we would be over-estimating (or inflating) the beaming effect and thus the derived mass of the companion. Added to this, if the Lambertian phase function is assumed, a new dependency with $\sin 2\theta$ appears in the reflection effect. As described in Faigler & Mazeh (2014), the new phase functions would be

$$\Phi^{\rm SR}_{\rm geo}(z) = -\sin i \left[\cos\delta_{\rm SR}\ \mathbf{\cos\theta} + \sin\delta_{\rm SR}\ \mathbf{\sin\theta}\right] \tag{2.41}$$

$$\Phi^{\rm SR}_{\rm Lam}(z) \approx \Phi^{\rm SR}_{\rm geo}(z) + 0.18\sin^2 i \left[\cos(2\delta_{\rm SR})\ \mathbf{\cos(2\theta)} + \sin(2\delta_{\rm SR})\ \mathbf{\sin(2\theta)}\right] \tag{2.42}$$

In Table 2.4, we summarize the dependencies of the different effects with the geometrical angle θ assuming or neglecting super-rotation and using the two phase functions fully described in § 2.3.1. In Fig. 2.9 we have computed the models for fixed amplitudes and inclination ($A_{\rm ellip} = 60$ ppm, $A_{\rm ref} = 30$ ppm, $A_{\rm beam} = 10$ ppm, $i = 80°$) for the different formulations showed in Table 2.4. We plot the residuals between different pairs of formulations assuming different phase shifts for the super-rotation effect ($\delta_{\rm SR} = 0, 0.1, 0.2$). In panel (a), we clearly see the interdependency between reflection and ellipsoidal modulations explained above, when assuming a wrong phase function. The inclusion of the super-rotation in panel (b), adds a phase shift in the residuals but still with the same shift and amplitude. Panels (c) and (d) show the inflation of the beaming effect when neglecting the super-rotation effect previously explained.

TABLE 2.4: Amplitudes of the different angle dependencies for the REB modulations (adapted from Table 1 in Faigler & Mazeh, 2014). We have just taken into account the second harmonic in the ellipsoidal effect. Note: SR = super-rotation.

$\Phi(z)$	SR?	$\cos\theta$	$\sin\theta$	$\cos 2\theta$	$\sin 2\theta$
Geometrical	N	$-A_{\rm ref}$	$A_{\rm beam}$	$-A_{\rm ellip}$	0
Lambert	N	$-A_{\rm ref}$	$A_{\rm beam}$	$-A_{\rm ellip}+$	0
				$+0.18\,A_{\rm ref}\,\sin i$	
Geometrical	Y	$-A_{\rm ref}\cos\delta_{\rm SR}$	$A_{\rm beam}+$	$-A_{\rm ellip}$	0
			$+A_{\rm ref}\sin\delta_{\rm SR}$		
Lambert	Y	$-A_{\rm ref}\cos\delta_{\rm SR}$	$A_{\rm beam}+$	$-A_{\rm ellip}+$	$-0.18\,A_{\rm ref}\,\sin i\sin 2\delta_{\rm SR}$
			$+A_{\rm ref}\sin\delta_{\rm SR}$	$+0.18\,A_{\rm ref}\,\sin i\cos 2\delta_{\rm SR}$	

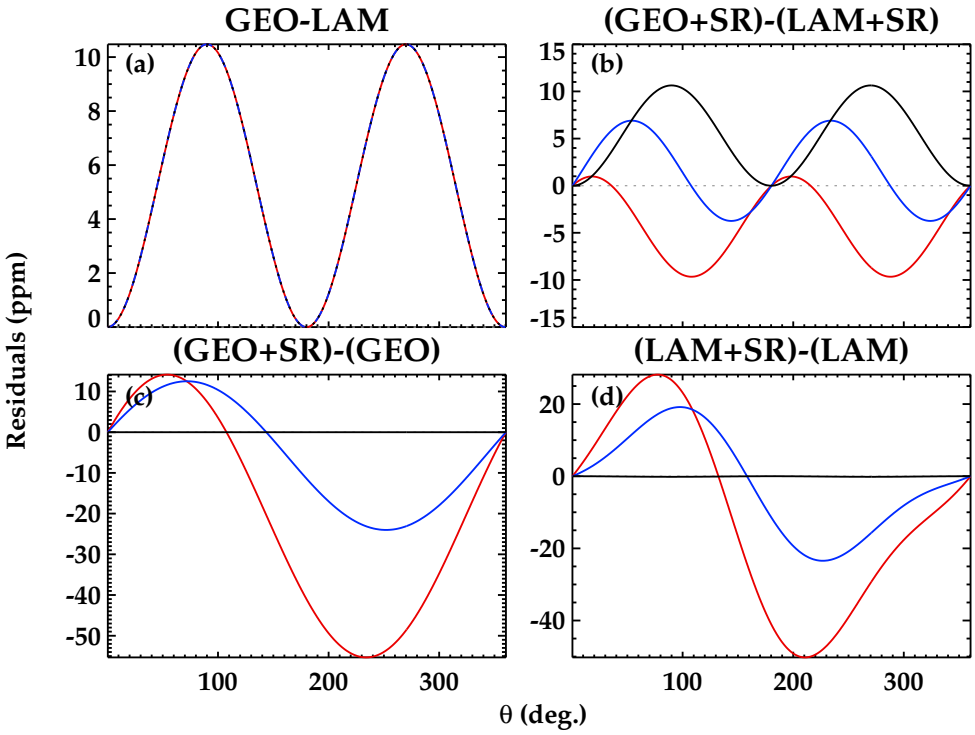

FIGURE 2.9: Differences between the different formulations in Table 2.4 for models with fixed amplitudes and orbital inclination ($A_{\rm ellip}$ = 60 ppm, $A_{\rm ref}$ = 30 ppm, $A_{\rm beam}$ = 10 ppm, i = 80°). The title of each panel describes the difference computed. We have used three different phase shifts for the super-rotation effect: $\delta_{\rm SR}$ = 0 (black), $\delta_{\rm SR}$ = 0.1 (blue), and $\delta_{\rm SR}$ = 0.2 (red), in phase units.

2.4 Asteroseismology

We have used asteroseismology in part of the work presented in this dissertation.[8] Cool stars ($T_{\rm eff} < 7000$ K) with a convective envelope may show solar-like oscillations, that is, pressure oscillation modes stochastically excited by turbulent motions (e.g., Christensen-Dalsgaard, 2012). These are acoustic modes of high radial order. The long timespan and high-precision photometry obtained by CoRoT[9] and *Kepler* has increased the possibilities of detecting and modeling these stellar pulsations, which provide invaluable information about the stellar interiors and physical properties of the star such as surface gravity, effective temperature, mass, radius, or age.

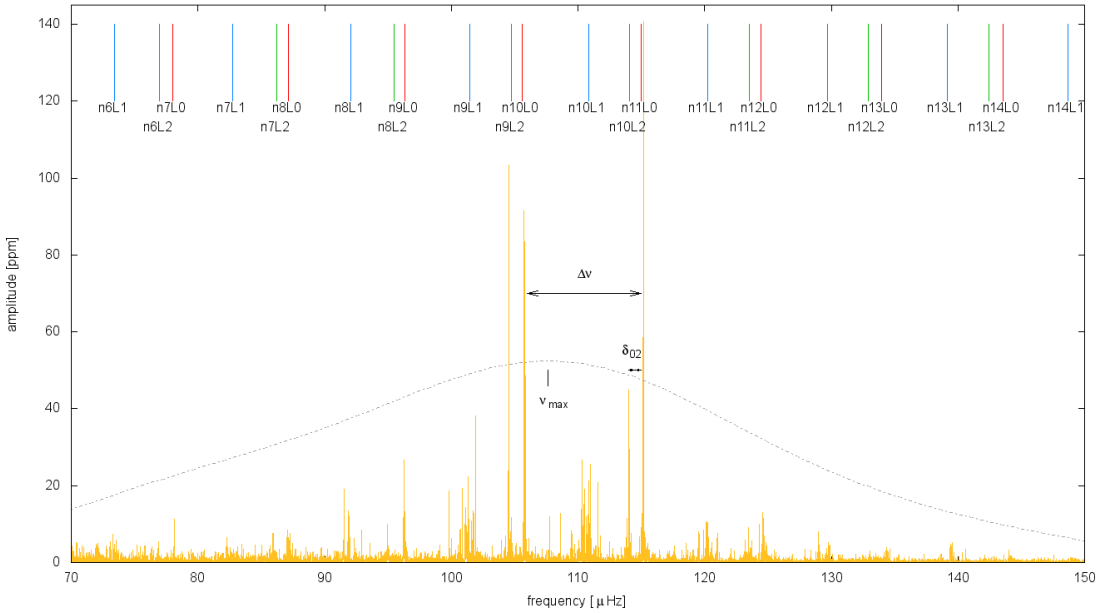

FIGURE 2.10: Power spectrum of the *Kepler* data of Kepler-91 showing the frequency at maximum power ($\nu_{\rm max}$), and the frequency separation ($\Delta\nu$).

The power spectrum of the photometric data in this type of stars presents a regular pattern modulated by a Gaussian shape and are characterized by two global parameters (see Fig. 2.10): the **frequency at maximum power** (thereafter $\nu_{\rm max}$) and the **frequency separation** ($\boldsymbol{\Delta\nu}$) between consecutive radial order (n) modes with the same angular degree (ℓ), see Fig. 2.10. These quantities are linked via **scaling relations** ($\Delta\nu \propto \rho^{1/2}$, $\nu_{\rm max} \propto g/T_{\rm eff}^{1/2}$) to global stellar parameters such as total mass, radius, and effective temperature (Belkacem et al., 2011, Brown et al., 1991, Kjeldsen & Bedding, 1995, Ulrich, 1986). These relations read as

$$M_\star = \left(\frac{\nu_{\rm max}}{\nu_{\rm max,\odot}}\right)^3 \left(\frac{\Delta\nu_\odot}{\Delta\nu}\right)^4 \left(\frac{T_{\rm eff}}{T_{\rm eff,\odot}}\right)^{3/2} \tag{2.43}$$

[8] This section has been adapted from Lillo-Box et al. (2014a). The asteroseismic analysis of this paper was lead by Joesfina Montalbán.

[9] The CoRoT space-based telescope obtained long baseline precise photometry (down to 100 ppm) for more than 150 000 stars (see Schneider et al., 1998).

$$R_\star = \frac{\nu_{\max}}{\nu_{\max,\odot}} \left(\frac{\Delta\nu_\odot}{\Delta\nu}\right)^2 \sqrt{\frac{T_{\rm eff}}{T_{\rm eff,\odot}}}. \tag{2.44}$$

These equations allow us to derive the stellar mass and radius (once we have an estimate of the effective temperature) independently of the chemical composition and of stellar modeling. They are, however, approximate (empirical) relations and must be calibrated. The validity of $\Delta\nu \propto \rho^{1/2}$ can be tested with predictions from models, as done by White et al. (2011), Miglio et al. (2013a), and Mosser et al. (2013). The second relation cannot be tested with models, and only a theoretical justification has been proposed by Belkacem et al. (2011). Nevertheless, comparisons between global parameters derived from seismology and those obtained from interferometry and spectroscopy of solar-like pulsators indicate that $\nu_{\max}$ is a very good proxy of the surface gravity and stellar radius (Huber et al., 2012, Miglio et al., 2012, Morel & Miglio, 2012, White et al., 2013). These studies suggest that, in the analyzed domain, Eqs. 2.43 and 2.44 can provide stellar radius and mass with an uncertainty of 4% and 10%, respectively (Huber et al., 2013, and references therein), and that is a significant improvement over the classical spectroscopic/photometric approach. This is crucial in the determination of the planet properties since all techniques provide parameters scaled to the stellar ones (e.g., $R_p/R_\star$ in the case of transits, or $M_p \sin i/M_\star$ for the radial velocity).

These scaling relations are being extensively used in the framework of stellar population studies (Hekker et al., 2011, 2009, Miglio et al., 2013b, 2009, Mosser et al., 2011, 2010) and of exoplanet parameter determination (see review by Moya, 2011) to characterize dwarfs and red giant solar-like pulsators detected by CoRoT and *Kepler*. In particular, scaling relations have been recently applied to derive the stellar parameters of 66 *Kepler* planet-host candidates presenting solar-like oscillations (Huber et al., 2013). Although the information from global parameters $\Delta\nu$ and $\nu_{\max}$ is extremely valuable for studying planetary systems, better and additional constraints (for instance stellar age[10]) can be expected from the modeling of **individual frequencies**.

For solar-like oscillations, the power spectrum shows a χ^2 statistic distribution with two degrees of freedom. Then, a maximum likelihood estimation (MLE) is applied, a method widely used in determining p-mode parameters in the Sun and solar-like stars. Following Anderson et al. (1990), the likelihood function used for the MLE is

$$S = \sum [M_i + \frac{O_i}{M_i}] \tag{2.45}$$

where O_i are the data and M_i is the model, composed of Lorentzian profiles:

[10]The determination of the age was crucial, for instance, in the case of HR 8799 to determine the properties of the directly imaged companion (see Moya et al., 2010).

$$M_i = \sum \frac{A_i(\Gamma_i/2)^2}{[(\nu - \nu_i)^2 + (\Gamma_i/2)^2]} + N(\nu), \tag{2.46}$$

being ν_i the oscillation frequency, Γ_i the line width, A_i the amplitude of each Lorentzian profile, and $N(\nu)$ the noise. Here, $N(\nu)$ is fitted using two components: constant white noise modeling the photon noise (W), and one Harvey-like profile (Harvey, 1985), which reproduces the convective contribution to the background, typically granulation:

$$N(\nu) = \frac{A}{[1 + (\nu/B)^\alpha]} + W \tag{2.47}$$

where A is related with the amplitude of the granulation, B has its characteristic timescale, and α is a positive parameter characterizing the slope of the decay.

The detailed properties of the oscillation modes depend on the stellar structure. In red giant stars, because of the contraction of the inert He core and the expansion of the hydrogen rich envelope, modes with frequencies in the solar-like domain can propagate in the gravity and acoustic cavities (internal and external regions respectively), thus presenting a mixed gravity-pressure character (Christensen-Dalsgaard, 2004, Dupret et al., 2009, Dziembowski et al., 2001, Montalbán et al., 2010). While the solar-like spectra of main sequence pulsators are mainly made of a moderate number of acoustic modes for each angular degree, those of red giants can present a large number of non-radial g-p mixed modes in addition to radial modes.

2.5 Forthcoming and future instrumentation

The future of high-precision photometry is guaranteed with the forthcoming space-based missions *CHEOPS*, *TESS*, *PLATO*. In Table 2.5, we summarize the expected precisions and main characteristics of these missions as compared to *Kepler* and CoRoT. These missions have different goals and strategies, so they will mainly look for planets in different niches or will characterize known systems.

The *CHEOPS* mission (Broeg et al., 2013) will have the main goal of serving as follow-up of known planetary systems, characterizing their atmospheres and detecting new components in the system. The main goals are the characterization of super-Earths, unveil the physics and formation process of Neptunes, and build a collection of "golden-targets" for exoplanetology. The *TESS* mission (Ricker et al., 2014) will be a short-duration all-sky survey visiting multiple fields during 1 month each. With these characteristics, *TESS* will be a planet hunter that will provide numerous candidates (from Earth to sub-Neptunes) in close orbits (< 30 days) around bright stars for subsequent ground-based follow-up. In the future, the *PLATO* mission (Rauer

TABLE 2.5: Main characteristics of the most important past, current, and forthcoming space-based missions with high-accurate photometers.

Mission	Launch	Precision	Dur.	V mag	Strategy
CoRoT	12/2006	~ 40 ppm / 6hr / 11.5th mag	6 yr	6-16	2 ecliptic fields
Kepler	03/2009	~ 10 ppm / 6hr / 10th mag	4 yr	7-17	*Kepler* field
K2	03/2014	~ 50 ppm / 6hr / 12th mag	2 yr	7-17	Ecliptic fields (80 days/field)
CHEOPS	~2017	~ 20 ppm / 6hr / 9th mag	3.5 yr	6-12	Follow-up
TESS	~2017	~ 60 ppm / 6hr / 9th mag	2 yr	4-13	All sky. 1 month/field
PLATO	~2024	~ 34-80 ppm / 6hr / 11th mag	6 yr	< 16	50% sky. 2 long pointings (2-3 yr)+ + 8 step-stare (2-5 months) fields

et al., 2014) will provide a longer baseline of 2-3 years for two fields and 2-5 months for other 8 fields, covering a total of 50% of the sky. Both the expected precision and the long baseline will allow the detection and characterization of small bodies and super-Earths in the habitable zones of their parent stars. The long baseline will also allow for asteroseismology studies, crucial to accurately and precisely determine the properties of the detected planets.

All these missions will look for the effects described in this chapter and will be able to populate void exoplanet niches.

Chapter 3

High-spatial resolution imaging from the ground

Contents

"To them, I said, the truth would be literally nothing but the shadows of the images."

Allegory of the Cave[1]

The Republic, Book VII (around 380 B.C.E.)

Plato (427-347 B.C.E.)

[1]Translation by Benjamin Jowett (Vintage, 1991).

3.1 The need for high-spatial resolution imaging in the planet hunt

In the previous chapter we have shown that high-precision photometers such as *Kepler* and CoRoT need to spread the incoming light into a sufficient number of pixels to reach the required precision for detecting extrasolar planets. A similar methodology is applied from the ground when high-precision photometry is needed, for instance by defocusing the telescope to detect primary and secondary planetary eclipses (e.g., Southworth et al., 2009). With such a large PSF, blended sources (either bounded or background/foreground), could clearly contaminate the light curves and consequently affect the derived orbital and planet parameters. Indeed, the presence of an additional star could lead, for example, to the definite rejection of the candidate (see O'Donovan et al., 2006). There are several configurations that can mimic a planetary-like transit. The most relevant are (see Fig 3.1):

(I a) Eclipsing binary (EB).- a small substellar object transiting a warmer star (the smallest stars and brown dwarfs have the same size as Jupiter due to electron degeneracy and its effect on the equation of state).

(I b) EB+background star(s).- a stellar binary blended with one or more background stars. The blended sources would dilute the transit of the EB, that could have depths typical of planetary transits.

(I c) Grazing EB.- a grazing eclipse of an EB.

(I d) Background EB.- a background eclipsing binary blended by the light of the main target.

(I e) Long-term starspot.- the presence of a long-lived stellar spot can produce periodical dips in the light curve with the rotational period of the star that could be misinterpreted as a planetary transit.[2]

Additionally, there are other configurations with blended stars that even including planets, their properties would be affected by the presence of blended sources. The most simple ones are

(II a) Background planetary system.- This would not strictly be a false positive since there is actually a planet in the system. However, it rejects the brightest target as a planet host and strongly affects the properties of the planet (which would appear smaller).

(II b) Planetary system with a blended star.- A real planet orbiting the brightest star with a blended source diluting the transit depth can also be miss-identified or erroneously characterized.

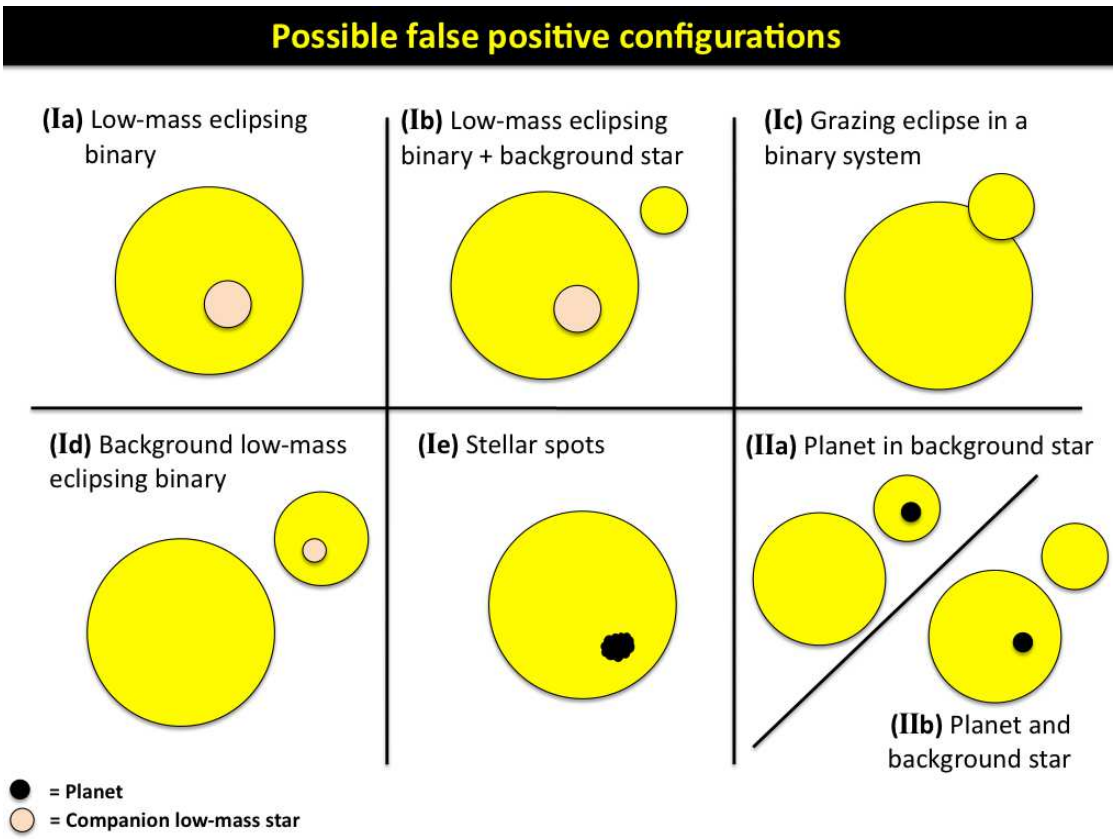

FIGURE 3.1: Representation of some of the possible configurations mimicking a planetary transit or contaminating the light curve of high-precision photometers.

As an example, we can imagine the case of a blended planetary system, with a true planet orbiting its host star and a blended background source contaminating the light curve (II b in Fig. 3.1). The amount of dilution depends on the magnitude difference (or **contrast**) between the host and the blended star (**Δm**). In the simple case in which Eq. 2.4 is valid, the undiluted planet-to-star radius ratio is given by

$$\left(\frac{R_p}{R_\star}\right)_{\text{undiluted}} = \sqrt{1 + 10^{-\Delta m/2.5}} \left(\frac{R_p}{R_\star}\right)_{\text{obs}} \tag{3.1}$$

At maximum, the correction factor is obtained when $\Delta m = 0$ and so the undiluted radius would be $\sim 41\%$ larger than that calculated directly from the measurement of the transit depth (Eq. 2.5). The presence of such a blended source could also affect the total transit duration (t_{1-4}), and the total transit flat duration (t_{2-3}).

Similarly, the radial velocity technique uses high-resolution spectra obtained with either fiber-fed or long-slit spectrographs. Close background/foreground stars can fall inside the fiber (with typical diameters of 1-2 arcsec) or inside the slit width (typically below 1 arcsec) and thus contaminate the spectra and so the radial velocity data. In section § 4.3.2, we will analyze how

[2]Note that stellar spots might be present in any configuration, thus complicating the light curve analysis.

the radial velocity precision is affected by blended lines, for example, due to the presence of a diluted star. The measured radial velocity in this case can have a scatter of the order of hundreds of m/s, depending of the spectral type and systemic radial velocity of the blended star.

Given this argumentation, it is clear the need of high-spatial resolution images of the host stars in order to unveil possible close contaminant sources. The probability of a chance-aligned background/foreground source for a given target is strongly dependent (as expected) on its galactic latitude and requested magnitude range, and less importantly on its galactic longitude. In Fig. 3.2, we show the expected number of stars closer than 2, 6, and 10 arcsec as a function of the galactic latitude for the *Kepler* field. We have simulated this by using the TRILEGAL tool,[3] assuming the default parameters, and for the magnitude range from $V = 14$ mag to $V = 21$ mag. From this simple exercise, we can conclude that the probabilities of having a blended chance-aligned source inside the typical *Kepler* apertures of 6-10 arcsec is non-negligible.

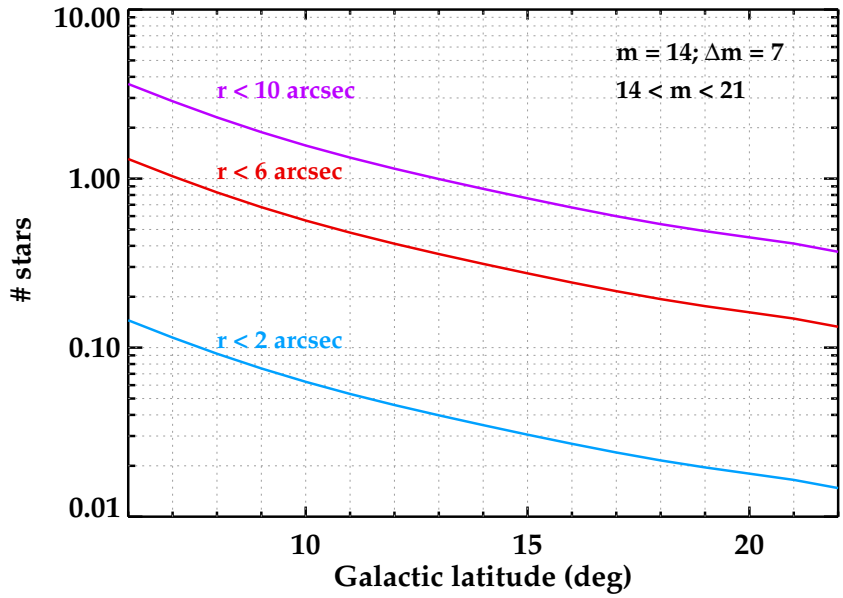

FIGURE 3.2: Expected number of stars closer than 2, 6, and 10 arcsec for a $m = 14$ mag star and companion sources as faint as $m = 21$ mag, as a function of the galactic latitude across the *Kepler* field.

Besides, high-resolution images have been extensively used to feed statistical validation tools of planetary candidates, mainly from the *Kepler* mission. These techniques examine the likelihood of the different false positive scenarios, measuring the confidence in the planetary interpretation of the transit signal. The most relevant tools in this regard are BLENDER (Torres et al., 2011), that has been used in the validation of a large amount of planet candidates (such as Lissauer et al., 2014, Rowe et al., 2014); and PASTIS (Díaz et al., 2014a). In section § 5.4, we will provide more detailed examples on how these algorithms can be used to validate small planets that are beyond the precision of direct techniques such as radial velocity or TTV.

[3] See `http://stev.oapd.inaf.it/cgi-bin/trilegal` and Girardi et al. (2005)

Finally, the role of multiplicity in planet formation and evolution still remains unclear. At present, a handful number of planets around one of the components of a binary system (satellite or S-type systems) and circumbinary planets revolving in wide orbits around the two components of a binary system (P-type) have been discovered. High-resolution images of close planet host candidates can reveal bounded companions in wide orbits (S-type systems), increasing this sample.

3.2 The atmosphere as a foe

The quality of the observations from ground-based telescopes is limited by several factors. The cause of these limitations is the atmosphere, a thick layer of anisotropic air. It creates a turbulent shell between the telescopes and the targets. This turbulence is mainly due to variations of the air temperature (T) and pressure (P) that provoke motions of the different air bubbles both locally and at large scales. The refractive index of the air depends on these parameters as $n(P,T,\lambda) \propto \lambda^{-2}PT^{-1}$, and the velocity of a light ray is decreased by this refraction index as $v = c/n$. Consequently, the flat incoming wavefront from space is distorted along its path through the atmosphere (see Fig. 3.3). This distortion (called **seeing**) translates into a blurring of the image.

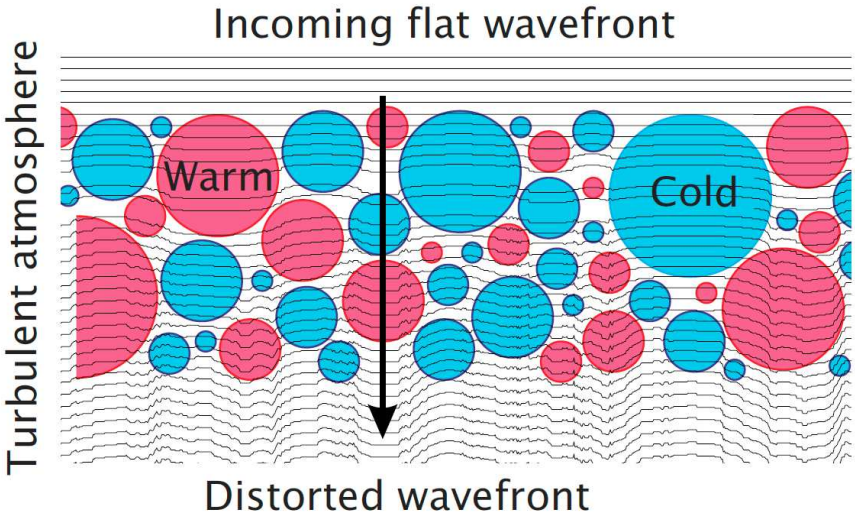

FIGURE 3.3: Scheme of the different temperature and pressure regions in the atmosphere and their effect on the flat wavefront from the stars. Figure extracted from Hormuth et al. (2008) and adapted from Egner (2007).

The importance of understanding the atmospheric turbulence lays in the possibility of resolving astronomical sources (such as close visual binaries) or extended structures (such as structures of galaxies or storms in Solar System planets). The theoretical shape of a point-like source as seeing by the circular aperture of a telescope is given by the Airy disk. This particular shape is

characterized by a maximum peak and its subsequent harmonics (see Fig. 3.4). The resolving power of a particular telescope of diameter $D_{\rm tel}$ observing at a wavelength λ is described by the minimum angular separation that two point-like sources can have to be discriminated by the telescope. According to the Rayleigh criterion, if both sources have the same brightness, this minimum angular separation occurs when the first harmonic of the point-spread function (PSF) of one of the sources coincides with the first minimum of the second source. This separation is given by

$$\alpha_{\rm res} = 1.22\,\frac{\lambda}{D_{\rm tel}}. \tag{3.2}$$

Note from this equation that larger telescopes and observations at longer wavelengths provide the best resolutions. Another way of characterizing this separation is by calculating the full-width at half-maximum (FWHM) of the PSF. In the case of absence of any other source of diffraction (i.e., **diffraction limited** or DL[4]), this value is simply given by

$$\mathrm{FWHM}_{\rm DL} = 1.02\,\frac{\lambda}{D_{\rm tel}}. \tag{3.3}$$

As an example, for the case of a 2.2m telescope observing in the Sloan i band ($\lambda_{\rm eff} = 7630$Å), we would be able to resolve two sources separated by 87 mili-arcsec (mas, i.e., 0.087 arcsec), corresponding to a $\mathrm{FWHM}_{\rm DL} = 0.073$ arcsec. This is what it would be expected with a perfect optical system

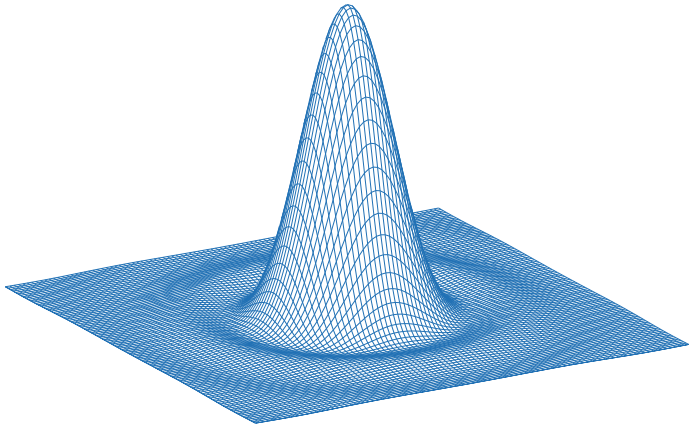

FIGURE 3.4: Airy disk representation.

However, in the presence of this air layer and sufficient short exposure times, the resulting image is a composition of different speckles with similar sizes as the Airy disk but spread into a larger area (see Fig. 3.5, middle panel). For longer exposures, these speckles are combined to conform a broader PSF. We then say that the images are **seeing limited** (see Fig. 3.5, left panel). The FWHM of a seeing limited image from a point-like source can be described as

[4]We here follow the notation in Hormuth et al. (2008).

FIGURE 3.5: Simulation of a long-exposure time image (left panel), a short-exposure time (mid panel) and a diffraction-limited image (right) of the same target (note the Airy disk). Figure adapted from Fig. 1.2 in Felix Hormuth's dissertation (Hormuth, 2007).

$$\mathrm{FWHM_{SL}} = 0.98\,\frac{\lambda}{r_0}, \tag{3.4}$$

where r_0 is the so-called Fried parameter (Fried, 1965). This parameter is a measurement of the strength of the distortions caused by turbulence in the atmosphere. Interestingly, in the seeing limited regime there is no dependence in r_0 with the size of the telescope aperture. The Fried parameter depends on the angle between the zenit, the line of sight, the altitude of the observatory, the observing wavelength, and a function describing the refractive index at different heights. Typical values for this parameter at the most important observatories and under good seeing conditions are $r_0 = 10 - 20$ cm. Consequently, for observations in the Sloan i band, the seeing limited resolution is $\mathrm{FWHM_{SL}} = 1.02$ arcsec.

An important parameter to take into account when trying to obtain high-spatial resolution images is the typical time in which the atmosphere changes. In this sense, the **speckle coherence time** is defined as the time difference at which the normalized autocorrelation function of the intensity at a fixed position in the focal plane drops to 1/e. In other words, it is the typical time at which the speckle patterns show good correlation, meaning that the atmosphere has not change by a significant amount (i.e., it is "frozen" during this timespan). Thus, exposure times below the speckle coherence time will "freeze" the atmosphere, providing close-to diffraction limited images. The typical coherence time for a 0.7 arcsec seeing in the V-band is around 100 ms (milliseconds).

Strehl ratio: measuring the quality of astronomical images

Ground-based observations have to deal with the presence of the atmosphere. We can measure the quality of the images by comparing the observed FWHM with the expected value for the given optics used. This is, however, a non complete picture of how the turbulence is affecting our observations. Instead, we should measure the percentage of energy emitted by the star that is being collected in the central peak of the PSF. In this context, Strehl (1902) described a parameter currently known as the **Strehl ratio** (hereafter **SR**). It is theoretically defined as the

ratio between the peak intensity of the observed PSF over the peak that we would see in absence of any atmosphere and with a diffraction limited optical system, SR = $\max(I_{observed})/\max(I_{DL})$. In consequence, the more spread is the energy, the smaller the Strehl ratio and then the poorer quality of the image. This expression can be approximated by SR = $\exp(-\sigma^2_{wf})$ for SR > 15%. In this approximation, σ^2_{wf} is the variance of the wavefront phases due to the presence of a turbulent medium. In the case of absence of a perturbed medium, the wavefront is flat and so $\sigma^2_{wf} = 0$ and SR = 100%. Equivalently, a SR =50% implies a standard deviation of $\sigma_{wf} = 0.83$ radians, which represents a measurement of how distorted is the incoming wavefront.

In practice, the distortions of the received wavefront are too large to be calculated by the above expressions. Instead, approximated expressions can be used. For instance, in the case of the pipeline provided for the AstraLux instrument at Calar Alto Observatory (Hormuth et al., 2008), they calculate what they call the pseudo-Strehl ratio of the observed image and divide it by the pseudo-Strehl ratio of the theoretical PSF of the optical system (see § 3.5). The pseudo-Strehl ratio is defined as the quotient between the peak of the PSF and the total flux of the PSF profile.

3.3 High-spatial resolution techniques from the ground

In the previous section, we have shown the effects of the atmosphere on the incoming flat wavefront from a point-like source. Several techniques have been developed in order to go beyond the seeing-limited regime and towards the diffraction-limited regime. In the following, we provide a summary of these techniques, used to obtain high-resolution images from the ground.

Adaptive optics.- In this technique, the aberrations in the wavefront of the incoming light are actively corrected by accordingly modifying the shape of the primary deformable mirror of the telescope. A sensor measures the shape of the wavefront. This information is then used to compute the needed shape of the deformable mirror and is translated to the actuators. Adaptive optics (AO) has provided very good results in the near-infrared regime, with typical spatial resolutions of the order of <0.1 arcsec. However, the number of required actuators is much larger in the optical than in the near-infrared (e.g., around 2300 in the V-band against $\sim$ 70 in the K-band for a 8-m telescope) and thus the vast majority of the AO instruments work in this wavelength regime. But, the advanced technology used makes these instruments expensive as compared to other techniques.

Speckle imaging.- The speckle imaging consists on getting thousands of short-exposure time images of the target (Labeyrie, 1970). Each individual frame contains different speckles, which are actually copies of the diffraction limited image (see mid and right panels of Fig. 3.5). This technique performs a complex and computationally time consuming auto-correlation of the individual images, looking for patterns of groups of speckles and finally adding them together to

increase the signal-to-noise. Then, after some processing methods are applied (see, for example, Howell et al., 2011), the image is reconstructed and we can obtain an almost diffraction limited image, with spatial resolution $\sim$ 0.05 arcsec and large contrasts at very small angular separations. However, this technique works well only for stars brighter than $V \sim 11$ mag (owing to have sufficient speckles with high signal-to-noise ratio). Also, the typical field of view for these type of systems is typically smaller than ~2 arcsec, being insufficient for some follow-up programs (see analysis in Lillo-Box et al., 2014b).

Lucky imaging.- The lucky-imaging technique is a simple and economic approach of getting near diffraction-limited images. It is based on the same principles as the speckle technique but with a different reduction process. It selects the best (least blurred) short-exposure frames from a large sample (typically > 10000 frames). The selection is based on the measurement of the Strehl ratio explained in the previous section. The term "lucky" comes from the definition of Fried (1978) of the probability of obtaining a "lucky" short exposure image with an Strehl ratio larger than 37% through a turbulent atmosphere. The only requirement of this technique is having a sufficiently bright star in the field in order to measure the Strehl ratio on each frame. Typical resolutions with this technique are 0.1 arcsec for equally bright stars and typical selection rates of $\sim$ 10%. It can be applied at different wavelength regimes with no extra costs, in particular, optical and near-infrared. The main disadvantage is that only $\sim$ 10% of the total frames are used in the final stacked image.

Speckle holography.- This technique was proposed by Schödel & Girard (2012). It consists on iteratively improve the PSF from each speckle on every short-exposure frame and using multiple (not only one) reference star. Its main advantage respect to the lucky-imaging is that it uses every frame (so no frame selection is needed) to compute the final image. Consequently, it improves the observing efficiency, detecting fainter sources for the same exposure time. In respect to AO, it can reach similar and even higher Strehl ratios. Interestingly, it can be combined with AO. Its disadvantage is that it only gets significant improvement in crowded fields where several reference stars can be used.

3.4 The Blended Source Confidence parameter

The techniques described above are very different and sometimes it is difficult to compare the output of complementary surveys. We have developed a statistical procedure in order to compare the high-resolution images obtained by different techniques. Additionally, this procedure can also serve to test the quality of a unique high-resolution image. The outcome is a parameter that provides the probability of the observed star to have a blended, undetected, visual companion with a certain maximum contrast of Δm. We call this parameter as the **Blended Source Confidence** (**BSC**, Lillo-Box et al., 2014b). In the following sections, we describe the scheme

and equations to obtain this parameter for a given high-spatial resolution observation of a particular target.

3.4.1 Sensitivity curve

The first step is to calculate the sensitivity curve of the observed image, i.e., the faintest source detectable as a function of the angular separation from the main target. Although there are several methodologies to obtain this sensitivity curve, we here describe a comprehensive and simple scheme that can be easily implemented.[5]

According to the particular instrument, we fit the observed PSF of the target to a known two-dimensional function describing the theoretical PSF of the instrument (e.g., a two-dimensional gaussian or, as it is the case of AstraLux, a combination of a Moffat function and a Gaussian). Then this PSF is scaled by a factor of Δm (i.e., $F_2 = F_1 10^{-0.4\Delta m}$) at different positions of the image. For instance, we used 20 angular separations between $\alpha = 0.1$ and $\alpha = 3.0$ arcsec and 20 relative magnitudes (Δm) between 0 and 10 magnitudes. For every pair $[\alpha, \Delta m]$, we added 20 artificial stars distributed at random angles (i.e., 400 artificial stars for every angular separation). Then, we run a detection algorithm (the same that we will then use to detect real companions) to try to detect these artificially added companions (see Fig. 3.6). The sensitivity curve (C_{sens}) is then computed as the contour line in the $[\alpha, \Delta m]$ plane, corresponding to the detection of the 70% of the artificially added stars with a 5σ minimum requirement (see Fig. 3.7). In our case, we carried out this task in the IDL environment, using the *find* and *aper* routines (among others) to detect the potential companions and obtain the aperture photometry.

3.4.2 *A priori* probability

Let us now, as a first step, assume a particular target with a magnitude m at galactic latitude b. The expected number of stars within an angular separation r from our target and with magnitudes in the range $[m, m + \Delta m]$ is given by

$$\begin{aligned} N(r, b, m, \Delta m) &= \int_{0''}^{r} 2\pi\alpha\rho(b, m, \Delta m)d\alpha \\ &= \pi r^2 \rho(b, m, \Delta m), \end{aligned} \tag{3.5}$$

where $\rho(b, m, \Delta m)$ represents the number of stars per unit area (i.e., the density of stars), and depends on the galactic latitude (b) of the target and the requested magnitude range $[m, m+\Delta m]$.

[5] Indeed, this approach ws subsequently adopted by Gilliland et al. (2014), following our prescriptions.

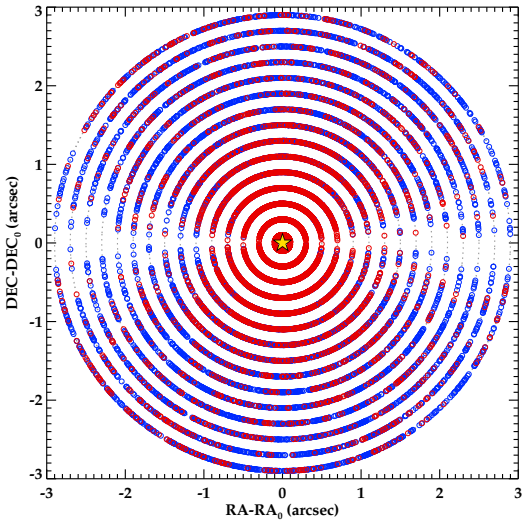

FIGURE 3.6: Demonstration of the proposed scheme to extract the sensitivity curve of a high-spatial resolution image of a particular target. Location of the artificially introduced sources. Detected (undetected) sources are represented in blue (red).

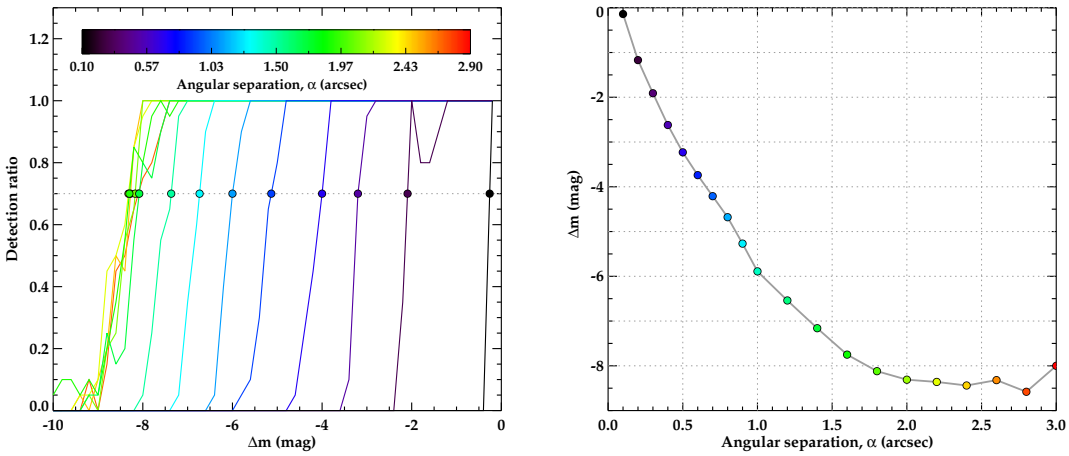

FIGURE 3.7: **Left:** Detection ratio of the artificially included sources as a function of the magnitude difference for the different angular separations (in color code). **Right:** Correspondent sensitivity curve extracted ($C_{\rm sens}$).

For small areas,[6] this value can be interpreted as the probability for this area to contain one chance-aligned star within this magnitude range.

In that case, we can define the probability of an object having a chance-aligned source within a certain magnitude range as $P_{\rm aligned} = N(r, b, m, \Delta m)$. This equation clearly shows that the probability of a chance-aligned source decays with the square of the angular separation as we approach to the target. Contamination sources above 3 arcsec can be easily detected by usual photometric observations (such as in Brown et al., 2011, or the UKIRT J-band survey observed

[6] With small area, we mean that it must be accomplished that $r < R_{max}$, where R_{max} is the radius that provides a value of unity for Eq. 3.5, i.e., $\int_0^{R_{max}} 2\pi\alpha\rho(b, m, \Delta m)d\alpha = 1$. We note that all studied targets in this dissertation accomplish $R_{max} > 3.0$ arcsec.

and supplied by Phil Lucas[7] for the *Kepler* field) or other techniques such as photocenter centroid analysis (see, for example, Batalha et al., 2010, for the *Kepler* case). Hence, in this work, we only take the 0-3 arcsec region into account.

We can now integrate P_{aligned} in the parameter space $\alpha = [0, 3]$ arcsec and $\Delta m = [0, \Delta m]$ to compute the total ***a priori*** **probability** of having a chance-aligned blended source ($P_{BS,0}$) with magnitude $m_{\text{target}} < m < m_{\text{target}} + \Delta m$ within 3 arcsec:

$$\begin{aligned} P_{BS,0} &= \int_{0''}^{3''} 2\pi\alpha\rho(b, m, \Delta m)\, d\alpha = \\ &= 9\pi\rho(b, m, \Delta m). \end{aligned} \tag{3.6}$$

3.4.3 Density of stars

For Eq. 3.6, we still need to calculate the expected density of stars for the given target (ρ). This parameter can be calculated in a similar way as Morton & Johnson (2011a). We can use the online tool TRILEGAL[8] to compute the number of expected stars within a magnitude range in a particular region of the sky. We used the default parameters for the bulge, halo, thin/thick disks, and the lognormal IMF (Initial Mass Function) from Chabrier (2001). For individual targets, this computation is easy and quick. However, for massive surveys, given that it is not possible to perform an automatic query in TRILEGAL (the user must proceed object by object), it is not possible to obtain individual populations for a large number of targets. Instead, we should apply a different approach. The strategy depends on the sample of targets and how are they distributed in the sky. We here explain the approach for the *Kepler* field, which will be used in chapter § 5.

The *Kepler* field is relatively large and encompasses around 12 degrees in both right ascension and declination (and almost 20 degrees in galactic latitude). As expected, we have found important differences in the stellar density from galactic latitudes that are close to the galactic disk compared to those farther from it. By neglecting the dependence of the ρ parameter with the galactic longitude, we obtained stellar populations with TRILEGAL for regions of 1 deg^2 centered at $b = 6°$ to $b = 22°$ in steps of 1° and a galactic longitude fixed to the center of the *Kepler* field (i.e., 76°), as seen in the left panel of Fig. 3.8. We then simulate stars up to a magnitude limit of $i_{SDSS} = 28$ mag inside each region according to the galactic model.

For a particular target at a galactic latitude b_{target} with a magnitude m and a needed contrast of Δm,[9] we determine $\rho(b_j, m, \Delta m)$ (the "j" subscript representing each galactic latitude for which

[7] See http://keplergo.arc.nasa.gov/ToolsUKIRT.shtml

[8] http://stev.oapd.inaf.it/cgi-bin/trilegal

[9] This required contrast depends on each particular problem and will be defined in section § 5 for the purposes of this work.

we run the TRILEGAL simulations) at all galactic latitudes in the grid by just counting stars within the magnitude range $[m, m+\Delta m]$ and dividing by the box area of 1 deg^2. Then we perform a low-order polynomial fit to ρ versus the galactic latitude values and infer the corresponding $\rho(b_{\rm target}, m, \Delta m)$ by evaluating the fitted function at $b_{\rm target}$ (see Fig. 3.8, right panel). We found that a fifth-order polynomial fits the data sufficiently well for the purposes of this work (see the example on the right panel of Fig. 3.8). By following this scheme, we can precisely estimate the density of stars in a concrete magnitude range at any position in the *Kepler* field.

3.4.4 The BSC parameter

We have previously described how we define the probability of having a blended source within some observational constraints (namely, the star position and the magnitude range of possible blended stars). Since we have calculated a sensitivity line for each observation ($C_{\rm sens}$), we can reduce the *a priori* probability ($P_{BS,0}$) by limiting this calculation to only that region where our high-spatial resolution image is not sensitive. In the angular separation versus magnitude difference plane, this non-sensitive zone is defined as the region between our sensitivity curve (C_{sens}) and the required maximum magnitude difference depending on the problem (Δm_{max}). In Fig. 3.9, this region has been shaded with diagonal blue lines. Hence, given a high-resolution image, the probability provided by Eq. 3.6 now integrates only over the diagonally shaded region (where we are not sensitive):

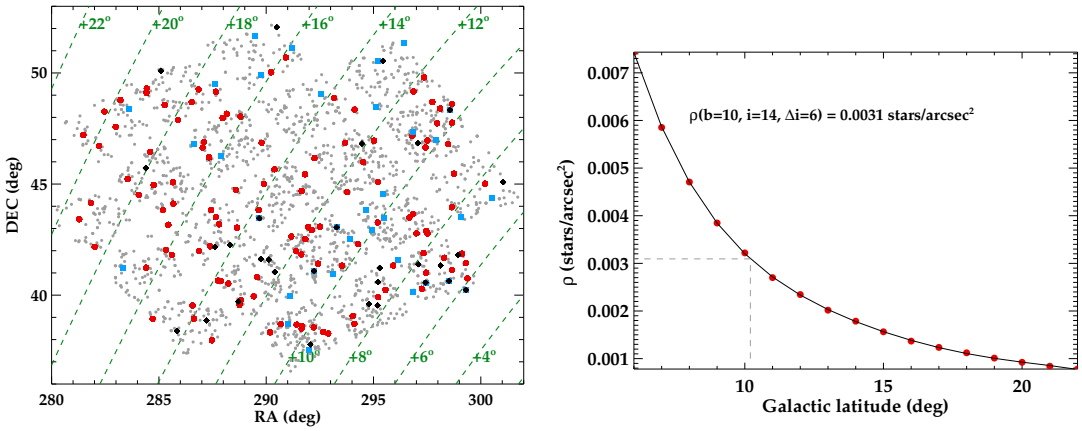

FIGURE 3.8: **Left:**Location of the targets studied in our AstraLux survey (red, blue, and black symbols, see § 5). Planet candidates of the *Kepler* sample from Batalha et al. (2013) are plotted as grey small circles. Iso-galactic latitude lines are marked as dashed inclined green lines parallels to the galactic plane. **Right:** Example of the determination of the ρ parameter for an object at $b = 10$ deg with a required magnitude range of $i = 14 - 20$ mag. Red filled circles represent the values calculated from the TRILEGAL simulation for each galactic latitude in the left panel (i.e., the $\rho[b, m, \Delta m]$ with b ranging from 6° to 22°), and the solid black line shows the corresponding fifth-degree polynomial fit. Gray dashed lines show the derived value at the requested galactic latitude in the example.

$$P_{BS} = P_{BS,0} - \int_{0''}^{3''} 2\pi\alpha \times \rho[b, m_i, \Delta m_0(\alpha)]\, d\alpha, \tag{3.7}$$

where $\Delta m_0(\alpha) = max[C_{sens}(\alpha), \Delta m_{max}]$. The second term in the right hand side of the expression represents the contribution of the high-resolution image.

It is thus clear that the better and deeper our image (i.e., the closer C_{sens} is to Δm_{max}), the more we diminish the blended source probability and thus improve the planetary candidacy. We can now determine an observational value of P_{BS} and define the **BSC parameter** as BSC = $1 - P_{BS}$, representing the confidence for this source not having blended sources in the specified magnitude range. We propose this parameter to be used in all high-resolution studies to compare the different surveys with the adaptive optics, speckle, or lucky-imaging techniques.[10]

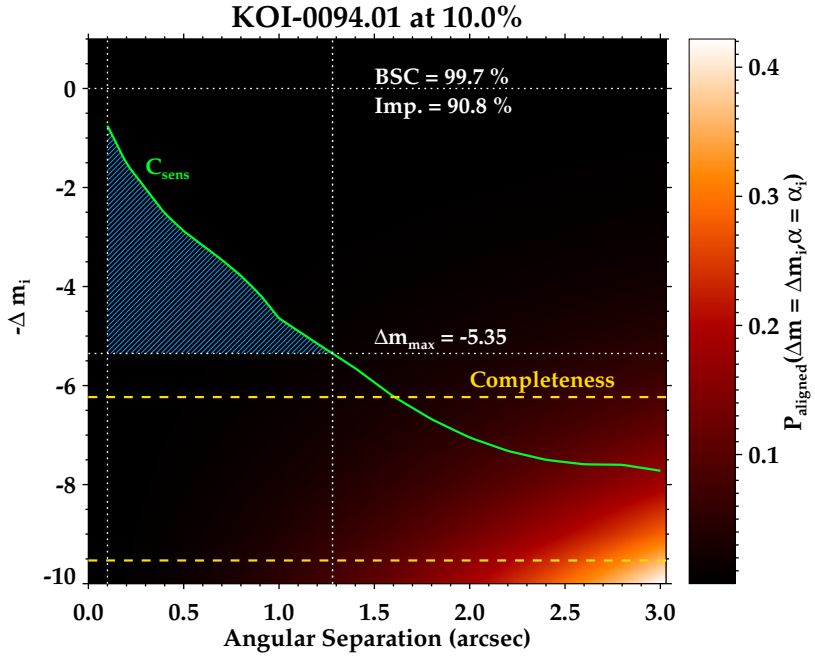

FIGURE 3.9: Example of the determination of the BSC parameter with CAHA/AstraLux observations for the *Kepler* candidate KOI-94[11]. The green solid line represents the 5σ sensitivity curve (C_{sens}). The lower horizontal dotted white line represents the maximum magnitude difference (Δm_{max}) requested for this problem. The two vertical white dotted lines show the lowest angular separation detectable in the image (left line) and the intersection between the sensitivity curve and the Δm_{max} (right line). The inaccessible region with this high-resolution image is shadowed with diagonal light blue lines. The background color code in the image represents the probability of having a chance-aligned background source for every angular separation and magnitude difference for the given KOI.

[10] A user-friendly web applet is being designed to provide the BSC value for any given sensitivity curve.

[11] This is a four-planet system currently confirmed by Hirano et al. (2012a) and Masuda et al. (2013), Kepler-89. A faint companion ($\Delta m_{\rm Kep}$ = 11.8 mag if bounded and $\Delta m_{\rm Kep}$ = 7.7 – 9.3 if not bounded) was found by Takahashi et al. (2013) at 0.6 arcsec. We note that this is below the 5σ sensitivity curve showed in this plot. Given the low probability for this source to be chance-aligned, it may be bounded to the planetary system.

3.4.5 Corrections to the BSC due to incompleteness

Every astronomical image is characterized by two values defining the magnitude limit for which all sources would be detected (completeness limit, $m_{\rm comp}$) and the faintest source detected in the image (detectability limit, $m_{\rm detect}$). All sources brighter than $m_{\rm comp}$ will be detected, while objects with $m_{\rm comp} < m < m_{\rm detect}$ would be detected with a certain probability. We can describe the decay in probability from $m_{\rm comp}$ to $m_{\rm detect}$ by an **incompleteness function**. In order to determine this function, we can fit the decay of the completeness histogram (number of sources detected per magnitude bin, for instance, in the astrometric field) between $m_{\rm comp}$ and $m_{\rm detect}$ with an exponential function like $f(x) = C + Ae^{-x/B}$, where $x = m - m_{complete}$. We can appropriately set $C = 0$ and $A = 1$, so that $f(m = m_{\rm comp}) = 1$ and $f(m > m_{\rm detect}) = 0$.

Back to the high-resolution image, in the calculation of the BSC, we should account for incompleteness if $m_{\rm target} + \Delta m_{\rm max} > m_{\rm comp}$ in the regions where $m_{\rm comp} > C_{\rm sens}$. We then have to correct the BSC for incompleteness of this region of the $[\alpha, \Delta m]$ diagram.

In Fig. 3.10, we can see an example of a high-resolution image with the incompleteness problem. Since the detectability limit is still below the sensitivity curve (i.e., $m + \Delta m_{max} < m_{detect}$), we still could detect a percentage of sources fainter than the completeness magnitude but not all of them. Thus the contribution of the vertically shaded region (hereafter incompleteness region) must be weighted by the incompleteness function.

The simplest approach to calculating $m_{\rm comp}$ and $m_{\rm detect}$ is by observing a globular cluster with a high density of stars with the same setup and exposure time as the science image. Given these limits, in the cases where the completeness line (upper yellow dashed line in Fig. 3.10) lays above the sensitivity curve ($C_{\rm sens}$, green line), the P_{BS} must be calculated as

$$\begin{aligned} P_{BS}^{corr} = P_{BS,0} - \int_{\alpha_0}^{3''} 2\pi\alpha\, \rho\Big(b, m_i, \Delta m_1(\alpha)\Big)\, d\alpha \;\; + \\ + \int_{\alpha_0}^{3''} d\alpha \int_0^{\Delta' m(\alpha)} 2\pi\alpha\, \rho\Big(b, m_{comp}, \Delta m_2(\alpha)\Big)\, e^{\frac{-\Delta m_2(\alpha)}{B}}\, d\Delta' m, \end{aligned} \tag{3.8}$$

where

$$\Delta m_1(\alpha) = max[m_i + C_{sens}(\alpha), m_i + \Delta m_{max}, m_{comp}] - m_i \tag{3.9}$$

$$\Delta m_2(\alpha) = max[m_i + C_{sens}(\alpha), m_i + \Delta m_{max}] - m_{comp} \tag{3.10}$$

and α_0 represents the angular separation at which $m + C_{sens}(\alpha = \alpha_0) = m_{comp}$. The second term corresponds to the contribution of the high-resolution image in the magnitude range where it is

complete (non-shaded region above the C_{sens} line in Fig. 3.10). The third term represents the weighted contribution of the high-resolution image according to our exponential incompleteness function derived above, and it is represented by the vertically shaded region in Fig. 3.10.

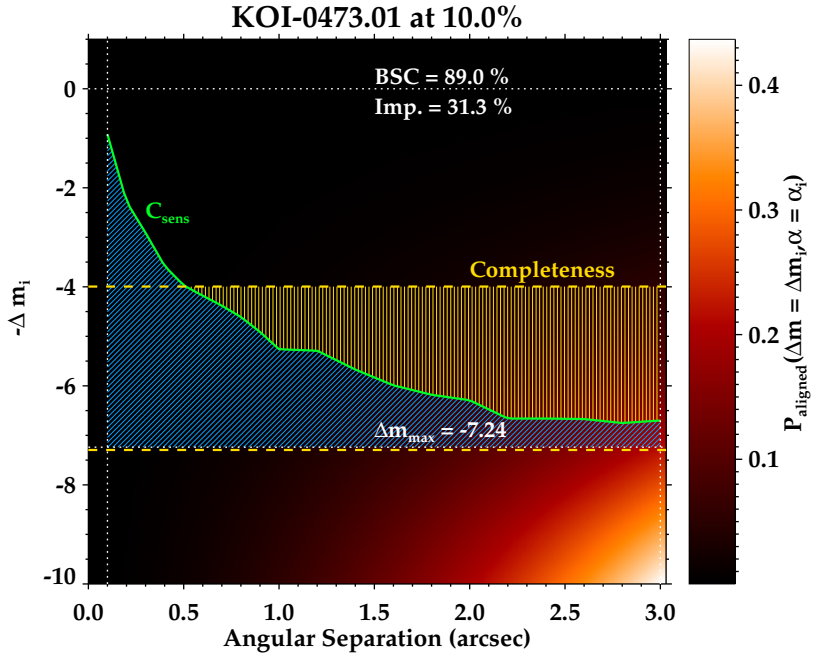

FIGURE 3.10: Example of a non-conclusive observation with CAHA/AstraLux, where the completeness level is above Δm_{max}. The upper and bottom dashed yellow lines represent the completeness and detectability levels, respectively. The incompleteness region is marked by the shaded region with vertical yellow lines. The color-code and legend is the same as in Fig. 3.9

3.5 AstraLux in a nutshell: instrument and reduction pipeline

In this work we have extensively used the AstraLux instrument, placed at the 2.2m telescope at the Calar Alto Observatory (Almería, Spain). Although a complete description of the instrument and reduction pipeline can be found on Felix Hormuth's Ph.D. dissertation (Hormuth, 2007), we here summarize the most relevant characteristics for the present work and the application to the *Kepler* search.

3.5.1 Overview of the instrument

The AstraLux instrument consists on a relatively simple camera composed by a quick shutter, able to obtain tens of frames per second, and a 512×512 pixels CCD of 16×16 μm each. According to the commissioning plate scale estimations, this is translated into ~0.04654 arcsec/pixel. It is possible to use a reduced window of the CCD, which allows to set shorter exposure times. For instance, reducing the chip to one fourth (i.e., 256 × 256 pixels) the single frame exposure time

TABLE 3.1: Coefficients linking the software and the physical gain in the AstraLux instrument (see Eq. 3.11).

k	a	b	c
0	−0.020981269	−0.0077822229	$-3.4432020 \times 10^{-5}$
1	0.0054692930	0.00041951355	4.1596610×10^{-6}
2	0.00030952551	$-4.4883595 \times 10^{-6}$	$-5.7290537 \times 10^{-8}$
3	$-8.7914694 \times 10^{-6}$	$-2.1410006 \times 10^{-8}$	$1.9775723 \times 10^{-10}$
4	9.4715544×10^{-8}	$5.6838745 \times 10^{-10}$	$1.6669195 \times 10^{-12}$
5	$-5.1625410 \times 10^{-10}$	$-4.1550787 \times 10^{-12}$	$-2.2139237 \times 10^{-14}$
6	$1.4603941 \times 10^{-12}$	$1.5230594 \times 10^{-14}$	$1.0367412 \times 10^{-16}$
7	$-1.7013942 \times 10^{-15}$	$-2.2456162 \times 10^{-17}$	$-1.7297170 \times 10^{-19}$

can be as short as 15 ms. Smaller windows (and thus shorter exposure times) are also possible but paying the price os smaller fields of view.

The physical gain (PG) can be adjusted from 1 to 2500 e^-/ADU in 255 steps (software gain, SG). It is important to note that the relation between both gains is non-linear. In a private communication, the principal investigator of the instrument (Felix Hormuth) provided us with an empirical expression relating both gains depending on the temperature of the CCD ($T_{\rm CCD}$):

$$\log_{10}(PG) = \sum_{k=0}^{8} SG^k a_k + T_{\rm CCD} \sum_{k=0}^{8} SG^k b_k + T_{\rm CCD}^2 \sum_{k=0}^{8} SG^k c_k \tag{3.11}$$

where the coefficients a, b, and c are presented in Table 3.1. When obtaining the absolute photometry of the targets with photometric standard stars, the different applied gains must be accounted for (Lillo-Box et al., 2012). In this dissertation, we have used the main target as the reference by using photometry from the *Kepler* input catalog (KIC, Brown et al., 2011). Details on this calibration will be given in § 5.1.3.

We must also define the individual exposure time ($T_{\rm exp}$) and the total number of frames (N_f) to be obtained. The former affects the spatial resolution (the longer exposure time the more blurred will be each frame) and is limited by the size of the selected window and the magnitude of the target. In other words, $T_{\rm exp}$ should be as small as possible but sufficient to detect the target. The total number of frames should be adjusted according to the required effective exposure time ($T_{\rm exp}^{\rm eff} = N_f \times T_{\rm exp} \times R_{\rm sel}$), where $R_{\rm sel}$ is the selection rate ($R_{\rm sel} \in [0, 1]$), representing the percentage of the best frames that will be selected by the pipeline to generate the final near diffraction-limited image.

3.5.2 Data reduction pipeline

The pipeline provided by the observatory and developed by Felix Hormuth to reduce the AstraLux data-cubes is also extensively explained in Hormuth (2007). Here, we summarize the main steps and the properties of its data-products.

Due to the large number of frames typically acquired ($N_f > 10000$), the outcome of the AstraLux observations is a data-cube. Given the appropriate calibration files (and file names), the pipeline computes the master bias and flat-field images. Then, it looks for a reference source in all frames of the scientific image. This is done by stacking the first two seconds of the raw images. Once the reference source is detected, it determines the Strehl ratio of this source on each frame. Then, the best quality frames are selected and appropriately aligned and stacked to conform the final image. The pipeline default products are images with 1%, 2.5% , 5%, and 10% of selection rate ($R_{\rm sel}$). In Fig. 3.11, we show the differences between the seeing limited, worst Strehl ratio frame, best Strehl ratio frame, and final 1% selection rate image for a 3000 frames observation of $T_{\rm exp} = 30$ milliseconds (ms) of the photometric standard star Ross-711.

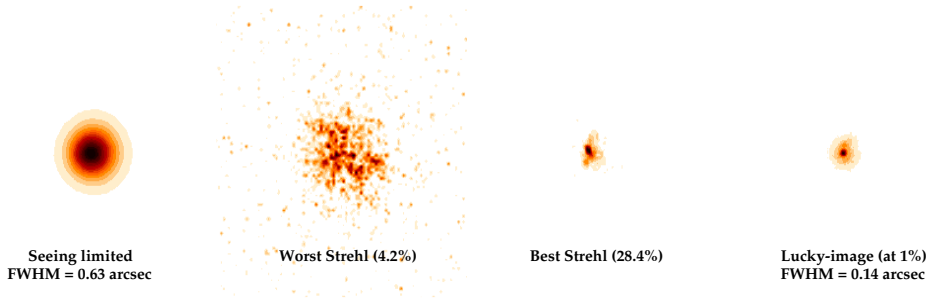

FIGURE 3.11: From left to right: (a) seeing limited image stacking 3000 frames for a photometric standard star (Ross-711); (b) frame with the worst measured Strehl ratio among the 3000 frames; (c) frame with the best Strehl ratio; (d) final image processed by the pipeline by selecting and stacking the 1% best frames.

For the purposes of the present work and advised by F. Hormuth, we have always used the 10% selection rate images. In Fig. 3.12, we show an example of the capabilities of AstraLux and its reduction pipeline. It shows the triple system GJ 900 that we observed in 2012, with the two faintest companions separated by 0.33 arcsec.

The PSF of the resulting processed image ($\mathrm{PSF_{obs}}$) of a single target can be approximated by the combination of a Moffat function and a theoretical $\mathrm{PSF_{th}}$ convolved with a Gaussian:

$$\mathrm{PSF_{obs}} = W\left(\frac{1}{r^2/\sigma_m^2 + 1}\right)^{\beta} + (1 - W)\,\left(\mathrm{PSF_{th}}(r)\; e^{-r^2/\sigma_g^2}\right) \tag{3.12}$$

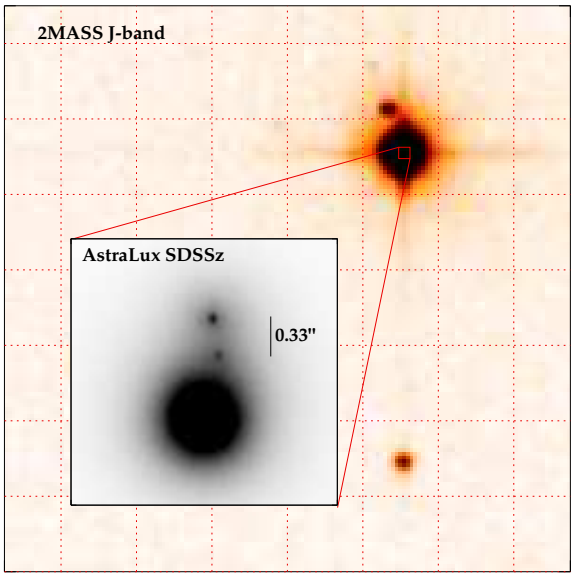

FIGURE 3.12: Example of the close triple system GJ 900 resolved with AstraLux. Image obtained in 2012 by J. Lillo-Box.

where W is a weight for each of the two components, σ_m is the width of the Moffat function, β is its corresponding law index, and σ_g is the width of the Gaussian profile. As determined in Hormuth (2007), approximated values for these parameters for the 10% of selection rate are: $W = 0.31$, $\sigma_g = 24.2$ mas, $\sigma_m = 270$ mas, and $\beta = 1.61$. These values provide residuals smaller than 0.5% of the peak intensity.

3.5.3 Calculation of the Strehl ratio and full-width at half-maximum

The pipeline of the observatory does not provide the Strehl and FWHM of the final image. Instead, we can calculate it as follows. First, the observed radial profile of the target is obtained and modeled by Eq. 3.12. The central region accounting for the 76% of the total energy distribution of the radial profile is calculated, which determines the equivalent FWHM (i.e., $\pm 1.17\sigma$ from the intensity peak), see right panel of Fig. 3.13. The Strehl ratio is obtained by comparing the pseudo-Strehl ratio of the observed radial profile to that of the theoretical PSF (blue profile in the left panel of Fig. 3.13). This pseudo-Strehl ratio is obtained by dividing the maximum value of the radial profile by its integrated energy.

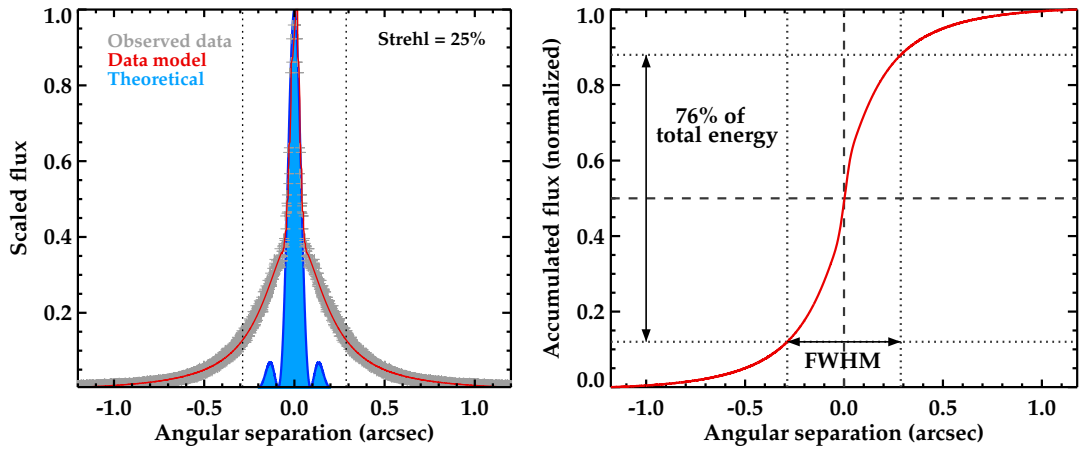

FIGURE 3.13: Example for the determination of the Strehl ratio (left) and full-width at half-maximum (FWHM) for a target given its radial profile from an AstraLux image (right). In the left panel the theoretical radial profile is shown in blue (to be compared to the observed profile in gray).

3.6 Forthcoming and future instrumentation

The new high-spatial resolution instrumentation is now focusing on efficiently obtaining high-contrast ratios at small angular separations. The latter state-of-the-art instruments in this category are GPI/Gemini South (Macintosh et al., 2014) and SPHERE/VLT (Dohlen et al., 2006). The first is capable of detecting 0.2 arcsec companions with contrast ratios of 10^6 (i.e., $\sim$ 15 mag) in one-two hours exposure time. For SPHERE, several modes are available but, in brief, it can achieve contrast ratios of 10^6 for a target at 0.3 arcsec in one hour exposure time. It is important to note that the main improvement in these instruments as compared to previous high-spatial resolution instruments (AstraLux/CAHA, FastCam/ORM, PHARO/, DSSI, etc.) is the large contrast, which allows the detection of giant planets at > 5 AU, where radial velocity is not sensitive and the probability of a transit is very low. Added to this, other proposed instruments for the future E-ELT telescope, namely METIS (Brandl et al., 2014) and EPICS (Kasper et al., 2010), will be capable of directly image planets in the low-mass (Earth-like) domain.

Regarding the space-based mission, starshades and coronograph missions are currently being designed by different groups, with the main aim of imaging Earth-like planets (see for instance, the New Worlds Mission[12]).

[12]http://newworlds.colorado.edu

Chapter 4

High-resolution spectroscopy: measuring radial velocities

Contents

"... eppur si muove"

Attributed to Galileo Galilei in 1633.[1]

[1] Sentence traditionally attributed to Galileo Galilei (1564-1642) when in 1633 he was forced to retract about his claim that Earth moves around the Sun.

4.1 Radial velocity imprints of planetary-mass companions

The Doppler effect is a well-known consequence of the motion of bodies emitting waves (such as sound or light). The length of these waves is enlarged or contracted depending on the relative velocity (v) between the transmitter and the receiver. Mathematically, the non-relativistic formula describing this change in wavelength is given by:

$$\frac{\Delta\lambda}{\lambda} = \frac{v}{c}, \tag{4.1}$$

where $\Delta\lambda = \lambda_0 - \lambda_1$, being λ_0 the originally emitted wavelength and λ_1 the finally received wavelength. Alternatively, the observed wavelength by the receiver can be expressed as:

$$\lambda_1 = \lambda_0 \left(1 - \frac{v}{c}\right). \tag{4.2}$$

It is clear from this equation that if the source is moving towards the observer/receiver then $\lambda_1 > \lambda_0$ (i.e., light is red-shifted), while if the source moves away the observer then $\lambda_1 < \lambda_0$ and so light is blue-shifted.

In the simple case of planet-star system where a planet of mass M_p orbits around a star of mass $M_\star$ with a period P in an orbit characterized by a semi-major axis a and an eccentricity e (see § 1.4), the gravitational pull of the planet induces a relative motion of the star around the center of masses of the system. As seen from Earth, only the radial component of the stellar motion (in the direction of the line of sight) is detectable.[2] This component, the velocity of the star along its tight orbit around the center of masses (hereafter the *radial velocity*), is given by

$$V_r(\theta) = V_{\rm sys} + K\,[\cos(\nu + \omega) + e\,\cos\omega] \tag{4.3}$$

where ω is the argument of the periastron of the orbit, $V_{\rm sys}$ is the radial component of the velocity of the center of masses of the system (also known as systemic velocity), and K is usually called as the semi-amplitude of the radial velocity, and is given by:

$$K = \frac{2\pi a}{P\sqrt{1-e^2}}\,\sin i \tag{4.4}$$

For the purposes of this work, we can use the Third Kepler's Law (see § 1.4) and the identities $a = a_p + a_\star$ and $M_p a_p = M_\star a_\star$ to rewrite Eq. 4.4 as:

$$K^3 = \frac{2\pi G}{P(1-e^2)^{3/2}} \left[\frac{M_p^3 \sin^3 i}{(M_\star + M_p)^2}\right], \tag{4.5}$$

[2] In the case of close stars, it is also possible to detect the tangential component by measuring proper motions in long baseline images. And the Gaia/ESA mission (currently in orbit) will do this by using very precise astrometry.

where the term in brackets is called the **mass function** ($\boldsymbol{F_M}$). By assuming that $M_p << M_\star$, we can present this equation in a more intuitive shape

$$K = \frac{28.4\text{m/s}}{\sqrt{1-e^2}} \frac{M_p \sin i}{M_{\text{Jup}}} \left(\frac{M_\star}{M_\odot}\right)^{-2/3} \left(\frac{P}{1yr}\right)^{-1/3} \tag{4.6}$$

The above assumption is usually valid for planetary systems. Although it depends on several factors, we can see that the difference between assuming the complete formulation (Eq. 4.5) and the simplified one (Eq. 4.6) is very small as compared to the absolute K value. For instance, in the case of a massive planet having $M_p = 13\ M_{\text{Jup}}$ around a low-mass star with $M_\star = 0.5 M_\odot$ in a 1-day period, the difference between the K value calculated by both expressions is just 1.6%. However, unless specified, we will use the complete Eq. 4.5 in our analysis.

Two important conclusions can be extracted from the derivation of the radial velocity expression:

- The RV semi-amplitude (K) depends on the projected mass of the planet ($M_p \sin i$), which provides just a lower limit to the its mass. In the case of planets with detected transits (as it will be the case of the majority of systems studied in this dissertation), the inclination values should be in the range $i = 60° - 90°$, so the true masses could just be < 15% larger ($1/\sin 60° \approx 1.15$) than the projected mass.

- The expected K value for a Jupiter-mass planet around a Solar-mass star in a similar orbit as Jupiter ($P = 11.8$ years) is $K \sim 12$ m/s. For a close-in orbit of a similar system, we obtain $K \sim 203$ m/s. For an Earth-mass planet around a solar-mass star in a 365-days period $K \sim 8.9$ cm/s. This increases to 64 cm/s for a 1-day orbit. In Fig. 4.1, we provide the K values for different planet masses at different orbital periods depending on the mass of the host star. The precision of different high-resolution spectrographs is marked for reference. The small K values expected for any planetary-mass objects at most orbital distances clearly shows the need for high-resolution stable spectrographs for exoplanetary exploration.

The precision reached with the CAFE spectrograph (which is extensively used in this dissertation and that will be described in § 4.4) is ~15 m/s. This allows the detection of Jupiter-mass planets at Jupiter orbital periods and closer to the star. Neptune-mass planets in close-in orbits of few days around low-mass stars (< 0.3 $M_\odot$) are also accessible with CAFE.

4.2 High-resolution spectroscopy for precise radial velocity

The increasing precision of high-resolution spectrographs has gone hand in hand with the improved high-precision photometers aiming at discovering and characterizing small extrasolar

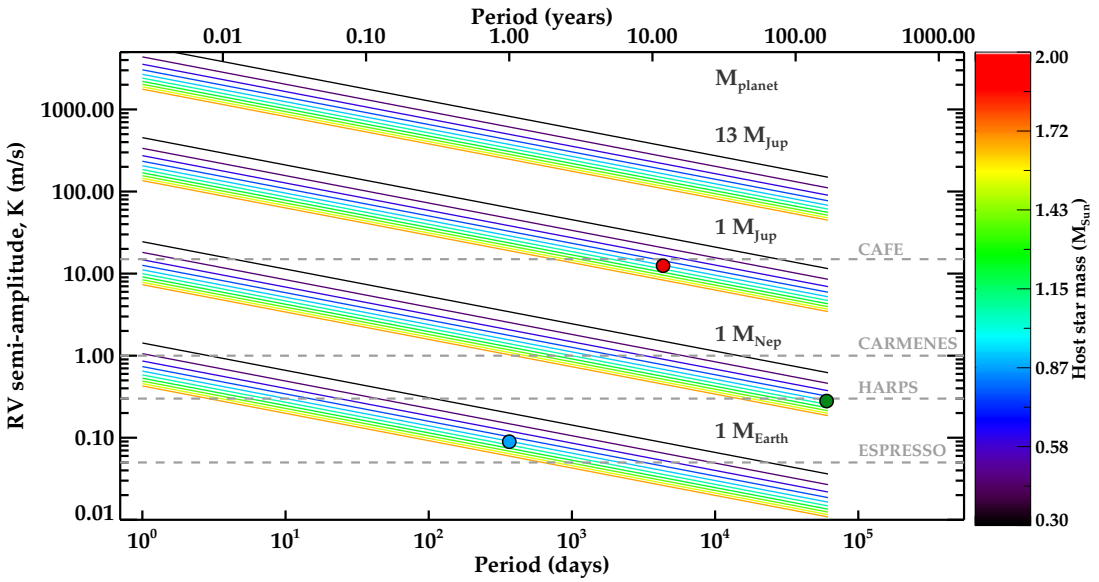

FIGURE 4.1: Radial velocity semi-amplitude expected for different planet masses (each set of colored lines) around stars of different masses (in color-code), as a function of the orbital period. The location of the Earth (blue circle), Neptune (green circle), and Jupiter (red circle) is also presented. The precision of current and forthcoming instruments for precise RV measurements is marked with horizontal dashed lines.

planets. However, although we showed in previous chapters that high-precision photometers allow the detection of Earth-size and even smaller planets, the evolution of high-resolution spectrographs has not yet reached the required precision to detect Earth-like planets (in terms of mass and orbital period). As we have seen in the previous section, precisions of the order of tens of cm/s are required to characterize Earth-like planets. Even Jupiter-mass planets require precisions of few tens of m/s. According to the Doppler effect equation, this implies sub-mÅ precisions in wavelength. Reaching this level of precision when measuring the line center of one spectral line would require spectral resolution of the order of $R \sim 10^7$. The alternative is the combination of thousands of spectral lines, which allows to reach this precision with resolutions $R \gtrsim 5 \times 10^4$.

Expected precision for a single spectrum

The expected uncertainty in the measurement of the line center of a spectral line with **relative contrast**[3] C and full-width at half maximum of FWHM, assuming that photon noise follows a Poisson distribution, is given by (Figueira, 2010)

$$\sigma_\lambda = \sqrt{\text{FWHM}}\,\frac{\sqrt{2-C}}{C}. \tag{4.7}$$

This expression shows that, as one would expect, broader and lower contrast spectral lines provide larger uncertainties in themeasurements of the line center. In terms of radial velocity, this

[3]The contrast is defined as the ratio between the height of the line and the continuum level.

uncertainty for a given line observed with a spectrograph of pixel scale px_{sc} and a signal-to-noise ratio S/N can be written as

$$\sigma_{RV} \propto \frac{\sqrt{\mathrm{FWHM}}}{\mathrm{S/N}} \frac{\sqrt{px_{sc}}}{C} f(C_{\mathrm{eff}}) \tag{4.8}$$

where $f(C_{\mathrm{eff}})$ is a function of the effective contrast of the line (see Figueira, 2010, and references therein).

When combining the information of a large spectral range (B) from the spectrum of a star of spectral type SpT, having a projected rotational velocity $v \sin i$, and observed with a spectrograph of spectral resolution R, the final expected RV precision is given by (according to simulations presented in Hatzes et al., 2010)

$$\sigma_{RV}(m/s) = Q \times (S/N)^{-1} \times R^{-3/2} \times B^{-1/2} \times f(\mathrm{SpT})^{-1/2} \times (v \sin i/2)^{-1}, \tag{4.9}$$

where Q is a constant factor that depends on the spectrograph and $f(\mathrm{SpT})$ is a function characterizing the density of lines in the spectrum, from $f(\mathrm{A-type}) = 0.1$ to $f(\mathrm{M-type}) = 10$, being $f(\mathrm{G-type}) = 1.0$. In the case of CAFE, we find that $Q_{\mathrm{CAFE}} \approx 3.5 \times 10^{12}$, while the estimated value for HARPS is $Q_{\mathrm{HARPS}} = 2.4 \times 10^{11}$ (Hatzes et al., 2010). Having half the spectral resolution of HARPS and twice its spectral coverage, the expected precision for CAFE is $\sigma_{RV}(\mathrm{CAFE}) \approx 10 \times \sigma_{RV}(\mathrm{HARPS}) \approx 15$ m/s.

Precision in long-term programs

Since the main program of this dissertation is to perform a long baseline RV follow-up, there are other technical aspects related to long-term observations that can severely affect the precision of the RV. Some of them can be corrected or calibrated *a posteriori*:

- **Instrumental changes.-** Their origin can be due to different causes like the change of the ThAr lamp, or any update in the instrument involving the change of the CCD, loss of vacuum, etc.
- **Charge Transfer Inefficiency (CTI).-** Dependencies of the relative RV values with the S/N of the spectrum. These are due to the inefficient transfer of the electrons from pixel to pixel during the readout process.
- **Other dependencies with the S/N-** There are other effects that can result in dependencies of the RV with the acquired S/N of each spectrum. In long-term surveys, this may play an important role due to the different seeing and extinction conditions during the different campaigns.

- **Temperature, pressure, and humidity changes.-** Changes in the conditions of the spectrograph chamber can modify the properties of the CCD (e.g., pixel size) and the refractive indexes of the different components of the instrument. An active control of these conditions can highly improve the stability of the instrument, but it is expensive. Instead, a minimum recording of the internal and chamber conditions is necessary to track possible correlations between RV drifts and changing conditions in the chamber (see § 4.4.3).

- **Moon illumination.-** If the relative RV of the Moon is close to the RV of the star and the light from the star is contaminated by the Sun light reflected by the Moon, it can contaminate the spectrum of the star, introducing RV shifts. This is usually a relevant effect for observations at Moon separations of $< 60°$, but could also be important at larger separations for low S/N spectra Santerne et al. (2009). This can be corrected by obtaining a simultaneous spectrum of the sky close to the Moon and then correct for it in the process of RV extraction (see Santerne et al., 2009).

These effects will be analyzed in the case of CAFE in section § 4.4.4. On the other side, there are some sources of uncertainty that reduce the precision of the RV measurements and cannot be corrected *a posteriori*. Here we summarize the most important ones:

- **Seeing.-** In both long-slit and fiber-fed spectrographs, the seeing can be an important source of dispersion difficult to correct *a posteriori*. A constant but large seeing may cause a reduction in the S/N of the spectrum, and thus a loss in RV precision. Spectra taken with different seeing conditions can have RV offsets of the order of several tens of m/s (see Boisse et al., 2010a,b), but this can be tracked with the observation of RV standard stars during the same night. However, the combination of a variable seeing during long exposures and a wrong centering or guiding shifts can importantly decrease the precision by adding random noise, being difficult to correct. Moreover, very good seeing conditions, with seeing values smaller than the fiber aperture are more sensitive to centering and guiding problems.

- **Centering.-** A non-homogeneous illumination of the fiber entrance due to a wrong centering of the object can also introduce RV variations depending on the relative position of the object in the different spectra taken. For instance, in Bouchy et al. (2013), the authors show RV drifts of ~ 25 m/s in SOPHIE when locating the star 1 arcsec away from the fiber center. There is no system in CAFE capable of controlling this star centering other than the by-eye homogeneity of the wings of the PSF minus fiber image in the guiding camera, so expert observers are required.

- **Guiding.-** The precision of the guiding system of the telescope is also important since it governs the different positions of the star in the fiber entrance along the exposure. This

affects the homogeneity of the illumination and thus the RV precision. However, guiding precision of the order of 0.1 arcsec are expected to cause systematics of the order of few m/s for seeing conditions similar to the fiber entrance diameter (Bouchy et al., 2013). Larger systematics will be obtained for better seeing conditions due to a more inhomogeneous illumination of the fiber. The guiding precision of the new tracking camera of the 2.2m telescope in CAHA provides guiding precisions of the order of 0.1-0.2 arcsec, which corresponds to RV differences of few m/s.

- **Extinction and BERV.-** The barycentric Earth radial velocity (BERV) corrects for the Earth motion in the Solar System and is usually calculated at mid-exposure time. However, for long-exposure time spectra this is not precise due to the different extinction and seeing conditions in the atmosphere. The correct time to calculate the BERV should be a photon weighted time. Its calculation is currently possible with the installation of exposuremeters such as in the case of HARPS, HARPS-N, or SOPHIE. The exposuremeter measures the stellar flux in real time and the flux weighted mean of the observation time. Additionally, it can be used to stop observations when the desired S/N is reached. CAFE does not have this capability but the uncertainties introduced by this effect should be of few m/s, below its expected precision.

- **Line smearing in long-exposures.-** The BERV changes by some tens of m/s during relatively long exposure times of $T_{\rm exp} > 1800$s. This produces an artificial broadening of the spectral lines, which diminishes the accuracy in the determination of the line center. However, its effect is expected to be small in our typical exposure times of $1800 - 2700$ s, given the expected precision of CAFE.

The seeing, centering, and guiding effects induce a non-uniform illumination in the fiber entrance of the telescope. This is reflected in slight variations of the line profiles and positions in the detector, which affects the RV measurements. To minimize these effects, the need of good scrambling imagers and octagonal fiber has been demonstrated (e.g., Boisse et al., 2010a, Bouchy et al., 2013, Hunter & Ramsey, 1992, Lovis et al., 2008). In particular, optical fibers have good scrambling properties but double scramblers are needed to reach precisions of ~ 10 m/s. The CAFE instrument lacks this double scrambler but its installation is under study by the observatory after our suggestion. Additionally, the installation of a centering system allowing an optimal positioning of the target in the fiber center may improve the instrument precision. Before these improvements are installed, additional uncertainties of 10-15 m/s are expected in the RV measurements due to non-uniform illumination problems, difficult to measure with this instrument.

4.3 Extracting the radial velocity

4.3.1 The cross-correlation approach

Although several techniques have been proposed to accurately extract the radial velocity from a high-resolution spectrum, the cross-correlation approach is the most commonly used (Baranne et al., 1979). This is due to several reasons, namely its simplicity and the amount of information that can be extracted from its shape.

This approach is based on the construction of the cross-correlation function (CCF) between the observed spectrum and a template. In the simplest (but very powerful) case, the template is just a list of central wavelengths of several spectral lines in the same wavelength range as the observed spectrum. In this case, the template is called a binary mask, being 1 inside the line profile (i.e., in the range $\lambda_0 \pm$ FWHM) and 0 outside the line (see Fig. 4.2). For every line, we move the mask across the problem line for different velocities according to the Doppler effect equation (Eq. 4.2). At every step, we get the total flux inside the binary mask (cross-correlate both spectra). In Fig. 4.2, we illustrate this process for one line.

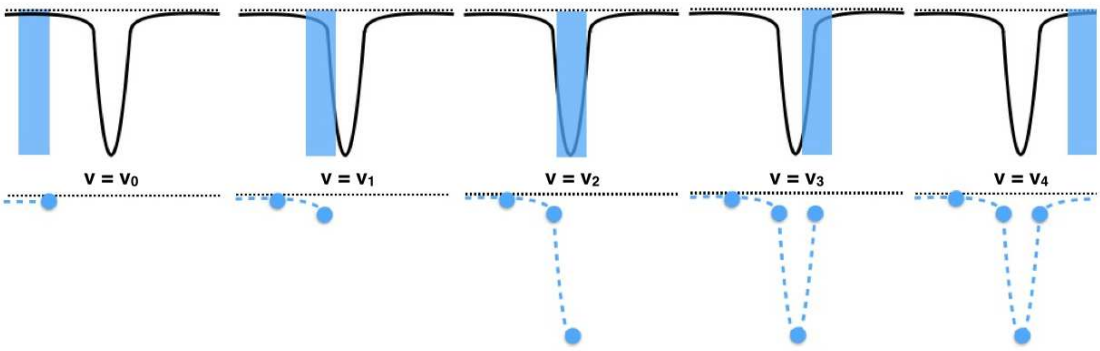

FIGURE 4.2: Cross-correlation for a single observed line (in black, top panels). The mask is represented by the transparent blue box. The bottom panels represent the construction of the CCF at every velocity shift of the mask.

There are 2 fundamental parameters when building the CCF and performing the cross-correlation:

- σ_{step} (km/s): step in velocities to shift the mask.
- σ_{width} (km/s): width of the mask boxes.

General rules for the selection of these parameters are: $\sigma_{\text{step}} < \sigma_{\text{width}}$, $\sigma_{\text{width}} <$ pixel size (km/s), $\sigma_{\text{step}} \sim \sigma_{\text{width}}/2$ (P. Figueira and N. Santos, *private communication*). It is important to not oversampling the CCF (a too small σ_{step} does not provide any relevant or additional information) neither under sampling the CCF (a too large σ_{step} would imply the loss of information when trying to fit a gaussian to the CCF).

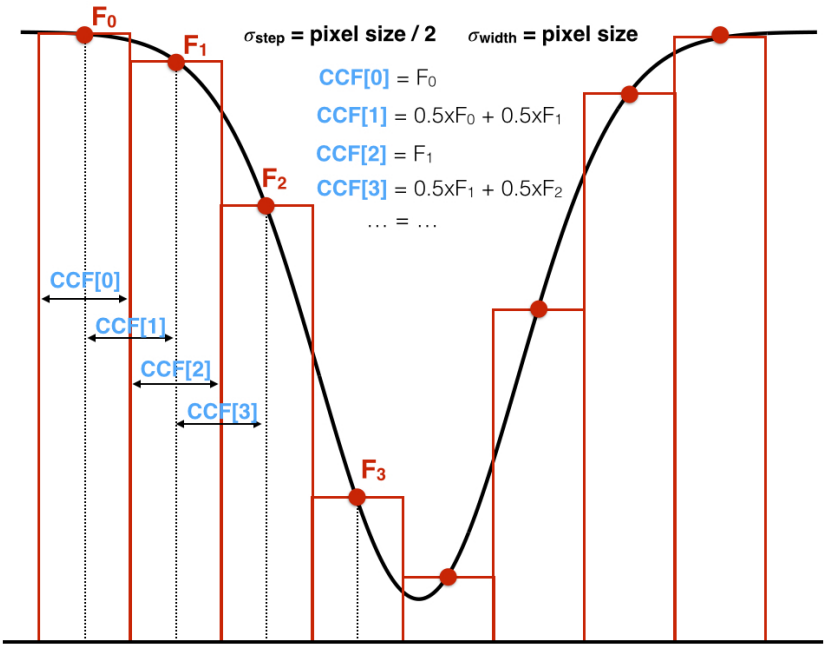

FIGURE 4.3: Detailed calculation of the CCF at different velocity steps. Here we have assumed $\sigma_{\rm width}$ =pixel size and $\sigma_{\rm step} = \sigma_{\rm width}/2$. The rectangles illustrate the pixel size and their corresponding measured fluxes.

Mathematically, the CCF of the i-th spectral line in an observed spectrum S correlated to a template mask T is computed as:

$$CCF_i[\mathrm{v}] = S[\lambda_i] \times T[\lambda_i(1 + \mathrm{v}/c)] \times w_i \tag{4.10}$$

where w_i are the weights applied to each line (normally the strength or contrast of the line in the original template used to construct the mask). In practice, we create an array of velocities v in a range $\mathrm{v} \in [-\mathrm{v}_A, +\mathrm{v}_A]$ with step σ_{step}. Then, for each velocity, we compute the flux of the observed spectrum in the range $[\lambda_{\rm v} - \sigma_{\rm width}, \lambda_{\rm v} - \sigma_{\rm width}]$, where $\lambda_{\rm v} = \lambda_0(1 + \mathrm{v}/c)$, being λ_0 the rest wavelength of this particular spectral line. This is schematically explained in Fig. 4.3. The output array with a cross-correlated value for each velocity is multiplied by the corresponding weight of the line. The complete CCF is then obtained by adding the weighted CCF_i of every line as:

$$CCF[\mathrm{v}] = \sum_i S[\lambda_i] \times T[\lambda_i(1 + \mathrm{v}/c)] w_i \tag{4.11}$$

While computing the CCF, two important sources of uncertainty must be taken into account. In particular, residuals from the *cosmic rays* elimination (or non-removed cosmic rays) can importantly affect the final radial velocity measurement, introducing artificial asymmetries in the CCF. We corrected for this by masquerading pixels with anomalously large flux values (over 10σ) and their surrounding ± 2 pixels. This is specially important in long-exposures ($T_{\rm exp} >$ 1800 s) where a large number of cosmic rays can hit the CCD.

Additionally, *telluric lines* can strongly affect the precision of the RV measurements. In particular, telluric lines close or blended with the selected lines in the mask can introduce important RV offsets and broadening of the CCF, thus decreasing its precision. At the expected precision of CAFE, only oxygen atmospheric lines could importantly affect our measurements (P. Figueira, 2014, *private communication*). When 1 m/s precision is aimed, other telluric lines such as water or OH must be taken into account. In particular, Cunha et al. (2014) studied the effect of micro-telluric lines for the cm/s precisions aimed by the forthcoming VLT ultra-high-resolution spectrograph ESPRESSO. In our case, the O_2 lines affecting the CAFE data are mainly concentrated in two bands of the optical spectrum, namely 6865 – 6970Å (order IDs #22 and #23 in the CAFE spectrum) and 7590 – 7700Å (orders IDs #14 and #15 in CAFE). The orders containing these bands should be (and were) avoided. Added to this, orders including Hα (ID #27), Hβ (ID #57) and other broad lines such as the sodium doublets (5890Å and 8200Å) should be (and were) removed from the calculation of the CCF.

4.3.2 Creating an appropriate mask

In this section we test the different criteria required for a line to be considered as part of the mask. We have used a high-resolution spectrum of the Sun as provided by BASS 2000[4] as a template. We normalize every 100 Å of this spectrum by dividing it by its median. In order to make the process clearer, we divide the entire spectrum into small ranges of 20 Å. On every 20 Å slice, we identify the major number of lines possible. In the following we summarize and quantify the different criteria used to select or reject every identified line:

1. Minimum line contrast

The contribution of weak absorption lines (small contrast) to the radial velocity information is small as compared to strong lines (large contrast). They introduce more noise than useful information to the CCF. The larger the contrast, the more precisely we could measure its center (and so its radial velocity shift). We have performed simulations to estimate the limiting contrast that would allow us obtaining final radial velocity precisions of ~ 10 m/s. We simulated 1000 lines with the same contrast and with the typical CAFE resolution. Then, we combined their CCFs to obtain the averaged radial velocity. This was done for different line contrasts in the range C =5%-100% and four different continuum noises, corresponding to S/N = 5, 8, 10, 20. The results are plotted in Fig. 4.4, left panel. From this plot it is clear that the combination of lines with contrast $C > 5\%$ in spectra of S/N> 10 provide the expected radial velocity precision. In the case of S/N< 10, only the combination of lines with contrasts $C > 50\%$ achieve this precision. Since the number of lines with $C > 50\%$ will be small, we prefer to loose here some precision by setting a minimum contrast for low S/N spectra of

[4]http://bass2000.obspm.fr

$C > 30\%$ but keep many more lines. In our purpose to compute a general mask, we will select lines with contrasts $C > 5\%$. Then, for every given star, if most of the spectra are taken with low S/N, we should only use mask lines with $C > 30\%$.

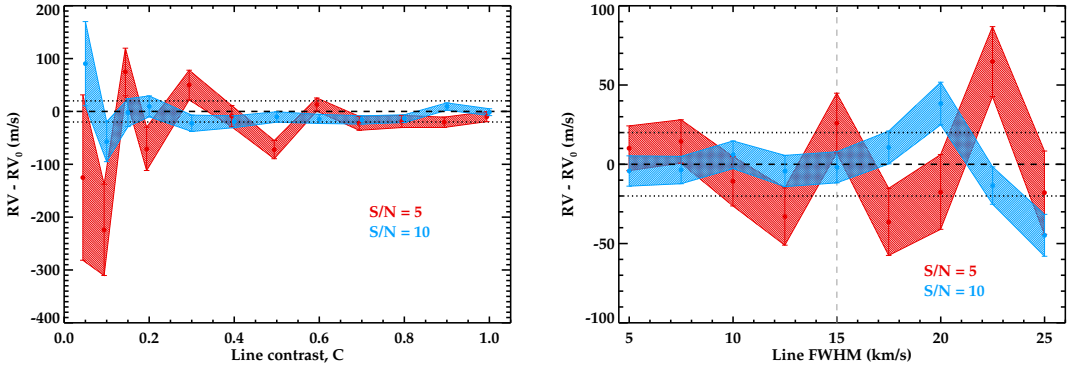

FIGURE 4.4: Line depth (left panel) and FWHM (right panel) criteria for line selection of the CCF mask. The color-code represents the median radial velocity of 1000 simulated lines over the standard deviation of all measurements.

2. Maximum FWHM

Broad lines can introduce more noise than information into the CCF. The closer the line width to the instrumental profile, the better precision in the determination of the line center (and thus of the radial velocity). We have performed a similar simulation than in the previous criterion but now fixing the line depth and allowing different FWHM values for the line width. The resolution element of CAFE as investigated by Aceituno et al. (2013) is $\mathrm{FWHM_{CAFE}} = 4.8$ km/s, where we have used the mean spectral resolution of $R = 62000$ (FWHM$= c/R$). The results show that lines broader than FWHM$=$ 15 km/s start to decrease the precision of the radial velocity measurement for a S/N$=$ 10 spectrum of 1000 lines. Although the dependency of the precision with the FWHM is softer than that measure for the line contrast, we decided to keep the FWHM$<$ 15 km/s limit to avoid blending problems with other lines.

3. Close detected lines

Only isolated lines are eligible to be part of the binary mask. Let us consider two lines A and B with center wavelengths, full-with at half-maximum, and contrast values of $[\lambda_A, \mathrm{FWHM}_A, I_A]$ and $[\lambda_B, \mathrm{FWHM}_B, I_b]$, respectively. We assume that both lines are "close" if the separation between their centers is:

$$\Delta \mathrm{v} = c\frac{\lambda_A - \lambda_B}{\lambda_A} < 2 \times \mathrm{FWHM}_A + 2 \times \mathrm{FWHM}_B. \tag{4.12}$$

As a general rule, this criterion is passed by lines which surrounding companions accomplish the above condition. However, we note that the error induced by the presence of a close detected line in the determination of the center of line A, depends on two factors: the separation and the depth ratio between both lines. For instance, a line 1000 times weaker

($I_B/I_A = 0.001$) at $\Delta v = 1 \times \mathrm{FWHM}_A$ will introduce a scatter in the determination of the RV clearly below the 1 m/s level (see some examples in Fig. 4.5). Thus, lines with detected close companions are still eligible under specific relative properties. In order to quantify this, we have simulated different line pairs in a range of contrast ratios and separations. A gaussian fit to the target line provides the shift induced by the presence of the blended line. The results are shown in the left panel of Fig. 4.6. We have used the 10 m/s contour as a limiting criterion. Thus, for a given line, if we detect a companion with a depth ratio I_B/I_A, we would keep line A if the separation between both lines is larger than the one provided by the 10 m/s contour at the corresponding depth ratio. For instance, if $I_B/I_A = 0.4$, we would keep line A if the separation between A and B is larger than $\sim$ 16 km/s, otherwise the line will be rejected (see dashed lines for this example in Fig. 4.6, left panel).

4. Close undetected lines

Added to the resolved lines, there could be some close lines not resolved by the detection algorithm. To account for these cases, we measure the symmetry of each line by determining the integrated flux ratio between the right (F_r) and left (F_l) half of the absorption line, i.e., $S = |F_l/F_r|$. The closer S is to unity, the less probable it contains a relevant blended line. We have simulated this for different contrast ratios and line separations to determine the limiting S that provides similar precisions than the 10 m/s contour. In the right panel of Fig. 4.6, we show these simulations and plot different $S-$contours as a reference ($S = 1.01, 1.05, 1.06, 1.1$) and over plot the calculated RV precision contours determined in the previous criterion. As we can see, the $S = 1.01$ contour coincides with a precision of around 10 m/s. Hence, we decided to keep every line with a symmetry value $S \in [0.99, 1.01]$ (values with $S < 1$ refer to cases where the unresolved line is at the right side of the target line).

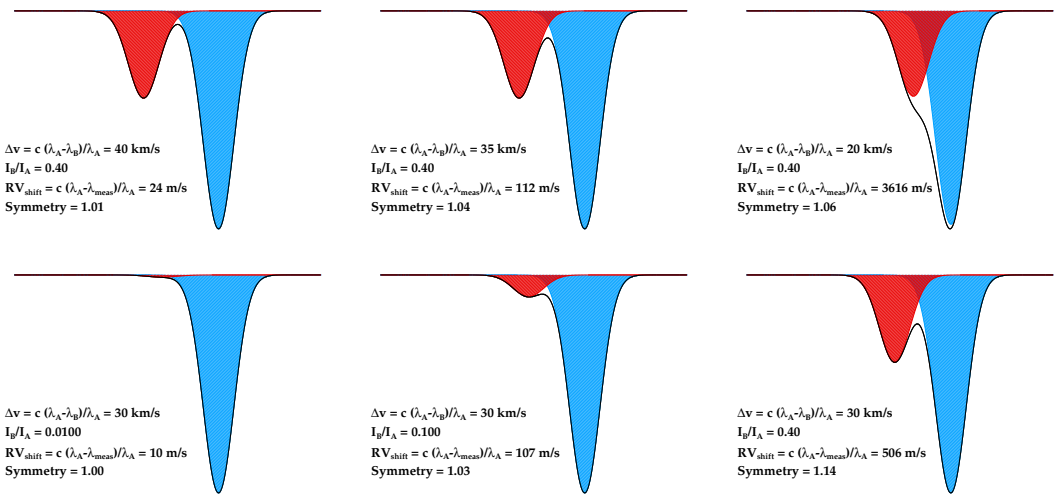

FIGURE 4.5: Radial velocity shift induced by companions at different separations (upper panels) and with different contrast ratios (bottom panels).

In summary, the final conditions to be fulfilled by each line to become part of the template binary mask are:

1. **Line depth.-** We only selected lines presenting at least 5% of absorption (30% in the case of very low S/N spectra).
2. **Line FWHM.-** We discard broad lines since they introduce more noise than information in the CCF. We only select lines with FWHM< 15 km/s.
3. **Close detected lines.-** Apart from all isolated lines, lines with detected close companions are eligible under contrast and separation conditions that still provide 10 m/s precision in the determination of the center of the line.
4. **Blended undetected lines.-** We require all detected lines to have a symmetry value in the range $S = [0.99, 1.01]$, being S the ratio between the left and right fluxes of the line , i.e., $S = F_{\rm left}/F_{\rm right}$.

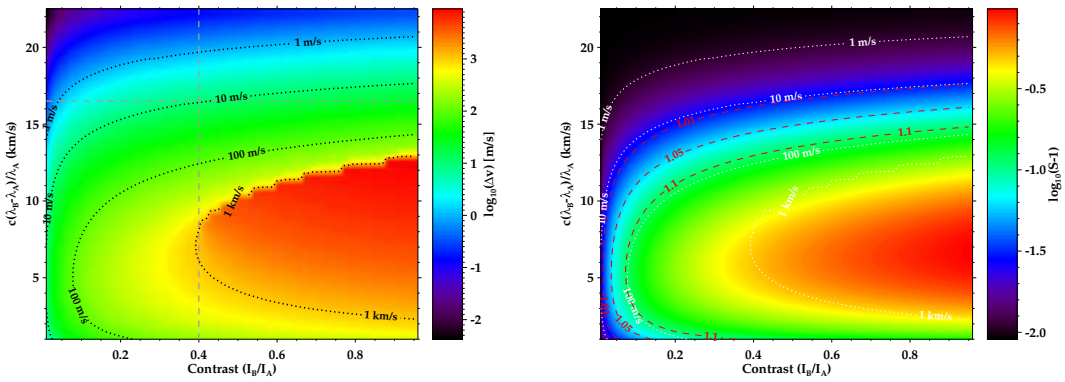

FIGURE 4.6: Left panel: radial velocity shifts due to the presence of a close detected line as a function of the line contrast and separation between lines. Right panel: measured symmetry of a line with a blended companion as a function of the line contrast and separation between both lines. Contours of the left panel are shown in the right panel as red dotted lines for reference.

4.3.3 The final mask and its precision

Applying all these criteria to the solar spectrum, we obtain a final sample of 2097 useful lines among the initially detected 11478 lines (≈ 18%). In Fig. 4.7 we show the number of lines that passed the different criteria for the different CAFE orders. As shown, the most limiting criterion is the depth of the line, which we have selected to be $C = 0.05$ (5%) for spectra with S/N> 10. Logically, at the bluest orders, the most restrictive criteria are those related to blended (detected or undetected) lines, since the density of spectral lines is larger in this region.

In order to test the accuracy and precision achievable with this mask for typical CAFE spectra, we have degraded the solar spectrum to the CAFE resolution and we have only used the

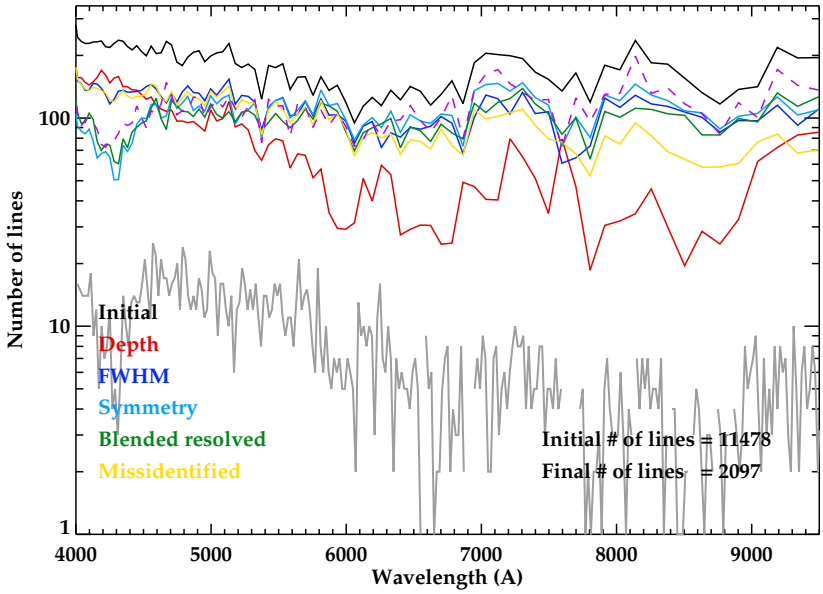

FIGURE 4.7: Number of lines accomplishing each of the requested criteria.

wavelength range visible by the instrument (based on the commisioning wavelength calibration provided in Aceituno et al., 2013). Additionally, we have added different levels of noise to the degraded spectrum. For each noise level, we simulated 300 spectra and computed the CCF to measure the corresponding RV. In Fig. 4.8, we show the results of this simulation.

In the left panel, we show all derived radial velocities for each noise level with small black filled circles. The median value and the standard deviation of all 300 measurements is highlighted as a colored circle and and error bar. In the right panel, we show the corresponding gaussian distribution of the 300 simulations per noise level. As expected, the less noisy is the spectrum, the best constrained is the radial velocity.

Interestingly, for $\sigma_{cont} = 0.0$ (i.e., S/N= ∞), we get $\Delta v(\sigma_{cont} = 0) = 8.5 \pm 2$ m/s. This can be considered as an offset of the mask, and could be due to a non perfect determination of the wavelength centers of the selected lines of the mask. This offset has been subtracted from all measurements.

For all S/N levels, the median value of the 300 simulated spectra lie inside $\pm$ 5 m/s, thus providing good precision over different S/N levels. What the standard deviation (σ_{RV}) of this simulations is telling us is that we have a 68.7% of probability that a given RV measurement is in the range $RV_{\rm true} \pm \sigma_{RV}$. For instance, given an observation with S/N= 10, we have 68.7% of probability that our measurement is closer to the true radial velocity than 23.7 m/s.

In summary, the accuracy of this mask is very good even for low S/N spectra. As expected, its precision drops when decreasing the S/N. We obtain standard deviations from the median value (i.e., precisions) of 2 m/s for S/N= 100, 5 m/s for S/N= 20, 22 m/s for S/N= 10, and 43 m/s for

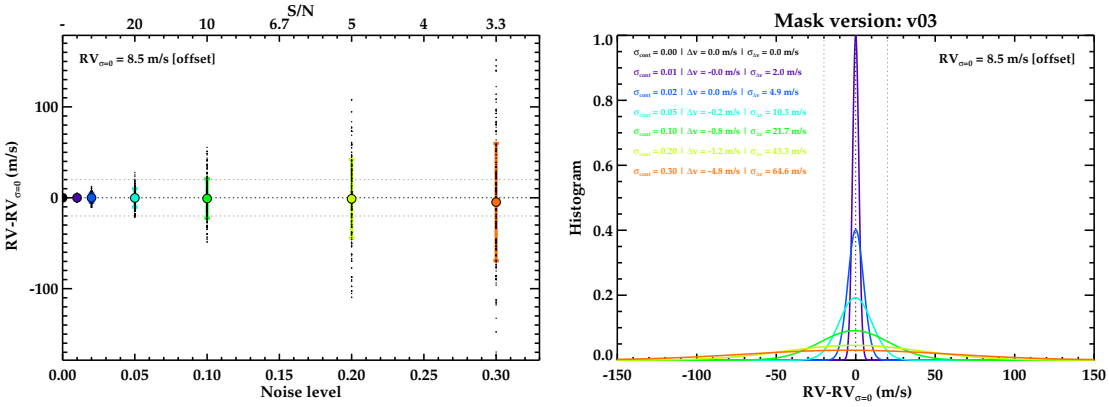

FIGURE 4.8: Simulation to determine the expected nominal accuracy and precision of the mask. **Left:** Radial velocities of the 300 simulated spectra for each noise level. the colored symbols represent the median and standard deviation of the calculated values. Note the offset of 8.5 m/s applied (see text). **Right:** Distribution of radial velocities for each noise level. The color code and the standard deviation of the measurements are shown in the legend.

S/N= 5. This is thus the expected systematic uncertainty due to the selection of spectral lines for the mask at each noise level. The former can be considered as the contribution of the mask to the final uncertainty of the calculated radial velocity for a G2V star.

4.3.4 The outcomes of the cross-correlation function: RV and beyond

The cross-correlation procedure (using the selected mask) provides a CCF for each observed spectrum. This CCF should be considered as a mean spectral profile of the star, since we have averaged thousands of these spectral lines. As such, additional information can be extracted from its profile, shape, and change with time.

Barycentric radial velocity

The first and basic outcome of the CCF is its centroid, providing the radial velocity of the star at the given time of observation. This radial velocity is obtained by fitting a four-terms Gaussian profile to the CCF. The center of this distribution is the radial velocity of the star. The uncertainty in the determination of this peak (σ_{CCF}) provides one of the contributions to the final RV uncertainty. It is computed by assuming uncertainties in the CCF values corresponding to assuming Poisson noise on the flux corresponding to every wavelength ($\sigma_{F_i}(\lambda_i) = \sqrt{F_i}$). This noise is accordingly propagated in the calculation of the CCF and the used to compute the uncertainty of the CCF center.

The calculated radial velocity must be referred to a rest frame. Thus, it must be corrected for the Earth motion. The rest frame is usually defined as the barycenter of the Solar System. This correction is usually called the barycentric Earth radial velocity (BERV) and depends on several factors, namely the geographical coordinates of the observatory, its altitude, the celestial

coordinates of the target, and the effective julian date of the observation. The expression for its calculus can be found in Lindegren & Dravins (2003) and several routines provide its value to few tens of cm/s precision. In particular, we use the *helcorr* routine in IDL. The final barycentric radial velocity of the star is then calculated as RV = RV_{CCF} + BERV.

Bisector analysis

Differences in the line profile of the stellar spectral lines can be directly attributed to different processes. In particular, pulsation or activity from stellar spots can modify the shapes of the spectral lines, which is reflected in variations of their centroids, and thus of the measured radial velocity. This is translated into strong correlations between the measured radial velocities and the corresponding shapes of the CCF at different epochs. This variation in the radial velocity values can be misinterpreted by the presence of additional bodies in the system. In Queloz et al. (2001), the authors identified the RV variations found in HD 166435 being caused by starspots present in the active star (see Fig. 4.9). These variations could perfectly mimic the RV signal produced by a hot-Jupiter planet in a Keplerian orbit.

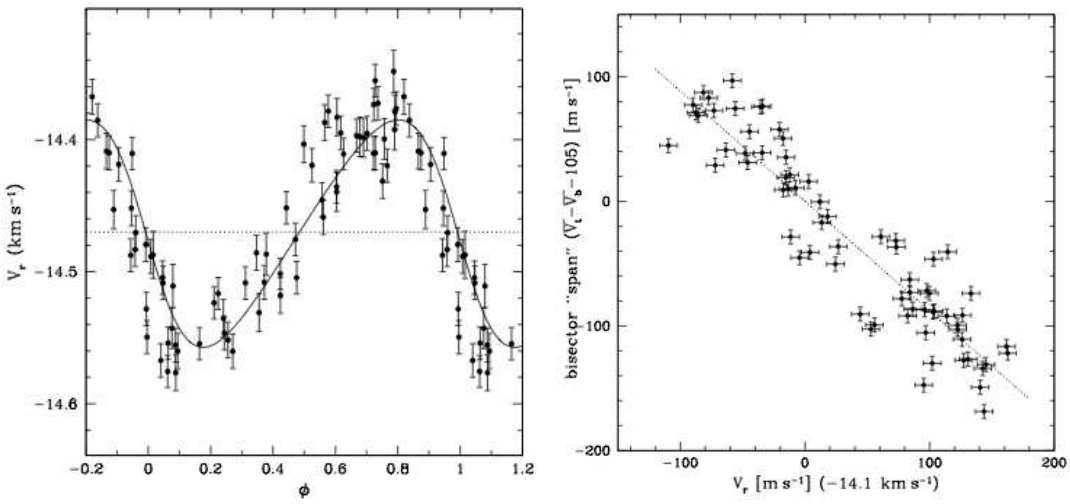

FIGURE 4.9: Figures adapted from Queloz et al. (2001). **Left:** Phase-folded radial velocity curve corresponding to HD 166435, showing a strong periodicity. **Right:** Corresponding correlation between the RV values and the BIS.

Aiming at quantifying the differences in the CCF shape (and thus in the spectral lines) due to stellar activity and/or pulsation, Queloz et al. (2001) proposed the bisector analysis. In brief, this technique measures the difference between the line-bisectors of the top (V_t) and bottom (V_b) vertical sections of the CCF (BIS= $V_t - V_b$, see Fig. 4.9, right panel). Radial velocity changes due to the reflex motion of the star because of the presence of another body in the system would be completely independent of the BIS values, while RV changes correlated with the BIS may indicate a line-profile variation origin. Other line profile indicators have been subsequently proposed to asses the possible correlations between RV and CCF profile changes like V_{span} (Boisse et al., 2011), FWHM variations (Dumusque et al., 2011), BIS^+ and BIS^- (Figueira

et al., 2013), or the bi-Gaussian (Figueira et al., 2013, Nardetto et al., 2006). We refer the interesting reader to Figueira et al. (2013) and references therein for a complete description of every indicator and the applicability for different cases. For the purposes of the present work, we used the *LineProf*[5] tool provided by P. Figueira (2014, *private communication*) and presented in Santos et al. (2014). This tool calculates all indicators given the CCF of the different spectra and checks for possible correlations with the calculated RVs. It provides the Pearson correlation coefficients for each of the different indicators.

The analysis of radial velocity signal induced by stellar activity has put into questioning the capabilities of the radial velocity method to detect Earth-like planets in the habitable zone of Sun-like stars. However, studies of long-term variation of stellar activity have shown that it is possible to correct for these effects and detect Earth-analogs with the forthcoming very-high-resolution spectrographs with $\sim$ 10 cm/s precision like ESPRESSO/VLT and CODEX/E-ELT Santos (2010). Simultaneous photometric observations are needed to correct these activity variations, as described in Aigrain et al. (2012) and Haywood et al. (2014).

4.3.5 Other approaches: maximum-likelihood estimation

Other approaches to extract the radial velocity from an observed spectrum have been proposed by different authors. In particular, different types of templates (such as synthetic spectra of similar spectral type as the problem star, unweighted binary masks, self-correlation with one of the epochs, the solar spectrum, etc.) have been tested.

Alternatively, Zucker (2003) developed a scheme to combine cross-correlation functions from the different orders based on maximum likelihood estimation. Zucker (2003) showed that maximum-likelihood parameter determination is equivalent to cross-correlation (see section 2 in that paper). The method assumes that the observed spectrum, $S(n)$, can be modeled by a template, $T(n)$, scaled by a constant (a_0), shifted by a determined number of bins (s_0) with the addition of random white Gaussian noise with a specific standard deviation (σ_0), $S(n) = a_0 T(n - s_0) + \mathcal{N}(0, \sigma_0^2)$. The natural logarithm of the likelihood function becomes

$$\ln L = -N \log \sigma_0 - \frac{1}{2\sigma_0^2} \sum_n [S(n) - a_0 T(n - s_0)]^2 + constant, \tag{4.13}$$

where N is the total number of bins (pixels) of the spectrum. The set of parameters $[\hat{s}, \hat{a}, \hat{\sigma}]$ maximizing the function provides the best fit of the modified template to the observations. In particular, $\hat{s}$ can be identified with the radial velocity of the star. This method assumes zero mean for both the template and the observed spectrum.

[5] This python code is available at https://bitbucket.org/pedrofigueira/line-profile-indicators

In the specific cases where this approach was used to extract the radial velocity, we employed a modified version of our genetic algorithm presented in Lillo-Box et al. (2014a) (*GAbox*, explained in depth in Appendix A), to find the set of parameters maximizing the likelihood in Eq. 4.13. We used synthetic spectra from Coelho et al. (2005) and used ATLAS09[6] to compute templates with similar spectral properties as the target star. *GAbox* searches for the best-fit set of parameters with no need of exploring the whole parameter space.

We have used this approach in different analysis, namely for Kepler-91b (section § 6.2) and in the case of fast rotators (section § 6.6). However, slightly better results in the case of slow rotating stars (such as Kepler-91) might be obtained by the CCF approach (P. Figueira, 2014, *private communication*).

A similar but more complex (and improved) implementation of this method was presented in Anglada-Escudé & Tuomi (2012) to be included in the pipeline for the HARPS instrument (HARPS-TERRA). The authors called this method as **template matching** and is based in the same principles explained above, fitting the observed spectrum to a high S/N template (being either a synthetic spectrum or the combination of all spectra of the target source) and obtaining the least-square set of parameters (mainly velocity shift and continuum level), including the Doppler shift of the spectrum (i.e., the radial velocity). While they obtained similar precisions for G- and K-type stars with both CCF and template matching, the latter method provided better results for M-type and active stars (see paper for details).

4.4 CAFE in a nutshell

4.4.1 Overview of the instrument

The Calar Alto Fiber-fed Échelle spectrograph (CAFE, Aceituno et al., 2013) was installed at the 2.2 m telescope of the Calar Alto observatory on May 24th, 2011. It is a high-resolution Échelle spectrograph (R = 57000 − 67000) covering the optical region of the spectrum between ~ 4000-9500 Å. This instrument was entirely designed and assembled at the observatory in order to replace the previous high-resolution spectrograph, FOCES (Pfeiffer et al., 1992). The aim was to improve the efficiency and precision of the instrument with respect to its predecessor. To that end and with the ultimate goal of achieving precisions of 15 m/s in radial velocity for stars brighter than 14 mag in the V-band, a new camera was designed and new more efficient and long-term stable fibers were used, also minimizing the number of movable parts. The instrument is placed in a stabilized room, avoiding any kind of vibrations, or temperature and pressure changes, which can reduce the precision of the instrument by a significant amount (see § 4.4.3). As its name clearly states, the dispersion element is fed by a fiber of 2.4 arcsec in diameter. It

[6] http://kurucz.harvard.edu/grids.html

is equipped an iKon-L CCD camera made by Andor Technologies, with 2048 × 2048 pixels of 13.5 μm. This CCD has a better quantum efficiency, lower readout-noise and higher read-out speed than that for FOCES. Its wavelength range is divided into 84 orders separated by ∼ 20 pixels in the blue part and ∼ 10 pixels in the red part.

4.4.2 The CAFE reduction pipeline

The data used for this dissertation were reduced by using the improved pipeline[7] provided by the observatory that delivers a fully reduced spectrum (see details in Aceituno et al., 2013). Prior to submitting any spectrum to the reduction pipeline, we run our own pre-pipeline routine to combined the several tens of bias and continuum images obtained during the evening and/or morning calibrations before and after the observations to obtain higher S/N calibration frames. This pre-pipeline also selects the corresponding ThAr frame to wavelength calibrate every science spectrum. The latter step is user-adjustable, being possible to select the closest ThAr frame to the science image or a combination of the several tens of ThAr frames obtained during the evening/morning calibrations. The outcome of this pre-pipeline is an automatic script ready to run the CAFE pipeline for all nights in a given campaign.

The CAFE pipeline does a complete processing of the spectra, including bias subtraction, order tracing and extraction, and flat-fielding (including an efficient cleaning of the fringing pattern). It uses hundreds of thorium-argon lines from the selected ThAr frame to wavelength calibrate the spectrum. Typical uncertainties of 1 mÅ per line (few tens of m/s) are achieved in this step.

We processed all our spectra with the observatory pipeline as explained above.

4.4.3 Improving CAFE: shutter, chamber monitoring, and S/N estimator

During our first runs with the instrument in 2012 and the first analysis of the data, we proposed some improvements to the observatory that were implemented by the end of that year and were fully operative since December 2012. Here we explain these and other improvements.

Shutter

During the first runs we detected that the ThAr heating time was of the order of 15-20 minutes. During this heating time, the intensity of the thorium and argon spectral lines varies significantly until the stabilization is reached. This had important implications in the observing strategy since we obtain one ThAr spectrum right after each scientific spectrum to perform the wavelength calibration with a reference as close to the science image as possible (to account for possible

[7] See Appendix on http://www.caha.es/CAHA/Instruments/CAFE/Cafe/CAFE.pdf

differences in the pixel size along the night mainly due to small temperature, pressure, and/or humidity changes). Instead, due to this heating time, one should wait 15-20 minutes until the lamp is completely stabilized. In order to quantify how this heating time affects the position of the centroid of the ThAr lines with time, we selected a set of 46 isolated and high S/N spots (thorium/argon lines in the 2D raw images) spread along the whole CCD (see Fig. 4.10). We obtained successive arc frames along several hours turning on and off the lamp at different moments and measuring the centroid position of every spot in every arc frame. In Fig. 4.11, we show the results of this test. We plot the relative position of every spot in every frame (black circles) and the median relative position of the 46 spots as colored circles (red for the X-position in the CCD and blue for the Y-position).

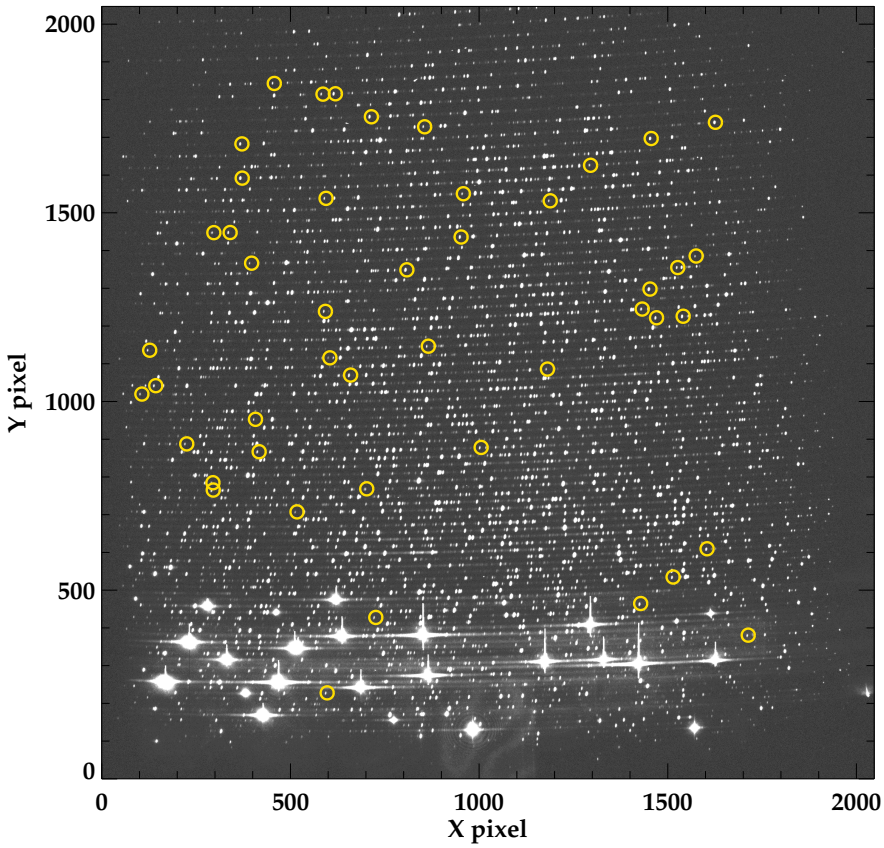

FIGURE 4.10: Selected spots for the centroid analysis in a ThAr frame.

From this analysis it is clear that the stabilization of the ThAr lines (and thus the stability of the wavelength calibration) takes more than 20 minutes once the lamp has been turned-on. We measured differences in the relative position of the spots of several tens of millipixels (mpix), which translates to several tens of m/s in the extracted radial velocity data. The solution for this (rather to waiting for 20 minutes every time we turned-on the lamp) is to keep the lamp on during the whole night when precise radial velocity data (at the level of $\sim$ 15 m/s) is needed.

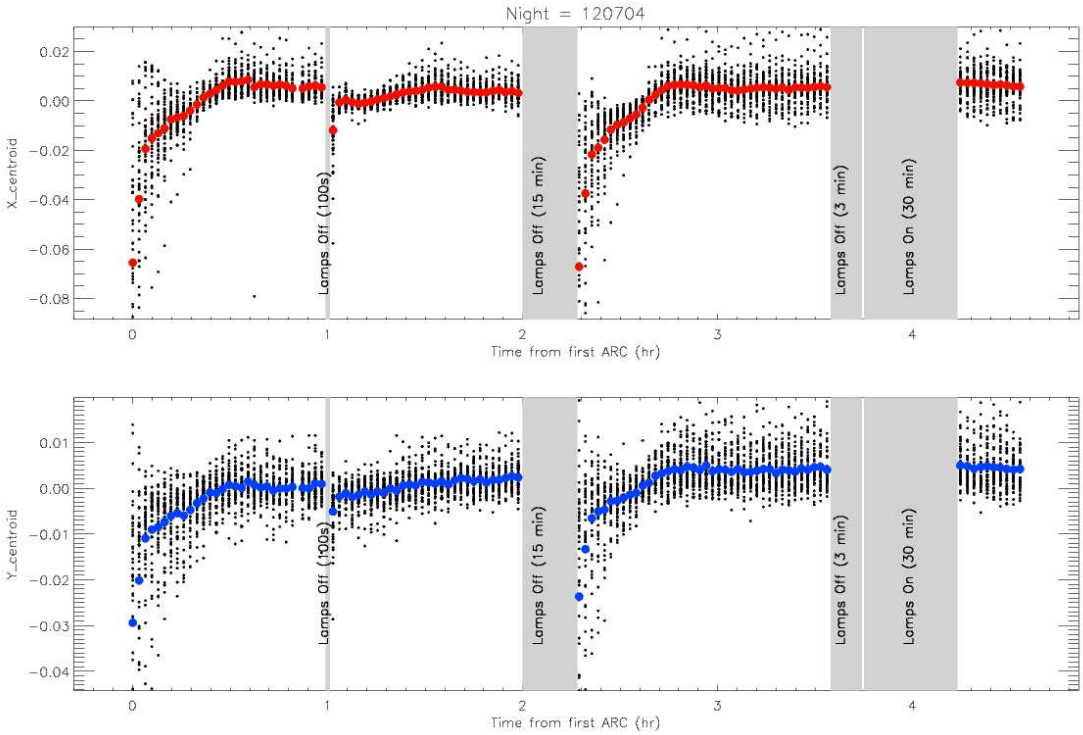

FIGURE 4.11: Analysis of stability of the selected set of ThAr spots in the raw 2D images of an arc frame. The individual relative positions of every spot on every image are shown as black circles. The median values of all 40 spots in every frame is shown as a colored circle, red for the X-axis and blue for the Y-axis. We mark the times when we turned off or turned on the lamp.

As a result of this study, we decided, together with the CAHA experts on the instrument (namely Jesús Aceituno and Sebastián Sánchez) to include a shutter in the optical path of the ThAr lamp in order to maintain the lamp on during the night observations, without contaminating the incoming science light from the target. The shutter was installed in December 2012 with successful results regarding the arc stability. In Fig. 4.12, we show the X-positions of all 46 spots along two different nights, before (left) and after (right) the shutter was installed. As shown, the mean dispersion of the spot locations is impressively reduced from 12 mpix to less than 0.1 mpix (more than two orders of magnitude). The new precision corresponds to few tens of cm/s of stability of the ThAr spots along the whole night.

Hence, we recommend to keep the lamp on during the whole night and use the shutter accordingly to obtain arc or scientific frames.

Chamber monitoring

As we have seen in the previous section, another important source of noise at this level of precision can be changes in the temperature, pressure, and/or humidity of the CAFE chamber. Although this is partially mitigated by the use of close ThAr frames to perform the wavelength calibration, an active control of the room conditions is advisable, as it is the case of, e.g.,

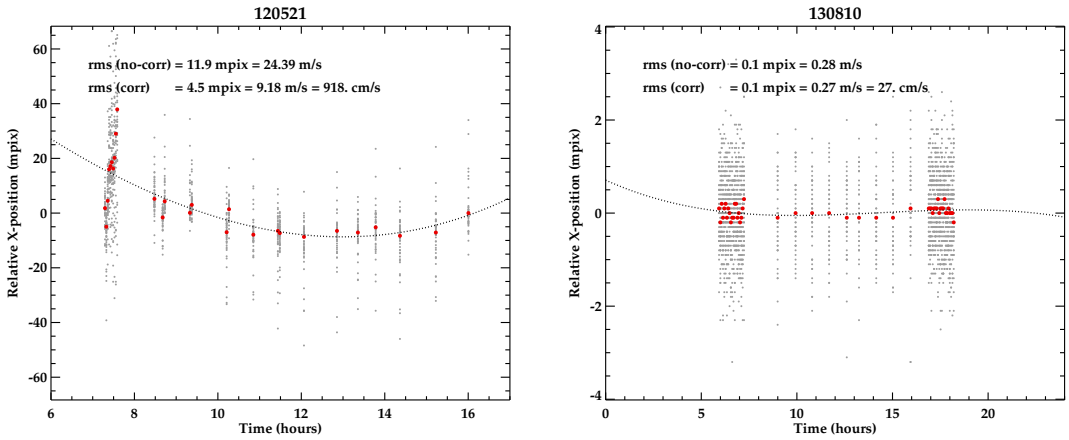

FIGURE 4.12: Relative position of the 40 selected ThAr spots prior (left) and after (right) the installation of the shutter. The root mean square (rms) of all frames at the night is shown on every panel.

HARPS-N (Cosentino et al., 2012). However, since such an active actuation was not possible due to economic restrictions, we suggested the installation of sensors to register these parameters in order to keep control on them and explain possible jumps or non-precise radial velocity measurements. After its installation on December 2012, we have detected variations in the grating room temperature of the order of 7°C along the entire year. As expected, this is correlated with the different seasons, getting colder in winter and hotter in summer.

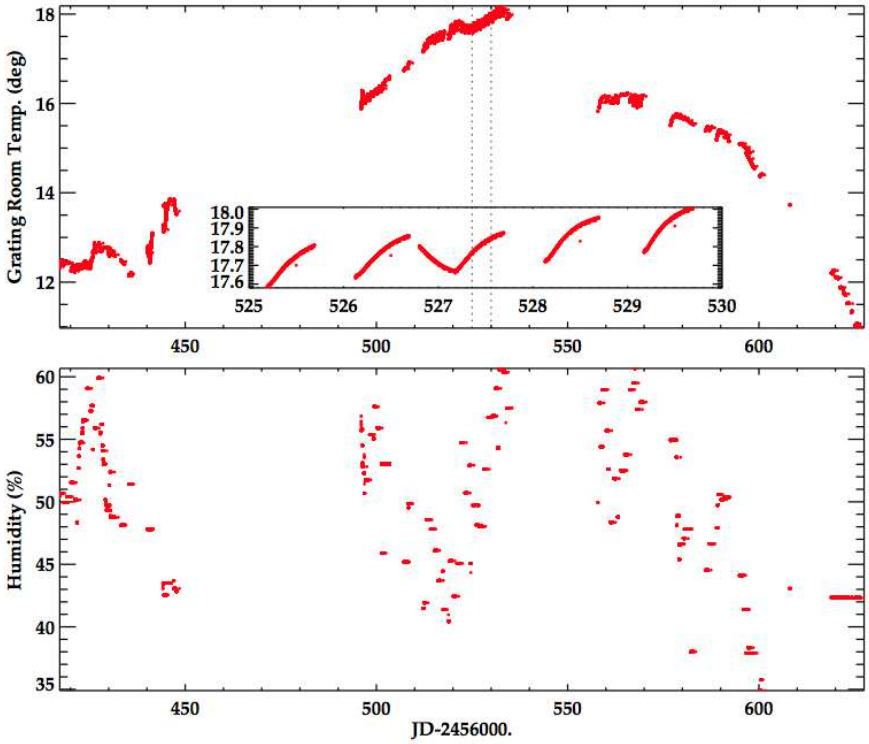

FIGURE 4.13: Grating room temperature (up) and humidity (bottom) along 2013.

On-the-fly S/N estimator

The need for an on-the-fly S/N estimator is clear for an instrument of these characteristics, where the observer needs to adapt the exposure times to the weather conditions in order to reach a certain S/N (in the absence of an exposuremeter as it is the case of SOPHIE and HARPS). In other high-resolution spectrographs such as FOCES, the software uses the 5% of the light to feed a exposuremeter for different purposes, including a S/N estimator which stops the exposition right when the desired S/N has been reached. This system is not available in CAFE and so we developed a tool to quickly obtain a rough estimation of the S/N of the spectrum.[8]

This routine takes the raw spectrum and proceeds with the following steps:

1. Sum the ten central columns of the raw image. This provide the signal as a function of the Y-pixel value, $S(y)$.

2. Look for the rough centers of the orders with enough signal (above 1-σ).

3. Re-center the above positions by fitting a gaussian function. This provides the center of order $n-th$, i.e., $y_0(n)$

4. Calculate the S/N of each detected order as

$$\mathrm{S/N_0}(n) = \frac{\int_{y_0(n)-2px}^{y_0(n)+2px} (S(y) - B)dy}{\sqrt{\int_{y_0(n)-2px}^{y_0(n)+2px} (S(y) - B + N[y_0(n)])dy}} \tag{4.14}$$

   where, B is the median value of the bias in the calibration frames and $N[y_0(n)]$ is the standard deviation of the inter-order pixels right above the $n-th$ order. The **mean zero-order signal-to-noise ratio** (**$\mathrm{S/N_0}$**) is then calculated as the average of the central orders 10 to 60 ($\sim 4500-8000$Å).

5. The results for each order are then plotted and the statistics of the calculation are prompted in the terminal.

In order to compare $\mathrm{S/N_0}$ with the more usually measured S/N ratio (the ratio between the signal and the scatter of the continuum at ~5500 Å), we obtained both values for a set of reduced spectra. The result is shown in Fig. 4.14. $\mathrm{S/N_0}$ is actually measuring the mean intensity of orders 10-60 as compared to the inter-order systematic deviations. Thus, $\mathrm{S/N_0}$ is much more sensitive to atmospheric changes such as clouds, seeing, or extinction than S/N. This will be very useful when trying to explain some RV correlations in the following section. The different levels of S/N achieved for the different targets plotted in this figure are due to the different spectral types and the convolution of their spectral energy distribution with the CAFE efficiency. Note that

[8]This routine is available at the observatory.

while S/N measures the signal-to-noise at one of the orders, S/N_0 provides a mean value for a wide range of the spectrum (~4500-8000 Å).

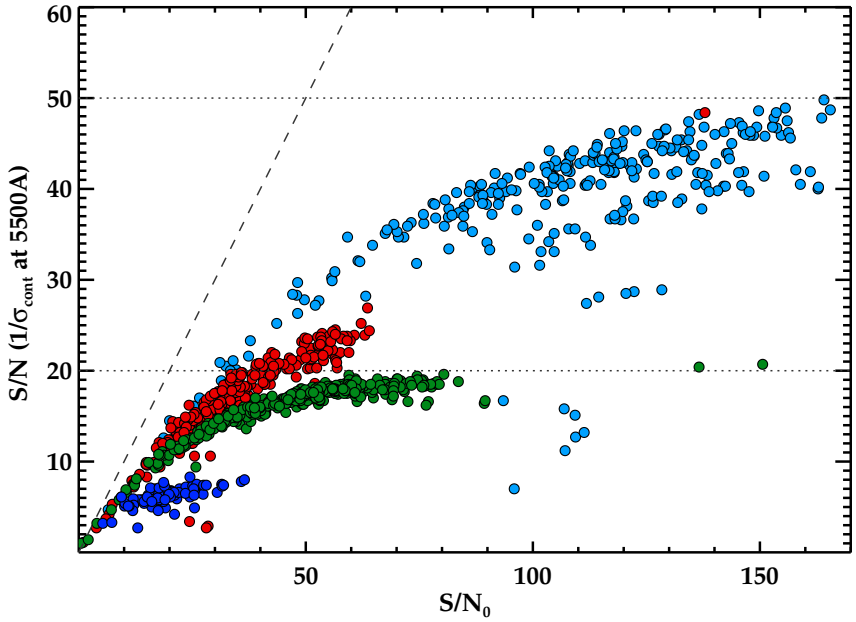

FIGURE 4.14: Signal-to-noise versus continuum noise for different objects, namely HD109358 (light blue), HD124292 (red), HD182488 (green), Kepler-91 (dark blue). The 1:1 line is represented by the dashed line. The S/N in the Y-axis is the common S/N, defined as the ratio between the signal and the scatter at ~5500Å. The different levels reached by each target is due to the convolved spectral energy distribution with the CAFE efficiency for each wavelength, which is different for the distinct spectral types of these targets (from G0 for HD109358 to K3 for Kepler-91).

4.4.4 Analysis of radial velocity standards

The long timespan of our CAFE observations have provided sufficient data as to detect important unaccounted effects of the instrument. In this subsection we analyze the radial velocity of the observed standard stars HD124292 (G8V, $RV = 37.773 \pm 0.100$ km/s), HD182488 (G9V, $RV = -21.462 \pm 0.046$ km/s), and HD109358 (G0V, $RV = 6.228 \pm 0.151$ km/s), which are known to be very stable (Chubak et al., 2012, Nidever et al., 2002). Indeed, HD182488 is located in the *Kepler* field so that it is a good tracer of possible instrumental or atmospheric changes affecting the radial velocity data. In this section, we study in detail a strong dependency of the RV measurements with the S/N of the spectra (particularly enhanced with the S/N_0), and the long-term stability of the instrument due to different events affecting CAFE (e.g., ThAr lamp changes, CCD reparation, etc.). In Fig. 4.15, we show a small part of the spectrum of these three standards, all of them having $S/N_0 \sim 50$ (but fairly different S/N).

Radial velocity dependency with the signal-to-noise ratio

The RV of the three standard stars shows a strong correlation with the S/N_0 of the spectrum,

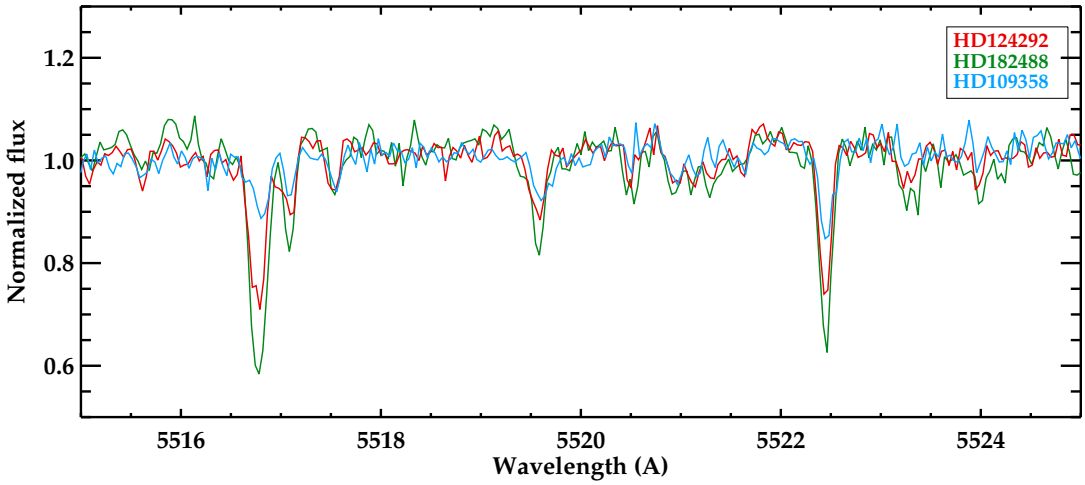

FIGURE 4.15: Spectra of the three RV standards. The three spectra have the same S/N_0 ($S/N_0 \sim 50$) and were corrected for their RV and the BERV. Despite having the same signal level (same S/N_0), the difference in the continuum scatter is noticeable (e.g., around 5518 Å). This is due to the different spectral types of these stars, whose spectral energy distribution is convolved with the CAFE efficiency, providing different noise levels for the same S/N_0.

which is apparently translated to other properties of the CCF. In Fig. 4.16, we show these dependencies with the S/N_0 of the spectrum, the FWHM of the CCF, the height of the CCF, and the measured bisector (BIS). From this figure, we can see a strong linear correlation of the RV with S/N_0. This effect could be due to different reasons. First, the wide range of S/N_0 for a single object observed with the same exposure time, would indicate that different atmospheric conditions (seeing, extinction, clouds, etc.) were present. This effect is usually called the *seeing effect* and has been detected in several circular fiber-fed spectrographs such as SOPHIE (Boisse et al., 2010a). As we explained in section § 4.2, this effect is due to a non-uniform illumination of the fiber entrance, which translates into different spot profiles and thus can induce RV offsets for spectra obtained at different conditions. As demonstrated by Bouchy et al. (2013), the installation of octagonal fibers and double scramblers provides a more uniform distribution of the light, which translates into more precise RV measurements under different atmospheric conditions.

The second possible reason for this dependency is a similar effect to the *charge transfer inefficiency* (CTI), also known to occur in space-based instruments like the Hubble Space Telescope (e.g. Goudfrooij et al., 2006, Massey et al., 2014), and in ground-based instruments like SOPHIE (Bouchy et al., 2009) and HARPS-N (Cosentino et al., 2014). This effect is due to the inefficiency of the CCD to transfer the electrons from one pixel to the next, resulting in a trap of the electrons in the original pixel. If an intensity I_0 is measured in pixel x_0, then, after the transfer to the next pixel in the readout process, this intensity will be diminished as $I_1 = I_0 \times (1 - \epsilon_{\rm CTI})$, where $\epsilon_{\rm CTI}$ characterizes the inefficiency of the transfer. Since this transfer will be done N times until the signal reaches the edge of the CCD, the final measurement would be $I_{\rm meas} = I_0 \times (1 - \epsilon_{\rm CTI})^N$. The important point here is that since the final value depends on the number of transfers, pixels

at the left side of the CCD will be more importantly affected (i.e., N is larger for them) than those at the right side. This results into a blue shift of the lines, introducing RV offsets of the order of several m/s. More importantly, $\epsilon_{\rm CTI}$ is proportionally larger at low fluxes, and so the effect is more important at high-S/N values, introducing important RV offsets.

The observed effect in the CAFE data could be due to any of these effects. Since there is no seeing monitoring measuring the seeing along the line of sight of the telescope, we cannot definitively affirm which of the two is the responsible for the RV dependency. More calibration data and analysis is needed to unveil its nature. For instance, measuring RV offsets of different ThAr frames obtained at different S/N levels (i.e., different exposure times) would indicate that the effect is due to a CTI in the CCD of CAFE. However, since an accurate calibration of the effect is out of the scope of this dissertation, we will use the current data to model this dependency and correct for it when necessary, regardless of its nature.[9]

We then performed a linear fit to the S/N_0 versus RV data and obtained the following expression to correct for this dependency:

$$RV_{corr}(m/s) = RV_{meas}(m/s) - [(-346.1 \pm 8.0) + (3.51 \pm 0.11) \times S/N_0] \quad (4.15)$$

In Fig. 4.17, we show the detrended RV values against the same parameters as in Fig. 4.16. This correction perfectly flattens the measured RV values with any of the aforementioned parameters.

However, in this dissertation we work with relative radial velocities, comparing different measurements of the same target at different epochs. Since all spectra of the same object will be acquired with similar S/N_0 levels, we do not expect this effect to be relevant in the large majority of the targets analyzed in this work. Indeed, if the differences in the S/N_0 levels of the different spectra are small, applying this correction could introduce more noise than the own correction, being thus inadvisable. The uncertainty introduced with this correction is large compared to the correction itself for small differences in the S/N_0 ($\Delta S/N_0$). Instead, this ratio decreases for large $\Delta S/N_0$ values. As a reference, we would recommend not to correct the RV measurements when the maximum difference of S/N_0 between the different spectra of the same object is $\Delta S/N_0 = (S/N_0)_{max} - (S/N_0)_{min} < 30$. We will see that this is the general case for most of the targets observed in this dissertation. In Fig. 4.18, we show the uncertainty of the correction over its absolute value for different S/N_0 differences and mark the suggested limit.

More calibration data is needed to definitively confirm whether this effect is actually due to a CTI-like or seeing effect. In particular, the analysis of the RV of ThAr spectra obtained at different S/N (different exposure times) can be very useful to better calibrate this effect and establish its origin.

[9] Calibration frames are being obtained at the observatory to unveil the source of this trend.

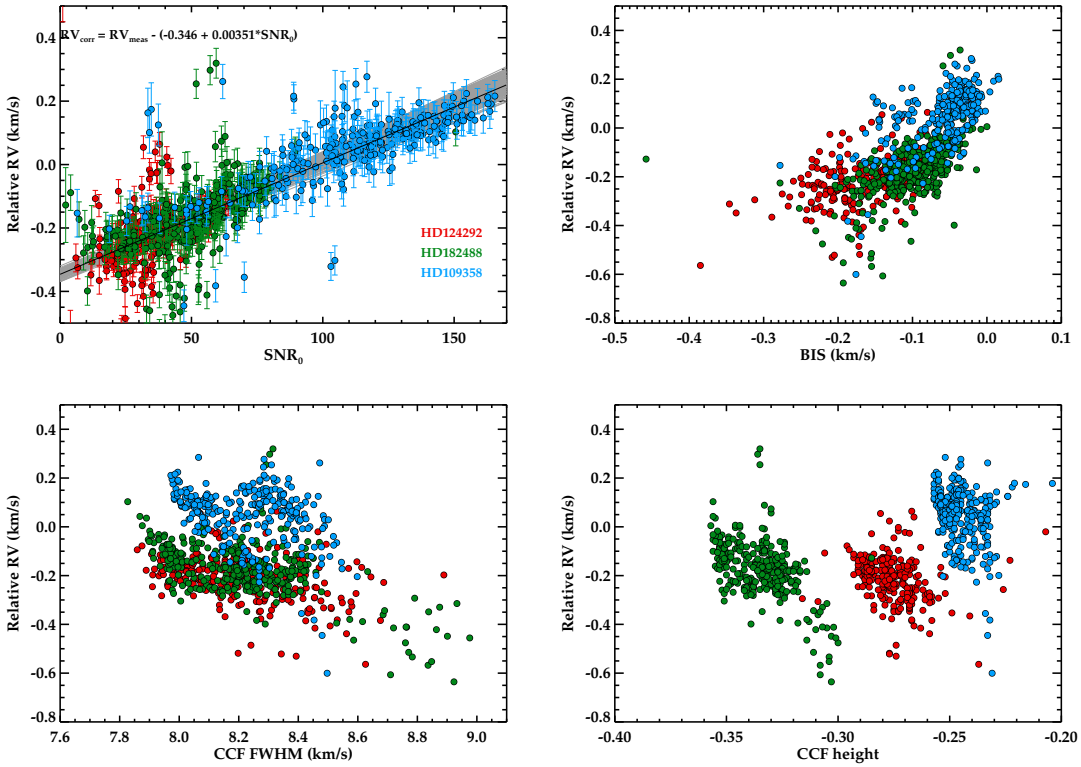

FIGURE 4.16: Dependency of the RV measurements (Y-axis) with different parameters (X-axis). The different colors represent the data for three different standards (see legend in the upper left panel). The RVs are already corrected for the long-term events explained in § 4.4.4. The differences in the height of the CCF in the bottom right panel are due to the diffeernt spectral types (see also Fig. 4.15).

Intra-night radial velocity drift

Due to the lack of an active control system, the ambient conditions of the CAFE room can vary along the night. This can introduce important RV variations. In order to evidence this, we carried out a simple test. We observed the same standard star (HD182488) twice during four nights, at the beginning and at the end of the night. All spectra were then reduced with two different arcs. Reduction A (hereafter RedA) is performed with the closest arc to every scientific image (usually prior or after the science spectrum). Reduction B (hereafter RedB) is performed with the combined arc obtained at the beginning of the night. We have used data from nights 2014-06-25 to 2014-06-28.

The radial velocity obtained by RedA (RV^A) and RedB (RV^B) is shown in Fig. 4.19, and they have been already corrected for the S/N_0 effect explained in the previous section. In this figure we show two panels. The left panel shows the obtained RVs for each reduction. In the right panel, we show the intrinsic RV scatter for each set of RVs. Two important conclusions can be extracted from this test:

- From the left panel we can see that the use of the closest arc provides RV with much

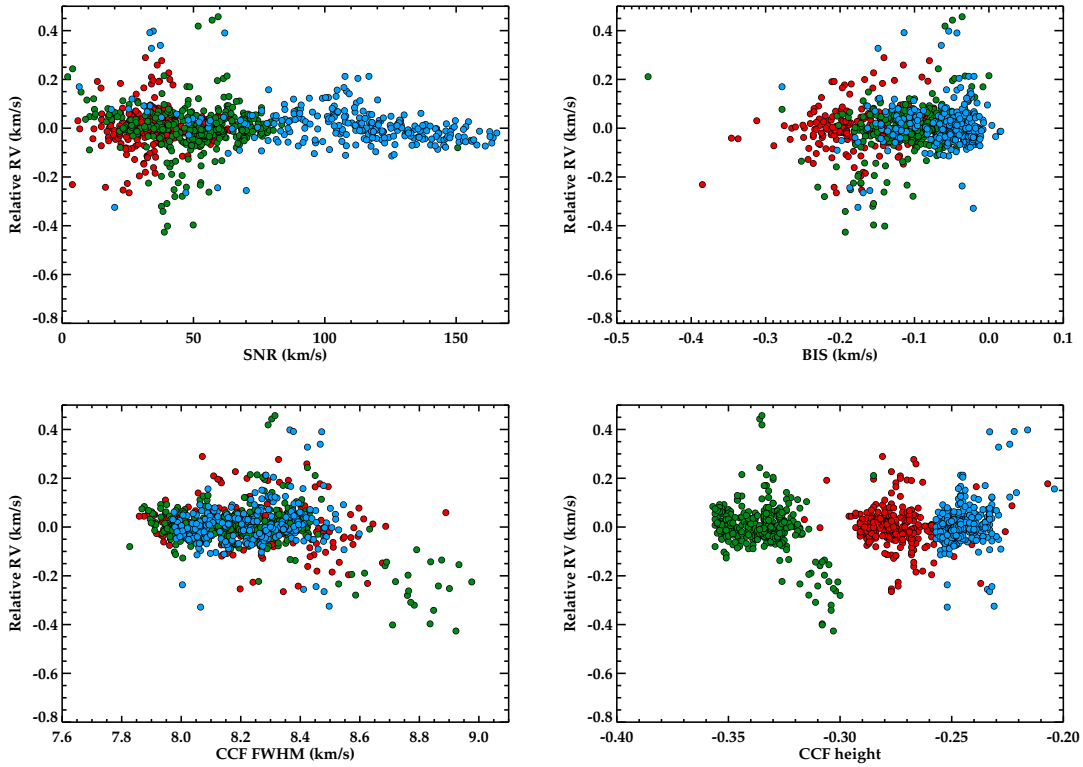

FIGURE 4.17: Dependency of the RV measurements (Y-axis) with different parameters (X-axis) after the CTI-like correction showed in Eq. 4.15. The different colors represent the data for three different standards (see legend in the upper left panel of Fig. 4.16). The RV are already corrected for the long-term events explained in § 4.4.4.

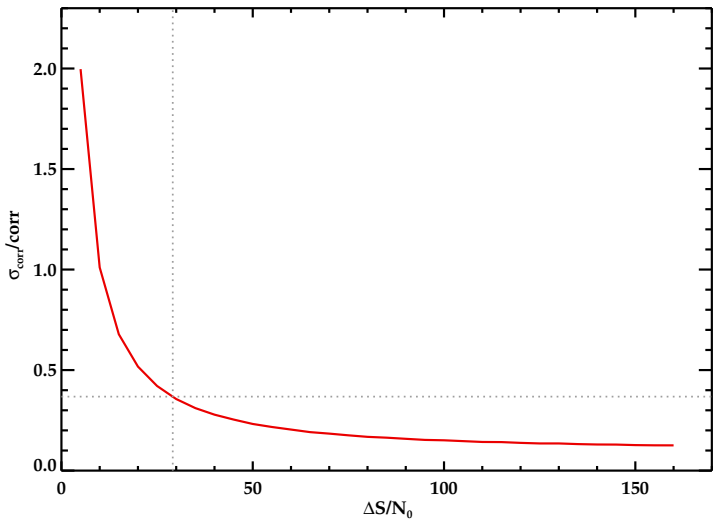

FIGURE 4.18: Relative uncertainty introduced when correcting for the CTI-like effect.

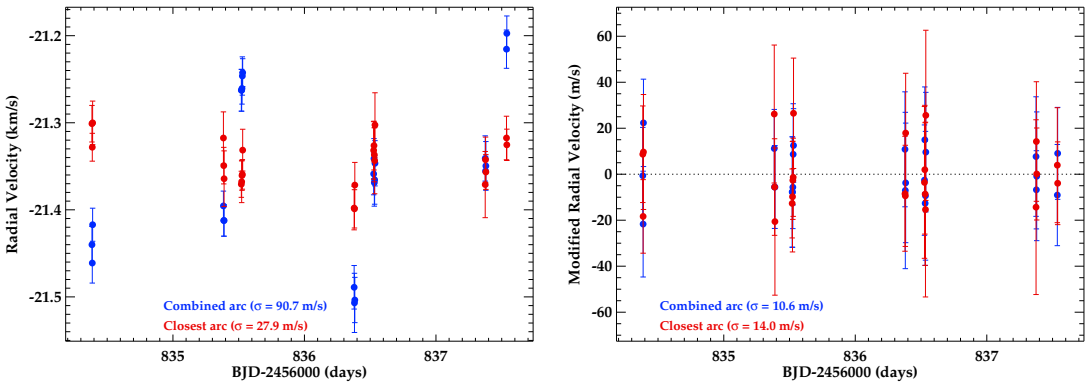

FIGURE 4.19: Intra-night radial velocity drift of CAFE. Difference between using master (blue) or the closest (red) arc in the wavelength calibration. In the **left panel** we show the RVs obtained and the corresponding scatters for each case. In the **right panel**, the median value of each dataset has been removed to show the intrinsic dispersion.

smaller dispersion (∼ 28 m/s) than the combined arc obtained at the beginning of the night (∼ 91 m/s). The differences in the RV of the RedB set between the spectra obtained at the beginning and at the end is quite important. The chamber monitoring indicates an increasing of the temperature of the CAFE room along the night, what could be the source of this difference. As a consequence, **this shows the importance of monitoring the RV drift of CAFE by obtaining several arc frames along the night.**

- From the right panel, however, we can see that the internal dispersion of the different sets of data is lower in the reduction where we used the combined arc (10 m/s for RedB compared to the 14 m/s for RedA). This can be directly attributed to the higher S/N of the combined arc, which in turn provides a more precise wavelength calibration. Consequently, **the use of a master arc (obtained by combining tens of arcs) improves the precision of the RV**.

These two conclusion imply that the better strategy for getting precise radial velocities with CAFE is to wavelength calibrate the spectra with the master arc obtained at the beginning (or end) of the night. The RVs obtained should then be corrected from the intra-night drift by cross-correlating the individual arc frames with the master arc. This strategy was not possible to apply in all of our runs due to the lack of the shutter in 2012, what prevented us from obtaining stable arc frames along the night. Thus, for homogeneity reasons we proceed by the alternative solution of using the closest arc to obtain the wavelength calibration of each science frame. However, for new observations, we strongly recommend the aforementioned observing strategy.

CAFE stability in long-term programs

Along our three years of observations with the instrument, we have observed several RV standards, monitoring them in a long timespan. During this period, there have been several technical

TABLE 4.1: Definition of the CAFE windows and corresponding offsets. The relative offsets are referred to event 2012a and the absolute offsets are referred to the literature values of the RV of these objects, namely 37.773 ± 0.100 km/s for HD124292 (Nidever et al., 2002),−21.462 ± 0.046 km/s for HD182488 (Chubak et al., 2012), and 6.228 ± 0.151 km/s for HD109358 (Chubak et al., 2012). The offsets have been calculated after being corrected for the S/N dependency.

Window ID	Date range (calendar) (YYYY.MM.DD)	Date range (JD-2456000)	Rel. offset (m/s)	Abs. offset (m/s)	Event
2012a	<2012.06.26	< 105	0.0	-12.5	ThAr lamp change
2012b	2012.06.26 - 2013.04.17	105-400	64.6	52.2	ThAr lamp change
2013a	2013.04.17 - 2013.06.22	400-466	79.9	79.0	CAFE condensation
2013b	2013.06.22 - 2014.02.11	466-700	-3.8	18.5	ThAr lamp change
2014a	2014.02.11 - 2014.06.10	700-819	8.6	-3.8	ThAr lamp change
2014b	2014.06.10 - 2014.08.09	819-879	-40.3	-52.8	ThAr lamp change
2014c	>2014.08.09	>879	0.0	0.0	ThAr lamp change

changes that could have affected the necessary stability of the instrument for the purposes of this work. In particular, we highlight several changes in the ThAr lamp and an important event on May-June 2013, when the instrument was repaired due to a vacuum loss that produced some condensation on the CCD. In Table 4.1, we summarize these events and define the CAFE windows with their corresponding date ranges. Every time that some of these events happens, jumps in the radial velocity and, more importantly, displacements of the orders in both axis can appear. The simplest way to account for these changes in to assume the possible existence of a RV offset when comparing measurements of long baseline programs. The number of needed offsets to fit for in the radial velocity signal would be $N-1$, being N the number of CAFE windows in which we have performed the observations for this particular object. This is similar to assuming that measurements from different CAFE windows come from different instruments.

We have calculated these offsets in the case of the standard stars observed during our long timespan. An iterative process was applied. We first corrected for the S/N-dependent effect (explained in the previous section) and then apply this correction to the RV measurements of the standards to calculate the offsets between each CAFE window. The relative offsets are defined as the difference between the median value at every window with respect to the RV measured in 2012a. The final relative offset is the mean of the three values corresponding to the three RV standards. For the absolute offsets, we took the literature RVs of these standards as a reference, being 37.773 ± 0.100 km/s for HD124292 (Nidever et al., 2002),−21.462 ± 0.046 km/s for HD182488 (Chubak et al., 2012), and 6.228 ± 0.151 km/s for HD109358 (Chubak et al., 2012). In Fig. 4.20, we show the measured offsets of the different CAFE windows for the three different standard stars used. The offsets are relatively small (below 100 m/s) but still significant for the aimed precision. Thus, we should either fit for the different offsets or apply those provided in Table 4.1.

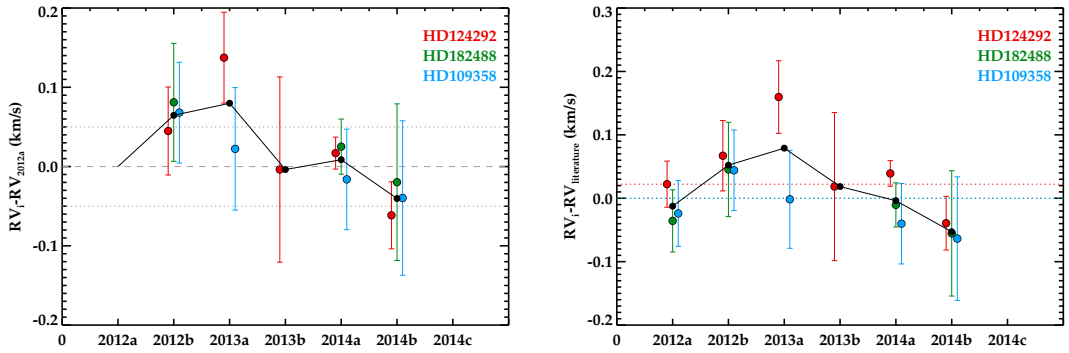

FIGURE 4.20: Relative (left) and absolute (right) offsets for the different CAFE windows. The different colors represent the three RV standards used in this study. The black symbols represent the mean values for each CAFE window and are presented in Table 4.1.

It is important to note from Fig. 4.20 that the RV precision of CAFE windows 2013a and 2013b is far worse than in other windows. This is also clear when looking at the uncertainties of the extracted RV measurements for the RV standards, which is comparatively larger as compared to other windows. We attribute this loss of precision in 2013 runs to the condensation of the CAFE CCD (during 2013a) and the posterior works on the instrument (in 2013b). Additionally, the results with the ThAr changed in 2013b seem to indicate that this lamp was not suitable for precise RV measurements, providing larger uncertainties in the wavelength calibration. Because of all these reasons we should take observations during 2013a and 2013b with some care.

As a final remark, correcting for the S/N-dependent effect and for the appropriate RV offsets for the different CAFE windows, we achieve RV stability at the level of 60 m/s in three years of observations. By avoiding the 2013a and 2013b data, this stability improves to 42 m/s for the three RV standards observed along this long baseline.

4.5 Forthcoming and future instrumentation

In our search for Earth-like planets, we already showed in Fig. 4.1 the need for obtaining precisions of few tens of cm/s in long-term baselines. Currently, few instruments have achieved sub-m/s precisions, being HARPS/MPG, HARPS-N/TNG, UVES/VLT, and HIRES/Keck the best examples. At that level of precision, many instrumental and physical effects (such as stellar activity, star centering in the fiber, etc.) must be taken into account. Hence, apart from a very-high-resolution spectrograph other calibration properties play a key role.

In the near future, the instrument CARMENES[10] (Amado et al., 2013, Quirrenbach et al., 2014) will be installed at the 3.5m telescope of Calar Alto Observatory.[11] The project around this

[10] https://carmenes.caha.es
[11] First light for CARMENES is expected on September 2015 and the survey is planned to start on January 2016.

instrument aims at detecting Earth-like planets in the habitable zone of M-dwarf stars. It will target 300 M-dwarfs during 5 years. Since these stars are less massive, precision of 1 m/s will be sufficient for achieving this goal.

In 2016, the instrument ESPRESSO (Pepe et al., 2010) will be installed at the VLT. Its capabilities will allow cm/s-level precision in G- and M-dwarfs, what would allow the characterization of Earth-like planets in the habitable zone of their stars. The instrument will also be prepared to work with the four UTs of the VLT, increasing the effective collecting area and reaching fainter stars. Finally, the CODEX instrument (Pasquini et al., 2008) has been proposed for the E-ELT. It will be capable of reaching 2 cm/s precision over long timespans of several years.

Part II

Scientific results: the evolution of planets across the Hertzsprung-Russell diagram. The CAB-MPIA follow-up of *Kepler* planets

In this second part of the dissertation, we present the scientific results, obtained by applying the different techniques described in Part I. These techniques were used in a comprehensive follow-up of the Kepler planet candidates. In Part II we show a complete picture of the process to confirm a planetary system detected by the transit method, from the target selection to the confirmation of several exoplanets by different techniques. This is done in a two-phase project:

In Chapter 5, we present the initial selection of the targets and the results of our high-spatial resolution survey on *Kepler* candidates. In Chapter 6, we explain the subsequent radial velocity follow-up of the best candidates. There, we present the confirmation an characterization of different extrasolar planets. In Chapter 7, we put our discoveries in context with the current population of known planets, highlighting the relevance of our discoveries.

Chapter 5

Multiplicity in planet host stars: the lucky imaging survey of *Kepler* planet host candidates

Contents

Outline and authored publications related to this chapter

In this chapter we present the first phase of the project, a high-spatial resolution survey of *Kepler* planet host candidates. The chapter is divided in five main sections. In section § 5.1, we describe the target selection and main properties of the planet candidates around them, the observations with AstraLux, and their reduction and calibration. In section § 5.2, we present the results of the survey. We provide a catalog of close sources to the host candidates and analyze the probability of not having blended undetected sources for those being isolated. We also compare our results to those of other high-spatial resolution surveys carried out in the *Kepler* sample. In section § 5.3, we discuss the implications of our findings in the study of the multiplicity rate of planet hosts. In section § 5.4, we show two examples in which our high-resolution images have been used to validate small size planets and in section § 5.5 we summarize other side projects for which we contributed with AstraLux images in the filler time of the *Kepler* survey. Note that all tables in this chapter were moved to the end of the chapter for a more confortable reading.

The main results of this survey have been published in Lillo-Box et al. (2012) and Lillo-Box et al. (2014b), see sections § 5.1 to § 5.3. Besides, these observations have been used in the validation and confirmation of planetary systems, co-authoring Barclay et al. (2013), Marcy et al. (2014), and Birkby et al. (2014), see section § 5.4. Our AstraLux observations of Saturn during the filler time of our programs (when the *Kepler* field was not yet visible) provided valuable information in the study of this Solar System planet, with our participation in Sánchez-Lavega et al. (2012) and Sánchez-Lavega et al. (2014), see section § 5.5.

5.1 Description of the survey

The main aim of this section is to provide a detailed description of our high-resolution survey of *Kepler* planet host candidates. In section § 5.1.1, we show the need and motivations for carrying out this study. In section § 5.1.2, we describe the target selection criteria and the properties of the final sample of observed targets. Finally, in section § 5.1.3, we summarize the performed observing runs and the reduction process, including photometric and astrometric calibrations of the images as well as the developed procedure to automatically detect companions in the AstraLux images. In this section we also estimate the completeness and detectability limits of the survey.

5.1.1 Motivations of this survey

In Chapter 3, we showed the need for high-spatial resolution images to validate and/or confirm the planetary nature of the thousands of candidates provided by the *Kepler* mission (and

in general by any high-precision photometric survey looking for planetary transits). Among the different false positive configurations presented in Chapter 3 (section § 3.1), some might be ruled out by the automatic pipeline implemented by the *Kepler* team (Borucki et al., 2011, Jenkins et al., 2010). In particular, the pipeline looks for differences in the depth of odd- and even-numbered eclipses. A significant difference could indicate that the system is actually an eclipsing binary (case Ia in § 3.1), with its period being twice that derived by the detection pipeline. Also, the pipeline performs an analysis of the photocentroid location of each frame to look for possible background eclipsing binaries (case Id in § 3.1), see Batalha et al. (2010). In this case, the relative position of the image centroid during and outside of the transit should be displaced. This technique is capable of identifying background eclipsing binaries typically as close as about 2 arcsec to the target (Batalha, 2014).[1] Additionally, low-resolution spectroscopy can easily reject physically bounded stellar companions (configuration Ic). However, configurations involving blended unassociated close stars (cases Ib, Id, and IIa,b) are the main sources of false positives in the sample of transiting planet candidates, and are difficult to detect by spectroscopic or photocentroid analysis. More specifically, cases IIa and IIb clearly shows the need for an intense high-resolution imaging follow-up program to validate the planetary nature of the transients. Owing to the *Kepler* long baseline, we expect few or no false positives due to starspots (Ie case).

Theoretical studies of the false positive probability of *Kepler* candidates conclude that obtaining high resolution images below 1-2 arcsec is crucial for confirming the planetary detections and their physical properties. As an example, an Earth-size planet transiting a faint star might have a false positive probability greater that 20% if it lacks high resolution imaging, which could potentially be decreased to less than 2% with a high resolution image (Morton & Johnson, 2011b). Several authors have acquired this kind of observations for other planet-host candidates, finding significant corrections to the planet-star properties. For instance, Daemgen et al. (2009) found stellar companions to three stars harboring planets. As a consequence, the updated values of the physical parameters differ by about 2% from the previous ones.

High-resolution spectroscopic surveys aiming at confirm the planetary mass of the candidates are expensive and highly telescope time consuming. This is because one needs to sample the planetary orbit at different phases (usually a minimum of 5 points spread along the orbital phases are required) to identify the planet and determine its orbital and physical properties. Also, close sources can contaminate the target spectra and thus diminish the radial velocity precision, masquerading the possible planets. Thus, a pre-survey of high-spatial resolution imaging is crucial to unveil possible blended sources and prioritize the best (isolated) host candidate for subsequent radial velocity follow-up or to minimize the impact of multiplicity. However, besides the recent state-of-the-art high-resolution spectrographs, the smallest (Earth-size and tinier) planets are not accessible with the RV technique. Thus, statistical validation of these systems is currently the

[1] Note that the *Kepler* pixel size is much larger, around 4×4 arcsec

only way to establish their planetary nature. In this statistical analysis, high-spatial resolution images play a key role in rejecting false positive scenarios. Several tools such as BLENDER (Torres, 2010) and PASTIS (Díaz et al., 2014b) make use of these type of observations to validate the smallest candidates.

Even if the planet is confirmed/validated, its formation and evolution scenarios (including its possible migration) require an accurate description of the effect of possible bounded stellar companions. The vast majority of planets found in multiple systems are actually S-type (the planet orbits one of the two components of the system, and the other component plays the role of a gravitational perturber, see Kley, 2010). These secondary objects make planet formation difficult since they interact dynamically with the system elements producing an extra heating of the protoplanetary disk. All of these factors may cause large changes in the planetary architecture and exoplanetary properties from those present when the planets formed around single stars. For instance, Eggenberger et al. (2004) found a statistical segregation in the planet mass for planets with orbital periods shorter than 40 days around single and multiple systems. Finding additional examples of planets in multiple-star systems can shed more light to the formation and evolution of planetary systems.

For all these reasons, we decided to carry out a high-spatial resolution survey of the *Kepler* candidates with AstraLux/CAHA, then selecting the best (isolated) targets for subsequent radial velocity follow-up with CAFE/CAHA to confirm their planetary nature and characterize them.

5.1.2 Target selection and characteristics

Among the large *Kepler* crop of planet candidates, we performed a target selection according to different criteria.

- **Magnitude.-** There were several reasons to limit the target list in magnitude. First, the maximum magnitude contrast that a hypothetical eclipsing binary must have to mimic a planetary transit of fractional depth δ is given by

$$\Delta m_{\rm Kep}^{\rm max} = m_{\rm EB} - m_{\rm target} = -2.5\ \log_{10}(\delta). \tag{5.1}$$

  This formula is valid for the *Kepler* bandpass. Thus, this is the magnitude that we would need to reach in our high-resolution observations to completely reject all eclipsing binary scenarios. The typical values of $\Delta m_{\rm Kep}^{\rm max}$ for the *Kepler* targets, ranges from $\Delta m_{\rm Kep}^{\rm max} \sim 2$ mag (for the largest planets with $\delta \sim 10\%$) to $\Delta m_{\rm Kep}^{\rm max} \sim 10$ mag (for the tiniest planets with $\delta \sim 0.01\% = 100$ ppm). Therefore, we decided to limit the sample to those targets where we could at least obtain an approximate magnitude contrast of $\Delta m_{\rm Kep}^{\rm max} = 5$ mag at separations

of 1 arcsec from the main target. The 2.2m/AstraLux instrumental configuration provides detectability limits of $i = 20 - 21$ mag ($m_{\rm Kep} \sim 19.5 - 20.5$ mag) in total exposure times of around 2700 s. We thus limited the magnitude of the targets to $m_{\rm Kep} < 16$ mag, with preference to targets with $m_{\rm Kep} < 14$ mag.

- **Subsequent RV follow-up.-** Due to the final goals of the survey and the limitations in magnitude of the CAFE/2.2m instrument/telescope configuration used to perform the subsequent follow-up of the isolated candidates, we favored targets with magnitudes below $m_{\rm Kep} < 14$ mag. Added to this, we also prioritized targets with relatively large radius according to the measured transit depths. These objects are like Jupiter-mass planets, easier to detect with the expected CAFE precision of 15 m/s. Based on their measured size and their orbital separation (also estimated by the *Kepler* team by assuming zero eccentricity), we estimated the expected radial velocity semi-amplitude with Eq. 4.6. We observed the targets with expected K values around three times above the expected CAFE precision (i.e., $K > 50$ m/s).

- **Requirements from the *Kepler* team.-** Since February 2012, we are part of the extended *Kepler* team dedicated to the follow-up of the candidates. In particular, we became part of this team contributing with the lucky-imaging observations. Thus, some of the targets that were included in our sample are small (Earth-sized) planets that could not be followed-up by CAFE. These observations were then used to validate the candidates with other techniques. Our results have been delivered to the CFOP through the XMFOP.[2]

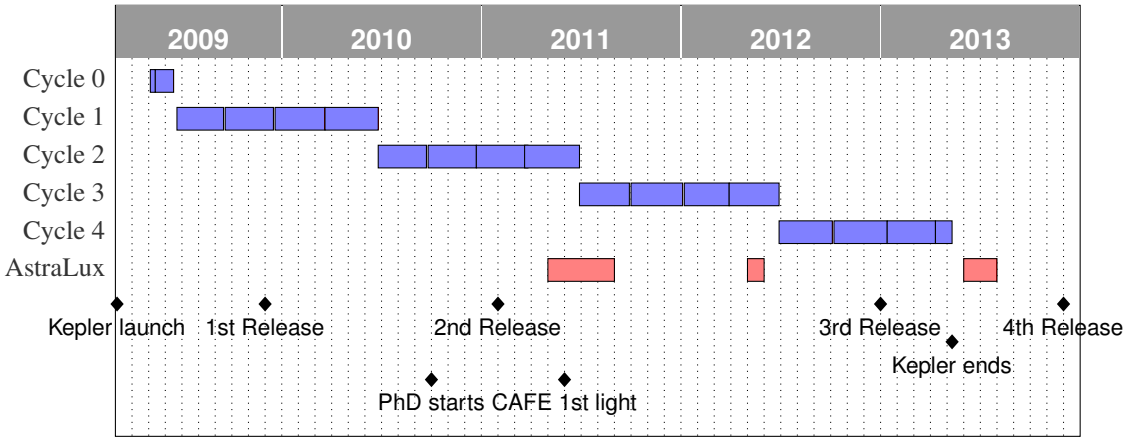

FIGURE 5.1: Gantt chart of the *Kepler* mission observations. The blue segments represent the different *Kepler* quarters. Approximate AstraLux observing campaigns are marked by red boxes.

These criteria are not mutually exclusive, i.e., they just represent some guidelines in the selection of the candidates. Thus, most of the targets did not accomplish all selection criteria since they

[2] XMFOP stands for *Kepler* Extended Mission Follow-up Observation Program.

had different objectives. Also, the different *Kepler* releases were delivered during our observing campaigns (see Gantt chart in Fig. 5.1) so the target list was updated as the candidates came out.

Since the status of the different planets changed during the different *Kepler* releases. Unfortunately, after some of these KOIs were observed, some of their hosted planet candidates were rejected for different reasons (re-analysis of the light curve by the *Kepler* team, radial velocity observations, etc.). Along this dissertation we will refer to the sample of targets still hosting confirmed/validated or candidate planets as the **active sample** (172 KOIs in total) and to those with all their candidates rejected as the **demoted sample** (61 KOIs). In Fig. 5.2, we show the distribution of the candidates depending on their magnitude and planet-to-star radius ratio.

In total, we have observed 233 KOIs hosting 392 planet candidates. Currently, 172 KOIs hosting 316 planet candidates are in the active sample, while 61 KOIs have all their 76 planet candidates demoted as false positives. In Fig. 5.3, we summarize this information.

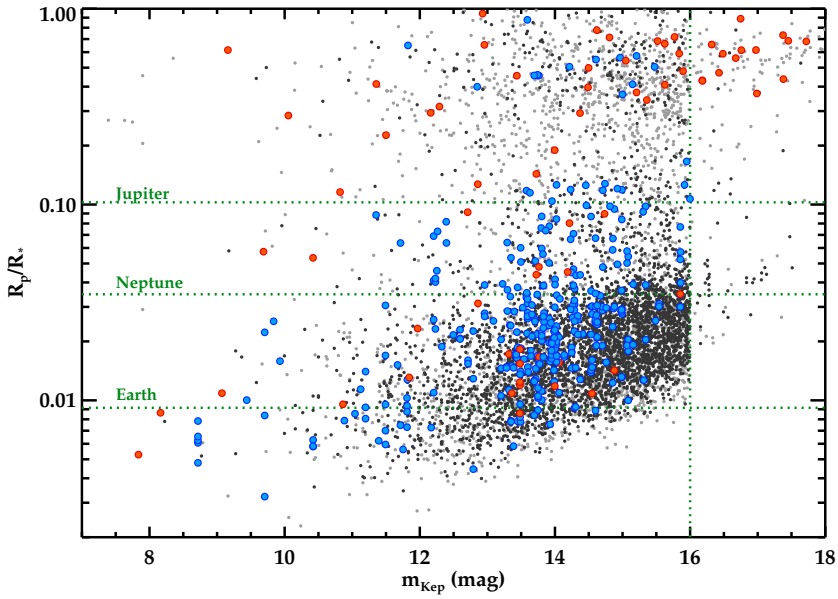

FIGURE 5.2: Planet-to-star radius ratio as a function of the *Kepler* magnitude for all KOIs. Planet candidates as for February 18th, 2015 are marked as black circles and false positives as gray circles. The sample of KOIs observed by AstraLux in our *Kepler* survey is represented by blue symbols for the active sample (316) and orange symbols for the demoted sample (76).

The final sample of targets observed during all our lucky-imaging campaigns thus consisted on 233 objects (including both active and demoted). The distribution of the expected planetary radii for the active sample as determined by the *Kepler* team is shown in Fig. 5.4 (right panel). Around 22% of the sample are Jupiter-size or larger planets, while 36% are Earth- or super-Earth-size. Although a larger sample of super-Jupiters was observed, most of them ($\sim$ 65%) have been demoted by subsequent analysis. It is important to highlight that the active sample is representative of the final sample of planet candidates provided by *Kepler* with similar percentages at all size ranges, i.e., 12.3% (20.2% in the final *Kepler* sample) are Earth-size, 23.7%

(32.2%) are super-Earth-size, 41.4% (43.6%) are Neptune-size, 13.0% (6.9%) are Jupiter-size, and 8.8% (3.1%) are super-Jupiter-size planet candidates.

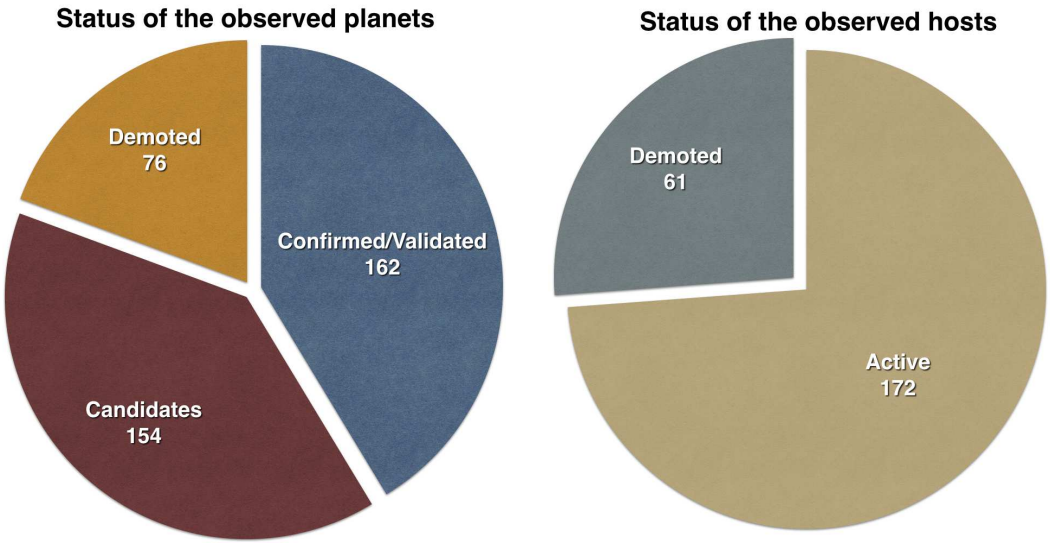

FIGURE 5.3: Pie chart showing the status of the 392 planet candidates orbiting around the 233 host stars observed in our survey. **Left:** Status of the individual planet candidates. **Right:** Status of the host stars, demoted being those host stars with any confirmed or candidate planet.

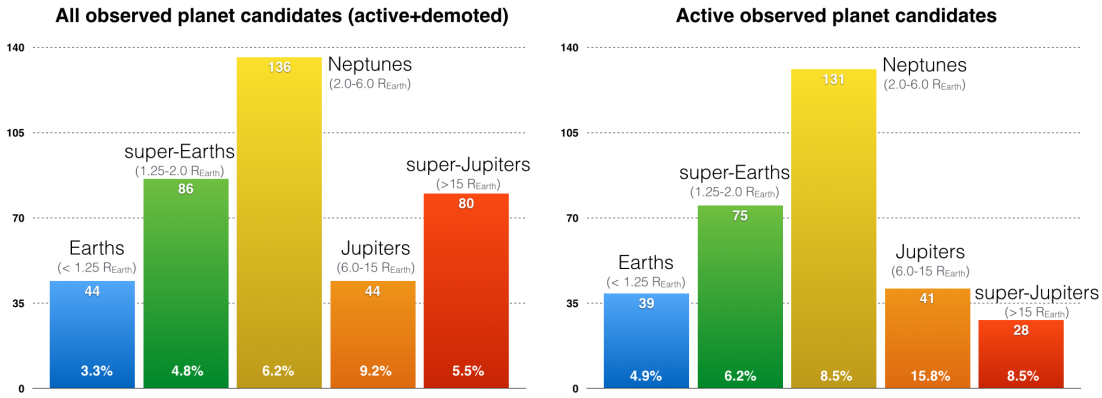

FIGURE 5.4: Distribution of planet sizes in our sample of KOIs observed with AstraLux. **Left:** Active plus demoted candidates. The ratios shown at the bottom of each category are referred to the total number of KOIs delivered by *Kepler*, including currently active and already demoted. **Right:** Active candidates. The ratios at the bottom are referred to active only candidates.

In Fig. 5.5 (left panel), we show the location of the targets in a $T_{\rm eff}$ vs. $\log g$ diagram, assuming the stellar parameters provided by the CFOP. We can see that we are observing planet hosts across the HR diagram, from low- to high-mass main-sequence stars and more evolved stars ascending the Red Giant Branch (RGB). Also, in the right panel of Fig. 5.5, we show the distribution of planets hosted by our targets according to their physical distance to the host star. We can see an important concentration of demoted large planets in close orbits. Most of these false positives are subsequently identified close eclipsing binaries. We also note that among our sample of 172 active systems, we have 53 confirmed/validated multi-planetary systems and 20

still to be confirmed. So, between 30% – 42% of the selected targets are systems with multiple planets (i.e., two or more).

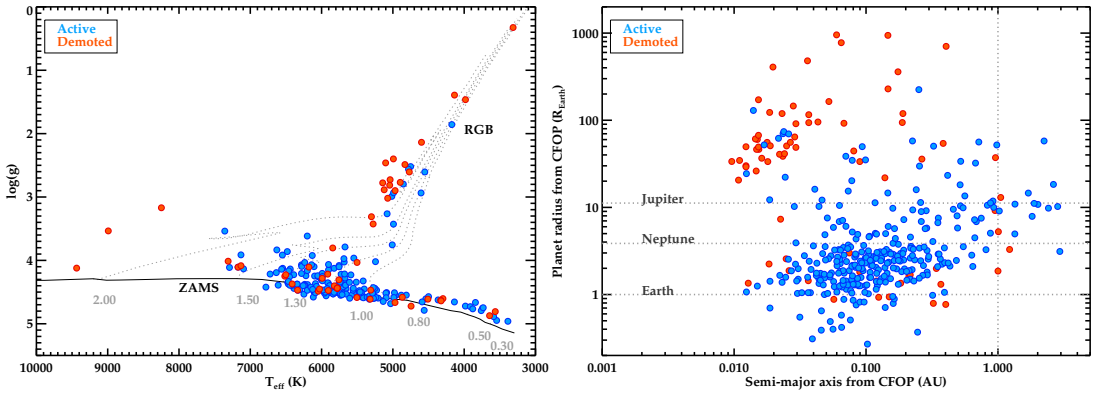

FIGURE 5.5: Properties of the sample of KOIs observed with AstraLux. **Left:** Hertzsprung-Russell diagram including the selected host candidates. Evolutionary tracks from Baraffe et al. (1998) for different masses are overplotted. **Right:** Orbital separation and radius of the planet candidates around the selected targets.

In Table 5.1, we provide information about the observed targets as well as magnitudes in the *Kepler* band , and in the i_{KIC}, and z_{KIC} bands from the KIC survey (Brown et al., 2010). We provide some properties of the stars summarized in Huber et al. (2014) and the number of planets confirmed/validated, candidates, and false positives on each system. According to the latter number, we classify the KOIs in the active (A) and demoted (D) samples.

5.1.3 Observations, data reduction, and calibration

Overview of the observing runs and strategy

The selected targets were observed along three visibility windows of the *Kepler* field from Calar Alto Observatory during 2011, 2012, and 2013. In total, we observed 233 KOIs (104 KOIs in 2011, 21 KOIs in 2012, and 108 KOIs in 2013) initially hosting 392 planet candidates (currently 316 in the active sample). In Table 5.2, we summarize the observing runs dedicated to this AstraLux survey.

We used exposure times for the single frames in the range 30 –100 milliseconds (which is below the coherence time of the atmospheric turbulence, see § 3.2) and set the number of frames accordingly to accomplish our depth requirement (typically 20000 – 40000 frames). The specific exposure time for each target was set according to its magnitude, the required magnitude contrast, and the weather conditions. In all cases, we used the full CCD array of the camera (24×24 arcsec). This observing setup ensures the aimed coverage both in contrast and angular separation from the main target. We observed all targets with the Sloan Digital Sky Survey *i* band (SDSSi). After the on-the-fly reduction done by the AstraLux pipeline, we checked for the

possible presence of close companions to the main target. If any, we proceed with observations in the SDSSz filter. The two filters give some color (spectral) information, providing hints about their possible bond to the main target. In the following we will use the letter *m* to refer to a magnitude in a non-specific filter and *i* and *z* for the magnitudes in the SDSSi and SDSSz filters.

Table 5.3 lists the observing characteristics (date, filter, individual exposure times, number of frames, image completeness,FWHM, and Strehl ratio) for each target.

Data reduction

Data cube images were reduced by using the online pipeline of the instrument (see Hormuth, 2007, and section § 3.5.2 of this dissertation), which performs basic reduction and selects the highest quality images. Then, it combines the best 1.0%, 2.5%, 5.0%, and 10% frames with the highest Strehl ratios (Strehl, 1902). It calculates the shifts between the single frames, performs the stacking, and resamples the final image to have half the pixel size (i.e., around 0.023 arcsec/pixel). As stated in section § 3.5.2, in this work we only use the 10% selection rate images. We chose this particular selection rate, since it provides the optimal compromise between a good angular resolution and a high magnitude contrast, according to our previous experience with the instrument and recommendations from Felix Hormuth (PI of the instrument).

Astrometric calibration

We acquired images of the M15 globular cluster in all three observing seasons to obtain the relative plate solution of the CCD. We used the more than 100 manually cross-matched sources with the Yanny et al. (1994) catalog (who provides accurate coordinates based on observations of the Hubble Space Telescope images) to obtain the plate scale and position angle of the CCD. We compared the angular separations and position angles of more than 1000 randomly selected star pairs in the latter catalog (separations in arcsec) and in our own catalog (separations in pixel units). The derived pixel size and position angle of the CCD for each observing season are shown in Table 5.4. We obtained typical uncertainties of 0.20 mas/px (around 1% of relative error) for the pixel size. This astrometric calibration assumes linearity along the whole CCD and neglects second-order distortions, but this is enough for the purposes of this dissertation. The reduced images with the four selection rates and the data cubes are available under request so that any interested researcher can reproduce the results and perform a more dedicated astrometric calibration if needed.

Source detection and photometric calibration

Sources were identified in each image by using our semi-automatic routine, specifically designed for the instrument. The algorithm first detects possible sources in the image whose integrated flux over an aperture of 10 pixels is at least three times greater than the corresponding sky flux (measured as the median value of all pixels, assuming that most of the image is not covered by

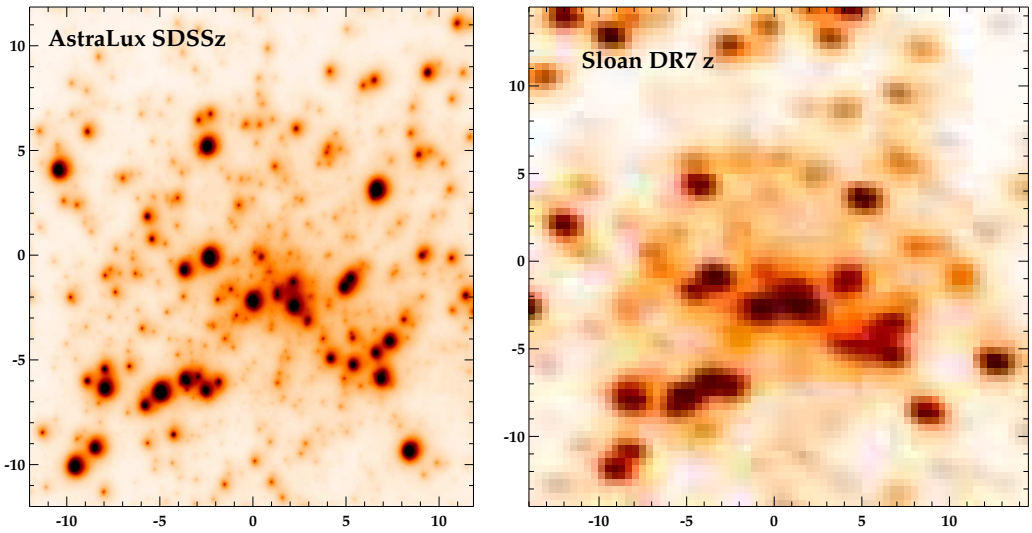

FIGURE 5.6: Image of M15 with AstraLux (left) and SDSS (right). M15 was used for astrometric calibration of the AstraLux images. North is up, East is left. X- and Y-axis are in arcsec units.

stars). Then, each source candidate is individually checked to fulfill the following criteria: i) not being at the edge of the image; ii) having a PSF-like radial profile shape (to reject possible artifacts and cosmic rays); and iii) having magnitudes in the range 0-30 mag to reject possible remaining bad pixel. All images were then manually inspected to check the final detected sources.

We then applied aperture photometry on the detected sources to measure the relative magnitudes between objects in the same image. We used the *aper* routine in IDL to extract the flux contained within a specified aperture. This aperture is selected for each image by taking into account the close objects in the field to avoid contamination of close companions. Thus, for each image, we have the instrumental magnitudes ($m_{\rm inst}$) for all sources and the magnitude differences with respect to the KOI (which we call $\Delta i/\Delta z$, where $\Delta m = m^{\rm KOI}_{\rm inst} - m^{\rm C/}_{\rm inst}$).[3] In most cases where a close companion (below 3 arcsec) was found, we obtained additional photometry in the SDSSz filter to characterize the secondary object.

Absolute calibration was then performed by using the KIC photometry of the KOI and the instrumental magnitudes and magnitude differences of the surrounding objects with respect to the KOI. First, KIC magnitudes were converted to SDSS magnitudes by using the photometric transformations presented by Pinsonneault et al. (2012) in their Eqs. 3 and 4. According to Brown et al. (2011), the KIC images have a full width at half-maximum of 2.5 arcsec. Hence, as stated by the authors, the KIC photometry is unable to resolve the components of close binary stars. According to this, we can consider that their PSF photometry cannot resolve visual companions closer than 2.5 arcsec, so the magnitudes of such KOIs account for the flux of all sources inside

[3]Note that with this definition, sources fainter than the KOI would have $\Delta m < 0$ while brighter sources would have $\Delta m > 0$.

such radius. Thus, we can distinguish between two cases to calibrate our photometry, KOIs with and without companions closer than 2.5 arcsec:

- **KOIs *without* companions closer than 2.5 arcsec.-** When any close companion was detected, we derived the photometric zero-point of our Astralux images ($Z_p^{\rm image}$) by using the KIC magnitudes of the KOIs calibrated to the SDSS filters ($m_{\rm KIC}^{\rm KOI}$),neglecting atmospheric or instrumental effects

$$Z_p^{\rm image} = m_{\rm KIC}^{\rm KOI} - m_{\rm inst.}^{\rm KOI} \tag{5.2}$$

  This zero-point is the applied to all detected sources in the image so $m_{cal} = m_{\rm inst.} + Z_p^{\rm image}$.

- **KOIs *with* companions closer than 2.5 arcsec.-** In the case where one or more close companions (CC) were found, we assume that the KIC magnitude of the KOI converted to the SDSS system ($m_{\rm KIC}^{\rm KOI}$) is actually the sum of the fluxes coming from all sources inside 2.5 arcsec. In this case, we have to add the fluxes of all sources inside 2.5 arcsec. Thus, since $m_{\rm cal} = m_{\rm inst} + Z_p$, then $F_{\rm cal} = F_{\rm inst} 10^{-Z_p/2.5} = F_{\rm inst} F_{Z_p}$, we have that

$$F_{\rm KIC}^{\rm KOI} = F_{Z_p} \left[F_{\rm inst}^{\rm KOI} + \sum_j F_{\rm inst}^{CC_j} \right], \tag{5.3}$$

  where j runs in the number of companions found within 2.5 arcsec. Equivalently, translating this equation to magnitudes, we have:

$$m_{\rm KIC}^{\rm KOI} = Z_p + m_{\rm inst}^{\rm KOI} - 2.5 \log \left(1 + \sum_j 10^{\Delta m_j/2.5} \right). \tag{5.4}$$

  Thus, the calibrated magnitude of the KOI after taking the close companions into account is given by

$$m_{\rm cal}^{KOI} = m_{\rm KIC}^{\rm KOI} + 2.5 \log \left(1 + \sum_j 10^{\Delta m_j/2.5} \right). \tag{5.5}$$

  Hence, the magnitude of the close companions can be determined as $m_{\rm cal} = m_{\rm cal}^{KOI} - \Delta m$.

This scheme was then applied to both filters i and z to obtain the absolute magnitudes of all detected objects.

Completeness and detectability limits

The mean completeness and limiting magnitudes of the images was determined by observing the M15 globular cluster. In this crowded field, we detected the largest number of sources possible with a 5σ criterion. Then, we measured the number of objects per magnitude bin of 0.5 mag on every photometric observation of M15. Computing the mean values of these bins we were able to construct the histogram shown in Fig. 5.7. This histogram was scaled to a 200-second

exposure-time image to account for the mean effective exposure time of our science images. The results show a mean completeness value of $i_{\rm comp}$ = 18.4 ± 0.3 mag and found that our faintest detected source has $i_{\rm detect}$ = 22.5 mag.

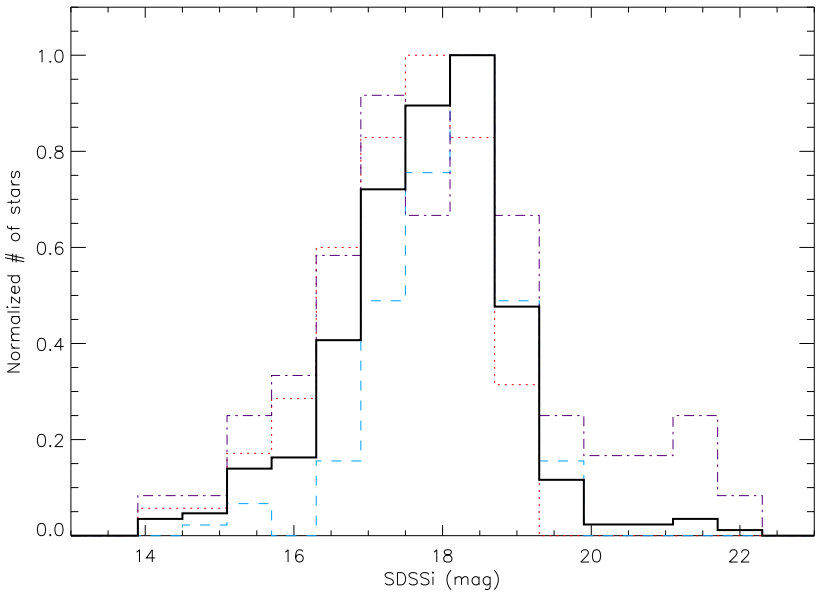

FIGURE 5.7: Mean completeness and detectability limits of our survey (black solid line) for a 200s effective exposure-time image. Red dotted line, blue dashed line, and purple dotted-dashed line represent the values for the three photometric nights considered, namely 2011-07-26, 2011-07-05 and 2011-07-07, respectively. Binsize is 0.5 magnitudes. The histograms have been normalized to their maximum value for visualization purposes.

Since these values were calculated for a particular exposure time but we set different exposure times for each target, the completeness and detectability limits should be scaled. For each particular science image, the scaled values of $i_{\rm comp}$ and $i_{\rm detect}$ are shown in Table 5.3.

5.2 Results and analysis

In this section, we present the results of our high-spatial resolution survey. The section has been divided into three different sub-sections. In section § 5.2.1, we summarize the general results of companion detection rates. In section § 5.2.2, we focus on the KOIs with detected companions closer than 6 arcsec, providing a catalog of close sources and analyzing them in terms of their possible physical association and their implications in the determination of the properties of the transiting objects. In section § 5.2.3, we provide the catalog of isolated KOIs (showing no companions closer than 6 arcsec). The reliability of this isolated nature is analyzed by rejecting some false positive scenarios that can be ruled out to a certain probability with our high-spatial resolution images. Finally, in section § 5.2.4, we use the BSC parameter as

a criterion to compare the goodness of our lucky-imaging survey to other similar works in the *Kepler* sample.

5.2.1 General results of the survey

Among the 233 KOIs observed (*demoted+active* samples), we found 78 of them (33.5%) having companions closer than 6 arcsec, while 155 KOIs (66.5%) where found to be isolated. Among the non-isolated sample, we detected at least one companion closer than 3 arcsec in 42 KOIs (18.0%), while at least one companion in the range 3-6 arcsec was found in 46 KOIs (19.7%).

Regarding the *active* sample only (with currently active planet candidates) consisting on 172 KOIs, we found companions closer than 6 arcsec in 57 of them (33.1%), while 115 were found to be isolated (66.9%). Among the non-isolated sample, we found close companions (< 3 arcsec) in 30 KOIs (17.4%), while at least one companion in the range 3-6 arcsec was found in 34 KOIs (19.8%).

These results are summarized in the pie chart diagrams showed in Fig. 5.8.

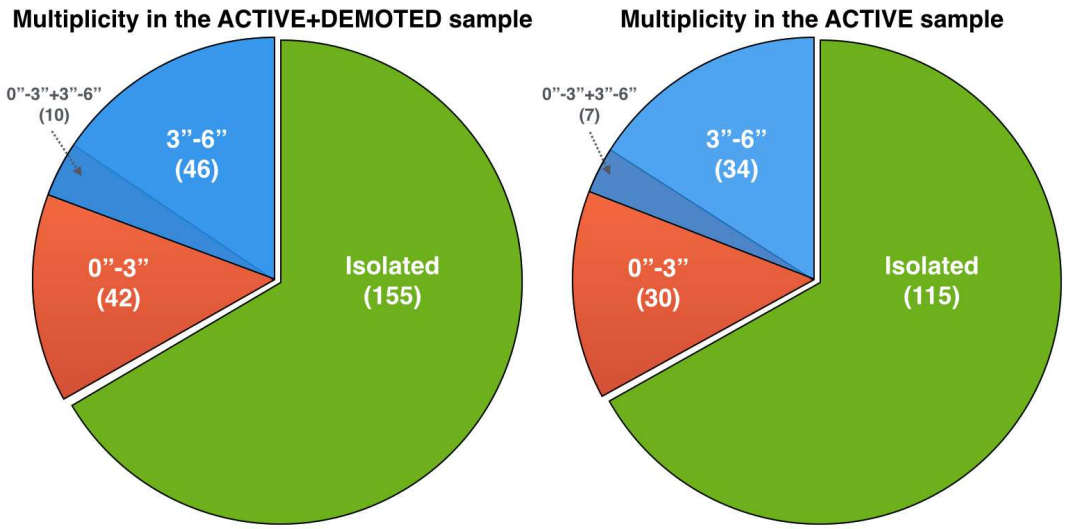

FIGURE 5.8: General results of the high-spatial resolution survey. Pie charts with the number of detected companions at different angular separations for the whole (left) and active (right) samples.

In Table 5.5, we provide the complete catalog of sources detected within 6 arcsec. Figure 5.9 shows their spatial distribution. This figure illustrates the high density of close visual companions and the need to obtain high resolution images of all candidates to better characterize the systems. These objects will be analyzed in section § 5.2.2.

The identified isolated KOIs are studied in more detail in section § 5.2.3. These targets are thus suitable to proceed with radial velocity studies, since no object has contaminated the *Kepler*

light curve within our sensitivity and detectability limits (presented in the next section). In the following section we will restrict our analysis to the *active* sample.

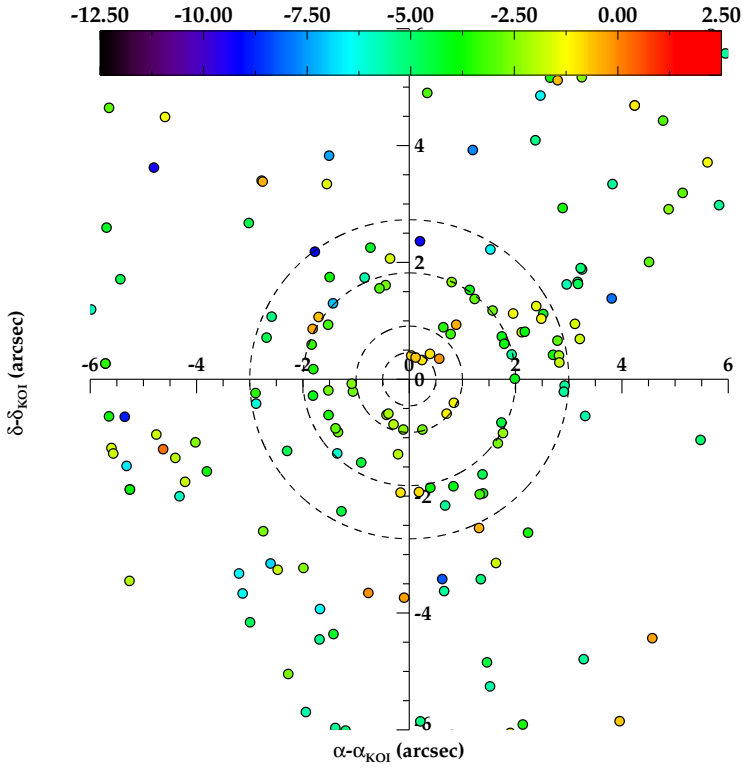

FIGURE 5.9: Location of the detected companions to the KOIs in our sample. Each filled circle corresponds to a detected source and its relative position in the projected sky with respect to the KOI. The colors represent the magnitude difference between the companion and the corresponding KOI. We have marked with dashed circles the 0.5, 1.0, 2.0, and 3.0 arcsec separations for visualization purposes.

5.2.2 Non-isolated host candidates: detection of blended sources

5.2.2.1 A catalog of close sources to *Kepler* host candidates

The mere presence of companions closer than 6 arcsec affects both the KOI status as a planet candidate and (if confirmed by other techniques) the derived planet properties, such as planet radius or impact parameter. Thus, the light curves of these targets should be studied in more detail, taking these additional sources into account. In Table 5.5, we provide the catalog of observed KOIs with companions closer than 6 arcsec, including the measured separations, angular positions and derived photometric information.

In Fig. 5.10, we show the AstraLux images of the 30 KOIs with detected companions closer than 3 arcsec, indicating their position in the image. While most of the companions farther than 3 arcsec are easily detectable by ground-based all sky surveys and low-resolution images, these

close companions are usually blended in such surveys. In this figure we have also overplotted the apertures defined by the *Kepler* team to extract the photometry and get the final light curves. As shown, the large majority of the detected companions lie inside these apertures, thus diluting the dips of the transiting objects. Consequently, the light curves of these targets should be re-analyzed, taking into account the dilution produced by these additional sources.

In most of these cases, we re-observed the target in the z band aiming at getting some color information $(i-z)$ of the companions to estimate their spectral types. This can be useful when trying to undilute the light curves. The photometric color was obtained as

$$(i-z)_{/C} = \Delta i - \Delta z + (i-z)_{KOI}, \tag{5.6}$$

where the subscript $/C$ denotes the values of the companion and $\Delta i = (i^{/C}_{\rm inst} - i^{KOI}_{\rm inst})$, and $\Delta z = (z^{/C}_{\rm inst} - z^{KOI}_{\rm inst})$.

5.2.2.2 Photometric characterization of the close companions

We applied two different methods to determine the spectral type (effective temperature) of the stellar companions according to their angular separation.

Spectral types for close companions (< 3 arcsec)

Assuming a main-sequence nature for the secondary, we were able to estimate their spectral types by using the $(i-z)$ color. Synthetic spectra from Pickles (1998) for main-sequence stars were convolved with the SDSSi and SDSSz transmission curves,[4] following the same scheme as in Daemgen et al. (2009) to derive a relation between the spectral type and the aforementioned $(i-z)$ color. We overploted our $(i-z)$ colors in this diagram to estimate the companion spectral types. The typical uncertainties depend on the spectral type since they are determined according to the photometric uncertainty in the calculation of the $(i-z)$ values. In particular, we note that, since the dependence of the spectral type on the aforementioned color is stronger for types later than K5-K6, uncertainties are much smaller than for earlier types, for which the dependence is weaker. Thus, only stellar companions with $i-z > 0.21$ (corresponding to a K5-K6 main-sequence star) are considered in this analysis. In Fig. 5.11, we show the results. Also, in column 10 of Table. 5.5, we provide the estimated spectral types of these close companions. As expected, these objects are cool, low-mass stars (late K or early M). Their physical association are discussed in section § 5.2.2.3.

[4] See http://www.sdss.org/dr3/instruments/imager/index.html

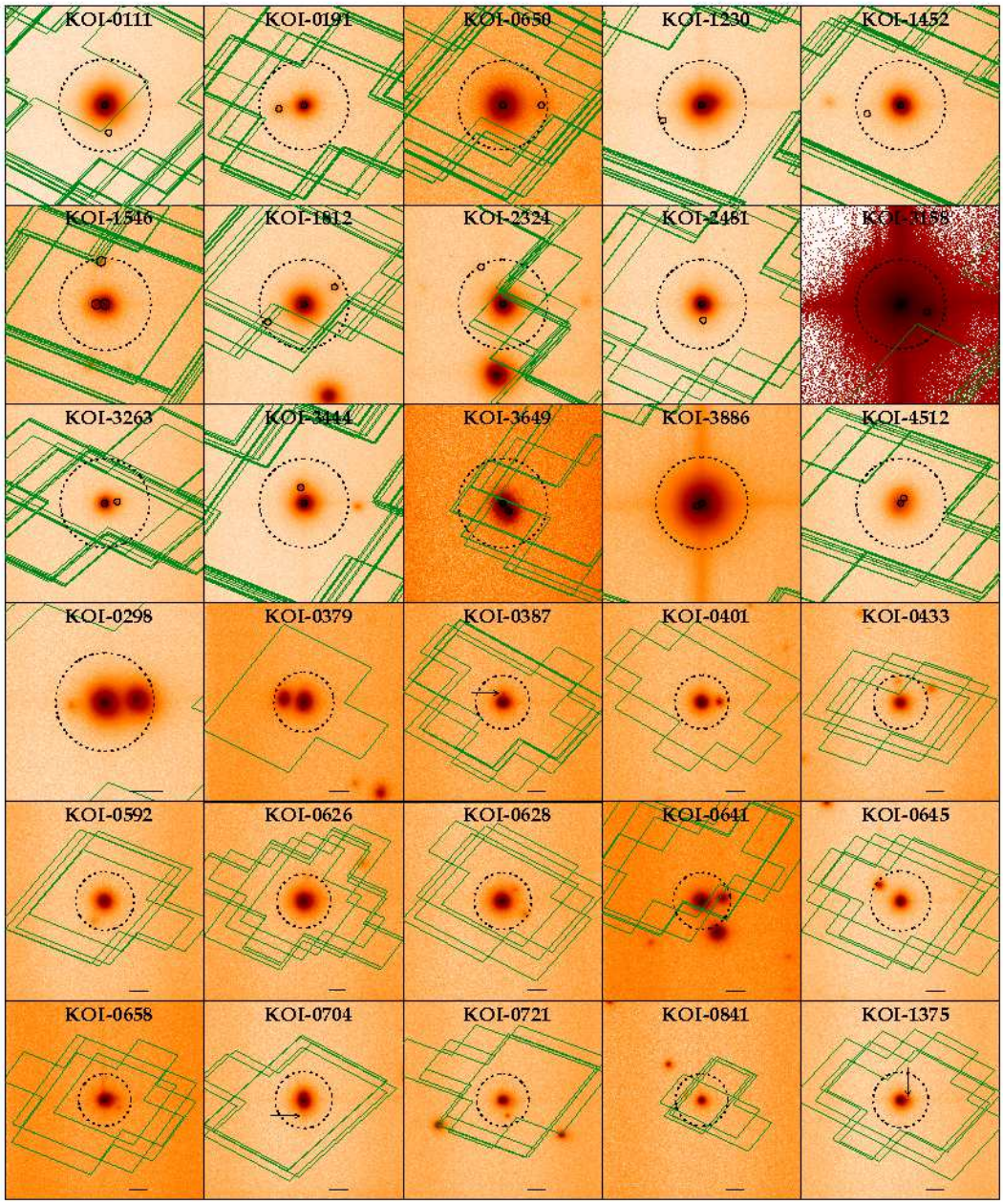

FIGURE 5.10: High-spatial resolution images obtained with AstraLux/CAHA of the 30 KOIs with detected companions closer than 3 arcsec. The dotted circles represent the 3 arcsec angular separations and the solid line circles show the location of the detected sources. The green lines show the *Kepler* apertures used to extract the photometry in different *Kepler* quarters.

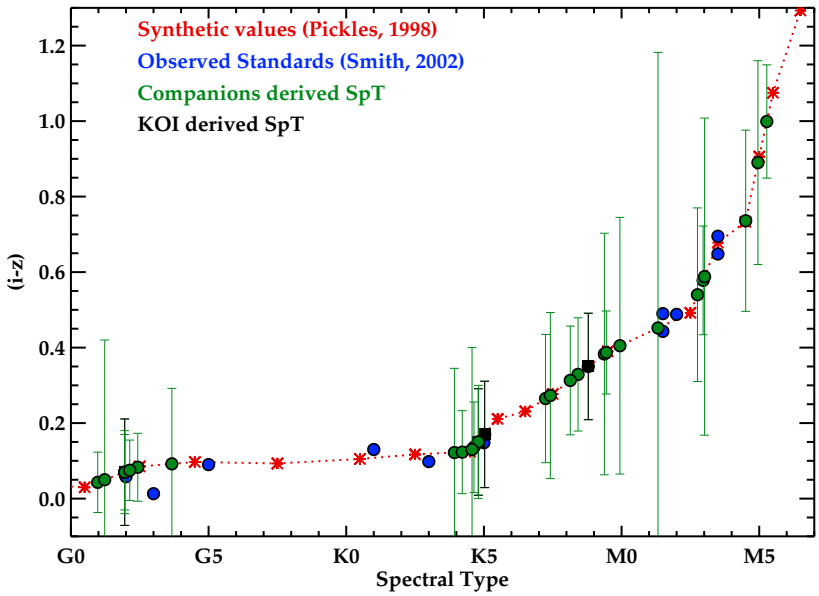

FIGURE 5.11: Spectral type estimation for the stellar companions. Red asterisks represent the synthetic values calculated by convolving the spectral library from Pickles (1998) with the transmission curves of the Sloan filters. Blue circles represent the position of standard stars from Smith et al. (2002). Green filled circles are the measurements for our detected companions and their uncertainties.

Spectral energy distributions for 3-6 arcsec companions

In these cases, where we lack information in the z filter, we searched for photometric information in public catalogs by using the last version of the Virtual Observatory SED Analyzer (Bayo et al., 2013, 2008). In cases where more than five photometric points are found, this tool fits a spectral energy distribution (SED) model to obtain the effective temperature of the source. Table 5.5 (column 10) shows the results for the sources for which this study was possible. Here we assumed a solar metallicity and two surface gravities to account for two possible types of companion at different evolutionary stages: main-sequence foreground or bounded stars ($\log g = 4.5$) or background giant stars ($\log g = 3.5$). According to the results, these companions are mostly K-type stars if we assume a main-sequence stage. We note that all KOIs are hotter (earlier spectral types) than the possible companions. We found an rms ~ 200 K between our fitting results and the KIC effective temperatures.

5.2.2.3 Physical association of the close companions

The formation mechanisms and evolution of planetary systems is known to be affected by the presence of bounded stellar companions. Thus, it is important to determine the possible physical bond of the close companions detected in this survey. Several multiple-star systems have been discovered, both circumbinary planets as for instance Kepler-16b (Doyle et al., 2011), and binary systems with the planet orbiting one of the components of the couple, as HD 196885Ab (see

Thebault, 2011). These objects represent a challenge for theoretical models of planet formation, for instance, in terms of orbital stability (Holman & Wiegert, 1999, see). Moreover, it has been discovered that around one fifth of known exoplanets inhabit double or multiple stellar systems (Desidera & Barbieri, 2007, Mugrauer & Neuhäuser, 2009, Thebault, 2011).

As a general rule, we showed in Eq. 3.5 that the expected number of chance-aligned stars within a particular sky-projected area is proportional to this area ($N = \pi r^2 \rho$, where ρ is the density of stars). In Fig. 5.12, we show the distribution of companions as a function of the projected angular separation to the KOI. Dashed lines show the expected number of chance-aligned sources in the range 14-21 mag for stellar densities $\rho = 0.0010, 0.0031, 0.0070$ stars/arcsec^2 (see section § 3.4.3). The blue dashed line (corresponding to $\rho = 0.0031$ stars/arcsec) shows the mean value for the *Kepler* field, while the gray lines represent the minimum and maximum densities in the *Kepler* field (maximum and minimum galactic latitudes, respectively). From this figure, we can see that the number of detected stars closer than ~2 arcsec is clearly overabundant, suggesting that the majority of these companions are not chance-aligned but instead bounded to the KOI.

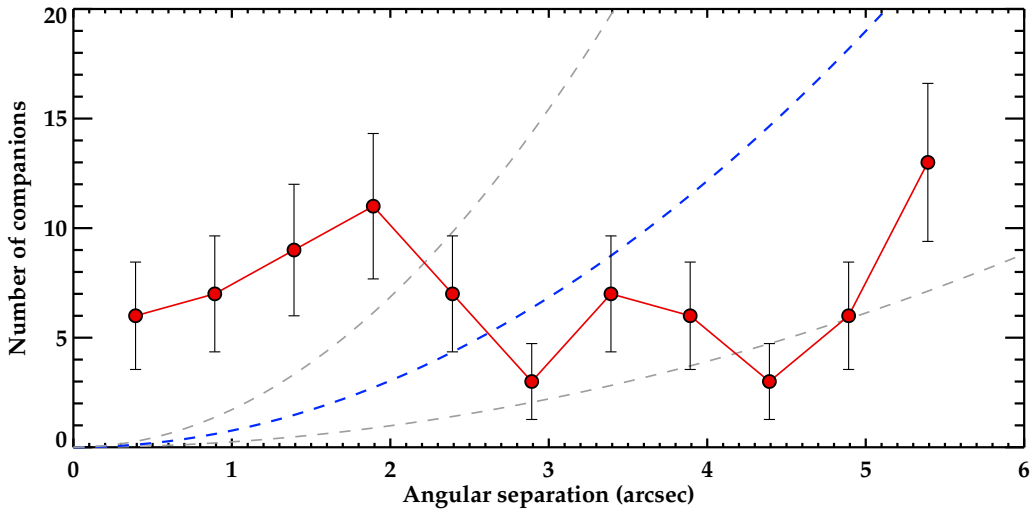

FIGURE 5.12: Number of detected companions as a function of the angular separation (red symbols and line). Uncertainties are assumed poissonian (i.e., $\sqrt{N}$). Dashed lines show the expected number of chance-aligned sources in the range 14-21 mag for stellar densities $\rho = 0.03, 0.1, 0.2$ stars/arcsec^2. The blue dashed line shows the mean value for the *Kepler* field.

In particular, for those KOIs with observations in both i and z filters, we can further constrain whether the close companions are bound or not to the central object by using the color information. We constructed an empirical Zero-Age main-sequence (ZAMS) based on the synthetic *griz* photometry derived by Ofek (2008) for Tycho-2 stars with Hipparcos B_T and V_T bands, as well as 2MASS JHK magnitudes (see Fig. 5.13). To reach the substellar domain, we added 109 brown dwarfs in the Pleiades region published by Moraux et al. (2003) and 943 substellar sources from Bouy et al. (2013) with *iz* photometry, assuming a distance to the cluster of 130 pc (Stello & Nissen, 2001).

As we are interested in possible binary stars, we computed the lower envelope of the ZAMS for the Ofek+Pleiades catalogs in an M_i vs. $(i-z)$ color-magnitude diagram. In this diagram, we forced the KOIs to be located in the empirical ZAMS according to their $(i-z)$ color. This provides a distance modulus that can now be applied to the corresponding companions. If both stars share a joint formation process (i.e., they are bounded), both should lie in the ZAMS.

In total, we obtained images in both i and z filters for 20 KOIs out of the 30 KOIs with detected close companions. Figure 5.13 shows the results for these targets and Fig. 5.14 zooms into the ZAMS region. We find that the location of 11 companions to 10 KOIs in this diagram is consistent with a common formation scenario, thus being possibly bounded. These companions are KOI-0379B,[5] KOI-387B, KOI-0401B, KOI-433B, KOI-628B, KOI-0641B, KOI-641C, KOI-0645B, KOI-0658B, KOI-1375B, and KOI-3158B. According to our spectral type analysis based on the $(i-z)$ color, the companion to KOI-3158 is a redder object in the range K5-M1 (assuming that it is a main-sequence star). Also, KOI-0433B and KOI-0658B lie in the low-mass domain of the diagram, implying that they could be either low-mass stars or even brown dwarf companions to the host stars. More interestingly, the two companions to KOI-641 have compatible positions with being physically associated. This would then be a triple S-type system with one of the companions being a low-mass or substellar object. Additionally, other two close objects could also lie within the ZAMS boundaries if we take into account the errors in the determination of this isochrone, namely KOI-0628B and KOI-1375B.

Although the orbital parameters must be revised to account for the detection of the blended object, *we can conclude that these systems are potential candidates to be S-type planetary systems*. In particular, a posterior work by Campante et al. (2015) validated the five planets orbiting **KOI-3158A (Kepler-444A b,c,d,e,f)** and confirmed the physical association of its close companion KOI-3158B with a period of 430 yr corresponding to an orbital separation of 65 AU, becoming a satellite-type (S-type) multi-planetary system as we suggested in Lillo-Box et al. (2014b). Also, the three planets around **KOI-401 (Kepler-149 b,c,d)** and **KOI-0658 (Kepler-203 b,c,d)** were validated by Rowe et al. (2014), although to our knowledge they did not take into account the close companions presented in this dissertation and in Lillo-Box et al. (2012, 2014b). In the following section we update the planet parameters according to these detections.

According to their position in the Hertzprung-Russell diagram of Fig. 5.13, the remaining close companions are probably background sources.

[5] Note that we follow the IAU convention regarding to nomenclature, i.e., capital letters for multiple stars and small letters for planets.

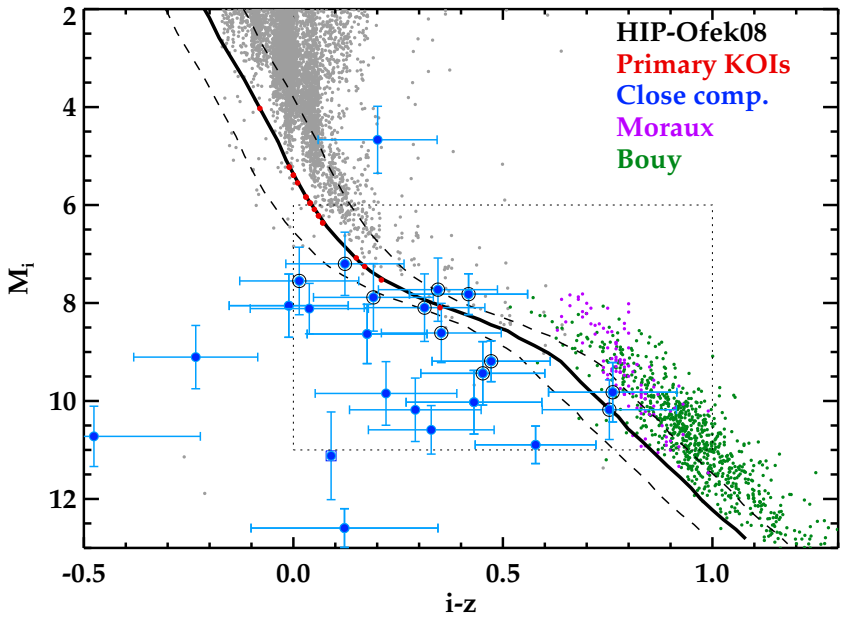

FIGURE 5.13: Estimation of the possible bond of the close companions (blue circles) to KOIs detected in both *i* and *z* filters (see section § 5.2.2.3). The primary sources are represented in red and the close companions in blue. The solid black line represents the empirical ZAMS obtained by using the synthetic *iz* photometry from Ofek (2008) (gray dots), the observed members of the Pleiades cluster by Moraux et al. (2003) (purple circles), and Bouy et al. (2013) (green circles). Possible bounded companions are marked with an open circle. In Fig. 5.14, we show a zoom-in to the marked square dotted region.

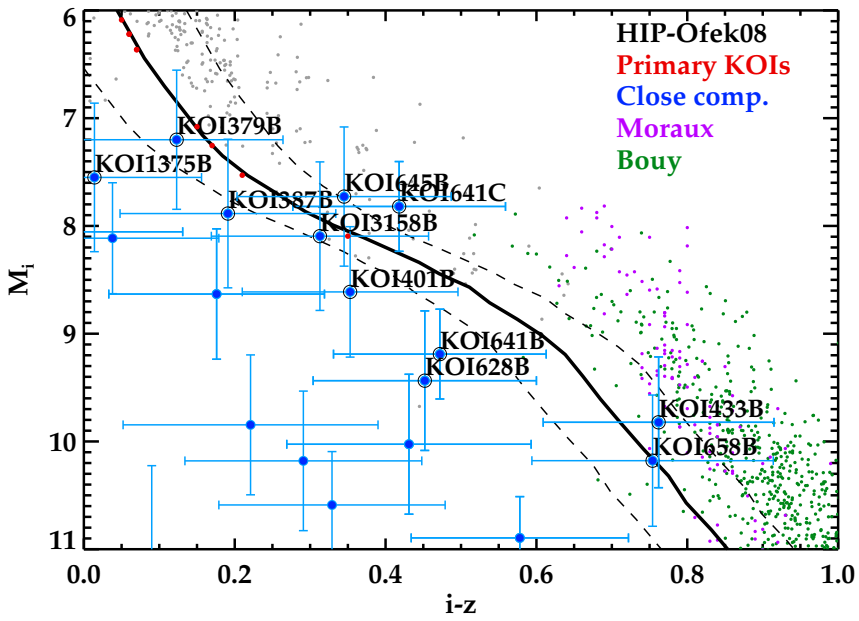

FIGURE 5.14: Zoom-in of Fig. 5.13 to the marked region. In this figure we show the KOI numbers of the possible bounded companions.

5.2.2.4 Update of the planet properties

The detected close companions blended in the *Kepler* apertures contaminate the light curves and dilute the transit signals. This dilution provokes erroneous estimation of the properties of the transiting body when modeling the eclipse. The algorithm to determine the planet properties from the transit, used by the *Kepler* team, deblends the light curves from sources detected by the KIC photometric survey on the *Kepler* field (Brown et al., 2011). Among the 30 active KOIs with detected companions closer than 3 arcsec in the present survey, none of them were detected by KIC observations.

Although several orbital and physical parameters can be affected by this dilution, in this dissertation we just provide corrections for the planet-to-star radius ratio. The correction of other parameters such as the semi-major axis of the orbit or the impact parameter (as well as as a fine correction of $R_p/R_\star$) involves new modeling of the transit signals, which is out of the scope of this work. The results for the affected planet candidates are listed in Table 5.6. The estimations clearly show the increase in the planetary radius caused by the unaccounted flux of the blended star.

In three cases (namely, KOI-1230.01, KOI-3649.01, and KOI-3886.01), the planet candidate has a new estimated radius that according to mass-radius relations by Chabrier & Baraffe (2000) would yield to a typical mass of the transiting object in the stellar regime. We also note that the largest extrasolar planets confirmed so far[6] have a maximum radius below 2.2 $R_{\rm Jup}$ (24.7 $R_\oplus$). These candidates are thus likely to be false positives.

5.2.3 Isolated host candidates: a bona-fide sample for subsequent follow-up

The large majority of the observed KOIs (66.5%) were found to be isolated within our sensitivity limits. In this section, we analyze how our high-spatial resolution images can rule out some of the possible false positive scenarios explained in § 3.1. Once the sensitivity curve have been calculated for the images of the isolated KOIs (see § 3.4.1), the relevant information to be determined is how well can we assure that no blended (chance-aligned) sources are contaminating the detected transit signal.

Generally, our high-spatial resolution images can play an important role in the rejection of two false positive scenarios. First and most critical, specific configurations of a blended unassociated eclipsing binary (case Id in § 3.1) can reproduce the detected planetary transit of the candidate. According to Morton & Johnson (2011a), this case is of particular importance for shallow transits (with apparent depths below 1000 ppm), which should be the case of small planets around

[6] According to `http://exoplanet.eu`

main-sequence stars (or larger planets around giant stars). In section § 5.2.3.1, we deeply investigate and quantify how our high-resolution images can reduce the probability of such scenario being the responsible of the detected transit. Secondly, even if the transiting object is actually eclipsing the target star (cases Ib and IIb in § 3.1), the mere presence of single blended sources not accounted for in the light curve analysis can importantly dilute the transit/eclipse depth. As a consequence, the transiting object would seem smaller than it actually is. This scenario is discussed and quantified in section § 5.2.3.2.

Other configurations, such as hierarchical triples or grazing eclipses, cannot be ruled out by high-spatial resolution images, but their occurrence probabilities are extremely low.

5.2.3.1 Rejecting background eclipsing binary scenarios

In this section, we analyze the possible presence of an undetected blended eclipsing binary (EB). We use the BSC parameter explained in § 3.4 to determine the probability for a given KOI to have a blended EB capable of mimicking the detected transit but undetected by our high-spatial resolution images.

Given a planet candidate, we can calculate the maximum contrast that an hypothetical blended EB must have to mimic a transit of fractional depth δ (see equation 7 in Morton & Johnson, 2011a). This equation reads

$$\Delta m_{\mathrm{Kep}}^{max} = m_{EB} - m_{target} = -2.5 \ \log_{10}(\delta). \tag{5.7}$$

This value is valid for the *Kepler* band. Since we are observing in the SDSSi band, we have to compute the magnitude conversion. If we use the KIC (*Kepler* Input Catalog) magnitudes, we can easily see that the *Kepler* and i magnitudes are linearly correlated. By performing a linear fitting, we obtain

$$i = 0.947 \cdot m_K + 0.510. \tag{5.8}$$

The linear correlation goodness of this fit is $r^2 = 0.98$, which is acceptable enough for this work. Thus, we can estimate the contrast in the i_{SDSS} band as $\Delta i = 0.947 \cdot \Delta m_K$, so that

$$\Delta i_{max} = 0.947 \cdot [-2.5 \ \log_{10}(\delta)]. \tag{5.9}$$

For clarity, we refer to this maximum contrast in the i band as Δm_{max}. This maximum contrast was described as a user-defined parameter in § 3.4, where we explained the BSC calculations. Here, we define this parameter with the above characteristics and introduce it in Eqs. 3.6 to 3.8 in order to calculate the BSC for background EBs with the appropriate magnitudes to mimic the measured planetary-like transit signal.

In order to maximize the power of the high-resolution observations, we need the completeness of the images to be fainter than $i_{\rm KOI} + \Delta i_{max}$. In other words, we define the completeness criterion as $i_{\rm comp} > i_{\rm KOI} + \Delta i_{max}$. In Fig. 5.15, we show that all observations have detectability limits roughly larger than this value (all purple points are around the 1.0 line and below 1.1), i.e., $i_{\rm det} > i_{\rm KOI} + \Delta i_{max}$. However, we have achieved the completeness criterion ($i_{\rm comp} > i_{\rm KOI} + \Delta i_{max}$) only for the 40% of the planets, gray points in the figure. Thus, for the remaining 60% we will need to apply the incompleteness correction explained in § 3.4.5. We note, however, that for most of the targets the completeness limit is very close to the requested $i_{\rm KOI} + \Delta i_{max}$ and the correction will not be very important.

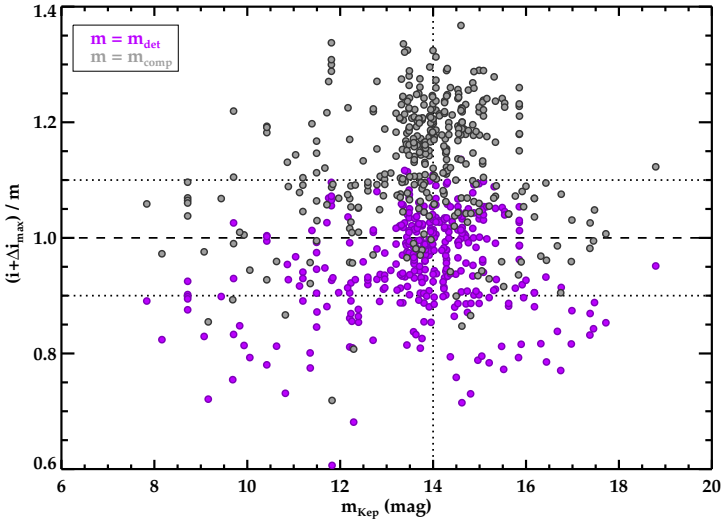

FIGURE 5.15: Ratio between the requested depth in magnitude and the actual completeness of the image as a function of the target magnitude.

We have calculated the P_{BS} parameter for all KOIs without companions closer than 3 arcsec. The results are presented in column 6 of Table 5.7. In this table, we also show $P_{BS,0}$ (corresponding to the *a priori* probability before any high-spatial resolution image) and the corresponding **improvement** obtained with our high-resolution observations. Complementarily, the BSC is defined as BSC= $1 - P_{BS}$ and BSC$_0$ = $1 - P_{BS,0}$. This parameter provides the level of confidence that any blended companion with the appropriate characteristics to mimic the detected planetary transit is blended within 3 arcsec.

The results show that our observations reduce the blended source probability by more than a half for the 62% of the planets studied. Among the sample of planet candidates around isolated stars in the active list (196 in total), only three had BSC$_0$ > 99%. After our high-resolution observations, we have increased this number to 31 planets with more than a 99% confidence that there is no background eclipsing binary mimicking the planetary transit. Although more tests should be done to completely validate them, **this result improves the confidence on their true**

planetary nature. We will compare the quality of different high-resolution imaging techniques in terms of the P_{BS} values in § 5.2.4.

5.2.3.2 Rejecting diluted single-star scenarios

In this second case, we assume that the eclipse is taking place in the brighter star and analyze the possible presence of other single-blended sources. In this case, the eclipse could have been produced by another stellar or sub-stellar object (case Ib in § 3.1) or by a true planet with a larger radius than that calculated from the transit signal (case IIb in § 3.1).

Let us start with the simple case of one single star blended in the *Kepler* aperture. The observed transit depth can be calculated as $\delta_{\rm obs} = (F_{\rm nt} - F_{\rm t})/F_{\rm nt}$, see Eq. 2.4.[7] In the presence of a secondary star contributing with a flux F_2, we have $F_{nt} = F_1 + F_2$ and $F_t = F_1(1-\epsilon) + F_2$, where ϵ is the actual fraction of the star covered by the transiting object and its value can be easily demonstrated to be equal to the true transit depth (i.e., $\epsilon = \delta_{\rm true}$). By using this, we can correct the transit depth due to the presence of a blended source as

$$\delta^{\rm true} = \delta^{\rm obs}\left(1 + 10^{-\Delta m/2.5}\right)^{1/2}, \tag{5.10}$$

where $\Delta m = m_2 - m_1$ represents the magnitude difference between the the blended (m_2) and the target star (m_1) in the *Kepler* band. At this point, as stated by Law et al. (2014), we can distinguish between two cases:

(a) The transited star is the *faintest* star ($\Delta m < 0$), case IIa.

(b) The transited star is the *brightest* star ($\Delta m > 0$), case IIb.

To get the true radius of the transiting object, case (a) or IIa requires some knowledge about the radius ratio between the two stars involved. This requires additional knowledge of both stars (which means more free parameters rather than just the magnitude difference), which is out of the scope of this theoretical analysis.

In case (b) or IIb, however, assuming that the transit depth is related to the radius ratio between the transiting object and the parent star as $\delta = (R_p/R_\star)^2$, the true radius of the transiting object is given by

$$R_p^{true} = R_p^{obs}\left(1 + 10^{-\Delta m/2.5}\right)^{1/2}. \tag{5.11}$$

[7] We remind the reader that $F_{\rm nt}$ stands for the flux out of transit and $F_{\rm t}$ for the flux on transit.

According to the most updated catalog of confirmed exoplanets,[8] the empirical maximum possible radius for a planet is $R_p^{max} \approx 2.2\ R_J$. Thus, we can calculate the maximum magnitude difference Δm_{max}^{dil} that the blended source can have (i.e., how faint could it be) to dilute the transit depth, such that a non-planetary object (i.e., $R_p > R_p^{max}$, regardless of its nature) appears as a true planet-size object:

$$\Delta m_{max}^{dil} = -2.5 \log \left[\left(\frac{R_p^{max}}{R_p^{obs}} \right)^2 - 1 \right]. \tag{5.12}$$

This equation indicates that the presence of undetected blended objects with magnitudes $m_1 < m_2 < m_1 + \Delta m_{max}^{dil}$ can dilute the eclipse depth of a non-planetary object down to the typical values of a planetary object transit. For instance, in the case of a transit providing a planetary radius of $R_p^{obs} = 2\ R_{\rm Jup}$, only blended stars with magnitude contrast smaller than 1.7 mag can dilute the transit so that the true radius of the transiting object is larger than the 2.2 $R_{\rm Jup}$ limit.

According to Eq. 5.12, case (b) only applies to candidates with $R_p^{obs} > 1.56\ R_{\rm Jup}$, since smaller planets would need companions brighter than the transited star (case (b), $\Delta m_{max}^{dil} < 0$). In our sample, only five objects have $R_p^{obs} \in [1.56, 2.20]\ R_{\rm Jup}$ (namely, KOI-0338.01, 1353.01, 1452.01, 2481.01, and 3728.01). For those cases, we can proceed exactly as we did for the blended eclipsing binary scenario to get the P_{BS}, but now we use Δm_{max}^{dil} as the maximum magnitude value to get the probability of the presence of a diluter source, P_{DS}. The results show that this probability is diminished from $P_{DS,0} = 10^{-3} - 10^{-2}$ to $P_{DS} = 10^{-5} - 10^{-4}$, i.e., from 0.1-1% to 0.001-0.01%. Although the starting probabilities were already small, our high-resolution images showing no blended sources within our detection limits practically discard this possibility as a false positive scenario for the observed candidates. Indeed, the two planets around **KOI-338 (Kepler-141)** and **KOI-1353.01 (Kepler-289b)** have recently been validated by Rowe et al. (2014), and we will present hints for the confirmation of **KOI-2481.01** by our RV analysis in section§ 6.7, while a brown dwarf nature is established for KOI-3728.01 (see § 6.6.3 and § 6.8).

We note that due to the mathematical shape of Eq. 5.12, we cannot perform this calculation for planet candidates with $R_p^{obs} > R_p^{max}$.

On the other hand, as stated by Law et al. (2014), case (a) would only affect few planet candidates with observed radii close to the limit $R_p^{obs} \approx 1.56\ R_J$ and presenting blended stars with very small radius. Thus, small planet candidates are not affected by this scenario, although the presence of blended sources can modify their properties, as we showed in section § 5.2.2.4.

For cases with more than one blended star, the P_{DS} probability is insignificant for case (b), since the probability of having two or more undetected sources within our sensitivity limits is far smaller.

[8] We have checked the radii of the radial velocity confirmed extrasolar planets provided by The Extrasolar Planet Encyclopedia (`http://exoplanet.eu`).

Thus, we can conclude that the dilution from single blended stars is not important in our sample. These blended stars can only slightly affect the properties but not the planetary nature.

5.2.4 A comprehensive comparison between different techniques

There are three main techniques that can provide high-resolution (diffraction limited) images from the ground: speckle imaging, adaptive optics, and lucky imaging. Among the high spatial resolution studies performed for the *Kepler* candidates, there are three main works that have provided exhaustive observations of the candidates apart from our survey. Howell et al. (2011) (hereafter H11) published the first results of the speckle imaging observations for 156 KOIs, using the 3.5m-telescope WIYN on Kitt Peak. Adams et al. (2012, 2013) (hereafter A12) provided the AO multiplicity results in the near-infrared regime for a total of 102 KOIs using both the 6.5m Multiple Mirror Telescope (MMT) and the Palomar Hale 5.1m telescope. A posterior shallow but extensive survey by Law et al. (2014) with Robo-AO (hereafter L14) provided AO observations for 715 KOIs, using the robotic Palomar 1.5m telescope (Cenko et al., 2006).

The distribution of *Kepler* magnitudes is similar for all surveys, peaking L14 and the present work at slightly fainter magnitudes ($m_{kep} \approx 14$) than H11 and A12 ($m_{kep} \approx 12$). In Fig. 5.16, we show this distribution for the four studies.

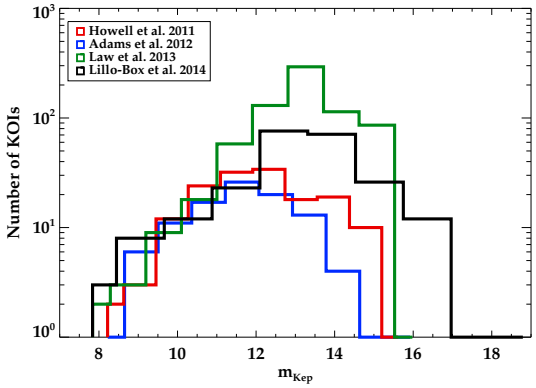

FIGURE 5.16: Distributions of *Kepler* magnitudes for the different high-spatial resolution surveys in the *Kepler* sample of planet host candidates.

However, since these works were published, some of their KOIs have also been demoted as planet candidates due to several reasons. In particular, 24 KOIs from H11 (out of 156, 15%), 16 KOIs from A12 (out of 102, 16%), and 17 KOIs from L14 (out of 714, 2.3%) currently do not present any planet candidate.[9] In our case, the percentage of demoted KOIs is higher (61 out of 233, 26%) because we observed several KOIs, which still had the *non-dispositioned* flag in the *Kepler* archive (meaning that they did not yet passed all requirements to be planet candidates) during the 2013 observing season and most of them turned out to be false positives.

[9] as of February 2015

FIGURE 5.17: Venn diagrams summarizing the results of the four main high-spatial resolution studies regarding the *Kepler* sample of planet host candidates.

The speckle imaging study by H11 provides the highest resolution images (with detection limits at 0.05 arcsec) but in a very small field of view that only allows to detect companions at a limiting separation of 1.4 arcsec. They also provide a typical depth magnitude limitation of $\Delta m = 4.0$ mag. The large majority of the transits of planet candidates could be mimicked by blended stellar systems fainter than this magnitude difference (as we can see in the fourth column of Tab. 5.7). With these observing limitations, they found that 4/127 KOIs (3%) with remaining planet candidates do present a stellar companion closer than 1.4 arcsec.

The AO work by A12 seems to be more complete in magnitude depth and field coverage (more than 20×20 arcsec). We have used their updated Tables 2 and 4 to compute statistics that could be compared to the H11 and our own study. In particular, they find that among their 85 KOIs with remaining planet candidates, 37 are isolated (no companion closer than 6 arcsec, 44 %), 12 KOIs (14%) present a stellar companion within 1.4 arcsec, 28 KOIs (33%) present a stellar companion within 3 arcsec, and 30 KOIs (35%) present at least one companion in the range 3-6 arcsec.

The recently published survey by Law et al. (2014) provides the largest catalog of AO observations of *Kepler* candidates. Their observations determine that 29 out of the 697 KOIs with remaining candidates (4.2%) present some companion within 1.4 arcsec, and 49 (7%) do present companions closer than 2.5 arcsec. Since this survey is limited to 2.5 arcsec of separation, we cannot include the remaining 648 in the isolated group.

All these numbers are summarized and compared to the lucky imaging results provided in this paper in Tables 5.8 and 5.9. Figure 5.17 also illustrates the coincident KOIs between the different works. In the next subsections, we compare these works to our survey, summarizing coincident objects and BSC results. For the latter, please note that all four studies provide 5σ-level sensitivity limits, so that direct comparison of the BSC values can be done.

Comparison with Howell et al. (2011)

Among the 12 coincident objects between H11 and this work, none of them present companions within 1.4 arcsec (the largest separation detectable by H11). Since sensitivity curves and photometric transformations of the filters used to the SDSS system are not provided by the authors for these targets, we cannot exactly compare how both studies have improved the BSC values. As a zero-order approximation, we can assume that the limiting magnitude presented in their Table 2 as Δ_{max} and calculated for an angular separation of 0.2 arcsec is constant over the 1.4 arcsec of spatial coverage and obtained in a similar filter.[10] We can then determine a zero-order BSC_{H11} and thus compare it to our values. The results (see Tab. 5.10) show that the speckle-imaging limiting magnitudes are smaller than the required magnitude differences to discard possible background configurations able to mimic the planetary transit (that we have called Δm_{max} in this dissertation). This happens for all 32 planet candidates orbiting the 12 common KOIs. In all cases, our AstraLux observations are better (in terms of reducing the BSC parameter) than the H11 observations. The small contribution of the H11 study to reduce the probability of a blended eclipsing binary is mostly due to the reduced field of view, which avoids detection of 1.5-3.0 arcsec companions, where the probability of having a background source is maximum in the 0-3 arcsec range.

Comparison with Adams et al. (2012, 2013)

Only four out of the ten coincident objects with Adams et al. (2012) present at least one companion below 6 arcsec:

KOI-0111 & KOI-0555. The companions to KOI-0111 and KOI-0555 detected by our survey are not detected by A12. Since the magnitude differences in both cases are relatively small (Δi = 6.1 for KOI-0111 and Δi = 3.8 for KOI-0555), the non-detection by A12 could mean that these companions are bluer, but we would need photometry in different bands to confirm this result.

KOI-0372. On the contrary, we do not detect any of the three faint companions to KOI-0372 with $\Delta m_{Kep} > 10.0$ due to their faintness (but we detect the farther and brighter companion at 5.94 arcsec). However, the maximum magnitude difference for a companion star that could mimic the planetary transit of the candidate KOI-0372.01 is $\Delta m_{max} = 4.99$, so that the detected companions by A12 do not affect the planetary candidacy of this object. The planet orbiting this target is prelimiray confirmed by our RV survey (see section § 6.5).

KOI-0115. This KOI hosts three planet candidates for which $\Delta m_{max}(.01) = 7.6$, $\Delta m_{max}(.02) = 8.8$, and $\Delta m_{max}(.03) = 11.1$. The observations from A12 detected two companions with magnitude differences below those values. We do not detect the closest target at 2.43 arcsec and $\Delta m_{kep} = 11.4$ mag due to sensitivity restrictions in the present study. However, this companion

[10] The filters used by H11 are similar to the I and R Johnson bands.

has a magnitude difference that is higher than the maximum difference that would affect any of the three planets. Hence, we could say that this is a negligible blended star for this system.

In the case of the six remaining KOIs with non-detected companions closer than 6 arcsec, we obtain smaller values of the blended source probability, given that our images are deeper for these particular objects. Table 5.10 summarizes these results compared to our values according to the updated sensitivity limits that are provided by A12 for each target in the *Kepler* band and transformed to the *i* filter using our own transformation determined in section § 5.2.3.1. In this case, we can see that A12 reduces the probability of having a background source more than H11. The only handicap of this survey is that possible blue non-negligible objects could not be detected by this survey (as we have shown in the cases of KOI-0555 or KOI-0111), since *Kepler* observations are performed in the optical wavelengths and A12 observations are obtained in J and Ks bands.

Comparison with Law et al. (2014)

A total of 112 KOIs have observations in both L14 and the present study. Among this subsample, 13 KOIs have detected companions within 2.5 arcsec (the largest separation that L14 can achieve). In four cases, both studies detect the companions (KOI-0401, KOI-0191, KOI-0628, and KOI-1375). In one case (KOI-0640), our survey does not detect the companion object at 0.44 arcsec with a contrast magnitude of 0.62 mag in the *i* band. We have examined the AstraLux image and concluded that the ambient conditions were poor for this particular night. This is also reflected in its sensitivity curve with poor quality. Finally, we have detected companions to the remaining eight KOIs (namely, KOI-0658, KOI-1452, KOI-0703, KOI-0704, KOI-0721, KOI-2481, KOI-0111, and KOI-1812) that were not detected by the L14 survey. In L14, the authors justify this non-detection compared to our previous study by arguing that the companions are fainter than their detections limits. However, all planet candidates in these eight planetary systems have calculated a Δm_{max} that is fainter than the calculated magnitude differences of the companion sources. Thus, the detected companions in our survey and those not detected by L14 can actually severely affect the candidacy of the planets or, at least, their properties, being non-negligible detections. It must be noted that we have detected companions in the range 2.5-6.0 arcsec for another 26 coincident KOIs that could also affect the derived properties of the planet candidate or even their candidacy and that are not detected in L14 due to field of view restrictions.

Since no individual sensitivity limits are provided for each KOI in L14, we can use their quality definition for each KOI (low, medium, or high), use the correspondent sensitivity curve in the $i_{\rm SDSS}$ band provided in their paper to estimate the BSC, and compare it to the values found for our isolated KOIs. The results are presented and compared in Table 5.11. In general, our observations reduce the P_{BS} by a more significant amount.

General comparison of *Kepler* high-resolution imaging surveys

We can compare the results of the surveys by using the BSC parameter defined in previous sections. In particular, we can estimate how each of these high-resolution surveys have contributed to the validation of the planet candidates by measuring how they have diminished the probability of a KOI to have a blended non-detected source. We can calculate the BSC parameter for each observed target in each survey and compare the BSC value prior and after the imaging observations. We can define the *Improvement* parameter as the relative difference between the prior BSC value and the new BSC value (i.e., $Improvement = (P_{BS,0} - P_{BS})/P_{BS,0}$). By doing so, we can summarize the results by the histograms shown in Fig. 5.18. According to it, A12 obtained a similar distribution of improvements than our work. The only handicap of this survey lies is that the targets were observed in the near-infrared while *Kepler* observations are performed in the optical band. Thus, they could have missed some bluer companions that affect the *Kepler* photometry. This was demonstrated in section § 5.2.4 with the cases of KOI-0111 and KOI-0555. On the contrary, we could be missing redder companions that are possibly bound (such KOI-0372B), which could have implications in the knowledge of the formation and evolution of the planetary system.

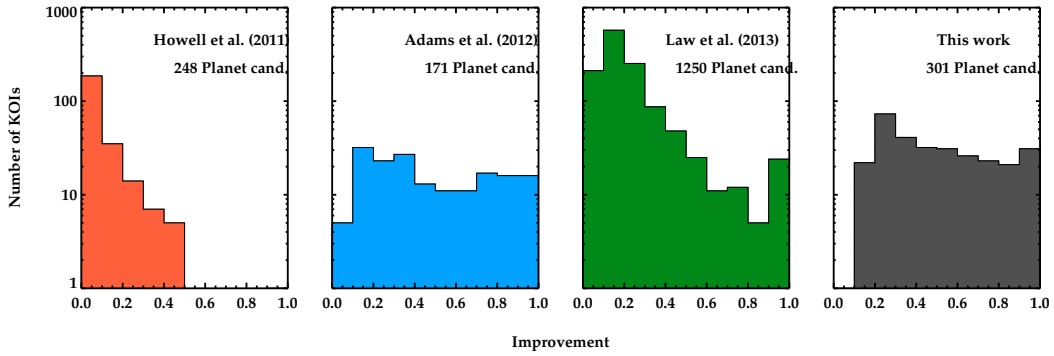

FIGURE 5.18: Comparison of the quality of the four main high-resolution surveys of the *Kepler* sample of planet candidates. The x-axis represents the improvement in the probability of a background, non-detected companion that could mimic the particular planetary transit.

The H11 speckle imaging study does not reduce the probability of a blended scenario in more than 10% for the large majority of their observations. This is mostly due to the limited contrast magnitude and small field of view that they use.

In the case of L14, they present the largest sample of high-resolution images, which are also observed in the optical range. Their distribution of Improvements is rather broad. With these observations, the 93% of the planet candidates hosted by their observed KOIs (1163 planet candidates in total) diminish the probability of a blended scenario by less than 50%. The remaining 7% of the planet candidates (87 in total) reduced this probability by more than 50%. However, since we calculated their P_{BS} by assuming the typical sensitivity curves that are provided by L14 for each target, according to their quality definition of the AO image (namely *low*, *medium*,

and *high*), we warn that applying the particular sensitivity curves for each KOI could modify these results.

Finally, our survey provides high-resolution observations for 233 *Kepler* host candidates (172 still active KOIs) in the optical range. Our results show improvements in the blended source probability above 50% for the 62% (186) of the planet candidates studied and below 50% for the remaining 38% (115) of the planet candidates.

In Fig. 5.19, we show all the companions detected by the four surveys. Empirical sensitivity curves according to these detections are also plotted for each of the surveys.

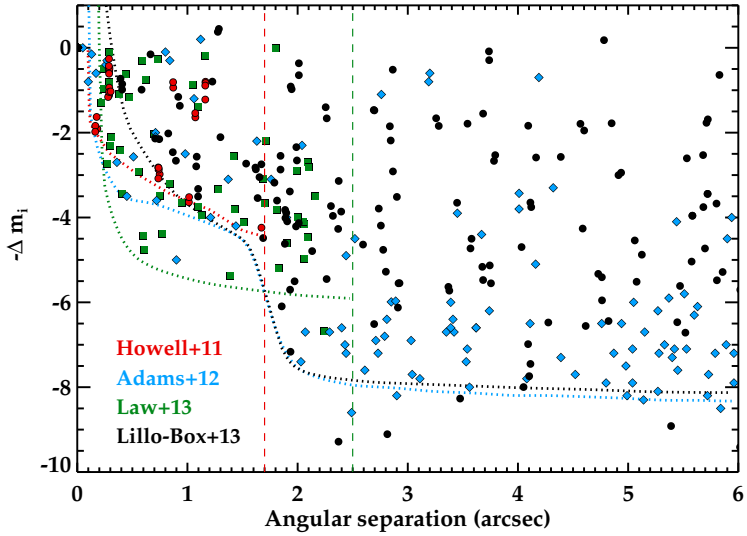

FIGURE 5.19: All companions detected by the different high-resolution surveys studied in this work: Adams et al. (2012) in blue filled diamonds, Howell et al. (2011) in red filled circles, Law et al. (2014) in green filled squares, and our work in black filled circles. The empirical sensitivity limits according to these detections are shown with dotted lines.

5.2.5 Update on posterior works

Since the publication of our survey in Lillo-Box et al. (2012) and Lillo-Box et al. (2014b), other works were published on high-spatial resolution surveys of *Kepler* candidates apart from those analyzed in previous sections. In this section, we briefly summarize their main results and the coincident objects with our work:

- Gilliland et al. (2014).- This work used the WFC3 onboard the Hubble Space Telescope to examine 23 KOIs in a field-of-view of 2.5 arcsec. They found 15 companions, six of them being probably bounded. We have no overlap objects with this work.
- Dressing et al. (2014).- In this work, the authors used the ARIES instrument at the 6.5m Multiple Mirror Telescope on Mt. Hopkins to obtain AO images in the near-infrared of

87 KOIs. They found 14 KOIs with companions closer than 3 arcsec (17%) and 39 KOIs with companion closer than 6 arcsec (41%), compatible with our results. We have no overlap objects with this work.

- Wang et al. (2014a).- The authors performed AO imaging on 56 KOIs and detected companions closer than 6 arcsec in 17 KOIs (30%), including 7 KOIs (~13%) with companions closer than 3 arcsec. The only one common target was KOI-111 for which we detected a companion at ~ 1.8 arcsec that was not detected by Wang et al. (2014a).

- Horch et al. (2014).- In this paper, the authors used the WIYN and Gemini-8m telescopes to obtain speckle imaging with the DSSI instrument in the optical range of 588 and 35 KOIs within 1 arcsec. They discovered companions in 41 of 588 targets observed with WIYN (7.0 ± 1.1%) and in 8 of 35 KOIs observed with Gemini (22.8 ± 8.1%). To our knowledge, as of today there is not table providing their results. Since their work does not make any comparison to previous works, we do not know whether there is any overlap with our sample.

- Everett et al. (2014).- In this paper the authors use AO and speckle, finding 7 close companions to 18 KOIs. There is overlap with KOI-115, where we found a companion not accesible by their field of view; and KOI-2593, for which no companions were found in both works.

5.3 Discussion: multiplicity rate in planet hosts

The presence of companions physically associated to planet host stars is known to affect the formation efficiency, migration, and dynamical evolution of planetary systems (e.g., Boss, 2006). This is reflected in the properties of the planets orbiting any star in a multiple-system, which may undergo several processes such as gravitational instabilities, dissipation, and or Kozai effects (see Lodieu et al., 2014, and references therein) .

The multiplicity rate (η) in planet hosts has been investigated even before the launch of the *Kepler* telescope (e.g., Daemgen et al., 2009, Mugrauer et al., 2005, Raghavan et al., 2006, and references therein). Seeing-limited and more recently diffraction-limited images of planet hosts have allowed the detection of close companions. As we have shown, different works have also analyzed the multiplicity in *Kepler* planet host candidates (e.g., Adams et al., 2012, 2013, Law et al., 2014, Lillo-Box et al., 2012, 2014b, Wang et al., 2014a). Now that some of these planets have been confirmed or validated, the number of planets in multiple-star systems has grown. Added to this, other works have obtained high-spatial resolution images of confirmed planet hosts (e.g., Lodieu et al., 2014, Ngo et al., 2014, Wang et al., 2014b), also increasing the sample.

All this new pieces of the puzzle have started to provide hints on the responses to key questions related to how multiplicity affects the formation/occurrence, migration, and dynamical evolution of planetary systems. Here we summarize how all these works, and in particular this dissertation, have shed more light to unveil the influence of multiple-star hosting systems.

Is the multiplicity rate different in planet hosts than in single stars? How this depends on the binary separation?

First, the difficulties in answering this question are mainly related to our difficulties of defining what a single star is. We cannot assure at 100% that a star is actually not hosting a planet because the large majority of planets (the Earth-size ones) are difficult to detect with the current instrumentation. Thus, all results comparing multiplicity in single and host stars suffer from this observational bias.

This said, Roell et al. (2012) provided a summary of the 57 detected planets in S-type systems. They found that the multiplicity rate of planet host stars is 12%, four times smaller than that for Solar-like stars ($\sim$ 46%, Raghavan et al., 2010). Previously, Raghavan et al. (2006) and Mugrauer & Neuhäuser (2009) suggested larger rates for multiplicity in planet hosts, $\sim$ 23% and $\sim$ 17% respectively. In either case, it seems quite clear from these works that multiple stellar systems inhibit somehow the presence of planets. This could be due to different reasons such as suppression of planet formation, gravitational instabilities leading to planetary ejection/engulfment in the early stages, etc.

Seeing-limited observations showed that the frequency and properties of planets orbiting one of the components of a wide binary system are not affected by the gravitational pull of the secondary star, confirming theorists' investigations. In particular, Desidera & Barbieri (2007) concluded that only stellar companions at separations closer than 100-300 AU can affect the formation, migration, and dynamical evolution of the planetary systems. More recently, Wang et al. (2014b) provided observational evidences that planet formation is suppressed in binary systems closer than 20 AU and affirmed in a posterior work (Wang et al., 2014a) that planets are less common in systems with stellar companions closer than 1500 AU.

In this dissertation, we have detected possibly bounded companions to validated/confirmed planet hosts. In particular, we found a close companion to KOI-3158 (Kepler-444A Campante et al., 2015) at 1.8 arcsec, which given the Hipparcos distance of 35.7 pc, provides a projected separation of the two targets of $\sim$ 65 AU. Also, we will see in section § 6.7 that we have found hints for a very compact S-type planetary system in KOI-2481, with the planet orbiting in a 33-days orbit ($\sim$ 0.23 AU) and a low-mass companion in a 193-days tight orbit ($\sim$ 0.76 AU). The definitive confirmation of this system would represent a challenge for the study of multiplicity in planet hosts, both in terms of existence and stability of the orbits.

Is there a difference in the multiplicity rate of different type of planets? How does multiplicity affects planet properties?

These two questions are directly related to whether the formation of binary systems allows only some type of planets to be formed. By analyzing the sample of 57 planets in S-type configurations, Roell et al. (2012) concluded that exoplanets on multiple-star systems tend to be more massive than planets around single stars (see Fig. 5.20, left panel). Although we are in the low-numbers regime, it appears that massive planets survive formation and evolution processes in multiple star systems more frequently than less-massive planets.

Do planets form in close binary systems? Which kind of planets can do so?

According to theoretical simulations, planet formation should be disrupted in multiple-star systems with small separations of ~10-200 AU (see, for instance, Desidera & Barbieri, 2007, Kraus et al., 2012, Thébault et al., 2006, and references therein). From an observational point of view, Eggenberger et al. (2004) presented a list of 15 planets in S-type binary systems with separations from ~20-6400 AU. The mostly packed system in the Roell et al. (2012) catalog of 57 S-type planetary systems had a separation between the two components of ~ 10 AU. These discoveries are in relatively good agreement with the theoretical simulations. However, all planets detected below 100 AU seemed to be rather massive, with typical masses larger than 1 $M_{\rm Jup}$. Added to this, according to this catalog, multi-planet systems are not found in binaries with separations smaller than 100 AU. Thus, these data showed that planets around close binaries are massive and single (see Fig. 5.20, right panel).

However, in this dissertation we have shown the presence of a probably bounded companion to the five-planet system Kepler-444 (KOI-3851, Campante et al., 2015), with a separation of ~ 65 AU. If we assume Earth-like density for the tiny planets validated in this system with $R_p = 0.31 - 0.51\ R_\oplus$, we obtain masses in the range $M_p = 0.03 - 0.13\ M_\oplus$, well below the limiting line proposed by Roell et al. (2012) as the limit for planets in binary systems (also below the limits of the right panel of Fig. 5.20). The other confirmed system below this line is the two confirmed planets around GJ 667C (Anglada-Escudé & Tuomi, 2012). In both cases, the planets lie below the critical planet-primary separation calculated by using the expression by Holman & Wiegert (1999) and so both systems are expected to be stable.

Additionally, we have evidences for the detection of an extremely packed S-type planetary system, KOI-2481 (see Chapter 6 and Lillo-Box et al., 2015c), with a Jupiter mass planet orbiting one of the components of a binary system with a projected separation of ~ 0.8 AU. In this case, the system appears to be at the edge of the critical binary separation.

The detection of the two packed S-type planetary systems with Earth-like and smaller planets (Kepler-444 and GJ 667C) puts into questioning that only massive planets can grow in close binary systems. Instead, this seems to be an observational bias rather than a real effect. Indeed,

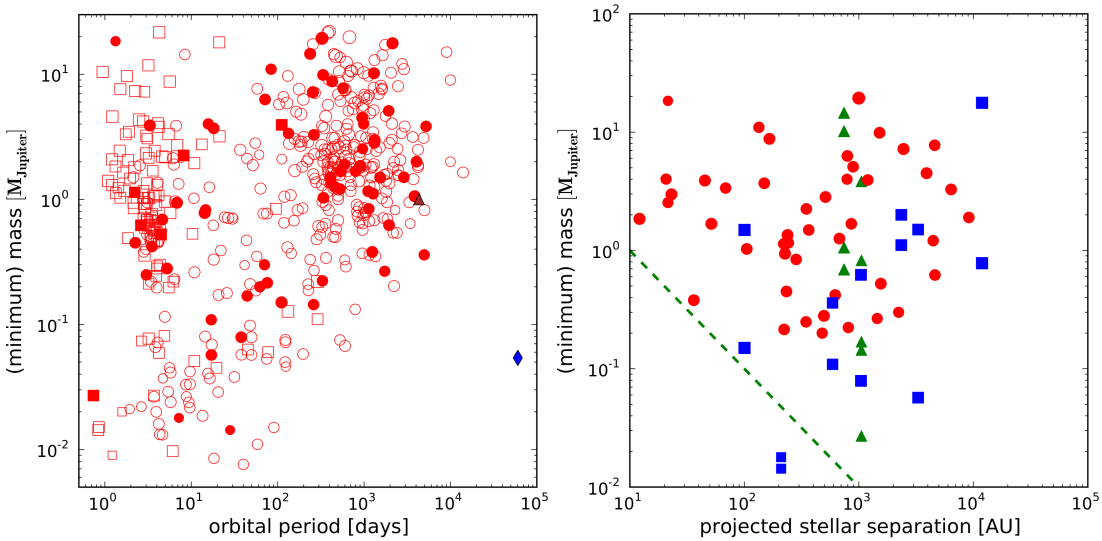

FIGURE 5.20: Adapted figures from Roell et al. (2012). **Left:** distribution of planets around single stars detected by RV (squares) and transits (circles), compared to planets found in S-type systems (filled symbols). **Right:** Minimum planetary masses as a function of the projected binary separation. The planets around Kepler-444 and KOI-2481 lie belw the empirical limit marked by the dashed line.

according to the theoretical expression of the critical semi-major axis provided by Holman & Wiegert (1999), it seems more realistic that less massive planets can more easily achieve close stable orbits than the more massive ones. On the other hand, the validation of the five planets in Kepler-444 and our detection of the close companion probably bounded reduces the lower limit of 100 AU found for a multi-planetary systems to survive in a multiple-star system down to $\sim$ 65 AU. Finally, the possible confirmation of KOI-2481 reduces the minimum projected separation of the two components of an S-type planetary system from 10 AU to $\sim$ 0.8 AU.

Are multi-planetary systems less common in multi-star systems?

Among the whole sample of 447 confirmed/validated multi-planetary systems, only 10 (2.2%) have known detected bounded companions. On the other hand, among the 742 known planets in single-planetary systems, 48 (6.4%) have known detected bounded companions. Although these ratios may suffer from many different biases, they can give us an idea about the rough ratio. Apparently, we have now found around three times more single-planet S-type planetary systems than multiple-planet S-type systems.

In our sample, we have found 10 KOIs with probably bounded companions. Among this sample, 5 KOIs are multiple and the other 5 are single planetary systems. Indeed, the planets orbiting three out of the five multiple systems have been validated, namely KOI-3851 (Kepler-444), KOI-401 (Kepler-149), and KOI-658 (Kepler-203); and the radii of all candidates are smaller than $5R_\oplus$ (except for KOI-433.02 with $R_p \sim 11\ R_\oplus$).

If the gravitational bond of these stellar companions to the 10 KOIs and the remaining planet candidates are confirmed we would have similar rates for multis to form in S-type planetary systems than for single planets. However, we warn about the low-number statistics and strong biases that can severely affect this values.

5.4 Validation of *Kepler* planetary systems

In this section we summarize two works in which we contributed by providing high-resolution observations used to validate the tiniest planet known to date (Kepler-37b, § 5.4.1; Barclay et al., 2013) and to confirm a sample of 49 small planets around 22 host stars in the *Kepler* sample (§ 5.4.2; Marcy et al., 2014). We briefly summarize our participation in the papers and refer to the corresponding papers for additional information about these systems.

5.4.1 Kepler-37 b: a sub-Mercury sized planet

The planet host candidate KOI-0245 was followed-up with AstraLux as part of our high-resolution imaging survey explained in the previous sections. These observations were used to validate the planet candidates detected by *Kepler*. In particular, three planets have been found and validated in this system, currently known as Kepler-37b,c,d after their validation by Barclay et al. (2013). In this paper, we analyzed this system by using different techniques. The stellar properties of the host star were determined by studying its solar-like oscillations detected in the *Kepler* light curve. The modeling yielded a stellar radius of $R_\star = 0.772 \pm 0.016\ R_\odot$ and a mass of $M_\star = 0.803 \pm 0.034\ M_\odot$. An accurate determination of these parameters was crucial to provide accurate estimations of the planetary sizes. The phase-folded transits of the planets were then modeled to obtain their orbital and physical properties. All planets had orbits consistent with being circular. The fitted transits are shown in Fig. 5.21 and the fitted parameters for the three planets in the system are shown in Table 5.12. This system hosts the tiniest planet known to date (Kepler-37b), having an estimated radius of $0.303^{+0.053}_{-0.073}\ R_\oplus$, smaller than the size of Mercury ($\sim 0.38\ R_\oplus$) and compatible with the size of the Moon ($\sim 0.27\ R_\oplus$).

Kepler-37 was observed with AstraLux/2.2m at Calar Alto Observatory under good seeing conditions (0.8 arcsec) on 2012 May 27th, using a Sloan i filter (see Fig. 5.21, right panel). This configuration allowed us to perform diffraction limited imaging of Kepler-37. We used the full camera array (24×24 arcsec) to cover the whole Kepler PSF. We took 30 000 frames of 30 milliseconds of exposure time (well below the typical timescale on which atmospheric turbulence changes). According to our sensitivity measurements on the final image (see Fig. 5.21, left panel), we did not detect any source at the 3-σ level for objects 2 magnitudes fainter at 0.25 arcsec from the target star, 4 magnitudes at 0.4 arcsec, 6 magnitudes at 0.5 arcsec, and

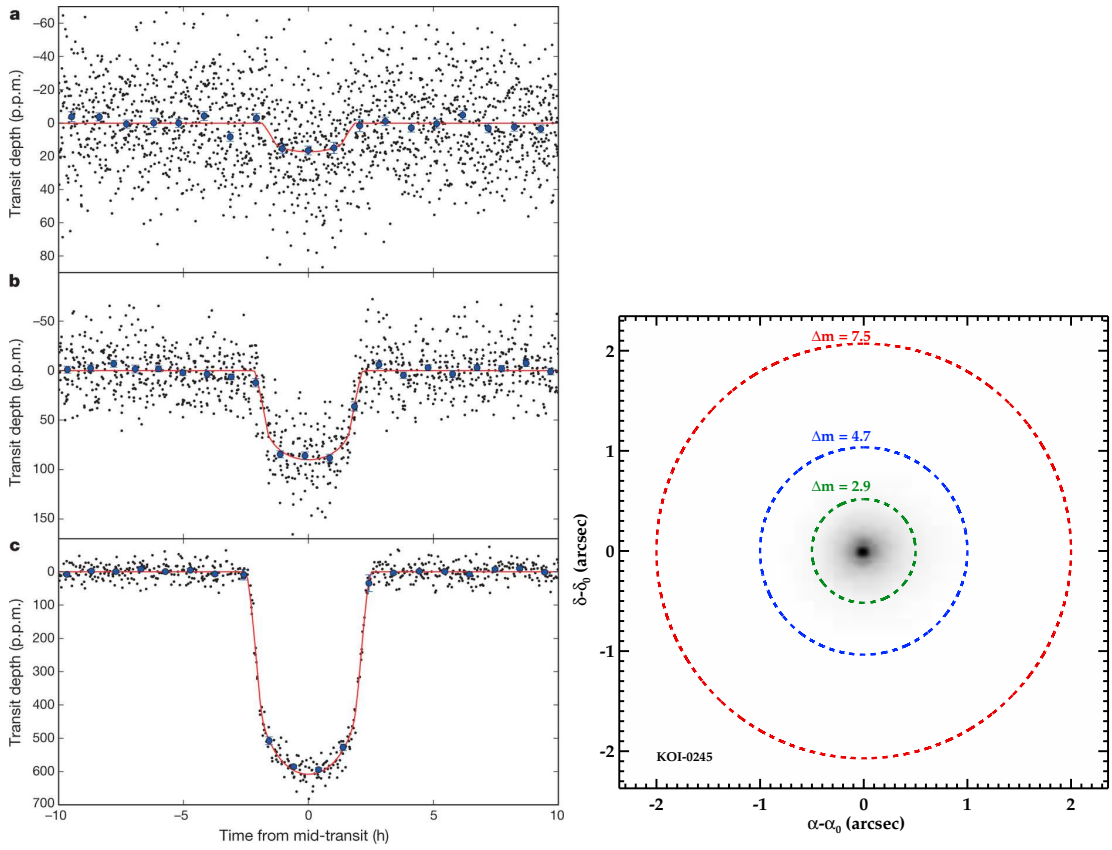

FIGURE 5.21: **Left:** Phase folded light curves of the three Kepler-37 system planets and their corresponding fitted models. **Right:** AstraLux image of Kepler-37 (KOI-245) and its sensitivity limits at different angular separations. Figures adapted from Barclay et al. (2013).

7 magnitudes at angular separations greater than 1.4 arcsec. The resulting BSC values for the three planets where 95.8%, 98.7%, and 99.9% for Kepler-37b,c,d respectively. These results agreed with other high-spatial resolution observations (AO using ARIES/MMT and speckle from DSSI/WYIN-3.5m and DSSI/Gemini-N) also used in this work.

These high-spatial resolution observations and other analysis were used to feed the BLENDER software. BLENDER analyses attempt to show that a blend scenario is much less likely than a planet interpretation by creating a wide array of synthetic light curves of various blend scenarios and comparing the goodness of fit to the synthetic light curves with that of the true planet model. We therefore explored possible astrophysical scenarios (blends) that can mimic a planet transit and determined that the planet configuration is the most likely in all three cases. In particular, the ratio of the planet prior to blend frequency yields an odds ratio that favors the planet interpretation by a factor of 262 for Kepler-37b, 287 for Kepler-37c, and $> 10^6$ for Kepler-37d. These results validate the planetary nature of these transiting objects in the Kepler-37 system, hosting the smallest planet known to date.

5.4.2 Validation of small planets in the *Kepler* sample: from gaseous to rocky

In Marcy et al. (2014), we analyzed the radial velocity and high-spatial resolution images of 22 *Kepler* stars hosting 49 small planets ($R_p < 3R_\oplus$). A long baseline of RV observations was used to determine or constrain the planetary masses and orbital parameters of these planets. Among the 49 candidates, 42 were detected by the transit signal in *Kepler* data and 7 were detected by the ground-based RV data obtained with HIRES/Keck. We contributed with AstraLux observations of four out of the 22 hosts (namely Kepler-37, Kepler-100, Kepler-102, and Kepler-409). Good quality on-site seeing of 0.7-0.9 arcsec during the observations combined with short exposure times lead to diffraction-limited images of the four targets in a 24 × 24 arcsec field of view. A total of 30 000 frames of 30 ms each were acquired for Kepler-37 and Kepler-409, and 40 000 frames were acquired for Kepler-100 (with 83 ms of exposure time) and Kepler-102 (with 68 ms of individual exposure time). No companions were found within our sensitivity limits.

5.5 Miscellaneous

We used the filler time of our AstraLux observations (when the *Kepler* field was not yet visible) to observe other interesting targets:

- **WTS-2 b.-** We contributed to the confirmation of the WTS-2 b extrasolar planet (Birkby et al., 2014) by providing high-spatial resolution images in the SDSSi and SDSSz bands. We detected a close companion to the host star at 0.6 arcsec, contrbuting 10.4 ± 1% and 13.1 ± 1% to the total light in these bands. The probability of a chance-aligned star for this star is lower than 0.26% so that the detected companion is probably a bounded star at an orbital separation of ∼ 600 AU. See paper for more details on this system.

- **Saturn's 2010 Great White Storm.-** We followed-up the evolution of the 2010 Great White Storm in Saturn by taking AstraLux observations in a timespan of several weeks (see Fig. 5.22, left panel). These observations were part of the work presented in Sánchez-Lavega et al. (2012), where the long-term evolution of the storm was analyzed.

- **Saturn's Hexagon.-** Subsequent images of Saturn with AstraLux during our filler time contributed to the analysis of the impressive hexagon-shaped storm on the Notrh-pole of the planet (see Fig. 5.22, right panel). This long-term follow-up of the hexagonal wave (Sánchez-Lavega et al., 2014) allowed an accurate determination of the true rotational period of the planet for the first time (10 hr 39 min 23.01s ± 0.01 s), a very contentious issue and very important to understand its climatology.

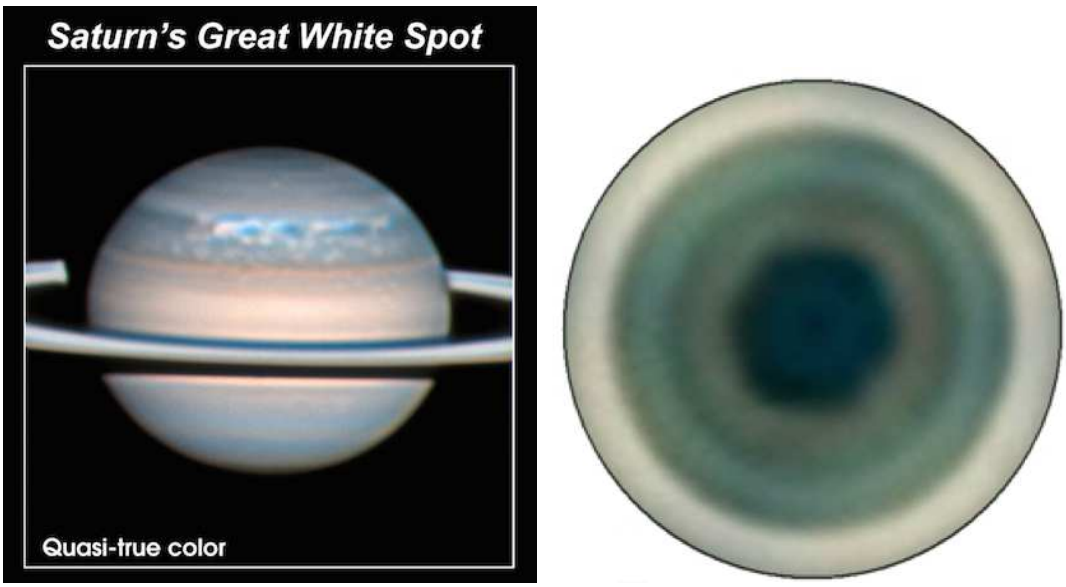

FIGURE 5.22: AstraLux images of Saturn's 2010 White storm (left panel, Sánchez-Lavega et al., 2012) and polar hexagon (right panel, Sánchez-Lavega et al., 2014).

5.6 Summary

In this chapter we have described our high-spatial resolution survey of *Kepler* planet host candidates performed with the AstraLux instrument at the 2.2m telescope in Calara Alto Observatory. In total, we observed 233 KOIs hosting 392 planet candidates. The main conclusions of this survey are as follows:

- We detected companions closer than 3 arcsec for 42 KOIs (18.0%) and companions at 3-6 arcsec for 46 KOIs (19.7%). By contrast, 155 KOIs (66.5%) appeared isolated within our sensitivity limits. Similar percentages are found for the *active* sub-sample of 172 KOIs.
- The possible physical association of the closest companions was analyzed and we concluded that companions to 10 KOIs are compatible with a joint formation.
- The parameters (transit depth and radius) of the planet candidates revolving around these hosts with close companions were updated.
- For the isolated sample, we determied the BSC parameter, indicating the probability that the target has no chance-aligned companions within the sensitivity limits obtained by our images. These results were compared to other high-spatial resolution surveys, concluding that the present survey combines a large sample of targets with a good contrast and angular separation, improving the BSC by more than 50% for the 62% of our sample.
- The results of this survey have resulted in some detections of potentially bounded companions that could represent a challenge for the study of multiplicity in planet hosts, such

as the case of the Kepler-444 (KOI-3158) planetary system with a possibly bounded companion at 65 AU. The Earth-like mass of the planets in this system found by Campante et al. (2015) puts into questioning that only massive planets can grow in close binaries.

- Although in the low-number statistics regime, we have found no differences between single-planet and multi-planet systems having bounded stellar companions physically associated. We warn that this conclusion may suffer from observational bias (observed single-planet system could be actually multiple and there is a non-zero probability that the detected companions are not physically associated).

TABLE 5.1: Properties of the 233 KOIs observed in our AstraLux survey as for February 24th, 2015.

KOI	KIC	RA	DEC	m_{Kep}	i_{KIC}	z_{KIC}	T_{eff}	$\log g$	$R_\star$	$M_\star$	nP/CP/PC/FP	Status
6	3248033	19:38:23.89	38:22:00.38	12.161	12.047	12.024	6178 ± 104	4.106 ± 0.175	1.58 ± 0.415	1.16 ± 0.162	1/0/0/1	D
12	5812701	19:49:48.9	41:00:39.56	11.353	11.245	11.26	6635 ± 142	4.193 ± 0.145	1.516 ± 0.885	1.312 ± 0.272	1/0/1/0	A
41	6521045	19:25:32.64	41:59:24.97	11.197	11.03	10.992	5825 ± 75	4.125 ± 0.009	1.49 ± 0.035	1.08 ± 0.063	3/3/0/0	A
49	9527334	19:28:59.77	46:09:53.36	13.704			5900 ± 106	4.509 ± 0.019	0.951 ± 0.159	1.065 ± 0.047	1/0/1/0	A
51	6056992	19:43:40.52	41:19:56.76	13.761			5780 ±	4.438 ±	1.0 ±	1.0 ±	1/0/1/0	A
69	3544595	19:25:40.39	38:40:20.49	9.931	9.739	9.705	5669 ± 75	4.466 ± 0.01	0.921 ± 0.02	0.909 ± 0.057	1/1/0/0	A
82	10187017	18:45:55.85	47:12:28.91	11.492	11.15	11.034	4812 ± 101	4.548 ± 0.042	0.755 ± 0.031	0.734 ± 0.048	5/5/0/0	A
94	6462863	19:49:19.94	41:53:28.04	12.205	12.057	12.039	6098 ± 101	4.247 ± 0.13	1.297 ± 0.27	1.081 ± 0.103	4/4/0/0	A
99	8505215	19:41:44.24	44:31:52.03	12.96	12.68	12.539	4965 ± 109	4.555 ± 0.048	0.736 ± 0.037	0.709 ± 0.053	2/0/1/1	A
111	6678383	19:10:25.11	42:10:00.4	12.596	12.442	12.397	5755 ± 119	4.081 ± 0.213	1.361 ± 0.225	0.814 ± 0.056	4/3/0/1	A
115	9579641	19:11:32.96	46:16:34.47	12.791	12.654	12.648	6391 ± 157	4.226 ± 0.166	1.332 ± 0.727	1.085 ± 0.283	3/2/1/0	A
131	7778437	19:56:23.41	43:29:51.32	13.797	13.64	13.621	6475 ± 169	4.349 ± 0.067	1.271 ± 0.927	1.314 ± 0.257	1/0/1/0	A
139	8559644	19:26:36.76	44:41:17.78	13.492	13.327	13.301	5906 ± 98	4.361 ± 0.074	1.145 ± 0.254	1.098 ± 0.074	2/2/0/0	A
149	3835670	19:06:31.22	38:56:44.16	13.397	13.167	13.075	5683 ± 113	4.026 ± 0.189	1.624 ± 0.359	1.022 ± 0.128	1/0/1/0	A
152	8394721	20:02:04.11	44:22:53.69	13.914	13.761	13.741	6388 ± 160	4.442 ± 0.05	1.037 ± 0.467	1.084 ± 0.209	4/4/0/0	A
156	10925104	19:36:29.14	48:20:58.28	13.738	13.334	13.155	3983 ± 80	4.721 ± 0.067	0.54 ± 0.06	0.56 ± 0.06	3/3/0/0	A
191	5972334	19:41:08.94	41:13:19.05	14.991	14.747	14.68	5700 ± 167	4.515 ± 0.046	0.87 ± 0.368	0.903 ± 0.107	4/0/4/0	A
196	9410930	19:38:03.18	45:58:53.9	14.465	14.238	14.182	5657 ± 110	4.441 ± 0.048	0.947 ± 0.063	0.903 ± 0.067	1/1/0/0	A
199	10019708	19:40:06.16	46:57:21.6	14.879	14.72	14.71	6418 ± 187	4.395 ± 0.058	1.171 ± 0.722	1.241 ± 0.255	2/0/1/1	A
209	10723750	19:15:10.33	48:02:24.83	14.274	14.131	14.095	6466 ± 150	4.373 ± 0.068	1.183 ± 0.716	1.205 ± 0.265	2/2/0/0	A
211	10656508	19:11:52.87	47:58:19.56	14.989	14.82	14.788	6343 ± 150	4.411 ± 0.054	1.137 ± 0.754	1.213 ± 0.261	1/0/1/0	A
212	6300348	19:44:33.55	41:36:11.45	14.858	14.663	14.559	6106 ± 176	4.497 ± 0.046	0.94 ± 0.375	1.013 ± 0.135	1/0/1/0	A
232	4833421	19:24:26.85	39:56:56.79	14.247	14.067	14.032	6103 ± 143	4.496 ± 0.044	0.949 ± 0.327	1.028 ± 0.117	5/5/0/0	A
238	7219825	19:47:59.67	42:46:55.06	14.061	13.891	13.819	6086 ± 104	4.367 ± 0.077	1.092 ± 0.184	1.012 ± 0.063	3/2/0/1	A
245	8478994	18:56:14.29	44:31:05.57	9.705			5417 ± 75	4.567 ± 0.04	0.772 ± 0.026	0.803 ± 0.068	4/4/0/0	A
298	12785320	19:21:58.62	52:03:19.87	12.713			5780 ±	4.438 ±	1.0 ±	1.0 ±	2/0/2/0	A
326	9880467	19:06:37.45	46:47:00.75	12.96			4751 ± 63	2.52 ± 0.115	11.536 ± 2.13	1.606 ± 0.295	2/0/2/0	A
330	11361646	19:47:26.21	49:09:43.37	13.928	13.73	13.64	6049 ± 153	4.257 ± 0.168	1.251 ± 0.618	1.031 ± 0.229	2/0/2/0	A
338	10552611	19:51:53.01	47:43:54.06	13.448	13.116	12.986	4173 ± 68	1.857 ± 0.104	18.939 ± 5.89	0.941 ± 0.357	2/2/0/0	A
339	10587105	19:03:33.21	47:52:49.36	13.763	13.616	13.586	6248 ± 154	4.533 ± 0.03	0.886 ± 0.34	0.977 ± 0.088	3/0/2/1	A
343	10982872	19:40:28.54	48:28:52.61	13.203	13.013	12.969	5726 ± 109	4.219 ± 0.132	1.243 ± 0.187	0.933 ± 0.078	3/3/0/0	A
345	11074541	19:06:05.95	48:41:00.96	13.34	13.005	12.846	4883 ± 99	4.549 ± 0.044	0.749 ± 0.035	0.725 ± 0.05	1/0/1/0	A
346	11100383	19:54:38.62	48:36:22.93	13.524	13.231	13.107	5088 ± 110	4.508 ± 0.066	0.806 ± 0.043	0.763 ± 0.061	1/0/1/0	A
349	11394027	19:07:24.64	49:15:42.05	13.586	13.382	13.322	5914 ± 157	4.354 ± 0.102	1.146 ± 0.581	1.081 ± 0.234	1/0/1/0	A
351	11442793	18:57:44.04	49:18:18.58	13.804	13.66	13.634	6238 ± 195	4.378 ± 0.099	1.054 ± 0.408	0.967 ± 0.144	7/6/1/0	A
366	3545478	19:26:39.4	38:37:09.32	11.714			6201 ± 124	3.616 ± 0.188	3.354 ± 0.457	1.694 ± 0.167	1/0/1/0	A
372	6471021	19:56:29.38	41:52:00.34	12.391	12.208	12.165	5838 ± 116	4.529 ± 0.017	0.897 ± 0.128	0.992 ± 0.048	1/0/1/0	A
375	12356617	19:24:48.29	51:08:39.4	13.293	13.111	13.028	5755 ± 112	4.101 ± 0.145	1.549 ± 0.381	1.105 ± 0.178	1/0/1/0	A
379	2446113	19:28:13.62	37:46:34.29	13.319	13.177	13.07	6546 ± 186	4.125 ± 0.21	1.594 ± 0.802	1.244 ± 0.27	2/0/1/1	A
385	3446746	19:28:51.62	38:32:54.93	13.435	13.211	13.128	5696 ± 155	4.417 ± 0.088	1.001 ± 0.38	0.954 ± 0.12	1/0/1/0	A
386	3656121	19:36:26.58	38:42:36.84	13.838	13.661	13.6	6197 ± 161	4.382 ± 0.091	1.06 ± 0.426	0.986 ± 0.158	2/2/0/0	A
387	3733628	19:08:52.49	38:51:45.08	13.577			4538 ± 92	4.607 ± 0.029	0.663 ± 0.029	0.65 ± 0.038	1/0/1/0	A
388	3831053	18:58:49.66	38:56:12.56	13.644			5687 ± 117	3.973 ± 0.198	1.775 ± 0.426	1.08 ± 0.187	1/0/1/0	A
393	3964109	19:36:06.99	39:03:06.66	13.542	13.395	13.369	6343 ± 129	4.411 ± 0.054	1.137 ± 0.529	1.213 ± 0.218	1/0/1/0	A
398	9946525	19:19:08.69	46:51:31.65	15.342	15.042	14.938	5271 ± 177	4.543 ± 0.033	0.838 ± 0.252	0.893 ± 0.071	3/2/1/0	A
401	3217264	19:03:24.88	38:23:02.84	14.001	13.729	13.632	5529 ± 199	4.526 ± 0.048	0.832 ± 0.354	0.848 ± 0.113	3/3/0/0	A
408	5351250	19:12:56.18	40:31:15.24	14.985	14.766	14.67	5862 ± 161	4.484 ± 0.053	0.931 ± 0.377	0.963 ± 0.123	4/4/0/0	A
416	6508221	19:07:27.71	41:59:20.68	14.29	14.019	13.908	5262 ± 168	4.598 ± 0.027	0.761 ± 0.177	0.846 ± 0.083	3/2/1/0	A
422	9214713	19:21:33.56	45:39:55.18	14.74	14.562	14.501	6230 ± 165	4.397 ± 0.081	1.047 ± 0.43	0.993 ± 0.162	1/0/1/0	A
431	10843590	18:49:50.52	48:15:25.62	14.262	14.004	13.955	5402 ± 184	4.452 ± 0.108	0.865 ± 0.421	0.774 ± 0.149	2/2/0/0	A
433	10937029	19:54:12.2	48:19:56.82	14.924	14.627	14.529	5551 ± 179	4.509 ± 0.043	0.899 ± 0.35	0.952 ± 0.084	2/0/2/0	A
435	11709124	19:19:07.32	49:53:47.51	14.534	14.342	14.282	5937 ± 162	4.559 ± 0.03	0.832 ± 0.35	0.916 ± 0.104	6/2/4/0	A
439	12470954	19:45:37.65	51:21:29.34	14.313	14.063	13.998	5438 ± 158	4.577 ± 0.02	0.825 ± 0.25	0.938 ± 0.063	2/0/1/1	A
463	8845205	20:00:49.46	45:01:05.3	14.708	13.999	13.497	3387 ± 59	4.961 ± 0.102	0.3 ± 0.05	0.3 ± 0.05	1/0/1/0	A
465	8891318	19:35:42.84	45:08:33.03	14.188	14.017	13.976	6240 ± 182	4.397 ± 0.076	1.064 ± 0.497	1.025 ± 0.202	1/0/0/1	A
473	10155434	19:47:14.08	47:10:18.98	14.673	14.433	14.335	5582 ± 153	4.551 ± 0.028	0.85 ± 0.315	0.937 ± 0.078	1/0/1/0	A
478	10990886	19:52:25.37	48:24:04.14	14.273	13.58	13.129	3744 ± 50	4.756 ± 0.072	0.5 ± 0.06	0.52 ± 0.06	1/0/1/0	A
481	11192998	19:32:38.44	48:52:52.29	14.701	14.446	14.359	5413 ± 173	4.59 ± 0.032	0.759 ± 0.235	0.819 ± 0.104	3/2/1/0	A
490	3239945	19:30:38.02	38:20:43.4	14.023	13.688	13.542	4978 ± 151	4.511 ± 0.069	0.808 ± 1.216	0.772 ± 0.131	4/2/2/0	A
496	4454752	19:15:01.19	39:33:49.13	14.411	14.135	14.028	5417 ± 164	4.325 ± 0.173	1.066 ± 0.419	0.877 ± 0.107	1/0/1/0	A
518	8017703	19:09:45.4	43:49:55.52	14.287	13.981	13.837	4590 ± 88	4.655 ± 0.034	0.595 ± 0.025	0.583 ± 0.03	3/3/0/0	A
520	8037145	19:38:40.31	43:51:11.74	14.55	14.255	14.105	5229 ± 178	4.47 ± 0.085	0.877 ± 0.318	0.826 ± 0.11	4/3/1/0	A
524	8934495	18:54:10.6	45:13:31.99	14.868	14.603	14.513	5361 ± 164	4.58 ± 0.026	0.799 ± 0.23	0.889 ± 0.071	1/0/1/0	A
528	9941859	19:08:24.27	46:53:47.33	14.598	14.364	14.278	5675 ± 160	4.338 ± 0.161	1.042 ± 0.372	0.861 ± 0.132	3/3/0/0	A
534	10554999	19:54:39.29	47:45:43.34	14.613	14.344	14.249	5294 ± 170	4.599 ± 0.027	0.761 ± 0.171	0.849 ± 0.079	2/2/0/0	A
548	12600735	19:18:00.16	51:41:08.63	14.02	13.874	13.845	6343 ± 153	4.375 ± 0.075	1.115 ± 0.563	1.069 ± 0.248	1/0/1/0	A
555	5709725	19:32:29.62	40:56:05.17	14.759	14.499	14.396	5252 ± 121	4.442 ± 0.089	0.898 ± 0.104	0.815 ± 0.073	2/0/2/0	A
561	6665695	18:48:01.11	42:10:35.5	14.005	13.732	13.63	5207 ± 159	4.595 ± 0.038	0.725 ± 0.138	0.756 ± 0.114	1/0/1/0	A
564	6786037	19:37:07.43	42:17:27.49	14.854	14.642	14.564	5960 ± 159	4.516 ± 0.038	0.906 ± 0.378	0.983 ± 0.117	3/0/3/0	A
567	7445445	19:27:48.46	43:04:28.96	14.338	14.126	14.01	5783 ± 162	4.508 ± 0.054	0.86 ± 0.369	0.869 ± 0.117	3/3/0/0	A

TABLE 5.1: continued.

KOI	KIC	RA	DEC	$m_{\rm Kep}$	$i_{\rm KIC}$	$z_{\rm KIC}$	$T_{\rm eff}$	$\log g$	$R_\star$	$M_\star$	nP/CP/PC/FP	Status
571	8120608	19:54:36.65	43:57:18.08	14.625	14.015	13.667	3761 ± 77	4.793 ± 0.078	0.46 ± 0.06	0.48 ± 0.06	5/5/0/0	A
579	8616637	19:14:20.17	44:44:01.68	14.137	13.858	13.745	5239 ± 171	4.585 ± 0.026	0.785 ± 0.194	0.868 ± 0.075	2/2/0/0	A
589	9763754	19:14:35.9	46:35:51.91	14.547	14.377	14.32	6116 ± 165	4.579 ± 0.03	0.782 ± 0.338	0.845 ± 0.081	1/0/0/1	A
592	9957627	19:37:51.04	46:49:17.22	14.292	14.102	14.014	6072 ± 157	4.411 ± 0.085	1.01 ± 0.371	0.96 ± 0.128	1/0/1/0	A
611	6309763	19:53:10.57	41:41:01.68	14.022	13.866	13.803	6343 ± 161	4.375 ± 0.077	1.115 ± 0.54	1.069 ± 0.239	1/0/1/0	A
617	9846086	19:49:40.48	46:38:39.34	14.608	14.386	14.309	5858 ± 161	4.495 ± 0.04	0.963 ± 0.416	1.056 ± 0.176	1/0/1/0	A
623	12068975	19:40:54.35	50:33:32.32	11.811	11.685	11.677	6004 ± 102	4.304 ± 0.016	1.12 ± 0.033	0.922 ± 0.059	4/4/0/0	A
624	3541946	19:22:41.55	38:41:27.64	13.597	13.39	13.346	5733 ± 152	4.551 ± 0.029	0.855 ± 0.329	0.947 ± 0.085	3/2/1/0	A
625	4449034	19:06:15.31	39:32:04.09	13.592	13.433	13.394	6481 ± 167	3.861 ± 0.31	2.343 ± 0.692	1.456 ± 0.243	1/0/1/0	A
626	4478168	19:40:46.41	39:32:22.81	13.49	13.339	13.289	6157 ± 92	4.449 ± 0.029	1.014 ± 0.16	1.05 ± 0.044	2/0/2/0	A
628	4644604	19:14:47.67	39:42:29.84	13.946	13.744	13.664	5741 ± 113	4.341 ± 0.143	1.008 ± 0.189	0.813 ± 0.072	1/0/1/0	A
632	4827723	19:17:40.28	39:56:42.04	13.359	13.124	13.052	5441 ± 106	4.504 ± 0.044	0.877 ± 0.135	0.894 ± 0.051	1/0/1/0	A
638	5113822	19:42:14.26	40:14:10.58	13.595	13.394	13.333	5989 ± 156	4.322 ± 0.136	1.131 ± 0.436	0.979 ± 0.165	2/2/0/0	A
640	5121511	19:49:00.63	40:17:18.96	13.332	13.058	12.96	5275 ± 121	4.429 ± 0.094	0.918 ± 0.132	0.825 ± 0.073	1/0/1/0	A
641	5131180	19:57:11.87	40:14:06.25	13.583	13.069	12.719	4137 ± 76	4.656 ± 0.042	0.594 ± 0.026	0.584 ± 0.032	1/0/1/0	A
644	5356593	19:19:52.02	40:31:57.58	13.725	13.474	13.369	5672 ± 177	3.788 ± 0.491	2.29 ± 1.011	1.173 ± 0.289	1/0/0/1	A
645	5374854	19:40:52.19	40:35:32.1	13.716	13.538	13.466	6282 ± 175	4.071 ± 0.285	1.549 ± 0.698	1.03 ± 0.232	2/0/2/0	A
650	5786676	19:21:35.08	41:02:24.29	13.594	13.293	13.188	5098 ± 167	4.518 ± 0.069	0.787 ± 1.226	0.746 ± 0.178	1/0/1/0	A
654	5941160	18:57:38.38	41:14:14.86	13.984	13.789	13.746	6053 ± 153	4.242 ± 0.177	1.277 ± 0.636	1.038 ± 0.233	2/2/0/0	A
658	6062088	19:48:21.6	41:23:16.91	13.989	13.789	13.697	5949 ± 152	4.5 ± 0.042	0.937 ± 0.382	1.013 ± 0.129	3/3/0/0	A
659	6125481	19:29:40.13	41:25:00.73	13.413	13.297	13.237	6722 ± 159	4.216 ± 0.132	1.466 ± 0.866	1.296 ± 0.277	1/0/1/0	A
664	6442340	19:26:32.32	41:50:01.89	13.484	13.287	13.214	5762 ± 113	4.38 ± 0.087	1.06 ± 0.192	0.981 ± 0.059	3/3/0/0	A
670	7033671	19:27:17.64	42:30:58.35	13.774	13.555	13.508	5672 ± 106	4.279 ± 0.124	1.204 ± 0.202	1.005 ± 0.073	1/0/1/0	A
671	7040629	19:35:33.65	42:31:40.68	13.749			6220 ± 177	4.242 ± 0.156	1.328 ± 0.843	1.123 ± 0.311	4/4/0/0	A
672	7115785	19:24:40.69	42:38:26.91	13.998	13.768	13.685	5514 ± 110	4.344 ± 0.126	1.043 ± 0.178	0.876 ± 0.07	3/2/0/1	A
676	7447200	19:30:00.81	43:04:59.34	13.822	13.371	13.142	3914 ± 82	4.73 ± 0.068	0.53 ± 0.06	0.55 ± 0.06	2/2/0/0	A
678	7509886	19:01:45.4	43:10:06.53	13.283	12.997	12.888	5244 ± 180	4.02 ± 0.481	1.56 ± 1.028	0.929 ± 0.144	2/2/0/0	A
682	7619236	19:40:47.52	43:16:10.23	13.916	13.692	13.614	5589 ± 102	4.229 ± 0.134	1.289 ± 0.231	1.026 ± 0.094	1/0/1/0	A
684	7730747	18:45:09.67	43:24:48.03	13.831	13.575	13.496	5548 ± 175	3.964 ± 0.383	1.793 ± 0.865	1.079 ± 0.277	1/0/1/0	A
685	7764367	19:41:54.18	43:29:35.31	13.949	13.77	13.766	6440 ± 165	4.136 ± 0.201	1.653 ± 0.917	1.365 ± 0.254	1/0/1/0	A
686	7906882	19:47:21.78	43:38:49.64	13.579	13.346	13.255	5559 ± 162	4.47 ± 0.077	0.885 ± 0.361	0.845 ± 0.119	1/0/1/0	A
693	8738735	18:59:01.16	44:57:21.72	13.949	13.802	13.775	6332 ± 156	4.472 ± 0.048	0.981 ± 0.413	1.041 ± 0.167	2/2/0/0	A
695	8805348	19:02:37.43	45:04:46.41	13.437	13.276	13.241	5741 ± 112	4.341 ± 0.143	1.008 ± 0.189	0.813 ± 0.071	1/0/1/0	A
703	9162741	19:39:38.88	45:34:00.07	13.361			6561 ± 182	4.14 ± 0.196	1.584 ± 0.839	1.272 ± 0.271	1/0/0/1	A
704	9266431	18:57:32.68	45:43:10.96	13.704	13.46	13.382	5470 ± 163	4.477 ± 0.073	0.884 ± 0.347	0.854 ± 0.11	1/0/1/0	A
709	9578686	19:09:19.87	46:12:12.64	13.94	13.716	13.662	5655 ± 155	4.532 ± 0.04	0.845 ± 0.364	0.888 ± 0.104	1/0/1/0	A
717	9873254	18:48:51.1	46:43:04.15	13.387	13.182	13.109	5665 ± 105	4.391 ± 0.065	1.095 ± 0.247	1.076 ± 0.062	2/0/2/0	A
721	9964801	19:48:16.42	46:50:03.4	13.645	13.439	13.396	6106 ± 162	4.099 ± 0.248	1.656 ± 0.773	1.256 ± 0.25	1/0/1/0	A
739	10386984	18:51:56.11	47:34:42.92	15.488	14.931	14.626	3733 ± 76	4.747 ± 0.071	0.51 ± 0.06	0.53 ± 0.06	1/0/1/0	A
800	3342970	19:26:36.85	38:29:40.77	15.541	15.341	15.262	6167 ± 174	4.444 ± 0.043	1.064 ± 0.536	1.149 ± 0.238	2/2/0/0	A
834	5436502	19:11:35.31	40:38:16.16	15.084	14.862	14.768	5858 ± 165	4.495 ± 0.038	0.963 ± 0.407	1.056 ± 0.172	5/5/0/0	A
841	5792202	19:28:56.82	41:05:09.17	15.855	15.571	15.491	5325 ± 107	4.558 ± 0.014	0.863 ± 0.046	0.981 ± 0.025	5/2/2/1	A
881	7373451	19:39:38.33	42:56:06.94	15.859	15.564	15.406	5330 ± 219	4.612 ± 0.034	0.718 ± 0.182	0.77 ± 0.116	2/0/2/0	A
884	7434875	19:14:34.2	43:02:21.45	15.067	14.755	14.63	5094 ± 168	4.589 ± 0.023	0.791 ± 0.106	0.884 ± 0.047	3/3/0/0	A
1032	2162635	19:27:54.61	37:31:57.18	13.862	13.497	13.296	5009 ± 81	3.755 ± 0.091	2.283 ± 0.625	1.083 ± 0.201	1/0/1/0	A
1096	3230491	19:20:43.93	38:19:18.99	14.709	14.481	14.391	5606 ± 158	4.597 ± 0.03	0.76 ± 0.27	0.832 ± 0.097	1/0/1/0	A
1174	10287723	19:47:17.19	47:21:14.51	13.447	12.997	12.712	4500 ± 153	4.572 ± 0.042	0.726 ± 0.039	0.717 ± 0.054	1/0/1/0	A
1187	3848972	19:24:17.1	38:59:56.54	14.489	14.253	14.179	5505 ± 162	4.586 ± 0.03	0.776 ± 0.24	0.848 ± 0.094	1/0/0/1	D
1192	3644071	19:24:07.72	38:42:14.08	14.215	13.969	13.879	5609 ± 159	4.346 ± 0.149	1.048 ± 0.375	0.889 ± 0.12	2/0/1/1	A
1230	6470149	19:55:47.56	41:48:43.74	12.263	11.914	11.729	5015 ± 97	2.99 ± 0.016	7.062 ± 0.258	1.782 ± 0.193	1/0/1/0	A
1236	6677841	19:09:33.89	42:11:41.4	13.659	13.518	13.523	6781 ± 157	4.422 ± 0.051	1.067 ± 0.426	1.097 ± 0.157	3/3/0/0	A
1268	8813698	19:19:33.51	45:00:20.41	14.814	14.645	14.589	6201 ± 179	4.472 ± 0.049	0.989 ± 0.431	1.058 ± 0.197	1/0/1/0	A
1353	7303287	19:49:51.68	42:52:58.22	13.956	13.764	13.691	6279 ± 171	4.095 ± 0.252	1.598 ± 0.831	1.158 ± 0.312	2/2/0/0	A
1356	7363829	19:28:28.78	42:55:54.04	15.206	14.978	14.909	5888 ± 188	4.398 ± 0.11	0.991 ± 0.364	0.9 ± 0.13	1/0/1/0	A
1375	6766634	19:13:16.9	42:15:41.09	13.709			5982 ± 193	4.468 ± 0.077	0.901 ± 0.363	0.869 ± 0.122	1/0/1/0	A
1376	6774826	19:24:03.26	42:16:59.28	13.997			7131 ± 220	3.913 ± 0.294	2.145 ± 0.677	1.373 ± 0.266	1/0/0/1	A
1421	11342550	19:10:36.11	49:09:21.79	15.305	15.087	15.006	5923 ± 161	4.445 ± 0.056	1.021 ± 0.453	1.059 ± 0.202	1/0/1/0	A
1426	11122894	18:52:50.2	48:46:39.51	14.232	14.063	13.985	6150 ± 151	4.423 ± 0.061	1.04 ± 0.478	1.04 ± 0.204	3/2/1/0	A
1452	7449844	19:33:07.57	43:03:20.91	13.63	13.525	13.478	7172 ± 211	4.107 ± 0.145	1.77 ± 1.007	1.46 ± 0.308	1/0/1/0	A
1477	7811397	19:10:36.95	43:30:20.58	15.917	15.655	15.554	5272 ± 215	4.598 ± 0.039	0.719 ± 0.164	0.749 ± 0.122	1/0/1/0	A
1527	7768451	19:46:41.11	43:29:54.2	14.879	14.621	14.497	5734 ± 186	4.527 ± 0.04	0.861 ± 0.374	0.911 ± 0.109	1/0/1/0	A
1529	9821454	19:08:09.48	46:38:24.46	14.307	14.152	14.116	6305 ± 155	4.458 ± 0.048	1.011 ± 0.433	1.066 ± 0.199	2/2/0/0	A
1546	5475431	19:54:03.29	40:38:22.64	14.456	14.236	14.208	5713 ± 165	4.541 ± 0.024	0.893 ± 0.282	1.01 ± 0.087	1/0/1/0	A
1573	5031857	19:47:23.08	40:08:19	14.373	14.185	14.1	6086 ± 157	4.511 ± 0.04	0.921 ± 0.363	1.003 ± 0.116	2/0/2/0	A
1574	10028792	19:51:40.05	46:57:54.47	14.6	14.372	14.292	5991 ± 189	4.205 ± 0.21	1.293 ± 0.572	0.977 ± 0.19	3/2/1/0	A
1596	10027323	19:50:02.37	46:57:40.54	15.157	14.758	14.572	3880 ± 143	4.765 ± 0.086	0.49 ± 0.07	0.51 ± 0.07	2/2/0/0	A
1684	6048024	19:34:08.28	41:19:47.64	12.849	12.717	12.709	6428 ± 134	4.377 ± 0.072	1.156 ± 0.603	1.16 ± 0.245	1/0/1/0	A
1701	7222086	19:50:04.58	42:46:37.42	11.041	11.047	11.077	7292 ± 226	4.112 ± 0.097	1.881 ± 1.325	1.67 ± 0.345	1/0/1/0	A
1725	10905746	18:54:30.92	48:23:27.61	13.496			3545 ± 84	4.948 ± 0.027	0.316 ± 0.14	0.323 ± 0.154	1/0/1/0	A
1779	9909735	19:53:55.88	46:47:37.04	13.297	13.077	13.029	5903 ± 165	4.15 ± 0.221	1.47 ± 0.717	1.113 ± 0.262	2/2/0/0	A
1781	11551692	19:10:25.34	49:31:23.73	12.231	11.884	11.744	4987 ± 93	4.586 ± 0.014	0.768 ± 0.048	0.829 ± 0.034	3/1/2/0	A
1800	11017901	19:01:04.46	48:33:36.03	12.394	12.179	12.119	5555 ± 171	4.44 ± 0.119	0.872 ± 0.419	0.764 ± 0.145	1/0/1/0	A

TABLE 5.1: continued.

KOI	KIC	RA	DEC	$m_{\rm Kep}$	$i_{\rm KIC}$	$z_{\rm KIC}$	$T_{\rm eff}$	log g	$R_\star$	$M_\star$	nP/CP/PC/FP	Status
1802	11298298	19:30:07.4	49:03:42.16	13.345	13.175	13.156	6126 ± 144	4.458 ± 0.045	1.021 ± 0.467	1.09 ± 0.223	1/0/1/0	A
1805	4644952	19:15:14.87	39:46:14.38	13.828	13.591	13.54	5903 ± 175	4.065 ± 0.249	1.784 ± 0.612	1.349 ± 0.174	3/3/0/0	A
1812	6279974	19:20:30.37	41:36:03.9	13.742	13.582	13.545	6258 ± 163	4.399 ± 0.081	1.039 ± 0.416	0.983 ± 0.149	1/0/1/0	A
1894	11673802	19:49:26.23	49:47:51.18	13.427	13.05	12.815	4992 ± 75	3.428 ± 0.022	3.79 ± 0.19	1.41 ± 0.214	1/0/1/0	A
1924	5108214	19:37:08.86	40:12:49.72	7.837	7.674	7.657	5844 ± 75	3.804 ± 0.011	2.49 ± 0.055	1.443 ± 0.08	1/0/0/1	D
1925	9955598	19:34:43.01	46:51:09.94	9.439	9.211	9.154	5460 ± 75	4.498 ± 0.009	0.893 ± 0.018	0.918 ± 0.057	1/1/0/0	A
2042	9111849	19:55:00.04	45:27:59.04	13.089	12.941	12.871	6628 ± 176	3.835 ± 0.354	2.403 ± 0.639	1.441 ± 0.233	1/0/1/0	A
2133	8219268	19:02:41.49	44:07:00.23	12.495	12.104	11.919	4605 ± 97	2.936 ± 0.013	6.528 ± 0.352	1.344 ± 0.169	1/1/0/0	A
2260	11811193	19:20:56.6	50:01:48.32	12.168	12.05	12.058	6444 ± 141	4.393 ± 0.065	1.112 ± 0.533	1.111 ± 0.228	1/0/1/0	A
2324	7746958	19:18:42.69	43:27:29.28	11.671			5780 ±	4.438 ±	1.0 ±	1.0 ±	1/0/1/0	A
2352	8013439	19:00:43.87	43:49:51.88	10.421			6550 ± 185	3.916 ± 0.319	2.058 ± 0.722	1.274 ± 0.284	3/2/1/0	A
2481	4476423	19:39:07.76	39:35:47.47	13.605	13.214	12.99	4553 ± 97	2.605 ± 0.016	10.472 ± 0.696	1.616 ± 0.256	1/0/1/0	A
2545	9696358	18:58:22.49	46:26:59.21	11.752	11.63	11.553	6131 ± 75	3.923 ± 0.04	2.134 ± 0.134	1.417 ± 0.093	1/0/1/0	A
2593	8212002	18:47:20.48	44:09:21.3	11.714			6141 ± 176	4.069 ± 0.263	1.712 ± 0.774	1.254 ± 0.263	1/0/1/0	A
2632	11337566	18:57:41.45	49:06:22.39	11.392	11.28	11.261	6461 ± 147	4.166 ± 0.188	1.529 ± 0.847	1.253 ± 0.278	1/0/1/0	A
2640	9088780	19:27:14.36	45:26:07.72	13.226	12.896	12.69	4854 ± 97	2.796 ± 0.009	7.478 ± 0.246	1.27 ± 0.11	1/0/1/0	A
2674	8022489	19:18:36.3	43:49:27.92	13.349	13.159	13.065	5988 ± 156	4.255 ± 0.175	1.236 ± 0.537	1.002 ± 0.196	3/0/3/0	A
2712	11098013	19:50:59.35	48:41:39.51	11.125	11.011	11.036	6450 ± 150	4.261 ± 0.132	1.32 ± 0.767	1.159 ± 0.285	1/0/1/0	A
3157	8738244	18:57:58.95	44:59:17.24	8.163	8.343	8.438	8247 ± 159	3.17 ± 0.382	7.762 ± 0.79	3.253 ± 0.224	1/0/0/1	D
3158	6278762	19:19:00.55	41:38:04.58	8.717			5032 ± 182	4.683 ± 0.037	0.593 ± 0.057	0.618 ± 0.047	5/5/0/0	A
3178	10991239	19:52:56.44	48:29:52.4	10.863			4136 ± 89	1.392 ± 0.03	44.448 ± 11.419	1.777 ± 1.122	1/0/0/1	D
3179	6153407	19:57:12.67	41:26:27.66	10.884			6237 ± 188	4.033 ± 0.304	1.683 ± 0.754	1.115 ± 0.3	1/0/1/0	A
3203	3122872	19:31:34.12	38:16:13.84	11.816	11.728	11.75	7095 ± 183	4.134 ± 0.183	1.523 ± 0.675	1.151 ± 0.254	1/0/1/0	A
3206	5612697	19:18:17.91	40:48:27.34	11.843			5780 ±	4.438 ±	1.0 ±	1.0 ±	1/0/0/1	A
3237	6587796	19:01:19.35	42:02:25.54	12.325	12.14	12.089	5838 ± 144	4.529 ± 0.03	0.897 ± 0.364	0.992 ± 0.109	1/0/1/0	A
3263	11853130	19:00:23.01	50:06:03.46	15.949	15.273	14.854	3587 ± 50	4.888 ± 0.08	0.38 ± 0.05	0.407 ± 0.06	1/0/1/0	A
3444	5384713	19:49:43.01	40:33:42.87	13.693	12.971	12.453	3842 ± 124	4.664 ± 0.072	0.598 ± 0.031	0.6 ± 0.034	4/0/4/0	A
3554	6426592	19:02:24.39	41:49:03.12	15.207	14.986	14.893	5780 ±	4.438 ±	1.0 ±	1.0 ±	1/0/1/0	A
3560	4848423	19:40:52.19	39:54:36.15	11.825	11.693	11.687	6466 ± 198	4.333 ± 0.211	0.989 ± 0.349	0.769 ± 0.084	1/0/1/0	A
3564	10960995	18:53:16.29	48:24:16.55	14.498	14.191	13.996	4868 ± 188	4.582 ± 0.051	0.708 ± 0.088	0.7 ± 0.1	1/0/0/1	D
3570	5023948	19:40:57.83	40:09:27.36	15.048	14.846	14.767	6413 ± 197	4.372 ± 0.186	0.941 ± 0.365	0.76 ± 0.079	1/0/0/1	D
3571	5113053	19:41:33.93	40:13:00.37	15.519	15.289	15.181	6516 ± 185	4.249 ± 0.154	1.279 ± 0.582	1.055 ± 0.222	1/0/0/1	D
3588	9656543	19:39:04.47	46:22:27.16	16.319	16.002	15.862	5503 ± 190	4.033 ± 0.354	1.616 ± 0.795	1.026 ± 0.27	1/0/0/1	D
3597	9366988	19:59:53.17	45:48:42.96	14.371	14.129	14.055	5914 ± 188	4.217 ± 0.204	1.271 ± 0.537	0.972 ± 0.181	1/0/0/1	D
3616	6058875	19:45:28.89	41:23:25.69	15.839	15.484	15.251	4745 ± 166	4.722 ± 0.045	0.536 ± 0.033	0.552 ± 0.033	1/0/0/1	D
3633	11858741	19:15:02.47	50:10:36.6	16.485			5780 ±	4.438 ±	1.0 ±	1.0 ±	1/0/0/1	D
3639	10491544	19:55:38.8	47:39:29.87	13.436	13.089	12.867	5073 ± 146	3.02 ± 0.308	4.61 ± 3.227	0.812 ± 0.366	1/0/0/1	D
3649	6066379	19:52:31.79	41:20:03.37	15.475	15.212	15.085	6282 ± 192	4.207 ± 0.19	1.343 ± 0.706	1.057 ± 0.269	1/0/1/0	A
3658	1575690	19:27:31.66	37:11:20.8	15.625	15.105	14.776	4298 ± 162	4.603 ± 0.051	0.675 ± 0.036	0.668 ± 0.048	1/0/0/1	D
3670	2167890	19:32:22.47	37:30:52.24	12.858	12.468	12.254	5039 ± 96	2.727 ± 0.477	11.828 ± 3.829	2.719 ± 0.419	1/0/0/1	D
3684	9394601	19:08:36.75	45:59:01.78	12.29	12.162	12.158	6337 ± 156	4.47 ± 0.05	0.971 ± 0.402	1.015 ± 0.143	1/0/0/1	D
3692	5903301	19:54:38	41:08:19.98	15.149	14.923	14.766	6200 ± 195	4.161 ± 0.229	1.382 ± 0.667	1.009 ± 0.222	1/0/1/0	A
3693	7695087	19:43:13.4	43:18:16.02	14.734	14.305	14.078	4969 ± 98	2.899 ± 0.448	9.433 ± 3.302	2.572 ± 0.42	1/0/0/1	D
3704	2569494	19:20:42.92	37:50:56.22	17.38	17.031	16.826	5311 ± 215	4.469 ± 0.09	0.866 ± 0.348	0.804 ± 0.134	1/0/0/1	D
3706	7770471	19:48:43.32	43:28:37.6	14.62	14.442	14.35	6502 ± 180	4.227 ± 0.151	1.407 ± 0.834	1.22 ± 0.289	1/0/0/1	D
3708	6314173	19:56:57.75	41:37:18.05	17.719	17.53	17.359	7311 ± 227	4.013 ± 0.213	1.959 ± 0.764	1.442 ± 0.258	1/0/0/1	D
3712	2437060	19:20:47.89	37:46:37.16	16.988	16.502	16.172	4599 ± 114	2.137 ± 0.454	23.673 ± 4.518	2.799 ± 0.515	1/0/0/1	D
3714	11564013	19:37:16.59	49:31:55.67	15.207	14.981	14.875	5821 ± 211	4.402 ± 0.161	0.898 ± 0.452	0.742 ± 0.125	1/0/0/1	D
3719	9837083	19:37:16.66	46:37:10.55	16.18			4330 ± 155	4.628 ± 0.057	0.639 ± 0.049	0.632 ± 0.061	1/0/0/1	D
3723	5471606	19:50:47.94	40:38:29.28	10.82			3982 ± 124	1.464 ± 0.235	32.244 ± 15.658	1.104 ± 0.436	1/0/0/1	D
3725	3459199	19:40:48.69	38:31:10.38	10.055	9.732	9.549	5102 ± 80	2.462 ± 0.515	15.458 ± 4.555	2.522 ± 0.531	1/0/0/1	D
3727	12023089	19:46:21.96	50:29:24.1	15.626	15.343	15.197	5319 ± 202	4.612 ± 0.062	0.654 ± 0.095	0.638 ± 0.076	1/0/0/1	D
3728	7515679	19:11:13.73	43:11:19.62	12.252	12.196	12.203	7358 ± 223	3.538 ± 0.315	4.037 ± 0.445	2.054 ± 0.169	1/0/1/0	A
3730	10879213	19:53:02.38	48:13:08.27	18.792			5780 ±	4.438 ±	1.0 ±	1.0 ±	1/0/0/1	D
3742	5565486	19:57:30.74	40:45:26.49	14.964	14.823	14.777	6609 ± 193	4.391 ± 0.059	1.135 ± 0.53	1.155 ± 0.244	1/0/1/0	A
3744	11303811	19:40:14.77	49:02:47.61	15.77	15.442	15.22	4970 ± 192	4.665 ± 0.051	0.591 ± 0.053	0.589 ± 0.052	1/0/0/1	D
3763	3114667	19:23:59.34	38:16:57.42	17.375			4324 ± 156	4.639 ± 0.065	0.616 ± 0.053	0.604 ± 0.065	1/0/0/1	D
3765	12109845	19:23:40.6	50:41:47	16.44	16.025	15.749	4561 ± 153	4.788 ± 0.06	0.469 ± 0.027	0.492 ± 0.035	1/0/1/0	A
3777	4075067	19:43:28.67	39:09:31.72	11.5	11.582	11.608	8992 ± 292	3.535 ± 0.34	4.832 ± 0.488	2.922 ± 0.204	1/0/0/1	D
3788	9405541	19:29:45.43	45:57:08.49	9.687	8.841	8.126	3314 ± 68	0.326 ± 0.174	123.724± 23.814	1.106 ± 0.365	1/0/0/1	D
3793	4037163	19:00:19.23	39:11:02.04	16.675			5780 ±	4.438 ±	1.0 ±	1.0 ±	1/0/0/1	D
3795	3338660	19:21:53.81	38:25:38.52	14.807	14.612	14.52	5992 ± 182	4.283 ± 0.168	1.171 ± 0.444	0.96 ± 0.161	1/0/0/1	D
3796	3338674	19:21:54.51	38:25:36.88	12.708	12.321	12.091	4897 ± 109	2.769 ± 0.408	9.407 ± 3.025	1.898 ± 0.644	1/0/0/1	D
3800	9593759	19:36:25.76	46:12:34.09	17.474	17.035	16.779	4770 ± 133	2.605 ± 0.31	9.67 ± 3.791	1.373 ± 0.424	1/0/0/1	D
3801	8827930	19:40:49.67	45:05:53.48	15.999	15.752	15.665	5825 ± 165	4.504 ± 0.033	0.965 ± 0.388	1.083 ± 0.165	1/0/1/0	A
3803	6286155	19:28:40.58	41:37:11.13	13.763	13.442	13.28	5277 ± 164	3.426 ± 0.323	4.168 ± 1.605	1.69 ± 0.32	1/0/0/1	D
3805	4663185	19:36:19.05	39:43:46.71	11.356	10.958	10.73	4831 ± 96	2.488 ± 0.388	15.637 ± 3.974	2.744 ± 0.493	1/0/0/1	D
3810	5769943	18:55:00.1	41:05:09.64	16.758	16.109	15.692	3644 ± 50	4.872 ± 0.06	0.39 ± 0.05	0.412 ± 0.05	1/0/0/1	D
3814	2997178	19:32:17.95	38:10:10.99	12.861	12.495	12.284	5122 ± 107	2.886 ± 0.469	9.828 ± 3.608	2.707 ± 0.384	1/0/0/1	D
3817	5636642	19:45:19.4	40:53:46.53	16.428	16.137	16.025	5758 ± 188	4.307 ± 0.179	1.084 ± 0.378	0.869 ± 0.141	1/0/0/1	D
3821	5956776	19:22:35.59	41:14:02.65	16.747	16.548	16.655	7172 ± 221	4.107 ± 0.15	1.77 ± 0.973	1.46 ± 0.295	1/0/0/1	D
3824	6516874	19:20:23.27	41:58:14.45	15.896	15.688	15.577	6046 ± 167	4.486 ± 0.045	0.972 ± 0.386	1.053 ± 0.171	1/0/0/1	D

TABLE 5.2: Description of the AstraLux observing runs.

Run ID	Dates	Type/Code	PI	Comments/Weather conditions
1	2011/06/06-12	Open/F11-2.2-025	J. Lillo-Box	60%
2	2011/07/01-10	GTO	D. Barrado	88%
3	2011/07/25-26	Open/H11-2.2-012	J. Lillo-Box	100%
4	2012/05/25-27	GTO	D. Barrado	100%
5	2013/06/10-23	Open/H13-2.2-010	J. Lillo-Box	100%
6	2013/07/12-17	GTO	D. Barrado	100%

Notes. We also obtained AstraLux time from additional DGT and DDT programs.

TABLE 5.1: continued.

KOI	KIC	RA	DEC	$m_{\rm Kep}$	$i_{\rm KIC}$	$z_{\rm KIC}$	$T_{\rm eff}$	$\log g$	$R_\star$	$M_\star$	nP/CP/PC/FP	Status
3827	5114623	19:42:55.88	40:15:38.81	15.36	15.13	15.074	6029 ± 171	4.452 ± 0.056	0.998 ± 0.427	1.025 ± 0.181	2/0/0/2	D
3842	9532637	19:37:26.32	46:07:31.4	17.453	16.978	16.694	4509 ± 168	4.612 ± 0.049	0.663 ± 0.057	0.656 ± 0.07	1/0/0/1	D
3845	11824218	19:46:27.82	50:01:18.15	13.724	13.365	13.16	4993 ± 123	2.399 ± 0.037	19.695 ± 0.594	3.546 ± 0.035	1/0/0/1	D
3849	8949316	19:22:04.55	45:14:07.34	16.182	15.491	14.944	3564 ± 63	4.808 ± 0.06	0.44 ± 0.05	0.454 ± 0.05	1/0/0/1	D
3853	2697935	19:09:52.29	37:57:59.9	10.63	10.323	10.196	5081 ± 118	3.265 ± 0.292	4.811 ± 2.32	1.554 ± 0.377	1/0/0/1	A
3873	8430105	19:26:14.07	44:29:17.48	10.42	10.127	9.97	5143 ± 101	2.777 ± 0.404	9.294 ± 3.478	1.884 ± 0.535	1/0/0/1	D
3886	8848288	20:04:11.35	45:05:15.47	9.837	9.465	9.288	4781 ± 76	2.562 ± 0.032	12.536 ± 2.203	2.088 ± 0.765	1/0/1/0	A
3890	8564976	19:35:05.31	44:38:18.49	13.226	12.865	12.677	4991 ± 91	2.933 ± 0.03	7.506 ± 0.793	1.761 ± 0.335	1/0/1/0	A
3919	4649440	19:20:33.05	39:45:54.73	12.956	12.647	12.49	5301 ± 159	3.311 ± 0.355	5.037 ± 1.792	1.893 ± 0.26	1/0/0/1	D
3925	10788461	19:12:39	48:09:54.54	14.026	13.782	13.702	5678 ± 184	4.215 ± 0.204	1.303 ± 0.573	1.015 ± 0.216	3/0/3/0	A
3940	5195945	19:37:15.09	40:19:11	12.93	12.572	12.373	5045 ± 96	2.814 ± 0.037	9.131 ± 0.869	1.983 ± 0.341	1/0/0/1	D
3993	2970804	19:04:25.67	38:06:27.46	9.16			5780 ±	4.438 ±	1.0 ±	1.0 ±	1/0/0/1	D
3998	7707742	19:55:35.89	43:23:44.31	16.975	16.807	16.705	7131 ± 225	4.084 ± 0.151	1.83 ± 1.02	1.483 ± 0.311	1/0/0/1	D
4013	4832225	19:22:59.19	39:54:39.71	9.072	9.323	9.477	9436 ± 291	4.122 ± 0.145	2.161 ± 0.903	2.256 ± 0.548	1/0/0/1	D
4016	5938970	18:53:22.68	41:12:06.26	14.073	13.6	13.385	4366 ± 129	4.624 ± 0.054	0.639 ± 0.048	0.628 ± 0.062	1/0/1/0	A
4033	4138557	19:02:22.1	39:12:22.56	11.968	11.795	11.751	5906 ± 155	4.475 ± 0.077	0.881 ± 0.362	0.845 ± 0.118	1/0/0/1	D
4351	5436161	19:11:02.2	40:39:25.34	14.999	14.714	14.562	5136 ± 165	4.648 ± 0.052	0.612 ± 0.062	0.608 ± 0.055	1/0/1/0	A
4355	4571004	19:36:49.89	39:40:48.41	13.482			5780 ±	4.438 ±	1.0 ±	1.0 ±	5/0/0/5	D
4512	12069414	19:41:48.14	50:32:31.6	15.314	15.006	14.885	5286 ± 226	4.517 ± 0.081	0.776 ± 0.425	0.722 ± 0.163	1/0/1/0	A

Notes. In the last column we show the status of the KOI, being active (A) or demoted (D).

TABLE 5.3: Observational information, completeness, and detectability magnitudes for the isolated KOIs observed with the Calar Alto/AstraLux instrument during the 2011 observational season (62 KOIs in total) and all targets observed during 2012 and 2013 seassons (20 and 57 respectively KOIs). Active KOIs (currently keeping at least one of their planet candidates) are shown in the upper part of the table and demoted KOIs are shown in the bottom part of the table

Active KOIs											
KOI ID	Others	kep (mag)	Date (yyyy-mm-dd)	Filter	T_{ind} (s)	#Frames	Eff.Time s	i_{comp} (mag)	i_{det} (mag)	FWHM[a] (arcsec)	Strehl (%)
12	L	11.353	2011-06-03	i	0.05	10000	50.0	16.9	20.2	0.630	19.5
41	H,A,L	11.197	2013-06-22	i	0.083	40000	332.0	19.0	22.3	0.265	15.8
49	H,L	13.704	2013-06-22	i	0.083	40000	332.0	19.0	22.3	0.195	35.9
51	-	13.761	2013-06-22	i	0.06	20000	120.0	17.8	21.1	0.269	30.8
69	H,A,L	9.931	2013-06-22	i	0.045	40000	180.0	18.3	22.6	0.333	12.5
82	H,A,L	11.492	2013-06-23	i	0.068	40000	272.0	18.7	22.0	0.318	21.6
94	H,A,L	12.205	2013-06-21	i	0.06	30000	180.0	18.3	21.6	0.445	21.6
111	H,A,L	12.596	2013-06-23	i	0.068	40000	272.0	18.7	22.0	0.324	28.0
115	A,L	12.791	2013-06-23	i	0.068	40000	272.0	18.7	22.0	0.336	28.1

TABLE 5.3: continued.

KOI ID	Others	kep (mag)	Date (yyyy-mm-dd)	Filter	T_{ind} (s)	#Frames	Eff.Time s	i_{comp} (mag)	i_{det} (mag)	FWHM[a] (arcsec)	Strehl (%)
139	L	13.492	2011-06-10	i	0.075	20000	150.0	18.1	21.4	0.391	31.9
149	L	13.397	2013-06-23	i	0.068	40000	272.0	18.7	22.0	0.357	30.7
152	L	13.914	2013-06-14	i	0.08	30000	240.0	18.6	21.9	0.225	38.8
156	L	13.738	2013-06-16	i	0.068	40000	272.0	18.7	22.0	0.336	31.1
191	L	14.991	2013-06-15	i	0.08	25000	200.0	18.4	21.7	0.311	48.1
191	L		2013-06-15	z	0.08	25000	200.0	-	-	0.311	69.9
196	H	14.465	2011-05-10	i	0.2	10000	200.0	18.4	21.7	0.392	28.5
199	-	14.879	2011-05-12	i	0.2	10000	200.0	18.4	21.7	0.246	34.6
209	L	14.274	2011-06-06	i	0.1	20000	200.0	18.4	21.7	0.282	35.9
211	L	14.989	2011-06-08	i	0.1	30000	300.0	18.8	22.1	0.393	48.9
238	L	14.061	2011-06-05	i	0.1	20000	200.0	18.4	21.7	0.206	37.1
245	H,A	9.705	2012-05-27	i	0.03	30000	90.0	17.5	20.8	0.276	26.7
330	L	13.928	2011-06-26	i	0.1	20000	200.0	18.4	21.7	0.217	36.5
338	-	13.448	2011-06-01	i	0.087	10000	87.0	17.5	20.8	0.326	28.7
338	-		2011-06-01	z	0.09	10000	90.0	-	-	0.320	34.7
339	L	13.763	2011-06-26	i	0.1	20000	200.0	18.4	21.7	0.220	33.3
345	L	13.34	2011-06-03	i	0.09	10000	90.0	17.5	20.8	0.652	33.3
346	-	13.524	2011-06-04	z	0.15	12000	180.0	-	-	0.479	31.2
349	L	13.586	2011-06-04	i	0.15	12000	180.0	18.3	21.6	0.319	24.0
351	-	13.804	2011-06-03	i	0.2	12000	240.0	18.6	21.9	0.523	21.5
366	H,L	11.714	2011-06-01	i	0.034	10000	34.0	16.5	19.8	0.238	32.4
372	H,A,L	12.391	2011-06-01	i	0.034	10000	34.0	16.5	19.8	0.327	29.9
372	H,A,L		2011-06-01	z	0.04	10000	40.0	-	-	0.263	41.5
385	L	13.435	2011-06-03	i	0.2	10000	200.0	18.4	21.7	0.711	25.5
386	L	13.838	2011-05-10	i	0.2	10000	200.0	18.4	21.7	0.435	23.3
388	L	13.644	2011-06-04	i	0.15	12000	180.0	18.3	21.6	0.429	23.3
393	L	13.542	2011-06-05	i	0.15	10000	150.0	18.1	21.4	0.350	16.2
398	H	15.342	2013-06-22	i	0.09	29999	270.0	18.7	22.0	0.250	45.3
416	L	14.29	2011-06-06	i	0.1	20000	200.0	18.4	21.7	0.291	55.0
422	-	14.74	2011-06-25	i	0.2	10000	200.0	18.4	21.7	0.413	12.9
422	-		2011-06-25	z	0.1	20000	200.0	-	-	0.273	41.4
431	L	14.262	2011-06-07	i	0.1	20000	200.0	18.4	21.7	0.369	32.3
435	L	14.534	2013-06-14	i	0.08	30000	240.0	18.6	21.9	0.247	40.5
463	L	14.708	2011-06-25	i	0.1	20000	200.0	18.4	21.7	0.352	34.4
473	-	14.673	2011-06-08	i	0.1	20000	200.0	18.4	21.7	0.470	45.6
478	L	14.273	2011-06-01	i	0.15	10000	150.0	18.1	21.4	0.333	25.7
481	L	14.701	2011-06-09	i	0.1	20000	200.0	18.4	21.7	0.434	46.1
496	-	14.411	2011-06-01	i	0.2	10000	200.0	18.4	21.7	0.323	27.7
518	-	14.287	2013-06-22	i	0.083	40000	332.0	19.0	22.3	0.271	34.6
524	-	14.868	2011-06-09	i	0.1	23000	230.0	18.6	21.9	0.436	49.2
528	L	14.598	2011-06-08	i	0.1	20000	200.0	18.4	21.7	0.498	45.7
534	L	14.613	2011-05-10	i	0.2	10000	200.0	18.4	21.7	0.340	30.5
561	L	14.005	2011-05-10	i	0.2	8000	160.0	18.2	21.5	0.429	24.0
564	L	14.854	2013-06-15	i	0.08	33750	270.0	18.7	22.0	0.311	44.3
567	L	14.338	2011-06-01	i	0.2	10000	200.0	18.4	21.7	0.376	25.5
571	L	14.625	2011-06-08	i	0.1	20000	200.0	18.4	21.7	0.426	37.4
579	L	14.137	2011-06-05	i	0.1	20000	200.0	18.4	21.7	0.233	34.8
611	L	14.022	2011-06-02	i	0.2	10000	200.0	18.4	21.7	0.337	24.5
617	-	14.608	2011-06-06	i	0.1	20000	200.0	18.4	21.7	0.338	37.2
624	L	13.597	2013-06-15	i	0.083	40000	332.0	19.0	22.3	0.377	28.7
625	L	13.592	2011-06-10	i	0.075	20000	150.0	18.1	21.4	0.306	31.6

TABLE 5.3: continued.

KOI ID	Others	kep (mag)	Date (yyyy-mm-dd)	Filter	T_{ind} (s)	#Frames	Eff.Time s	i_{comp} (mag)	i_{det} (mag)	FWHM[a] (arcsec)	Strehl (%)
632	L	13.359	2011-05-12	i	0.15	10000	150.0	18.1	21.4	0.250	29.4
638	A,L	13.595	2011-06-05	i	0.1	14000	140.0	18.0	21.4	0.373	27.9
640	L	13.332	2013-06-21	i	0.083	40000	332.0	19.0	22.3	0.577	28.5
650	L	13.594	2013-06-21	i	0.083	7766	64.5	17.2	20.5	0.534	28.4
654	L	13.984	2011-06-10	i	0.075	20000	150.0	18.1	21.4	0.345	34.8
659	L	13.413	2011-05-12	i	0.15	14000	210.0	18.5	21.8	0.235	29.1
664	L	13.484	2011-06-26	i	0.075	20000	150.0	18.1	21.4	0.184	39.2
670	-	13.774	2011-06-26	i	0.1	20000	200.0	18.4	21.7	0.215	36.2
672	-	13.998	2013-06-21	i	0.083	10498	87.1	17.5	20.9	0.659	45.5
676	L	13.822	2011-06-05	i	0.1	14000	140.0	18.0	21.2	0.319	29.6
678	-	13.283	2011-06-25	i	0.1	14000	140.0	18.0	21.3	0.304	28.3
682	L	13.916	2013-06-10	i	0.05	45000	225.0	18.5	21.8	0.314	38.3
684	L	13.831	2011-06-10	i	0.075	20000	150.0	18.1	21.4	0.295	33.1
686	L	13.579	2011-06-10	i	0.075	20000	150.0	18.1	21.4	0.303	29.9
693	-	13.949	2011-06-25	i	0.1	20000	200.0	18.4	21.7	0.290	32.3
695	L	13.437	2011-06-03	i	0.15	12000	180.0	18.3	21.6	0.559	13.8
709	L	13.94	2011-06-25	i	0.1	20000	200.0	18.4	21.7	0.231	35.2
717	L	13.387	2011-06-26	i	0.1	14000	140.0	18.0	21.3	0.194	36.5
739	L	15.488	2011-05-10	i	0.2	10000	200.0	18.4	21.7	0.390	37.9
800	L	15.541	2011-05-08	i	0.2	10000	200.0	18.4	21.7	0.397	37.2
800	L		2011-05-11	z	0.2	7580	151.6	-	-	0.376	58.0
834	L	15.084	2013-06-15	i	0.08	38000	304.0	18.9	22.2	0.251	45.6
884	L	15.067	2011-06-09	i	0.1	24000	240.0	18.6	21.9	0.420	53.1
1096	-	14.709	2013-06-10	i	0.09	30000	270.0	18.7	22.0	0.361	40.6
1174	-	13.447	2013-06-20	i	0.068	40000	272.0	18.7	22.0	0.277	30.5
1230	L	12.263	2013-06-12	i	0.04	40000	160.0	18.2	21.5	0.282	28.9
1236	L	13.659	2011-06-10	i	0.075	20000	150.0	18.1	21.4	0.477	31.1
1268	-	14.814	2011-06-07	i	0.15	20000	300.0	18.8	22.1	0.407	35.1
1353	L	13.956	2012-05-26	i	0.075	30000	225.0	18.5	21.6	0.287	34.5
1356	-	15.206	2013-06-11	i	0.1	30000	300.0	18.8	22.1	0.392	48.0
1421	-	15.305	2013-06-11	i	0.1	30000	300.0	18.8	22.1	0.342	48.7
1426	L	14.232	2011-06-25	i	0.1	20000	200.0	18.4	21.7	0.304	34.6
1452	L	13.63	2012-05-26	i	0.075	30000	225.0	18.5	21.8	0.309	31.0
1477	-	15.917	2013-06-11	i	0.1	30000	300.0	18.8	22.1	0.283	55.6
1529	L	14.307	2011-06-08	i	0.1	20000	200.0	18.4	21.7	0.437	52.3
1546	-	14.456	2013-07-16	i	0.08	22500	180.0	18.3	21.6	0.558	54.0
1596	L	15.157	2011-06-09	i	0.1	24000	240.0	18.6	21.9	0.409	49.0
1684	L	12.849	2012-05-25	i	0.075	30000	225.0	18.5	21.8	0.378	24.5
1701	L	11.041	2012-05-27	i	0.05	30000	150.0	18.1	21.4	0.277	27.0
1725	L	13.496	2013-06-13	i	0.04	40000	160.0	18.2	21.5	0.196	39.0
1779	L	13.297	2012-05-25	i	0.09	25000	225.0	18.5	21.8	0.303	27.3
1781	L	12.231	2012-05-25	i	0.05	30000	150.0	18.1	21.4	0.426	21.6
1800	-	12.394	2012-05-25	i	0.05	30000	150.0	18.1	21.4	0.395	24.6
1802	L	13.345	2013-06-16	i	0.083	40000	332.0	19.0	22.3	0.394	27.8
1805	L	13.828	2013-06-20	i	0.083	40000	332.0	19.0	22.3	0.443	32.6
1812	L	13.742	2013-06-19	i	0.068	40000	272.0	18.7	22.0	0.547	38.5
1894	L	13.427	2012-05-25	i	0.07	35000	245.0	18.6	21.9	0.261	32.1
1925	L	9.439	2012-05-27	i	0.03	30000	90.0	17.5	20.8	0.265	23.5
2042	L	13.089	2012-05-25	i	0.075	30000	225.0	18.5	21.8	0.363	25.5
2133	L	12.495	2012-05-25	i	0.05	30000	150.0	18.1	21.4	0.275	29.9
2260	L	12.168	2012-05-27	i	0.05	30000	150.0	18.1	21.4	0.256	29.9

TABLE 5.3: continued.

KOI ID	Others	kep (mag)	Date (yyyy-mm-dd)	Filter	T_{ind} (s)	#Frames	Eff.Time s	i_{comp} (mag)	i_{det} (mag)	FWHM[a] (arcsec)	Strehl (%)
2324	-	11.671	2012-05-27	i	0.05	30000	150.0	18.1	21.4	0.857	4.6
2352	L	10.421	2012-05-26	i	0.03	30000	90.0	17.5	20.8	0.225	28.2
2481	L	13.605	2012-05-26	i	0.05	30000	150.0	18.1	21.4	0.238	34.7
2481	L		2012-05-26	z	0.075	30000	225.0	-	-	0.266	39.1
2545	L	11.752	2012-05-26	i	0.03	30000	90.0	17.5	20.8	0.222	32.8
2593	L	11.714	2012-05-26	i	0.04	30000	120.0	17.8	21.1	0.287	27.5
2632	L	11.392	2012-05-26	i	0.05	30000	150.0	18.1	21.4	0.358	34.2
2640	L	13.226	2012-05-25	i	0.075	30000	225.0	18.5	21.8	0.336	16.2
2674	-	13.349	2013-06-14	i	0.08	30000	240.0	18.6	21.9	0.234	33.6
2712	-	11.125	2013-06-19	i	0.068	40000	272.0	18.7	22.0	0.314	21.1
3158	-	8.717	2013-06-15	i	0.03	40000	120.0	17.8	21.1	0.292	23.4
3158	-		2013-06-15	z	0.03	20000	60.0	-	-	0.246	35.4
3179	-	10.884	2013-06-19	i	0.083	40000	332.0	19.0	22.3	0.358	22.7
3203	-	11.816	2013-06-19	i	0.083	40000	332.0	19.0	22.3	0.419	20.7
3206	-	11.843	2013-06-19	i	0.083	40000	332.0	19.0	22.3	0.283	27.0
3237	-	12.325	2013-06-16	i	0.068	40000	272.0	18.7	22.0	0.351	22.7
3263	-	15.949	2013-06-11	i	0.07	43000	301.0	18.8	22.1	0.256	55.8
3444	-	13.693	2013-06-15	i	0.06	40000	240.0	18.6	21.9	0.910	64.3
3444	-		2013-06-15	z	0.06	30000	180.0	-	-	0.189	46.2
3554	-	15.207	2013-06-28	i	0.09	13333	120.0	17.8	21.1	0.329	54.7
3560	-	11.825	2013-07-14	i	0.04	30000	120.0	17.8	21.1	0.325	28.8
3649	-	15.475	2013-07-17	i	0.09	20000	180.0	18.3	21.6	0.631	8.4
3692	-	15.149	2013-07-17	z	0.09	29999	270.0	-	-	0.320	26.2
3728	-	12.252	2013-06-11	i	0.05	40000	200.0	18.4	21.7	0.387	25.9
3742	-	14.964	2013-06-29	i	0.09	13333	120.0	17.8	21.1	0.354	22.3
3765	-	16.44	2013-07-14	i	0.1	18000	180.0	18.3	22.4	0.343	68.3
3765	-		2013-07-17	z	0.1	18000	180.0	-	-	0.251	79.1
3801	-	15.999	2013-06-11	i	0.07	43000	301.0	18.8	22.1	0.262	65.2
3853	-	10.63	2013-06-28	i	0.045	40000	180.0	18.3	21.6	0.230	30.2
3886	-	9.837	2013-06-10	i	0.0295	25000	73.9	17.3	20.6	0.373	24.9
3886	-		2013-06-10	z	0.03	20000	60.0	-	-	0.309	30.8
3890	-	13.226	2013-06-13	i	0.05	35000	175.0	18.3	21.6	0.287	21.9
3925	-	14.026	2013-06-14	i	0.08	40000	320.0	18.9	22.2	0.253	36.7
4016	-	14.073	2013-06-16	i	0.083	36765	305.1	18.9	22.2	0.351	31.0
4351	-	14.999	2013-07-15	i	0.09	29999	270.0	18.7	22.0	0.274	39.3
4512	-	15.314	2013-07-16	i	0.09	36666	330.0	18.9	22.2	0.454	64.3
Demoted KOIs											
6	-	12.161	2013-06-23	i	0.068	40000	272.0	18.7	22.0	0.312	32.0
1187	-	14.489	2013-06-20	i	0.083	40000	332.0	19.0	22.3	0.266	36.0
1924	L	7.837	2012-05-27	i	0.03	30000	90.0	17.5	20.8	0.308	20.0
3157	-	8.163	2013-07-16	i	0.045	40000	180.0	18.3	21.6	0.560	7.1
3178	-	10.863	2013-07-16	i	0.04	30000	120.0	17.8	21.1	0.212	30.5
3564	-	14.498	2013-07-14	i	0.08	15000	120.0	17.8	21.1	0.278	21.1
3570	-	15.048	2013-07-14	i	0.09	13333	120.0	17.8	21.1	0.372	28.3
3571	-	15.519	2013-07-14	i	0.09	13333	120.0	17.8	21.1	0.360	24.5
3588	-	16.319	2013-07-15	i	0.1	12000	120.0	17.8	21.1	0.448	61.2
3597	-	14.371	2013-07-15	i	0.08	15000	120.0	17.8	21.1	0.347	38.8
3616	-	15.839	2013-07-15	i	0.09	20000	180.0	18.3	21.6	0.405	42.4
3616	-	15.839	2013-07-17	z	0.09	20000	180.0	-	-	0.578	13.9
3633	-	16.485	2013-07-17	z	0.1	12000	120.0	-	-	0.412	16.7
3639	-	13.436	2013-06-10	z	0.05	30000	150.0	-	-	0.245	44.6

TABLE 5.3: continued.

KOI ID	Others	kep (mag)	Date (yyyy-mm-dd)	Filter	T_{ind} (s)	#Frames	Eff.Time s	i_{comp} (mag)	i_{det} (mag)	FWHM[a] (arcsec)	Strehl (%)
3639	-	13.436	2013-06-28	i	0.06	20000	120.0	17.8	21.1	0.363	31.3
3658	-	15.625	2013-07-15	i	0.09	20000	180.0	18.3	21.6	0.518	60.0
3670	-	12.858	2013-06-12	z	0.04	20000	80.0	-	-	0.231	46.6
3684	-	12.29	2013-07-15	i	0.06	20000	120.0	17.8	21.1	0.415	24.8
3684	-	12.29	2013-07-17	z	0.1	20000	200.0	-	-	0.202	37.4
3693	-	14.734	2013-06-12	i	0.07	35000	245.0	18.6	21.9	0.349	16.4
3704	-	17.38	2013-07-17	i	0.1	18000	180.0	18.3	21.6	0.409	55.9
3706	-	14.62	2013-07-15	i	0.08	15000	120.0	17.8	21.1	0.373	42.3
3708	-	17.719	2013-07-14	i	0.1	18000	180.0	18.3	21.6	0.367	42.4
3712	-	16.988	2013-06-12	i	0.1	20000	200.0	18.4	21.7	0.380	77.8
3714	-	15.207	2013-07-14	i	0.09	29999	270.0	18.7	22.0	0.386	25.6
3719	-	16.18	2013-07-15	i	0.1	18000	180.0	18.3	21.6	0.501	82.3
3719	-	16.18	2013-07-17	i	0.1	18000	180.0	18.3	21.6	0.501	82.3
3723	-	10.82	2013-07-14	i	0.04	30000	120.0	17.8	21.1	0.320	26.1
3725	-	10.055	2013-06-10	i	0.03	25000	75.0	17.3	20.6	0.269	29.5
3727	-	15.626	2013-07-13	i	0.09	36666	330.0	18.9	22.2	0.440	22.2
3730	-	18.792	2013-07-13	i	0.1	18000	180.0	18.3	21.6	0.413	42.0
3744	-	15.77	2013-07-13	i	0.09	36666	330.0	18.9	22.2	0.371	15.2
3763	-	17.375	2013-07-12	i	0.1	18000	180.0	18.3	21.6	0.491	44.7
3777	-	11.5	2013-06-13	i	0.04	40000	160.0	18.2	21.5	0.229	29.1
3788	-	9.687	2013-06-10	i	0.03	45000	135.0	18.0	21.3	0.331	21.4
3793	-	16.675	2013-06-29	i	0.1	27000	270.0	18.7	22.0	0.700	8.7
3795	-	14.807	2013-06-28	i	0.08	15000	120.0	17.8	21.1	0.414	24.0
3796	-	12.708	2013-06-11	i	0.05	40000	200.0	18.4	21.7	0.372	26.4
3800	-	17.474	2013-06-13	i	0.1	18090	180.9	18.3	21.6	0.412	66.2
3803	-	13.763	2013-06-12	i	0.07	40000	280.0	18.8	22.1	0.236	37.9
3805	-	11.356	2013-06-13	i	0.03	30000	90.0	17.5	20.8	0.229	29.1
3810	-	16.758	2013-06-29	i	0.1	27000	270.0	18.7	22.0	0.330	72.2
3814	-	12.861	2013-06-12	i	0.04	40000	160.0	18.2	21.5	0.247	36.3
3817	-	16.428	2013-06-29	i	0.1	33000	330.0	18.9	22.2	0.276	45.4
3821	-	16.747	2013-06-28	i	0.1	33000	330.0	18.9	22.2	0.396	23.0
3824	-	15.896	2013-06-28	i	0.09	36666	330.0	18.9	22.2	0.432	70.3
3827	-	15.36	2013-06-12	i	0.08	40000	320.0	18.9	22.2	0.351	57.8
3842	-	17.453	2013-07-13	i	0.1	18000	180.0	18.3	21.6	0.386	72.2
3845	-	13.724	2013-06-13	i	0.07	40000	280.0	18.8	22.1	0.207	38.8
3849	-	16.182	2013-07-13	i	0.1	27000	270.0	18.7	22.0	0.366	60.2
3873	-	10.42	2013-06-13	i	0.03	30000	90.0	17.5	20.8	0.222	27.9
3919	-	12.956	2013-06-13	i	0.07	35000	245.0	18.6	21.9	0.246	33.4
3940	-	12.93	2013-06-13	i	0.06	40000	240.0	18.6	21.9	0.241	34.1
3993	-	9.16	2013-06-29	i	0.03	40000	120.0	17.8	21.1	0.349	23.5
3998	-	16.975	2013-06-29	i	0.1	33000	330.0	18.9	22.2	0.687	7.9
4013	-	9.072	2013-07-16	i	0.068	40000	272.0	18.7	22.0	0.472	9.1
4013	-	9.072	2013-07-17	z	0.068	40000	272.0	-	-	0.335	17.1
4033	-	11.968	2013-07-16	i	0.06	30000	180.0	18.3	21.6	0.269	28.3
4033	-	11.968	2013-07-17	z	0.06	30000	180.0	-	-	0.221	39.7
4355	-	13.482	2013-06-28	i	0.083	40000	332.0	19.0	22.3	0.331	38.4
					From 2012						
99	L	12.96	2011-07-05	i	0.0300	20000	60.0	16.34	19.94	0.249	22.6
131	L	13.797	2011-07-10	i	0.0750	20000	150.0	17.34	20.94	0.285	34.6
212	-	14.858	2011-07-09	i	0.1000	24000	240.0	17.65	21.25	0.392	46.9
232	L	14.247	2011-07-02	i	0.200	10000	200.0	18.40	22.00	0.261	26.8

TABLE 5.3: continued.

KOI ID	Others	kep (mag)	Date (yyyy-mm-dd)	Filter	T_{ind} (s)	#Frames	Eff.Time s	i_{comp} (mag)	i_{det} (mag)	FWHM[a] (arcsec)	Strehl (%)
238	L	14.061	2011-07-05	i	0.1000	20000	200.0	17.65	21.25	0.206	37.1
298	-	12.713	2011-06-12	i	0.0800	20000	160.0	17.41	21.01	0.431	25.1
298	-	12.713	2011-06-12	z	0.200	10000	200.0	—	—	0.256	31.3
326	-	12.96	2011-06-12	i	0.200	10000	200.0	18.40	22.00	0.268	33.6
343	L	13.203	2011-06-12	i	0.200	10000	200.0	18.40	22.00	0.272	25.2
372	A,H,L	12.391	2011-07-01	i	0.0340	10000	34.0	16.48	20.08	0.327	29.9
372	A,H,L	12.391	2011-07-01	z	0.0400	10000	40.0	—	—	0.263	41.5
375	-	13.293	2011-07-02	i	0.0870	10000	87.0	17.50	21.10	0.324	27.8
379	-	13.319	2011-07-25	i	0.1000	14000	140.0	17.65	21.25	0.327	28.8
379	-	13.319	2011-07-25	z	0.1000	14000	140.0	—	—	0.322	39.4
387	-	13.577	2011-07-02	i	0.0900	10000	90.0	17.53	21.13	0.270	27.9
387	-	13.577	2011-07-02	z	0.1000	10000	100.0	—	—	0.306	35.2
401	L	14.001	2011-07-05	i	0.200	10000	200.0	18.40	22.00	0.296	25.3
401	L	14.001	2011-07-05	z	0.200	10000	200.0	—	—	0.239	37.6
408	-	14.985	2011-07-09	i	0.150	20000	300.0			0.540	52.3
433	-	14.924	2011-07-07	i	0.1000	20000	200.0	17.65	21.25	0.387	44.0
433	-	14.924	2011-07-07	z	0.200	10000	200.0	—	—	0.405	44.0
439	L	14.313	2011-06-11	i	0.200	10000	200.0	18.40	22.00	0.373	26.5
465	L	14.188	2011-07-10	i	0.1000	20000	200.0	17.65	21.25	0.316	34.1
490	-	14.023	2011-07-03	i	0.200	12000	240.0			0.837	4.1
520	L	14.55	2011-07-08	i	0.200	10000	200.0	18.40	22.00	0.436	27.0
548	L	14.02	2011-06-09	i	0.200	10000	200.0	18.40	22.00	0.329	25.9
555	A,L	14.759	2011-06-10	i	0.200	10000	200.0	18.40	22.00	0.287	31.7
592	-	14.292	2011-07-07	i	0.1000	20000	200.0	17.65	21.25	0.437	33.8
592	-	14.292	2011-07-08	z	0.200	10000	200.0	—	—	0.440	47.6
611	L	14.022	2011-07-02	i	0.200	10000	200.0	18.40	22.00	0.337	24.5
623	H,L	11.811	2011-07-05	i	0.0300	10000	30.0	16.34	19.94	0.204	34.4
626	L	13.49	2011-07-04	i	0.150	12000	180.0	18.09	21.69	0.443	24.6
626	L	13.49	2011-07-04	z	0.150	12000	180.0	—	—	0.395	35.1
628	L	13.946	2011-07-04	i	0.200	10000	200.0	18.40	22.00	0.370	24.1
628	L	13.946	2011-07-04	z	0.200	8000	160.0	—	—	0.449	36.5
638	A	13.595	2011-07-05	i	0.1000	14000	140.0	17.65	21.25	0.373	27.9
641	-	13.583	2011-07-01	i	0.0870	10000	87.0	17.50	21.10	0.333	27.5
641	-	13.583	2011-07-01	z	0.0870	10000	87.0	—	—	0.347	34.7
644	L	13.725	2011-07-04	i	0.150	12000	180.0	18.09	21.69	0.409	25.3
644	L	13.725	2011-07-04	z	0.150	12000	180.0	—	—	0.317	35.7
645	-	13.716	2011-06-26	i	0.1000	20000	200.0	17.65	21.25	0.227	35.2
645	-	13.716	2011-06-26	z	0.1000	20000	200.0	—	—	0.240	43.5
658	L	13.989	2011-07-01	i	0.200	10000	200.0	18.40	22.00	0.280	30.1
658	L	13.989	2011-07-01	z	0.200	10000	200.0	—	—	0.320	34.7
671	-	13.749	2011-06-09	z	0.200	10000	200.0			-	-
685	L	13.949	2011-06-11	z	0.200	10000	200.0	—	—	0.252	37.8
685	L	13.949	2011-06-11	i	0.200	10000	200.0	18.40	22.00	0.264	27.6
703	L	13.361	2011-06-11	i	0.0500	12000	60.0	16.89	20.49	0.222	39.7
703	L	13.361	2011-06-11	z	0.200	10000	200.0	—	—	0.253	36.2
704	L	13.704	2011-07-05	i	0.1000	15000	150.0	17.65	21.25	0.335	29.2
721	L	13.645	2011-06-26	i	0.1000	14000	140.0	17.65	21.25	0.187	37.9
721	L	13.645	2011-06-26	z	0.1000	14000	140.0	—	—	0.232	44.0
841	-	15.855	2011-06-11	i	0.200	10000	200.0	18.40	22.00	0.240	42.5
841	-	15.855	2011-06-11	z	0.200	10000	200.0	—	—	0.289	57.9
881	-	15.859	2011-06-11	i	0.200	10000	200.0	18.40	22.00	0.247	43.1

TABLE 5.4: Plate solution for our photometric observations (see section § 5.1.3).

Parameter	Units	2011	2012	2013
# stars		100	179	239
Pixel scale	mas/px	23.89 ± 0.23	23.89 ± 0.23	23.61 ± 0.20
PA	degrees	1.74 ± 0.54	1.94 ± 0.57	1.96 ± 0.50

TABLE 5.3: continued.

KOI ID	Others	kep (mag)	Date (yyyy-mm-dd)	Filter	T_{ind} (s)	#Frames	Eff.Time s	i_{comp} (mag)	i_{det} (mag)	FWHM[a] (arcsec)	Strehl (%)
1032	L	13.862	2011-06-06	i	0.150	10000	150.0	18.09	21.69	0.387	23.5
1192	-	14.215	2011-07-06	i	0.1000	20000	200.0	17.65	21.25	0.298	25.1
1375	L	13.709	2011-07-06	i	0.0750	20000	150.0	17.34	20.94	0.229	36.3
1375	L	13.709	2011-07-06	z	0.0750	20000	150.0	—	—	0.263	43.2
1376	-	13.997	2011-07-07	i	0.1000	20000	200.0			0.506	35.3
1527	-	14.879	2011-07-07	i	0.0800	25000	200.0	17.41	21.01	0.412	50.4
1573	-	14.373	2011-07-08	i	0.200	10000	200.0	18.40	22.00	0.390	26.5
1574	-	14.6	2011-07-06	i	0.1000	20000	200.0	17.65	21.25	0.241	37.9

Notes.

[a] Due to the non-gaussian shape of the radial profile, this parameter is not exactly the FWHM. Instead, it represents the width that includes the same energy ratio as the FWHM (i.e., 76%).

TABLE 5.5: Photometry of the 57 active KOIs (upper part of the table) and 21 demoted KOIs (bottom part of the table) with detected companions that are closer than 6 arcsec.

Active KOIs										
KOI	Comp.	Ang.Sep. arcsec	Angle deg.	SDSSi mag.	SDSSz mag.	Δi mag.	Δz mag.	i-z mag.	SpT	Season
99	A	0.00 ± 0.00	0.00 ± 0.00	12.61 ± 0.10	–	0.000 ± 0.004	–	–	-	2011
99	B	3.475 ± 0.033	48.87 ± 0.54	20.87 ± 2.51	–	−8.268 ± 6.295	–	–	-	2011
111	A	0.00 ± 0.00	0.00 ± 0.00	12.38 ± 0.10	–	0.000 ± 0.003	–	–	$G0^{G5}_{F8}$	2013
111	B	1.856 ± 0.018	186.11 ± 0.50	18.47 ± 0.54	–	−6.095 ± 0.526	–	–	-	2013
115	A	0.00 ± 0.00	0.00 ± 0.00	12.59 ± 0.10	–	0.000 ± 0.003	–	–	$F8^{G2}_{F5}$	2013
115	B	4.051 ± 0.039	157.43 ± 0.50	20.59 ± 1.50	–	−7.997 ± 2.251	–	–	-	2013
131	A	0.00 ± 0.00	0.00 ± 0.00	13.57 ± 0.10	–	0.000 ± 0.003	–	–	-	2011
131	B	5.683 ± 0.055	154.05 ± 0.54	17.33 ± 0.25	–	−3.755 ± 0.051	–	–	-	2011
152	A	0.00 ± 0.00	0.00 ± 0.00	13.69 ± 0.10	–	0.000 ± 0.003	–	–	$G0^{G5}_{F8}$	2013
152	B	5.721 ± 0.056	160.17 ± 0.50	17.14 ± 0.23	–	−3.443 ± 0.044	–	–	-	2013
152	C	5.721 ± 0.056	160.17 ± 0.50	17.14 ± 0.23	–	−3.443 ± 0.044	–	–	-	2013
191	A	0.00 ± 0.00	0.00 ± 0.00	14.76 ± 0.10	14.69 ± 0.10	0.000 ± 0.004	0.000 ± 0.004	0.0700 ± 0.141	$G8^{K0}_{G8}$	2013
191	B	1.671 ± 0.016	96.09 ± 0.50	17.50 ± 0.10	17.74 ± 0.11	−2.746 ± 0.023	−3.049 ± 0.038	−0.233 ± 0.148	$A1^{A9}_{B1}$	2013
212	A	0.00 ± 0.00	0.00 ± 0.00	14.59 ± 0.10	–	0.000 ± 0.003	–	–	-	2011
212	B	4.936 ± 0.047	308.29 ± 0.54	17.54 ± 0.18	–	−2.944 ± 0.024	–	–	-	2011
232	A	0.00 ± 0.00	0.00 ± 0.00	14.00 ± 0.10	–	0.000 ± 0.003	–	–	-	2011
232	B	5.697 ± 0.055	21.69 ± 0.54	18.73 ± 0.38	–	−4.730 ± 0.132	–	–	-	2011
298	A	0.00 ± 0.00	0.00 ± 0.00	14.45 ± 0.10	14.53 ± 0.10	0.000 ± 0.008	0.000 ± 0.003	−0.0800 ± 0.141	-	2011
298	C	2.011 ± 0.019	272.76 ± 0.54	15.09 ± 0.10	14.89 ± 0.10	−0.646 ± 0.012	−0.365 ± 0.004	0.201 ± 0.142	-	2011
326	A	0.00 ± 0.00	0.00 ± 0.00	13.95 ± 0.10	–	0.000 ± 0.003	–	–	-	2011
326	B	3.542 ± 0.034	269.08 ± 0.54	15.74 ± 0.14	–	−1.789 ± 0.009	–	–	-	2011
343	A	0.00 ± 0.00	0.00 ± 0.00	12.94 ± 0.10	–	0.000 ± 0.003	–	–	-	2011
343	B	5.077 ± 0.049	145.23 ± 0.54	18.46 ± 0.52	–	−5.515 ± 0.256	–	–	-	2011
375	A	0.00 ± 0.00	0.00 ± 0.00	13.05 ± 0.10	–	0.000 ± 0.003	–	–	-	2011
375	B	5.471 ± 0.053	155.79 ± 0.54	18.66 ± 0.52	–	−5.614 ± 0.256	–	–	-	2011
379	A	0.00 ± 0.00	0.00 ± 0.00	13.48 ± 0.10	13.42 ± 0.10	0.000 ± 0.003	0.000 ± 0.003	0.0600 ± 0.141	-	2011
379	B	1.946 ± 0.019	80.03 ± 0.54	14.46 ± 0.10	14.33 ± 0.10	−0.976 ± 0.004	−0.913 ± 0.004	0.123 ± 0.141	-	2011
387	A	0.00 ± 0.00	0.00 ± 0.00	14.04 ± 0.10	14.05 ± 0.10	0.000 ± 0.003	0.000 ± 0.003	−0.0100 ± 0.141	-	2011

TABLE 5.5: continued.

KOI	Comp.	Ang.Sep.	Angle	SDSSi	SDSSz	Δi	Δz	i-z	SpT	Season
		arcsec	deg.	mag.	mag.	mag.	mag.	mag.		
387	B	0.8953 ± 0.0086	350.57 ± 0.54	16.70 ± 0.10	16.51 ± 0.10	−2.662 ± 0.016	−2.461 ± 0.014	0.191 ± 0.143	-	2011
401	A	0.00 ± 0.00	0.00 ± 0.00	13.75 ± 0.10	13.71 ± 0.10	0.000 ± 0.003	0.000 ± 0.003	0.0400 ± 0.141	-	2011
401	B	1.994 ± 0.019	269.60 ± 0.54	16.40 ± 0.10	16.05 ± 0.10	−2.655 ± 0.018	−2.342 ± 0.016	0.353 ± 0.143	-	2011
433	A	0.00 ± 0.00	0.00 ± 0.00	14.58 ± 0.10	14.54 ± 0.10	0.000 ± 0.003	0.000 ± 0.003	0.0400 ± 0.141	-	2011
433	B	2.396 ± 0.023	5.33 ± 0.54	18.44 ± 0.11	17.68 ± 0.10	−3.861 ± 0.053	−3.139 ± 0.027	0.762 ± 0.153	-	2011
433	C	3.783 ± 0.036	292.93 ± 0.54	17.25 ± 0.10	17.07 ± 0.10	−2.666 ± 0.018	−2.530 ± 0.016	0.176 ± 0.143	-	2011
435	A	0.00 ± 0.00	0.00 ± 0.00	14.27 ± 0.10	–	0.000 ± 0.003	–	–	$G8^{K0}_{G5}$	2013
435	B	4.850 ± 0.047	34.75 ± 0.50	16.05 ± 0.14	–	−1.779 ± 0.009	–	–	-	2013
439	A	0.00 ± 0.00	0.00 ± 0.00	13.99 ± 0.10	–	0.000 ± 0.003	–	–	-	2011
439	B	5.520 ± 0.053	15.98 ± 0.54	20.71 ± 0.83	–	−6.715 ± 0.680	–	–	-	2011
520	A	0.00 ± 0.00	0.00 ± 0.00	14.18 ± 0.10	–	0.000 ± 0.003	–	–	-	2011
520	B	5.802 ± 0.056	271.27 ± 0.54	17.85 ± 0.22	–	−3.672 ± 0.038	–	–	-	2011
548	A	0.00 ± 0.00	0.00 ± 0.00	13.81 ± 0.10	–	0.000 ± 0.003	–	–	-	2011
548	B	4.729 ± 0.045	132.99 ± 0.54	19.14 ± 0.45	–	−5.329 ± 0.194	–	–	-	2011
555	A	0.00 ± 0.00	0.00 ± 0.00	14.43 ± 0.10	–	0.000 ± 0.003	–	–	-	2011
555	B	4.120 ± 0.040	22.38 ± 0.54	18.18 ± 0.25	–	−3.755 ± 0.053	–	–	-	2011
592	A	0.00 ± 0.00	0.00 ± 0.00	14.06 ± 0.10	14.00 ± 0.10	0.000 ± 0.003	0.000 ± 0.003	0.0600 ± 0.141	-	2011
592	B	2.320 ± 0.022	151.15 ± 0.54	18.02 ± 0.11	17.73 ± 0.11	−3.962 ± 0.052	−3.731 ± 0.047	0.291 ± 0.157	-	2011
623	A	0.00 ± 0.00	0.00 ± 0.00	11.62 ± 0.10	–	0.000 ± 0.003	–	–	-	2011
623	B	5.680 ± 0.055	201.60 ± 0.54	14.15 ± 0.16	–	−2.529 ± 0.015	–	–	-	2011
626	A	0.00 ± 0.00	0.00 ± 0.00	13.29 ± 0.10	13.25 ± 0.10	0.000 ± 0.001	0.000 ± 0.003	0.0400 ± 0.141	-	2011
626	B	2.777 ± 0.027	348.46 ± 0.54	18.05 ± 0.15	18.52 ± 0.21	−4.762 ± 0.106	−5.278 ± 0.183	−0.476 ± 0.254	-	2011
628	A	0.00 ± 0.00	0.00 ± 0.00	13.73 ± 0.10	13.70 ± 0.10	0.000 ± 0.003	0.000 ± 0.003	0.0300 ± 0.141	-	2011
628	B	1.813 ± 0.017	310.92 ± 0.54	17.33 ± 0.11	16.88 ± 0.10	−3.601 ± 0.038	−3.179 ± 0.026	0.452 ± 0.148	-	2011
628	C	2.756 ± 0.026	239.18 ± 0.54	17.92 ± 0.12	17.49 ± 0.11	−4.191 ± 0.065	−3.790 ± 0.046	0.431 ± 0.162	-	2011
641	A	0.00 ± 0.00	0.00 ± 0.00	13.19 ± 0.10	12.98 ± 0.10	0.000 ± 0.003	0.000 ± 0.003	0.210 ± 0.141	-	2011
641	B	2.264 ± 0.022	276.82 ± 0.54	14.85 ± 0.10	14.38 ± 0.10	−1.663 ± 0.009	−1.401 ± 0.007	0.472 ± 0.141	-	2011
641	C	3.739 ± 0.036	205.75 ± 0.54	13.48 ± 0.10	13.06 ± 0.10	−0.292 ± 0.004	−0.084 ± 0.003	0.418 ± 0.141	-	2011
645	A	0.00 ± 0.00	0.00 ± 0.00	13.61 ± 0.10	13.60 ± 0.10	0.000 ± 0.003	0.000 ± 0.003	0.0100 ± 0.141	-	2011
645	B	2.845 ± 0.027	50.41 ± 0.54	15.79 ± 0.10	15.45 ± 0.10	−2.185 ± 0.012	−1.850 ± 0.011	0.345 ± 0.142	-	2011
650	A	0.00 ± 0.00	0.00 ± 0.00	13.23 ± 0.10	–	0.000 ± 0.028	–	–	$K2^{K2}_{K1}$	2013
650	B	2.594 ± 0.025	268.09 ± 0.50	17.87 ± 0.59	–	−4.638 ± 0.584	–	–	-	2013
658	A	0.00 ± 0.00	0.00 ± 0.00	13.75 ± 0.10	13.70 ± 0.10	0.000 ± 0.003	0.000 ± 0.003	0.0500 ± 0.141	-	2011
658	B	1.906 ± 0.018	239.69 ± 0.54	17.84 ± 0.12	17.09 ± 0.11	−4.091 ± 0.066	−3.387 ± 0.035	0.754 ± 0.160	-	2011
671	A	0.00 ± 0.00	0.00 ± 0.00	13.95 ± 0.10	–	0.000 ± 0.003	–	–	-	2011
671	B	4.092 ± 0.039	66.85 ± 0.54	20.94 ± 0.90	–	−6.985 ± 0.805	–	–	-	2011
685	A	0.00 ± 0.00	0.00 ± 0.00	13.70 ± 0.10	13.70 ± 0.10	0.000 ± 0.003	0.000 ± 0.003	0.000 ± 0.141	-	2011
685	B	3.377 ± 0.032	270.68 ± 0.54	19.43 ± 0.58	19.34 ± 0.57	−5.725 ± 0.327	−5.635 ± 0.320	0.0900 ± 0.479	-	2011
704	A	0.00 ± 0.00	0.00 ± 0.00	13.43 ± 0.10	–	0.000 ± 0.003	–	–	-	2011
704	B	1.637 ± 0.016	179.45 ± 0.54	16.97 ± 0.11	–	−3.542 ± 0.038	–	–	-	2011
721	A	0.00 ± 0.00	0.00 ± 0.00	13.40 ± 0.10	13.37 ± 0.10	0.000 ± 0.003	0.000 ± 0.003	0.0300 ± 0.141	-	2011
721	B	1.890 ± 0.018	195.18 ± 0.54	17.41 ± 0.12	17.20 ± 0.12	−4.013 ± 0.067	−3.822 ± 0.066	0.221 ± 0.169	-	2011
841	A	0.00 ± 0.00	0.00 ± 0.00	15.52 ± 0.10	15.45 ± 0.10	0.000 ± 0.004	0.000 ± 0.004	0.0700 ± 0.141	-	2011
841	B	1.986 ± 0.019	69.12 ± 0.54	19.73 ± 0.14	20.95 ± 0.37	−4.210 ± 0.099	−5.504 ± 0.356	−1.224 ± 0.395	-	2011
841	C	5.723 ± 0.055	41.05 ± 0.54	17.21 ± 0.10	17.22 ± 0.10	−1.687 ± 0.010	−1.768 ± 0.012	−0.0110 ± 0.142	-	2011
881	A	0.00 ± 0.00	0.00 ± 0.00	15.49 ± 0.10	–	0.000 ± 0.003	–	–	-	2011
881	B	5.390 ± 0.052	191.76 ± 0.54	24.41 ± 2.41	–	−8.916 ± 5.820	–	–	-	2011
1032	A	0.00 ± 0.00	0.00 ± 0.00	13.42 ± 0.10	–	0.000 ± 0.001	–	–	-	2011
1032	B	5.858 ± 0.056	86.43 ± 0.54	18.70 ± 0.42	–	−5.285 ± 0.169	–	–	-	2011
1174	A	0.00 ± 0.00	0.00 ± 0.00	12.91 ± 0.10	–	0.000 ± 0.003	–	–	$K5^{K5}_{K4}$	2013
1174	B	5.060 ± 0.049	237.48 ± 0.50	17.45 ± 0.34	–	−4.541 ± 0.103	–	–	-	2013
1192	A	0.00 ± 0.00	0.00 ± 0.00	13.90 ± 0.10	–	0.000 ± 0.003	–	–	-	2011
1192	B	5.806 ± 0.056	344.60 ± 0.54	19.38 ± 0.50	–	−5.480 ± 0.242	–	–	-	2011
1230	A	0.00 ± 0.00	0.00 ± 0.00	11.83 ± 0.10	–	0.000 ± 0.003	–	–	$K3^{K3}_{K2}$	2013
1230	B	2.814 ± 0.027	109.07 ± 0.50	20.94 ± 7.21	–	−9.108 ± 7.206	–	–	-	2013
1375	A	0.00 ± 0.00	0.00 ± 0.00	14.09 ± 0.10	14.09 ± 0.10	0.000 ± 0.003	0.000 ± 0.003	0.000 ± 0.141	-	2011
1375	B	0.7442 ± 0.0072	267.99 ± 0.54	16.25 ± 0.10	16.23 ± 0.10	−2.153 ± 0.010	−2.139 ± 0.011	0.0140 ± 0.142	-	2011
1452	A	0.00 ± 0.00	0.00 ± 0.00	13.46 ± 0.10	–	0.000 ± 0.003	–	–	$F8^{G0}_{F5}$	2012
1452	B	2.371 ± 0.023	102.02 ± 0.57	22.75 ± 7.76	–	−9.284 ± 7.761	–	–	-	2012
1452	C	4.763 ± 0.046	85.26 ± 0.57	19.42 ± 0.37	–	−5.953 ± 0.361	–	–	-	2012
1546	A	0.00 ± 0.00	0.00 ± 0.00	14.57 ± 0.10	–	0.000 ± 0.004	–	–	$K1^{K1}_{K0}$	2013
1546	B	0.5839 ± 0.0057	88.80 ± 0.50	15.55 ± 0.10	–	−0.987 ± 0.006	–	–	-	2013
1546	C	2.901 ± 0.028	3.22 ± 0.50	18.08 ± 0.11	–	−3.515 ± 0.042	–	–	-	2013
1546	D	4.113 ± 0.040	164.16 ± 0.50	18.21 ± 0.11	–	−3.648 ± 0.047	–	–	-	2013
1546	E	4.615 ± 0.045	198.72 ± 0.50	21.12 ± 0.68	–	−6.557 ± 0.669	–	–	-	2013
1573	A	0.00 ± 0.00	0.00 ± 0.00	14.12 ± 0.10	–	0.000 ± 0.003	–	–	-	2011
1573	B	4.033 ± 0.039	297.73 ± 0.54	18.81 ± 0.33	–	−4.697 ± 0.101	–	–	-	2011
1574	A	0.00 ± 0.00	0.00 ± 0.00	14.30 ± 0.10	–	0.000 ± 0.003	–	–	-	2011
1574	B	5.125 ± 0.049	224.00 ± 0.54	19.18 ± 0.38	–	−4.877 ± 0.134	–	–	-	2011
1725	A	0.00 ± 0.00	0.00 ± 0.00	13.95 ± 0.10	–	0.000 ± 0.003	–	–	-	2013
1725	B	4.093 ± 0.040	98.31 ± 0.50	15.79 ± 0.14	–	−1.837 ± 0.010	–	–	-	2013

TABLE 5.5: continued.

KOI	Comp.	Ang.Sep.	Angle	SDSSi	SDSSz	Δi	Δz	i-z	SpT	Season
		arcsec	deg.	mag.	mag.	mag.	mag.	mag.		
1781	A	0.00 ± 0.00	0.00 ± 0.00	11.81 ± 0.10	–	0.000 ± 0.001	–	–	$K2^{K3}_{K2}$	2012
1781	B	3.447 ± 0.033	332.14 ± 0.57	15.46 ± 0.22	–	−3.653 ± 0.037	–	–	-	2012
1802	A	0.00 ± 0.00	0.00 ± 0.00	13.11 ± 0.10	–	0.000 ± 0.003	–	–	$G2^{G5}_{F8}$	2013
1802	B	5.446 ± 0.053	239.86 ± 0.50	19.58 ± 0.72	–	−6.469 ± 0.511	–	–	-	2013
1812	A	0.00 ± 0.00	0.00 ± 0.00	13.54 ± 0.10	–	0.000 ± 0.003	–	–	$G2^{G8}_{F8}$	2013
1812	B	2.368 ± 0.023	297.19 ± 0.50	17.81 ± 0.13	–	−4.269 ± 0.086	–	–	-	2013
1812	C	2.695 ± 0.026	114.07 ± 0.50	20.05 ± 0.68	–	−6.512 ± 0.677	–	–	-	2013
2324	A	0.00 ± 0.00	0.00 ± 0.00	13.96 ± 0.10	–	0.000 ± 0.004	–	–	-	2012
2324	B	2.910 ± 0.028	28.42 ± 0.57	20.08 ± 0.71	–	−6.123 ± 0.707	–	–	-	2012
2324	C	4.781 ± 0.046	173.04 ± 0.57	13.78 ± 0.10	–	0.180 ± 0.004	–	–	-	2012
2324	D	5.576 ± 0.054	269.99 ± 0.57	19.00 ± 0.28	–	−5.039 ± 0.261	–	–	-	2012
2481	A	0.00 ± 0.00	0.00 ± 0.00	13.17 ± 0.10	13.02 ± 0.10	0.000 ± 0.003	0.000 ± 0.003	0.150 ± 0.141	$K4^{K5}_{K4}$	2012
2481	B	1.097 ± 0.011	183.16 ± 0.57	16.68 ± 0.11	16.34 ± 0.10	−3.505 ± 0.039	−3.326 ± 0.031	0.329 ± 0.150	$K8^{M2}_{K5}$	2012
3158	A	0.00 ± 0.00	0.00 ± 0.00	14.03 ± 0.10	14.04 ± 0.10	0.000 ± 0.003	0.000 ± 0.003	−0.0100 ± 0.141	$F4^{K4}_{A4}$	2013
3158	B	1.845 ± 0.018	252.17 ± 0.50	16.90 ± 0.10	16.59 ± 0.10	−2.870 ± 0.021	−2.547 ± 0.018	0.313 ± 0.144	$K8^{M1}_{K5}$	2013
3263	A	0.00 ± 0.00	0.00 ± 0.00	15.31 ± 0.10	–	0.000 ± 0.004	–	–	-	2013
3263	B	0.8260 ± 0.0081	274.52 ± 0.50	17.33 ± 0.10	–	−2.019 ± 0.012	–	–	-	2013
3444	A	0.00 ± 0.00	0.00 ± 0.00	12.92 ± 0.10	12.57 ± 0.10	0.000 ± 0.003	0.000 ± 0.003	0.350 ± 0.141	$K8^{M2}_{K5}$	2013
3444	B	1.080 ± 0.010	9.62 ± 0.50	15.72 ± 0.10	15.14 ± 0.10	−2.795 ± 0.021	−2.567 ± 0.019	0.578 ± 0.144	$M2^{M4}_{M0}$	2013
3444	C	3.579 ± 0.035	264.38 ± 0.50	17.42 ± 0.14	17.30 ± 0.17	−4.501 ± 0.100	−4.729 ± 0.141	0.122 ± 0.223	$K3^{K8}_{A7}$	2013
3649	A	0.00 ± 0.00	0.00 ± 0.00	15.82 ± 0.10	–	0.000 ± 0.020	–	–	-	2013
3649	B	0.6649 ± 0.0065	214.19 ± 0.50	15.97 ± 0.11	–	−0.154 ± 0.022	–	–	-	2013
3886	A	0.00 ± 0.00	0.00 ± 0.00	9.79 ± 0.10	9.62 ± 0.10	0.000 ± 0.003	0.000 ± 0.003	0.170 ± 0.141	$K4^{K4}_{K4}$	2013
3886	B	0.4080 ± 0.0040	114.58 ± 0.50	10.65 ± 0.10	10.61 ± 0.10	−0.854 ± 0.004	−0.986 ± 0.004	0.0380 ± 0.141	$F8^{K5}_{A7}$	2013
4016	A	0.00 ± 0.00	0.00 ± 0.00	13.51 ± 0.10	–	0.000 ± 0.003	–	–	$K5^{K5}_{K5}$	2013
4016	B	5.583 ± 0.054	34.90 ± 0.50	17.47 ± 0.25	–	−3.958 ± 0.054	–	–	$M7^{M7}_{M6}$	2013
4016	C	5.583 ± 0.054	34.90 ± 0.50	17.47 ± 0.25	–	−3.958 ± 0.054	–	–	$M7^{M7}_{M6}$	2013
4512	A	0.00 ± 0.00	0.00 ± 0.00	15.37 ± 0.10	–	0.000 ± 0.008	–	–	$K3^{K4}_{K2}$	2013
4512	B	0.3922 ± 0.0038	327.99 ± 0.50	16.10 ± 0.10	–	−0.728 ± 0.011	–	–	-	2013
					Demoted KOIs					
465	A	0.00 ± 0.00	0.00 ± 0.00	13.95 ± 0.10	–	0.000 ± 0.003	–	–	-	2011
465	B	3.677 ± 0.035	130.75 ± 0.54	19.12 ± 0.43	–	−5.163 ± 0.178	–	–	-	2011
465	C	4.588 ± 0.044	192.89 ± 0.54	18.21 ± 0.30	–	−4.261 ± 0.078	–	–	-	2011
644	A	0.00 ± 0.00	0.00 ± 0.00	14.20 ± 0.10	14.19 ± 0.10	0.000 ± 0.003	0.000 ± 0.003	0.0100 ± 0.141	-	2011
644	B	2.697 ± 0.026	63.31 ± 0.54	15.68 ± 0.10	15.66 ± 0.10	−1.476 ± 0.006	−1.467 ± 0.006	0.0190 ± 0.141	-	2011
703	A	0.00 ± 0.00	0.00 ± 0.00	13.95 ± 0.10	13.95 ± 0.10	0.000 ± 0.003	0.000 ± 0.003	0.000 ± 0.141	-	2011
703	B	1.936 ± 0.019	33.82 ± 0.54	21.12 ± 1.36	19.65 ± 0.34	−7.165 ± 1.356	−5.702 ± 0.330	1.463 ± 1.403	-	2011
3564	A	0.00 ± 0.00	0.00 ± 0.00	13.95 ± 0.10	–	0.000 ± 0.003	–	–	-	2013
3564	B	4.912 ± 0.048	102.03 ± 0.50	16.95 ± 0.19	–	−3.002 ± 0.025	–	–	-	2013
3616	A	0.00 ± 0.00	0.00 ± 0.00	14.91 ± 0.10	14.94 ± 0.10	0.000 ± 0.011	0.000 ± 0.016	−0.0300 ± 0.141	$F2^{K1}_{A2}$	2013
3616	B	1.276 ± 0.012	212.33 ± 0.50	14.53 ± 0.10	14.50 ± 0.10	0.376 ± 0.010	0.445 ± 0.014	0.0390 ± 0.142	$G0^{K5}_{A7}$	2013
3639	A	0.00 ± 0.00	0.00 ± 0.00	13.95 ± 0.10	13.95 ± 0.10	0.000 ± 0.003	0.000 ± 0.003	0.000 ± 0.141	$F7^{K4}_{A5}$	2013
3639	B	3.281 ± 0.032	37.91 ± 0.50	15.61 ± 0.13	15.79 ± 0.15	−1.661 ± 0.007	−1.842 ± 0.011	−0.181 ± 0.142	$A2^{F1}_{B3}$	2013
3639	C	4.601 ± 0.045	110.25 ± 0.50	15.74 ± 0.14	15.89 ± 0.15	−1.792 ± 0.008	−1.950 ± 0.012	−0.158 ± 0.142	$A3^{F3}_{B4}$	2013
3670	A	0.00 ± 0.00	0.00 ± 0.00	–	14.12 ± 0.10	–	0.000 ± 0.003	–	-	2013
3670	B	1.299 ± 0.013	117.65 ± 0.50	–	16.22 ± 0.10	–	−2.107 ± 0.011	–	-	2013
3670	C	1.897 ± 0.018	92.89 ± 0.50	–	18.01 ± 0.11	–	−3.892 ± 0.055	–	-	2013
3670	D	4.822 ± 0.047	242.77 ± 0.50	–	20.56 ± 0.58	–	−6.441 ± 0.575	–	-	2013
3684	A	0.00 ± 0.00	0.00 ± 0.00	13.95 ± 0.10	13.95 ± 0.10	0.000 ± 0.001	0.000 ± 0.003	0.000 ± 0.141	$F7^{K4}_{A5}$	2013
3684	B	3.755 ± 0.037	233.00 ± 0.50	19.50 ± 0.48	19.07 ± 0.48	−5.551 ± 0.221	−5.130 ± 0.222	0.421 ± 0.344	$M0^{M4}_{G2}$	2013
3684	C	4.102 ± 0.040	38.97 ± 0.50	21.69 ± 1.29	21.40 ± 1.38	−7.740 ± 1.656	−7.452 ± 1.882	0.288 ± 2.511	$K7^{---}_{---}$	2013
3693	A	0.00 ± 0.00	0.00 ± 0.00	13.95 ± 0.10	–	0.000 ± 0.006	–	–	-	2013
3693	B	4.275 ± 0.042	205.37 ± 0.50	20.43 ± 1.13	–	−6.475 ± 1.269	–	–	-	2013
3704	A	0.00 ± 0.00	0.00 ± 0.00	14.10 ± 0.10	–	0.000 ± 0.004	–	–	-	2013
3704	B	1.533 ± 0.015	317.43 ± 0.50	16.83 ± 0.10	–	−2.730 ± 0.022	–	–	-	2013
3704	C	2.865 ± 0.028	282.98 ± 0.50	17.02 ± 0.10	–	−2.914 ± 0.026	–	–	-	2013
3704	D	4.164 ± 0.041	122.78 ± 0.50	16.69 ± 0.10	–	−2.586 ± 0.019	–	–	-	2013
3712	A	0.00 ± 0.00	0.00 ± 0.00	13.95 ± 0.10	–	0.000 ± 0.010	–	–	-	2013
3712	B	5.829 ± 0.057	321.51 ± 0.50	14.59 ± 0.15	–	−0.640 ± 0.013	–	–	-	2013
3714	A	0.00 ± 0.00	0.00 ± 0.00	13.95 ± 0.10	–	0.000 ± 0.003	–	–	-	2013
3714	B	4.761 ± 0.046	224.26 ± 0.50	19.36 ± 0.45	–	−5.408 ± 0.196	–	–	-	2013
3719	A	0.00 ± 0.00	0.00 ± 0.00	13.95 ± 0.10	–	0.000 ± 0.003	–	–	-	2013
3719	B	5.533 ± 0.054	261.90 ± 0.50	16.56 ± 0.17	–	−2.605 ± 0.018	–	–	-	2013
3777	A	0.00 ± 0.00	0.00 ± 0.00	13.99 ± 0.10	–	0.000 ± 0.003	–	–	-	2013
3777	B	1.687 ± 0.016	186.36 ± 0.50	18.47 ± 0.15	–	−4.485 ± 0.110	–	–	-	2013
3777	C	1.884 ± 0.018	257.21 ± 0.50	18.61 ± 0.16	–	−4.621 ± 0.124	–	–	-	2013
3788	A	0.00 ± 0.00	0.00 ± 0.00	13.96 ± 0.10	–	0.000 ± 0.001	–	–	-	2013
3788	B	2.263 ± 0.022	67.85 ± 0.50	19.41 ± 0.24	–	−5.451 ± 0.213	–	–	-	2013
3805	A	0.00 ± 0.00	0.00 ± 0.00	13.95 ± 0.10	–	0.000 ± 0.003	–	–	-	2013
3805	B	3.684 ± 0.036	199.67 ± 0.50	19.43 ± 0.53	–	−5.474 ± 0.274	–	–	-	2013
3805	C	4.389 ± 0.043	285.00 ± 0.50	16.52 ± 0.17	–	−2.572 ± 0.019	–	–	-	2013

TABLE 5.5: continued.

KOI	Comp.	Ang.Sep.	Angle	SDSSi	SDSSz	Δi	Δz	i-z	SpT	Season
		arcsec	deg.	mag.	mag.	mag.	mag.	mag.		
3842	A	0.00 ± 0.00	0.00 ± 0.00	13.95 ± 0.10	–	0.000 ± 0.006	–	–	-	2013
3842	B	3.684 ± 0.036	247.05 ± 0.50	15.50 ± 0.15	–	−1.552 ± 0.013	–	–	-	2013
3940	A	0.00 ± 0.00	0.00 ± 0.00	13.97 ± 0.10	–	0.000 ± 0.003	–	–	-	2013
3940	B	2.132 ± 0.021	256.74 ± 0.50	18.76 ± 0.17	–	−4.792 ± 0.141	–	–	-	2013
4013	A	0.00 ± 0.00	0.00 ± 0.00	14.27 ± 0.10	14.22 ± 0.10	0.000 ± 0.003	0.000 ± 0.001	0.0500 ± 0.141	$G1^{K5}_{A8}$	2013
4013	B	0.9166 ± 0.0089	62.14 ± 0.50	15.43 ± 0.10	15.58 ± 0.10	−1.157 ± 0.005	−1.367 ± 0.005	−0.160 ± 0.141	$A2^{F2}_{B4}$	2013
4033	A	0.00 ± 0.00	0.00 ± 0.00	14.04 ± 0.10	14.03 ± 0.10	0.000 ± 0.003	0.000 ± 0.003	0.0100 ± 0.141	$F7^{K4}_{A5}$	2013
4033	B	1.617 ± 0.016	110.55 ± 0.50	16.86 ± 0.10	16.89 ± 0.10	−2.823 ± 0.021	−2.865 ± 0.026	−0.0320 ± 0.145	$F2^{K1}_{A2}$	2013
4033	C	2.925 ± 0.028	276.42 ± 0.50	19.58 ± 0.28	19.58 ± 0.32	−5.548 ± 0.261	−5.551 ± 0.305	0.00700 ± 0.425	$F7^{M0}_{O7}$	2013
4355	A	0.00 ± 0.00	0.00 ± 0.00	14.48 ± 0.10	–	0.000 ± 0.003	–	–	-	2013
4355	B	2.864 ± 0.028	93.15 ± 0.50	14.99 ± 0.10	–	−0.516 ± 0.004	–	–	-	2013

TABLE 5.6: Estimation of the new parameters of the planet candidates orbiting the KOIs with detected companions closer than 3 arcsec.

Planet	Depth (ppm)		R_p/R_s (%)			R_p ($R_\oplus$)	
candidate	CFOP	New	CFOP	New[a]	Sec.[b]	CFOP[c]	New[d]
Lillo-Box et al. (2012)							
298.01	274	472± 67	1.41±0.04	2.2±0.2	2.6± 0.3	1.40	2.16
379.01	292	422± 24	1.6±0.1	2.1±0.1	3.1± 0.2	2.58	3.38
379.02	136	196± 11	1.1±0.1	1.40±0.04	2.1± 0.1	1.83	2.31
387.01	1122	1137± 75	3.3±0.3	3.4±0.1	29.4± 73.4	2.18	2.23
401.01	2103	2363± 132	4.1±0.2	4.9±0.1	13.8± 3.1	6.57	7.82
401.02	1618	1818± 101	4.2±0.2	4.3±0.1	12.1± 2.7	6.67	6.85
433.01	2864	3048± 76	5.10±0.04	5.5±0.1	21.8± 4.2	5.60	6.06
433.02	13690	14570± 365	11.7±0.1	12.1±0.2	47.6± 9.3	12.90	13.27
592.01	539	561± 19	2.6±0.1	2.37±0.04	11.7± 4.9	2.74	2.48
626.01	374	378± 4	1.8±0.1	1.94±0.01	19.2± 8.7	2.09	2.30
628.01	476	504± 21	2.2±0.2	2.24±0.05	9.3± 3.4	1.87	1.90
641.01	1002	2225± 90	3.1±1.3	4.7±0.1	4.3± 0.1	1.83	2.82
644.01	23950	30367± 591	13.87±0.03	17.4±0.2	33.7± 1.2	33.16	41.67
645.01	201	239± 5	1.61±0.05	1.55±0.02	3.6± 0.2	2.53	2.44
645.02	257	305± 7	1.59±0.03	1.75±0.02	4.0± 0.2	2.51	2.75
658.01	505	517± 8	2.1±0.1	2.27±0.02	14.7± 5.0	2.03	2.18
658.02	484	496± 8	2.1±0.1	2.23±0.02	14.4± 4.9	2.02	2.13
658.03	166	170± 3	1.2±0.1	1.30±0.01	8.5± 2.9	1.14	1.25
703.01	130	131± 1	1.04±0.05	1.142±0.003	17.9± 12.1	1.36	1.50
721.01	276	284± 2	1.63±0.03	1.685±0.007	9.9± 1.4	2.76	2.86
841.01	2967	3071± 45	5.4±0.1	5.54±0.04	29.6± 6.3	5.44	5.56
841.02	4962	5136± 7	7.0±0.2	7.2±0.1	38.3± 8.1	7.05	7.19
1375.01	2608	2651± 99	5.3±0.6	5.1±0.1	40.0± 44.8	6.65	6.44
Lillo-Box et al. (2014b)							
111.01	496	497.3 ± 1.7	2.107 ± 0.020	2.2301 ± 0.0038	43 ± 28	2.14	2.26
111.02	455	456.2 ± 1.6	2.024 ± 0.023	2.1359 ± 0.0036	41 ± 26	2.05	2.16
111.03	598	599.6 ± 2.0	2.328 ± 0.026	2.4487 ± 0.0042	47 ± 30	2.36	2.48
111.04	56	56.15 ± 0.19	0.76 ± 0.11	0.7493 ± 0.0013	14.5 ± 9.3	0.77	0.76
191.01	14611	32000 ± 5800	11.520 ± 0.051	17.9 ± 1.6	16.4 ± 1.2	11.00	17.10
191.02	664	1450 ± 260	2.426 ± 0.036	3.82 ± 0.34	3.49 ± 0.26	2.30	3.62
191.03	194	425 ± 77	1.291 ± 0.043	2.06 ± 0.19	1.89 ± 0.14	1.24	1.98
191.04	659	1440 ± 260	2.402 ± 0.073	3.80 ± 0.34	3.48 ± 0.26	2.30	3.64
1230.01	6998	6998 ± 17	8.259 ± 0.018	8.366 ± 0.010	700 ± 6100	37.10	37.58
1546.01	14150	19568 ± 79	10.624 ± 0.084	13.989 ± 0.028	22.61 ± 0.12	9.50	12.51

TABLE 5.6: continued.

Planet	Depth (ppm)		R_p/R_s (%)			R_p ($R_\oplus$)	
candidate	CFOP	New	CFOP	New[a]	Sec.[b]	CFOP[c]	New[d]
1812.01	1258	1277.8 ± 4.1	4.053 ± 0.065	3.5746 ± 0.0058	28.5 ± 2.9	4.80	4.23
2324.01[e]	149	149.39 ± 0.66	1.10 ± 0.46	1.2222 ± 0.0027	24 ± 21	0.32	0.36
2481.01	793	820 ± 12	2.750 ± 0.072	2.865 ± 0.021	15.3 ± 3.3	20.60	21.46
3158.01	26	56.8 ± 10.0	0.47 ± 0.12	0.753 ± 0.066	0.707 ± 0.055	0.30	0.49
3158.02	43	91 ± 16	0.73 ± 0.11	0.959 ± 0.084	0.900 ± 0.070	0.47	0.62
3158.03	48	103 ± 18	0.63 ± 0.12	1.017 ± 0.089	0.954 ± 0.074	0.41	0.66
3158.04	52	111 ± 20	0.65 ± 0.28	1.055 ± 0.093	0.990 ± 0.077	0.42	0.68
3158.05	73	157 ± 28	0.78 ± 0.14	1.25 ± 0.11	1.178 ± 0.091	0.51	0.81
3263.01	23226	26485 ± 95	16.88 ± 0.99	16.274 ± 0.029	43.44 ± 0.56	7.00	6.75
3444.01	199	219.6 ± 6.9	1.59 ± 0.77	1.482 ± 0.023	4.64 ± 0.72	1.04	0.97
3444.02	3285	3620 ± 110	8.8 ± 4.9	6.017 ± 0.095	18.9 ± 2.9	5.74	3.93
3444.03	96	105.8 ± 3.3	0.96 ± 0.49	1.028 ± 0.016	3.22 ± 0.50	0.63	0.67
3649.01	110642	1301000 ± 41000	44.6 ± 2.7	114.1 ± 1.8	34.774 ± 0.050	65.36	167.18
3886.01[e]	441	1350 ± 300	1.86 ± 0.12	3.68 ± 0.41	2.56 ± 0.14	25.38	50.31
4512.01	3989	5954 ± 53	5.68 ± 0.00	7.717 ± 0.034	10.994 ± 0.099	6.19	8.41

Notes. Parameters from the CFOP are subjected to constant changes according to the new analysis of the *Kepler* team. Here we present the values published at the moment of presenting the results in Lillo-Box et al. (2012) and Lillo-Box et al. (2014b). In the former work, the values were mainly obtained from Batalha et al. (2013), whereas in the second case, the values were mainly obtained from Burke et al. (2014). [(a)] New planet-to-star radii ratio assuming no limb-darkening. [(b)] Planet-to-star radius assuming that the host is actually the secondary companion detected at less than 3 arcsec. [(c)] Planet radii calculated by the *Kepler* project (`http://exoplanetarchive.ipac.caltech.edu`) [(d)] Planet radii assuming the new depth and no limb-darkening. Please note that this could be the cause that the new derived radii are smaller than catalog radii in some cases. No error is presented since no error in the stellar radii is given. [(e)] According to the UKIRT J-band catalog of the *Kepler* field, it remains unclear to us if the detected companions to these KOIs in this paper match some of the targets in the UKIRT catalog.

TABLE 5.7: Results of the blended source probability prior ($P_{BS,0}$) and after (P_{BS}^{LB14}) the AstraLux images for 222 planet candidates around isolated KOIs from all three observing runs ($Type$ = 0) and KOIs with detected companions at 3-6 arcsec from the 2012 and 2013 observing runs ($Type$ = 1). See sections § 3.4 and 5.2.3.1 for more details.

Active KOIs								
Planet	Type[a]	m_{kep}	Δm_{max}	$P_{BS,0}$	P_{BS}	Improve	P_{appEB}	P_{BB}
candidate		mag	mag	%	%	%	%	%
12.01	0	11.35	-4.83	1.8	0.7	61.5	0.0431	0.0003
41.01	0	11.20	-8.62	6.1	1.9	68.5	0.0404	0.0008
41.02	0	11.20	-9.77	10.1	5.8	42.1	0.0404	0.0024
41.03	0	11.20	-9.61	9.4	5.2	44.9	0.0404	0.0021
49.01	0	13.70	-7.31	8.1	3.4	57.7	0.0245	0.0008
51.01	0	13.76	-3.75	2.9	0.1	97.9	0.0241	0.0000
69.01	0	9.93	-8.45	4.1	1.5	63.7	0.0501	0.0007
82.01	0	11.49	-7.15	1.3	0.2	84.7	0.0307	0.0001
82.02	0	11.49	-8.46	2.5	1.0	60.2	0.0307	0.0003
82.03	0	11.49	-8.99	3.1	1.6	48.5	0.0307	0.0005

TABLE 5.7: continued.

Planet candidate	Type[a]	m_{kep} mag	Δm_{max} mag	$P_{BS,0}$ %	P_{BS} %	Improve %	P_{appEB} %	P_{BB} %
82.04	0	11.49	-9.73	4.2	2.7	35.7	0.0307	0.0008
82.05	0	11.49	-10.36	5.3	3.8	28.1	0.0307	0.0012
94.01	0	12.21	-5.35	3.7	0.3	90.8	0.0342	0.0001
94.02	0	12.21	-7.37	10.6	4.1	61.2	0.0342	0.0014
94.03	0	12.21	-6.44	6.8	1.2	82.2	0.0342	0.0004
94.04	0	12.21	-9.21	23.8	17.2	27.6	0.0342	0.0059
115.01	1	12.79	-7.63	4.5	1.9	57.1	0.0272	0.0005
115.02	1	12.79	-8.84	7.4	4.8	34.7	0.0272	0.0013
115.03	1	12.79	-11.03	14.8	12.2	17.5	0.0272	0.0033
139.01	0	13.49	-5.82	3.9	0.9	76.4	0.0250	0.0002
139.02	0	13.49	-9.03	15.2	12.0	21.0	0.0250	0.0030
149.01	0	13.40	-7.14	6.0	2.6	56.4	0.0253	0.0007
152.01	1	13.91	-5.98	13.6	3.3	75.7	0.0235	0.0008
152.02	1	13.91	-7.36	25.1	14.4	42.6	0.0235	0.0034
152.03	1	13.91	-7.50	26.6	16.0	40.1	0.0235	0.0038
152.04	1	13.91	-7.88	31.3	20.7	34.1	0.0235	0.0049
156.01	0	13.74	-7.72	9.9	6.2	37.3	0.0244	0.0015
156.02	0	13.74	-8.27	12.4	8.7	29.8	0.0244	0.0021
156.03	0	13.74	-6.81	6.7	3.0	55.0	0.0244	0.0007
196.01	0	14.46	-4.67	4.0	0.4	90.0	0.0234	0.0001
199.01	0	14.88	-4.72	4.8	1.0	80.2	0.0236	0.0002
199.02	0	14.88	-8.57	23.4	19.2	18.2	0.0236	0.0045
209.01	0	14.27	-5.31	2.8	0.6	79.4	0.0241	0.0001
209.02	0	14.27	-6.20	4.3	1.9	55.2	0.0241	0.0005
211.01	0	14.99	-4.99	3.1	0.6	80.0	0.0245	0.0002
238.01	0	14.06	-7.80	23.9	16.4	31.3	0.0233	0.0038
238.02	0	14.06	-9.07	39.0	31.5	19.2	0.0233	0.0074
245.01	0	9.71	-7.61	0.9	0.1	84.5	0.0444	0.0001
245.02	0	9.71	-9.53	2.3	1.3	45.9	0.0444	0.0006
245.03	0	9.71	-11.42	5.3	4.2	20.2	0.0444	0.0019
245.04	0	9.71	-10.82	4.1	3.1	26.0	0.0444	0.0014
330.01	0	13.93	-8.34	16.3	11.9	27.0	0.0239	0.0028
330.02	0	13.93	-10.20	29.0	24.6	15.2	0.0239	0.0059
338.01	0	13.45	-8.21	16.0	12.6	21.7	0.0252	0.0032
338.02	0	13.45	-9.90	29.8	26.3	11.7	0.0252	0.0066
339.01	0	13.76	-8.40	7.1	5.1	28.1	0.0246	0.0013
339.02	0	13.76	-8.44	7.2	5.2	27.7	0.0246	0.0013
339.03	0	13.76	-8.52	7.4	5.4	26.9	0.0246	0.0013
345.01	0	13.34	-6.84	3.3	2.2	33.6	0.0253	0.0005
349.01	0	13.59	-7.68	5.1	3.2	36.7	0.0248	0.0008
351.01	0	13.80	-4.93	1.4	0.1	90.5	0.0247	0.0000
351.02	0	13.80	-5.66	2.0	0.5	72.3	0.0247	0.0001
351.03	0	13.80	-7.69	4.8	3.3	31.4	0.0247	0.0008
351.04	0	13.80	-7.97	5.4	3.9	28.2	0.0247	0.0010
351.05	0	13.80	-9.07	7.8	6.3	19.5	0.0247	0.0015
351.06	0	13.80	-9.43	8.6	7.1	17.5	0.0247	0.0018
366.01	0	11.71	-5.73	2.4	0.7	69.7	0.0373	0.0003
372.01	0	12.39	-4.99	4.2	0.8	80.5	0.0330	0.0003
385.01	0	13.44	-8.38	19.0	16.1	15.1	0.0253	0.0041
386.01	0	13.84	-7.16	16.7	9.9	40.9	0.0238	0.0024
386.02	0	13.84	-7.44	18.9	12.0	36.2	0.0238	0.0029

TABLE 5.7: continued.

Planet candidate	Type[a]	m_{kep} mag	Δm_{max} mag	$P_{BS,0}$ %	P_{BS} %	Improve %	P_{appEB} %	P_{BB} %
388.01	0	13.64	-8.16	8.4	6.1	27.3	0.0247	0.0015
393.01	0	13.54	-8.34	23.6	17.4	26.3	0.0248	0.0043
398.01	0	15.34	-4.75	3.8	0.9	76.3	0.0247	0.0002
398.02	0	15.34	-6.53	8.5	5.4	36.5	0.0247	0.0013
398.03	0	15.34	-7.87	13.5	10.4	22.9	0.0247	0.0026
416.01	0	14.29	-6.62	6.0	3.1	47.6	0.0239	0.0007
416.02	0	14.29	-6.97	6.9	4.1	41.3	0.0239	0.0010
416.03	0	14.29	-9.30	15.5	12.7	18.4	0.0239	0.0030
422.01	0	14.74	-4.23	2.6	0.8	69.6	0.0239	0.0002
431.01	0	14.26	-6.99	4.0	2.4	40.1	0.0246	0.0006
431.02	0	14.26	-7.29	4.5	2.9	35.5	0.0246	0.0007
435.01	1	14.53	-6.71	5.8	3.3	43.0	0.0241	0.0008
435.02	1	14.53	-4.94	2.6	0.3	89.0	0.0241	0.0001
435.03	1	14.53	-7.66	8.5	5.9	29.8	0.0241	0.0014
435.04	1	14.53	-8.58	11.5	8.9	21.9	0.0241	0.0022
435.05	1	14.53	-7.31	7.4	4.9	33.9	0.0241	0.0012
435.06	1	14.53	-8.81	12.3	9.7	20.5	0.0241	0.0023
463.01	0	14.71	-6.12	17.9	9.0	49.5	0.0228	0.0021
473.01	0	14.67	-7.24	16.0	11.0	31.3	0.0233	0.0026
478.01	0	14.27	-6.49	10.2	6.0	41.3	0.0233	0.0014
481.01	0	14.70	-7.15	10.1	7.0	31.0	0.0238	0.0017
481.02	0	14.70	-7.98	13.8	10.6	22.8	0.0238	0.0025
481.03	0	14.70	-7.05	9.7	6.6	32.2	0.0238	0.0016
496.01	0	14.41	-7.91	14.3	10.5	26.3	0.0236	0.0025
518.01	0	14.29	-7.06	6.9	3.6	47.1	0.0240	0.0009
518.02	0	14.29	-7.60	8.5	5.3	38.0	0.0240	0.0013
518.03	0	14.29	-6.79	6.1	2.9	52.9	0.0240	0.0007
524.01	0	14.87	-7.14	6.1	4.1	31.9	0.0247	0.0010
528.01	0	14.60	-7.45	7.5	5.3	29.8	0.0242	0.0013
528.02	0	14.60	-7.10	6.6	4.3	34.1	0.0242	0.0011
528.03	0	14.60	-7.42	7.4	5.2	30.2	0.0242	0.0013
534.01	0	14.61	-7.40	19.1	14.3	25.2	0.0232	0.0033
534.02	0	14.61	-7.98	24.0	19.2	20.1	0.0232	0.0044
561.01	0	14.01	-7.78	5.8	4.2	26.9	0.0245	0.0010
564.01	0	14.85	-7.56	21.9	15.6	28.6	0.0233	0.0036
564.02	0	14.85	-5.66	9.7	3.5	63.7	0.0233	0.0008
564.03	0	14.85	-9.03	35.6	29.3	17.6	0.0233	0.0068
567.01	0	14.34	-7.43	12.7	8.6	32.2	0.0235	0.0020
567.02	0	14.34	-7.80	14.7	10.6	27.8	0.0235	0.0025
567.03	0	14.34	-7.62	13.8	9.7	29.7	0.0235	0.0023
571.01	0	14.62	-7.44	28.1	20.1	28.7	0.0229	0.0046
571.02	0	14.62	-7.25	26.0	17.9	31.1	0.0229	0.0041
571.03	0	14.62	-7.79	32.4	24.4	24.9	0.0229	0.0056
571.04	0	14.62	-7.43	27.9	19.8	28.9	0.0229	0.0045
571.05	0	14.62	-7.86	33.2	25.2	24.3	0.0229	0.0058
579.01	0	14.14	-8.21	10.7	7.8	26.9	0.0240	0.0019
579.02	0	14.14	-8.18	10.5	7.7	27.1	0.0240	0.0018
611.01	0	14.02	-5.60	11.8	2.9	75.4	0.0233	0.0007
617.01	0	14.61	-5.10	6.6	1.6	76.2	0.0232	0.0004
624.01	0	13.60	-7.35	10.8	5.2	52.3	0.0247	0.0013
624.02	0	13.60	-7.39	11.0	5.3	51.4	0.0247	0.0013

TABLE 5.7: continued.

Planet candidate	Type[a]	m_{kep} mag	Δm_{max} mag	$P_{BS,0}$ %	P_{BS} %	Improve %	P_{appEB} %	P_{BB} %
624.03	0	13.60	-8.54	17.7	12.1	31.9	0.0247	0.0030
625.01	0	13.59	-6.94	5.7	3.2	44.0	0.0248	0.0008
632.01	0	13.36	-8.52	13.0	9.9	23.8	0.0255	0.0025
638.01	0	13.60	-7.04	15.2	8.8	41.8	0.0246	0.0022
638.02	0	13.60	-6.96	14.6	8.3	43.2	0.0246	0.0020
640.01	0	13.33	-7.50	21.1	10.8	48.8	0.0259	0.0028
654.01	0	13.98	-8.21	8.4	6.5	23.2	0.0243	0.0016
654.02	0	13.98	-8.43	9.1	7.1	21.5	0.0243	0.0017
659.01	0	13.41	-8.33	15.2	10.0	34.1	0.0253	0.0025
664.01	0	13.48	-8.64	15.8	11.8	25.3	0.0251	0.0029
664.02	0	13.48	-9.51	21.5	17.5	18.6	0.0251	0.0044
664.03	0	13.48	-9.48	21.2	17.3	18.8	0.0251	0.0043
670.01	0	13.77	-8.46	15.9	11.5	27.8	0.0242	0.0028
672.01	0	14.00	-7.60	11.4	8.9	22.5	0.0238	0.0021
672.02	0	14.00	-7.04	9.1	6.5	28.3	0.0238	0.0015
672.03	0	14.00	-10.86	30.8	28.2	8.4	0.0238	0.0067
676.01	0	13.82	-5.90	5.5	2.0	63.5	0.0241	0.0005
676.02	0	13.82	-6.52	7.4	3.8	49.1	0.0241	0.0009
678.01	0	13.28	-8.44	7.2	5.2	27.4	0.0255	0.0013
678.02	0	13.28	-8.52	7.4	5.4	26.7	0.0255	0.0014
682.01	0	13.92	-5.35	5.8	0.8	85.4	0.0238	0.0002
684.01	0	13.83	-7.26	4.1	2.6	36.1	0.0246	0.0006
686.01	0	13.58	-4.36	3.5	0.1	96.8	0.0247	0.0000
693.01	0	13.95	-8.26	7.4	5.4	27.8	0.0244	0.0013
693.02	0	13.95	-8.09	7.0	4.9	29.6	0.0244	0.0012
695.01	0	13.44	-7.66	5.2	3.7	29.5	0.0251	0.0009
709.01	0	13.94	-7.57	6.6	4.2	36.8	0.0243	0.0010
717.01	0	13.39	-8.47	5.4	3.9	27.1	0.0251	0.0010
717.02	0	13.39	-9.90	8.4	6.9	17.3	0.0251	0.0017
739.01	0	15.49	-7.41	7.2	5.6	23.0	0.0256	0.0014
800.01	0	15.54	-7.22	24.2	19.3	20.3	0.0243	0.0047
800.02	0	15.54	-7.16	23.5	18.6	20.9	0.0243	0.0045
834.01	0	15.08	-5.84	6.8	2.9	57.4	0.0241	0.0007
834.02	0	15.08	-7.72	14.3	10.4	27.4	0.0241	0.0025
834.03	0	15.08	-8.35	17.4	13.5	22.5	0.0241	0.0033
834.04	0	15.08	-9.27	22.0	18.1	17.8	0.0241	0.0044
834.05	0	15.08	-8.11	16.2	12.3	24.2	0.0241	0.0030
884.01	0	15.07	-5.95	6.7	3.4	48.2	0.0242	0.0008
884.02	0	15.07	-6.02	6.9	3.7	46.6	0.0242	0.0009
884.03	0	15.07	-7.89	14.1	10.8	22.9	0.0242	0.0026
1096.01	0	14.71	-4.89	5.4	0.7	87.7	0.0234	0.0002
1174.01	1	13.45	-6.76	7.9	2.5	68.0	0.0252	0.0006
1236.01	0	13.66	-7.24	6.3	3.8	39.2	0.0246	0.0009
1236.02	0	13.66	-8.19	9.3	6.8	26.7	0.0246	0.0017
1236.03	0	13.66	-7.93	8.4	5.9	29.5	0.0246	0.0015
1268.01	0	14.81	-4.77	3.5	0.3	90.3	0.0239	0.0001
1353.01	0	13.96	-4.50	5.2	0.2	96.9	0.0235	0.0000
1353.02	0	13.96	-7.98	26.0	18.1	30.2	0.0235	0.0043
1356.01	0	15.21	-5.20	6.9	2.1	69.0	0.0240	0.0005
1421.01	0	15.30	-4.85	3.0	0.7	76.8	0.0250	0.0002
1426.01	0	14.23	-7.17	4.4	2.7	37.6	0.0246	0.0007

TABLE 5.7: continued.

Planet candidate	Type[a]	m_{kep} mag	Δm_{max} mag	$P_{BS,0}$ %	P_{BS} %	Improve %	P_{appEB} %	P_{BB} %
1426.02	0	14.23	-5.60	2.2	0.6	71.8	0.0246	0.0002
1426.03	0	14.23	-5.54	2.1	0.6	73.7	0.0246	0.0001
1452.01	1	13.63	-4.50	2.7	0.1	96.6	0.0246	0.0000
1477.01	0	15.92	-4.60	4.5	1.4	68.1	0.0256	0.0004
1529.01	0	14.31	-8.46	9.8	7.8	20.4	0.0241	0.0019
1529.02	0	14.31	-9.42	12.9	10.9	15.5	0.0241	0.0026
1546.01	1	14.46	-4.38	9.1	0.6	93.9	0.0226	0.0001
1596.01	0	15.16	-8.11	28.4	22.7	20.1	0.0237	0.0054
1596.02	0	15.16	-6.88	18.0	12.3	31.6	0.0237	0.0029
1684.01	0	12.85	-6.59	6.4	1.5	76.7	0.0283	0.0004
1701.01	0	11.04	-9.70	17.2	11.9	30.8	0.0453	0.0054
1725.01	1	13.50	-6.40	2.4	0.8	65.0	0.0250	0.0002
1779.01	0	13.30	-6.63	8.6	2.7	69.0	0.0259	0.0007
1779.02	0	13.30	-7.12	10.8	4.6	56.9	0.0259	0.0012
1781.01	1	12.23	-6.42	1.7	0.3	82.1	0.0292	0.0001
1781.02	1	12.23	-7.47	2.8	1.3	55.5	0.0292	0.0004
1781.03	1	12.23	-6.81	2.1	0.6	72.8	0.0292	0.0002
1800.01	0	12.39	-6.01	1.4	0.1	89.3	0.0280	0.0000
1802.01	1	13.35	-7.61	6.9	3.5	49.0	0.0254	0.0009
1805.01	0	13.83	-7.22	8.7	4.2	52.0	0.0242	0.0010
1805.02	0	13.83	-7.65	10.4	5.9	43.4	0.0242	0.0014
1805.03	0	13.83	-8.36	13.7	9.2	32.8	0.0242	0.0022
1894.01	0	13.43	-8.20	12.8	8.2	36.3	0.0253	0.0021
1925.01	0	9.44	-9.30	3.5	1.7	50.8	0.0490	0.0009
2042.01	0	13.09	-7.32	12.6	5.8	54.2	0.0271	0.0016
2133.01	0	12.49	-7.98	4.3	2.3	46.0	0.0283	0.0007
2260.01	0	12.17	-9.95	8.9	7.1	20.8	0.0303	0.0021
2324.01	1	11.67	-9.06	7.1	5.8	18.4	0.0351	0.0020
2352.01	0	10.42	-10.12	4.6	3.2	30.1	0.0409	0.0013
2352.02	0	10.42	-10.39	5.1	3.7	27.0	0.0409	0.0015
2352.03	0	10.42	-10.44	5.2	3.8	26.4	0.0409	0.0016
2545.01	0	11.75	-10.61	7.7	6.4	17.2	0.0312	0.0020
2593.01	0	11.71	-10.03	5.6	4.3	23.0	0.0306	0.0013
2632.01	0	11.39	-10.25	5.5	4.8	12.5	0.0323	0.0015
2640.01	0	13.23	-7.94	8.8	5.0	42.6	0.0259	0.0013
2674.01	0	13.35	-6.07	3.6	0.5	86.0	0.0254	0.0001
2674.02	0	13.35	-9.60	15.4	11.9	22.9	0.0254	0.0030
2674.03	0	13.35	-9.84	16.5	13.0	21.3	0.0254	0.0033
2712.01	0	11.12	-8.99	8.0	4.0	49.7	0.0419	0.0017
3179.01	0	10.88	-9.93	26.6	18.1	32.0	0.0486	0.0088
3203.01	0	11.82	-8.84	13.5	7.7	43.3	0.0371	0.0028
3206.01	0	11.84	-8.87	8.1	5.4	33.5	0.0345	0.0018
3237.01	0	12.32	-8.12	4.6	2.1	53.7	0.0294	0.0006
3444.01	1	13.69	-8.79	41.8	30.9	26.2	0.0242	0.0075
3444.02	1	13.69	-5.97	12.3	2.3	81.1	0.0242	0.0006
3444.03	1	13.69	-9.48	54.1	43.1	20.3	0.0242	0.0104
3554.01	0	15.21	-1.36	0.4	0.0	99.7	0.0246	0.0000
3560.01	0	11.82	-0.90	0.1	0.0	99.8	0.0376	0.0000
3728.01	0	12.25	-6.61	2.6	0.4	83.5	0.0304	0.0001
3742.01	0	14.96	-1.66	1.9	0.0	99.2	0.0228	0.0000
3765.01	0	16.44	-2.50	1.6	0.1	95.2	0.0263	0.0000

TABLE 5.7: continued.

Planet candidate	Type[a]	m_{kep} mag	Δm_{max} mag	$P_{BS,0}$ %	P_{BS} %	Improve %	P_{appEB} %	P_{BB} %
3801.01	0	16.00	-4.49	7.9	2.5	68.5	0.0251	0.0006
3853.01	0	10.63	-7.53	2.5	0.4	83.6	0.0437	0.0002
3890.01	0	13.23	-6.51	5.8	1.7	71.7	0.0261	0.0004
3925.01	0	14.03	-6.92	5.1	2.3	54.5	0.0242	0.0006
3925.02	0	14.03	-8.08	8.0	5.2	34.6	0.0242	0.0013
3925.03	0	14.03	-8.17	8.3	5.5	33.5	0.0242	0.0013
4016.01	1	14.07	-6.92	4.8	2.4	50.3	0.0243	0.0006
4351.01	0	15.00	-5.59	5.8	2.3	60.2	0.0241	0.0006
Demoted KOIs								
6.01	0	12.16	-8.13	14.3	8.3	42.1	0.0346	0.0029
1187.01	0	14.49	-6.44	10.6	4.7	55.6	0.0233	0.0011
1924.01	0	7.84	-10.29	4.7	3.2	32.9	0.0199	0.0006
3157.01	0	8.16	-9.70	1.3	1.0	22.1	0.0498	0.0005
3178.01	0	10.86	-6.40	2.1	0.1	93.2	0.0444	0.0001
3564.01	1	14.50	-1.51	0.2	0.0	99.2	0.0246	0.0000
3570.01	0	15.05	-1.66	1.2	0.0	99.5	0.0233	0.0000
3571.01	0	15.52	-0.91	0.7	0.0	99.7	0.0240	0.0000
3588.01	0	16.32	-0.83	0.6	0.0	99.8	0.0255	0.0000
3597.01	0	14.37	-2.47	1.7	0.0	99.5	0.0229	0.0000
3616.01	1	15.84	-3.65	7.6	1.3	82.8	0.0246	0.0003
3639.01	1	13.44	-3.63	1.8	0.0	98.2	0.0253	0.0000
3658.01	0	15.62	-3.71	5.8	0.0	100.0	0.0244	0.0000
3684.01	1	12.29	-2.57	0.2	0.0	99.0	0.0294	0.0000
3693.01	1	14.73	-5.60	9.8	3.3	66.0	0.0231	0.0008
3704.01	1	17.38	-1.51	2.2	0.1	97.1	0.0226	0.0000
3706.01	0	14.62	-0.52	0.2	0.0	100.0	0.0230	0.0000
3708.01	0	17.72	-0.74	2.5	0.0	99.8	0.0159	0.0000
3712.01	1	16.99	-1.99	2.8	0.1	97.0	0.0246	0.0000
3714.01	1	15.21	-4.71	4.4	0.9	79.4	0.0243	0.0002
3719.01	1	16.18	-3.49	4.2	1.0	76.5	0.0255	0.0003
3719.01	1	16.18	-3.49	4.2	1.0	76.6	0.0255	0.0003
3723.01	0	10.82	-6.66	4.5	3.0	34.2	0.0485	0.0014
3725.01	0	10.05	-6.67	2.6	0.3	89.3	0.0524	0.0001
3727.01	0	15.63	-5.37	8.0	3.3	59.1	0.0248	0.0008
3730.01	0	18.79	-0.84	1.9	0.8	56.4	-0.0023	-0.0000
3744.01	0	15.77	-4.91	6.6	2.2	66.9	0.0251	0.0005
3763.01	0	17.38	-0.68	0.9	0.0	100.0	0.0224	0.0000
3777.01	1	11.50	-7.52	9.0	1.9	78.8	0.0415	0.0008
3788.01	1	9.69	-8.87	3.1	1.2	60.7	0.0485	0.0006
3793.01	0	16.68	-3.26	3.0	0.6	81.6	0.0262	0.0001
3795.01	0	14.81	-0.76	0.3	0.0	99.9	0.0234	0.0000
3796.01	0	12.71	-6.80	5.8	1.6	72.7	0.0290	0.0005
3800.01	0	17.47	-3.48	7.0	4.2	40.1	0.0226	0.0009
3803.01	0	13.76	-6.61	8.0	2.6	67.6	0.0242	0.0006
3805.01	1	11.36	-4.77	1.3	0.0	96.3	0.0416	0.0000
3810.01	0	16.76	-3.48	2.8	0.8	72.7	0.0265	0.0002
3814.01	0	12.86	-7.33	11.1	5.1	54.2	0.0285	0.0014
3817.01	0	16.43	-4.54	15.7	6.3	59.7	0.0250	0.0016
3821.01	0	16.75	-4.03	6.9	2.5	63.3	0.0254	0.0006
3824.01	0	15.90	-5.26	8.2	3.8	53.8	0.0252	0.0010
3827.01	0	15.36	-5.35	14.8	5.6	62.0	0.0237	0.0013

TABLE 5.7: continued.

Planet candidate	Type[a]	m_{kep} mag	Δm_{max} mag	$P_{BS,0}$ %	P_{BS} %	Improve %	P_{appEB} %	P_{BB} %
3827.02	0	15.36	-5.41	15.2	6.0	60.4	0.0237	0.0014
3842.01	1	17.45	-0.87	1.0	0.0	100.0	0.0227	0.0000
3845.01	0	13.72	-6.36	6.0	1.4	75.9	0.0244	0.0004
3849.01	0	16.18	-4.03	4.4	1.1	73.9	0.0257	0.0003
3873.01	0	10.42	-5.55	0.7	0.0	94.6	0.0452	0.0000
3919.01	0	12.96	-7.68	8.5	3.8	55.0	0.0274	0.0010
3940.01	1	12.93	-7.31	11.0	4.0	63.9	0.0280	0.0011
3993.01	0	9.16	-7.99	1.3	0.9	32.5	0.0483	0.0004
3998.01	0	16.98	-4.28	18.7	9.0	52.2	0.0236	0.0021
4013.01	1	9.07	-10.63	6.5	5.5	16.6	0.0484	0.0026
4033.01	1	11.97	-7.18	3.0	0.7	76.7	0.0322	0.0002
4355.01	1	13.48	-7.83	17.9	9.8	45.3	0.0251	0.0025
4355.02	1	13.48	-7.85	18.1	10.0	44.9	0.0251	0.0025
4355.03	1	13.48	-7.57	16.0	7.9	50.7	0.0251	0.0020
4355.04	1	13.48	-8.10	20.2	12.1	40.2	0.0251	0.0030
4355.05	1	13.48	-7.38	14.8	6.7	54.8	0.0251	0.0017

Notes.

[a] $Type = 0$ for isolated KOIs (no companions within 6 arcsec from the host star) and $Type = 1$ for KOIs with at least one companion between 3-6 arcsec (see Table 5.5 for photometric information about the detected companions).

TABLE 5.8: Multiplicity results for the four main works on high-resolution imaging on the *Kepler* sample of candidates. We show the number of detected companions for different separation ranges. The lower part of the table shows the statistics regardless whether the KOI still hosts planet candidates. We have 56 KOIs that have been demoted in the latest *Kepler* releases and are not classified as planet hosts any longer. In the case of Howell et al. (2011), there are 24 demoted KOIs, there are 16 for Adams et al. (2012, 2013), and there are 17 for Law et al. (2014). These results are presented int the third section of this table.

Targets with remaining planet candidates (current valid KOIs)							
Study	Technique[a]	Observed	Isolated	0.0″-1.4″	0.0″-2.5″	0.0″-3.0″	3″-6″
Howell et al. 2011	speckle, opt	131	—	4 (3%)	—	—	—
Adams et al. 2012,2013	AO, near-IR	85	37 (44%)	12 (14%)	23 (27%)	28 (33%)	30 (35%)
Law et al. 2013	AO, opt	697	—	29 (4%)	49 (7%)	—	—
Lillo-Box et al. 2011-2013	lucky, opt	174	117 (67%)	9 (5%)	25 (14%)	30 (17%)	34 (20%)
All targets observed (valid and demoted KOIs)							
Study	Technique[a]	Observed	Isolated	0.0″-1.4″	0.0″-2.5″	0.0″-3.0″	3″-6″
Howell et al. 2011	speckle, opt	155	—	9	—	—	—
Adams et al. 2012,2013	AO, near-IR	101	45	16	28	34	36
Law et al. 2013	AO, opt	714	—	31	51	—	—
Lillo-Box et al. 2011-2013	lucky, opt	234	154	14	36	43	48
Demoted KOIs							
Study	Technique[a]	Observed	Isolated	0.0″-1.4″	0.0″-2.5″	0.0″-3.0″	3″-6″
Howell et al. 2011	speckle, opt	24	—	5	—	—	—
Adams et al. 2012,2013	AO, near-IR	16	8	4	5	6	6
Law et al. 2013	AO, opt	17	—	2	2	—	—
Lillo-Box et al. 2011-2013	lucky, opt	56	38	5	11	13	13

Notes.
[(a)] Technique and wavelength range (opt = optical, near-IR = near-infrared) used in the study.

TABLE 5.9: Summary of coincident KOIs in the main high-resolution surveys of the Kepler sample.

	Lillo-Box	Adams+12	Howell+11	Law+13
Lillo-Box	233	10	12	112
Adams+12		102	74	66
Howell+11			156	85
Law+13				714

TABLE 5.10: Comparison between the improvements in the BSC parameter (in %) obtained by using the H11 (Howell et al., 2011), the A12 (Adams et al., 2012), and our high-resolution images (LB14) for all planet candidates involved (28 in H11 and 27 in A12). In all cases, the BSC has been improved with respect to the speckle images and the A12 study. Note that the common target KOI-0623 to H11 is not presented here because we detected a stellar companion closer than 3 arcsec. The small improvement of the H11 study is mostly due to the reduced field of view, which avoids detection of 1.5-3.0 arcsec companions, where the probability of having a background source is maximum in the 0-3 arcsec range.

Planet candidate	$P_{BS,0}$ %	P_{BS} (%) H11	A12	LB14	Planet candidate	$P_{BS,0}$ %	P_{BS} (%) H11	A12	LB14
41.01	6.10	5.9	4.3	1.9 111.04	13.00	12.6	8.0	9.9	
41.02	10.10	9.9	8.2	5.8	115.01	4.50	-	2.5	1.9
41.03	9.40	9.2	7.6	5.2	115.02	7.40	-	5.4	4.8
49.01	8.10	7.4	-	3.4	115.03	14.80	-	12.8	12.2
69.01	4.10	4.0	2.0	1.5	196.01	4.00	2.8	-	0.4
82.01	1.30	1.2	0.4	0.2	245.01	0.90	0.9	0.3	0.1
82.02	2.50	2.4	1.5	1.0	245.02	2.30	2.3	1.7	1.3
82.03	3.10	3.0	2.1	1.6	245.03	5.30	5.3	4.7	4.2
82.04	4.20	4.1	3.2	2.7	245.04	4.10	4.1	3.5	3.1
82.05	5.30	5.2	4.3	3.8	366.01	2.40	2.0	-	0.7
94.01	3.70	3.1	0.9	0.3	372.01	4.20	3.4	0.2	0.8
94.02	10.60	10.0	6.5	4.1	398.01	3.80	2.5	-	0.9
94.03	6.80	6.2	2.7	1.2	398.02	8.50	7.2	-	5.4
94.04	23.80	23.2	19.7	17.2	398.03	13.50	12.2	-	10.4
111.01	5.40	5.1	0.9	2.3	638.01	15.20	-	3.2	8.8
111.02	5.60	5.3	1.0	2.6	638.02	14.60	-	2.7	8.3
111.03	4.90	4.6	0.7	1.9					

TABLE 5.11: Comparison between the blended source probabilities (P_{BS}, in %) obtained by using the L13 (Law et al., 2014) and our high-resolution images (LB14) for coincident planet candidates (167 in total).

Planet candidate	$P_{BS,0}$ (%)	P_{BS} (%) L13	LB14	Planet candidate	$P_{BS,0}$ (%)	P_{BS} (%) L13	LB14	Planet candidate	$P_{BS,0}$ (%)	P_{BS} (%) L13	LB14
12.01	1.80	0.0	0.7	416.02	6.90	5.9	4.1	709.01	6.60	5.2	4.2
41.01	6.10	4.6	1.9	416.03	15.50	14.5	12.7	717.01	5.40	4.6	3.9
41.02	10.10	8.5	5.8	431.01	4.00	2.9	2.4	717.02	8.40	7.7	6.9
41.03	9.40	7.9	5.2	431.02	4.50	3.4	2.9	739.01	7.20	5.3	5.6
49.01	8.10	7.1	3.4	435.01	5.80	4.9	3.3	800.01	24.20	20.6	19.3
69.01	4.10	3.1	1.5	435.02	2.60	1.6	0.3	800.02	23.50	20.0	18.6
82.01	1.30	0.6	0.2	435.03	8.50	7.5	5.9	834.01	6.80	5.1	2.9
82.02	2.50	1.8	1.0	435.04	11.50	10.5	8.9	834.02	14.30	12.6	10.4
82.03	3.10	2.4	1.6	435.05	7.40	6.4	4.9	834.03	17.40	15.7	13.5
82.04	4.20	3.5	2.7	435.06	12.30	11.3	9.7	834.04	22.00	20.3	18.1
82.05	5.30	4.6	3.8	463.01	17.90	10.7	9.0	834.05	16.20	14.5	12.3
94.01	3.70	1.9	0.3	478.01	10.20	2.5	6.0	884.01	6.70	5.1	3.4
94.02	10.60	8.8	4.1	481.01	10.10	7.5	7.0	884.02	6.90	5.3	3.7
94.03	6.80	5.0	1.2	481.02	13.80	11.1	10.6	884.03	14.10	12.5	10.8
94.04	23.80	22.0	17.2	481.03	9.70	7.1	6.6	1230.01	4.10	0.02	0.2
111.01	5.40	4.5	2.3	528.01	7.50	6.6	5.3	1236.01	6.30	5.5	3.8
111.02	5.60	4.7	2.6	528.02	6.60	5.6	4.3	1236.02	9.30	8.5	6.8
111.03	4.90	4.1	1.9	528.03	7.40	6.5	5.2	1236.03	8.40	7.6	5.9
111.04	13.00	12.1	9.9	534.01	19.10	14.7	14.3	1353.01	5.20	0.8	0.2
115.01	4.50	3.7	1.9	534.02	24.00	19.6	19.2	1353.02	26.00	21.6	18.1
115.02	7.40	6.6	4.8	561.01	5.80	4.7	4.2	1426.01	4.40	3.3	2.7
115.03	14.80	13.9	12.2	564.01	21.90	19.3	15.6	1426.02	2.20	1.1	0.6
139.01	3.90	3.0	0.9	564.02	9.70	7.1	3.5	1426.03	2.10	1.0	0.6
139.02	15.20	14.3	12.0	564.03	35.60	33.0	29.3	1452.01	2.70	0.4	0.1
149.01	6.00	5.3	2.6	567.01	12.70	9.9	8.6	1529.01	9.80	6.3	7.8
152.01	13.60	10.9	3.3	567.02	14.70	11.9	10.6	1529.02	12.90	9.4	10.9
152.02	25.10	22.4	14.4	567.03	13.80	10.9	9.7	1596.01	28.40	25.5	22.7
152.03	26.60	24.0	16.0	571.01	28.10	14.0	20.1	1596.02	18.00	15.1	12.3
152.04	31.30	28.7	20.7	571.02	26.00	11.8	17.9	1684.01	6.40	1.9	1.5
156.01	9.90	5.5	6.2	571.03	32.40	18.2	24.4	1701.01	17.20	14.7	11.9
156.02	12.40	8.0	8.7	571.04	27.90	13.7	19.8	1725.01	2.40	1.6	0.8
156.03	6.70	2.4	3.0	571.05	33.20	19.1	25.2	1779.01	8.60	7.4	2.7
191.01	6.80	3.4	0.8	579.01	10.70	8.9	7.8	1779.02	10.80	9.6	4.6
191.02	28.00	24.6	21.5	579.02	10.50	8.8	7.7	1781.01	1.70	0.4	0.3
191.03	43.50	40.1	36.9	611.01	11.80	6.1	2.9	1781.02	2.80	1.5	1.3
191.04	28.20	24.8	21.6	624.01	10.80	8.5	5.2	1781.03	2.10	0.7	0.6
209.01	2.80	1.2	0.6	624.02	11.00	8.7	5.3	1802.01	6.90	5.6	3.5
209.02	4.30	2.7	1.9	624.03	17.70	15.4	12.1	1805.01	8.70	6.6	4.2
211.01	3.10	1.9	0.6	625.01	5.70	4.2	3.2	1805.02	10.40	8.3	5.9
238.01	23.90	19.5	16.4	632.01	13.00	11.3	9.9	1805.03	13.70	11.7	9.2
238.02	39.00	34.6	31.5	638.01	15.20	11.5	8.8	1812.01	7.30	5.3	3.1
330.01	16.30	10.7	11.9	638.02	14.60	11.0	8.3	1894.01	12.80	8.3	8.2
330.02	29.00	23.3	24.6	640.01	21.10	19.2	10.8	1924.01	4.70	4.4	3.2
339.01	7.10	6.0	5.1	650.01	8.60	6.7	7.4	1925.01	3.50	3.0	1.7
339.02	7.20	6.1	5.2	654.01	8.40	7.0	6.5	2042.01	12.60	11.3	5.8
339.03	7.40	6.3	5.4	654.02	9.10	7.7	7.1	2133.01	4.30	3.7	2.3
345.01	3.30	2.4	2.2	659.01	15.20	13.1	10.0	2260.01	8.90	7.5	7.1
349.01	5.10	2.8	3.2	664.01	15.80	13.8	11.8	2352.01	4.60	4.0	3.2
366.01	2.40	0.04	0.7	664.02	21.50	19.5	17.5	2352.02	5.10	4.5	3.7
372.01	4.20	0.01	0.8	664.03	21.20	19.3	17.3	2352.03	5.20	4.7	3.8
385.01	19.00	16.4	16.1	676.01	5.50	0.2	2.0	2481.01	16.60	13.1	10.0
386.01	16.70	14.7	9.9	676.02	7.40	1.9	3.8	2545.01	7.70	6.7	6.4
386.02	18.90	16.9	12.0	682.01	5.80	2.6	0.8	2593.01	5.60	4.8	4.3
388.01	8.40	7.1	6.1	684.01	4.10	3.1	2.6	2632.01	5.50	4.7	4.8
393.01	23.60	22.0	17.4	686.01	3.50	0.3	0.1	2640.01	8.80	7.3	5.0
416.01	6.00	5.0	3.1	695.01	5.20	4.2	3.7				

TABLE 5.12: Derived properties of the Kepler-37 planetary system.

Parameter	Kepler-37b	Kepler-37c	Kepler-37d
R_p ($R_\oplus$)	$0.303^{+0.053}_{-0.073}$	$0.742^{+0.065}_{-0.083}$	$1.99^{+0.11}_{-0.14}$
Period (days)	$13.367308^{+0.000058}_{-0.000085}$	$21.301886^{+0.000046}_{-0.000044}$	$39.792187^{+0.000040}_{-0.000043}$
i (deg)	$88.63^{+0.30}_{-0.53}$	$89.07^{+0.19}_{-0.33}$	$89.335^{0.043}_{0.047}$
a (AU)	$0.1003^{+0.0008}_{-0.0011}$	$0.1368^{+0.0011}_{-0.0014}$	$0.2076^{+0.0016}_{-0.0022}$
Depth (ppm)	$11.9^{+2.6}_{-3.1}$	$81.1^{+2.6}_{-2.9}$	$574.9^{+3.2}_{-3.5}$

Chapter 6

Confirming the planetary nature of transiting candidates: radial velocity and light curve modulations

Contents

Outline and authored publications related to this chapter

In this chapter we present the results concerning the confirmation of planetary systems in the *Kepler* sample by using radial velocity observations and light curve modulations. We describe the selected targets and the general characteristics of the radial velocity observations in section § 6.1. The subsequent sections describe in more detail our results for particular systems, namely Kepler-91 (§ 6.2), Kepler-432 (§ 6.3), Kepler-447 (§ 6.4), KOI-372 (§ 6.5), the analysis of some false positives and fast rotators found in our selected sample (§ 6.6), the preliminary results of yet not finished analysis of some of the targets (§ 6.7), and the analysis of light curve modulations of a sample of substellar companions in the brown dwarf/planetary-mass domain (§ 6.8). The work presented in this chapter was done in close collaboration with Thomas Henning, Luigi Mancini, and Simona Ciceri from the MPIA, with the additional cooperation of Nuno Santos and Pedro Figueira from CAUP. The results have been published in different refereed papers, namely Kepler-91 (Lillo-Box et al., 2014b,c), Kepler-432 (Ciceri et al., 2015), Kepler-447 (Lillo-Box et al., 2015b), KOI-372 (Mancini et al., 2015, in prep., in preparation), substellar companions (Lillo-Box et al., 2015c, in preparation), and the binaries and fast rotators (Lillo-Box et al., 2015a).

6.1 Description of the CAB-MPIA survey

6.1.1 Motivations and target selection

The main goal of the *Kepler* mission was to detect the first Earth-like planet in the habitable zone of a Sun-like star. For this reason, most of the high-precision radial velocity efforts from the follow-up program (by using the highest-resolution spectrographs like HARPS-N/TNG or

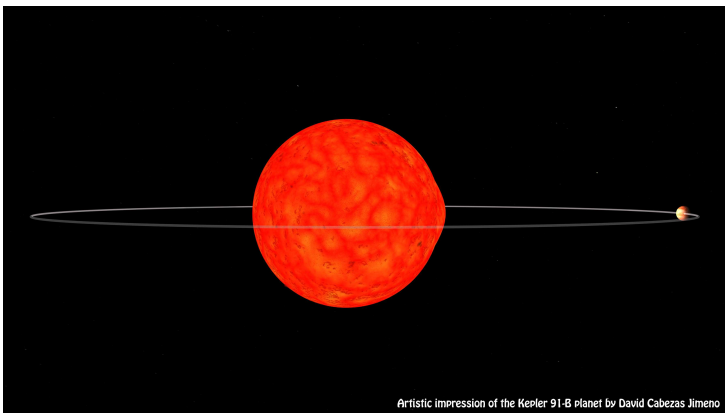

FIGURE 6.1: Artistic view of the Kepler-91 planetary system. The planet is not to scale but the size of the star is proportional to the planet separation. Credit: David Cabezas Jimeno.

HIRES/Keck) have been focused on the smallest candidates orbiting around main-sequence stars. Complementarily, we have focused on the sample of giant planets orbiting stars at different evolutionary stages, from main-sequence hosts to stars ascending the red giant branch close to the Helium-flash. These targets have radial velocity amplitudes typically larger than several tens of m/s, which is clearly feasible with CAFE. We selected the targets accomplishing the following criteria:

- **Target is isolated.-** The main source of targets for this part of the project is the isolated sample of candidates found by our high-spatial resolution survey presented in Chapter 5. However, due to strategic reasons, we also selected some targets for which close (but negligible) stellar companions were detected. Additionally, we selected other targets not observed in our AstraLux survey but having publicly available high-spatial resolution images at the CFOP obtained by other groups.
- **Detectable RV.-** The expected radial velocity semi-amplitude must be detectable with CAFE. We estimated this value by assuming the stellar masses provided by the CFOP at the moment of starting the observations and assuming Jupiter-like densities for candidates with derived radius larger than 8 $R_\oplus$ and Neptune-like density for those showing radius in the range $3 - 8\ R_\oplus$.
- **Magnitude limit.-** According to the commissioning data, targets with magnitudes above $m_{\rm Kep} > 14$ are not suitable for CAFE for planet-detection purposes. Those targets would require exposure times longer than 2-hours to achieve the necessary S/N for precise RV. In absence of an exposuremeter, this long exposures can importantly diminish the RV precision and accuracy.

In total, we have being following 32 planet candidates transiting 30 host stars, including two multiple systems (KOI-338 and KOI-972). The derived properties of these candidates, as determined by the *Kepler* team (Batalha et al., 2013, Borucki et al., 2010, Burke et al., 2014), are

summarized in Table 6.1. The selected targets were observed with CAFE in a long baseline of more than two years (from 2012 to 2014) divided in several runs of few days each. This has allowed us to follow from very short-period candidates (such as Kepler-91) to very long-period objects of several hundreds of days (like KOI-375), as shown in Table 6.1. The phase coverage of our RV observations, the number of spectra acquired per target, and the status and publications for each of the 32 planet candidates is summarized in Table 6.2. In the "Disposition" column of this table, we also show the current status of the different targets, being FP = False Positive, PC = Planet Candidate, FR = Fast Rotator, HS = Hot Star, Confirmed = planet confirmed by the publication stated in the last column, Confirmed? = planet confirmed in our preliminary analysis, Validated = planet statistically validated, EB = Eclipsing Binary as established by the publication in the last column.

Since our observations started right after the delivery of the candidates by the *Kepler* team, in some cases no reconnaissance spectra had yet been taken by the *Kepler* follow-up observing program (KFOP). Thus, we lacked information about the effective temperature or rotational velocity of the star. This is the reason why some of the targets were discarded after the first spectra were taken. After the reduction, some of them presented large rotational velocities ($v \sin i > 20$ km/s), what prevented precise RV analysis. This was the case of KOI-12, KOI-131, KOI-366, KOI-625, KOI-972, KOI-3728. However, the observations of these fast rotators were used to set upper limits to their masses (see § 6.6.3). Others showed large radial velocity variations indicating a stellar nature for the comapanion. These targets are also analyzed in § 6.6.4.

Added to this, after having obtained several CAFE spectra, the nature of four of the targets being followed in this project was established by other groups. We briefly summarize these results:

- **KOI-338 (Kepler-141).-** The two close-in giant planets orbiting this star were validated by Rowe et al. (2014).
- **KOI-368.-** The transiting object orbiting this hot ($T_{\rm eff} \sim 9000\,K$) and fast rotating ($v \sin i \sim$ 90 km/s) star was suggested to be an M-dwarf by Zhou & Huang (2013) according to the analysis of the secondary eclipse. Given this high temperature, few spectral lines are available, which prevents any RV analysis. Its spin-orbit misalignment has also been a matter of debate by other authors (Ahlers et al., 2014).
- **KOI-977.-** This candidate was stablished as a false positive by Hirano et al. (2015). Their results show that this is a triple system with a giant star ($R_\star > 20\,R_\odot$) and an eclipsing binary consisting on a sun-like and a later-type star displaying ellipsoidal variations. However, theur results are not yet conclusive and more work on this system is still needed.

- **KOI-1894.-** The planetary nature of this candidate was established by Sato et al. (2015) at the $\sim 2-3\sigma$ level by using radial velocity and REB analysis. This lead the authors to put an upper-limit to the mass of the transiting planet of 0.39 $M_{\rm Jup}$.

An additional sample of several KOIs were selected because we found REB modulations in the *Kepler* light curves compatible with the presence of planetary-mass or substellar companions (i.e., with amplitudes for this modulations < 300 ppm). The light curve of some of these targets is preliminary analyzed in 6.8; and RV observations are currently ongoing. The properties of the this sample are presented in Table 6.3.

6.1.2 Observations and data reduction

The development of this survey has gone hand-in-hand with our understanding of the CAFE instrument and its peculiarities. In Chapter 4, we already explained the characteristics of the instrument, the improvements suggested by our team (and implemented by the observatory), and the analysis of the RV standard stars. Taking this peculiarities into account, the typical observational strategy in a given night consisted on:

- Getting several tens of calibration frames (bias, flats, arcs) during the evening (usually 30 bias, 30 flats and 30-50 arcs).
- Observing radial velocity standards. We usually observed two to three standards (the same ones along the 3-years baseline, namely HD109358, HD124292, and HD182488) before starting the scientific observations. This allowed us to monitor RV jumps in the different CAFE windows (see section § 4.4.4).
- Observing the scientific targets. Since the selected targets had magnitudes in the range 12-14 mag, long-exposure times were needed to achieve the necessary S/N. Owing to avoid a large number of cosmic ray hits on the CCD, vigneting of the telescope, or guiding problems, we split the whole exposure time in different frames of maximum exposure time of 2700 s. Usually, one to three frames per target were obtained depending on the magnitude of the targets and the atmospheric conditions (extinction, seeing, etc.). Also, arc frames were taken before and after the target to wavelength calibrate the spectrum.
- Getting calibration frames at the end of the night. The same set of calibration frames as that obtained during the evening were also obtained at the end of the night.

The reduction of the scientific frames was performed by following the steps explained in section § 4.4.2. In the following sections, we present the different results obtained for the selected targets.

TABLE 6.1: Ancillary information from selected targets for RV follow-up (32 planets around 30 hosts).

KOI	Kepler-ID	KIC	Planet	Disp.	Method	RA (hours)	Dec (deg)	Period (days)	$R_p/R_\star$	a (AU)	R_p ($R_\oplus$)	$T_{\rm eff}$ (K)	log g cgs	$R_\star$ ($R_\odot$)	$M_\star$ ($M_\odot$)	$m_{\rm Kep}$ mag
12		5812701	.01	PC(FR)	RV	19:49:48.9	41:00:39	17.855219698	0.0883	0.1463	14.63	6635	4.193	1.516	1.3120	11.353
131		7778437	.01	PC(FR)	RV	19:56:23.41	43:29:51	5.014234575	0.0758	0.0629	10.53	6475	4.349	1.271	1.3140	13.797
338	Kepler-141	10552611	.01	Validated	RV	19:51:53.01	47:43:54	7.010627450	0.0186	0.0703	38.6	4173	1.857	18.939	0.9410	13.448
338	Kepler-141	10552611	.02	Validated	RV	19:51:53.01	47:43:54	3.107638730	0.0078	0.0409	16.16	4173	1.857	18.939	0.9410	13.448
340		10616571	.01	EB	RV	19:50:39.52	47:48:05	23.673092809	0.1427	0.1669	18.44	5774	4.335	1.183	1.1030	13.057
366		3545478	.01	PC(FR)	RV	19:26:39.4	38:37:09	75.112218740	0.0636	0.4156	23.3	6201	3.616	3.354	1.6940	11.714
368		6603043	.01	PC	RV	19:23:25.1	42:05:12	110.321654340	0.0842	0.5832	18.79	9274	4.154	2.043	2.1720	11.375
371		5652983	.01	EB	RV	19:58:42.28	40:51:23	498.391140000	0.0553	1.4223	19.37	5198	3.614	3.207	1.5520	12.193
372		6471021	.01	Confirmed	RV	19:56:29.38	41:52:00	125.628876210	0.0816	0.4899	8	5838	4.529	0.897	0.9920	12.391
375		12356617	.01	Confirmed?	RV	19:24:48.29	51:08:39	988.881117700	0.0639	2.0091	10.81	5755	4.101	1.549	1.1050	13.293
625		4449034	.01	PC(FR)	RV	19:06:15.31	39:32:04	38.138530840	0.8775	0.2514	224.53	6481	3.861	2.343	1.4560	13.592
684		7730747	.01	PC	RV	18:45:09.67	43:24:48	4.034914596	0.0385	0.0509	7.56	5548	3.964	1.793	1.0790	13.831
686		7906882	.01	EB	RV	19:47:21.78	43:38:49	52.513546589	0.1177	0.2594	11.38	5559	4.470	0.885	0.8450	13.579
972		11013201	.01	PC(FR)	RV	18:48:00.07	48:32:32	13.118966756	0.0178	0.1376	8.28	7221	3.488	4.240	2.0180	9.275
972		11013201	.02	PC(FR)	RV	18:48:00.07	48:32:32	7.821931080	0.0053	0.0975	2.47	7221	3.488	4.240	2.0180	9.275
977		11192141	.01	PC	RV	19:30:52.71	48:51:07	1.353770439	0.2254	0.0234	387.97	4283	2.012	15.76	0.9310	10.523
1020		2309719	.01	PC	RV	19:31:43.4	37:36:23	54.356370780	0.2139	0.283	33.13	6058	4.144	1.418	1.0230	12.899
1032		2162635	.01	Confirmed?	RV	19:27:54.61	37:31:57	1500.140677200	0.0735	2.634	18.35	5009	3.755	2.283	1.0830	13.862
1299	Kepler-432	10864656	.01	Confirmed	RV	19:33:07.73	48:17:09	52.501076800	0.0272	0.3036	12.39	4995	3.331	4.160	1.3530	12.183
1463		7672940	.01	EB?	RV	19:13:02.07	43:22:35	1064.268141000	0.1422	2.1525	33.75	6340	3.833	2.173	1.1740	12.328
1800	Kepler-447	11017901	.01	Confirmed	RV	19:01:04.46	48:33:36	7.794301316	0.0636	0.0704	6.06	5555	4.440	0.872	0.7640	12.394
1894		11673802	.01	PC	RV	19:49:26.23	49:47:51	5.287897870	0.0171	0.0665	7.09	4992	3.428	3.790	1.4100	13.427
2133	Kepler-91	8219268	.01	Confirmed	RV+REB	19:02:41.49	44:07:00	6.246680050	0.0215	0.0733	15.39	4605	2.936	6.528	1.3440	12.495
2481		4476423	.01	Confirmed?	RV	19:39:07.76	39:35:47	33.854258600	0.0139	0.2402	15.96	4553	2.605	10.47	1.6160	13.605
3725		3459199	.01	FP	RV	19:40:48.69	38:31:10	1.570518040	0.2848	0.036	480.77	5102	2.462	15.46	2.5220	10.055
3728		7515679	.01	FP(FR)	RV+REB	19:11:13.73	43:11:19	5.546083665	0.0459	0.078	20.24	7358	3.538	4.037	2.0540	12.252
3788		9405541	.01	FP	RV	19:29:45.43	45:57:08	5.552645413	0.0574	0.0649	776.04	3314	0.326	123.7	1.1060	9.687
3853		2697935	.01	FP?	RV	19:09:52.29	37:57:59	21.513071730	92.429	0.1755	48558.7	5081	3.265	4.811	1.5540	10.630
3873		8430105	.01	FP	RV	19:26:14.07	44:29:17	63.328904200	0.0534	0.3844	54.23	5143	2.777	9.294	1.8840	10.420
3890		8564976	.01	EB?	RV	19:35:05.31	44:38:18	152.827700000	0.0393	0.676	32.24	4991	2.933	7.506	1.7610	13.226
3919		4649440	.01	FP	RV	19:20:33.05	39:45:54	19.370696930	0.6536	0.1747	359.53	5301	3.311	5.037	1.8930	12.956
5684		9475697	.01	Confirmed?	RV	19:43:29.5	46:00:52	206.801125	0.0258	0.9381	24.34	5048	2.978	8.611	2.5710	11.128

TABLE 6.2: Status of the planet candidates followed-up with CAFE.

KOI	Planet	Kepler-ID	Disp.	Phase coverage	Comments	Sect.	Publication
12	.01		PC(FR)			§ 6.6.3	**Lillo-Box et al. (2015a)**
131	.01		PC(FR)			§ 6.6.3	**Lillo-Box et al. (2015a)**
338	.01	Kepler-141b	Validated			§ 6.1.1	Rowe et al. (2014)
338	.02	Kepler-141c	Validated			§ 6.1.1	Rowe et al. (2014)
340	.01		EB			§ 6.6.4	**Lillo-Box et al. (2015a)**
366	.01		PC(FR)			§ 6.6.3	**Lillo-Box et al. (2015a)**
368	.01		FP?(HS,FR)		A-type host, M-dwarf companion	§ 6.1.1	Zhou et al. (2013)
371	.01		EB			§ 6.6.4	**Lillo-Box et al. (2015a)**
372	.01		Confirmed			§ 6.5	**Mancini et al. (2015)**
375	.01		Confirmed?		Possible detection	§ 6.7	-
625	.01		PC(FR)			§ 6.6.3	**Lillo-Box et al. (2015a)**
684	.01		Confirmed?		RV rms= 37 m/s	§ 6.7	-
686	.01		EB			§ 6.6.4	**Lillo-Box et al. (2015a)**
972	.01		PC(FR)			§ 6.6.3	**Lillo-Box et al. (2015a)**
972	.02		PC(FR)			§ 6.6.3	**Lillo-Box et al. (2015a)**
977	.01		FP?			§ 6.1.1	Hirano et al. (2015)
1020	.01		FP		Double-lined CCF	§ 6.7	**Uploaded on CFOP**
1032	.01		Confirmed?		Possible detection	§ 6.7	-
1299	.01	Kepler-432b	Confirmed			§ 6.3	**Ciceri et al. (2015)**
1463	.01		EB?			§ 6.6.4	**Lillo-Box et al. (2015a)**
1800	.01	Kepler-447b	Confirmed			§ 6.4	**Lillo-Box et al. (2015b)**
1894	.01		Confirmed			§ 6.1.1	Sato et al. (2015)
2133	.01	Kepler-91b	Confirmed			§ 6.2	**Lillo-Box et al. (2014a,c)**
2481	.01		Confirmed?		Detection of a third object	§ 6.7	**Lillo-Box et al. (2015d, in prep.)**
3725	.01		EB			§ 6.6.4	**Lillo-Box et al. (2015a)**
3728	.01		FP(FR)		Brown dwarf	§ 6.6.3	**Lillo-Box et al. (2015a)**
3788	.01		FP		It was "not-dispositioned"	-	-
3853	.01		FP?		Heartbeat signal	§ 6.6.5	**Lillo-Box et al. (2015a)**
3873	.01		FP		It was "not-dispositioned"	§ 6.1.1	-
3890	.01		EB?			§ 6.6.4	**Lillo-Box et al. (2015a)**
3919	.01		FP?		RV rms= 40 m/s	§ 6.7	-
5684	.01		Confirmed?		Possible detection	§ 6.7	-

Notes. The phase coverage column indicates which region of the orbital phase (from 0 to 1 in steps of 0.1) have been observed with CAFE (green). Additional runs are approved in semester 2015A and further runs are requested for 2015B. Bold face in the "Publication" column highlight the works in which we have participated.

TABLE 6.3: Ancillary information from selected targets for the study of REB modulations. Data obtained from the CFOP (uncertainties are not provided for clarity reasons).

KOI	Kepler-ID	KIC	Planet	Disp.	Method	RA (hours)	Dec (deg)	Period (days)	$R_p/R_\star$	a (AU)	R_p ($R_\oplus$)	$T_{\rm eff}$ (K)	$\log g$ cgs	$R_\star$ ($R_\odot$)	$M_\star$ ($M_\odot$)	$m_{\rm Kep}$ mag
554		5443837	.01	PC	REB	19:21:24.27	40:41:13	3.658494470	0.0731	0.0476	7.96	6108	4.471	0.997	1.072	14.545
1074		10272640	.01	PC	REB	19:25:06.15	47:19:46	3.770552098	0.1084	0.0486	13.01	6302	4.388	1.098	1.07	15.439
1546		5475431	.01	PC	REB	19:54:03.29	40:38:22	0.917569588	0.1253	0.0186	12.22	5713	4.541	0.893	1.01	14.456
3728		7515679	.01	PC	REB	19:11:13.73	43:11:19	5.546083665	0.04592	0.078	20.24	7358	3.538	4.037	2.054	12.252
3886		8848288	.01	PC	REB	20:04:11.35	45:05:15	5.566506330	0.0253	0.0786	34.67	4781	2.562	12.53	2.088	9.837
5220		5986270	.01	PC	REB	19:53:31.3	41:17:47	1.534680255	0.0192	0.0344	31.85	4961	3.5	4.47	2.3090	12.224
5713		9780149	.01	PC	REB	19:42:24.62	46:31:03	2.506027000	0.3600	0.0352	50.95	5780	4.438	1.000	1.00	12.294

6.2 Kepler-91 b: a planet at the end of its life

In this section we present the observations, analysis, and discussion involving the confirmation and characterization of the extrasolar planet Kepler-91b. This work was published in Lillo-Box et al. (2014a) and Lillo-Box et al. (2014c).

6.2.1 Context

We present the confirmation of the planetary nature of the extrasolar planet Kepler-91 b (KOI-2133, KIC 8219268), a close-in giant planet orbiting a K3III star ascending the red giant branch (RGB). We achieve this confirmation by exploiting the high-precision photometry provided by the *Kepler* mission (Borucki et al., 2010) and analyzing the radial velocity data obtained with CAFE. The accuracy of the *Kepler* light curve allows us to detect small variations (of the order tens of parts per million) in the out-of transit signal of the host star. These light curve modulations are caused by the combination of three main factors already presented in § 2.3, namely the reflected light from the planet, the ellipsoidal variations, and the Doppler beaming. The theory and equations involving these effects are described in § 2.3. The *Kepler* light curve also showed stellar pulsations that are crucial to obtain accurate parameters for the host star by using the asteroseismology (see section § 2.4). The radial velocity data allowed a cross-validation of the planetary-mass of the transiting object.

We analyze all the available data to firmly conclude that the transiting object is a very close-in hot-Jupiter planet in a stage previous to be engulfed by its host star.

6.2.2 Observations

***Kepler* photometry.-** We used the PDCSAP fluxes provided by the *Kepler* MAST.[1] Neither light curve detrending nor outlier rejection were necessary in this case. But, in order to check how these corrections could improve the quality of our data, we applied an iterative rejection process. First, the entire dataset has been split into continuous sections (i.e., regions without temporal gaps). Each section was then fitted with a fifth-degree polynomial. Typical duration of the different sections are around 25-30 days (roughly one third of a *Kepler* quarter). Then, we divided the data by this fitted model and removed those points above 3σ. We iterated this process until no further outliers were detected. While the standard deviation of the raw PDCSAP flux ($\approx$ 1152 days) is $\sigma_{\rm raw}$ = 400 ppm, the cleaned light curve yields $\sigma_{\rm cleaned}$ = 380 ppm. Since the improvement is below 5%, we preferred not to apply any correction to the PDCSAP flux to prevent possible artificially added trends.

[1] https://archive.stsci.edu/kepler/

High-spatial-resolution imaging.- We observed Kepler-91 as part of our high-spatial resolution imaging survey explained in Chapter § 5. The observations were performed on May 25, 2012, with a mean seeing of 0.8 arcsec. We obtained 30 000 images of 50 ms exposure time in the full CCD array of the camera (24×24 arcsec^2). Data reduction and analysis were done by following the procedures explained in Chapters 2 and 5. The calculated probability of an undetected blended source in this high-spatial resolution image is $P_{BS} = 2.3\%$ (BSC= 97.7%). This implies a probability for the presence of an eclipsing binary able to mimic the planetary transit of Kepler-91b of $P_{\rm BGEB} = 0.0007\%$. The only relevant configuration that could mimic a planetary transit and cannot be rejected by our high-spatial resolution images is a diluted binary in a triple system. However, Morton & Johnson (2011a) provide an estimation of the probability for a given transit depth, period, and primary mass that such eclipse is produced by a hierarchical triple system. The authors conclude that for a given system with a one solar-mass primary star and a ten-days orbital period (similar to our system), the probability of such an appropriate hierarchical triple system is of the order of 0.001 % for diluted eclipse depths in the range 100 – 20 000 ppm. Thus, with these considerations, we can assume that Kepler-91 is isolated, and neither its light curve nor its radial velocity are affected by a close companion or a chance-aligned object along the line of sight.

High-resolution spectroscopy.- High-resolution spectra were collected with CAFE during the *Kepler* observing window of May-July 2012. The exposure time for Kepler-91, a $m_{\rm Kep} = 12.5$ mag giant (spectral type K3 III), was set between 1800 s and 2700 s, depending on the weather conditions (seeing, atmospheric transparency, etc.). We typically obtained from two to three spectra per night for this object. In total, 40 spectra were acquired in 20 nights, with a median S/N of 11. The spectra were reduced by using the observatory pipeline (see section § 4.4.2). The data presented here were taken during the earlier periods of operations of the instrument, when the thermal and vibrational control systems were still not fully operational. The radial velocity data were extracted by using the template matching technique, following the alternative approach to CCF explained in § 4.3.5. The combination of all spectra provided a high-resolution and high S/N spectrum of the target, that is used to derive the stellar properties.

6.2.3 Analysis

6.2.3.1 Properties of the host star

In the characterization of exoplanet properties, it is crucial to obtain the most accurate host-star parameters (radius, mass, effective temperature, age, etc.). The inference of both orbital and physical properties of the planet strongly depends on how well the stellar parameters are known (Seager & Mallén-Ornelas, 2003). We have used our wealth of data on Kepler-91 to accurately determine these physical parameters following independent methods: model fit to the spectral

energy distribution (SED), model fitting the high S/N spectrum, individual characterization of particular spectral lines, asteroseismology, and comparison with isochrones and evolutionary tracks. Table 6.4 provides a summary of all stellar parameters derived by these methods. Descriptions of each of them follows.

TABLE 6.4: Summary of the results for the host star properties from the different methods explained in section § 6.2.3.1.

Ref.	$M_*(M_\odot)$	$R_*(R_\odot)$	$\log g$	ρ (kg/m^3)	[Fe/H]^b	$T_{\rm eff}$ (K)	Age (Gyr)
KIC10	1.45	7.488	**2.852 ± 0.5**	4.86	**0.509 ± 0.5**	**4712 ± 200**	N/A
TCE	1.49	7.59	**2.85**	4.80	(-0.2)^a	**4837**	2.66 ± 0.83
Huber13	1.344 ± 0.169	6.528 ± 0.352	2.94 ± 0.17	6.80	**0.29 ± 0.16**	**4605 ± 97**	N/A
SED	N/A	N/A	< 3.5	N/A	**0.4 ± 0.2**	**4790 ± 110**	N/A
Spec.	N/A	N/A	**3.0 ± 0.3**	N/A	**0.11 ± 0.07**	**4550 ± 75**	N/A
Sc.Rel.	$1.19^{+0.27}_{-0.22}$	$6.20^{+0.57}_{-0.51}$	2.93 ± 0.17	**7.0 ± 0.4**	N/A	(4550 ± 75)^a	N/A
Freq.	**1.31 ± 0.10**	**6.30 ± 0.16**	**2.953 ± 0.007**	**7.3 ± 0.1**	(0.11 ± 0.07)^a	(4550 ± 75)^a	**4.86 ± 2.13**

Notes. Parameters in bold represent primary values (i.e. a directly determined parameter by this method). Values in neither bold nor brackets have been calculated based on other previously determined or assumed parameters. The expression N/A reflects parameters that cannot be determined by the corresponding method. $^{(a)}$ Assumed (input) parameter, also in parenthesis. $^{(b)}$ Note that $[M/H] \approx \log(Z/Z_\odot)$

Spectral energy distribution (SED).- We used the Virtual Observatory SED Analyzer (VOSA,[2] Bayo et al., 2013, 2008) to model the SED of this target. VOSA uses Bayesian inference to compute the expected values for the effective temperature, surface gravity, metallicity, and interstellar extinction. We have used ancillary photometric data to build and fit the SED of Kepler-91. In particular, we used the KIC photometry in the *g, r, i, z* filters (Brown et al., 2011), the 2MASS JHKs photometry (Cutri et al., 2003), WISE (Wide-field Infrared Survey) bands W1 to W4 (Wright et al., 2010), the *Kepler* band (Borucki et al., 2010), and UBV photometry from Everett et al. (2012). Table 6.5 summarizes this information.

The Bayesian analysis from VOSA reveals that Kepler-91 has an effective temperature of $T_{\rm eff}$ = 4790 ± 110 K with metallicity being slightly oversolar [Fe/H] = 0.4 ± 0.2 (see summary in Table 6.4). We have set the extinction range to A_V = [0.0, 1.0] mag. The output expectance and variance from the Bayesian probabilities is A_V = 0.43 ± 0.15 magnitude. The surface gravity, however, is not very well constrained, but the probability distribution function seems to indicate that $\log g$ < 3.5. These values are in good agreement to the ones obtained by the KIC study (Brown et al., 2011) and Huber et al. (2013).

High-resolution and high-S/N spectrum.- We centered our study in the metallicity and effective temperature values that will be crucial for better constraining the parameter space in our own asteroseismic modeling. A previous inspection of the spectrum shows the lack of lithium at 6707.8 Å, indicating the evolved stage of the host star.

[2] http://svo2.cab.inta-csic.es/theory/vosa/

TABLE 6.5: Photometric data used in the spectral energy distribution fitting.

Band	Magnitude[a]	Reference[b]	Band	Magnitude[a]	Reference[b]
U	15.297	E12[c]	J	10.790 ± 0.026	2MASS, C03
B	13.986	E12[c]	H	10.235 ± 0.030	2MASS, C03
V	12.884	E12[c]	Ks	10.136 ± 0.021	2MASS, C03
g'	13.407	KIC, B11[d]	W1	10.032 ± 0.023	WISE, W10
r'	12.406	KIC, B11[d]	W2	10.157 ± 0.020	WISE, W10
i'	12.104	KIC, B11[d]	W3	10.049 ± 0.040	WISE, W10
z'	11.919	KIC, B11[d]	W4	9.380	WISE, W10
Kep	12.495	Kepler, B10			

Notes. [(a)] We assume 1% error when no errors are provided by the catalogues. [(b)] E12 = Everett et al. (2012), B11 = Brown et al. (2011), B10 = Borucki et al. (2010), C03 = Cutri et al. (2003), and W10 = Wright et al. (2010) [(c)] Johnson-like filters. More details can be found in Everett et al. (2012). [(d)] Sloan-like filters. More details can be found in Brown et al. (2011).

Metallicity.- We followed the specific prescriptions for giant stars described by Gray et al. (2002). This scheme uses a small part of the spectrum (from 6219.0 Å to 6261.5 Å) that was verified to mainly depend on the stellar metallicity. The method uses the percentage of stellar continuum absorbed by the atmospheric elements of the star. This percentage is what the authors call *line absorption* (LA). After masking specific lines that strongly depend on the effective temperature, they were able to fit a second-order polynomial relating [Fe/H] as a function of the LA. Since the authors do not provide the coefficients of this polynomial, we used the results in their Table 4 to perform our own fit. It is important to note the clear difference between stars with $T_{\rm eff}$ above and below 4830 K (although the physical reason is unknown, as the authors claim in their work). We divided the calibration sample into two groups according to this separation (hot for $T_{\rm eff} > 4830$ K and cold for $T_{\rm eff} < 4830$) and fit two different second-order polynomials of the form [Fe/H] = $a_0 + a_1 x + a_2 x^2$ with x being the masked line absorption in % (i.e., LA). Coefficients for the fit of both groups are reported in Table 6.6. In the left-hand panel of Fig. 6.2 we have plotted these polynomials together with the tested giant stars in Gray et al. (2002), with stars hotter than 4830 K in red and cooler in blue.

TABLE 6.6: Coefficients of the second-order polynomial fit ([Fe/H]= $a_0 + a_1 x + a_2 x^2$) to the line absorption values.

Group	a_0	a_1	a_2
Hot ($T_{\rm eff} > 4830$ K)	−1.60 ± 0.15	0.326 ± 0.046	−0.0142 ± 0.0036
Cold ($T_{\rm eff} < 4830$ K)	−1.968 ± 0.090	0.357 ± 0.022	−0.0152 ± 0.0013

We measured the masked LA for our spectrum finding that 12.8 ± 0.7 % of the light coming from the star is absorbed by chemical elements. Owing to the non-negligible segregation in temperature, we investigated the dependence of the LA with this parameter. The right-hand panel of Fig. 6.2 shows the values for the test giants. There is a clear lack of such objects in

the upper right region of the figure (high temperatures and high LA values). It is clear from this figure that for the measured LA of Kepler-91, the effective temperature is not expected to lie above 4830 K. We therefore used the coefficients corresponding to the cool polynomial to compute the metallicity. The uncertainty has been calculated by a quadratic sum of the error of the LA parameter and the standard deviation of the residuals of the test giants with respect to the fitted polynomial.[3] Our final estimation is [Fe/H] = 0.11 ± 0.07, which agrees within the errors with the one obtained by Huber et al. (2013), [Fe/H] = 0.29 ± 0.16.

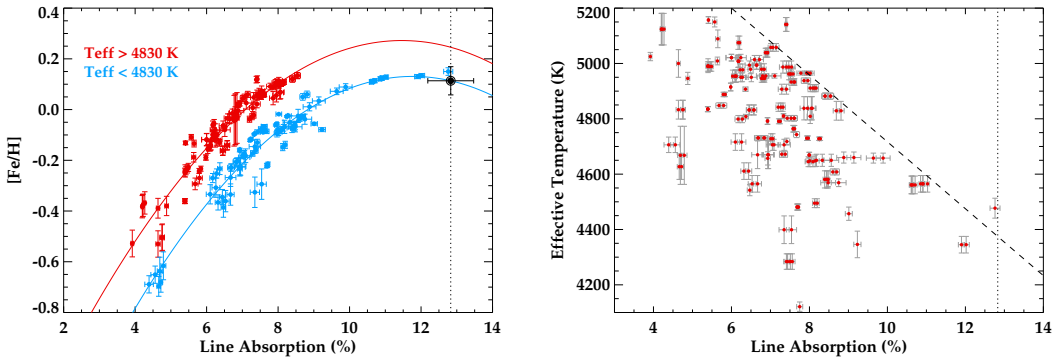

FIGURE 6.2: **Left:** Determination of the stellar metallicity of Kepler-91. We show data from giants compiled by Gray et al. (2002) to parametrize the line absorption parameter (LA) with the iron abundance [Fe/H]. Two samples are shown: giants with $T_{\rm eff} > 4830$ K (red) and giants with $T_{\rm eff} < 4830$ K (blue). Solid lines represent the fitted second-order polynomials to the test data. The dotted vertical line shows the obtained LA for Kepler-91 and the black circle its determined position in the diagram. **Right:** Effective temperature versus LA showing that Kepler-91 should be considered in the cool group of giants regarding the left panel segregation. The red circles show the position of the test giants, and the dashed line represents an estimated empirical limit to the temperature for each LA.

Effective temperature & $v \sin i$.- We have used four line pairs in the spectrum to estimate the stellar effective temperature. As explained in Gray & Brown (2001), just one of the lines in the pair is temperature sensitive, so that their depth ratio can be used to estimate $T_{\rm eff}$. We used the pairs NiII/VI at 6223.99/6224.51 Å, FeI/VI at 6232.65/6233.20 Å, VI/FeI at 6251.83/6252.57 Å, and FeI/VI at 6255.95/6256.89 Å. As a first step, to estimate the rotational velocity, we synthesized a grid of models using the ATLAS09[4] software for metallicities [Fe/H]=0.0-0.2, effective temperatures in the range 4400-4800 K (50 K step), surface gravities from 2.5 to 3.5, and rotational velocities from 1.0 to 12.0 km/s in steps of 0.1 km/s (turbulence velocity fixed to 2.0 km/s). A global fit to the spectrum provides a posterior distribution for the $v \sin i$ parameter with an expectance and variance values of $v \sin i = 6.8 \pm 0.2$ km/s. By setting the rotational velocity in the calculated range, considering three values for the surface gravity ($\log g = 2.5$, 3.0, and 3.5), and building a finer grid of temperatures with 25 K step, we proceeded to a least-square analysis of the four line pairs. A Bayesian analysis provides the next expectance and

[3] This implies that the uncertainty in the metallicity is at 1σ level. Here we prefer to keep the 1σ uncertainty to constrain, as much as possible, the parameter space for subsequent asteroseismic analysis with high computational time use.

[4] http://kurucz.harvard.edu/grids.html

variance values for the different gravity values: 4600 ± 46 K for $\log g = 2.5$, 4550 ± 47 K for $\log g = 3.0$, and 4500 ± 50 K for $\log g = 3.5$. As a compromise between these values we adopt an effective temperature of $T_{\rm eff} = 4550 \pm 75$ K, whose central value nearly corresponds to the surface gravity determined by the asteroseismology (Huber et al., 2013, and our own calculations in the next section).

Asteroseismology.-[5] We have used both the scaling relations and the individual analysis of 38 frequencies in the power spectrum of the *Kepler* light curve to obtain accurate physical properties of Kepler-91. The equations and theory of these techniques were explained in section § 2.4.

Scaling relations.- Huber et al. (2013) derived the global parameters of the power spectrum: $\Delta\nu = 9.39 \pm 0.22$ μHz and $\nu_{max} = 108.9 \pm 3.0$ μHz. We used the A2Z pipeline (Mathur et al., 2010) to re-determine them, obtaining $\Delta\nu = 9.48 \pm 0.88$ μHz and $\nu_{max} = 109.4 \pm 6.1$ μHz, in good agreement at the 1σ level with the previous study, and leading to a mean density around 2% higher than that reported in Huber et al. (2013). The updated scaling relation suggested by Mosser et al. (2013) implies an additional increase in the density of 2% with respect to what is obtained with Eqs. 2.43 and 2.44. According to Mosser et al. (2013), these equations should be corrected by a factor of $(1 - 4\zeta)$ and $(1 - 2\zeta)$ respectively (with $\zeta = 0.038$ for red giants), and the reference values for the Sun should be changed to $\nu_\odot = 3104$ μHz and $\Delta\nu_\odot = 138.8$ μHz. By using these updated scaling relations and effective temperature ($T_{\rm eff} = 4550 \pm 75$ K), we derive the following stellar mass, radius, and mean density: $M_\star = 1.19^{+0.27}_{-0.22}\, M_\odot$, $R_\star = 6.20^{+0.57}_{-0.51}\, R_\odot$, and $\rho_\star = 7.04 \pm 0.44$ kg/m^3 (uncertainties have been calculated by performing Monte Carlo Markov Chain simulations). The corresponding stellar luminosity and surface gravity are: $\log g = 2.93 \pm 0.17$ (cgs), and $L = 14.8^{+3.9}_{-3.3}\, L_\odot$.

Individual frequencies.- The high S/N of the Kepler-91 power spectrum allows to detect 38 individual frequencies. The individual frequencies of Kepler-91 were obtained by fitting the power spectrum of the signal to a model. The background was fitted prior to extracting the modes parameters and then held as a fixed value. For fitting the modes, all the parameters were allowed to vary with no bond among them. The entire spectrum was fitted at once between 65 and 145 μHz. The initial values for the p-mode parameters were extracted from the observed spectrum. The formal uncertainties were obtained from the Hessian matrix in the MLE procedure. The results are given in Table 6.7 and plotted in Fig. 6.3 in an échelle diagram.

As summarized in Table 6.7, the oscillation spectrum of Kepler-91 presents seven radial modes, seven quadrupole modes, and 23 $\ell = 1$ modes. The arrangement of $\ell = 2$ and $\ell = 0$ modes on well defined vertical ridges in the échelle diagram suggests that the observed $\ell = 2$ modes are trapped well in the acoustic cavity and behave as pure pressure modes. Therefore, from

[5] The asteroseismology analysis of Kepler-91 was lead by Josefina Montalbán and Andrés Moya, with the additional collaboration of Mauro Barbieri.

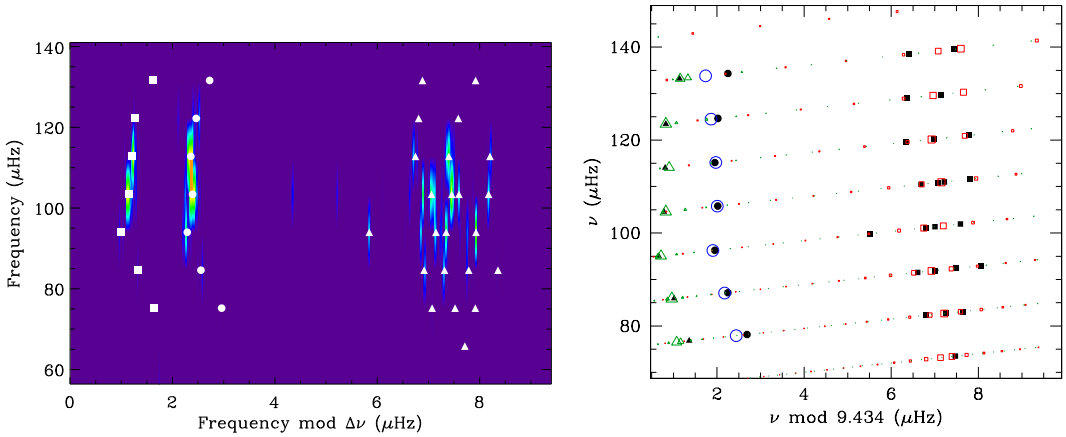

FIGURE 6.3: **Left:** Échelle diagram of the power spectrum of the data with the fitted modes over-plotted. Circles for $l = 0$, triangles for $l = 1$, and squares for $l = 2$. The power spectrum is fitted using maximum likelihood estimation. **Right:** Comparison between observational (black solid dots and white symbols in the left panel) and theoretical (open symbols) frequencies in the échelle diagram for a typical good fitting of radial and non-radial modes. Circles correspond to radial modes, squares to dipole modes, and triangles to quadrupole ones. The size of the theoretical symbols is an indication of the expected amplitude based on the value of the inertia mode (Houdek et al., 1999). The asymptotic period spacing for this model is 76s.

TABLE 6.7: Pulsating modes observed for Kepler-91 ordered by frequency.

l	ν	$\delta\nu$	l	ν	$\delta\nu$	l	ν	$\delta\nu$	l	ν	$\delta\nu$
1	73.510	0.035	1	92.386	0.017	0	105.792	0.012	1	121.002	0.013
2	76.835	0.022	1	92.958	0.025	1	110.459	0.043	2	123.468	0.028
0	78.160	0.031	2	95.004	0.020	1	110.995	0.035	0	124.663	0.024
1	82.271	0.013	0	96.289	0.016	1	110.855	0.019	1	129.008	0.017
1	82.720	0.023	1	99.843	0.009	1	111.574	0.011	1	129.783	0.027
1	83.115	0.020	1	101.146	0.028	2	114.018	0.018	2	133.215	0.030
2	85.924	0.014	1	101.345	0.013	0	115.159	0.011	0	134.326	0.046
0	87.156	0.019	1	101.929	0.007	1	119.546	0.021	1	138.483	0.040
1	91.514	0.012	2	104.557	0.010	1	120.198	0.012	1	139.520	0.023
1	91.913	0.012									

Notes. The first column gives the spherical degree, the second the frequency in μHz, and the third the error in determining the frequency.

individual $\ell = 0$ and $\ell = 2$ frequencies, we can derive quantities, such as the large and small frequency separations, and try to use them as observational constrains in our analysis (Bedding et al., 2010, Huber et al., 2010, Montalbán et al., 2010). We have computed the mean large frequency separation for radial modes directly from frequencies ($\Delta\nu(n,\ell) = \nu_{n,\ell} - \nu_{n-1,\ell}$), and by fitting the asymptotic relation $\nu_{n\ell} \approx (n + \ell/2 + \epsilon)\Delta\nu$ (Gough, 1986, Tassoul, 1980, Vandakurov, 1967). In the first case we got $\langle\Delta\nu_0\rangle = 9.434\,\mu$Hz with a standard deviation $0.1\,\mu$Hz, and $\Delta\nu = 9.37 \pm 0.02\,\mu$Hz in the second one. Dipole modes, given their p-g mixed character, do not follow the asymptotic relations for pressure modes, a certain regularity is expected, however, in the period spacing between consecutive radial orders (Beck et al., 2011, Bedding et al., 2011,

Mosser et al., 2011), for similarity with the asymptotic behavior of pure gravity modes (Tassoul, 1980). From the detected dipole modes we got a mean value of the period spacing of mixed modes (ΔP_{obs}) of the order of 53s. This quantity is smaller than the asymptotic period spacing (Bedding et al., 2011, Christensen-Dalsgaard, 2012, Montalbán et al., 2013, Mosser et al., 2011, 2012) which, according to the Mosser et al. (2012) estimation for a RGB star with $\Delta\nu \approx 9.5\,\mu$Hz, should be slightly lower than 80s (Fig. 6.3, right panel).

In our fit we also included the spectroscopic constraints (i.e., $T_{\rm eff} = 4550 \pm 75$ K and [Fe/H]= 0.11 ± 0.07). When taking different solar mixtures and the uncertainties in metallicity determination into account, the constraint used in our fit is then $Z/X = 0.019 \pm 0.005$. (Z and X are the metal and hydrogen mass fractions, respectively.)

We used the stellar evolution code ATON (Ventura et al., 2008) to compute a grid of stellar models with masses between 1.0 and 1.6 $M_\odot$ in steps of 0.02 $M_\odot$, helium mass fraction of $Y = 0.26 - 0.32$ in steps of 0.01, metal mass fractions of $Z = 0.01$, 0.015, 0.0175, 0.020, and 0.025, and mixing length parameter $\alpha_{\rm MLT}$ =1.9, 2.05 and 2.2. The step in radius between consecutive models in the evolutionary tracks is of the order of $5\times10^{-3}\,R_\odot$. For each model with a large frequency separation (from scaling law) within 10% of the observed value, we computed the adiabatic oscillation frequencies for $\ell = 0$, 1, 2 modes using LOSC (Montalbán et al., 2010, Scuflaire et al., 2008). We also derived the theoretical values of $\langle\Delta\nu_0\rangle$ and $\langle\delta\nu_{02}\rangle$.

The theoretical values of the frequencies and frequency separations differ in general from the observational ones, because of the so-called near-surface effects. The model frequencies were therefore corrected using the method described in Kjeldsen et al. (2008). The power-law correction was applied to radial and non-radial modes. To take the different sensitivity of non-radial modes to surface layers into account, the surface correction of non-radial modes was multiplied by a factor $Q^b_{n,\ell}$, where $Q_{n,\ell}$ corresponds to the ratio of the mode inertia to the inertia of the closest radial mode (Aerts et al., 2010, chapter 7). We considered several values of the exponent b in the surface-correction law: $b = 5, 6, 7, 8$.

For the individual frequency fitting, we evaluated the agreement between models and observations by using different merit functions (reduced χ^2, $\sum_N((\nu_{obs} - \nu_{theor})^2/\sigma_\nu^2)/N$, including or not the dipole modes). The merit function for radial and quadrupole modes leads to a mean density of $\rho = 7.3 \pm 0.1$ kg/m^3. This value does not significantly depend on the assumed b parameter in the surface-effects correction. The mean density derived from frequency fitting is therefore 5.8% higher than derived from the classic scaling relations (Eqs. 2.43 and 2.44), and 3.7% higher than that provided by their updated version (Mosser et al., 2013). This discrepancy between both methods agrees with other studies (see for instance Fig. 4 in Belkacem et al., 2013).

We have also evaluated the fit of the dipole modes in two different ways: one taking only the most trapped modes into account, those with lowest inertia between two radial modes and another taking all the dipole mixed modes into account. The results obtained by these two methods are consistent and provide two different minima in the stellar mass-radius domain: one around 1.25 $M_\odot$ and the second around 1.45 $M_\odot$. Excluding solutions with effective temperature deviating by more than 3σ reduces the parameters space to $M_\star = 1.31 \pm 0.10\ M_\odot$, $R_\star = 6.30 \pm 0.16\ R_\odot$, $\log g = 2.953 \pm 0.007$, and an age of 4.86 ± 2.13 Gyr.

The frequencies of radial modes vary as $\rho^{1/2}$. Given the steps used in stellar radius and mass, we can expect a typical change in frequencies between different models of the order of 0.8%, that is, 0.9 μHz. That value is much more than the intrinsic precision of the observational frequencies. The computation of non radial frequencies for such as evolved object is very time consuming. Moreover, given the uncertainties linked to the surface effects and its correction (see i.e., Gruberbauer et al., 2012), a denser grid of models is not worth it.

6.2.3.2 Primary transit

The transit of this system has already been previously fitted by Tenenbaum et al. (2012), hereafter TCE. The orbital and physical parameters calculated in that paper are summarized in the second column of Table 6.8. However, as shown in section § 6.2.3.1, the physical parameters of the host star are now more precisely determined. In particular, effective temperature, surface gravity, and metallicity are quite different from what is assumed by TCE (see Table 6.4). The dependency of these parameters with the transit shape resides on the limb darkening coefficients. By trilinearly interpolating the Claret & Bloemen (2011) tabulated values of the four quadratic limb darkening coefficients, we find that the relative differences between adopting the TCE stellar parameters and our determined parameters are of the order of 17%, 40%, 20%, and 7%, respectively. Thus, a new transit fitting is needed for this system.

In TCE, the authors assumed zero eccentricity for the orbit. The effect of a non-zero eccentricity in the shape of the transit is known to be small for low values of e. It would produce asymmetries in the ingress and egress slopes since the planet-to-star distance at both orbital positions would be different. To test this possibility and due to the subtleness of this effect, we have carried out a Kolmogorov-Smirnov test between both sides of the transit. The results show a 70% probability that the ingress is equal to the egress. Several binnings were tested yielding similar results. Since the magnitude of the asymmetries could be very small and given that there is a non-negligible probability of 30% that the ingress is different from the egress, we find it justified to try fitting the transit with a non-zero eccentricity.

By allowing a non-circular orbit, the transit shape depends on six free parameters: planet-to-star radius ratio (R_p/R_*), orbital eccentricity (e), argument of the periastron (ω), semi-major axis

TABLE 6.8: Results for the analysis of the primary transit and the light-curve modulations of Kepler-91. Comparison with the values obtained by (Tenenbaum et al., 2012, TCE).

	Transit fitting			**REB fitting**	
Parameter	TCE[a]	e = fixed[b]	e =free[b]	e = fixed[c]	e = free[c]
e	0.0	0.0	$0.13^{+0.12}_{-0.12}$	0.0	$0.066^{+0.013}_{-0.017}$
ω ($^\circ$)	0.0	0.0	37^{+150}_{-125}	0.0	$316.8^{+21}_{-7.4}$
$M_p(M_{\rm Jup})$	N/A[d]	N/A[d]	N/A[d]	$0.84^{+0.16}_{-0.32}$	$0.88^{+0.17}_{-0.33}$
a/R_*	2.64 ± 0.23[e]	$2.40^{+0.12}_{-0.12}$	$2.37^{+0.10}_{-0.12}$	$2.36^{+0.10}_{-0.35}$	$2.45^{+0.15}_{-0.30}$
R_p/R_* (10^{-2})	2.115 ± 0.072	$2.255^{+0.031}_{-0.097}$	$2.200^{+0.046}_{-0.075}$	$2.255^{+0.031}_{-0.097}$ [f]	$2.255^{+0.031}_{-0.097}$ [f]
i ($^\circ$)	71.4 ± 2.5	$68.5^{+1.0}_{-2.0}$	$66.6^{+2.0}_{-1.0}$	75^{+14}_{-15}	78^{+10}_{-15}
$\phi_{\rm offset}(10^{-3})$	N/A	$1.14^{+0.74}_{-0.79}$	$-0.5^{+0.7}_{-2.0}$	6^{+23}_{-22}	2^{+23}_{-22}
$\chi^2_{\rm red}$	3.40	2.86	2.86	5.16	3.92
BIC	637	624	633	1460	1411

Notes. [a] Values from the last results of the threshold crossing events by Kepler team (TCE, Tenenbaum et al., 2012). [b] Results from the re-analysis of the primary transit with our genetic algorithm (see section § 6.2.3.2). [c] Results from the fitting of the REB modulations (see section § 6.2.3.3). [d] Parameter not derivable by this method. [e] Derived value from the equation $r = a(1-e^2)/(1+e\cos\nu)$ and assuming that the primary transit occurs at true anomaly $\nu = \pi/2 - \omega$. [f] Assumed parameters from the transit fitting.

to stellar radius ratio (a/R_*), inclination (i), and a phase offset ($\phi_{\rm offset}$) . This sixth parameter is included to account for possible deviations in the measured time of mid-transit (T_0). Limb darkening coefficients are fixed to the central values of the $T_{\rm eff}$, $\log g$, and [Fe/H] since we have checked that, under their confident limits, the quadratic coefficients just vary below 4%, 6%, 3%, and 1%. Monte Carlo Markov Chain (MCMC) simulations show that these changes are inside the error bars of the final fitted parameters.

We used *GAbox* to model-fit our data (see Appendix A). The large amount of free parameters led us to note that the solution is *multi-valuated*. Different sets of solutions fit the data equally well, having χ^2 values inside the 99% of confidence (i.e., presenting differences in the χ^2 value lower than 16.812[6] with respect to the χ^2_{min}). Although from statistics we cannot choose a particular set of parameters, we selected the one with the smallest relative errors in all parameters. The parameters of this model are shown in the fourth column of Table 6.8. Uncertainties have been estimated by using 99% confident contours in χ^2 maps for each pair of parameters. The largest upper and lower uncertainties for all pairs have been used. Interestingly, the selected model has a non-zero eccentricity of $e = 0.13 \pm 0.12$. But, other models inside the 99% of confidence interval provide a variety of eccentricities ($e < 0.28$), planet-to-star radius ($R_p/R_\star \in [0.021, 0.023]$), semi-major axis ($a/R_\star \in [2.2, 2.8]$, correlated with the inclination parameter), and inclination

[6] Corresponding to the 99% confidence level for a six free parameters proble.

($i \in [65°, 73°]$). It is important to note that, for the calculated stellar radius, all solutions restrict the planet radius to $1.3 - 1.4\ R_{\rm Jup}$. The χ^2 value for the adopted eccentric model is $\chi^2_{\rm red} = 2.86$.

We have also run *GAbox* by assuming zero eccentricity, which leaves only four free parameters for the system. In this case, the least relative error solution provides a $\chi^2_{\rm red} = 2.86$, and all statistically possible solutions provide parameters within the error bars of this model.

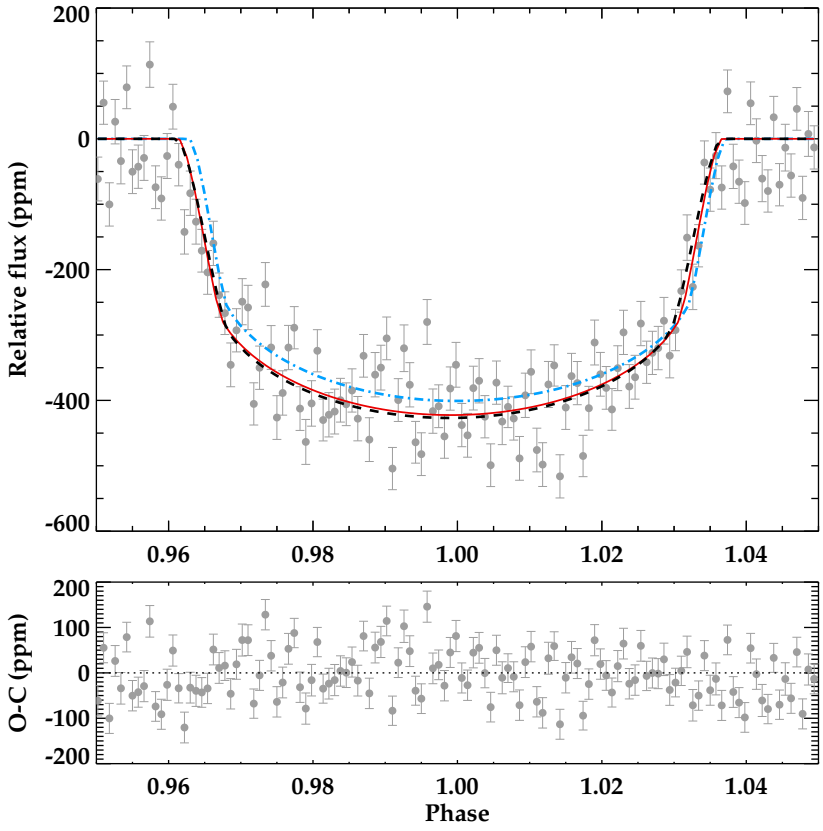

FIGURE 6.4: Best-fit solutions for the transit of Kepler-91 b according to different model schemes: assuming parameters from Tenenbaum et al. (2012) (dot-dashed blue line), assuming zero eccentricity (dashed black line), and leaving the eccentricity as a free parameter (solid red line). Residuals for our circular model are presented in the lower panel.

For comparison purposes, we have also reproduced the model fitted by TCE with their limb darkening coefficients and orbital and physical parameters. This model produces $\chi^2_{\rm red} = 3.41$. All three models (TCE, $e = 0$, and $e \neq 0$) are plotted in Fig. 6.4. Both quantitatively (by comparing the χ^2 value) and qualitatively (by inspecting the aforementioned figure), our $e = 0$ (fixed) solution improves the quality of the fit from that of TCE. However, to evaluate whether including the eccentricity as a free parameter improves the fit of the transit or not, we have used the Bayesian information criterion (BIC, see for example, Schwarz, 1978, Smith et al., 2009). For a given model solution, the BIC value is calculated as $\mathrm{BIC} = \chi^2_{min} + k \ln N$, where N is the number of observed points, and k is the number of free parameters. A difference greater than 3 in the BIC values of both models indicates positive evidence against the higher BIC value,

and a difference greater than 10 indicates strong evidence. Since BIC(e = 0, fixed) = 624 and BIC(e = free) = 633, the eccentric case is not favored over the zero eccentricity scenario. This means that we do not need the eccentricity to correctly fit the observed transit. However, we have proved that there is a combination of e, ω that also reproduces the transit with similar values for the $R_p/R_\star$, $a/R_\star$ (within confident limits), and inclination parameters. Then, we can conclude that the primary transit fitting itself is not enough to determine whether the orbit of the transiting object is eccentric or not.

6.2.3.3 Light curve modulations

When inspecting the out-of-transit region of the phase-folded light curve (LC) of Kepler-91, a clear double-peaked modulation is apparent (see Fig. 6.5). This light curve variation is known to be caused by the REB modulations explained in section § 2.3.

Some of the parameters involved in Eqs. 2.18 to 2.31 can be fixed based on previous sections (see Table 6.9 for a summary of the adopted values). This leaves six free parameters: eccentricity (e), longitude of periastron (ω), planet mass (M_p), semi-major axis to stellar radius ratio ($a/R_\star$), inclination (i), and phase offset ($\phi_{\rm offset}$). In the lower part of Table 6.9, we set some constraints to the free parameters to restrict the fitting process.

Since the amplitude of the REB modulations is quite small (100-150 ppm), we have used a larger bin size in this analysis (60 minutes with a 3σ rejection algorithm). The region where a possible occultation is located has been masked out ($\phi = [0.66, 0.72]$). We used *GAbox* to model fit the free parameters, obtaining 4000 convergence solutions (see detailed explanations in Appendix A). Owing to account for the errors introduced by non-fitted parameters (such as $T_{\rm eff}$, $\log g$, $R_p/R_\star$, etc.), we have run MCMC simulations, allowing these parameters to vary inside their confidence limits. Posterior distributions provide the 1σ uncertainties.

Since six free parameters are fitted, we cannot statistically disentangle sets of convergence solutions with a difference in the measured χ^2-value of $\Delta\chi^2 = \chi^2 - \chi^2_{min} < 16.812$. However, we can choose the model that minimizes the relative errors among the sample of solutions. In particular, this model is also the one that minimizes the error in the companion's mass, a key parameter for confirming its planetary nature. This solution is shown in the last column of Table 6.8. More importantly, most of the aforementioned possible solutions are contained within the confidence limits of these parameters. In Fig. 6.6, we show the location of all possible solutions in two-dimensional diagrams marking the location of the final adopted value and the median value for all solutions. All common parameters with the transit analysis agree within the error bars, thus providing a *self-consistent* solution for the orbital and physical parameters.[7] For comparison

[7] This way, the complete set of parameters provides the best-fit, rather than selecting the best parameters individually from the median of the distribution of solutions.

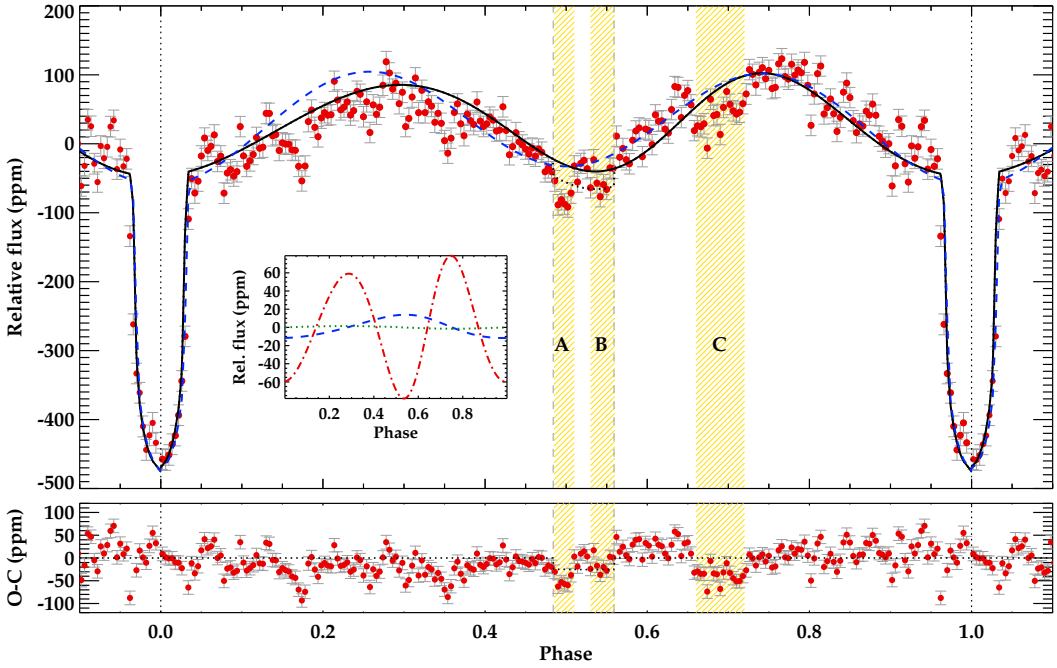

FIGURE 6.5: Best-fitted model to the REB modulations of Kepler-91 for an assumed circular orbit (dashed blue line) and the best non-circular model (solid black line). Red circles show the folded light curve assuming the period obtained by the *Kepler* team and binned to 29.4 minutes intervals (similar to the real cadence of observations. In the small panel we show the individual contributions of ellipsoidal (red dotted-dashed line), reflection (blue dashed line), and Doppler beaming (green dotted line). The lower panel shows the residuals after subtracting the non-circular model to the observed data. The three shadowed regions marked as A, B, and C represent the three detected dims (see section § 6.2.3.4). The theoretical location of the secondary eclipse according to the architecture of the system is marked with vertical grey dashed lines in the upper panel. By removing the contribution of the planet reflection in this region, we obtain the dotted black line.

purposes, we have estimated a mean amplitude for each modulation, assuming the star-planet distance equal to the semi-major axis.[8] Our derived parameters provide peak-to-peak amplitudes of $A_{ellip} = 121^{+32}_{-33}$ ppm, $A_{ref} = 25^{+15}_{-15}$ ppm, and $A_{beam} = 3^{+1}_{-2}$ ppm. As expected, the most relevant effect in this system is the ellipsoidal modulation, given the small separation between the planet and the star.

We also ran the fitting algorithm by assuming zero eccentricity. The best-fit model is shown in Fig. 6.5. In this case, the improvement in the fit by accounting for non-zero eccentricity becomes clear and could be quantitatively measured by comparing the BIC values of both models: $BIC_{e=0} - BIC_{e\neq0} = 59$. This difference is largely greater than six, which indicates that the REB modulations are clearly described better by an eccentric model.

The detection of this ellipsoidal modulation confirms the presence of a physically bound planetary-mass companion to Kepler-91 *without* the need for a radial velocity study. It is important to note

[8] Since the best solution provides a non-circular orbit, the amplitude itself varies with the orbital position of the planet.

TABLE 6.9: Inputs and ranges for the free parameters in the REB fitting of Kepler-91.

Fixed parameters (input)			
Parameter	Value	Description	Origin
$T_{\rm eff}$	4550 ± 75 K	Effective temperature	Spectroscopy (§ 6.2.3.1)
$\log g$	2.953 ± 0.007	Surface gravity	Asteroseismology (§ 6.2.3.1)
[Fe/H]	0.11 ± 0.07	Stellar metallicity	Spectroscopy (§ 6.2.3.1)
P	6.246580 ± 0.000082 days	Orbital period	Light curve (Batalha et al., 2013)
Ω	$0°$	Longitude of the ascending node	Assumed
$\lambda_{\rm eff}^{Kepler}$	575 nm	Effective wavelength of the Kepler band	
M_*	$1.31 \pm 0.10\ M_\odot$	Stellar mass	Asteroseismology (§ 6.2.3.1)
R_*	$6.30 \pm 0.16\ R_\odot$	Stellar radius	Asteroseismology (§ 6.2.3.1)
R_p/R_*	$2.255^{+0.031}_{-0.097} \times 10^{-2}$	Planet-to-star radius	Transit fitting (§ 6.2.3.2)
Free parameters (output)			
Parameter	[Lower limit , Upper limit]	Description	
e	$[0.0, 0.5]$	Eccentricity	
ω	$[0°, 360°]$	Argument of periastron	
M_p	$[0.5 M_{\rm Jup}, 6.0 M_{\rm Jup}]$	Planet-to-star mass ratio	
$a/R_\star$	$[1.5, 5.0]$	Semi-major axis to stellar radius ratio	
i	$[60°, 90°]$	Orbital inclination	
$\Phi_{\rm offset}$	[-0.05,0.05]	Phase offset in phase units	

that all statistically possible solutions mentioned before fit the data with companion masses between 0.5 M_{Jup} and 1.1 M_{Jup}, confirming the planetary nature of the object orbiting Kepler-91.

6.2.3.4 Additional eclipses

Since the orbital parameters have been constrained in previous sections, we can use the Wallenquist (1950) equation to determine the location of the secondary transit (see Eq. 2.13). By using the orbital parameters from the REB analysis, the secondary eclipse should be centered at $\phi_{sec} = 0.53$. The duration of the secondary eclipse is expected to be similar to that of the primary due to the small eccentricity of the orbit (i.e., around 10-11 hours).

However, after removing the signal produced by the REB variations, five clear dips in the light curve can be detected (see Fig. 6.7). The first one is located at the mid orbital period ($\phi_A \approx 0.5$, labelled as A in Fig. 6.7). Its duration of $d_A \approx 4.5 - 6.0$ hours is shorter than the primary transit (about 11 hours), which prevents this from being the secondary eclipse. Another small dip (labelled as B) is found at $\phi_B = 0.54$, which would correspond to the expected location of the mid-eclipse. However, its duration of only 5-6 hours, combined with its low S/N, also prevents us from confirming this as the secondary eclipse.

A third dip (C) is found at $\phi \approx 0.68$. In this case, the duration of the possible occultation is close to the primary transit's duration ($d_C \approx 11 - 12$ hours). However, its location prevents this from being the secondary eclipse of the confirmed planet Kepler-91b. Finally, although less evident than the previously analyzed dips, there are two more occultations at $\phi \approx 0.17$ (D) and $\phi \approx 0.35$

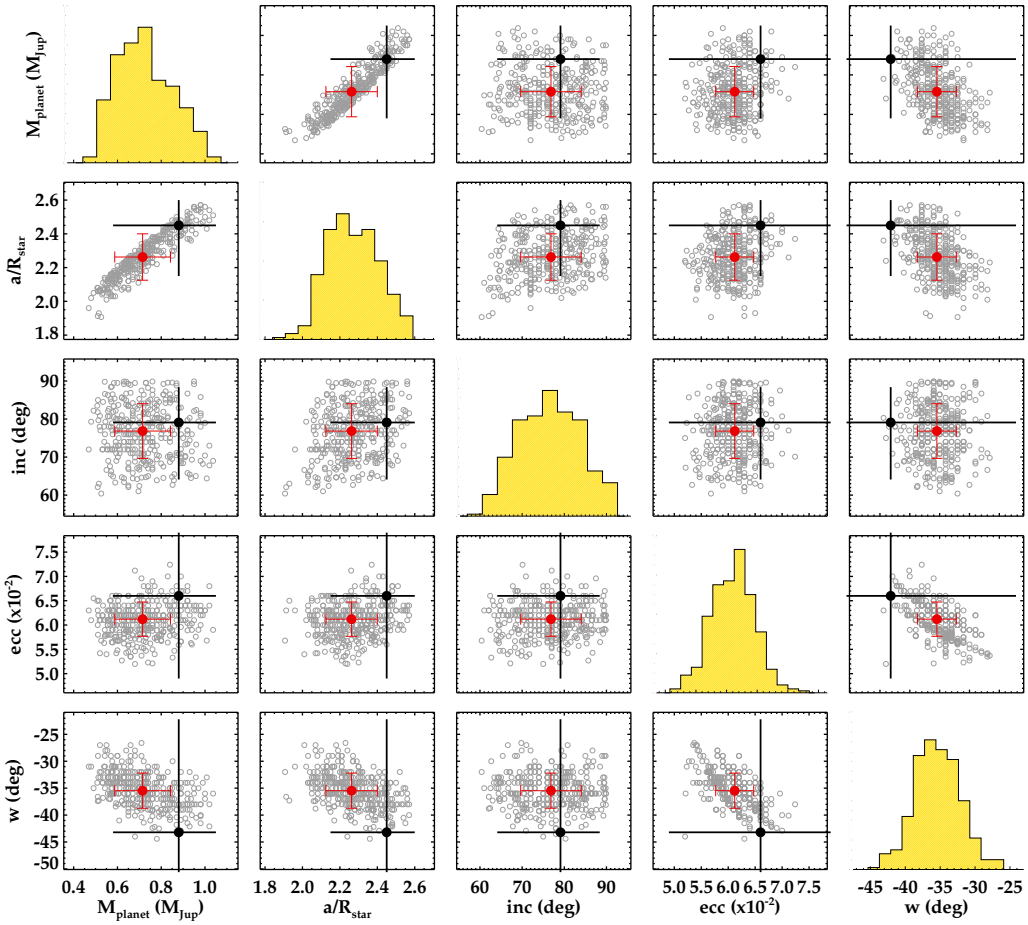

FIGURE 6.6: Possible solutions for the REB modulation fitting (see section § 6.2.3.3). Each grey open circle (and its correspondent error bars) represents a possible solution for the REB modulations whose χ^2 value is statistically valid as compared to the minimum χ^2 obtained with the genetic algorithm. We have marked the adopted model in black, being the one that presents the least relative errors. The red symbol corresponds to the most repeated value (and standard deviation deviation) for each parameter in the whole set of statistically acceptable solutions.

(E). Similar reasons to those stated for the previous dips discard these other possibilities as the occultation of Kepler-91b.

We can conclude that none of the previously discussed dips agree with the expected location and duration of the occultation of this planet. According to our fitting, the contribution of the planet reflection at such orbital phases would yield a theoretical depth of $D_{\rm sec} = 25 \pm 15$ ppm for the secondary eclipse. Interestingly, this coincides with the depth of the observed dip labelled as B in Fig. 6.7. However, the theoretical location of the secondary eclipse encompasses both A and B dips. Thus, although observationally we do not detect a clear secondary eclipse accomplishing all theoretical constraints, we can set an upper limit of 40 ppm for its depth. This would agree with the depth of the two minima, A and B. In other words, the combined position and duration of both dips make plausible, with caveats, the identification of the secondary eclipse. However, more work is needed to unveil the origin of such dips and to confirm its detection.

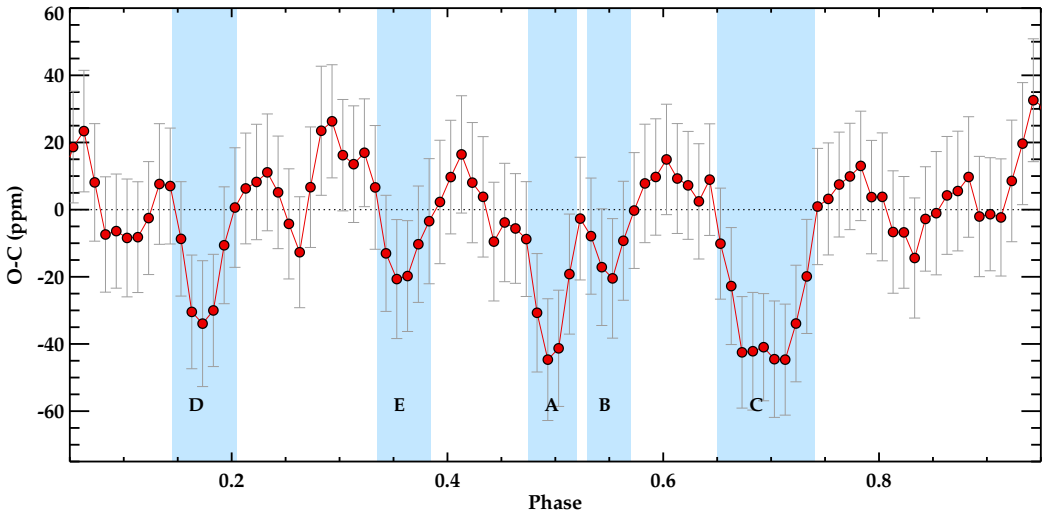

FIGURE 6.7: Zoom to the residuals of the REB and transit fitting of Kepler-91b with a larger bin size of 1.5 hours. Shaded regions mark the estimated positions of the five intriguing dips.

In any case, the explanation for the three individual dips is beyond the scope of this work and should be addressed by further analysis of this planetary system.[9] We have already shown that A and B could be part of the secondary eclipse. Some explanations for dips C, D, and E that should be studied more in detail by future works are listed here:

- **Large Trojan body.-** Dip D is located right at the expected conjunction time for the Lagrangian point L4, suggesting the presence of a Trojan body (or set of bodies), like the large bodies detected in the L4 and L5 Lagrangian points of Jupiter. Given the approximated depth of $\delta_D \sim 30$ ppm, the hypothesized Trojan should have a maximum size of $\sim 3.8\ R_\oplus$. According to theoretical studies by Laughlin & Chambers (2002), the only restriction for the stability of a planet+Trojan system is that the total mass of both objects ($M_T + M_p$) must not exceed the $\sim 4\%$ of the mass of the host star. In this case, even assuming an Earth-like density for the Trojan (providing an upper mass limit of $< 53 M_\oplus$), this condition is well accomplished. Hence, this hypothesis is plausible given the current data from a stability point of view.

- **Outer resonant and transiting planet.-** Any of the detected dips could be due to a resonant outer planet transiting the host star. This possibility forces non-coplanarity of the orbits since for the measured inclination of $i \approx 66°$, planets in longer-period orbits would not transit the parent star. The existence of such planets would explain the non-circular orbit of Kepler-91b despite its closeness to the parent star. Indeed, the subsequent work by Sato et al. (2015) on this system found a RV drift in their 1-year baseline observations with Subaru/HDS, suggesting the existence of additional companions.

[9] We have submitted some telescope proposals to test the different scenarios.

- **Exomoon.-** A large exomoon blocking the reflected light from the planet's day side could explain dips C and/or E, occurring right before and after the occultation of the planet when its day side is faced towards us. This configuration would require that the moon's period were an integer number of the planet's period around the host star. Again, this possibility would need an exhaustive stability study.

- **Instrumental and/or stellar activity effects.-** Subtle effects of the *Kepler* reduction pipeline, combined with some activity effect on the stellar surface or even the detected pulsations explained in section § 6.2.3.1 could also explain any of the detected dips.

6.2.3.5 Transit timing variations: hints of additional bodies

NOTE: The results presented in this section are preliminary and were not published in Lillo-Box et al. (2014a,c).

Description of the observed TTVs and TDVs

Mazeh et al. (2013) provided precise determinations of the transit timing variations (hereafter TTVs) and transit duration variations (TDVs) for the whole sample of KOIs detected in Quarters 1 to 9. The results show that Kepler-91b suffers one of the largest TTVs in the KOI sample studied. The median absolute deviation of these TTVs was found to be 71 minutes, but larger values until 261 ± 28 minutes have been found. However, we do not see any temporal correlation that could reveal the obvious presence of another single outer planet perturbing the orbit of Kepler-91b (see Fig. 6.8). Also, relatively large TDVs have also been found for this object. The maximum observed value being $TDV_{max} = 58 \pm 12$ s, with a standard deviation for the whole transit measurements of $\delta_{TDV} = 19$ s.

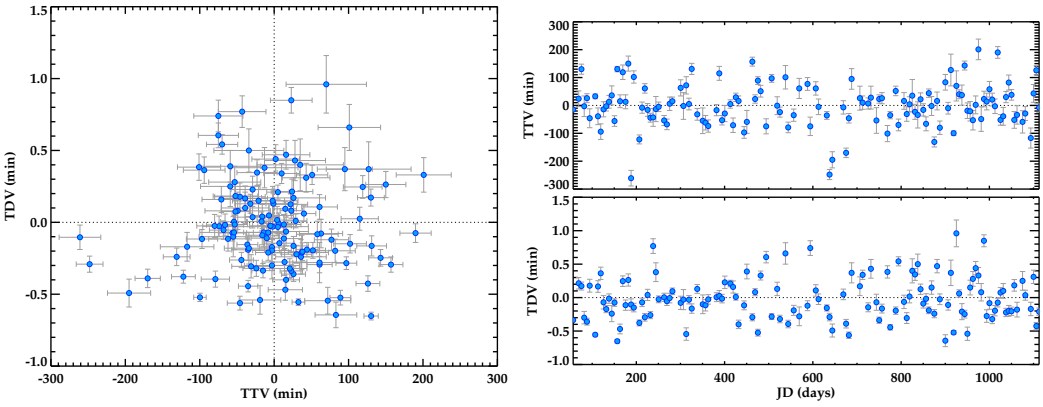

FIGURE 6.8: **Left:** Transit timing variations (TTVs) versus transit duration variations (TDVs) for Kepler-91b as determined by Mazeh et al. (2013). **Right:** Dependence of the TTVs and TDVs with the julian date. No significant periodicity is found above the Nyquist frequency.

Possible causes of the large TTVs

There are several configurations that can cause a delay and/or advance of the primary eclipse timings of a particular planet transiting its host star. We here investigate the best well-known causes trying to explain the observed large non-modulated TTVs.

1. **Inner perturber**. The presence of an inner planet can cause important TTVs, and the more eccentric is the orbit of the inner planet the larger TTVs are induced in the outer (transiting) planet. Let us label as 1 to the perturbing inner planet and as 2 to the outer transiting planet. These variations are modulated as a cosine, according to equation [14] in Agol et al. (2005):

$$\delta t_{inner} = \frac{P_2 a_1 \mu_1 \sqrt{1-e_2^2}}{2\pi a_2 (1 - e_2 \sin\omega_2)} \cos\theta_1(t) + \omega_1 \tag{6.1}$$

where $\theta_1(t)$ is the true anomaly of the transiting planet and ω_i is the argument of the persiastron of planet i. Since we can only measure δt_{inner} at the time of the transit, the best way to detect the effect of these inner planet is measuring the standard deviation of the observed TTVs. According to expression [16] in Agol et al. (2005), this standard deviation is given by:

$$< \sigma_2 >_{inner} = \frac{P_2 a_1 \mu_1 \sqrt{1-0.75e_1^2}}{2^{3/2}\pi a_2 (1-e_2^2)^{1/4}} \tag{6.2}$$

We have tested several possibilities for the inner planet properties (eccentricity, mass and semi-major axis). We found that for a $M_1 \approx M_2$ object orbiting in a very close orbit to Kepler-91b ($a_1/a2 \approx 1$), the standard deviation of the TTVs should be of the order of 1.5 minutes. This is clearly below the observed 76 minutes of standard deviation by Mazeh et al. (2013). *Thus, the TTVs cannot be (at least completely) caused by an inner planet.* Additionally, the closeness of Kepler-91 b to its host star makes unlikely the presence of another planet in a closer orbit.

2. **Outer perturber**. Let's suppose now another configuration consisting on an outer (non-transiting) planet (labelled as 2) and our inner (transiting) planet (labelled as 1). If the outer planet were in a circular orbit, being the inner planet in a near-circular orbit, it would be impossible for us to detect any TTV since the induced change in the period of the inner planet would be constant against time. However, if the outer planet has an eccentricity $e_2 \neq 0$, according to Haswell (2010), the maximum TTV induced if the reduced mass of the planet is $\mu_2 = M_2/M_*$, and it orbits with a semi-major axis of a_2, and an orbital period P_2, is given by:

$$\delta t_1^{max} \approx \mu_2 e_2 \left(\frac{a_1}{a_2}\right)^3 P_2 \tag{6.3}$$

Our RV data presented in section § 6.2.3.6 does not show RV variations other than that of Kepler-91b at the level of $\sim$ 50 m/s, which provides an upper limit for the mass of the possible outer planet of $0.5M_1$, i.e., $M_2 < 0.5\ M_{\rm Jup}$. Thus, let us assume a possible outer planet having this upper mass limit, $M_2 < 0.5\ M_{\rm Jup}$, with an eccentricity of $e_2 = 0.5$ and $n = a_2/a_1$. Note that, due to the large impact parameter of Kepler-91b, it is possible that the outer planet does not transit the stellar disk from our position. As a first approximation, using the third Kepler law we have $P_2 = P_1 n^{3/2}$. Hence, for $M_\star = 1.31 M_\odot$, we have $\delta t_1^{max}(min) \approx 1.6 \cdot n^{-3/2}$. Since, by definition, $a_2 > a_1$ (i.e., $n > 1$[10]), it should be $\delta t_1^{max} < 1.6$ min. Less-massive planets would yield to smaller values. Since the measured TTVs are much larger than this upper limit, *we can discard the outer non-resonant planet as the source of the TTVs.*

3. **Resonant perturber**. The previous calculations of planet perturbers in non-resonant orbits have assumed that the perturbation to the orbit of each planet is small. However, this is not the case for resonant-orbits where planets suffer large perturbations on their orbital parameters. This implies that a resonant outer planet will induce larger TTVs than non-resonant planets. Agol et al. (2005) investigated this possibility for a first order $j : j+1$ resonance, in the case of $j \approx j+1$ (and so $P_1 \approx P_2$). In this case, the maximum induced TTV on the transiting planet due to the perturber non-transiting outer planet is given by:

$$\delta t_{resonant}^{max} \approx \frac{P}{4.5j} \cdot \frac{M_{\rm pert}}{M_{\rm pert} + M_{\rm trans}} \tag{6.4}$$

We have represented in Figure 6.9 the maximum TTVs induced according to this expression depending on the mass of the perturber and the value of j. We have also over-plotted the contours corresponding to our maximum observed TTV ($TTV^{max} = 261 \pm 28$ minutes). Given that no additional transits are found, we can constrain the possible j-values and set the maximum j from which we would not see any transit of the perturber planet. Assuming coplanarity of both planets, we find that $j < 5$. Additionally, the radial velocity that will be presented in section § 6.2.3.6 constraints the mass of any outer companion with a mass larger than Kepler-91b for these resonant configurations. These constraints leave us only the following possibilities: (i) a 1:2 resonant planet of $M_{\rm pert} \sim 0.15\ M_{\rm Jup}$ (ii) a 2:3 resonant planet with a mass of $M_{\rm pert} \sim 0.26 - 0.35\ M_{\rm Jup}$, (iii) a 3:4 resonant planet with a mass of $M_{\rm pert} \sim 0.44 - 0.70\ M_{\rm Jup}$, and (iv) a 4:5 resonant planet with $M_{\rm pert} \sim 0.8 - 0.9\ M_{\rm Jup}$. So *there are three possible resonant configurations that could explain the large TTVs found for Kepler-91b.*

[10]Indeed, since we do not see any other transit from an outer planet, it should be $n > b_1/R_\star$, being $b_1/R_\star$ the impact parameter of the inner, transiting, planet in stellar radius.

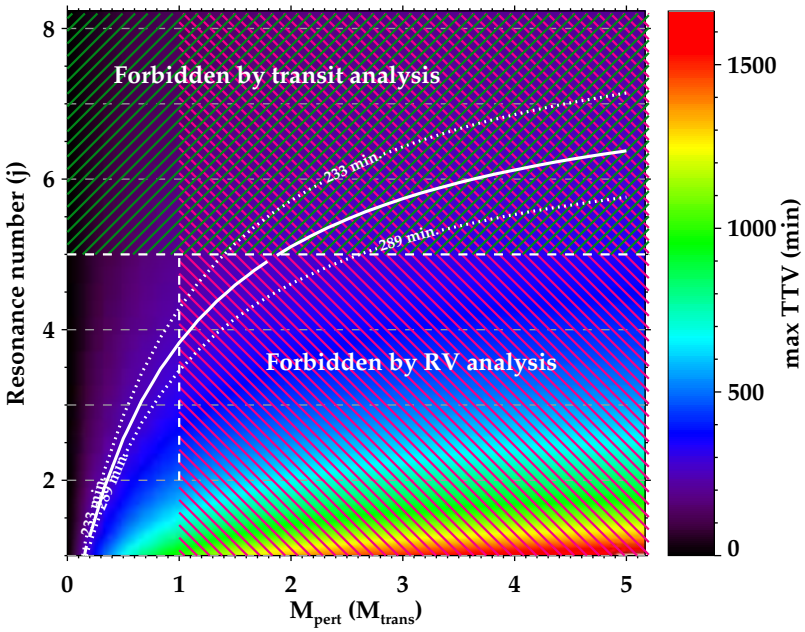

FIGURE 6.9: Estimated values for the maximum TTVs (in color-code) produced by a first order resonant perturber of mass $M_{\rm pert}$ in a j:j+1 orbit. We have over-plotted the contours corresponding to our maximum observed TTVs. The shaded regions are forbidden since it would yield to a visible transit of the perturber (green shaded region for $j > 5$), which is not seen in the *Kepler*light curve; and because our RV constraints (magenta shaded region).

4. **Exomoon**. The presence of an exomoon orbiting around the planet also can cause large TTVs. As stated in Kipping (2009), if exists, the satellite's period around the barycenter (P_{SB}) will always be less than 60% of the barycenter period around the star (P_B), i.e., $P_{SB}/P_B < 0.6$ (see equation 12 in the mentioned paper). Thus, due to a similar reason as for the inner planet, we can only reliably measure the RMS amplitude (i.e., the scatter) which scales as $\propto a_{SB}M_S$, where M_S is the mass of the satellite. The barycenter of the two-body system would actually orbit the star in a period of $P_B \sim 6.24$ days (as determined from the transit of Kepler-91 b). Since the transit has the same shape in every orbit (otherwise we would have not seen any jump but a large scatter in the folded light curve), we conclude that P_B must be a multiple integer of P_{SB}, i.e., $P_B = n \cdot P_{SB}$. According to Kipping et al. (2012), $n = \sqrt{3/\mathfrak{D}^3}$ and $\mathfrak{D} < 1$. This implies a contraint in the value of $\mathfrak{D}$ so that $\sqrt{3/\mathfrak{D}^3}$ must be an integer. In our case, $\mathfrak{D} < 0.75$ and so $n > 2$ and $P_{SB} < P_B/3$.

   According to Kipping (2009), the maximum amplitude of the TTVs for a M_S mass satellite orbiting the planet-satellite barycenter with a semi-major axis of a_{SB} is:

$$\delta t^{max}_{exomoon} \approx \frac{a_{SB}M_S}{\sqrt{2}M_P} \cdot \frac{P_B}{2\pi a_B} \tag{6.5}$$

   where M_P is the mass of the planet and a_B is the semi-major axis of the orbit of the barycenter around the star. If we use the Newton's Law of gravity, we can write a_{SB} as a

function of the period of P_{SB}). By setting $P_M = n \cdot P_P$ with n being an integer number, we can re-write the above equation as:

$$\delta t^{max}_{exomoon} \approx \frac{M_M}{M_P^{2/3}} \cdot \frac{P^{5/3}}{2\pi\sqrt{2}a_P} \cdot \left(\frac{G}{4n\pi}\right)^{1/3} \tag{6.6}$$

In the following section, we find some possible solutions for the possible detection of an exomoon when correcting the transit times from the measured TTVs. By introducing the values provided by the best solutions in the above equation, we find $\delta t^{max}_{exomoon}(B4) = 10 - 19$ minutes. Since the measured scatter in the Mazeh et al. data is 71 minutes, we can conclude that an exomoon itself cannot induce the observed TTV scatter.

We have explored the main possible causes for the detection of the large TTVs. The conclusion is that only four specific resonant configurations of the type j:j+1 (1:2, 2:3, 3:4, and 4:5) can produce by themselves the detected maximum TTV.

Finally, we warn that the above calculations were done by assuming coplanar orbits for the planets involved. This study shows that more work is needed on this interesting system to unveil all the detected features. In particular, Kepler-91b is an excellent candidate to be followed-up by the forthcoming high-precision space-based photometers such as *TESS*, *CHEOPS*, and *PLATO*.

6.2.3.6 Radial velocity

Table 6.10 summarizes the observing characteristics (Julian date, exposure time, S/N, and phase) as well as the RV values for each epoch. In Fig. 6.10, we show the phase-folded RV data.

Prior to fitting a Keplerian orbit to the RV data, we performed a Lomb-Scargle periodogram (Fig. 6.11) to check whether we detect the planetary signal at the expected period ($T = 6.246580 \pm 0.000082$ days as determined by Batalha et al., 2013). The longest period explored was set to the longest timespan between our observations (i.e., $T_{max} = t_{max} - t_{min} = 62$ days, where t_{max} and t_{min} are the earliest and latest Julian dates in our observations). Since the observations are unevenly separated, the shortest period searched was set to the median of the inverse time interval between data points, as was proposed by Debosscher et al. (2007) and Ivezić et al. (2013), $T_{min} = \overline{\Delta t} = 2.8$ days.[11] The significant peak in the power spectrum (with a false-alarm probability[12] of $FAP = 0.09\%$, over the 0.1% level) coincides with the expected period of the planet. This provides clear confirmation for the detection of a periodic signal. Consequently, we can affirm that we are detecting the RV signal of Kepler-91b.

[11] Eyer & Bartholdi (1999) claimed that for most practical cases, lower periodicities (higher frequencies) can be detected even for strongly (but randomly) under-sampled observations.

[12] Calculated by using the *astroML* python module (Vanderplas et al., 2012) and its bootstrapping package.

TABLE 6.10: Observational data and radial velocity for Kepler-91. Julian date is calculated at mid-observation.

Julian Date (days)-2456000	$\overline{S/N}$	Phase	RV (km/s)	Julian Date (days)-2456000	$\overline{S/N}$	Phase	RV (km/s)
079.3736990	10.2	0.6936	$-61.849^{+0.102}_{-0.086}$	102.5440124	11.4	0.4029	$-61.994^{+0.082}_{-0.071}$
079.4035263	10.9	0.6983	$-61.916^{+0.111}_{-0.096}$	102.5786588	11.6	0.4084	$-62.060^{+0.087}_{-0.073}$
079.4383387	11.6	0.7039	$-61.905^{+0.099}_{-0.084}$	103.4294963	11.6	0.5446	$-61.942^{+0.085}_{-0.073}$
080.6188492	10.0	0.8929	$-61.973^{+0.106}_{-0.090}$	103.4647180	10.6	0.5502	$-61.992^{+0.111}_{-0.089}$
080.6408499	9.5	0.8964	$-62.006^{+0.095}_{-0.085}$	111.6216095	10.9	0.8561	$-62.030^{+0.100}_{-0.089}$
089.6348116	11.3	0.3363	$-62.059^{+0.092}_{-0.078}$	112.3867977	11.4	0.9786	$-62.133^{+0.127}_{-0.105}$
092.4534211	11.3	0.7875	$-61.933^{+0.091}_{-0.079}$	112.4215921	11.5	0.9841	$-62.023^{+0.124}_{-0.105}$
092.4885156	11.5	0.7931	$-61.910^{+0.081}_{-0.073}$	116.4573650	11.1	0.6302	$-61.874^{+0.101}_{-0.081}$
093.3820328	11.1	0.9361	$-61.984^{+0.092}_{-0.080}$	116.4939625	11.3	0.6361	$-61.851^{+0.105}_{-0.086}$
093.4167639	11.4	0.9417	$-62.027^{+0.098}_{-0.080}$	121.3892272	10.8	0.4197	$-62.057^{+0.116}_{-0.096}$
094.3825217	11.4	0.0963	$-62.023^{+0.092}_{-0.078}$	121.4241545	11.0	0.4253	$-62.129^{+0.115}_{-0.092}$
094.4174484	11.6	0.1019	$-62.055^{+0.088}_{-0.077}$	123.5107198	10.8	0.7594	$-62.069^{+0.116}_{-0.097}$
094.6184378	10.6	0.1341	$-62.018^{+0.081}_{-0.067}$	123.5616251	11.0	0.7675	$-61.968^{+0.100}_{-0.080}$
094.6431432	10.5	0.1380	$-62.149^{+0.091}_{-0.080}$	128.3874072	10.5	0.5401	$-61.984^{+0.110}_{-0.090}$
095.6096755	10.7	0.2928	$-62.205^{+0.090}_{-0.075}$	128.4226132	11.1	0.5457	$-62.014^{+0.105}_{-0.087}$
095.6444425	10.5	0.2983	$-62.175^{+0.109}_{-0.094}$	131.3837431	11.4	0.0197	$-61.955^{+0.100}_{-0.086}$
096.4018846	10.3	0.4196	$-62.051^{+0.157}_{-0.129}$	131.4186423	11.5	0.0253	$-61.993^{+0.099}_{-0.086}$
096.4367742	9.6	0.4252	$-61.906^{+0.139}_{-0.115}$	140.3877688	11.0	0.4612	$-61.973^{+0.093}_{-0.077}$
099.3819275	10.7	0.8966	$-62.062^{+0.115}_{-0.095}$	140.4227569	10.8	0.4668	$-61.895^{+0.121}_{-0.105}$
099.4167349	10.5	0.9022	$-61.971^{+0.106}_{-0.091}$	141.5906808	10.6	0.6537	$-61.944^{+0.164}_{-0.134}$

We then used the RVLIN software[13] (Wright & Howard, 2009) and its additional package BOOTTRAN for parameter uncertainties estimation with bootstrapping (described in Wang et al., 2012) to fit our RV data to a Keplerian orbital solution. Since we have extensive observations of its transit, the period of the planet can be far more accurately and precisely determined by the transit analysis. Thus, we decided to fix the period to that provided by Batalha et al. (2013). Because of the relatively large uncertainties in the RV and incomplete coverage of the RV curve, we also decided to fix the eccentricity of the orbit to the slightly non-circular value determined by Lillo-Box et al. (2014a), $e = 0.066^{+0.013}_{-0.017}$. The free parameters for this fitting were the semi-amplitude of the RV variations (K), the systemic velocity of the system (V_{sys}), and the orbital argument of the periastron (ω).

We used the asteroseismic determination of the stellar mass of the host star, $M_\star = 1.31 \pm 0.1\ M_\odot$, to obtain a precise value of the minimum mass of the transiting object (i.e., $M_p \sin i$). Moreover, we know that the orbit of this planet is highly inclined with respect to our line of sight. We assumed the inclination from the transit fit ($i = 68.5^{+1.0}_{-2.0}$ degrees), which is supported by previous light curve analysis such as Tenenbaum et al. (2012), who derived $i = 71.4 \pm 2.5$ degrees, in good agreement with our value. Thus, we can directly determine the absolute mass of the orbiting object.

[13] http://exoplanets.org/code/

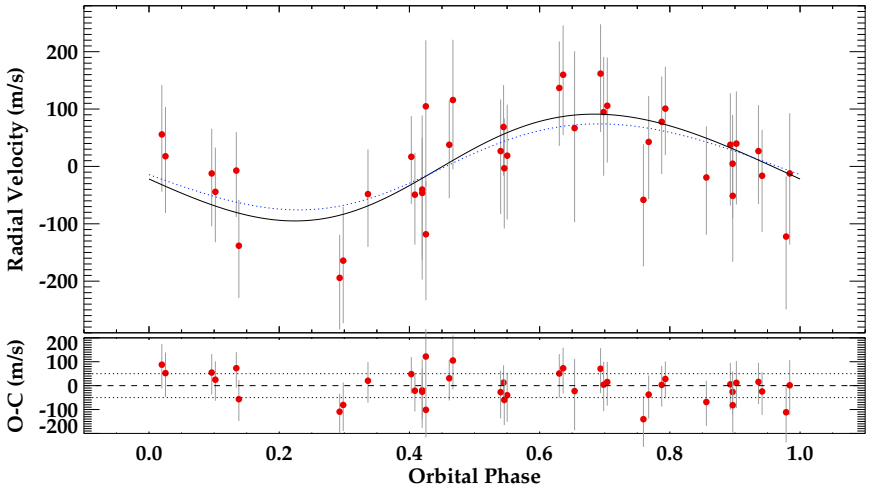

FIGURE 6.10: Radial velocity data of Kepler-91 (red circles). The solid black line shows the fit to the acquired radial velocity data by assuming the period obtained by the *Kepler* team (Batalha et al., 2013) and the small eccentricity derived in section § 6.2.3.3 using the light curve modulations (REB). The dotted line represents the independent curve obtained by using the parameters extracted from the analysis of the REB modulations.

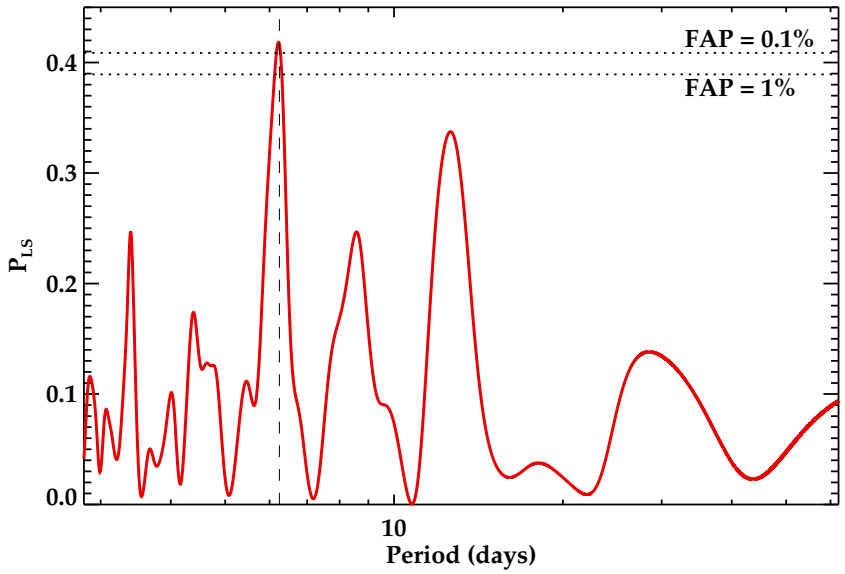

FIGURE 6.11: Lomb-Scargle periodogram of the radial velocity data of Kepler-91 obtained with CAFE. The dotted lines show the false-alarm probability levels of $FAP = 0.1\%$ and $FAP = 1\%$. The vertical dashed line shows the period derived by transit detection. The detected peak at 6.23 ± 0.03 days in this RV periodogram has an FAP= 0.09%.

The results of the RVLIN fitting process are shown in the third column of Table 6.11. The best fit model is plotted in Fig. 6.10. We investigated the significance of that fit against a constant model (which would imply that we are just detecting noise). We infer a Bayesian information criterion (BIC[14]) for the constant model and for the RV model of $\mathrm{BIC}_{const.} = 30.5$ and $\mathrm{BIC}_{RV} = 27.8$.[15]

[14] BIC= $\chi^2 + k \log N$, where $\chi^2 = \sum \frac{(RV_{model} - RV_{obs})^2}{\sigma^2_{RV}}$, k is the number of free parameters, and N is the number of data points.

[15] Assuming a circular orbit, we obtain $\mathrm{BIC}_{RV(e=0)} = 28.3$.

This implies a ΔBIC= 2.7, which provides positive (although not strong) evidence for the RV model (positive detection) against the constant model (negative detection). Alternatively, we obtain a value of 12.7 for an F-test with weighted residuals.[16] This value is higher than the corresponding value of the F-distribution for a 99% confidence level, $F_{0.01}(p_2 - p_1, N - p_2) = F_{0.01}(3, 36) = 4.38$. Thus, we can confirm that the detected RV variability is significant at 99% confidence level with respect to pure noise.

The radial velocity data confirm the Jupiter-like mass ($M_p \sin i = 1.01 \pm 0.18\ M_{Jup}$) of the planet orbiting Kepler-91. Using our previous value for the inclination, the absolute mass becomes $M_p = 1.09 \pm 0.20\ M_{Jup}$. This result agrees well, within the uncertainties, with the derived mass from the REB analysis in § 6.2.3.3 ($M_p = 0.88^{+0.17}_{-0.33}\ M_{Jup}$). Moreover, the semi-major axis $a_{RV} = 0.0726 \pm 0.0019$ AU also agrees extremely well with the value determined by the light curve modulations, of $a_{REB} = 0.072^{+0.002}_{-0.007}$ AU. The corresponding radial velocity model using the photometrically derived parameters obtained in the REB analysis is also plotted in Fig. 6.10 for comparison purposes.

6.2.4 Summary and discussion

We have used different types of observations and techniques to confirm the planetary nature of the extrasolar planet Kepler-91b. We applied several techniques to accurately derive the host star properties and two independent techniques to derive the planet and orbit characteristics. We conclude that Kepler-91b is a giant gaseous planet orbiting a giant K3III star ascending the RGB. The light curve modulations seem to favor a slightly eccentric orbit. In the following we compare our results to other posterior works and analyze the properties of this system based on our data.

Properties of the planetary system By considering the whole analysis, we report in Table 6.11 the parameters calculated for the Kepler-91 system according to the radial velocity and light curve analysis.

Regarding stellar parameters, from all determinations of the effective temperature and metallicity, we have chosen our spectroscopically calculations since they are the most precise ones and lie within the uncertainty limits of other studies. Thanks to its high precision as compared to other methods, asteroseismology determinations of the rest of the stellar parameters have been assumed. According to both asteroseismology and the analysis of the isochrones and evolutionary tracks, we estimate a stellar age of 2.7 − 7.0 Gyr. Given the calculated stellar parameters (stellar radius, effective temperature, and extinction), we can estimate a distance to Kepler-91

[16] $F = \frac{\chi_1^2 - \chi_2^2}{p_2 - p_1} / \frac{\chi_2^2}{N - p_2}$, where p_1 and p_2 are the free parameters of both models (so that $p_2 > p_1$), and N the number of data points.

by assuming the bolometric corrections polynomials defined by Flower (1996) and re-calculated by Torres (2010). The calculations provide a value of $d = 1030^{+150}_{-130}$ pc.

When it comes to the orbital parameters, we have demonstrated that an eccentric orbit is required to better describe the REB modulations. Thus, this parameter (together with the argument of the periastron) is better constrained by this technique rather than by the transit fitting or the radial velocity (which is too noisy to derive these parameters). Both studies agree on the high inclination of the orbit and provide similar values. We thus use the REB modulation analysis value due to its higher precision.

We used evolutionary tracks from Girardi et al. (2002) and assumed the effective temperature, metallicity, stellar radius, and mass from our spectroscopic and asteroseismic studies to compute the time that the radius of the star Kepler-91 will reach the current planet's orbital pericenter. If we only take this evolutive constraint into account, we conclude that Kepler-91b will be engulfed by the stellar atmosphere in less than 55 Myr. It is important to note that other non-negligible effects inducing instabilities on the planetary orbit could speed up the planet engulfment. As a result, this result can be considered as an upper limit to the remaining life of the planet. The first clear evidence of planet engulfment was published by Adamów et al. (2012). The authors showed the signs of a post-planet engulfment scenario for BD+48 740, where the presence of a highly eccentric ($e = 0.67$) secondary planet and an overabundance of lithium in the stellar spectrum could be caused by the previous engulfment of an inner planet. With a similar stellar mass, Kepler-91 could be in the immediately previous stage of BD+48 740, the scenario before the planet engulfment. In Chapter 7, we will place this planet and the other planets discovered by this survey, in context with the large crop of planets that have been currently confirmed.

Finally, given the planetary mass and radius obtained by the REB modulation and transit fitting studies, respectively, we can derive a mean density of $< \rho_p >= 0.33^{+0.10}_{-0.05}\ \rho_{\rm Jup}$, placing Kepler-91b in the giant gaseous planet locus of the mass-radius diagram of known exoplanets (Fortney et al., 2007). As for HD209458b, Kepler-91b seems to have an inflated atmosphere probably due to the strong stellar irradiation of its host star.

Stellar irradiation on the planet

The extremely close-in orbit of Kepler-91b and the large size of its host star imply a large stellar irradiation on the planet's atmosphere, which should have been playing an important role in the evolution of this planetary system. The equilibrium temperature of the planet is given by López-Morales & Seager (2007):

$$T_{eq} = T_\star \left(\frac{R_\star}{a}\right)^{1/2} [f(1 - A_B)]^{1/4} \tag{6.7}$$

where $A_B = \frac{3}{2}A_g$ is the Bond albedo if we assume Lambert's law. According to Eq. 2.18, the geometric albedo for the calculated parameters is $A_g = 0.154$. The f parameter describes the redistribution of the incident stellar flux in the planet's atmosphere and goes from $f = 1/4$, when the energy is instantaneously redistributed in the atmosphere, to $f = 2/3$, when the energy is instantaneously re-radiated to space. The equilibrium temperature in both extreme cases would be $T_{eq}(f = 2/3) = 2460^{+120}_{-40}$ K and $T_{eq}(f = 1/4) = 1920^{+100}_{-30}$ K. Note that we have not considered the effect on the planet equilibrium temperature of the actual fraction illuminated by the host star, as discussed in Guillot (2010).

Given the calculated stellar and orbital parameters, we obtain that around 70% of the planet atmosphere would be illuminated by the host star (in contrast to the approximately 50% illuminated for planets on wider orbits). The extra angle illuminated of the planet as counted from the perpendicular axis to the orbital plane is, at the periastron (apastron) of the orbit, $\alpha = 22.7^{+1.7}_{-1.1}$ ($20.8^{+2.3}_{-1.0}$) degrees (see Fig. 6.12). The angular size of the star as seen from the planet is given by $\tan(\beta/2) = R_\star/a$ so that, for this system, we obtain $\beta = 46.5^{+3.4}_{-0.3}$ degrees at pericenter passage. This value is well above the rest of the known planetary systems, with $\beta < 10°$. The implications of this effect on any determination of the planet and orbital parameters must be investigated by future works. In particular, the phase function function of the planet and so the reflection modulation would be affected by this additionally illuminated surface. Additionally, given the estimated high temperature of the planet, the depth of the transit could also be affected, indicating a smaller radius. These effects could be noticiable in high-precision photometric missions and should be taken into account in very close-in planets around giant stars, where it could be more relevant.

Comparison to other works

Two works claimed a non-planetary nature for Kepler-91b, one of them (Esteves et al., 2013, E13) prior to our confirmation in Lillo-Box et al. (2014a)[17] and the other (Sliski & Kipping, 2014, S14) published after our RV paper (Lillo-Box et al., 2014c). The first work was subsequently corrected by their authors in Esteves et al. (2014), E14, where they provide new fittings for the REB modulations and conclude that Kepler-91b is, indeed, a planet. On the other hand, three posterior works (Angerhausen et al., 2014, Barclay et al., 2015, Sato et al., 2015) provided additional independent proofs for the planetary nature of this object, as we had already demonstrated in Lillo-Box et al. (2014a,c). The parameters derived by all these works are shown in Table 6.11

E13, calculated a large value for the geometric albedo of the transiting object ($A_g = 2.49^{+0.55}_{-0.60}$), what led them to argue a self-luminous nature and thus discard its planetary nature. They derived a mass of $5.92^{+0.68}_{1.12} M_{\rm Jup}$ and obtained discrepant day/night-side and equilibrium temperatures

[17] This paper was sent to the journal on the 31 May 2013.

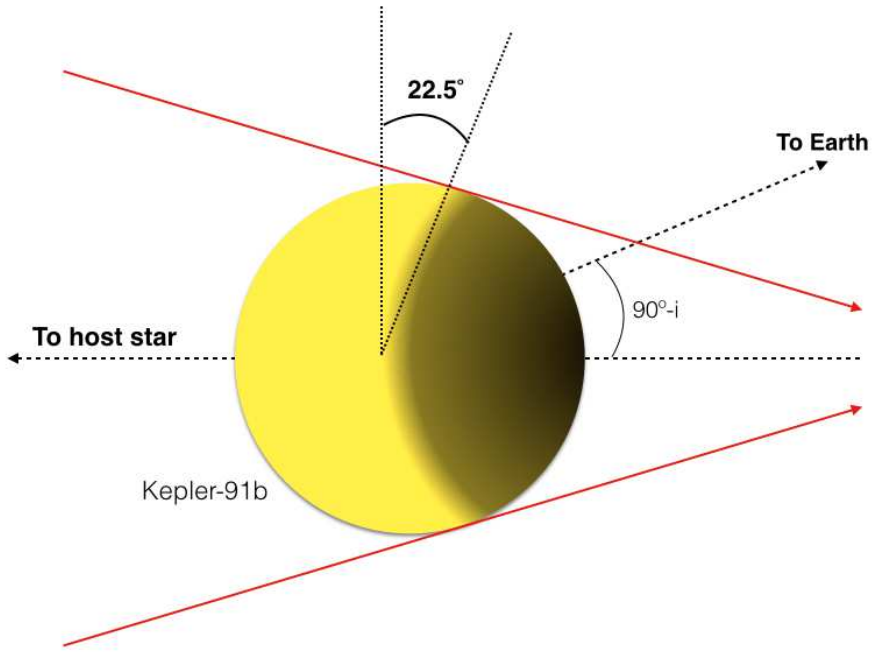

FIGURE 6.12: Diagram illustrating the irradiation of the host star onto the planet surface at mid-transit. The red lines represent the boundaries of the stellar irradiation that hits the planet surface.The yellow part represents the dayside. The black part represents the night side.

based on a claimed detection of the secondary eclipse. However, as we noted and Angerhausen et al. (2014) concluded as well, the detection of the secondary eclipse is neither clear nor conclusive. Moreover, given the derived mass by E13 for this companion with a Jupiter-like radius, it is difficult to explain their proposed stellar nature. This was subsequently corrected by E14, who estimated a geometric albedo of $A_g = 0.39^{+0.18}_{-0.19}$ assuming that dips A+B conform the secondary eclipse of the planet (what we cannot assure due to the reasons provided in § 6.2.3.4).

S14 also classified Kepler-91b as a false positive. They compared the asteroseismic determination of the stellar density $\rho_{\star,astero} = 6.81 \pm 0.32\ kg/m^3$ (derived by Huber et al., 2013), with the observed value $\rho_{\star,obs} = 43.47^{+0.67}_{-3.35}\ kg/m^3$ derived by them directly from transit fitting. Based on the large discrepancy between the two values, they concluded that to explain this disagreement, the orbit of the planet would have to be highly eccentric such that the planet is essentially expected to be in-contact with the star. Basically, their derived observed stellar density corresponds to a semi-major axis of the companion of $a/R_\star = 4.476^{+0.023}_{-0.118}$, similar to that of Esteves et al. (2013), $a/R_\star = 4.5$. The authors claimed that the two determinations of the semi-major axis are independent, but they both used the same set of photometric data and the same observational effect (the transit signal).

Barclay et al. (2015) provided the clues for disentangling the misclassification of Kepler-91b as a false positive by S14. As explained by Barclay et al., the star exhibits temporally correlated noise due to stellar granulation which they model as a Gaussian Process. They hypothesize that it is this noise component that led S14 to suspect that Kepler-91b was a false positive. Their

TABLE 6.11: Derived parameters from different works on Kepler-91.

	Lillo-Box et al. (2014a,c)		Barclay et al. (2015)	Sato et al. (2015)
Parameter	LC	RV		
$M_p \sin i$ ($M_{\rm Jup}$)	-	1.01 ± 0.18	-	-
R_p ($R_{\rm Jup}$)	$1.384^{+0.011}_{-0.054}$	-	$1.308^{+0.061}_{-0.074}$	1.40 ± 0.04
M_p ($M_{\rm Jup}$)	$0.88^{+0.17}_{-0.33}$	1.09 ± 0.20	0.73 ± 0.13	0.66 ± 0.06
ρ_p ($\rho_{\rm Jup}$)	$0.33^{+0.10}_{-0.05}$	$0.41^{+0.13}_{-0.08}$	$0.40^{+0.10}_{-0.09}$	0.24
$a/R_\star$	$2.45^{+0.15}_{-0.30}$	2.48 ± 0.12	$2.469^{+0.011}_{-0.011}$	$2.253^{+0.046}_{-0.045}$
a (AU)	$0.072^{+0.002}_{-0.007}$	0.0726 ± 0.0019	-	-
i (deg.)	$68.5^{+1.0}_{-1.6}$	-	$69.12^{+0.58}_{-0.88}$	$67.37^{+0.63}_{-0.65}$
e	$0.066^{+0.013}_{-0.017}$	-	$0.040^{+0.040}_{-0.016}$	$0.0519^{+0.0095}_{-0.0088}$
ω (deg.)	$316.8^{+21}_{-7.4}$	-	355.8	$302.8^{+8.7}_{-7.1}$
K (m/s)	-	93 ± 17	$67.1^{+9.4}_{-8.3}$	-
V_{sys} (km/s)	-	-62.011 ± 0.011	-	-

joint RV+light curve analysis yielded similar planet and orbital parameters as those derived by us.

A posterior work by Sato et al. (2015) also provided a joint RV+light curve analysis, again showing the planetary nature of Kepler-91 b. Additionally, they found a 20 m/s trend in their their precise measurements with Subaru/HDS along one year baseline, which suggests the presence of additional bodies in the system.

All the analysis presented in this section together with the results obtained by the aforementioned works suggest that Kepler-91 b is not the only body orbiting its host star. However, more precise radial velocity data and short-cadence high-precision photometry can shed more light to the detection of these hypothesized additional bodies.

6.3 Kepler-432 b: a massive planet in a highly eccentric orbit transiting a red giant

In this section we present the confirmation and characterization of the extrasolar planet Kepler-432b. This work was published in Ciceri et al. (2015).

6.3.1 Context

Up to now, more than 50 exoplanets have been detected around evolved giants with Doppler spectroscopy, and their general characteristics are different from those found orbiting main sequence (MS) stars. According to the study of Jones et al. (2014), they are more massive, prefer low-eccentricity orbits, and have orbital semi-major axes of more than 0.5 AU with an overabundance of between 0.5 and 0.9 AU. Furthermore, the correlation between stellar metallicity and the number of planets seems to be reversed compared with MS stars, even though there is still an open debate on this matter (see discussion in Jones et al., 2014). In this context, the discovery of more exoplanets around evolved stars is vital to enlarge the sample and better characterize the statistical properties of these planetary systems. The cases in which the parent stars are K or G giants, which are known to evolve from F- and A-type MS stars, are also very interesting for planet formation and evolution theories and help to form a better demographic picture of planets around early-type (more massive and hot) stars.

Here we describe the confirmation via RV measurements of the transiting planet Kepler-432 b (KOI-1299.01, KIC10864656), which we show to be a massive gas giant moving on a very eccentric orbit around an evolved K giant star that is ascending the red giant branch. Both Kepler-432 b and Kepler-91 b are on tight orbits and present physical characteristics that deviate from the systems detected so far by the RV method. This work was contemporaneously submitted with that by Ortiz et al. (2015), who also confirmed the planetary nature of Kepler-432 b. Both researches were carried out in independent manner by using CAFE and FIES/NOT.

6.3.2 Observations

***Kepler* photometry.-** Kepler-432 was continuously monitored by *Kepler*, being observed in 17 quarters with the long-cadence mode (29.4 min) and during 8 quarters in short-cadence mode ($\sim$ 1 min). It shows a periodic dimming in the light curve every 52.5 days.

High-spatial resolution imaging.- In this case, we did not obtained AstraLux images of this target. Instead, we analyzed two high-resolution images of Kepler-432 in J and K bands that were obtained with the NIRC2 imager mounted on the Keck II telescope, used in adaptive optics mode.[18] In these images, there is a clear detection of a nearby star at 1.1 arcsec, which is much fainter than Kepler-432 A, with $\Delta J = 5.68 \pm 0.04$ mag and $\Delta K = 5.19 \pm 0.01$ mag. We translated these differences into *Kepler*-band magnitudes by using the formulae from Howell et al. (2012), obtaining that component B is 6.68 ± 0.17 mag fainter than Kepler-432 A.

[18] The images were published by David Ciardi on the Community Follow-up Observing Program (CFOP, https://cfop.ipac.caltech.edu/home/), who kindly allowed us their use in this work.

TABLE 6.12: Photometric and physical properties of Kepler-432 from previous studies and our own results.

Parameter	Value	Reference
$R_\star$ ($R_\odot$)	4.160 ± 0.120	Huber et al. (2013)
$M_\star$ ($M_\odot$)	1.353 ± 0.101	Huber et al. (2013)
$\rho_\star$ (g cm^{-3})	0.02650 ± 0.00049	Huber et al. (2013)
$T_{\rm eff}$ (K)	4850 ± 100	This work
$\log g$ (cgs)	3.0 ± 0.5	This work
m_{Kep} (mag)	12.183	NASA Archive

Notes. The data taken from the NASA Exoplanet Archive are available on `http://exoplanetarchive.ipac.caltech.edu`.

High-resolution spectroscopy.- We obtained 28 spectra of Kepler-432 during 16 nights of observations carried out in the 2013 and 2014 seasons. The exposure time was 1800 s for most spectra, but increased to 2700 s for six spectra to compensate for the presence of thin clouds. The spectra were reduced by using the observatory pipeline (see section § 4.4.2). The radial velocity data were extracted by using the CCF approach as explained in § 4.3.1. We combined all spectra shifted at the same rest frame to obtain a high-resolution and high S/N spectrum of the target, used to obtain the stellar properties.

6.3.3 Analysis

Properties of the host star

Huber et al. (2013), making use of the asteroseismology technique, refined some parameters of this system. These were updated by Burke et al. (2014). We summarise relevant parameters in Table 6.12. Besides, we used the high-resolution and high-S/N spectrum of Kepler-432 to determine its general properties in an independent way. Following the methodology described in Fossati et al. (2010), we inferred the effective temperature of the star $T_{\rm eff}$ and its surface gravity $\log g$. The derived properties are also summarized in Table 6.12.

Orbital and physical properties from a joint light curve and RV analysis

To determine the physical parameters of the system, we simultaneously modeled the *Kepler* photometry and the CAFE RVs using the JKTEBOP code (see Southworth, 2013, and references therein). The parameters of the fit were chosen to be the fractional radii of the two objects ($r_\star = R_\star/a$ and $r_{\rm p} = R_{\rm p}/a$, where a is the orbital semi-major axis), orbital inclination (i), orbital period (P), reference transit midpoint (T_0), velocity amplitude ($K_\star$), systemic velocity ($V_{\rm sys}$) of the system, the eccentricity (e), and argument of periastron (ω).

The *Kepler* long- and short-cadence data were each converted from flux to magnitude units. Data with more than two transit durations from a transit midpoint (approximately 95% of the

datapoints for both cadences) were rejected to aid computational efficiency. Each transit was rectified to zero differential magnitude by subtracting a linear or quadratic polynomial trend versus time, fitted to the out-of-transit data points. The short-cadence data were additionally treated by iteratively rejecting 3σ outliers, totaling 1.2% of the data points. Error bars for the data for each cadence were assigned to force a reduced chi-squared of $\chi^2_\nu = 1$. The radial velocity error bars were scaled by $\sqrt{1.8}$ to achieve the same goal.

The very low ratio of the radii means that the transit is shallow and the partial phases (ingress and egress) are short. Their length is poorly determined by the data, leading to i and $r_\star$ being highly correlated. The solution is indeterminate without outside constraints. Fortunately, the asteroseismic density from Huber et al. (2013) can be used to rescue the situation: under the assumption that $M_\star \gg M_\mathrm{p}$, the density is directly related to $r_\star$ (Seager & Mallén-Ornelas, 2003). We therefore fixed $r_\star$ at the value for the known density (Table 6.12) and fitted for i. Limb darkening was specified using the quadratic law, whose coefficients were fixed at the theoretical values given by Sing (2010). We also assumed that, neglecting the detected B component, no other light came from the planet or from any additional object along the same sightline. The low sampling rate of the long-cadence data was dealt with as in Southworth (2011).

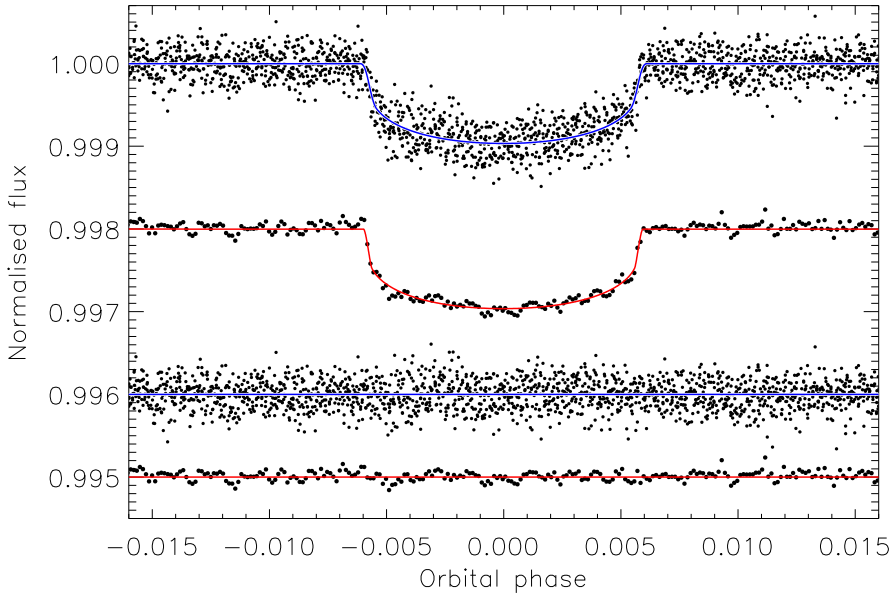

FIGURE 6.13: *Kepler* long-cadence (top light curve) and short-cadence (bottom light curve) data around transit. The JKTEBOP best fits are shown using solid lines. The residuals of the fits are shown offset towards the base of the figure. We phase-binned the short-cadence data by a factor of 100 to make this plot clearer. Figure from Ciceri et al. (2015).

The best fits are shown in Figs. 6.13 and 6.14; the scatters around the best fits were 0.19 mmag and 0.42 mmag for the long- and short-cadence. To determine error estimates, we ran Monte Carlo and residual-permutation (Southworth, 2008) simulations and adopted the larger of the two error bars for each parameter. We also needed to account for the uncertainty in $r_\star$. We did this by calculating solutions with $r_\star$ fixed at its asteroseismic value plus/minus its error bar to

determine the effect on each parameter, and added this in quadrature to the uncertainty from the Monte Carlo and residual-permutation simulations.

The result of this process was values for $r_\star$, r_p, i, P, T_0, $K_\star$, V_{sys} and e. Independent results were calculated for both cadences and found to be consistent. We adopted those from the short-cadence data because they yield parameter values with a better precision. The final physical properties of the system were then calculated using standard formulae, and the uncertainties were propagated with a Monte Carlo approach. These results are collected in Table 6.13.

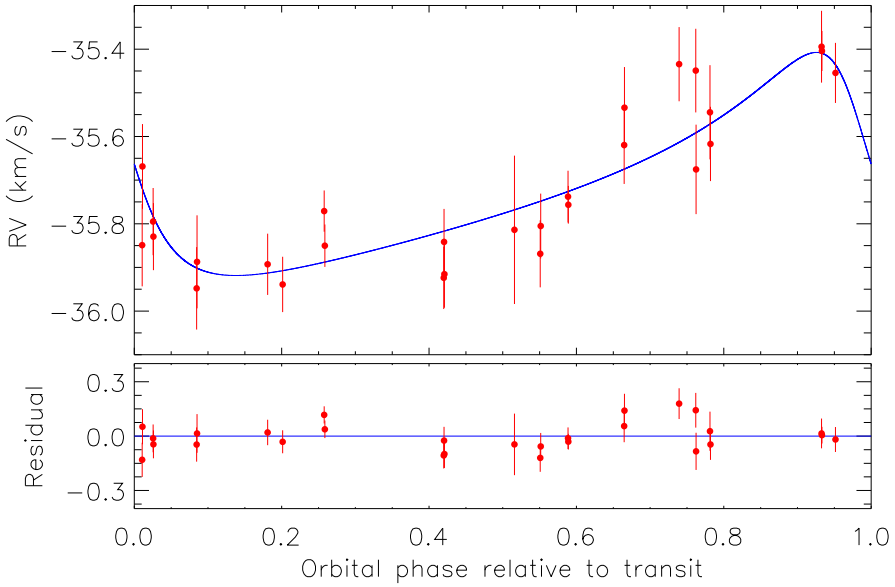

FIGURE 6.14: Upper panel: phased RVs for Kepler-432 red points) and the best fit from JKTEBOP (blue line). Lower panel: residuals of RVs versus best fit. Figure from Ciceri et al. (2015).

Rejection of blend scenarios

Owing to unveil the origin of the RV variations, we obtained a Lomb-Scargle periodogram of the RVs without considering the transit times from the photometry. Among the first three peaks we found P = 51.95 d (with a false-positive probability of FAP= 0.0136), a value similar to that obtained from the *Kepler* photometry. This strongly suggests that the object causing the periodic transits is also causing the RV variations.

Assuming that the object is transiting component A and using the relations from Lillo-Box et al. (2014b), we estimated the dilution effect of the faint star on the depth of the transit events, finding a correction of 0.01 $R_\oplus$ for the radius of the eclipsing object. This correction is much smaller than the uncertainty in our measurement of the radius of Kepler-432 b. Another possibility is that the B component might be an eclipsing binary. However, since we detected an RV signal of a planetary-mass object with the same periodicity as the transit signal and the companion is very faint, this scenario is very unlikely. Instead, the most probable scenario is that the planet is

TABLE 6.13: Measured properties of the Kepler-432 planetary system.

Parameter	Value
T_0 (BJD/TDB)	2455477.02906 ± 0.0014
P (d)	52.50097 ± 0.00021
$K_\star$ (km s^{-1})	0.256 ± 0.021
$V_{\rm sys}$ (km s^{-1})	-35.73 ± 0.014
e	0.535 ± 0.030
ω (degrees)	61.3 ± 7.9
$r_\star$	0.06374 ± 0.00039
$r_{\rm p}$	0.001763 ± 0.000022
i (degrees)	88.9 ± 1.3
$a/R_\star$	15.689 ± 0.096
$M_{\rm p}$ ($M_{\rm Jup}$)	4.87 ± 0.48
$R_{\rm p}$ ($R_{\rm Jup}$)	1.120 ± 0.036
$g_{\rm p}$ (m s^{-2})	96 ± 11
$\rho_{\rm p}$ ($\rho_{\rm Jup}$)	3.46 ± 0.48
a (AU)	0.3034 ± 0.0089

orbiting component A and that B only acts as a diluting source, having very weak implications on the planet (and orbital) properties derived from the light curve.

Additionally, other possible source of false positives is stellar activity, which could mimic the presence of a planetary body in the RV signal. To rule out this possibility, we determined the bisector velocity span (BVS) from the same spectra from which we obtained the RV measurements. The BVS values are plotted in Fig. 6.15 together with the best-fitting line, which is consistent with a horizontal line. This means that we did not find any significant correlation between RV and BVS, which rejects the stellar activity as the source of the RV variations.

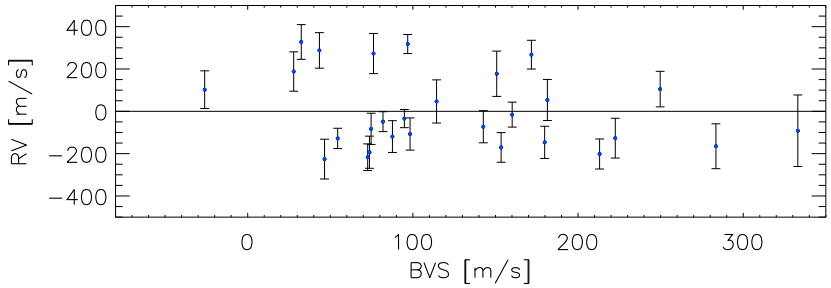

FIGURE 6.15: Radial velocity (RV) versus bisector velocity span (BVS) for Kepler-432. Figure from Ciceri et al. (2015).

6.3.4 Summary and discussion

We confirmed the planetary nature of Kepler-432 b, a planet with a mass of 4.87 ± 0.48 $M_{\rm Jup}$ and a radius of 1.120 ± 0.036 $R_{\rm Jup}$, orbiting a K2III giant that is ascending the red giant branch.

The planet has an eccentric orbit ($e = 0.535 \pm 0.030$) with a period of 52.50097 ± 0.00021 days. After Kepler-56 b,c and Kepler-91 b, Kepler-432 b becomes the fourth known transiting planet orbiting an evolved star. These planets have quite different characteristics from those detected by the RV method, and cover regions of parameter spaces that were considered to be void until now, see Chapter 7. They are also important indicators of the formation processes and evolutionary scenarios for planets around early-type stars.

Mazeh et al. (2013) found no significant transit-time variations for Kepler-432, and our RV data do not show any hint of a trend caused by a longer-period companion. More RVs and a longer time-span are necessary to constrain the possible presence of a third body that might be responsible for the location and eccentricity of Kepler-432 b.

Since Kepler-432 A is still evolving and expanding, this planetary system is also very interesting from a dynamical point of view. Currently, the planet reaches the minimum distance of $7.29 \pm 0.52\,R_\star$ at periastron, while at apastron is $24.08 \pm 0.85\,R_\star$ away. However, at the end of the red giant branch, the star will have a radius of $\sim 8\,R_\odot$ and, if we exclude a possible orbital decay due to angular momentum transfer mechanism, the distance of the planet from the star at periastron will be $\sim 3.8\,R_\star$. This means that the planet will not be directly devoured by its parent star (unless it experiment a spiral infall due to gravitational perturbations), but will instead accompany it towards a more distant common fate.

The contemporaneous work by Ortiz et al. (2015) (using data from CAFE and FIES) found a linear radial velocity trend of $\dot{\gamma} = 0.44 \pm 0.04$ m/s per day (in their 120-days baseline), suggesting the presence of a third long-period companion planet, which could be the cause for the large eccentricity found. A posterior work by Quinn et al. (2014), claimed the detection of the second planet (Kepler-432c) by using long-term observations in a $\sim$ 1200 days timespan with TRES instrument. Their analysis favor the presence of an outer planet with a period of $\sim$ 410 days and a minimum mass of $M_c \sin i = 2.5\ M_{\rm Jup}$, see references for further details.

Based on the works by Villaver & Livio (2009) and Kunitomo et al. (2011a), Ortiz et al. determined that Kepler-432 b will not survive the RGB phase of its host star, so that it will be swallowed by the star before reaching the tip of the RGB.

6.4 Kepler-447 b: a hot-Jupiter with an extremely grazing transit

In this section we present the observations, analysis, and discussion involving the confirmation and characterization of the extrasolar planet Kepler-447b. This work was published in Lillo-Box et al. (2015b).

6.4.1 Context

The *Kepler* light curve (LC) of Kepler-447 (KOI-1800, KIC 11017901; RA=$19^h01^m04^s.46$, DEC=48°33'36") shows a V-shaped dip with a periodicity of 7.79430132 ± 0.00000182 days (Burke et al., 2014). According to Huber et al. (2014), this object is a G8 main-sequence star that is slightly less massive ($M_\star = 0.764^{+0.145}_{-0.049}\ M_\odot$) and smaller ($R_\star = 0.872^{+0.49}_{-0.120}\ R_\odot$) than the Sun. Usually, V-shaped eclipses are classified as false positives. They are mainly identified as eclipsing binaries with stars of similar sizes or grazing stellar eclipses. However, the combination of transit and radial velocity measurements can reveal the planetary nature of the transiting object. If a planetary mass is found for the transiting object, the V-shape is then explained as a grazing planetary eclipse. To date, just one planetary grazing eclipse has been reported and confirmed as achieving the grazing criterion ($b + R_p/R_\star > 1$) over 3σ (WASP-67b, Hellier et al., 2012, Mancini et al., 2014). Also, a few other planets are known to transit their star in near-grazing orbits, but with the grazing criterion achieved below the 3σ level, such as WASP-34b (Smalley et al., 2011) or HAT-P-27/WASP-40 (Anderson et al., 2011, Béky et al., 2011). So far, *Kepler* has discovered none.

The discovery of such grazing planetary transits opens an interesting window. In this configuration, any (even small) gravitational perturbation due to the presence of additional bodies in the system (such as outer planets, exomoons, Trojans, etc.) would modify the standard Keplerian orbit of the planet. Such an effect would possibly induce a periodic variation in the impact parameter of the orbit that would be detectable in the transit data, so that these bodies could become indirectly detectable (e.g., Kipping, 2010). The observational imprints of other effects (such as planet rotation and oblateness or stellar pulsations) could be augmented in such interesting configurations.

In this section, we present the radial velocity and light curve analysis that yielded to the confirmation of this planetary system.

6.4.2 Observations

***Kepler* photometry.-** We have retrieved the *Kepler* photometry of this target from quarters Q1-Q17 (more than 1400 days, only with the long-cadence mode, 29.4 minutes). During Q4, the detector channels 5, 6, 7, and 8 in Module 3 of the charge-coupled device (CCD) failed. Consequently, any source falling in this detectors at any quarter could not be observed. Owing to the rotation of the spacecraft, Kepler-447 felt in this broken down module on Q4, Q8, Q12, and Q16. Thus, no data were acquired for this KOI during those quarters.

We used the simple aperture photometry (SAP) flux and its corresponding uncertainties provided by the *Kepler* team to compute the final light curve. From this analysis we removed any data

point with a quality flag in the processed light curves (SAP_QUALITY) equal to 128 (cosmic ray correction). In section § 6.4.4 we analyze the source and the effect of these datapoints on the light curve. Artificial (well-known) strong trends in the *Kepler* data and modulations due to stellar activity were significant in this case. Consequently, we needed to detrend the fluxes to analyze the transit signal. We used a cubic spline function to model the out-of-transit modulations, selecting the nodes by measuring the mean fluxes of one-day bins. This simple and quick approach provided a clean and flat light curve in the out-of-transit region, while keeping the transit unperturbed.

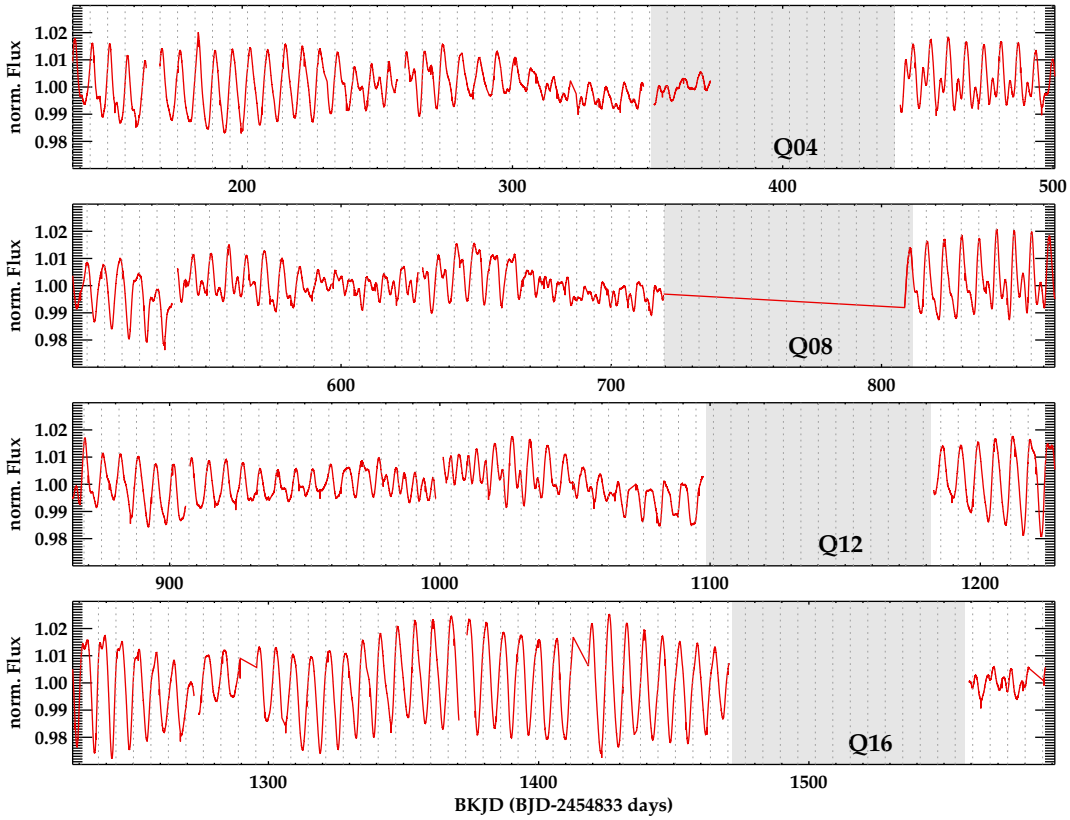

FIGURE 6.16: Photometric time series of Kepler-447 as obtained by the *Kepler* telescope. The simple aperture photometry (SAP) is plotted in red. The quarters in which the source felt in the death detector channels of the CCD are marked as shaded regions (see § 6.4.2). The vertical dotted lines are plotted with a periodicity equal to the measured rotational period by McQuillan et al. (2013b).

High-spatial resolution imaging.- Kepler-447 was part of our high-resolution imaging survey of *Kepler* candidates (see Chapter 5 and Lillo-Box et al., 2012, 2014b). In this case, the high-resolution image and its posterior analysis revealed a BSC value of 99.9%. This implies a 0.1% of probability of having a blended (undetected) source contaminating the *Kepler* light curve. Thus, we assume along this work that Kepler-447 is an isolated target.

High-resolution spectroscopy.- We obtained 21 high-resolution spectra of the target with CAFE, sampling the different orbital phases of the planet candidate. The spectra were reduced by using the dedicated pipeline provided by the observatory (see section § 4.4.2). The RV measurements were obtained by following the cross-correlation approach (see section § 4.3.1). In Table 6.14, we show the observing data and the final RV values for each epoch. We applied several line profile tests[19] to check for possible dependencies of the RV variation with stellar activity. We found no positive correlations between both sets of values in any of the performed tests. In particular, the bisector analysis (BIS, Queloz et al., 2001) provides a Pearson's correlation coefficient of 0.007, thus showing no correlation of the RV with the line profile indicator. We show the BIS values against their corresponding RVs in Fig. 6.17. This may indicate that the RV is not correlated with possible line profile asymmetries caused by stellar inhomogeneities such as spots.

We have also computed the periodogram of the radial velocity data (see lower panel of Fig. 6.17). It shows a relevant peak at the expected period from the transit analysis, with a false-alarm probability (FAP) of FAP < 0.01 %. This also indicates that the object transiting the host star is actually producing the RV variations.

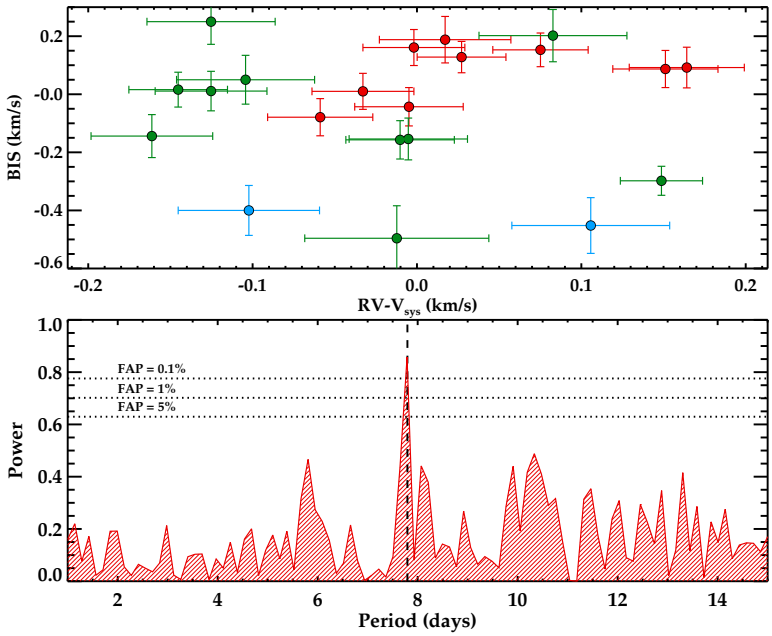

FIGURE 6.17: Bisector analysis and periodogram for Kepler-447. Upper panel: bisector analysis as a function of the measured radial velocity obtained during runs on 2012 (red symbols), 2013 (light blue), and 2014 (green). Lower panel: periodogram of the radial velocity data showing the significant peak at the corresponding transit period (vertical dashed line).

[19]By using the python code provided by P. Figueira (available at https://bitbucket.org/pedrofigueira/line-profile-indicators), explained in Figueira et al. (2013) and presented in Santos et al. (2014).

TABLE 6.14: Measured radial velocities for Kepler-447 by using the CAFE/CAHA spectrograph.

Julian Date (days)-2456000	$\overline{S/N}$	Phase	RV (km/s)	Julian Date (days)-2456000	$\overline{S/N}$	Phase	RV (km/s)
76.593035	26.0	0.941	$1.421^{+0.027}_{-0.027}$	801.517625	9.5	0.948	$1.308^{+0.036}_{-0.036}$
77.536041	23.5	0.062	$1.335^{+0.032}_{-0.032}$	801.552053	10.9	0.953	$1.396^{+0.045}_{-0.045}$
80.543287	25.7	0.448	$1.361^{+0.031}_{-0.031}$	812.524544	11.9	0.360	$1.303^{+0.033}_{-0.033}$
88.515082	15.3	0.471	$1.392^{+0.031}_{-0.031}$	812.556916	11.9	0.365	$1.209^{+0.042}_{-0.042}$
88.549981	17.4	0.475	$1.389^{+0.033}_{-0.033}$	817.599630	7.0	0.012	$1.301^{+0.056}_{-0.056}$
89.381498	17.1	0.582	$1.469^{+0.029}_{-0.029}$	818.585851	11.4	0.138	$1.168^{+0.030}_{-0.030}$
89.416506	13.8	0.587	$1.411^{+0.040}_{-0.040}$	818.553484	10.9	0.134	$1.188^{+0.034}_{-0.034}$
90.523633	23.6	0.729	$1.545^{+0.032}_{-0.032}$	859.401764	7.3	0.375	$1.188^{+0.039}_{-0.039}$
91.376159	18.8	0.838	$1.558^{+0.035}_{-0.035}$	823.582348	13.8	0.778	$1.462^{+0.025}_{-0.025}$
523.571588	11.6	0.288	$0.928^{+0.043}_{-0.043}$	842.549205	11.5	0.213	$1.152^{+0.037}_{-0.037}$
597.302622	18.2	0.748	$1.136^{+0.048}_{-0.048}$				

6.4.3 Analysis

6.4.3.1 Stellar properties: rotation and physical parameters

The SAP flux extracted by the *Kepler* pipeline shows a clear variability at the level of $\sim 4\%$ (peak to peak, see Fig. 6.16). This type of variations has been detected in many other sources with well-sampled photometric time series. They are related to the rotation of the star and the presence of stellar spots on its surface. In particular, McQuillan et al. (2013b) analyzed the photometric modulation caused by starspots in the *Kepler* sample of planet candidates. They calculated the rotational periods for several hundreds of KOIs by using the autocorrelation function technique (ACF), described in McQuillan et al. (2013a) and obtained a rotational period for Kepler-447 of $P_{\rm rot} = 6.459 \pm 0.003$ days. Added to this, we have computed the Lomb-Scargle periodogram of the light curve (see Fig. 6.18). It shows a clear set of peaks around $P_{\rm rot}$, with the highest one at $P_{\rm peak} = 6.4723 \pm 0.0003$ days. Additional but less significant peaks are found at larger periodicities, but their analysis is beyond the scope of the current work. Both the orbital and the stellar rotation share similar periodicities. This could be due to some on-going synchronization between the stellar rotation and the orbital period due to similar processes studied in binary stars, such as tidal friction (Zahn, 1966) or hydrodynamical mechanisms (Tassoul, 1987).

At this point, it is worth to mention that the presence of stellar spots producing the high-amplitude photometric modulations implies the existence of stellar activity. This could contaminate the transit signal with possible spot crossing events such as those detected in other hot-Jupiters around active stars (e.g., Désert et al., 2011, Silva-Valio & Lanza, 2011). These signals can also be used to measure sizes, temperatures, and positions of the spots (Silva, 2003), as well as the spin-orbit alignment between the planetary orbit and the stellar rotation axis (e.g.,

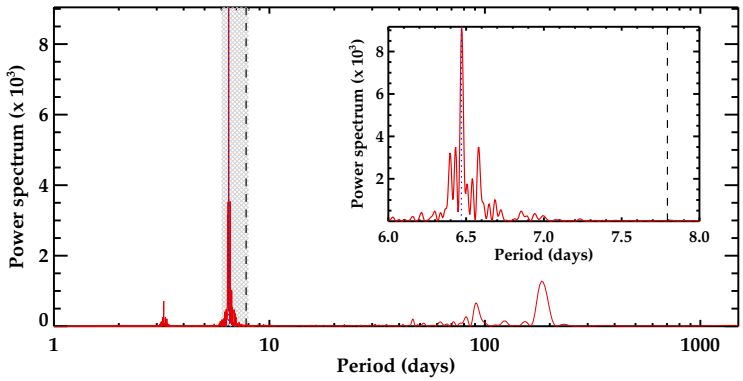

FIGURE 6.18: Lomb-Scargle periodogram of the complete *Kepler* light curve (red line) for Kepler-447. A zoom into the shaded region around the rotational period of the star (~6.5) days is shown in the small panel. The vertical dashed line corresponds to the orbital period, while the dotted vertical line is the measured rotational period by McQuillan et al. (2013b).

Sanchis-Ojeda & Winn, 2011). However, the long-cadence data obtained for Kepler-447 and the short duration of its transit prevent this kind of studies in this system with the current data.

Added to the stellar rotation, we used the CAFE spectra to obtain the physical properties of the host star. We combined all high-resolution spectra by shifting them according to their measured RV to obtain a moderate S/N spectrum. The final combination provides $S/N_0 = 65$. This spectrum was used to obtain the stellar parameters of the host star. We derived the effective temperature, surface gravity, and metallicity by using spectral synthesis, using the Fe I spectral lines as described in Pepe et al. (2011). The results show that Kepler-447 is a G8V star with $T_{\rm eff} = 5493 \pm 62$ K, $\log g = 4.40 \pm 0.10$, and $[{\rm Fe/H}] = +0.07 \pm 0.05$. These values agree with the photometrically obtained by Huber et al. (2014) except for the metallicit2y, which is sub-solar in the latter work but with much larger uncertainties ($[{\rm Fe/H}]_{\rm H14} = -0.40^{+0.36}_{-0.26}$). In Table 6.15, we show both sets of stellar properties.

By using these parameters, we can estimate the stellar mass and radius by applying the parametrization presented in Torres (2010). We estimated the uncertainties in these parameters by running 10^5 Monte Carlo trials obtained from a Gaussian distribution of the input values (i.e., $T_{\rm eff}$, $\log g$, and [Fe/H]) and the coefficients of the parametrization (see Table 1 in Torres, 2010). We then take the 68% limits (1σ) as the estimated uncertainties. According to this, we obtain $M_\star = 1.00 \pm 0.21\ M_\odot$ and $R_\star = 1.03 \pm 0.16\ R_\odot$. These values are assumed throughout this work for further estimation of orbital and physical properties of the transiting companion. For completeness, we also derive those properties by assuming the values provided by Huber et al. (2014).

TABLE 6.15: Stellar parameters for Kepler-447 as derived by different techniques.

Parameter	Huber et al. (2014)	This work
$T_{\rm eff}$ (K)	5555^{+171}_{-133}	5493 ± 62
$\log g$ (cgs)	$4.440^{+0.119}_{-0.308}$	4.40 ± 0.10
[Fe/H]	$-0.40^{+0.36}_{-0.26}$	0.07 ± 0.05
$M_\star$ ($M_\odot$)	$0.764^{+0.145}_{-0.049}$	1.00 ± 0.21
$R_\star$ ($R_\odot$)	$0.872^{+0.419}_{-0.120}$	1.03 ± 0.16

6.4.3.2 Simultaneous fit of the radial velocity and transit signals

Due to the aforementioned peculiar characteristics of this system, we decided to perform a simultaneous fit of the RV and transit data. This is because both effects share key parameters that could importantly affect the results of the other dataset (in particular the eccentricity and the argument of the periastron). The orbital period ($P_{\rm orb}$) and the mid-transit time (T_0) were fixed to the values measured by Burke et al. (2014).

In total, ten free parameters are needed to model both datasets: radial velocity semi-amplitude (K), eccentricity (e), argument of periastron (ω), systemic velocity of the system ($V_{\rm sys}$),[20] two RV offsets ($v_{\rm off1}$ and $v_{\rm off2}$, see § 4.4.4), semi-major axis to stellar radius ($a/R_\star$), planet-to-star radius ratio ($R_p/R_\star$), inclination (i), and a phase offset in the transit center to include possible unaccounted uncertainties in the determination of the transit epoch ($\phi_{\rm off}$).

Among these free parameters, six are needed to model the transit signal by using the Mandel & Agol (2002) formulation (i.e., $R_p/R_\star$, e, ω, $a/R_\star$, i, and $\phi_{\rm off}$), see section § 2.2.1. According to the recommendations from Müller et al. (2013) for high impact parameter transits, we fixed the limb-darkening coefficients to the theoretical values. We performed a trilinear interpolation of the determined stellar properties ($T_{\rm eff}$, $\log g$, and [Fe/H]) on the non-linear four terms limb-darkening values calculated by Claret & Bloemen (2011) for the *Kepler* band. The resulting values used in the transit fit are $a_1 = 0.5895$, $a_2 = -0.2477$, $a_3 = 0.8538$, and $a_4 = -0.4166$.

Due to the short duration of the transit ($\sim$ 1.13 hour) and the long cadence data obtained for this object (i.e., 29.4 minutes), there is a remarkable effect to take into account in the transit modeling. It is based in the fact that we try to fit long-cadence (timely binned) data with a theoretical transit model with infinite resolution (i.e., unbinned). In practice, the long-cadence data smooths the transit signal, producing a broader transit. If the transit is grazing, this also translates into a shallower depth. This effect was already highlighted by Kipping (2010), who warned about large errors in the derived parameters if not accounted for. By definition, this

[20] We note that this $V_{\rm sys}$ is not the absolute systemic velocity of the system since it is not corrected from the possible instrumental offsets, although this should be of some tens of m/s.

binning effect is larger for short (with sampling step of the order of the transit duration) and grazing transits, such as the present case. As explained by Kipping (2010), there are several ways to correct for it. The simplest (but most efficient) is to compute the light curve model with a short cadence sampling (e.g., 1 minute) and then bin the model with the actual cadence of the observed data. We used this approach in our analysis.

By assuming Keplerian orbit, we used Eq. 4.3 to model the reflex motion of the star due to an orbiting single planet. The true anomaly at each epoch was obtained by solving the Kepler equation according to the eccentricity and phase of the planet (see section § 1.4).

We used our genetic algorithm *GAbox* (see Appendix A) to explore the parameter space owing to find the set of parameters that best reproduces the current data. We broadly restricted the parameter space according to our knowledge of the data. The adopted ranges for each of the free parameters are summarized in Table 6.16.

Due to the different number of datapoints on each dataset ($N_{\rm RV} = 21$ and $N_{\rm LC} = 994$), we used the reduced chi-square ($\chi^2_{\rm red}$) as the minimization parameter in order to equally weight both effects. Mathematically, this minimization parameter is expressed as $\chi^2_{\rm red} = \chi^2_{\rm red,RV} + \chi^2_{\rm red,LC}$. The distribution of the 1500 convergence solutions found by *GAbox* in the parameter-parameter space is plotted in Fig. 6.19. In this figure we can see that all parameters but the planet radius are very well constrained. However, as it is shown by the color-code in Fig. 6.19, the least-square solution is located in the middle of the preferred region, suggesting that the adopted solution is a good compromise for all parameters ($\chi^2_{\rm red,RV} = 1.2$ and $\chi^2_{\rm red,LC} = 1.8$). We adopted this least-square set of parameters as our final solution.

The uncertainties were obtained by running Monte-Carlo Markov Chain (MCMC) simulations with the Metropolis-Hasting algorithm. We ran 10^6 steps and discarded the 10% firsts to avoid dependence on the priors, which were set to the *GAbox* solution. We used 3σ levels as the adopted uncertainties. The final parameters are shown in Table 6.16, and the results of this fit are presented in Fig. 6.20.

Given the obtained parameters in Table 6.16, we can derive the mass of the companion revolving around Kepler-447 by using its relation with the semi-amplitude of the RV signal (see Eq. 4.5). By assuming the stellar properties, we can obtain absolute values for the planetary mass and radius. Due to the relative disagreement between the stellar mass and radius obtained by Huber et al. (2014) and the present work (although still within the 1σ uncertainties), we decided to get absolute parameters for both sets of stellar properties. However, we refer to the final results to those obtained from our spectroscopic values (see § 6.4.3.1). We thus obtain a mass of $M_p = 1.35^{+0.48}_{-0.46}\ M_{\rm Jup}$ for the companion object, establishing its planetary nature. The large uncertainty is a consequence of the uncertainty in the stellar mass. Similarly, by using the $R_p/R_\star$ ratio, we obtain a planetary radius of $R_p = 1.65^{+0.59}_{-0.56}\ R_{\rm Jup}$. We should note that $R_p/R_\star$ is

not very well constrained due to the short duration and grazing shape of the transit signal (see Fig. 6.19). This is translated in a relatively large uncertainty for this parameter.

TABLE 6.16: Parameters of the joint fitting of the radial velocity and transit data for Kepler-447.

Parameter	Range	Value[a]	Units
K	$[50, 250]$	141^{+42}_{-42}	m/s
e	$[0.0, 0.5]$	$0.123^{+0.037}_{-0.036}$	
ω	$[0, 360]$	$98.3^{+1.1}_{-11.0}$	deg.
V_{sys}	$[1.0, 2.0]$	$1.39^{+0.11}_{-0.11}$	km/s
$a/R_\star$	$[10, 40]$	$20.41^{+0.36}_{-0.19}$	
$v_{\rm off1}$	$[-1000, 1000]$	-363^{+88}_{-20}	m/s
$v_{\rm off2}$	$[-1000, 1000]$	-84^{+24}_{-25}	m/s
$R_p/R_\star$	$[0.01, 0.50]$	$0.165^{+0.049}_{-0.048}$	
i	$[80, 90]$	$86.55^{+0.24}_{-0.32}$	deg.
$\phi_{\rm off}$	$[10, 20]$	$1.22^{+0.37}_{-0.11}$	min.

Notes. [(a)] Uncertainties are 3σ.

6.4.4 Discussion

Derived properties of the planetary system

In previous sections, we have shown that the companion transiting Kepler-447 has a planetary mass of $M_p = 1.37^{+0.48}_{-0.46}\ M_{\rm Jup}$ and a large radius of $R_p = 1.65^{+0.59}_{-0.56}\ R_{\rm Jup}$. According to these values, the resulting mean density of the planet would be $\rho_p = 0.30^{+0.71}_{-0.24}\ \rho_{\rm Jup}$. This low density indicates an inflated atmosphere for the planet. Although several inflation mechanisms could be taking place, the eccentricity found for this close-in giant planet suggests that tidal heating could be the main mechanism (e.g., Jackson et al., 2008). Note that at periastron passage, the planet approaches its host star at a distance of $r_{\rm per}/R_\star = 17.89^{+0.80}_{-0.75}$. The non-negligible eccentricity found could be due to a third body in the system, preventing the circularization process and enhancing the tidal heating.

The semi-major axis of the planetary orbit is $a = 0.069^{+0.006}_{-0.008}$ AU as calculated by using the third Kepler law (assuming the mass of the host and the orbital period). We then obtain an impact parameter of $b = 1.076^{+0.112}_{-0.086}$, confirming that the transit is highly grazing. At mid-transit, only around 20% of the planet disk actually eclipses the star (i.e., $A_{\rm ecl}/A_{\rm pl} = 0.20^{+0.30}_{-0.23}$). This explains the V-shape of the transit for this planetary mass companion. Given this impact parameter and the calculated planet-to-star radius ratio, we obtain a grazing criterion of $b + R_p/R_\star = 1.24^{+0.12}_{-0.10}$ (3σ uncertainties), clearly above the 3σ level. This confirms that Kepler-447b is the second

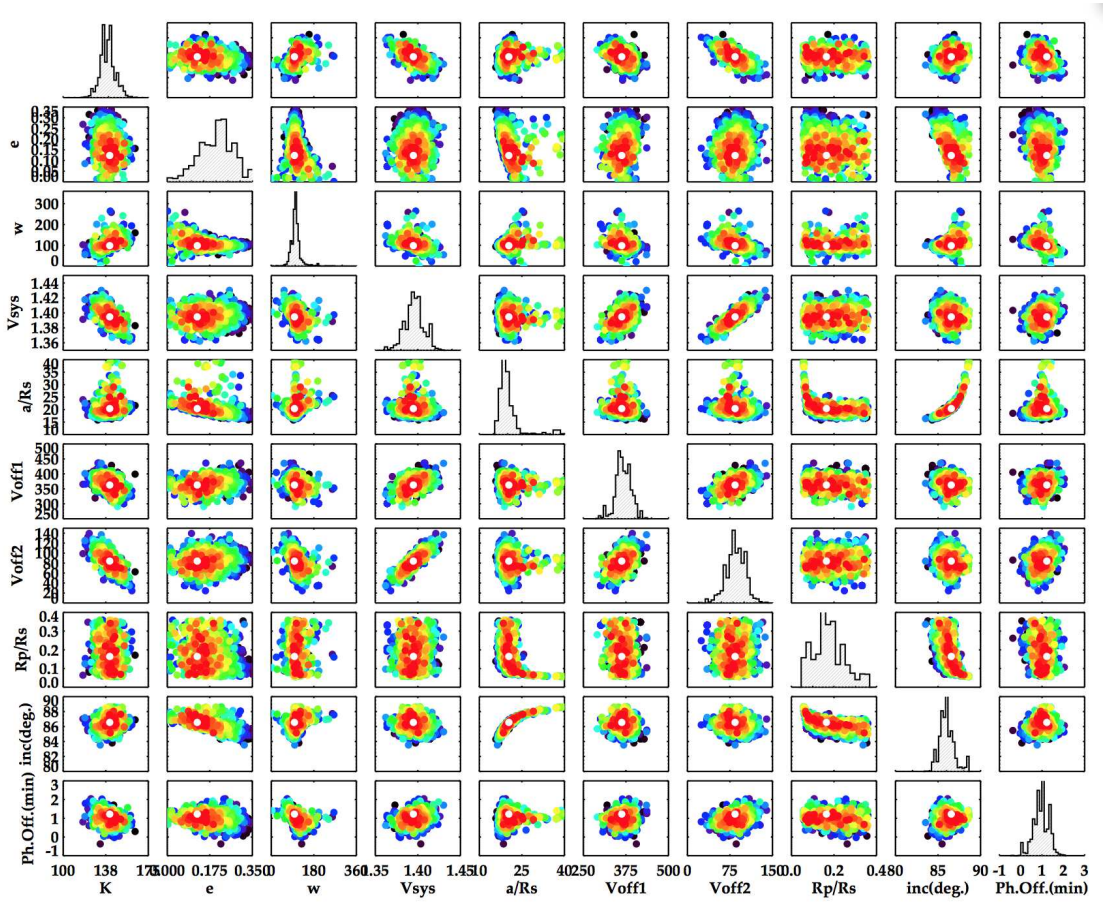

FIGURE 6.19: Parameter-parameter representation of the 1500 convergence solutions of the transit fitting using *GAbox*. In color-code we represent the combined reduced chi-square statistic of the RV and transit fitting models (dark colors represent poorer chi-square models). The diagonal panels show the histograms of the distribution of the individual parameters within all solutions. The white circle represents the least-square model.

known planet with a grazing transit, and the first in the *Kepler* sample, as mentioned before. The first planet known to accomplish this criterion was WASP-67b (Hellier et al., 2012, Mancini et al., 2014) which was analyzed with short-cadence data from the ground. According to the Exoplanet Archive,[21] Kepler-447b is the most grazing transiting exoplanet found to date, with the least fraction of its projected area covering the stellar disk. We have illustrated this in Fig. 6.21.

In Fig. 6.22, we show a scheme of the pole-on and face-on views of the system. As it is shown, the planet does not produce a secondary eclipse due to the slightly inclined and the non-circular orbit. This is in agreement with the lack of a secondary eclipse for such a large and close-in planet.

In Table 6.17 we present all derived physical and orbital properties for this system by assuming both sets of stellar parameters from our own analysis of the high-resolution and moderate S/N

[21] http://exoplanet.eu

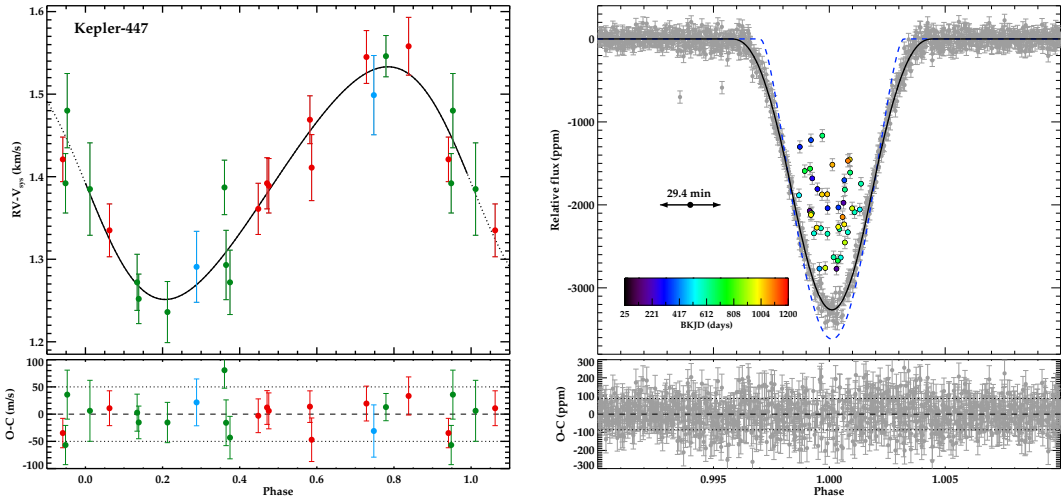

FIGURE 6.20: **Left panel:** Phase-folded radial velocity data obtained during runs on 2012 (red symbols), 2013 (light blue), and 2014 (green). The black line shows the best fit model. The lower left panel shows the residuals of the model fit, with a rms of 31 m/s. **Right panel:** transit fitting of Kepler-447b. In the upper panel, we show the detected transit in the *Kepler* light curve. We mark in color the outliers of the transit that have been removed from the fitting process (see § 6.4.2), and that are mostly due to the misidentification of cosmic rays by the *Kepler* pipeline. The color-code is shown in the color bar and relates to the corresponding Barycentric *Kepler* Julian Date (BKJD = BJD-2454833 days). The final fitted model is represented by the solid black line. We have also included with a dashed blue line the original (not binned) model from which it is calculated (see § 6.4.3.2). The bottom panel shows the residuals of the fit, with a rms of 101 ppm.

spectrum of the star (solution A) and from Huber et al. (2014), solution B.

The effect of cosmic rays in short-duration transits

The *Kepler* pipeline processes the data and tries to correct for the presence of possible cosmic rays inside the aperture of a target. This correction is sometimes affected by erroneous identification of cosmic rays in the transit time interval of long-cadence data when the duration of the transit is short as compared to the cadence. When this situation happens, the pipeline tries to correct the photometry and erroneously assigns larger fluxes for the in-transit data in the mentioned configurations. The result of this in the phase-folded light curve is a transit somehow filled by outlier data points symmetrically distributed around the mid-transit time. These outliers in the transit region could be erroneously interpreted as hints for the detection of other real configurations (such as additional bodies or spot-crossing events). The *Kepler* team provides information about which data points have been corrected for the possible existence of a cosmic ray by flagging them in the SAP_QUALITY field of the delivered data files with the flag 128.[22]

[22] See description of all SAP_QUALITY flags in the latest version of the Kepler archive manual at https://archive.stsci.edu/kepler/manuals/archive_manual.pdf.

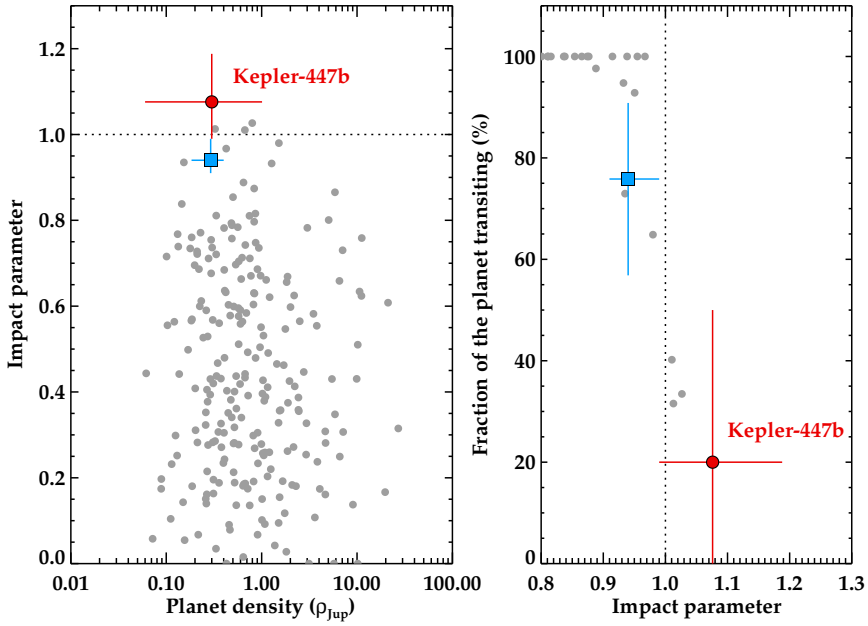

FIGURE 6.21: **Left panel:** impact parameter versus planetary density of known exoplanets with available information. **Right panel:** fraction of the projected planet transiting its host star as a function of the impact parameter. In both panels, Kepler-447b has been highlighted in red color and big circle symbol, including uncertainties. For reference, WASP-67b is also highlighted in light blue color with a square symbol. The values for the rest of the known planets are obtained from the Extrasolar Planet Encyclopedia (`http://exoplanet.eu`). For clarity reasons, we do not include their uncertainties.

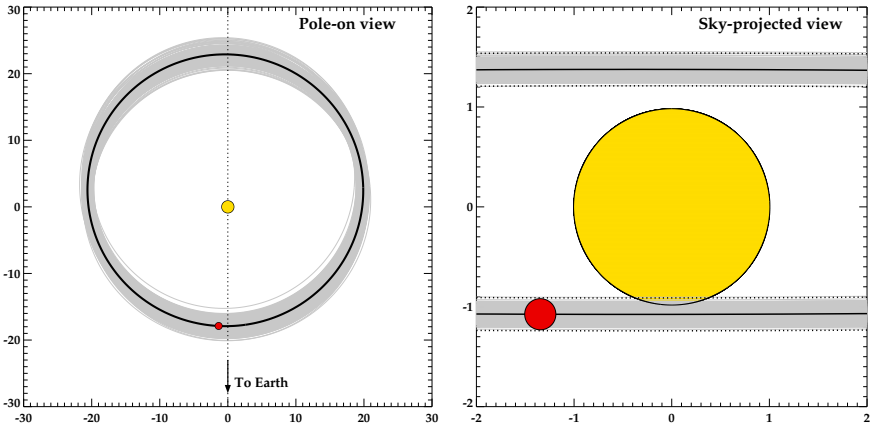

FIGURE 6.22: Orbital scheme the solution found for the orbit of the planet Kepler-447b (red filled circle). *Left panel*: Pole-on view of the orbit (separation from the star in units of the stellar radius). We show 500 orbits by bootstrapping the parameters inside their uncertainty limits. *Right panel*: Face on view of the orbit as projected in the sky (separation from the star in units of the stellar radius). We have marked the path of the planet between the dotted lines. The gray solid lines represent 500 orbits by bootstrapping the impact parameter. We can see that the transit is always grazing independently of the parameters taken inside the uncertainty limits.

TABLE 6.17: Derived physical and orbital parameters from the fitted solution of the joint analysis for Kepler-447.

Parameter	Derived parameters		Units	Assumptions[c]
	Sol. A[a]	Sol. B[b]		
$R_\star$	$\mathbf{1.05^{+0.19}_{-0.19}}$	$0.915^{+0.143}_{-0.100}$	$R_\odot$	$M_\star$, $\log g$
a	$\mathbf{0.0769^{+0.0062}_{-0.0079}}$	$0.0703^{+0.0036}_{-0.0023}$	AU	$P_{\rm orb}$, $M_\star$
b	$\mathbf{1.076^{+0.112}_{-0.086}}$	$1.076^{+0.112}_{-0.086}$		$a/R_\star$, i, e, ω
$T_{\rm dur}$	$\mathbf{1.135^{+0.016}_{-0.016}}$	$1.135^{+0.016}_{-0.016}$	hr	TR model
M_p	$\mathbf{1.37^{+0.48}_{-0.46}}$	$1.14^{+0.38}_{-0.34}$	$M_{\rm Jup}$	K, $M_\star$, $P_{\rm orb}$
R_p	$\mathbf{1.65^{+0.59}_{-0.56}}$	$1.40^{+0.89}_{-0.42}$	$R_{\rm Jup}$	$R_p/R_\star$, $R_\star$
$< \rho_p >$	$\mathbf{0.30^{+0.71}_{-0.24}}$	$0.42^{+0.74}_{-0.37}$	$\rho_{\rm Jup}$	M_p, R_p
$A_{\rm ecl}/A^\dagger_{\rm pl}$	$\mathbf{20^{+30}_{-23}}$	20^{+30}_{-23}	%	b, $R_p/R_\star$

Notes. All uncertainties cover the 99.7% of the probability distribution (i.e., 3σ). [a] Stellar radius and mass obtained from our spectroscopic analysis. [b] Stellar radius and mass obtained from Huber et al. (2014). [c] Assumed parameters in the estimation of the derived properties. † Fraction of the planet's projected area eclipsing the stellar disk at mid-transit (in %).

Due to the very specific situations in which this effect can play an important role and contaminate the transit region of a planetary transit, there are few cases where this instrumental effect has been reported. In particular, in Herrero et al. (2013), the authors misidentify the erroneously corrected data points in the eclipse interval with a spot-crossing event in the system LHS 6343. In a recent work by Montet et al. (2014), the authors identified the data points corresponding to this spot-crossing event in LHS 6343 as flagged data points with the SAP_QUALITY equal to 128, and thus being cosmic rays misidentifications by the *Kepler* pipeline.

In the case of Kepler-447, the version of the pipeline used in the first twelve quarters produced this kind of misidentifications, while no erroneous detection was found in the remaining quarters. The ~12% of the data points inside the transit time interval during the whole *Kepler* mission were tentatively identified (and thus corrected by the pipeline) as cosmic rays (see Fig. 6.23). If the quality flags are not taken into account, the result is a transit somehow filled by outlier data points (see Fig. 6.20, right panel) that could be erroneously interpreted as true signals caused by other real configurations. Besides this, owing to the extremely large impact parameter of the transit of Kepler-447b, which is thus a planetary grazing transit, these flagged data points could by chance be mimicking the signal induced by some of those configurations. It is thus worthwhile to warn about this effect and to highlight the importance to take the quality flags provided by the *Kepler* team into account in short-duration transit events.

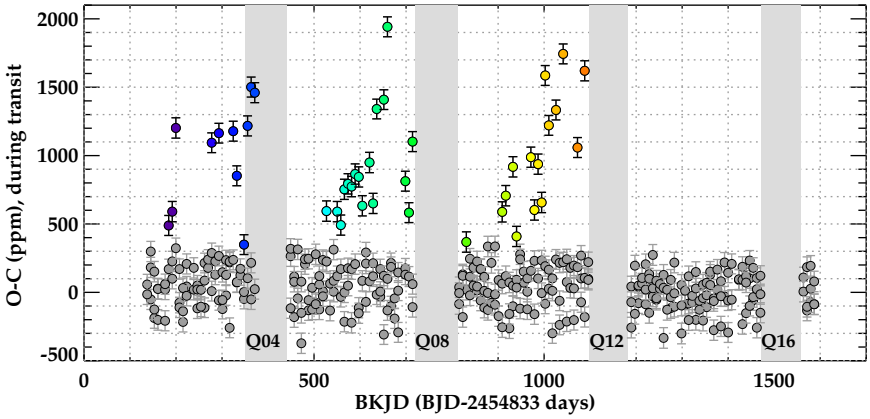

FIGURE 6.23: Flux difference between the observed measurement and the transit model for data points inside the transit region. Outliers mostly due to the misidentification of cosmic rays by the *Kepler* pipeline are marked in the same color code as in the right panel of Fig. 6.20. The *Kepler* quarters of the mission with few or no data for this KOI due to the failure of CCD Module 3 are highlighted as gray shaded regions (see § 6.4.2).

6.5 KOI-0372: a young extrasolar system with two giant planets on wide orbits

In this section we summarize the most updated results of a submitted paper regarding the detection of the two-planet system KOI-372. This work was led by Luigi Mancini (Mancini et al., 2015, in prep.) and our contribution is focused on the observations and analysis of the radial velocity data of the inner (transiting) planet KOI-372 b.

6.5.1 Observations

***Kepler* photometry.-** The *Kepler* spacecraft monitored KOI-372 from quarters Q0 to Q17. It presents a $\sim$ 0.2% dimming in its light curve with a period of $\sim$ 125 days (Borucki et al., 2011). This periodic dimming is actually caused by the transit of a Jupiter-like planet candidate, KOI-372 b, moving on a quite wide orbit around the star. Twelve transits of KOI-372 b are present in the *Kepler* long cadence light curve. We have labelled them from -5 to 6 (see Fig. 6.24). Two of the transits are incomplete (-2 and -1); two are most likely contaminated by star spots (5 and 2); and three were also covered in short cadence (4, 5 and 6). The complete *Kepler* light curve is shown in Fig. 6.25, which highlights a significant stellar variability (0.0470 $\pm$ 0.0002 mmag peak-to-peak). McQuillan et al. (2013b) found a periodic photometric modulation in the light curve and, by assuming that it is induced by a star-spot activity, estimated a stellar rotation period of 11.769 $\pm$ 0.016 days. This value is in good agreement with that found by Walkowicz & Basri (2013), i.e. 11.90 $\pm$ 3.45 days also based on *Kepler* data.

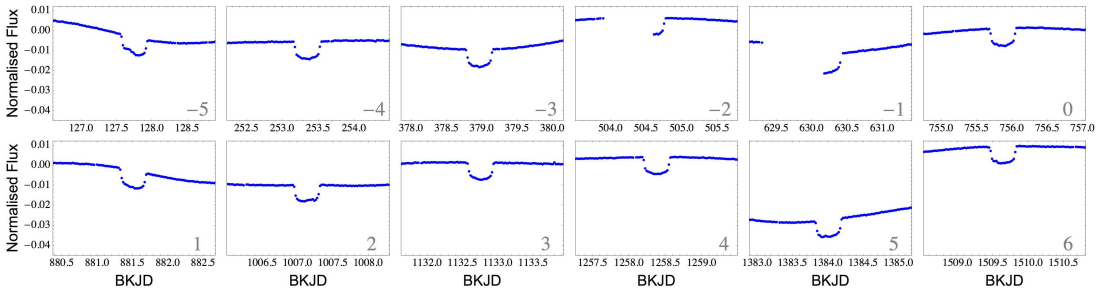

FIGURE 6.24: The 12 transit events of KOI-372 b observed by *Kepler*. The transits at epoch -5 and 2 are affected by star-spot-crossing events. Times are in BKJD (Barycentric Kepler Julian Date – equivalent to BJD(TDB)-2454833.0). Figure from Mancini et al. (2015, in prep.).

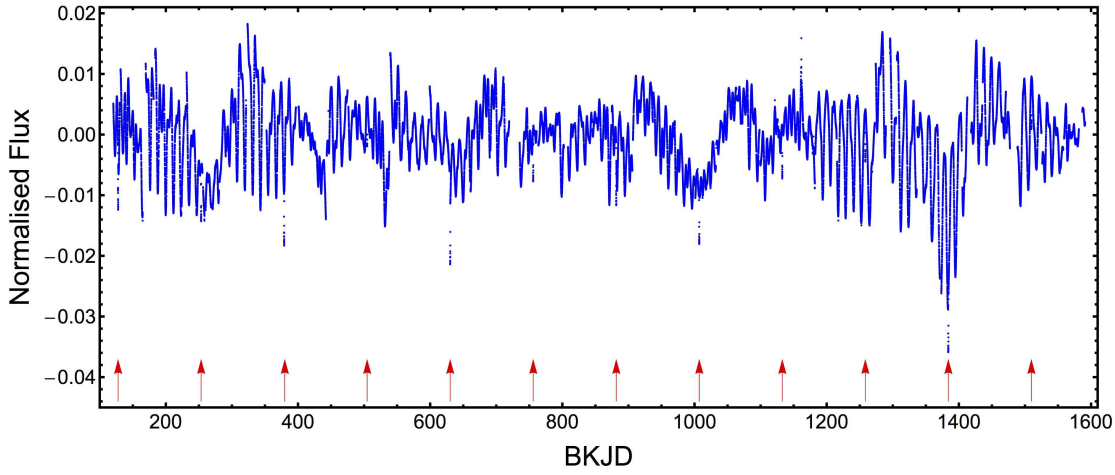

FIGURE 6.25: The entire *Kepler* light curve data of KOI-372. The large stellar variability can be reasonable interpreted as induced by a star-spot activity. Times are in BKJD (Barycentric Kepler Julian Date – equivalent to BJD(TDB) minus 2454833.0). The red arrows mark the mid-times of the twelve transits of KOI-372 b. Figure from Mancini et al. (2015, in prep.).

High-spatial-resolution imaging.- We observed this target with AstraLux, finding a 5.94 arcsec companion with $\Delta i = 4.64 \pm 0.18$ mag. Additionally, Adams et al. (2012) found other faint and red companions (see Table 6.18). We have estimated the dilution effect caused by each companion, finding that it is very small for the three closest companions, roughly 0.023% in total and thus negligible. The companion labelled as "E", correspond to our detection with AstraLux and is another *Kepler* target known as KIC 6471028. As it lies outside the *Kepler* aperture, this star does not contaminate KOI-372.

High-resolution spectroscopy.- We monitored KOI-372 between July 2012 and April 2015 with CAFE (i.e., four years of baseline). We used thorium-argon (ThAr) exposures obtained after each science spectrum to wavelength-calibrate the corresponding data. The final spectra have signal-to-noise ratios in the range S/N = 7–16. We obtained the RV by using the CCF approach (see § 4.3.1). Since we took several consecutive spectra, we decided to combine the

TABLE 6.18: Nearby visual companions around KOI-372 (from Adams et al., 2012) and their dilution effect on the depth of the transit events.

Companion	Distance ($''$)	K_s (mag)	ΔK_s	Dilution
B	2.49	23.2	8.6	0.005 %
C	3.56	22.4	8.0	0.01 %
D	4.99	22.7	8.2	0.008 %
E[a]	5.94	17.1	4.0	1.31 %

Notes. [a]Also known as KIC 6471028.

RV values of the corresponding pairs in the cases where their individual signal-to-noise was low (i.e., S/N < 10) and mutual discrepancies were larger than 50 m s^{-1}. This procedure can also diminish the effect of the stellar activity on the radial velocity (although here the expected amplitudes are of the order of few tens of m s^{-1}). Additionally, we rejected the results of different nights showing sudden changes in the atmospheric conditions (humidity, temperature, and wind speed), according to the Calar Alto weather station.[23]

6.5.2 Analysis

Spectral analysis and the age of KOI-372

We derived the spectroscopic parameters of the host star KOI-372 from the co-added CAFE spectrum, which has a S/N ratio of about 40 per pixel at 5500 Å. Following the procedures described in Gandolfi et al. (2015, 2013), we used a customized IDL software suit to fit the composite CAFE spectrum to a grid of synthetic theoretical spectra. The latter were calculated with the stellar spectral synthesis program SPECTRUM (Gray & Corbally, 1994) using ATLAS9 plane-parallel model atmospheres (Kurucz, 1979), under the assumptions of local thermodynamic equilibrium (LTE) and solar atomic abundances as given in Grevesse & Sauval (1998). This analysis was carried out by Davide Gandolfi and the details can be found in Mancini et al. (2015, in prep.). The results are shown in Table 6.19. In summary, we found that KOI-372 has an effective temperature of $T_{\rm eff} = 5820 \pm 80$ K, $\log g_\star = 4.4 \pm 0.1$ (cgs), [Fe/H]$= -0.01 \pm 0.07$ dex, $v_{\rm micro} = 1.1 \pm 0.1$ km/s, $v_{\rm macro} = 3.2 \pm 0.6$ km/s, and $v \sin i_\star = 4.4 \pm 0.5$ km/s. According to the Straizys & Kuriliene (1981) calibration scale for dwarf stars, the effective temperature of KOI-372 translates to a G2 V spectral type.

The CAFE co-added spectrum of KOI-372 reveals the presence of a moderate Li I 6707.8 Å absorption doublet (Fig. 6.26). We estimated the photospheric lithium abundance of the star by fitting the Li doublet using ATLAS9 LTE model atmospheres. We fixed the stellar parameters to the values given in Table 6.19 and allowed our code to fit the lithium content. Adopting a correction for non-LTE effects of +0.006 dex (Lind et al., 2009), we measured a lithium abundance

[23] Publicly available at http://www.caha.es/weathernng_es.html

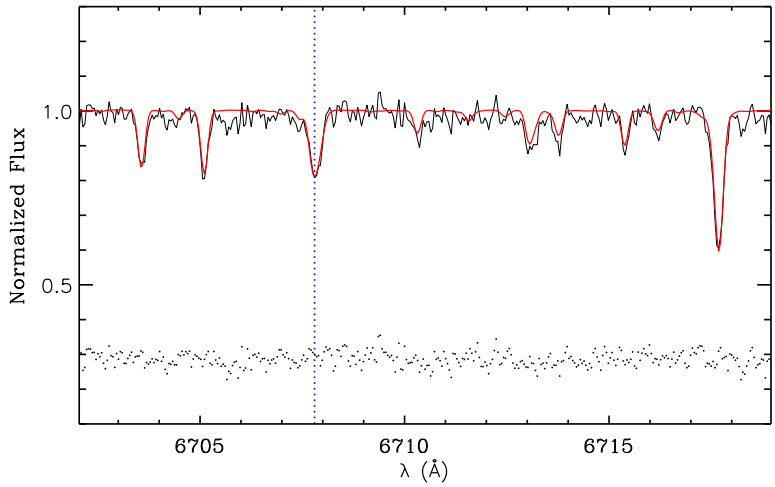

FIGURE 6.26: CAFE co-added spectrum of KOI-372 (black line) encompassing the Li I 6707.8 Å absorption doublet. The best fitting ATLAS9 spectrum is overplotted with a thick red line. The vertical dashed line marks the position of the Li doublet. The lowest part of the plot displays the residuals to the fit. Figure from Mancini et al. (2015, in prep.).

of $A(\mathrm{Li}) = \log(n(\mathrm{Li})/n(\mathrm{H})) + 12 = 2.48 \pm 0.12$ dex. The photospheric lithium content and the short rotation period of KOI-372 suggest that the star is relatively young. The lithium content of KOI-372 is intermediate between the average lithium abundance measured in early G-type stars of 0.6-Gyr-old open clusters ($A(\mathrm{Li}) = 2.58 \pm 0.15$ dex) and that of 2-Gyr-old open clusters ($A(\mathrm{Li}) = 2.33 \pm 0.17$ dex; Sestito & Randich, 2005). We used Eq. (32) from Barnes & Kim (2010) and the rotation period of KOI-372 to infer its gyro-age. The results show a gyro-age of 1.0 ± 0.3 Gyr, which confirms the relatively young scenario. Our estimation is in good agreement with the 1.15 Gyr gyro-chronological age predicted by Walkowicz & Basri (2013).

Physical properties of the system

The *Kepler* light curve was analyzed with the JKTEBOP code (Southworth, 2013), after modifying it to allow fitting for individual times of mid-transit. The *Kepler* long- and short-cadence data were fitted separately, accounting for the long effective exposure times in the long-cadence data by oversampling the fitted model by a factor of five. A quadratic limb darkening law was used, with the linear term fitted and the quadratic term fixed to 0.27 (Sing, 2010). Details on the uncertainty calculation can be found in Mancini et al. (2015, in prep.).

The analysis of the radial velocity is done separately in this dissertation,[24] fixing the orbital period P_{orb} and reference transit midpoint T_0 to the values measured from the transit times. In this prelimiary fitting, we fixed the eccentricity to a circular orbit.[25] With these assumptions, we obtain a fairly good fitting of the RV variation compatible to a $M_p = 1.11 \pm 0.21\ M_{\mathrm{Jup}}$. This

[24] A new CAFE run will take place in mid-May, that will allow us to improve the phase coverage of the orbit. Then we will proceed with a simultaneous fit of the RV and the LC.

[25] The observations in mid-May 2015 will allow us to better constrain the eccentricity of the orbit.

TABLE 6.19: Final parameters of the planetary system KOI-0372.

Parameter	Nomen. and Unit	Value
Stellar parameters		
R.A. (J2000)		$19^{h}56^{m}29{:}39^{s}$
Dec. (J2000)		$41°52'00.3''$
Kepler magnitude	K_p (mag)	12.39
Effective temperature	T_{eff} (K)	5820 ± 80
Iron abundance	[Fe/H] (dex)	-0.01 ± 0.07
Lithium abundance	A(Li) (dex)	2.5 ± 0.1
Microturb. velocity	v_{micro} (km/s)	1.1 ± 0.1
Macroturb. velocity[a]	v_{macro} (km/s)	3.2 ± 0.6
Proj. rotat. velocity	$v \sin i_\star$ (km/s)	4.4 ± 0.5
Age[b]	(Gyr)	1.0 ± 0.3
Spectral type[c]		G2 V
Rotation period[d]	P_{rot} (day)	11.769 ± 0.016
Mass	$M_\star$ ($M_\odot$)	$1.014 \pm 0.044 \pm 0.027$
Radius	$R_\star$ ($R_\odot$)	$1.122 \pm 0.083 \pm 0.010$
Mean density	$\rho_\star$ ($\rho_\odot$)	0.72 ± 0.16
Surface gravity	$\log g_\star$ (cgs)	$4.344 \pm 0.065 \pm 0.004$
Planetary parameters (KOI-372 b)		
Mass	M_p (M_{Jup})	1.11 ± 0.20
Radius	R_p (R_{Jup})	$0.882 \pm 0.088 \pm 0.008$
Mean density	ρ_p (ρ_{Jup})	1.61 ± 0.56
Equilibr. temperature	T_{eq} (K)	423 ± 16
Orbital parameters		
Time of mid-transit	T_0 (BJD_{TDB})	2455588.8710 ± 0.0030
Period	P_{orb} (days)	125.63243 ± 0.00071
Semi-major axis	a (au)	$0.4937 \pm 0.0073 \pm 0.0044$
Inclination	i (degree)	89.845 ± 0.086
Fractional star radius	r_A	0.01057 ± 0.00078
Fractional planet radius	r_b	0.000854 ± 0.000085
RV semi-amplitude	K_A (m/s)	45.2 ± 9.1
Barycentric RV	γ (km/s)	10.431 ± 0.007

Notes. Where there are two error bars, the first is a statistical error, coming from the measured spectroscopic and photometric parameters, while the second is a systematic error and is given only for those parameters which have a dependence on theoretical stellar models. [a] Using the calibration equations of Doyle et al. (2014). [b] From gyrochronology. [c] With an accuracy of ± 1 sub-class. [d] From McQuillan et al. (2013b). Table from Mancini et al. (2015, in prep.).

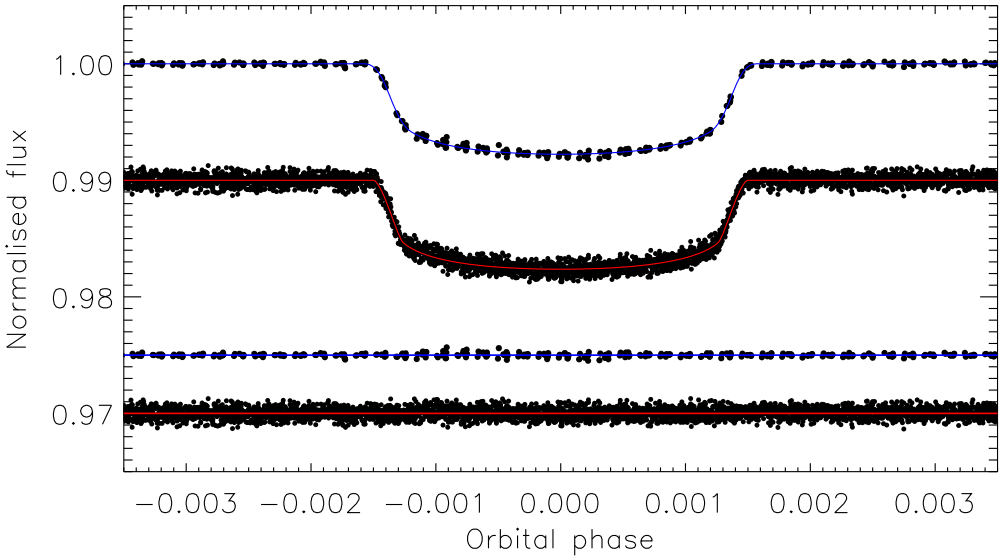

FIGURE 6.27: Phase-folded *Kepler* long-cadence (top light curve) and short-cadence (bottom light curve) data zoomed around transit phase. The TTVs were removed from the data before plotting. The JKTEBOP best fits are shown using solid lines. The residuals of the fits are plotted at the base of the figure. Figure from Mancini et al. (2015, in prep.).

solution is favored against a non-detection (straight line) with a BIC difference between both models of ΔBIC= 3.7. Figures 6.28 and 6.29 show the observed data and the fitted circular model.

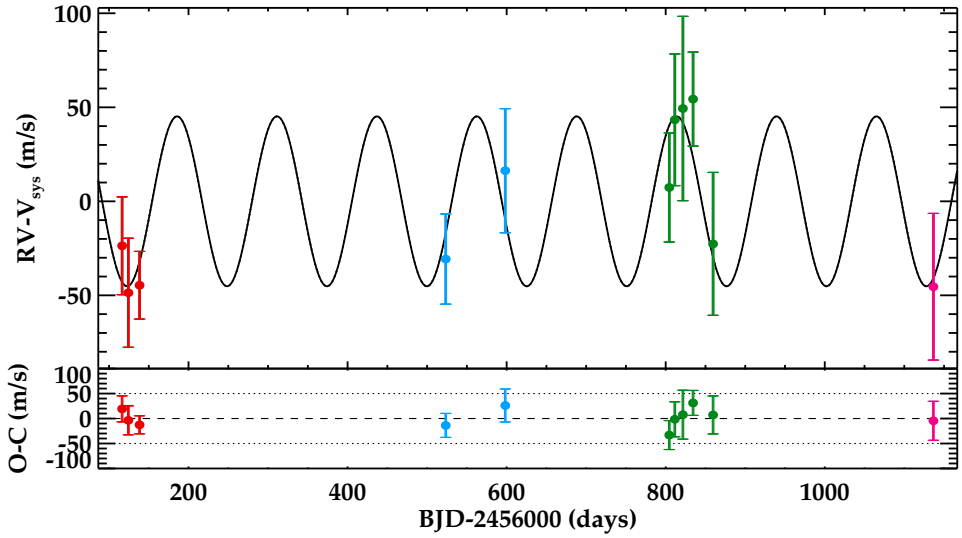

FIGURE 6.28: Radial velocity of KOI-372 as a funcion of the barycentric Julian date. The solid line represents the best fit circular model. Each color represents a different CAFE run, namely 2012 (red), 2013 (blue), 2014 (green), and 2015 (magenta).

Planet KOI-372 c from transit time variation

The analysis of the individual transits of KOI-372 b allowed us to detect transit timing variations,

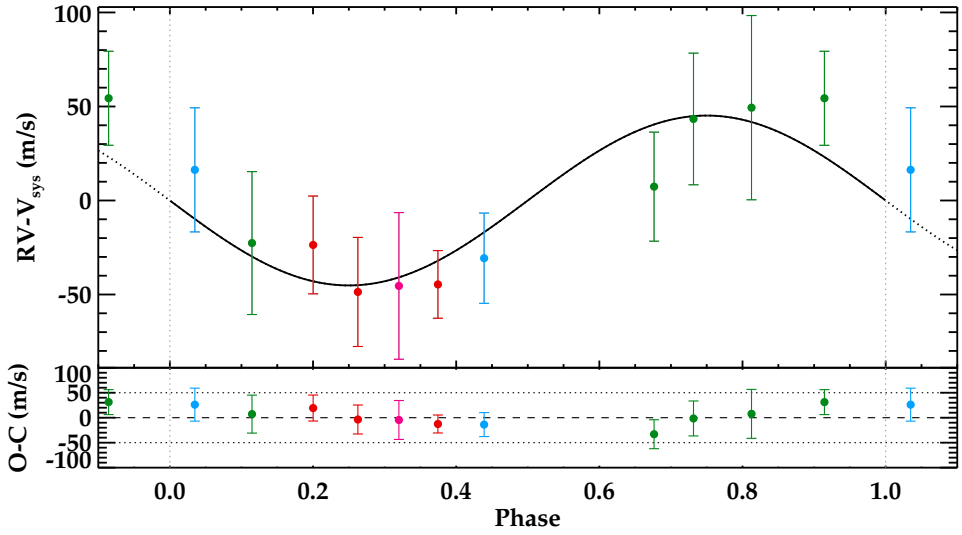

FIGURE 6.29: Phase-folded radial velocity of KOI-372 with the best-fit model represented by the solid line. Each color represent a different CAFE run, namely 2012 (red), 2013 (blue), 2014 (green), and 2015 (magenta).

which could be a sign of the presence of additional bodies in this system. We obtained the epochs of mid-transit for each of them with JKTEBOP (except for the -5 and 2 transits that were affected by starspots and were determined by the PRISM[26] and GEMC[27] codes, Tregloan-Reed et al. 2015, 2013). The residuals to a straight line fit of these epemerids is shown in Fig. 6.30, displaying a clear variation. Following the method described in Mazeh et al. (2015), we found that there is no significant correlation between the observed TTV and the local slope of the light curve at the transit times, suggesting that the TTV is likely induced by an unseen companion.

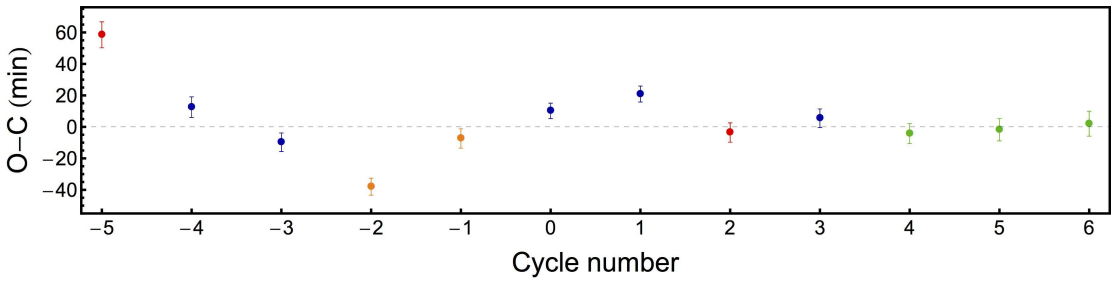

FIGURE 6.30: O–C diagram for the timings of KOI-372 b at mid-transit versus a linear ephemeris. The timings in blue refer to those coming from the *Kepler* long-cadence data, while those marked with green are from short-cadence data. The red points refer to the two long-cadence transits affected by star spots. The two incomplete long-cadence transits are marked with orange points. Figure from Mancini et al. (2015, in prep.).

The preliminary modeling with the TRADES (TRAnsits and Dynamics of Exoplanetary Systems; Borsato et al., 2014) code suggests the existence of an outer planet with a period of

[26] Planetary Retrospective Integrated Star-spot Model.
[27] Genetic Evolution Markov Chain.

$\sim$ 460 days and more massive than Neptune ($M_c < 0.3\ M_{\rm Jup}$). The analysis is currently ongoing and the final values will be provided in Mancini et al. (2015, in prep.) when the complete analysis of the RV is finished by using the mid-May 2015 CAFE data.

6.6 Eclipsing binaries and fast rotators in the CAB-MPIA survey

In this section we present the results for 13 *Kepler* Objects of Interest showing large radial velocity variations or large rotational velocities that prevent planet detection. This work was published in Lillo-Box et al. (2015a).

6.6.1 Context

We analyze 13 specific candidates in our sample that have shown either large RV variations or broadened spectra owing to the fast rotation of the host stars. The former cases are thus false positive planets, which detected eclipses are caused by stellar objects. The fast rotating stars are not suitable for high-precision radial velocity studies to detect variations due to planetary-mass objects since the spectral lines are broadened.

Among the studied candidates, we have found an eclipsing binary that shows heartbeat-like modulations on its light curve, KOI-3853. This effect was explained and explored by Kumar et al. (1995) and is due to tidal distortions in eccentric binary systems. The first object discovered whose light curve is mainly dominated by this type of modulation was KOI-54 (Welsh et al., 2011). Since then, only a few more cases have been found (e.g., Thompson et al., 2012), but more cases are needed to understand and test theoretical models regarding how pulsations are induced from the dynamic tidal distortion. Interestingly, the RV analysis of KOI-3853 also shows indications of a possible third, substellar companion.

6.6.2 Observations

***Kepler* photometry.-** The objects analyzed in this section were first classified by the *Kepler* mission as potential planet hosts by the detection of planetary-like transits. We used the long cadence data of quarters Q1-Q17 of the *Kepler* mission to analyze the light curves of some of these *Kepler* objects of interest (hereafter KOIs). We used the PDCSAP flux and detrended these data by using simple spline fitting to every set of data without jumps longer than one day. We used one-day averaged flux bins as nodes for the spline fitting. In specified cases (such as in KOI-3853), we removed some parts of the light curve in the calculation of the nodes in order not to smooth or even eliminate non artificial modulations (such as primary transits, eclipses, or other real variations).

High-spatial resolution imaging.- Nine out of the 13 KOIs were observed in our AstraLux survey. For the remaining targets, we used ancillary high-resolution images from Law et al. (2014) and the UKIRT J-band survey[28] of the *Kepler* sample, which are publicly available in the CFOP and provided by D. Ciardi. In Table 6.20 we summarize the main results obtained for each of the KOIs of the present study, including the calculated blended source confidence (BSC) and the number of detected visual companions closer than 6.0 arcsec.

High-resolution spectroscopy.- We obtained several CAFE epochs for the 13 KOIs. The data were reduced as described in § 4.4.2. The radial velocity data was obtained by using the template matching approach (§ 4.3.5) in the case of the fast rotators and the CCF approach (§ 4.3.1) for the slow rotators. In Tables 6.24 to 6.36 (at the end of this chapter) we provide the calculated radial velocities and the observing information (signal-to-noise, Julian date, and phase) for each epoch and KOI. The RV data was analyzed by using the RVLIN software[29] (Wright & Howard, 2009) and its additional package BOOTTRAN for parameter uncertainties estimation with bootstrapping (Wang et al., 2012) to fit our RV data to a Keplerian orbital solution.

TABLE 6.20: Ancillary data and calculated BSC values for the KOIs studied in section § 6.6

KOI	High-Res Im.[a] Ref.	Comp. (< 6″)	Sep. arcsec.	Δm mag (band)	BSC %
Group A - Eclipsing binaries					
340.01	L13[b]	0			99.99
371.01	L13[b]	0			96.0
686.01	LB14	0			99.9
3725.01	LB14	0			99.7
3853.01	LB14	0			99.6
Group B - Fast rotators					
12.01	LB14	0			99.3
131.01	LB12	1	5.54″	3.48 (i_{SDSS})	-
366.01	LB14	0			99.3
625.01	LB14	0			96.8
972.01	CFOP	0			-
972.02	CFOP	0			-
3728.01	LB14	0			99.6
Group C - Unsolved cases					
1463.01	CFOP	1	5.47″	6.9 (Kep.)	-
3890.01	LB14	0			98.3

Notes. Uncertainties in the angular separation of the companions and in their magnitude difference have been omitted for clarification purposes. We refer to the corresponding references for more information about this fact. [(a)] LB12 = Lillo-Box et al. (2012), L13 = Law et al. (2014), LB14 = Lillo-Box et al. (2014a), CFOP = no reference found in the bibliography but companion tables of the UKIRT J-band survey by D. Ciardi are available in the CFOP. [(b)] The maximum angular separation explored in Law et al. (2014) is 2.5 arcsec.

[28] http://keplergo.arc.nasa.gov/ToolsUKIRT.shtml
[29] http://exoplanets.org/code/

6.6.3 Fast rotators: upper mass limits to transiting companions

Planets orbiting fast-rotating stars are more difficult to detect by the RV method. The line broadening produced by this effect prevents an accurate measurement of the line shift, significantly increasing the uncertainties for high $v \sin(i)$ values. Six fast rotators ($v \sin(i) > 20$ km/s) were found in our sample.

As stated before, we can just provide an upper limit to the mass of the companion of these KOIs. We have assumed circular orbits for all of them, as well as the lack of blended companions contaminating the RV data (see Table 6.20). A simple circular model was fitted to the RV data by fixing the period and time of mid-transit calculated by the *Kepler* team from the analysis of the eclipse. Thus, only two free parameters were fitted, the RV semi-amplitude (K) and the systemic velocity ($V_{\rm sys}$). We ran one MCMC chain of 10^6 steps and discarded the first 10% to avoid dependency on the priors. The results for all six fast rotators are presented in Table 6.21. According to these results, all KOIs but KOI-3728 are compatible with having $K = 0$ km/s (non-detection) within the uncertainties. Thus, we can take $\sigma_{RV} = K + 3 \times \sigma_K$ (where σ_K is the uncertainty in K) as the upper limit of the semi-amplitude of the RV variations caused by an undetected companion.

In the case of KOI-3728, the solution for K is not compatible with zero, thus suggesting a possible detection of the RV variations provoked by the transiting companion. According to this analysis, the companion would have a mass of $0.068 \pm 0.041\ M_{\odot}$. However, owing to the large uncertainties and for consistency with the structure of this section, we prefer to maintain this KOI in the fast rotators group, although highlighting the possible detection of a stellar-like companion. The large $v \sin i$, instead, does not allow us to ensure such a detection. A quick analysis of its light curve suggests the presence of ellipsoidal variations. A simple fit to these variations provide a sub-stellar mass for the companion object, in agreement with that measured by the RV (see § 6.8).

The RV amplitude (K) induced by the companion (if any) detected in these KOIs should be smaller than the aforementioned upper limit (σ_{RV}), i.e., $K < \sigma_{RV}$. This amplitude was defined in Eq. 4.6. We can determine the maximum mass that accomplishes $K = \sigma_{RV}$. This value represents the maximum projected mass ($M^{max}_{\rm comp} \sin i$) of the hypothetic companion orbiting the star and inducing the detected transit signal. The calculated maximum masses of the hypothetic companions ($M^{max}_{\rm comp} \sin i$) are listed in Table 6.21.

All but two KOIs (KOI-972 and KOI-3728) have upper mass limits in the substellar regime ($\sim 80\ M_{\rm Jup}$), although we have clear hints that KOI-3728.01 is a brown dwarf as explained above. Indeed, in two cases (namely KOI-366 and KOI-625), the upper mass limit is close or even below the deuterium-burning limit ($\sim 13\ M_{\rm Jup}$), suggesting that the objects transiting these stars are likely planets.

TABLE 6.21: Upper limits for the mass of the transiting companion to KOIs with large $v \sin i$ values (fast rotators, Group B).

Group B - Fast rotators					
KOI	$v \sin i$	K (km/s)	V_{sys} (km/s)	σ_K (km/s)	$M_{\rm comp}^{max} \sin i$ ($M_{\rm Jup}$)
12.01	70 ± 5^{a}	0.140 ± 1.425	-18.6 ± 1.1	1.565	25.2 ± 3.7
131.01	$26^{\dagger,b}$	1.400 ± 1.995	-9.0 ± 1.8	3.395	35.8 ± 5.0
366.01	35 ± 2^{c}	0.027 ± 0.255	8.5 ± 0.2	0.282	8.70 ± 0.59
625.01	25 ± 2^{c}	0.120 ± 0.510	-25.87 ± 0.42	0.630	14.1 ± 1.6
972.01	120 ± 5^{c}	2.200 ± 3.300	-14.1 ± 2.4	5.500	106.8 ± 2.6
972.02	120 ± 5^{c}	2.200 ± 3.300	-14.1 ± 2.4	5.500	89.9 ± 2.1
3728.01	$55^{\dagger,a}$	4.810 ± 2.775	-52.6 ± 2.4	7.585	111.6 ± 6.3

Notes. † No uncertainties provided. $v \sin i$ values are obtained from different studies in the CFOP: $^{(a)}$ Values obtained from the analysis of TrES spectra by A. Byerla. $^{(b)}$ Values obtained from the analysis of Lick spectra by H. Isaacson. ^{c} Values obtained from the analysis of McDonald or TrES spectra by S. Quinn.

TABLE 6.22: Results of the fitting to the observed RVs for the eclipsing binaries and unsolved KOIs.

KOI	K (km/s)	e	ω (deg.)	$M_{\rm comp} \sin i^{(a)}$ ($M_{\odot}$)	inc.$^{(b)}$ (deg.)	$F_M{}^{(c)}$ ($M_{\rm Jup}$)	a (AU)
Group A - Eclipsing binaries							
0340 B	16.28±0.11	0.5138±0.0059	239.71±0.58	0.2144±0.0058	89.95	7.000±0.091	0.1614±0.0054
0371 B	8.252±0.086	0.4070±0.0081	94.75±0.47	0.445±0.014	89.95	23.15±0.82	1.424±0.047
0686 B	6.3±1.7	0.52±0.15	63±12	0.089±0.018	89.38	0.88±0.45	0.259±0.015
3853 B	26.98±0.48	0.3956±0.0084	130.8±1.3	0.527±0.043	50.42	35.5±2.2	0.175±0.014
3853 C	2.1±1.3	0.56±0.20	312±21	0.030±0.016	–	0.011±0.019	0.171±0.014
Group C - Unsolved cases							
1463 B	> 3.3	> 0.18	[80,200]	> 0.183 ± 0.030	89.95	> 4.15	2.15 ± 0.19
3890 B	> 2.5	> 0.33	[0,82]	> 0.097 ± 0.014	89.95	> 0.27	0.676 ± 0.040

Notes. $^{(a)}$ Companion mass assuming primary mass from Huber et al. (2014). $^{(b)}$ Orbital inclination provided by the *Kepler* team. $^{(c)}$ Mass function, defined as: $F_M = M_{\rm comp}^3 \sin^3 i/(M_{\rm comp} + M_{\star})^2$. This parameter is directly obtained from the RV fit and does not depend on the primary mass.

6.6.4 Eclipsing binaries: false positives in the *Kepler* sample

We have found seven candidates that show large RV variations, which are incompatible with the presence of planetary-mass companions. Among them, we have clear RV solutions for five KOIs, while more data is still needed for two of them (namely KOI-1463.01 and KOI-3890.01). The variations are modulated with the same period as detected by the transit method using *Kepler* data. In the following, we analyze each of these false positives. In Table 6.22 we present the fitted orbital and physical parameters for those KOIs with a clear Keplerian fit to the RV. Figure 6.31 shows the measured radial velocities and the corresponding RV models of these KOIs.[30]

[30] KOI-3725 is not presented in this figure because of its large $v \sin i$ prevents a precise RV study.

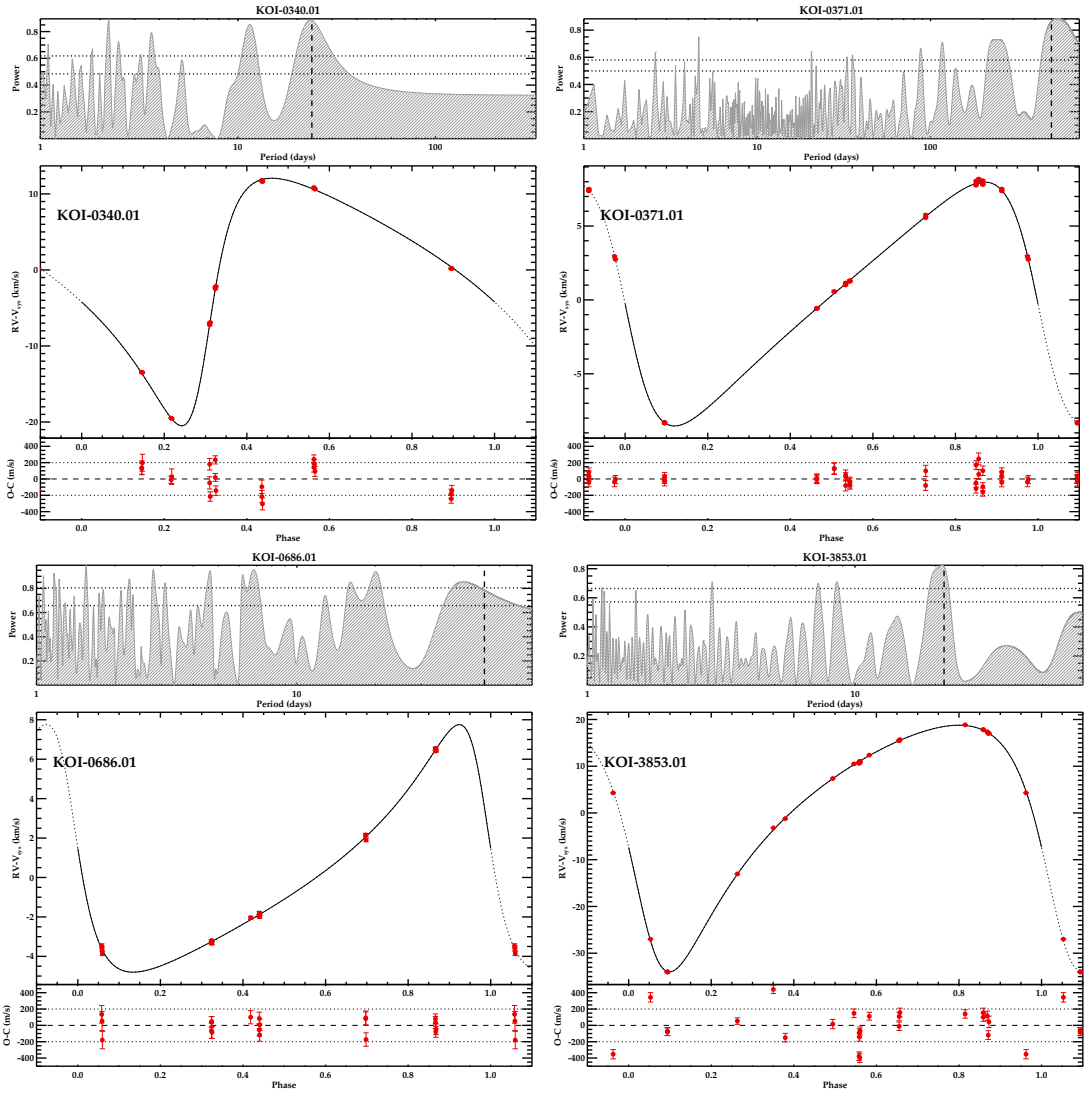

FIGURE 6.31: Radial velocity analysis of the detected binary systems. In each set of images and for every KOI, we show the periodogram of the radial velocity data (upper panel), the fit to the data (middle panel), and the residuals of the fit (lower panel).

KOI-0340.01

This planetary candidate was announced by the *Kepler* team in the first release of the mission (Borucki et al., 2010). Its *Kepler* light curve presents transit-like dims every 23.673188 ± 0.000014 days. It was included in the catalog of eclipsing binaries[31] presented and updated in Matijevič et al. (2012). Also, Santerne et al. (2012) used the SOPHIE instrument to obtain two RV measurements at quadrature phases assuming circular orbit, and derived a semi-amplitude of $K = 34.577 \pm 0.074$ km/s with this assumption, finally concluding that this system should be a single-line spectroscopic binary.

The modeling of our CAFE data (obtained at eight different phases) provides a highly eccentric orbit ($e = 0.513 \pm 0.005$) for the companion. The fitted RV semi-amplitude provides a value

[31] http://archive.stsci.edu/kepler/eclipsing_binaries.html

of $K = 16.28 \pm 0.11$ km/s. Assuming a host mass of $M_\star = 1.10 \pm 0.07\ M_\odot$ provided by the CFOP, we derived a stellar mass for the transiting object of $M_2 \sin i = 0.214 \pm 0.006\ M_\odot$. The L-S periodogram indicates a period for the RV data in good agreement with the period obtained with the transits method, thus indicating that both effects are produced by the same object (see Fig. 6.31). The non-planetary nature of the object transiting KOI-0340 is thus clear from this analysis so that we can firmly and definitively discard this candidate as a planet.

We also detect the secondary eclipse of this system. We used a simple model of a binary box with linear ingress and egress dependencies (enough for the purposes of this work) to measure its depth, location, and duration (see Fig. 6.32). The period and time of mid-eclipse were assumed from those calculated by the *Kepler* team. The results show a depth of $\delta_{\rm sec} = 650.6 \pm 6.6$ ppm, located at $\phi = 0.31862 \pm 0.00002$ and lasting $d = 0.01005 \pm 0.00023$ in phase units, equivalent to $d = 5.70 \pm 0.13$ hours. By assuming the primary eclipse depth provided by the *Kepler* team ($\delta_{\rm pri} = 22335$ ppm, no uncertainty provided), we can infer a surface temperature ratio since

$$\frac{\delta_{\rm pri}}{\delta_{\rm sec}} = \left(\frac{T_A}{T_B}\right)^4, \tag{6.8}$$

where $\delta_{\rm pri}$ is the depth of the deepest eclipse, $\delta_{\rm sec}$ the depth of the smaller eclipse, and T_A/T_B the ratio of effective temperatures of both stars. By using this equation, we obtain a temperature ratio of $T_A/T_B = 2.421 \pm 0.006$.

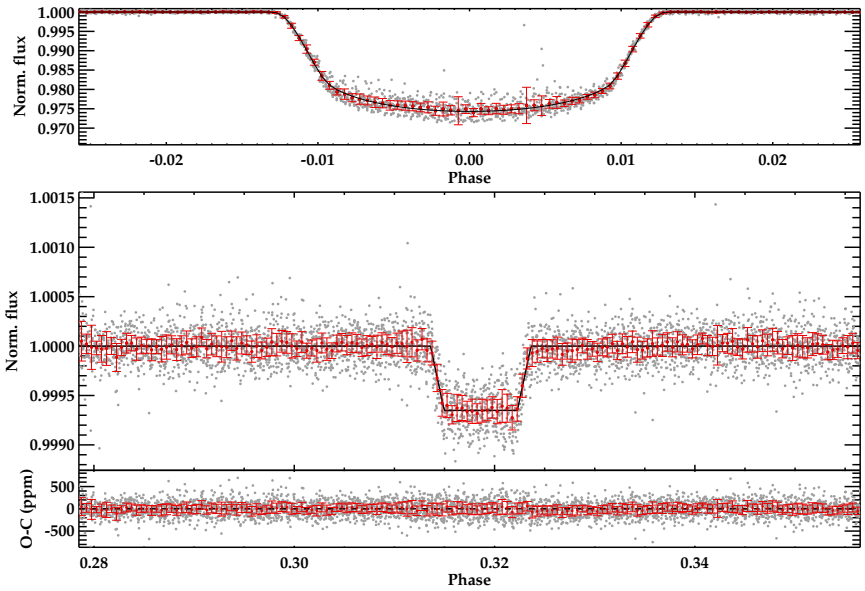

FIGURE 6.32: Detrended *Kepler* light curve of KOI-0340. In all panels small gray circles represent the *Kepler* data and the red filled circles is a binning of the whole data with a bin size of 0.005 in phase (~ 2.8 hours). Upper panel shows a zoom to the primary transit and the fitted primary eclipse with a solid black line. Middle panel shows the detected secondary eclipse and the fit as a solid black line. The lower panel shows the residuals of the fit, with a standard deviation of 173 ppm in the original dataset and 36 ppm in the binned light curve.

Given the orbital configuration from the RV analysis, the expected location of the secondary eclipse according to Eq. 2.13 is $\phi = 0.335 \pm 0.010$, if we assumed the inclination provided by the *Kepler* team. The difference between the expected time of mid-eclipse and the measured time is 9.3 ± 5.7 hours. The source of this discrepancy is unknown but could be due to an underestimation of the uncertainties in the RV parameters or an inaccurate determination of the time of eclipse, translated into a small shift in the phase-folded light curve.

Additionally, owing to the high eccentricity found for this system, we decided to perform a dedicated modeling of the primary eclipse.[32] We used the Mandel & Agol (2002) light curve models and obtained the non-linear four-terms limb-darkening parameters by interpolating the stellar parameters provided by Huber et al. (2014) to the values in Claret & Bloemen (2011) for the *Kepler* band. We fixed the eccentricity and argument of the periastron to the values found in the radial velocity analysis and leave the inclination (i), semi-major axis to primary radius (a/R_A), and radius ratio (R_B/R_A) as free parameters. The results for this fit are $i = 89.6° \pm 0.2°$, $a/R_A = 21.82 \pm 0.34$, and $R_B/R_A = 0.1452 \pm 0.0007$. This model is shown in the upper panel of Fig. 6.32. The main difference with the *Kepler* team parameters ($i_{\rm Kep} = 89.95°$, $(a/R_A)_{\rm Kep} = 14.31983 \pm 0.00722$, and $(R_B/R_A)_{\rm Kep} = 0.142771^{+0.000068}_{-0.000048}$) is the semi-major-to-stellar-radius ratio. This is due to their assumption of circular orbit, while we have found a relatively high value for the eccentricity from both the RV and the secondary eclipse analyses.

KOI-0371.01

A periodic transit signal of $P_{\rm orb} = 498.3928 \pm 0.0042$ days was detected by *Kepler* for this star. No significant difference in the depth of the two single eclipses is found in this case, so we maintain the period of this KOI as calculated by the *Kepler* team. The analysis of our RV data (with a timespan of 722 days) shows large relative variations for the stellar host. We find a clear (although broad) peak in the RV periodogram corresponding to the same periodicity as the transit signal (see Fig. 6.31). According to our fit of the RV modulations, we find that the companion source has a minimum mass of $M_2 \sin i = 0.445 \pm 0.014\ M_\odot$. The physically bounded stellar companion is calculated to be at $a = 1.424 \pm 0.047$ AU, with a highly eccentric orbit of $e = 0.407 \pm 0.008$. Thus, we can reject this planetary candidate and establish its binary nature.

KOI-0686.01

This planet candidate was released in the second catalog of *Kepler* planet candidates. The RV analysis reveals large variations with a clear modulation. The analysis of the AstraLux images of this object yielded a 0.1% of probability that this KOI has an undetected blended background

[32] The *Kepler* team assumes circular orbits in the transit fitting.

star. Thus, it is highly probable that these RV variations come from a bounded companion to the KOI-0686 system.

The analysis of the detected transits by the Kepler team provided an orbital period of $P_{\rm orb}$ = 52.513565 ± 0.000015 days. If we assume the same period and mid-transit time for the RV signal, we can obtain a model solution for the RV data. This fit provides a stellar mass for the companion transiting object of $M_B \sin i$ = 0.089±0.018 $M_\odot$. We can thus confirm that KOI-0686 is an eclipsing binary. We note that a contemporary work by Díaz et al. (2014b) also obtained the same conclusion, with the fitted parameters in good agreement within the uncertainties.

KOI-3725.01

The observations for this object were started while its status was "not-dispositioned" in the *Kepler* catalog. This meant that the light curve analysis had not yet passed all the required criteria to be considered as a planet candidate. After the target was observed with CAFE, the *Kepler* team updated its status to "false positive". Our analysis of the light curve shows a clear difference in the depth of the odd and even eclipses, thus tagging this system as an eclipsing binary. Given this, we must consider a double period such as the one published by the *Kepler* team (i.e., $P_{\rm orb}$ = 3.1409940 ± 0.0000008 days instead of 1.5704970 ± 0.0000004 days).

Our high-spectral resolution data and light curve analysis confirm that this system is an eclipsing binary, showing large RV variations over the observed timespan and differences in the odd/even eclipse depths. However, the small number of phases acquired and the contaminated spectrum by the presence of two possible sets of lines, with a very broad one (suggesting high rotational velocities) prevent us from performing any detailed RV analysis.

The clear odd/even differences in the eclipse depths (see Fig. 6.33) is also a clear sign of an eclipsing binary. According to this, the actual periodicity of this binary system is $P_{\rm orb}$ = 3.1409940 ± 0.0000008. The temperature ratio between both stars can be estimated from the depth ratio of both eclipses following Eq. 6.8. In this case, a simple fitting to the Gaussian-like eclipses (enough for the purposes of this paper) provides δ_1 = 2732 ± 30 ppm and δ_2 = 1803 ± 35 ppm (see fitted functions over-plotted in the bottom panel of Fig. 6.33). This implies a temperature ratio of T_A/T_B = 1.109 ± 0.006.

KOI-1463.01

Only four phases (14 spectra in total) have been obtained with CAFE for this long-period candidate ($P_{\rm orb}$ = 1064.2681410 ± 0.0001434 days). Our RV data (with a timespan of 691 days) shows large variations of ∼ 7.5 km/s, which do not correspond to a planetary-mass object (see Fig. 6.34, left panel). However, the low number of epochs acquired and the timespan (shorter

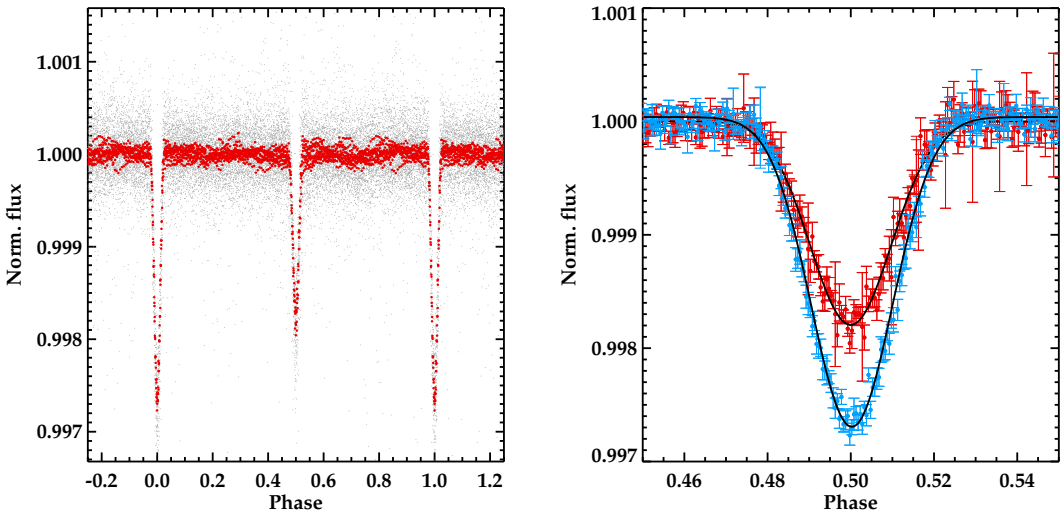

FIGURE 6.33: Detrended *Kepler* light curve of KOI-3725 and phase-folded by using the new calculated period (i.e., $P_{\rm orb} = 3.1409940 \pm 0.0000008$ days), twice that published by the *Kepler* team. Left panel shows the entire phase of the system. Right panel shows a zoom to the odd and even transits (in different colors and symbols). The primary transit has been shifted to $\phi = 0.5$ for comparison purposes. The transit model is shown as solid gray lines.

than the orbital period) prevents us from extracting definite conclusions about this system. We used a radial velocity model including non-zero eccentricity to fit the available data. The free parameters used were thus the RV semi-amplitude, the eccentricity, the argument of the periastron, and the systemic velocity of the system.

We ran a Monte-Carlo Markov-Chain with 10^6 steps to estimate these parameters and detect the correlations between them because of the lack of a complete sampling of the orbital phases. The degeneracy in the parameter space is important, but we must point out that all solutions provide eccentricities that are higher than $e > 0.18$ and semi-amplitude values higher than $K > 3.3$ km/s. This corresponds to a lower mass limit for the companion transiting object of $M_B^{min} = 0.183 \pm 0.030\ M_\odot$. In the left panel of Fig. 6.34, we show a random sample of solutions obtained for this system.

The transiting companion is probably a star, according to the present data, suggesting that KOI-1463.01 is a false positive. The solution to this system is still open, and more RV data in a longer timespan is needed (since *Kepler* will no longer observe this target). We also note that Hirano et al. (2012b) suggest that this candidate could actually be a late-type stellar companion transiting the star, which they base on their analysis of the flux variations.

KOI-3890.01

This planet candidate was detected as transiting its host star with a periodicity of 152.82630 ± 0.00099 days. Our RV analysis shows a clear trend with a variation of 3 km/s in a timespan

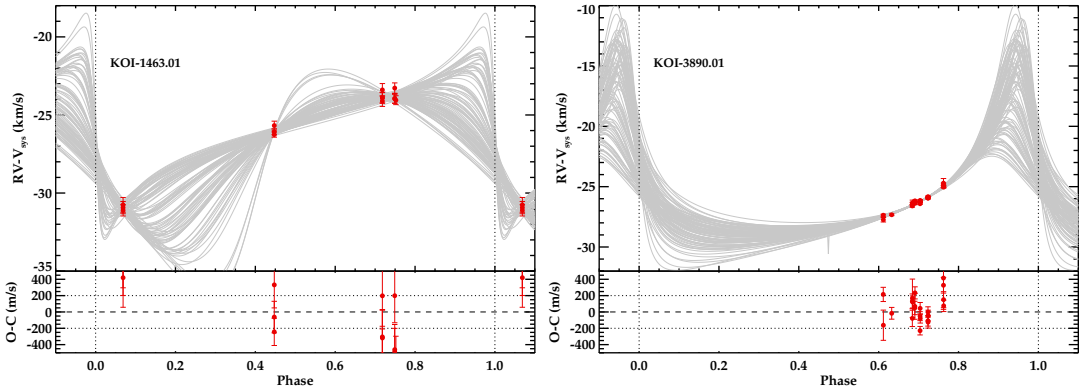

FIGURE 6.34: Radial velocity analysis of the two unsolved systems. We show one hundred random solutions accepted in our MCMC run. The residuals to the median solution are found in the lower panel

of 305.2 days (see Fig. 6.34, right panel). Since we do not detect transit depth differences in the odd and even transits, we can fix the period and mid-transit time to what was measured in the light curve analysis by the *Kepler* team. Also, the narrow range of phases covered by our observations ($\phi \in [0.6, 0.8]$) means that we cannot constrain the eccentricity and argument of the periastron of the orbit. We then proceed in the same manner as with KOI-1463 by running an MCMC chain and analyzing the range of parameters. By doing so, we obtain a minimum RV semi-amplitude of $K > 2.5$ km/s. This translates into a minimum mass for the transiting companion such that $M_B > 0.097 \pm 0.014\ M_\odot$, with a minimum eccentricity of $e > 0.33$. In the right hand panel of Fig. 6.34, we show a random sample of solutions for this degenerated system.

However, we must warn that in this case, the F-test comparing the RV model to a simple straight line provides a value of 3.6, slightly favoring the false positive detection against a null detection model. Thus, although this candidate is likely to be a binary, we cannot draw definite conclusions given the current data (mainly owing to the small phase coverage). More RV at different phases is needed to better understand this system.

6.6.5 The curious case of KOI-3853: a possible heartbeat triple system.

Radial velocity analysis

This KOI has been reported as a possible false positive in the Kepler database.[33] The derived period according to the light curve analysis is $P_{\rm orb} = 21.512905 \pm 0.000050$ days. The analysis of our high-resolution spectra obtained in 14 different phases reveals a large RV variation incompatible with a planetary-mass, thus confirming that KOI-3853.01 is not a planet. When fitting the RV with a single object, an important periodic trend is found in the residuals. We tried to fit

[33] http://exoplanetarchive.ipac.caltech.edu

the RV data by assuming the presence of a third body in the system (see Fig. 6.35). The fit in this case was significantly improved. We can measure the significance of such improvement by using the Bayesian inference criterion (BIC). We obtain a difference in the BIC value of ΔBIC > 100, showing strong evidence for the three-bodies against the two-bodies model.

Interestingly, the period of the less massive companion (i.e., component C) is similar (in agreement within 3σ uncertainties) to the more massive companion (i.e., component B), hence being in a near 1:1 mean motion resonance (MMR). The periodogram of the RV data shows a double (blended) peak around the period corresponding to the eclipse observed in the *Kepler* data. Both peaks have a false alarm probability (FAP) below 1%. To test the validity of the second periodicity in the data, we fixed the fitted parameters obtained for component B and ran 10×10^5 MCMC chains to fit the residuals of the data. We let the period of the possible C component vary in the range 1-71 days. The posterior distribution of the combined chains clusters around the estimated period provided by the joint fit (within the uncertainties).

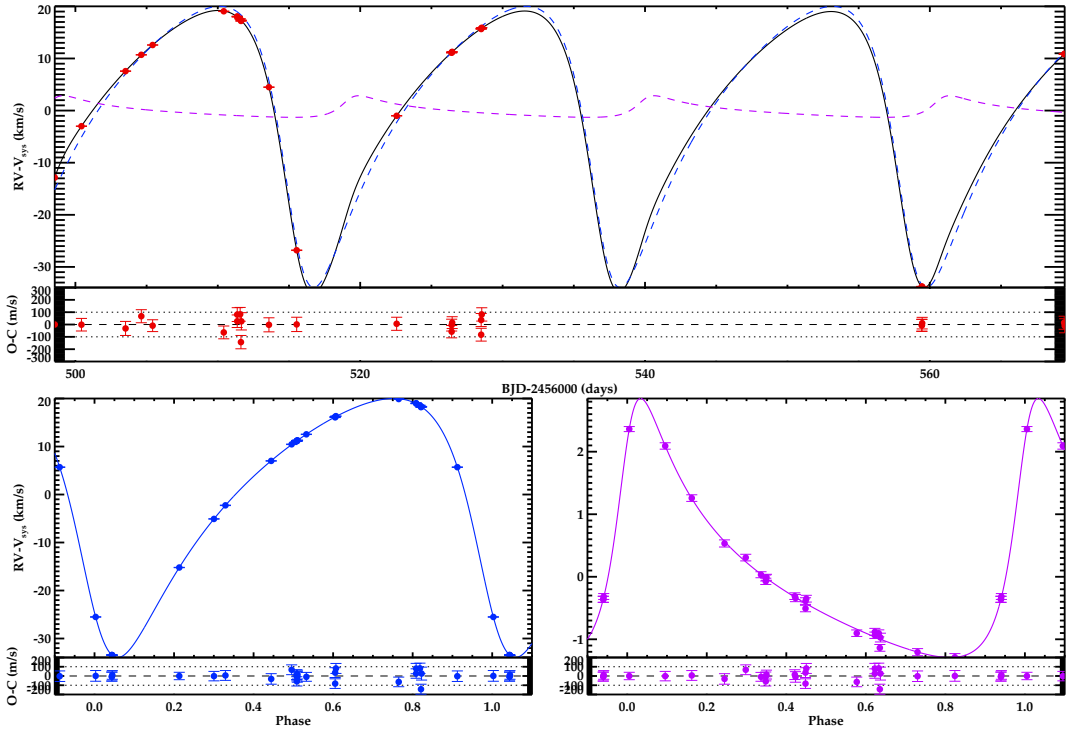

FIGURE 6.35: Radial velocity analysis of the detected components of KOI-3853. Upper panel shows the RV solution for the whole system (black solid line) and the two contributions of the B component (dashed blue) and C component (dashed purple). Lower panels show the individual contributions of components B (left panel) and C (right panel).

All these three tests performed with our RV data (BIC, periodogram, and MCMC analysis) favor the existence of a third component in near 1:1 MMR against the two-bodies-only configuration. The orbits of the two possible companions would be oriented in opposition, i.e., the difference in the argument of the periastron of both eccentric orbits agrees with being 180°. According to the fitted models, and assuming the stellar mass for the A component provided in Table 6.1,

the minimum masses of the two companions would be $M_B \sin i_B = 0.527 \pm 0.044\ M_\odot$ and $M_C \sin i_C = 0.030 \pm 0.016\ M_\odot$. The mass difference between both components is significantly large, with the less mass component in the substellar/planetary-mass regime.

The unusual architecture of the proposed scenario would require a more detailed study of its stability (which is beyond the scope of the present work). Simulations of 1:1 mean motion resonances in the planetary-mass regime by Antoniadou et al. (2014) show that these configurations are stable under specific mass ratio conditions, $m_C/m_B < 0.0205$. Although our objects are more massive, we note that this condition is fulfilled (within the uncertainties) for the KOI-3853 system. However, as stated before, more work is needed to analyze the stability of this system.

Stellar pulsations induced by the massive companion could also explain the correlated residuals in the RV fit. The light curve of this target presents the so-called *heartbeat* effect, which is produced by tidal interactions induced by the more massive stellar companion. In Willems & Aerts (2002), the authors describe and calculate the RV variations induced by tides in close binary systems. According to them, there are specific resonant configurations that can lead to radial velocity variations that are even larger than 5 km/s, thus a relevant explanation for the presence of the modulated residual of this close binary. However, an accurate description of this system is beyond the scope of this work. Future analysis studying the heartbeat-like modulation and the stellar modes induced by the close massive companion could reject the existence of the substellar companion in the 1:1 resonant orbit.

Light curve analysis

The light curve of KOI-3853 shows an interesting effect just discovered in a few tidally distorted binaries, the *heartbeat* pulsation. The shape of the light curve modulation due to this effect is well understood and was parametrized by Kumar et al. (1995). In particular, in the case of KOI-3853, its shape corresponds to a highly inclined orbit with the periastron oriented behind the plane of the sky. An accurate model fitting of this modulation is beyond the scope of this paper, but future work will focus on this object and characterize it fully.

However, the *heartbeat* is not the only imprint in the light curve of this system. A transit-like shape appears in the middle of the tidal modulation. The *Kepler* team identified this transit as a potential candidate with a planetary nature. After removing the heartbeat signal by a simple cubic spline fitting, the eclipse shows a maximum depth of around 2000 ppm. However, it is filled by some data points at lower depths. Interestingly, we can detect duration and depth variations in the individual eclipses (see Fig. 6.37 and 6.38). Figure 6.38 displays the depth of the individual eclipses as a function of time. A clear trend is visible and suggests that the eclipsing body is rapidly changing its impact parameter.

Our RV analysis suggests that the motion variations of the primary star (A) are described well with the presence of two companions, a massive stellar object (component B) and a substellar

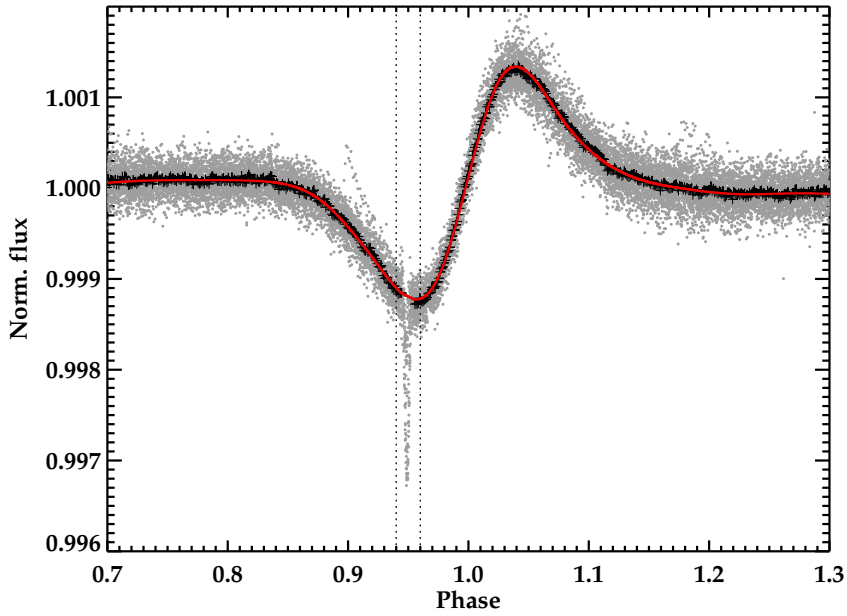

FIGURE 6.36: Detrended *Kepler* light curve of KOI-3853, phase-folded using the period published by the *Kepler* team. The heartbeat effect and the eclipse are clearly visible. The red line shows the spline function fit to remove the effect. Vertical dotted lines show the region zoomed in Fig. 6.37.

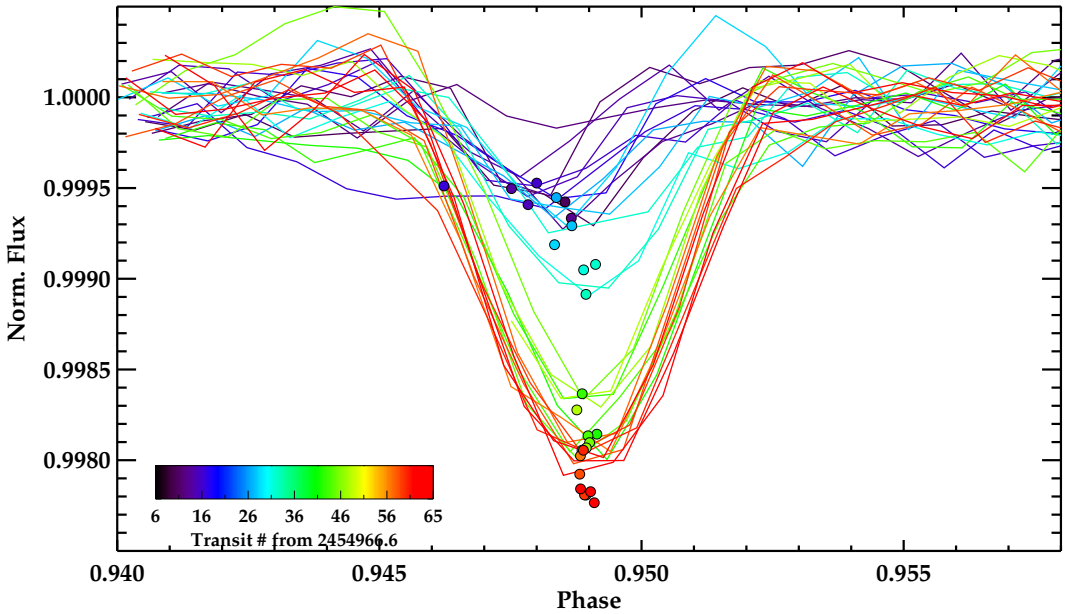

FIGURE 6.37: Individual eclipses in the KOI-3853 system. The color code represents the transit number (equivalent to the Julian date) since BJD = 2454966.6 days. The filled circles show the location (timing and depth) of the peak of the eclipse for each individual transit. We have omitted timespans in which *Kepler* data is not available at the phases of interest. The light curve has been firstly detrended and then removed from the heartbeat effect.

companion (component C) in a near 1:1 mean motion resonance. Both objects would revolve in eccentric orbits around the primary (massive) star. Based on this, we suggest some possible explanations for the depth, duration, and time variation of the detected eclipses:

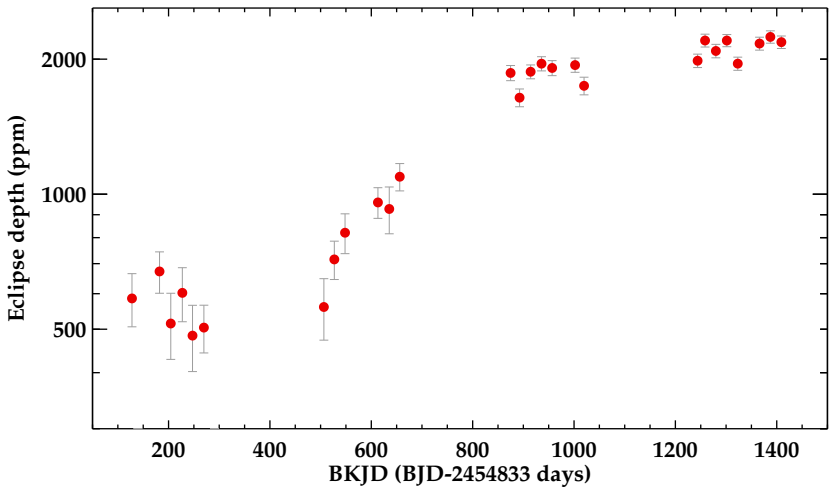

FIGURE 6.38: Variation in the eclipse depth of the KOI-3853 system in the timespan of *Kepler* observations.

- *Orbital wobble of component B*. In this case, we assume that the eclipse and the heartbeat signal are produced by component B. The presence of a third-body in the system (either component C or a satellite companion) can periodically vary the impact parameter of component B, thus changing both the duration and the depth of the eclipse. Since we know from the shape of the heartbeat effect that the orbital inclination should be high, this should be a grazing eclipse of component B over component A. In the first periods of Fig. 6.37, the projected location of component B in the plane of the sky would be at impact parameters $b \gtrsim 1+R_B/R_A$ so that we see a small eclipse or no at all. By contrast, in the last periods, the impact parameter decreases so that the eclipse is deeper. A longer timespan could have confirmed this hypothesis by detecting periodic variations of the eclipse depth.

- *Orbital wobble of component C*. In this case, we assume that the eclipse is produced by component C and the heartbeat is produced by component B. Our RV analysis suggests two eccentric orbits in opposition, i.e., with their pericenters differing by 180°. Component B, maybe in a higher inclined orbit (since we do not see any other dip in the LC), could be perturbing the orbit of component C, provoking an orbital wobble able to change its impact parameter and thus the eclipse depth.

- *Orbital circularization*. If the system is being circularized, with component B orbiting closer to component A every period, the eclipse depth and duration will be increased with time. Since within the timespan of *Kepler* data, we do not see a new turn back to smaller depths, we cannot discard this possibility.

With the current data, none of the previous conclusions can be rejected so that the problem remains open. However, our RV analysis suggests the presence of a third component in near 1:1 mean motion resonance. Future observations and study will shed more light on this and will try to unveil the nature of this system. In particular, a dedicated stability study is required to check the dynamical plausibility of the co-orbiting substellar object in 1:1 mean motion resonance. As mentioned above, the mass ratio between the two companions would agree with the allowed ratio for a triple system in 1:1 mean motion resonance as calculated by Antoniadou et al. (2014), although we warn that this study was specifically performed for planetary-mass systems.

6.6.6 Summary and discussion

We have analyzed the RV data obtained with the CAFE spectrograph for 13 KOIs and the *Kepler* light curves of some of them. In the majority of the eclipsing binaries found in this work (Group A), we found that the lighter component is a very low-mass star (VLMS). Zhou et al. (2014) and Díaz et al. (2014b) have published the latest results on this kind of objects (see also references therein), adding more examples to the reduced number of well-characterized VLMSs (with detected eclipses and RV variations). Added to this, our RV analysis suggests substellar masses for the transiting companions of the fast-rotating stars (Group B).

In Fig. 6.39, we show the mass-radius diagram for the companions found around these KOIs. In the case of KOI-0340 B, the radius provided by the *Kepler* team was well below the expected value provided by any isochrone. We then decided to make a dedicated primary eclipse fit to account for the derived high eccentricity. By assuming the primary radius obtained by Huber et al. (2014), the new radius of the companion, although larger, still lies below the expected value. This could be attributed to an underestimation of the radius of the primary star (R_A). We can estimate R_A from the a/R_A ratio obtained by the primary eclipse fitting and the a value obtained in the RV analysis. The resulting updated stellar radius is $R_A = 1.589 \pm 0.021\ R_\odot$. If we now use this value and the radii ratio between both components obtained from the eclipse fitting (R_B/R_A), we obtain $R_B = 0.231 \pm 0.021\ R_\odot$. This new value agrees perfectly with the expected given its mass and its evolutionary stage.

In the case of the fast rotator KOI-0972, the calculated upper mass limit for its transiting objects (assigning this mass limit to every candidate) also lies below the isochrones of VLMSs. The *Kepler* team detected two planet candidates in this system, with measured radii $R_{.01} = 6.1 \pm 1.4\ R_\oplus$ and $R_{.02} = 1.73 \pm 0.57\ R_\oplus$. There are thus two explanations for the discrepancy in the location of these objects in the mass-radius diagram: i) an underestimation of the stellar radius, or ii) a real planetary nature of the candidates, with corresponding masses well below our upper limits. The former explanation is plausible since the host seems to be a subgiant star, and the Darmouth models used to determine the radius could be biased for this kind of stars (see Huber

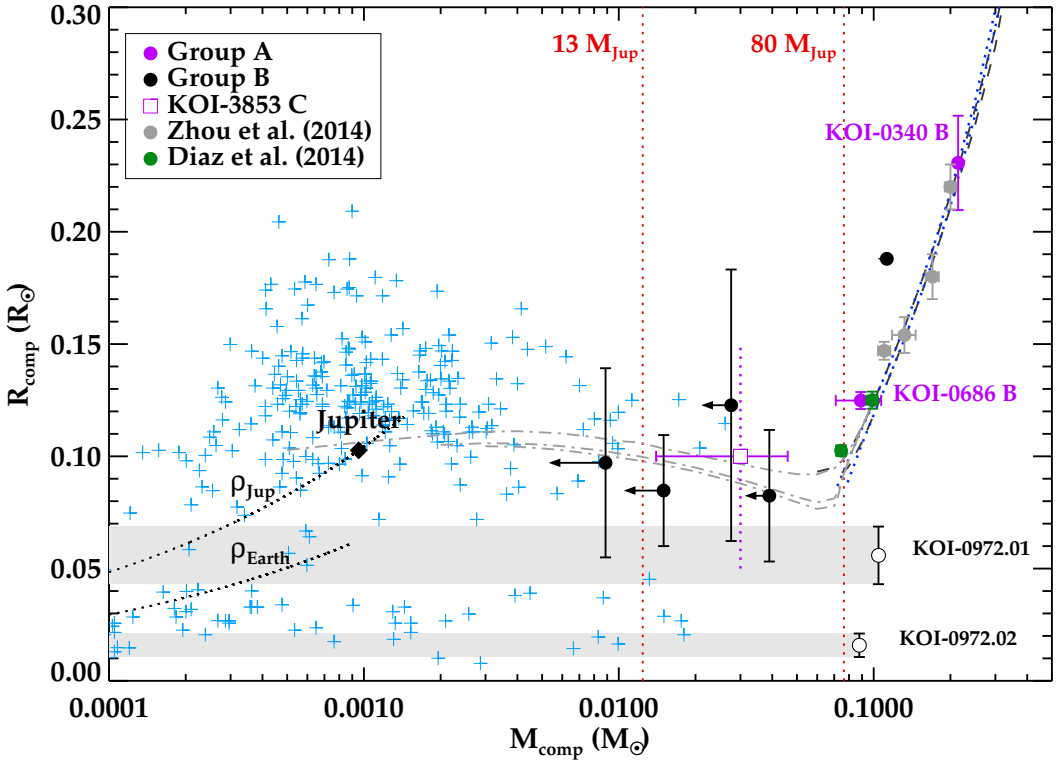

FIGURE 6.39: Mass-radius diagram of the companion objects with $M < 0.3\ M_{\odot}$ found to some of the analyzed KOIs in groups A and B. The open square shows the location of the possible third body in the KOI-3853 (i.e., KOI-3853 C), with an *ad hoc* assumed radius of $0.1\ R_{\odot}$. The dotted vertical error bar indicates our unknown about its actual size. We used the isochrones of 1 Gyr and 5 Gyr (from top to bottom) from Baraffe et al. (1998) for solar metallicity (dotted dark blue line) and [Fe/H]=-0.5 (dashed light blue line). In the case of masses below $0.1\ M_{\odot}$, we used the Baraffe et al. (2003) isochrones (dotted-dashed gray lines) of 1, 5, and 10 Gyr (from top to bottom). The arrows in the Group B KOIs indicate that their masses are just upper limits. The dashed regions illustrates the range of masses allowed for the KOI-0972 planet candidates. For reference, we have plotted the known planets with provided masses and radius published in the exoplanet encyclopedia (www.exoplanet.eu) as light blue plus signs.

et al., 2014). The latter possibility is represented in Fig. 6.39 by the shadowed regions. We can see that they would agree with having planetary-like densities, in agreement with their measured radii, if their masses are well below our detection limits.

According to the mass-radius diagram and isochrones, we can also obtain an estimation of the radius of the suggested third component in KOI-3853 (i.e., KOI-3853 C). By assuming the calculated mass obtained by RV and the isochrones between 1-5 Gyr, the radius of this object should be in the range $R_C \approx 0.08 - 0.11\ R_{\odot}$ (or equivalently $\approx 0.78 - 1.07\ R_{\rm Jup}$).

6.7 Preliminary results of ongoing analysis

In this section, we present the preliminary results for the remaining targets in this survey. In these cases, the analysis is still ongoing and the results are neither definite nor conclusive in most cases.

In Chapter 4 and Fig. 4.1, we showed that CAFE precision is able to detect Jupiter-mass planets at Jupiter orbital periods (i.e., ~ 4300 days). Some of the targets selected for this follow-up have estimated periods from the transit analysis of hundreds (and even thousands) of days. The phase coverage of some of them is still not completed but in this section we present their preliminary result. Additionally, we include the results of a marginal detection of KOI-684.01 and upper-mass limits to KOI-3919.01.

KOI-375.01: a massive planet in a 1000-days orbit

This planet candidate has a transit period of 988.8811177 ± 0.00091140 days as estimated by Burke et al. (2014). According to the CFOP, this is a Jupiter-size planet with $R_p = 10.81 \pm 2.66\ R_\oplus$ orbiting a Main-Sequence G5V star more massive than the Sun ($R_\star = 1.549 \pm 0.3810\ R_\odot$, $M_\star = 1.105 \pm 0.178\ M_\odot$). This relatively faint target ($m_{\rm Kep} = 13.3$ mag) has been followed-up along the three-years of CAFE observations, covering a total timespan of 712 days. Although this is still less than one orbital period, we have marginally detected the radial velocity signal of the planet. We fixed the RV offsets to those calculated for the RV standards in section § 4.4.4. We have also assumed circular orbit due to the lack of sufficient phase coverage to fit for this parameter and the argument of the periastron. We have also assumed the period and time of mid-transit from the analysis of the *Kepler* team. The best fit model is shown in Fig. 6.40. This preliminary result suggests that KOI-375 is a massive planet of $M_p = 11.2 \pm 1.8\ M_{\rm Jup}$ orbiting with a semi-major axis $a = 2.005 \pm 0.091$ AU, in the frontier of the brown dwarf domain. Its location is close to the habitable zone of its host star (estimated by using the HZ calculator explained in Kopparapu et al., 2013), which is $a_{\rm HZ} = 0.75 - 1.78$ AU.

However, still more data at key phases like $\phi = 0.25$ is needed to completely establish its planetary nature and characterize its orbit.[34]

KOI-1032.10: a possible hidden massive planet

This is the longest period planet that has been followed up by our survey, $P = 1500.1406772$ days, no uncertainty provided (Burke et al., 2014). With this period and the baseline of the *Kepler* mission, only two transits have been observed by the mission. According to the CFOP data, the host is a sub-giant K1IV star, that would have just left the Main-Sequence ($M_\star = 1.08 \pm 0.20\ M_\odot$, $R_\star = 2.28 \pm 0.63\ R_\odot$). Our CAFE observations, with a timespan of 718 days does not show

[34] Our mid-May campaign with CAFE could provide these data.

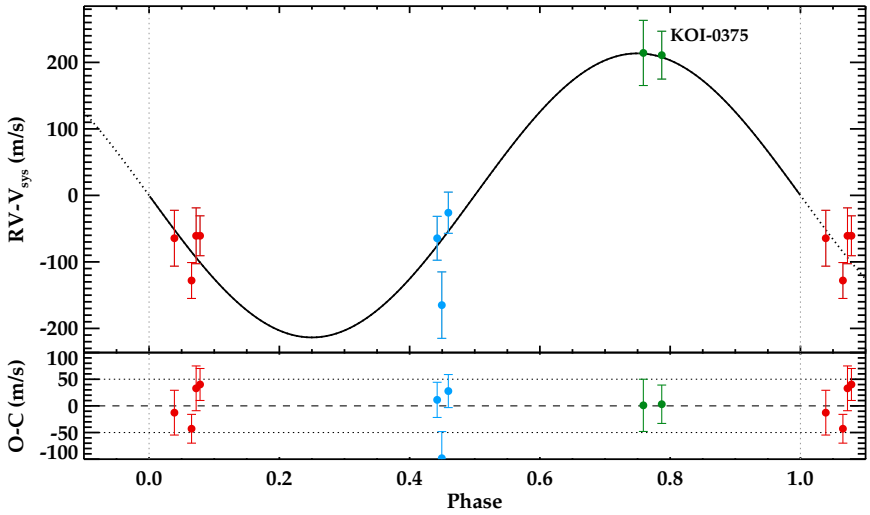

FIGURE 6.40: Preliminary RV analysis of KOI-375. The color code indicates the different epochs of the CAFE data: 2012 (red), 2013 (blue), and 2014 (green).

any RV variation compatible with the measured period by *Kepler*. Instead, we find strong RV variations at shorter time scales so we decided to test shorter-period orbits. To that end, we left the period and time of transit as free parameters. Again, we fixed the RV offsets between the CAFE windows to those determined in section § 4.4.4. We tested two approaches, leaving the eccentricity as a free parameter and fixing it to a circular orbit (and thus fixing $\omega = 90°$). We find the following results:

- *Eccentric orbit.-* We obtain a well-fitted signal with a periodicity of $P = 272.0 \pm 3.2$ days with a semi-major axis of $a = 0.843 \pm 0.052$ AU. This signal would correspond to a massive Jupiter with $M_p = 7.39 \pm 0.59$ $M_{\rm Jup}$ in an eccentric orbit of $e = 0.48 \pm 0.08$ and $\omega = 158.3° \pm 7.5°$. The corresponding BIC value for this model is BIC= 7.1. We show this model in Fig. 6.41, left panel.

- *Circular orbit.-* By fixing the eccentricity and argument of the periastron to that of a circular orbit, we obtain a different period of $P = 316.5 \pm 9.2$ days for a more massive planet of $M_p = 11.4 \pm 3.2$ $M_{\rm Jup}$ and $a = 0.93 \pm 0.06$ AU. In this case we obtain BIC= 10.4. We show this model in Fig. 6.41, right panel.

With this analysis, the current data seems to suggest the presence of a massive planet at a shorter period than that calculated by *Kepler*. We obtain slightly better evidence for the eccentric model than for the circular model (ΔBIC= 3.3). It is important to note that in both cases, depending on the age of the host star, this giant planet could be within the estimated (optimistic) habitable zone of its host star as estimated from the HZ calculator by Kopparapu et al. (2013), $a_{\rm HZ} = 0.78 - 1.89$ AU for a solar luminosity. In section § 7.4, we will discuss this HZ for some of the planets studied in this dissertation, including the two possible planets in this system.

However, as stated, more data is still needed to confirm this detection and to better explore the parameter space regarding the period, and orbital configuration.

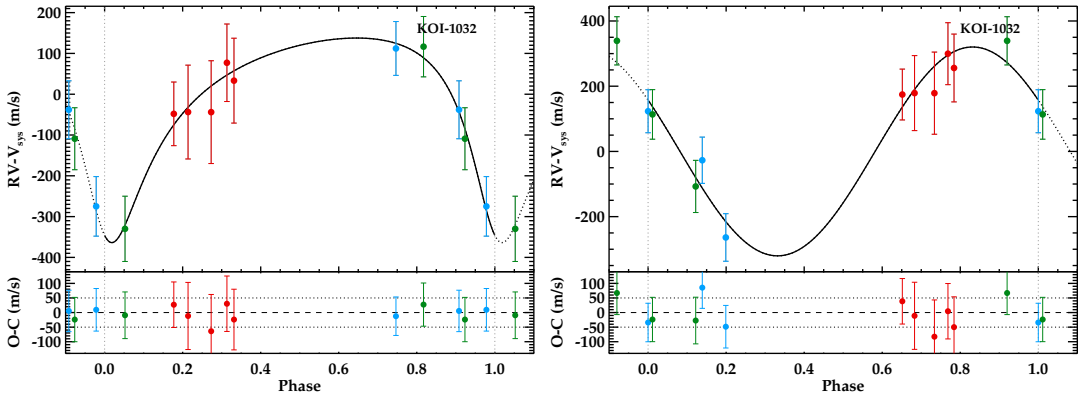

FIGURE 6.41: Preliminary RV analysis of KOI-1032 with the detection of a shorter-period planet than that detected by *Kepler*. We show the best fit eccentric (left) and circular (right) solutions. The color code indicates the different epochs of the CAFE data: 2012 (red), 2013 (blue), and 2014 (green).

KOI-5684: a possible two-planet system in 3:1 MMR

This planet candidate detected by *Kepler* orbits its host star every $P = 206.801125 \pm 0.002678$ days. According to the CFOP, the host star is a K1III giant star ($T_{\rm eff} = 5080 \pm 72$ K, $\log g = 2.98 \pm 0.03$) with an estimated mass of $M_\star = 2.57 \pm 0.17\ M_\odot$ and a stellar radius of $R_\star = 8.61 \pm 0.46\ R_\odot$. The measured radius suggests that this is a giant planet with $R_p = 24.3 \pm 1.3\ R_\oplus$. Our RV observations with CAFE have a reduced timespan of 60 days, just covering a small part of the orbit. However, we have detected anomalous RV variations that could be explained with the presence of a resonant planet at the 3:1 MMR, being the transiting planet in the outer orbit. In other words, our RV data suggests with strong evidence the presence of an inner planet with $P_c = P_b/3$. We have performed a RV fitting by assuming the period of the detected planet and its time of transit and have provided a guess for the second planet as being $P_c = P_b/3$. We also assumed the RV offsets calculated for the RV standards in section § 4.4.4. The results show an extremely good fit with an rms of 48 m/s (see Fig. 6.42). According to this, the estimated masses for the two bodies are $M_{p,b} = 14.24 \pm 0.83\ M_{\rm Jup}$ for the outer (transiting) body and $M_{p,c} = 7.07 \pm 0.52\ M_{\rm Jup}$ for the inner body. The measured depth of the transit for the outer planet is $\delta_b = 716 \pm 46$ ppm. The non detection of the inner body could be due to its smaller radii or the lack of coplanarity. A Jupiter-size planet around this star would have an expected depth of ~ 140 ppm, what should be detectable with *Kepler*. Instead, assuming edge-on orbit for the external planet, a slightly more inclined orbit for the inner planet ($i < 86°$) would not produce a transit.

More RV data and a more dedicated analysis of the *Kepler* light curve will shed more light to the origin of the detected RV variations.

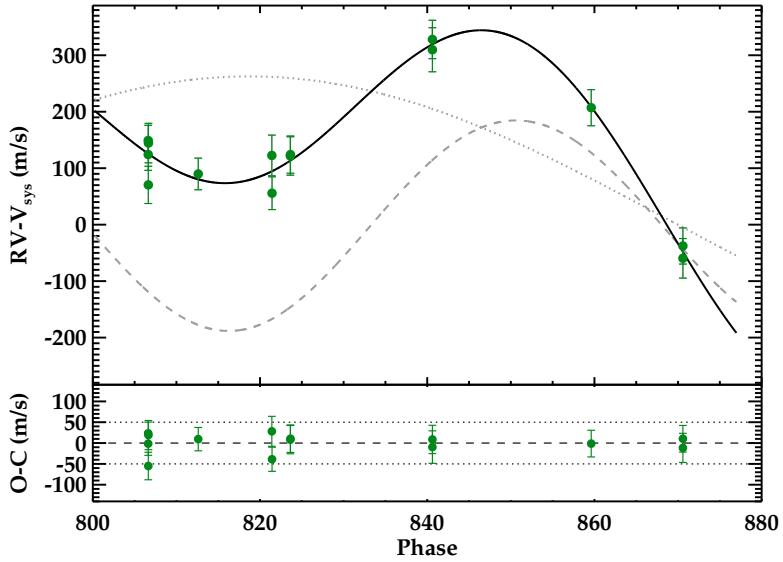

FIGURE 6.42: Preliminary RV analysis of KOI-5684 with the detection of a possible inner planet in 3:1 MMR. In the upper panel, the mode for the outer planet is shown as a gray dotted line while the model for the inner planet is represented by a gray dashed line. The joint model is shown with a black solid line. The color code indicates that all data was obtained in 2014.

KOI-2481: a possible extremely packed S-type planetary system

We have found large radial velocity variations in the CAFE data of this target. However, its periodicity does not match with that of the transiting object. *Kepler* found a periodic transit signal of $P = 33.8542586 \pm 0.0007913$ days around this K3III giant star $T_{\rm eff} = 4550 \pm 100$ K, $\log g = 2.61 \pm 0.02$) with an estimated mass of $M_\star = 1.62 \pm 0.26\ M_\odot$ and a large stellar radius of $R_\star = 10.47 \pm 0.70\ R_\odot$. The preliminary fit of the radial velocity suggests a longer period of 190 ± 0.3 days in a highly eccentric orbit of 0.7 ± 0.2 for a stellar object with $M_2 = 0.5 \pm 0.2\ M_\odot$. In Fig. 6.43, we show the results for a one-object fit with the period as a free parameter. The large variations are clear but they clearly show a different periodicity than that of the transit signal. In the right panel of such figure we provide a zoom to the 2012 data, with a better sampling. It shows anomalous radial velocity variations that could be due to the transiting object, having a high eccentricity around $e \sim 0.6$ (represented by the model in the residuals for which we have assumed the period of the transiting object).

KOI-684: a possible super-Neptune planet

This candidate is known to transit its host star in a short-period of $4.034914596 \pm 0.000002613$ days. Its transit yields an estimated radius for the planet candidate of $R_p = 7.56 \pm 3.64\ R_\oplus$ by assuming the stellar radius provided by the CFOP ($1.79 \pm 0.87\ R_\odot$). Our CAFE data has a long timespan of hundreds of days and has a good phase coverage (see Fig. 6.44, left panel). These data do not allow a conclusive model fit but it serves to set an upper limit to the mass of the transiting body. To that end, we tried to fit these data with a circular model by fixing the period and

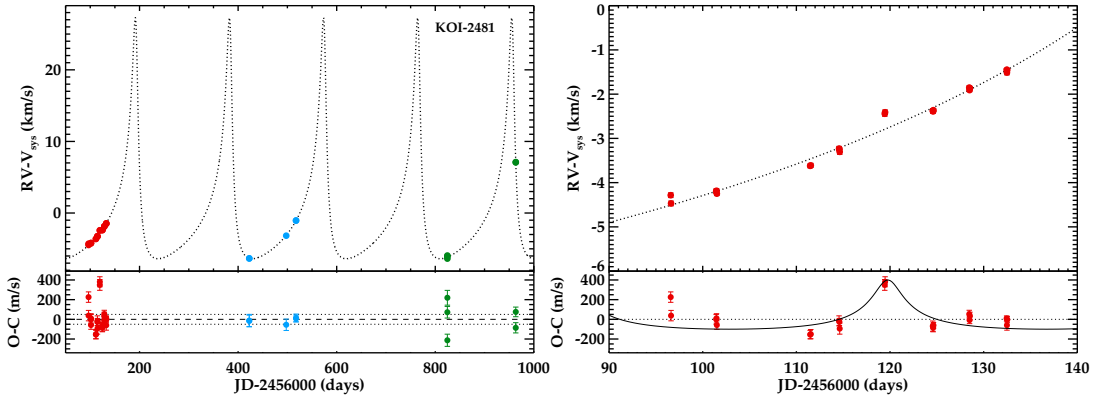

FIGURE 6.43: Preliminary RV analysis of KOI-2481 with the detection of a longer-period object than that detected by *Kepler*. We show the complete RV curve along the whole timespan of CAFE observations (left) and zoom to the 2012 data (right). In the residuals of the right panel (bottom plot), we have over-plotted a simple model for a giant planet in an eccentric orbit with the same period as the detected transit. The color code indicates the different epochs of the CAFE data: 2012 (red), 2013 (blue), and 2014 (green).

time of transit to the *Kepler* values and we obtained a mass of $M_p = 0.55 \pm 0.26\ M_{\rm Jup}$. Although the detection is at the $\sim 2\sigma$ level, we can establish the planetary nature of this candidate at this confidence level. The upper mass limit would then be $M_p < 0.81\ M_{\rm Jup}$. However, more precise data is needed to completely establish its neptunian nature and characterize its orbit.

KOI-3919: a possible "false" false-positive

The candidate KOI-3919 was catalogued as a false positive by the *Kepler* team due to significant secondary event. Our radial velocity data does not show significant variations above 40 m/s with relatively good phase coverage (in the range $\phi = 0.4 - 0.8$) for this $P_{\rm orb} \sim 19$ days candidate, see right panel of Fig. 6.44. From these data, we can do a similar analysis as for KOI-684 to set an upper mass limits to the mass of the transiting object. By doing so, we obtain $Mp = 0.17 \pm 0.21\ M_{\rm Jup}$. This non-detection provides an upper mass limit of $Mp < 0.38\ M_{\rm Jup}$ for this $R_p \sim 1.25\ R_{\rm Jup}$. A stellar body would induce much larger RV variations. Hence, the light curve of this target clearly needs further analysis to unveil the true nature of the primary and secondary eclipses.

6.8 Substellar companions from light curve modulations

In this section we present the preliminary results of a work in progress in collaboration with Álvaro Ribas, Bruno Merín, and Hervé Bouy. This work is dedicated to the detection and characterization of massive planets and brown dwarf companions in the *Kepler* sample of planet candidates.

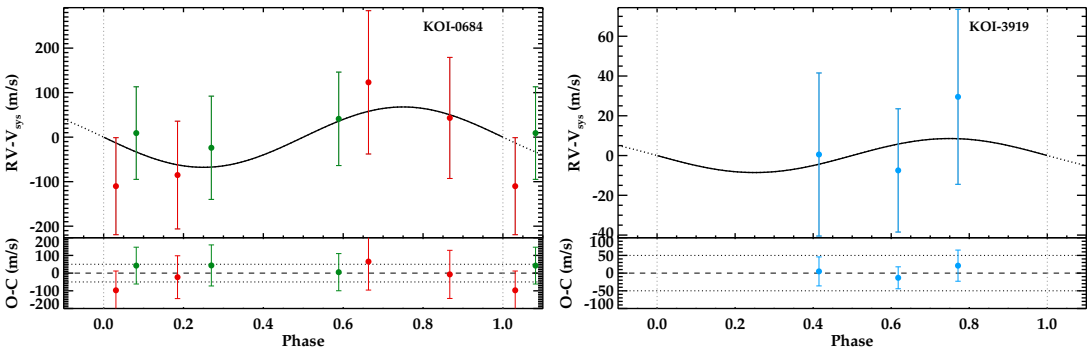

FIGURE 6.44: **Left:** Preliminary RV analysis of KOI-684 with the possible detection of the planet. **Right:** Preliminary RV analysis of KOI-3919 showing the small RV variations, incompatible with a stellar nature for the transiting object.

The explanation for the paucity of substellar objects in close-in orbits (< 3 AU) around FGK stars (also known as the brown dwarf desert) has been discussed for long time (e.g., Armitage & Bonnell, 2002). Radial velocity searches in the past have revealed this apparent desert, which was seen as a proof for the planet-like formation scenario for brown dwarfs (BDs). Additionally, massive planets are not found in close-in orbits around FGK stars. This similar process may indicate similarities in the formation and evolution of both type of objects, which could share identical migration processes.

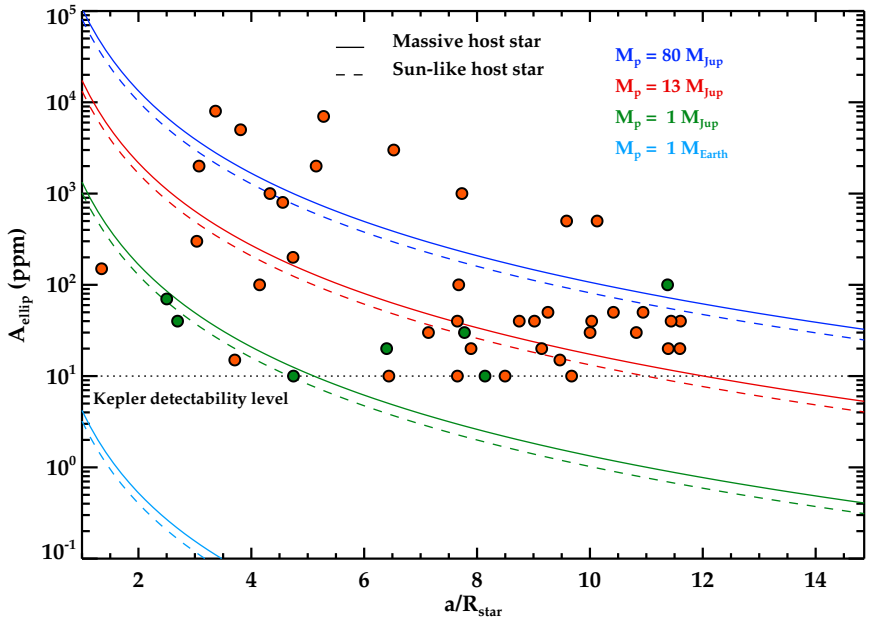

FIGURE 6.45: Estimation of the ellipsoidal modulation amplitude for different *Kepler* planets at different orbital separations. Orange symbols represent planet candidates while green symbols represent confirmed candidates. The Y-axis for each case was estimated form the peak-to-peak intensity in the out-of-eclipse region of the *Kepler* light curve. The solid (dashed) lines represent the amplitudes at different orbital separations for different masses of the companion around a 1.5 $M_\odot$ (1.0 $M_\odot$).

Besides, the number of brown dwarfs with measured radius is very small. Measuring masses and

radius of these substellar objects may help constraining theoretical models. In this regard, the *Kepler* mission has provided unprecedented photometric precision, providing long baseline light curves for more than 150 000 stars. Apart from the transit/eclipse detection, we showed in section § 2.3 that modulations in the out-of-transit region due to the presence of close companions can also be detected.

From our experience with Kepler-91 (see section § 6.2), we decided to carry out a massive search for light curve modulations compatible with planets and brown dwarfs. Among the whole sample of candidates we selected several hundreds by manual inspection of the detrended and phase-folded light curves, looking for the characteristic double-peak provoked by the ellipsoidal modulations. Based on the expected amplitude of this modulation compatible with a substellar object ($M_2 < 80\ M_{\rm Jup}$, see Fig. 6.45), we performed a second selection of candidates to be fully analyzed by our algorithms.

We have preliminary results for six out of the whole sample of selected candidates. In this preliminary analysis, we did not fit for the transit signal, removing this region from the phase-folded light curve. We fitted for the reflection, ellipsoidal, and beaming effects. We used the geometric phase function not including the super-rotation effect. Also, we only used the second harmonic of the ellipsoidal modulation, rejecting higher orders. This process ends up with seven free parameters, namely M_p, $a/R_\star$, i, $R_p/R_\star$, e, ω, and A_g. We have assumed the mass of the star as coming from the CFOP.

TABLE 6.23: Lightcurve fitting for the preliminary analysis of the analysis of KOIs.

KOI ID	M_p ($M_{\rm Jup}$)	$a/R_\star$	i (deg.)	R_p ($R_{\rm Jup}$)	e	ω (deg.)	A_g
554.01	$69.1^{+11.7}_{-8.7}$	$6.5^{+0.2}_{-0.5}$	$75.6^{+13.3}_{-15.6}$	$0.45^{+0.47}_{-0.25}$	$0.0442^{+0.00647}_{-0.00682}$	$152.9^{+11.7}_{-15.9}$	$0.55^{+1.29}_{-0.43}$
1074.01	$104.2^{+11.6}_{-99.5}$	$8.5^{+9.7}_{-3.2}$	$75.6^{+11.5}_{-15.3}$	$1.08^{+2.84}_{-0.24}$	$0.186^{+0.124}_{-0.110}$	$241.0^{+4.6}_{-58.0}$	$1.76^{+0.85}_{-1.71}$
1546.01	$249.2^{+2.3}_{-44.6}$	$6.7^{+0.5}_{-0.1}$	$60.4^{+27.8}_{-0.2}$	$0.40^{+0.20}_{-0.39}$	$0.121^{+0.00773}_{-0.00817}$	$128.4^{+3.8}_{-4.4}$	$0.00020^{+0.89}_{-0.00017}$
3728.01	$72.1^{+3.7}_{-5.8}$	$7.7^{+0.2}_{-0.4}$	$86.5^{+3.2}_{-5.0}$	$0.98^{+2.49}_{-0.93}$	$0.0593^{+0.00669}_{-0.0534}$	$286.6^{+2.5}_{-286.6}$	$0.35^{+0.54}_{-0.35}$
3886.01	$24.0^{+0.4}_{-12.8}$	$5.1^{+0.06}_{-1.2}$	$89.8^{+0.7}_{-9.7}$	$2.60^{+0.26}_{-0.027}$	$0.0125^{+0.00687}_{-0.0114}$	$79.1^{+14.8}_{-256.8}$	$0.57^{+0.020}_{-0.46}$
5220.01	$9.9^{+1.4}_{-2.6}$	$6.3^{+0.2}_{-0.7}$	$89.4^{+0.3}_{-4.2}$	$2.62^{+0.086}_{-0.055}$	$0.0652^{+0.0223}_{-0.0315}$	$8.6^{+25.9}_{-48.2}$	$0.0018^{+0.17}_{-0.0018}$
5713.01	$65.8^{+1.0}_{-10.8}$	$7.9^{+0.4}_{-0.2}$	$61.6^{+24.7}_{-1.4}$	$0.87^{+3.54}_{-0.19}$	$0.0476^{+0.00912}_{-0.0134}$	$359.3^{+0.3}_{-8.7}$	$-0.10^{+0.0082}_{-0.0091}$

The preliminary results for these objects, with the particular restrictions described in the above paragraph, are summarized in Table 6.23. The fitted models to the out-of-eclipse signal are plotted for the seven cases in Fig. 6.46. The results show that five out of the six targets are compatible with substellar masses and the remaining is compatible with a stellar mass. Note that these are very close substellar companions revolving at $a/R_\star < 10$ and transiting their parent stars. Indeed, KOI-5220.01 shows a planetary-mass and this preliminary analysis seems

to confirm its planetary nature. Additionally, KOI-3886.01 displays a mass compatible with that of a massive planet. However, this analysis has not yet taken into account the possible dilution induced by the close companion found in Chapter 5. Thus, more work and a more dedicated model fitting of these targets is needed to definitively confirm their nature.

This prelimiray work and the on-going massive analysis of the REB modulations for all KOIs will provide masses for the closest transiting objects and upper mass limits for longer-period objects. It also shows the power of the valuable information provided by the *Kepler* light curves, which allows the determination of masses without the need for radial velocity follow-up. Additionally, the mass and radius of just a few number of brown dwarfs are known. These results could provide both parameters, which are of key importance for the calibration of theoretical models.

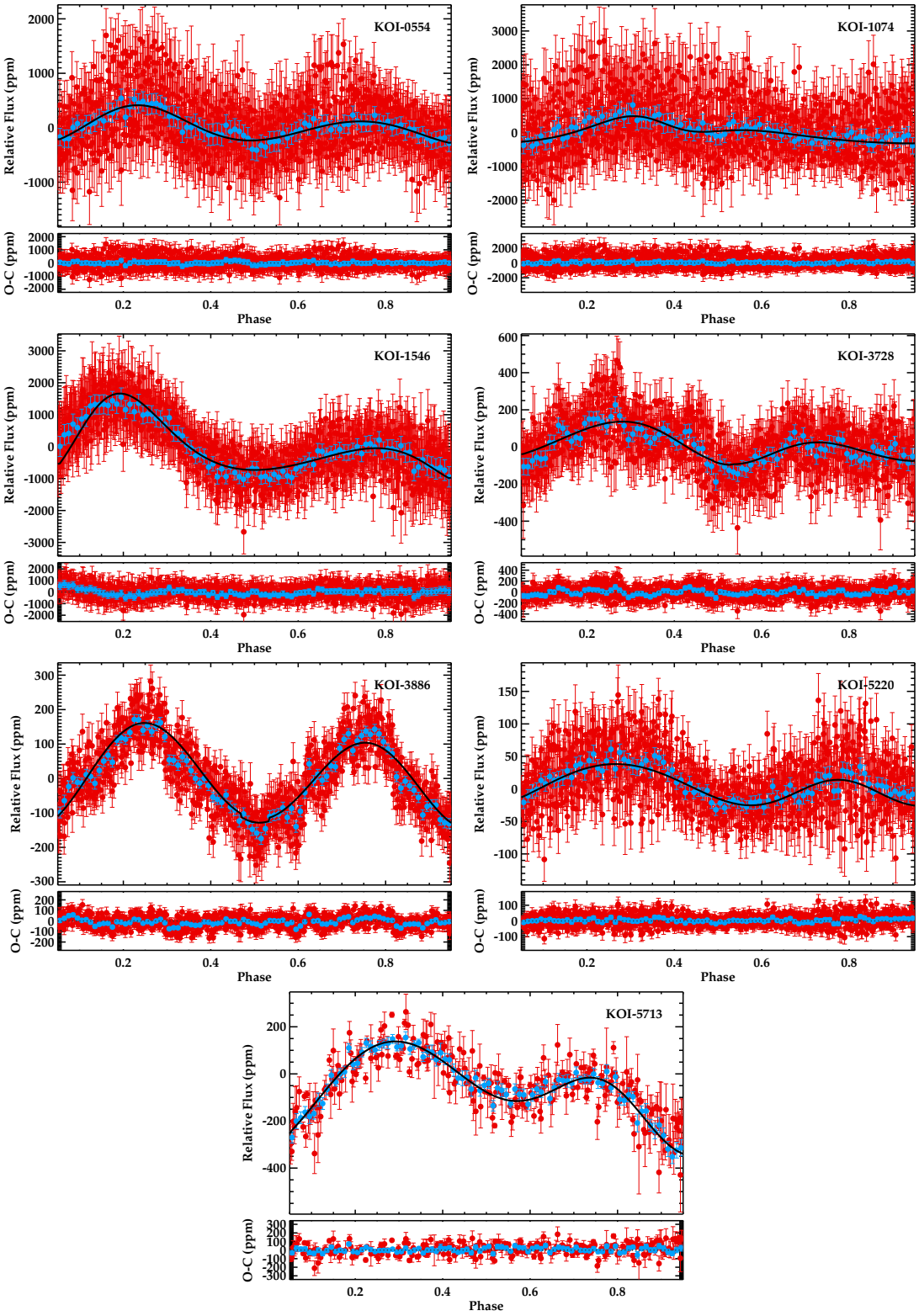

FIGURE 6.46: Results of the light curve modulations fitting for a sample of KOIs. Red symbols represent light curves binned with a bin size of 0.1% of the period while blue symbols have a bin size equal to 1% of the period. The solid black line in the upper panel of each figure shows the best-fit model to the data according to the relatively simple modellization explained in section § 6.8.

Tables of section § 6.6

TABLE 6.24: KOI-0012: measured radial velocities. The S/N ratio in Tables 6.24 to 6.36 are calculated as the median signal over the scatter of a continuum region close to 5500 Å.

Julian Date (days)-2456000	$\overline{S/N}$	RV (km/s)	Julian Date (days)-2456000	$\overline{S/N}$	RV (km/s)	Julian Date (days)-2456000	$\overline{S/N}$	RV (km/s)
66.442058	14.4	$-18.3^{+6.5}_{-4.7}$	72.463525	15.5	$-18.1^{+3.1}_{-2.7}$	87.634276	15.5	$-18.5^{+4.6}_{-1.2}$
66.454881	24.0	$-9.4^{+5.1}_{-4.7}$	76.518732	18.1	$-19.2^{+2.4}_{-3.4}$	90.630156	21.5	$-18.9^{+3.3}_{-4.4}$
66.467705	19.0	$-9.6^{+5.6}_{-5.7}$	76.533549	34.2	$-17.5^{+1.6}_{-3.4}$	115.379299	21.0	$-16.5^{+2.8}_{-4.5}$
69.439270	15.0	$-18.4^{+7.1}_{-6.2}$	76.548365	28.8	$-17.6^{+1.6}_{-1.8}$	115.391505	29.9	$-18.0^{+2.0}_{-1.5}$
69.451609	21.1	$-23.0^{+7.2}_{-1.4}$	77.602751	22.5	$-21.4^{+3.6}_{-1.4}$	115.403712	21.1	$-20.7^{+3.3}_{-1.2}$
69.463949	14.7	$-19.5^{+6.7}_{-2.5}$	77.615244	30.5	$-19.0^{+2.1}_{-2.8}$	117.381785	22.3	$-18.7^{+2.3}_{-1.5}$
70.434806	24.8	$-18.1^{+1.7}_{-2.2}$	77.627738	20.5	$-13.5^{+3.8}_{-3.5}$	117.393940	27.0	$-14.3^{+3.6}_{-1.3}$
70.447044	31.4	$-20.6^{+1.8}_{-1.3}$	78.457637	23.3	$-19.3^{+3.5}_{-2.5}$	117.406095	15.0	$-20.9^{+8.6}_{-1.7}$
70.459281	19.1	$-21.8^{+2.8}_{-1.3}$	78.472721	29.5	$-19.0^{+1.9}_{-2.3}$	129.381270	17.0	$-21.9^{+4.8}_{-1.7}$
71.431319	23.0	$-18.9^{+2.7}_{-1.3}$	78.487805	17.8	$-14.8^{+3.9}_{-2.7}$	129.393473	27.8	$-20.0^{+2.8}_{-2.5}$
71.456236	25.8	$-19.2^{+1.5}_{-1.6}$	80.406010	19.8	$-21.3^{+4.0}_{-2.0}$	129.405676	21.9	$-18.7^{+2.0}_{-1.5}$
71.532211	53.8	$-16.6^{+1.4}_{-2.8}$	80.418276	31.2	$-19.8^{+3.0}_{-7.5}$	180.442531	21.3	$-21.2^{+3.9}_{-1.7}$
71.608528	30.3	$-16.6^{+1.6}_{-2.1}$	80.430543	24.1	$-17.7^{+2.5}_{-4.6}$	180.464569	23.0	$-19.5^{+1.9}_{-2.7}$
71.632761	29.8	$-19.4^{+1.7}_{-1.4}$	82.602553	20.3	$-19.6^{+1.7}_{-1.7}$	180.464653	41.1	$-19.6^{+1.8}_{-2.1}$
72.439229	23.2	$-17.9^{+1.9}_{-3.1}$	82.614673	26.2	$-20.2^{+1.8}_{-2.1}$	180.486860	25.9	$-20.2^{+1.4}_{-1.7}$
72.451377	27.8	$-17.7^{+1.8}_{-3.2}$	82.626794	16.6	$-16.7^{+3.3}_{-1.7}$			

TABLE 6.25: KOI-0131: measured radial velocities

Julian Date (days)-2456000	$\overline{S/N}$	RV (km/s)	Julian Date (days)-2456000	$\overline{S/N}$	RV (km/s)	Julian Date (days)-2456000	$\overline{S/N}$	RV (km/s)
111.576836	7.0	$-6.2^{+1.7}_{-1.4}$	120.636824	6.5	$-5.3^{+3.1}_{-3.4}$	497.517894	4.2	$-8.7^{+4.4}_{-8.8}$
115.458790	9.1	$-7.8^{+1.6}_{-1.1}$	418.567422	6.5	$-12.1^{+9.3}_{-2.2}$	514.364588	4.6	$-8.1^{+8.9}_{-2.2}$
115.493531	7.4	$-10.7^{+2.8}_{-2.3}$	418.599802	7.6	$-11.8^{+2.8}_{-0.11}$	514.401807	11.2	$-21.5^{+5.3}_{-2.9}$
115.493595	14.0	$-11.6^{+4.4}_{-1.8}$	418.632175	12.2	$-10.5^{+2.9}_{-4.8}$	514.402164	7.0	$-8.7^{+2.1}_{-2.8}$
115.528462	8.0	$-8.1^{+2.4}_{-2.0}$	436.501911	7.1	$159.32^{+0.12}_{-4.4}$	514.438668	5.2	$3.3^{+6.2}_{-3.6}$
119.544606	4.5	$-8.4^{+2.6}_{-1.3}$	436.538388	6.5	$0.0^{+4.8}_{-5.1}$	529.484818	8.7	$-12.1^{+4.0}_{-2.3}$
120.530916	7.0	$-8.7^{+1.4}_{-3.3}$	436.573185	5.2	$-10.0^{+4.7}_{-2.6}$	529.521132	12.7	$-13.4^{+2.6}_{-4.0}$
120.566218	6.2	$-5.0^{+4.1}_{-3.0}$	497.439970	5.2	$-3.5^{+6.5}_{-4.2}$	529.521166	7.2	$-6.1^{+3.4}_{-11}$
120.583937	13.4	$-7.9^{+2.9}_{-2.9}$	497.475725	6.2	$-5.3^{+3.1}_{-11}$	529.557411	4.5	$-12.9^{+3.4}_{-1.8}$
120.601789	6.2	$-8.5^{+3.2}_{-4.6}$	497.477863	9.5	$-11.4^{+5.0}_{-2.5}$			

TABLE 6.26: KOI-0340: measured radial velocities

Julian Date (days)-2456000	$\overline{S/N}$	RV (km/s)	Julian Date (days)-2456000	$\overline{S/N}$	RV (km/s)	Julian Date (days)-2456000	$\overline{S/N}$	RV (km/s)
111.395672	13.8	$-103.499^{+0.045}_{-0.045}$	116.633232	9.5	$-72.401^{+0.074}_{-0.057}$	127.489427	15.8	$-83.806^{+0.063}_{-0.058}$
111.431211	12.8	$-103.559^{+0.095}_{-0.095}$	119.579846	11.6	$-73.268^{+0.059}_{-0.061}$	133.386589	12.5	$-97.467^{+0.069}_{-0.071}$
113.605011	12.5	$-91.229^{+0.075}_{-0.075}$	119.612757	19.6	$-73.172^{+0.055}_{-0.054}$	133.404004	15.2	$-97.457^{+0.085}_{-0.074}$
113.621494	17.8	$-91.001^{+0.071}_{-0.058}$	119.614455	12.4	$-73.262^{+0.057}_{-0.063}$	133.421419	8.1	$-97.52^{+0.10}_{-0.055}$
113.637977	12.5	$-90.909^{+0.058}_{-0.082}$	119.643968	9.2	$-73.381^{+0.061}_{-0.069}$	137.604302	9.5	$-86.483^{+0.048}_{-0.056}$
116.598403	7.8	$-72.213^{+0.082}_{-0.074}$	127.454588	15.5	$-83.850^{+0.054}_{-0.10}$	137.621876	14.1	$-86.268^{+0.050}_{-0.085}$
116.615818	12.6	$-72.333^{+0.074}_{-0.059}$	127.472007	21.9	$-83.789^{+0.056}_{-0.048}$	137.639450	9.9	$-86.171^{+0.058}_{-0.050}$

TABLE 6.27: KOI-0366: measured radial velocities

Julian Date (days)-2456000	$\overline{S/N}$	RV (km/s)	Julian Date (days)-2456000	$\overline{S/N}$	RV (km/s)	Julian Date (days)-2456000	$\overline{S/N}$	RV (km/s)
66.494606	15.4	$6.8^{+1.2}_{-1.0}$	82.469641	15.4	$8.3^{+1.3}_{-0.41}$	112.644079	15.4	$7.45^{+0.52}_{-0.46}$
69.490469	15.4	$7.7^{+1.8}_{-1.6}$	82.487003	15.4	$7.94^{+0.78}_{-0.39}$	118.374379	15.4	$8.19^{+0.47}_{-0.31}$
71.558576	15.4	$7.85^{+0.37}_{-0.28}$	82.504365	15.4	$7.77^{+0.84}_{-0.25}$	118.398555	15.4	$8.79^{+0.40}_{-0.24}$
71.570735	15.4	$7.15^{+0.38}_{-0.31}$	92.591566	15.4	$9.07^{+0.40}_{-0.53}$	118.398689	15.4	$9.00^{+0.29}_{-0.53}$
71.582894	15.4	$7.50^{+0.40}_{-0.27}$	92.615777	15.4	$9.11^{+0.38}_{-0.71}$	118.423132	15.4	$8.06^{+0.38}_{-0.33}$
72.599880	15.4	$9.06^{+0.32}_{-0.30}$	92.615814	15.4	$9.06^{+0.33}_{-0.30}$	126.369758	15.4	$7.87^{+0.51}_{-0.61}$
72.612031	15.4	$8.80^{+0.31}_{-0.77}$	92.640099	15.4	$8.93^{+0.44}_{-0.45}$	126.382150	15.4	$7.93^{+0.55}_{-0.28}$
72.624182	15.4	$8.37^{+0.36}_{-0.72}$	101.543893	15.4	$7.17^{+0.44}_{-0.41}$	126.394542	15.4	$9.36^{+0.64}_{-0.26}$
76.440887	15.4	$9.00^{+0.93}_{-0.42}$	101.561229	15.4	$8.64^{+0.34}_{-0.34}$	130.380236	15.4	$7.95^{+0.36}_{-0.51}$
76.466954	15.4	$9.54^{+0.65}_{-0.46}$	101.578566	15.4	$8.69^{+0.30}_{-0.30}$	130.392427	15.4	$8.29^{+0.31}_{-0.42}$
76.467735	15.4	$9.95^{+0.88}_{-0.29}$	110.385278	15.4	$7.93^{+0.62}_{-0.39}$	130.404619	15.4	$9.46^{+0.32}_{-0.24}$
76.492240	15.4	$8.27^{+0.50}_{-1.1}$	110.397526	15.4	$7.46^{+0.65}_{-0.56}$	139.381895	15.4	$7.75^{+0.57}_{-0.51}$
79.543631	15.4	$9.61^{+0.55}_{-0.68}$	110.409774	15.4	$7.57^{+0.88}_{-0.32}$	139.394228	15.4	$8.35^{+0.51}_{-0.25}$
79.555913	15.4	$8.67^{+0.39}_{-0.32}$	112.619832	15.4	$8.67^{+0.34}_{-0.27}$	139.406562	15.4	$8.41^{+0.53}_{-0.44}$
79.568194	15.4	$8.59^{+0.34}_{-0.33}$	112.631955	15.4	$7.36^{+0.49}_{-0.47}$			

TABLE 6.28: KOI-0371: measured radial velocities

Julian Date (days)-2456000	$\overline{S/N}$	RV (km/s)	Julian Date (days)-2456000	$\overline{S/N}$	RV (km/s)	Julian Date (days)-2456000	$\overline{S/N}$	RV (km/s)
121.454974	11.8	$-65.169^{+0.052}_{-0.052}$	505.601217	6.5	$-53.219^{+0.049}_{-0.053}$	803.627383	9.6	$-65.601^{+0.055}_{-0.059}$
121.467317	17.7	$-65.138^{+0.049}_{-0.053}$	505.612199	9.8	$-53.152^{+0.049}_{-0.059}$	824.620384	5.5	$-64.962^{+0.067}_{-0.048}$
121.479659	13.2	$-65.200^{+0.053}_{-0.061}$	505.623181	7.5	$-52.957^{+0.058}_{-0.059}$	824.642337	5.2	$-64.965^{+0.070}_{-0.049}$
436.604913	13.7	$-58.579^{+0.061}_{-0.068}$	528.419975	10.2	$-53.651^{+0.053}_{-0.049}$	838.397849	9.2	$-64.515^{+0.066}_{-0.053}$
436.629188	13.7	$-58.399^{+0.068}_{-0.054}$	528.438254	18.5	$-53.526^{+0.054}_{-0.050}$	838.416113	14.1	$-64.386^{+0.062}_{-0.049}$
497.381256	9.6	$-53.264^{+0.054}_{-0.053}$	528.456533	15.7	$-53.573^{+0.059}_{-0.055}$	838.434376	10.2	$-64.406^{+0.051}_{-0.054}$
497.394856	15.2	$-53.194^{+0.053}_{-0.072}$	559.495749	11.7	$-58.079^{+0.059}_{-0.067}$	843.450061	11.3	$-64.246^{+0.059}_{-0.048}$
497.408455	10.8	$-52.975^{+0.053}_{-0.060}$	560.496212	14.5	$-58.283^{+0.049}_{-0.070}$	843.466246	16.1	$-64.224^{+0.053}_{-0.062}$
500.645274	5.6	$-52.852^{+0.072}_{-0.049}$	803.605301	9.3	$-65.603^{+0.050}_{-0.066}$	843.482431	11.2	$-64.270^{+0.048}_{-0.053}$
500.669675	9.0	$-53.041^{+0.060}_{-0.058}$	803.616342	13.5	$-65.618^{+0.048}_{-0.051}$			

TABLE 6.29: KOI-0625: measured radial velocities

Julian Date (days)-2456000	$\overline{S/N}$	RV (km/s)	Julian Date (days)-2456000	$\overline{S/N}$	RV (km/s)	Julian Date (days)-2456000	$\overline{S/N}$	RV (km/s)
71.489198	11.6	$-25.97^{+0.55}_{-0.45}$	88.573506	1.7	$-28.8^{+4.2}_{-0.89}$	94.589328	9.8	$-25.77^{+0.98}_{-1.6}$
71.506591	16.5	$-25.80^{+0.62}_{-0.59}$	88.592027	9.8	$-26.27^{+0.74}_{-0.67}$	102.432371	9.3	$-24.9^{+1.1}_{-0.56}$
71.523984	11.6	$-26.13^{+0.65}_{-0.64}$	88.597524	13.0	$-23.8^{+1.9}_{-0.99}$	102.469438	9.1	$-26.92^{+0.99}_{-0.54}$
72.496141	10.7	$-26.39^{+0.79}_{-1.1}$	88.627038	7.8	$-24.6^{+1.7}_{-1.8}$	102.469462	15.6	$-31.2^{+2.5}_{-0.72}$
72.513475	15.2	$-25.29^{+0.84}_{-0.55}$	91.459181	8.3	$-25.9^{+1.4}_{-0.85}$	102.506577	7.8	$-24.3^{+1.8}_{-0.45}$
72.530808	10.7	$-25.5^{+1.3}_{-0.49}$	91.493991	15.7	$-25.1^{+1.3}_{-0.75}$	121.559629	8.1	$-25.2^{+1.1}_{-0.73}$
77.443828	11.6	$-25.57^{+0.69}_{-0.89}$	91.494063	9.0	$-26.1^{+1.2}_{-0.84}$	121.594577	13.7	$-24.1^{+1.2}_{-3.8}$
77.462844	16.5	$-26.31^{+0.59}_{-0.62}$	91.528730	9.5	$-26.64^{+0.95}_{-0.90}$	121.594628	7.6	$-26.5^{+1.6}_{-2.3}$
77.481860	11.8	$-26.66^{+0.65}_{-5.3}$	92.525138	11.2	$-25.37^{+0.91}_{-0.95}$	121.629474	7.8	$-24.7^{+1.3}_{-1.9}$
79.476176	9.0	$-25.5^{+1.1}_{-0.92}$	92.542705	16.1	$-26.08^{+0.97}_{-1.9}$	127.526771	9.7	$-25.03^{+0.99}_{-1.1}$
79.493735	14.0	$-27.39^{+0.96}_{-3.5}$	92.560272	10.9	$-25.77^{+0.86}_{-1.1}$	127.561701	9.0	$-26.1^{+1.0}_{-1.1}$
79.511293	10.4	$-25.08^{+0.63}_{-2.4}$	93.453444	10.2	$-25.0^{+1.2}_{-1.4}$	127.561732	16.5	$-25.92^{+0.89}_{-1.9}$
80.462852	8.2	$-29.7^{+5.4}_{-3.5}$	93.471006	14.6	$-24.2^{+1.7}_{-1.2}$	127.596724	8.9	$-26.22^{+0.61}_{-0.92}$
80.487557	13.2	$-23.6^{+4.4}_{-0.62}$	93.488568	10.3	$-27.6^{+1.7}_{-1.0}$	137.461469	8.5	$-25.1^{+1.1}_{-2.4}$
80.512261	10.1	$-25.4^{+1.0}_{-1.4}$	94.519592	10.9	$-26.06^{+0.94}_{-0.85}$	137.497308	7.9	$-23.3^{+1.9}_{-1.3}$
87.567872	7.5	$-25.5^{+4.1}_{-1.2}$	94.554529	18.6	$-25.0^{+1.1}_{-0.41}$	137.498740	15.2	$-27.1^{+1.9}_{-0.72}$
87.585564	10.0	$-25.7^{+2.8}_{-0.95}$	94.554666	10.3	$-25.29^{+0.89}_{-1.1}$	137.537443	9.5	$-26.52^{+0.64}_{-1.00}$
87.603257	6.2	$-24.7^{+2.7}_{-0.71}$						

TABLE 6.30: KOI-0686: measured radial velocities

Julian Date (days)-2456000	$\overline{S/N}$	RV (km/s)	Julian Date (days)-2456000	$\overline{S/N}$	RV (km/s)	Julian Date (days)-2456000	$\overline{S/N}$	RV (km/s)
91.564471	9.5	$-29.153^{+0.081}_{-0.081}$	110.542846	7.5	$-34.89^{+0.12}_{-0.093}$	124.524128	6.5	$-34.625^{+0.075}_{-0.069}$
91.581828	13.9	$-29.146^{+0.085}_{-0.082}$	110.560305	11.0	$-34.77^{+0.11}_{-0.061}$	129.435272	10.8	$-33.343^{+0.081}_{-0.085}$
91.599185	7.0	$-29.397^{+0.082}_{-0.073}$	110.577764	6.4	$-35.15^{+0.11}_{-0.075}$	130.540005	10.0	$-33.237^{+0.076}_{-0.060}$
100.433076	8.2	$-24.792^{+0.073}_{-0.067}$	124.453660	6.9	$-34.620^{+0.093}_{-0.081}$	130.574986	18.8	$-33.098^{+0.077}_{-0.11}$
100.468077	16.2	$-24.749^{+0.060}_{-0.066}$	124.488780	8.2	$-34.500^{+0.061}_{-0.076}$	130.575012	11.1	$-33.291^{+0.077}_{-0.068}$
100.468144	9.7	$-24.886^{+0.067}_{-0.12}$	124.488856	13.1	$-34.515^{+0.068}_{-0.077}$	130.609940	10.6	$-33.159^{+0.069}_{-0.077}$
100.503013	9.5	$-24.834^{+0.066}_{-0.11}$						

TABLE 6.31: KOI-0972: measured radial velocities

Julian Date (days)-2456000	$\overline{S/N}$	RV (km/s)	Julian Date (days)-2456000	$\overline{S/N}$	RV (km/s)	Julian Date (days)-2456000	$\overline{S/N}$	RV (km/s)
100.376405	58.2	$-8.2^{+4.2}_{-3.4}$	114.503592	53.2	$-8.5^{+8.7}_{-4.4}$	126.348892	37.8	$-8.8^{+3.3}_{-3.5}$
100.388716	86.3	$-12.9^{+3.4}_{-2.6}$	114.651427	40.6	$-10.0^{+3.2}_{-5.5}$	127.358229	47.4	$-11.2^{+4.6}_{-5.1}$
100.401026	64.0	$-15.4^{+3.0}_{-4.0}$	115.359156	38.5	$-11.3^{+5.2}_{-4.3}$	128.359248	34.8	$-14.9^{+8.8}_{-4.7}$
101.610586	41.2	$-12.8^{+4.5}_{-4.8}$	115.507564	44.8	$-14.1^{+3.8}_{-5.1}$	129.361016	37.8	$-15.5^{+3.3}_{-3.7}$
101.622675	61.7	$-11.7^{+4.5}_{-5.8}$	115.655973	22.7	$-10.7^{+5.5}_{-4.1}$	130.359776	54.4	$-16.1^{+4.6}_{-3.3}$
101.634765	45.9	$-15.4^{+5.1}_{-2.5}$	116.430815	41.5	$-17.0^{+4.1}_{-3.0}$	131.358377	41.9	$-14.1^{+3.8}_{-4.4}$
102.370604	61.3	$-18.8^{+6.3}_{-11}$	117.360460	34.2	$-15.8^{+5.1}_{-2.7}$	132.358859	40.2	-4^{+11}_{-14}
102.382723	89.3	$-9.3^{+2.3}_{-4.8}$	117.399590	41.8	$-13.1^{+4.9}_{-5.3}$	133.361742	46.1	$-14.0^{+4.5}_{-0.92}$
102.394841	65.1	$-7.7^{+2.7}_{-4.5}$	117.438719	24.0	$-14.9^{+6.1}_{-3.0}$	137.356202	41.2	$-22.5^{+6.5}_{-16}$
103.602984	62.3	$-13.2^{+8.8}_{-5.1}$	118.353116	34.0	$-18.9^{+5.4}_{-2.9}$	138.359861	43.1	$-19.0^{+5.4}_{-15}$
103.615092	87.4	$-16.4^{+6.6}_{-4.8}$	119.361354	23.1	$-18.7^{+5.7}_{-3.0}$	140.360137	37.0	$-7.7^{+5.0}_{-2.8}$
103.627200	61.2	$-10.7^{+5.7}_{-4.8}$	120.384560	29.7	$-22.0^{+4.6}_{-3.7}$	141.354705	39.0	$-16.0^{+4.2}_{-3.6}$
110.363523	34.3	$-13.4^{+6.5}_{-4.2}$	121.363682	40.7	$-16.2^{+3.5}_{-8.6}$	418.660632	37.0	$-15.0^{+4.7}_{-1.9}$
111.366741	39.7	$-15.0^{+5.2}_{-2.5}$	122.427018	41.9	$-13.0^{+3.4}_{-3.1}$	420.646028	15.4	$-27^{+20}_{-5.9}$
112.358116	48.0	$-12.2^{+5.5}_{-4.6}$	123.355871	30.5	$-6.7^{+6.6}_{-4.1}$	420.658684	21.2	$-82.22^{+0.97}_{-37}$
113.357987	34.7	$-6.4^{+5.9}_{-4.8}$	124.352637	41.6	$-14.2^{+3.9}_{-3.3}$	426.552329	13.7	$6^{+16}_{-3.1}$
114.355757	34.3	$-11.8^{+5.3}_{-3.7}$	125.446545	41.2	$-12.2^{+3.5}_{-8.5}$	435.646207	34.0	$4^{+12}_{-4.2}$

TABLE 6.32: KOI-1463: measured radial velocities

Julian Date (days)-2456000	$\overline{S/N}$	RV (km/s)	Julian Date (days)-2456000	$\overline{S/N}$	RV (km/s)	Julian Date (days)-2456000	$\overline{S/N}$	RV (km/s)
114.381820	12.8	$-30.76^{+0.47}_{-0.47}$	517.458750	13.2	$31.76^{+0.28}_{-0.41}$	838.477732	12.2	$306.20^{+0.33}_{-0.39}$
114.399160	19.8	$-30.93^{+0.39}_{-0.36}$	805.527896	7.3	$305.37^{+0.34}_{-0.34}$	838.494471	16.1	$305.52^{+0.29}_{-0.19}$
114.416499	15.2	$-31.11^{+0.36}_{-0.17}$	805.560558	3.2	$306.09^{+0.41}_{-0.33}$	838.511211	8.9	$305.54^{+0.31}_{-0.34}$
517.378382	14.5	$31.18^{+0.17}_{-0.28}$	805.560620	11.3	$305.58^{+0.34}_{-0.31}$	841.587718	6.9	$305.43^{+0.29}_{-0.29}$
517.418566	20.1	$31.36^{+0.19}_{-0.34}$	805.593404	7.5	$305.57^{+0.34}_{-0.29}$			

TABLE 6.33: KOI-3725: measured radial velocities

Julian Date (days)-2456000	$\overline{S/N}$	RV (km/s)	Julian Date (days)-2456000	$\overline{S/N}$	RV (km/s)	Julian Date (days)-2456000	$\overline{S/N}$	RV (km/s)
500.625109	14.2	$-51.3^{+3.9}_{-2.1}$	504.571903	29.6	$-30.9^{+1.2}_{-0.97}$	841.530484	14.6	$-15.0^{+2.1}_{-1.5}$
501.383460	19.2	$-46.2^{+2.0}_{-1.4}$	504.609225	22.8	$-41.9^{+1.1}_{-0.73}$	841.536254	20.6	$-29.0^{+2.7}_{-1.1}$
503.425012	23.2	$-42.1^{+1.4}_{-1.3}$	517.650133	21.0	$-45.20^{+0.79}_{-1.3}$	841.542025	14.2	$-29.1^{+1.4}_{-2.9}$
504.534581	19.0	$-50.2^{+1.4}_{-1.2}$						

TABLE 6.34: KOI-3728: measured radial velocities

Julian Date (days)-2456000	$\overline{S/N}$	RV (km/s)	Julian Date (days)-2456000	$\overline{S/N}$	RV (km/s)	Julian Date (days)-2456000	$\overline{S/N}$	RV (km/s)
354.369018	10.1	$-36.3^{+5.3}_{-3.4}$	511.418066	9.2	$-44^{+10}_{-3.6}$	523.540289	15.3	$-48.6^{+3.2}_{-1.9}$
354.379993	14.7	$-37.0^{+3.8}_{-2.5}$	512.472273	6.9	$-54^{+11}_{-2.5}$	525.518022	14.4	$-47.9^{+4.7}_{-2.7}$
354.390968	10.1	$-34.5^{+5.3}_{-16}$	513.408866	11.6	$-48.6^{+5.6}_{-3.0}$	525.536150	20.8	$-55.7^{+4.6}_{-26}$
498.570987	12.2	$-57.8^{+4.4}_{-25}$	513.427128	18.5	$-50.7^{+5.0}_{-2.2}$	525.554278	14.8	$-53.9^{+5.4}_{-2.6}$
498.583268	16.9	$-58.4^{+3.1}_{-15}$	513.445391	13.7	$-50.9^{+6.0}_{-6.9}$	528.567258	11.1	$-45.1^{+4.2}_{-11}$
498.595550	11.5	$-58.3^{+2.9}_{-17}$	514.605639	14.4	$-56.9^{+5.2}_{-4.3}$	559.339189	16.7	$-57.0^{+3.7}_{-2.5}$
500.576958	4.8	-30^{+20}_{-35}	514.623762	20.1	$-49^{+10}_{-3.3}$	559.371563	15.8	$-57.1^{+2.0}_{-3.9}$
500.602103	6.8	$-67^{+25}_{-3.6}$	514.641885	14.0	$-59.8^{+7.4}_{-4.5}$	559.403933	14.8	$-53.7^{+5.5}_{-6.7}$
501.428000	3.9	$-49^{+17}_{-8.2}$	517.590081	14.0	$-45.7^{+4.9}_{-6.4}$	567.330058	14.7	$-50.1^{+2.6}_{-4.8}$
510.446736	6.1	$-51^{+19}_{-9.7}$	517.606266	18.5	$-48.7^{+5.6}_{-3.1}$	567.367052	15.0	$-47.4^{+2.5}_{-4.0}$
510.468900	8.9	$-51^{+15}_{-4.4}$	517.622450	11.4	$-50.4^{+4.0}_{-1.4}$	567.403480	14.6	$-50.2^{+3.2}_{-3.8}$
510.491065	6.8	$-24^{+28}_{-5.7}$	523.503712	13.5	$-47.3^{+3.7}_{-5.6}$	597.418633	12.6	$-48^{+25}_{-3.2}$
511.390550	11.0	$-53.3^{+4.5}_{-4.9}$	523.522001	20.9	$-49.4^{+4.7}_{-2.2}$	597.418633	9.3	-47^{+14}_{-76}
511.404308	14.7	$-56.3^{+4.0}_{-5.7}$						

TABLE 6.35: KOI-3853: measured radial velocities

Julian Date (days)-2456000	$\overline{S/N}$	RV (km/s)	Julian Date (days)-2456000	$\overline{S/N}$	RV (km/s)	Julian Date (days)-2456000	$\overline{S/N}$	RV (km/s)
498.550774	19.3	$-88.037^{+0.040}_{-0.040}$	511.624458	11.8	$-57.982^{+0.054}_{-0.070}$	528.494410	28.8	$-59.539^{+0.052}_{-0.049}$
500.427256	6.8	$-78.182^{+0.051}_{-0.051}$	511.656257	9.6	$-57.901^{+0.070}_{-0.057}$	528.515065	43.6	$-59.420^{+0.053}_{-0.047}$
503.522251	23.8	$-67.622^{+0.057}_{-0.057}$	513.591688	26.4	$-70.695^{+0.057}_{-0.058}$	528.535719	32.7	$-59.298^{+0.054}_{-0.053}$
504.628523	24.9	$-64.491^{+0.053}_{-0.053}$	515.538671	25.8	$-101.989^{+0.058}_{-0.053}$	559.438923	28.5	$-108.981^{+0.049}_{-0.057}$
505.425120	25.4	$-62.606^{+0.048}_{-0.048}$	522.559858	24.5	$-76.193^{+0.053}_{-0.050}$	559.449900	39.6	$-108.981^{+0.048}_{-0.056}$
510.419882	21.0	$-56.134^{+0.052}_{-0.052}$	526.420908	35.1	$-64.086^{+0.050}_{-0.048}$	559.460877	27.4	$-109.009^{+0.047}_{-0.048}$
511.363906	25.3	$-57.187^{+0.051}_{-0.051}$	526.439128	45.2	$-64.033^{+0.048}_{-0.052}$	569.430575	25.6	$-64.360^{+0.053}_{-0.053}$
511.553563	33.1	$-57.133^{+0.056}_{-0.056}$	526.457348	27.8	$-63.921^{+0.048}_{-0.054}$	569.467568	16.5	$-64.290^{+0.057}_{-0.048}$
511.569631	14.5	$-57.611^{+0.056}_{-0.054}$						

TABLE 6.36: KOI-3890: measured radial velocities

Julian Date (days)-2456000	$\overline{S/N}$	RV (km/s)	Julian Date (days)-2456000	$\overline{S/N}$	RV (km/s)	Julian Date (days)-2456000	$\overline{S/N}$	RV (km/s)
499.397905	6.7	$-27.368^{+0.087}_{-0.087}$	511.496364	2.8	$-26.35^{+0.16}_{-0.074}$	516.552987	9.4	$-25.955^{+0.073}_{-0.38}$
499.438485	4.1	$-27.74^{+0.19}_{-0.19}$	511.535899	5.5	$-26.176^{+0.074}_{-0.052}$	516.554295	16.9	$-25.835^{+0.064}_{-0.098}$
502.629346	6.2	$-27.330^{+0.072}_{-0.072}$	513.484972	7.6	$-26.418^{+0.052}_{-0.072}$	516.589283	10.0	$-25.870^{+0.066}_{-0.070}$
510.526583	5.0	$-26.60^{+0.10}_{-0.100}$	513.522807	14.2	$-26.240^{+0.055}_{-0.056}$	522.447180	3.2	$-24.71^{+0.38}_{-0.090}$
510.564787	2.5	$-26.35^{+0.24}_{-0.24}$	513.523404	8.2	$-26.140^{+0.072}_{-0.065}$	522.485030	12.2	$-24.798^{+0.096}_{-0.055}$
510.577098	8.2	$-26.391^{+0.090}_{-0.074}$	513.560045	8.5	$-26.260^{+0.056}_{-0.073}$	522.485601	7.2	$-24.970^{+0.098}_{-0.064}$
510.639922	7.1	$-26.387^{+0.074}_{-0.082}$	516.520616	9.8	$-25.942^{+0.065}_{-0.066}$	522.522308	8.8	$-25.041^{+0.070}_{-0.096}$
511.457622	8.2	$-26.370^{+0.082}_{-0.16}$						

Chapter 7

The CAB-MPIA planets in context

Contents

Outline

In this chapter, we put in context the properties of the planets analyzed in this dissertation with the large crop of known planets. We discuss how our discoveries could contribute to our understanding of the whole process of planet formation, evolution, and death. Section 7.1 provides a general overview of the analyzed systems regarding planet and host properties as well as their orbital charcateristics. In § 7.2 we show how Kepler-91b and Kepler-432 have started to populate the niche of planets in close-in orbits around evolved stars. In section § 7.3, we focus on the giant planets in our sample that are located in the habitable zone of their host stars, which opens the window to find minor co-orbital bodies potentially habitable.

In the different diagrams included in this chapter to illustrate the location of the characterized planets, we will always use the following color-code depending on the status of the planets, namely confirmed (including those with preliminary analysis suggesting their planetary nature) and validated planets with CAFE data will be represented as blue filled circles (●); those already published by our CAFE data will be represented by large blue open circles (○); planets with yet inconclusive results are plotted as violet filled circles (●); detected false positives are shown as orange filled circles (●); detected brown dwarfs are shown as brown filled circles (●); planets confirmed by other works in which we have participated by providing the high-spatial resolution images (Barclay et al., 2013, Marcy et al., 2014) are represented by green filled circles (●).

Additionally and to put our planets in context, we have used the list of confirmed planets from the exoplanet.eu website. These planets are represented by gray "plus" symbols (+) unless other code is specified.

7.1 A general view

The planets presented in this dissertation occupy different regions of the widely used diagrams characterizing the exoplanetary population. In this section, we provide a general overview of their properties, putting them in context with the currently known sample of confirmed planets. We do this by answering three key questions:

What are the physical properties of the CAB-MPIA planets?

Thanks to the combination of the three techniques explained in the first part of this dissertation, we have been able to characterize several planets by obtaining their masses (based on radial velocity observations and REB analysis) and radii (thanks to the *Kepler* data). This information is directly related to planet density and thus bulk composition. In Fig. 7.1 we show their location in a mass versus radius diagram. As shown, we have analyzed planets in a large range of densities, from super-Earths and Neptunes in Marcy et al. (2014) and Barclay et al. (2013) to inflated Jupiters with our CAFE spectroscopic follow-up. Our work has been mainly dedicated to the latter group. Kepler-91 b and Kepler-447 b have a clear inflated radius due to their closeness to the host star. This is also the case of other followed planets with preliminary confirmation like KOI-3919.01, KOI-2481.01, and KOI-5684.01. Also, Kepler-432 b and the preliminary results for KOI-375.01 show that these are massive Jupiters with the expect radius according to theoretical models (Baraffe et al., 2003). By contrast, KOI-372.01 is much more dense and lies in the limit of the desert between massive Neptune-size planets and small Jupiters.

What are the orbital characteristics of the CAB-MPIA planets?

We have studied planets at different orbital periods, from very packed planetary systems like Kepler-91 ($P \sim 6.2$ days) to very long-period planets like KOI-375.01 ($P \sim 988$ days), see Figs. 7.2 and 7.3. Also, in our sample we find planets with completely edge-on orbits and very inclined orbital planes such as Kepler-91 b ($i \sim 68°$) and the largest impact parameter found in a planetary transit, Kepler-447 b, with $b \sim 1.07$ (i.e., only around 20% of the projected planet disk blocks the light coming from the star). We have also found non-negligible eccentricities for the confirmed planets, some of which are really close-in with orbital periods below 10 days. The origin of this eccentricity in short-period planets is unknown and may be due to different causes like additional companions, tidal instabilities, or the own migration history of the system. Also,

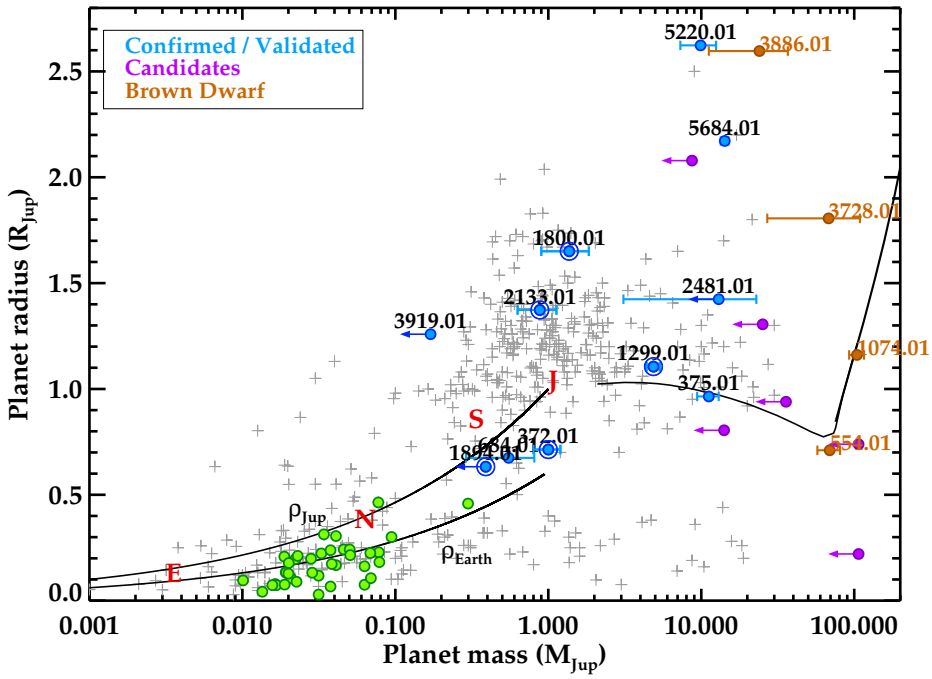

FIGURE 7.1: Mass-radius diagram for planets in the CAB-MPIA survey. The leftward arrows indicate upper mass limits that have been calculated for the corresponding planets. The color-code is as follows. Confirmed (including preilinary analysis) and validated planets with CAFE data are represented as blue filled circles, those already published are represented with large blue open circles, planets with yet inconclusive results are plotted as violet filled circles, detected false positives are shown as orange filled circles, detected brown dwarfs are shown as brown filled circles, planets confirmed by other works in which we have participated by providing the high-spatial resolution images (Barclay et al., 2013, Marcy et al., 2014) are represented by green filled circles. Other known planets are represented by gray plus symbols. We also show the location of some Solar System planets by their initial capital letters, namely Jupiter, Saturn, Neptune, and Earth. The solid black lines at the left of the panel represent iso-density lines corresponding to that of Jupiter (upper line) and Earth (bottom line). The theoretical line at larger masses corresponds to the 5 Gyr isochrone from Baraffe et al. (1998) for solar metallicity, while for masses below 100 $M_{\rm Jup}$, we used the Baraffe et al. (2003) isochrone of 5 Gyr.

as we will see in section 7.3, some of the characterized planets lie within the habitable zone of their stars.

What are the physical properties of the CAB-MPIA host stars?

The host stars of the planets analyzed in this project are in a wide range of evolutionary stages, from main-sequence stars with masses $\sim 1.0\,M_{\odot}$ (as in the cases of Kepler-447 and KOI-372), to more massive and evolved stars in the sub-giant phase or ascending the red giant branch like in the case of Kepler-91 and Kepler-432 (see Fig. 7.4). The latter group is crucial in our understanding of the co-evolution of planets and their hosts after the main sequence phase. We have confirmed the closest planet to an RGB giant star as of today. In section § 7.2, we will discuss the impact of these discoveries in our understanding of planet formation and evolution.

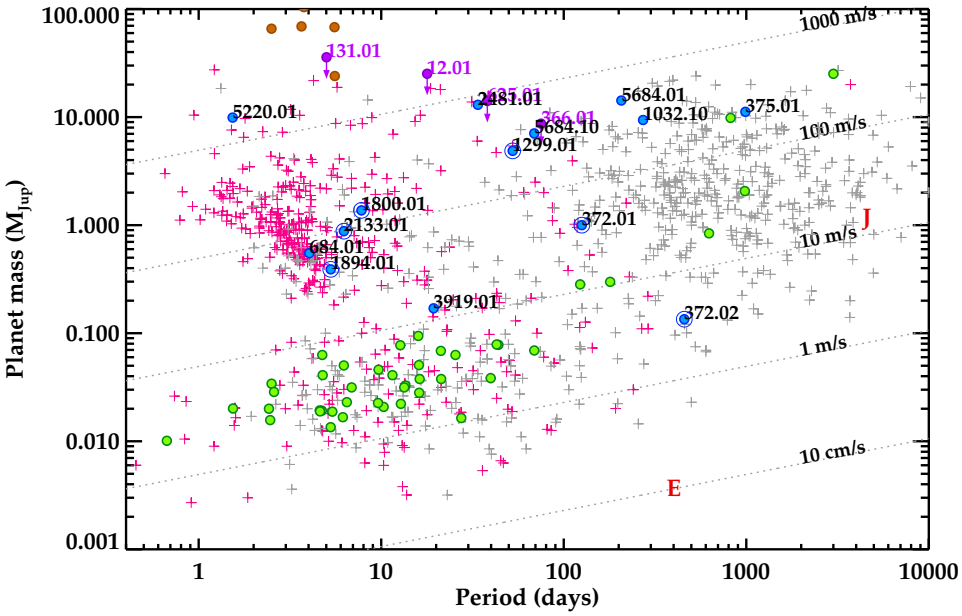

FIGURE 7.2: Mass-period diagram for planets in the CAB-MPIA survey. The downward arrows indicate upper mass limits that have been calculated for the corresponding KOIs. The color-code for circle symbols is explained at the beginning of this chapter. Dotted lines represent the expected RV semi-amplitude for a solar-mass star and a circular orbit. The location of the Earth and Jupiter is marked by their capital letters for reference. Known planets (from `exoplanet.eu`) are marked with plus symbols in gray (detected by radial velocity) and magenta (detected by transits).

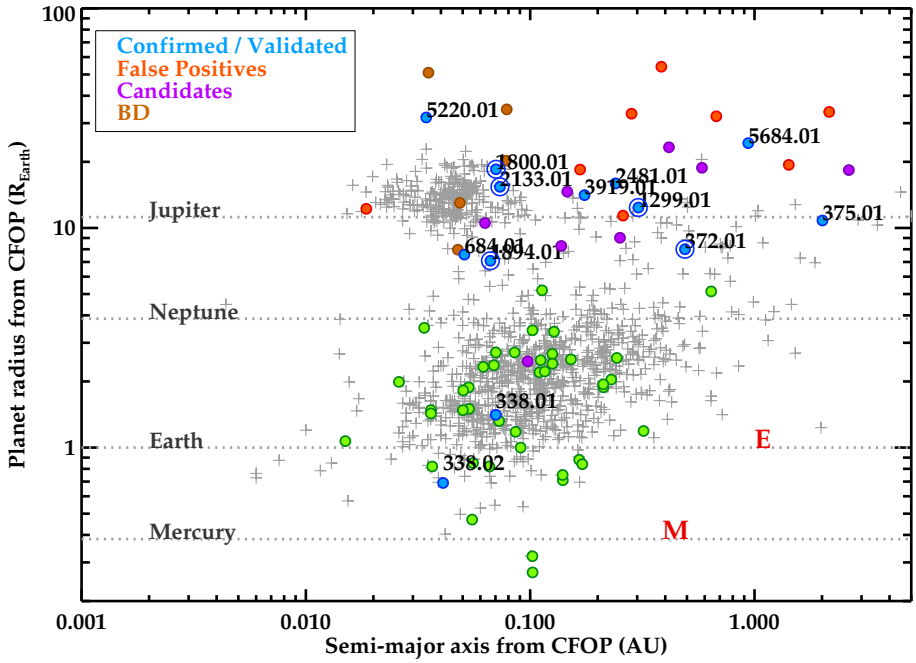

FIGURE 7.3: Radius versus orbital semi-major axis for the planets studied in the CAB-MPIA survey. The color-code is explained at the beginning of this chapter.

7.2 Planets around giant stars: the twilight of planetary systems

From a theoretical point of view, giant planets around red giant stars have been extensively studied in the recent years (Burkert & Ida, 2007, Kunitomo et al., 2011b, Passy et al., 2012, Villaver & Livio, 2009). Observationally, a few tens of exoplanets have been found so far to be orbiting these evolved stars (e.g., Adamów et al., 2012, Johnson et al., 2007, Jones et al., 2013).

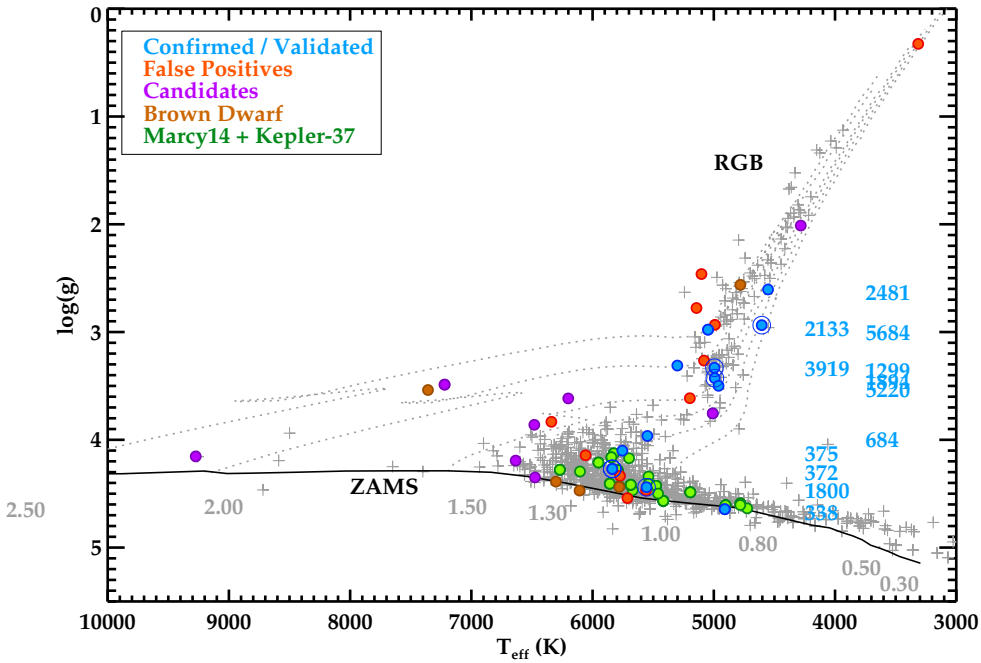

FIGURE 7.4: HR-like diagram of the planet hosts studied in this dissertation. The color code is indicated at the beginning of this chapter. Dotted lines represent the different evolutionary tracks for host stars of different masses (indicated in gray). The Zero-Age Main Sequence (ZAMS) is also marked as a solid black line for reference.

Giant stars evolved from F- and A-type main-sequence stars, for which precise radial velocity studies are difficult (owing to the small number of absorption lines present in their spectrum and their rapid rotation). Hence, although some have been detected by transit searches like *Kepler*, its planetary nature is difficult to establish. As a result of this, very few planets have been found so far orbiting the more massive main-sequence stars (i.e., F- and A-type). By contrast, these stars evolve off the main-sequence by cooling down and expanding their external layers (while contracting their cores), slowing their rotational velocities to conserve the angular momentum. Thus, K- and G-type giants with slower rotational velocities had F- and A-type progenitors in the main-sequence stage. In consequence, looking for planets on these more evolved stars (with much more sharper absorption lines) can help to better constrain the demography of planets around early-type stars, probing the efficiency of planet formation mechanisms for the different mass ranges of the host star. Hence, the discovery of planets around K and G giants and sub-giants is crucial for planet formation theories.

In addition, there is a paucity of planets with short periods around stars ascending the red giant branch (RGB, Johnson et al., 2007). The reason could be two-fold. On one hand, it could be explained by a scarcity of close-in planets around early-type main-sequence stars ($M_\star > 1.2\ M_\odot$). The lack of close-in planets around early type stars was hypothesized to be related to different migration mechanisms for planets around stars of different masses (Udry et al., 2003), owing to the shorter dissipation timescales of the protoplanetary disks of these stars, what prevents the formed planets from migrating to close-in orbits (Burkert & Ida, 2007). The latter was also favored by simulations of Currie (2009) and observationally proved by Ribas et al. (2015), who showed the dependency of the gas disk lifetime on the stellar mass, preventing the formation of close-in ($a < 0.5$ AU) planets around the more massive hosts.

On the other hand, the paucity of planets around these evolved stars has been considered by theoretical studies as an evidence for the planet engulfment/disruption even at the first stages of the evolution off the main-sequence of their parents. Villaver & Livio (2009) calculated how tidal interactions in the sub-giant and giant stages can lead to the final engulfment of the close-in planets and how this process is more efficient for more massive planets. Complementarily, in Villaver et al. (2014), the authors analyze the effects of the evolution of the planet's orbital eccentricity, mass-loss rate, and planetary mass on the survivability of planets orbiting massive stars ($M_\star > 1.5\ M_\odot$). They concluded that the planet mass is a key parameter for the engulfment during the sub-giant phase, with the more massive planets more likely falling into the stellar envelope during this phase (for the same initial orbital parameters). Also, planets located at $2 - 3\ R_\star$ when the star begins to leave the main sequence, may suffer orbital decay due to the influence of stellar tides. Any planet closer than this orbital distance may be engulfed by the star in the sub-giant phase.

However, these results are based on a limited sample of confirmed exoplanets around RGB stars. Therefore the detection of extremely close-in planets around post main-sequence (giant and sub-giant) stars is crucial to constrain theoretical models about how planets are destroyed by their hosts. Because of this reason, several long-term projects have focused on the search for planets around giant stars (e.g., TAPAS: Niedzielski et al., 2015; EXPRESS: Jones et al., 2011).

In this dissertation we have characterized some giant planets at different stages of their lives. In Fig. 7.4, we show the location of their hosts on an HR diagram. As shown, a relatively large percentage of our targets occupy regions corresponding to evolved stages, in their way to or even ascending the RGB. Among them, we have published the confirmation of Kepler-91 b (KOI-2133, § 6.2) and Kepler-432 b (KOI-1299, § 6.3). Added to this, we also followed KOI-1894 b that was firstly confirmed by Sato et al. (2015). Moreover, our preliminary analysis in section § 6.7 showed clear hints for the confirmation of KOI-2481.01, KOI-3919.01, KOI-1032.10 and the possible two-planet system KOI-5684.01 and KOI-5684.10. By contrast, the planetary nature of six of the targets in the RGB region was rejected by this and/or other works.

The confirmed planets in this work revolving around giant hosts have began to populate the previously isolated region of close-in planets to giant stars (see Fig. 7.5). Of particular interest is the case of Kepler-91b, which we determined to the very close to its engulfment. We used evolutionary tracks from Girardi et al. (2002) and assumed the effective temperature, metallicity, stellar radius, and mass from our spectroscopic and asteroseismic studies to compute the time that the envelope of the star will reach the current planet's orbital pericenter. If we only take this evolutive constraint into account, we conclude that Kepler-91b will be engulfed by the stellar atmosphere in less than 55 Myr. It is important to note that other non-negligible effects inducing instabilities on the planetary orbit due to the influence of stellar tides on this close-in planet ($a/R_\star \sim 2.45$ or, equivalently, $a \sim 0.07$ AU) should speed up the planet engulfment. As a consequence, this estimate can be considered as an upper limit to the planet's life.

The first clear evidence of planet engulfment was published by Adamów et al. (2012). The authors showed the signs of a post-planetary engulfment scenario for BD+48 740, where the presence of a highly eccentric ($e = 0.67$) secondary planet and an overabundance of lithium in the stellar spectrum could be caused by the previous engulfment of an inner planet. With a similar stellar mass, Kepler-91 could be in the immediately previous stage of BD+48 740, the scenario before the planet engulfment. Thus, we are contributing to build a complete scenario containing all the scenes of planet evolution from the craddle to the grave.

Its small planet-star separation places Kepler-91b as the closest planet to a host giant star known so far. Our derived orbital distance implies that more than 8% of the sky as seen from the planet is covered by the star (compared to the 0.0005% covered by the Sun from the Earth). This reinforces the idea that the planet under study is at the end of its life, with its host star rapidly inflating while ascending the RGB. Since we have found no overabundance of lithium in the spectrum of the host star, this might indicate that no previous engulfment took place in this sytem. No signs of planetary evaporation (such as a dust tail imprint in the transit or the presence of neutral magnesium in the ultraviolet like in HD 209458 b, Bourrier et al. 2015) the planet is still not being evaporated (at least the material has not been incorporated into the stellar atmosphere) and that no previous engulfment seems to have happened.

From the sample of confirmed exoplanets[1] (with derived masses), only Kepler-91 b is closer than $a/R_\star = 3.0$. Given the mass of the host star, at the main-sequence its radius was $\sim 1.14\ R_\odot$ (assuming it had a $\log g = 4.44$) and so the orbital distance of the planet was $(a/R_\star)_{MS} \sim 13.4$ (assuming no orbital migration in the post-MS phase). Thus, it was save from being engulfed during the sub-giant phase. In the case of Kepler-432 b, the planet also survived the sub-giant phase. Both systems, demonstrate that close-in planets exist around intermediate-mass stars. Given the mentioned short time scales for the dissipation of the protoplanetary disk in this massive stars, our results might suggest that the main mechanism driving the migration of giant

[1] http://exoplanet.eu/

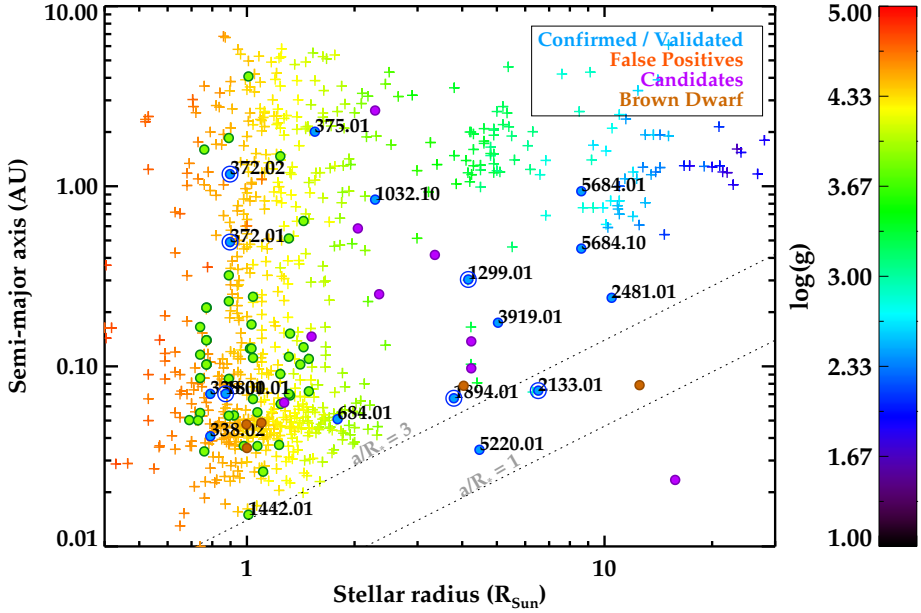

FIGURE 7.5: Stellar radius versus orbital semi-major axis of the planet for planets in the CAB-MPIA survey. The color code for planets of our survey (filled circles) is indicated at the beginning of this chapter. Known planets are represented by the "plus" symbol and they are color-coded according to the surface gravity of the host star as indicated by the color bar. The dotted lines mark the $a = R_\star$ and $a = 3R_\star$ limits, the firs corresponding to the stellar surface and the second to the approximate engulfment limit derived by Villaver et al. (2014).

planets to close-in orbits around intermediate-mass stars seems to be other than planet-disk interactions. Instead, in single-planetary systems, the star-planet gravitational interaction may drive the migration of the planets to close-in orbits in this intermediate-mass hosts (planet-planet scattering in multi-planetary systems could also play a role). A low efficiency of this mechanism or subsequent engulfment by the host star may explain the paucity of these planets around evolved stars.

Interestingly, the planet Kepler-407 b (KOI-1442.01), that was confirmed in Marcy et al. (2014), orbits its main-sequence star in a very tight orbit of 0.6 days ($\sim$ 14 hours), corresponding to $a/R_\odot \sim 3.22$, being one of the closest-in planets known to orbit around a main-sequence star (see Fig. 7.5). Although the mass of its host is similar to that of the Sun, the estimations by Villaver et al. (2014) indicate that this planet will not survive the sub-giant phase and will be quickly engulfed once the star will leave the main sequence due to the dominant stellar tides. Indeed, among the confirmed planets around main-sequence stars (mostly with $M_\star < 1.3\ M_\odot$) only few of them have $a/R_\odot \sim 2 - 3$, being thus secure from subsequent engulfment in the sub-giant phase (see Fig. 7.5).

Added to this, Kepler-91 b and later on Kepler-432 b are the first known planets to transit an evolved star. This may help us understanding the physical evolution of gas giants as their hosts evolve off the main-sequence. With these discoveries, we can start thinking about how the evolution of the parent stars affect the physical properties of their planets (such as the atmospheric

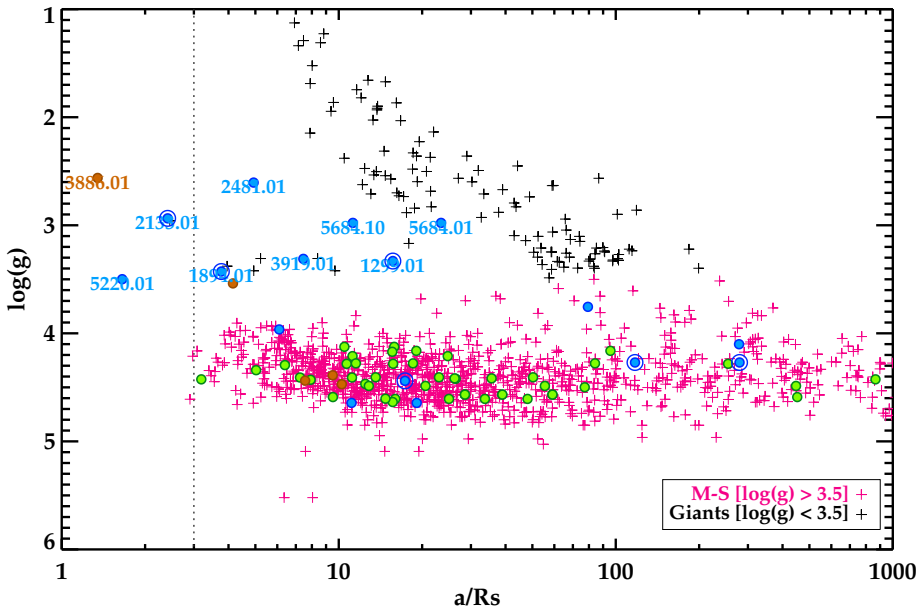

FIGURE 7.6: Semi-major axis to stellar radius ratio versus host surface gravity for planets of the CAB-MPIA survey. The color-code is explained at the beginning of this chapter. "Plus" signs represent the sample of known planets (as stated by `exoplanet.eu`). Their color indicate their evolutionary stage, being main-sequence ($\log g > 3.5$, magenta) and sub-giant or giant ($\log g < 3.5$, black) stars.

evaporation in HD209458, Bourrier et al. 2015; or EPIC 201637175 b by Sanchis-Ojeda et al. 2015). However, we just know a handful number of confirmed planets with derived masses and radius, so more detections are needed to start answering this question from an observational point of view. The definite confirmation of KOI-3919.01, KOI-2481.01, and the two-planet system KOI-5684 (with more precise measurements of their radial velocity variations) will significantly increase the population of transiting planets around giant stars, allowing a better comprehension of the influence of stellar evolution on planetary systems.

7.3 Close-in hot-Jupiters: implications on planet formation and evolution

The two competing scenarios to explain planet formation (namely core accretion - CA- and gravitational instability - GI-, see section § 1.3) have different consequences in the properties of the formed planets. In the CA mechanism, due to the higher efficiency of water ice to aggregate dust grains, it is expected that planets form beyond the ice-line at 5-10 AU (Helled & Vazan, 2013). On the contrary, GI allows the formation of massive planets and brown dwarfs in a wide range of orbital separations. However, none of these theories is able to explain the existence of a large number of Jupiter-like planets in close-in orbits ($a < 0.5$ AU) around their host (see Fig. 7.2). The alternative explanation suggests that these planets may have suffered migration

processes from their original place of birth. But we still lack a clear explanation of when this migration starts, what mechanism drives this migration and what are its consequences for the evolution of other planets being formed in the system.

We already showed in section § 1.3 the three proposed migration processes (namely planet-disk interactions, planet-planet scattering, and planet-star tidal interactions). We showed that these mechanisms play different roles at different time scales, showing the importance of detecting planets at different orbital separations and different ages.

In this work we have detected several close-in Jovian planets at different evolutionary stages. For instance, KOI-372 is a young analog of the Sun, with an estimated age of $\sim 1.0 \pm 0.3$ Gyr and hosting a Jupiter-mass planet at ~ 0.4 AU. Similarly, Kepler-447 hosts a very close-in Jupiter planet orbiting at ~ 0.07 AU. In the sub-giant phase we have found KOI-684.01 and Kepler-432 b, a sub-Jupiter-like planet at orbiting at ~ 0.05 AU and a massive planet at ~ 0.3 AU, respectively. Finally, several planets have been characterized in the RGB, mainly Kepler-91 b, a hot-Jupiter in a 0.07 AU orbit around its giant host.

Additionally, we have found potential brown dwarf companions (e.g., KOI-3728.01) orbiting in really close-in orbits ($a/R_\star < 12$) around its primary star. Also, we found upper mass limits in the brown-dwarf domain for the transiting companions of four fast rotators. Interestingly, these slightly more massive companions are also found in close-in orbits to their primary stars. Due to their large masses, they are not expected to form by core-accretion but instead by disk fragmentation. In this case, their closeness could be explained by other type of migration mechanisms as clump-clump scattering or clump-spiral wave interaction (Boley et al., 2010). This could also be the reason for the presence of the less massive hot-Jupiters found in close-in orbits. However, in principle, both planet formation mechanisms are not mutually exclusive and can predominate over the other in different environments. The objects characterized in this dissertation provide additional evidences in order to understand this process.

7.4 Gas giants as potential hosts of habitable minor bodies

Since the first discoveries of extrasolar planets there has been a debate on the properties that a planet must have to be considered as "habitable". In this section we follow the habitability description provided in Kopparapu et al. (2013),[2] whose equations allow the determination of an optimistic and pessimistic **habitable zones (HZ)**, depending on the definition of the outer edge (see paper for additional information[3]). Although in principle one tends to think in the

[2] The definition of the habitable zone has been discussed in several works, starting with Hart (1978), Papagiannis (1992), or Kasting et al. (1993).

[3] The HZ calculator is also available through the website:
http://depts.washington.edu/naivpl/sites/default/files/index.shtml

habitable zone as a range of planet-star separations, this may lead to confusions when comparing planets around stars at different evolutionary stages. This is because the HZ of a star is defined by the region around the host star in which the **effective stellar incident flux** is of the order of $S_{\mathrm{eff}} \sim 0.3 - 1.7$. In order to translate this to an orbital distance, the luminosity of the star (and thus its evolutionary stage) is required, since $d_{\mathrm{HZ}} = (L/L_{\odot})/(S_{\mathrm{eff}}/S_{\mathrm{eff},\oplus})$.

In Fig. 7.7, we plot the planets studied in a T_{eff} vs. semi-major axis diagram. In yellow, we mark the expected HZ for a solar-age and solar-mass star. We can see in this case that some of the planets around giant stars analyzed here lie inside this HZ. However, the luminosity of these giant stars is much larger than that of the Sun. Hence, a new diagram taking the evolutionary stage of the star into account is needed. As stated by Kopparapu et al. (2013), the key point that determines the HZ is the stellar incident flux on the planet, see Fig. 7.8. This parameter just depends on the effective temperature of the star and the planet-star separation. In order to place every planet on this diagram, we need to know its evolutionary stage to determine the luminosity of its star. We have done this by interpolating the corresponding evolutionary track of each host given its calculated surface gravity and effective temperature. In cases were the age of the star has been determined, we use this value to directly obtain the luminosity without interpolating in the $\log g$ vs. T_{eff} diagram.

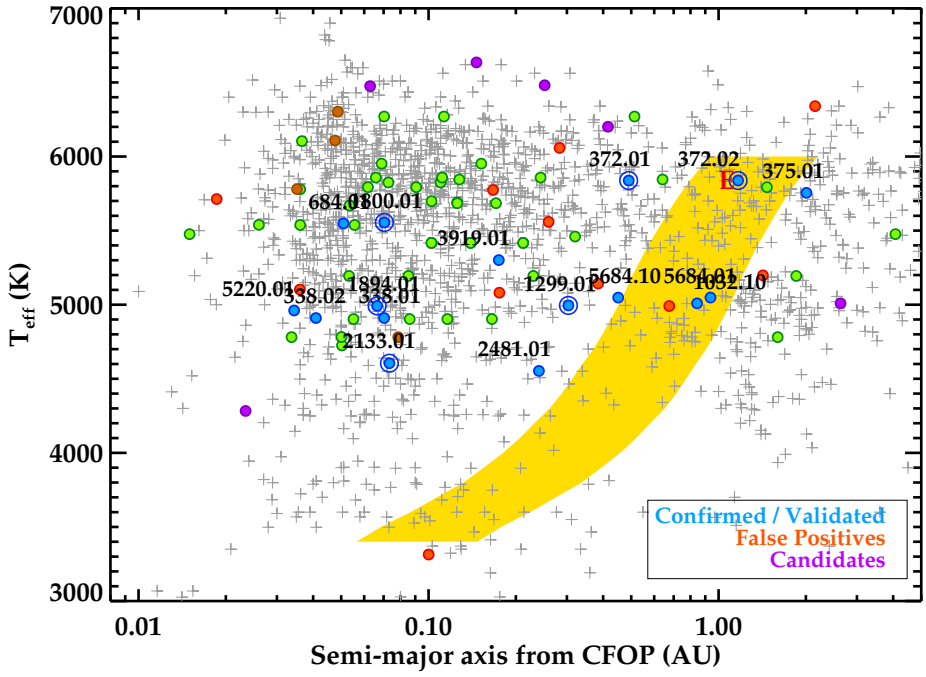

FIGURE 7.7: Semi-major axis versus effective temperature for planets in the CAB-MPIA survey. The habitable zone corresponding to a solar age, metallicity, and mass star is plotted for reference as yellow shaded region. This region is however not appropriated for some of the planets of this survey since some of their hosts are in really different evolutionary stages (see Fig. 7.8).

In this new, more reliable, diagram taking the evolutionary stage of the star into account, we find that five among the studied planet candidates lie inside the conservative HZ defined by

Kopparapu et al. (2013), see Fig. 7.8. In particular, in Marcy et al. (2014), we provided updated parameters for the third planet in the system Kepler-68 (KOI-246.10, firstly detected by Gilliland et al., 2013), **Kepler-68 d**, a Jupiter-mass planet around a solar-like star orbiting at a Mars-like distance ($a \sim 1.4$ AU). Besides, we detected and confirmed via TTVs a second non-transiting planet on KOI-372 (**KOI-372 c** or KOI-372.02), determined to have a Neptune-like mass and orbiting in a ~ 1.17 AU orbit. Also, our preliminary results on the RV data for **KOI-375.01** suggest the confirmation of the transiting massive planet ($M_p = 11.2 \pm 1.8\ M_{\rm Jup}$), revolving in a ~ 2 AU orbit around its solar-mass star recently evolved off the main-sequence. Additionally, the low-mass stellar companion (as derived by our preliminary RV analysis) to KOI-1463 (**KOI-1463.01**, with a lower-mass limit of 0.183 $M_\odot$) also lies inside the habitable zone of its primary star.

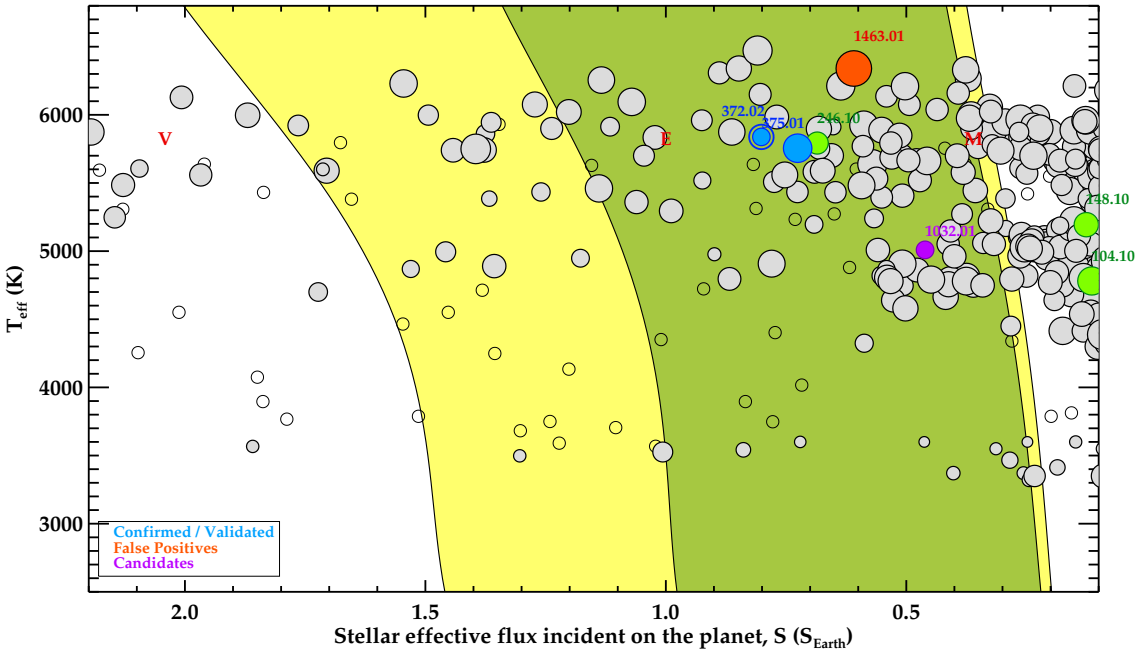

FIGURE 7.8: Habitable zone in terms of effective incident stellar flux on the planet. The yellow region represent the optimistic habitable zone (HZ), with the left limit corresponding to the "recent Venus" and the right limit to the "early Mars". The conservative HZ is marked as the green region and is limited by the runaway greenhouse on the left and the maximum greenhouse on the right. Filled symbols correspond to planets with determined mass (i.e., confirmed) and its size depends on this mass. Open circles correspond to validated planets (no available mass). Colored filled circles correspond to the targets from our survey with the color code explained at the beginning of this chapter.

In total, we have 5 companions (two confirmed gas giants, preliminary confirmation of another gas giant, one yet unconfirmed gas giant, and a low-mass star) in the habitable zone of their corresponding star. Although these objects cannot be habitable because of their gaseous nature, they can potentially host exomoons and/or exo-Trojans that would be habitable given their separations to the primary star. In the case of KOI-1463.01, in principle it cannot host any Trojan because of gravitational stability conditions. The only option in this case would by an S-type

planet orbiting in the combined HZ of the two stars. This calculation, however, is out of the scope of this dissertation and will not be analyzed here.

Besides, it is interesting to see the evolution of the habitable zone in these systems. In Fig. 7.9. we show the rough HZ in terms of incident stellar flux and how the evolution of the star has changed the range of orbital separations that can potentially host habitable planets. In this figure, each line represents the location of the corresponding planet with age with respect to the habitable zone of its host. We can see that all but one of the planets that are now in the HZ of their stars have remained there practically since the stabilized on their current orbits. However, in the case of the more evolved KOI-1032 system, the evolution of the host star off the main sequence has moved its HZ to the orbital region were this planet candidate is located. On the contrary, we can see that while Venus was formed inside the optimistic HZ of the Solar System, the evolution of the Sun slightly increasing its luminosity over the years has taken out Venus from the HZ. This interesting diagram shows how the evolution of the star affects the habitability of its planets.

In the case of the four gas giants, since they actually formed farther away, at orbits beyond $\sim$ 4 AU, and were subsequently moved to these closer orbits by Type II migration mechanisms before the dissipation of the protoplanetary disk, it is even more likely that they have captured more massive rocky (Earth-like) exomoons and exo-Trojans during this process (Tinney et al., 2011). For instance, the trojan bodies co-orbiting with Jupiter librate around its Lagrangian points L4/L5 with relatively high inclinations and eccentricities, which may indicate that they were captured during the migration of Jupiter rather than formed *in situ* (e.g., Jewitt & Sheppard, 2005). Additionally, the large number of natural rocky satellites harbored by the gas giants in the Solar system (more than 60 are known in Jupiter and Saturn) and the hundreds of trojan bodies co-orbiting at their Lagrangian points (see Fig. 7.10, left panel) indicate that their formation is not just casual but instead a byproduct of the formation and early migration of gas giants. Indeed, we now know that some Jupiter and Saturn moons, despite of being well beyond the habitable zone of the Solar System, could host (or have hosted) liquid water like in Titan in Saturn (Baland et al., 2011), Europa in Jupiter (Schmidt et al., 2011), or the case of Enceladus in Saturn (Waite et al., 2009), specially below thick layers of ice or other materials.

Following this reasoning, the probability for a gas giant planet to harbor rocky moons is high. Thus, looking for exomoons orbiting gas giants in the habitable zone of their stars is not inconsequential but key in our aim to look for extraterrestrial life. While the radial velocity semi-amplitude or transit depth of Earth-like planets at the HZ of solar-like stars is of few cm/s and ppm (respectively), the detection of gas giants at those distances are much easier. Detecting those giant planets is the first step to look for potentially habitable exo-Trojans and exomoons. In this regard, the HEK (Hunt for Exomoons with *Kepler*, Kipping et al., 2012) project and the

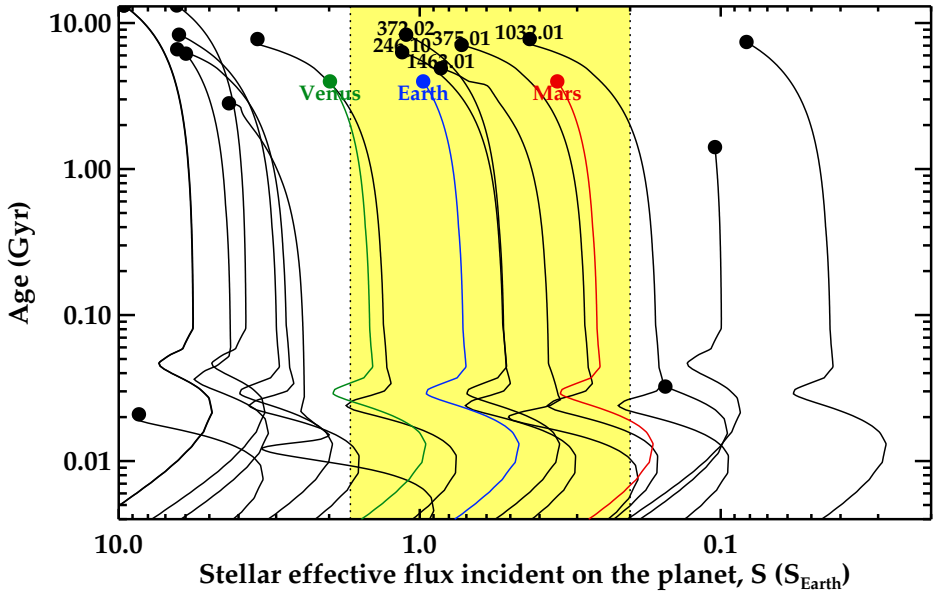

FIGURE 7.9: Evolution of the habitable zone for different planets of the present work. We show the stellar incident flux on the planet along the evolution of the star until the current state. The HZ is marked by the yellow shaded region. For reference, we plot the evolution of habitability of Venus, Mars, and the Earth.

forthcoming TROY project (a search for co-orbital bodies around known planets, Lillo-Box et al., 2015, in preparation) will focus on the quest for these interesting minor bodies.

Tinney et al. (2011) investigated the conditions for the habitability of these (somehow exotic but theoretically plausible) systems. They concluded that given the mass of $> 0.22\ M_{\oplus}$ required for an object to retain an atmosphere (Kaltenegger, 2000) and the lack of such massive regular moons (contemporaneously formed in the debris disk of the gas giant) in the Solar System, the only way for a massive gas giant to harbor a $> 0.22\ M_{\oplus}$ exomoon would be to capture it during its inward migration (i.e., irregular exomoons, showing larger eccentricities). The interested reader is encouraged to perouse the references included in Tinney et al. (2011). Regarding the habitability of exo-Trojans librating around the L4/L5 points of a gas giant in the habitable zone of its star, Dvorak et al. (2004) showed that stable configurations for these bodies are plausible. Interestingly, Laughlin & Chambers (2002) determined that the minimum mass requirement for a trojan body to be long-term stable is that the total mass of the planet and the Trojan does not exceed the $\sim 4\%$ of the mass of the host star. For instance, in a solar-mass star, the upper limit for a Trojan co-orbiting with a Jupiter-mass planet would be 40 $M_{\rm Jup}$. Given this large upper limit, Earth-mass Trojans co-orbiting with gas giants could be clearly stable (see scheme in Fig. 7.10, right panel).

All these reasons highlight the importance of detecting any kind of planet lying in the HZ of its host star (not just Earth-like worlds), which could be a potential host of minor habitable

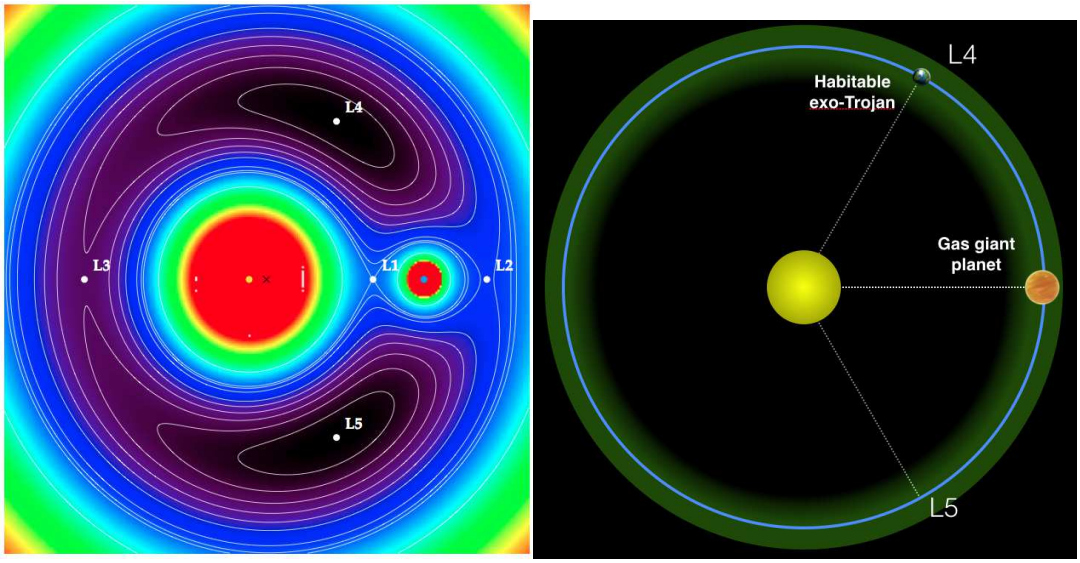

FIGURE 7.10: **Left:** Schematic representation of the equipotential surfaces in the two body problem of a Jupiter-like planet around a solar-like star. The Lagrangian stability regions are marked. **Right:** Schematic view of a gas giant planet in the HZ of its host star (green shadowed region) and harboring a rocky planet at the L4 Lagrangian point. Size of the bodies is not to scale.

worlds. To date, 122 planets have been confirmed in the HZ of their host stars. Among them, just 11 (9%) have Earth-like properties in terms of mass and radius. The remaining 91% are gas giants or Neptune-like planets that have migrated from their original place of birth to their current locations. The three objects confirmed/preliminary-confirmed/validated in this work (KOI-246.10, KOI-375.01, and KOI-372.02[4]) can be included in this latter group, thus being potential targets for subsequent searches of minor bodies.

[4]We do not include KOI-1032.01 because its planetary nature is not yet demonstrated.

Chapter 8

Conclusions and future work

Along this thesis we have detailed the different techniques and sets of observations in *Part I* (chapters 2, 3, and 4) and the scientific results achieved with these different pieces of information in *Part II* (chapters 5, 6, and 7).

We have carried out a comprehensive procedure to characterize a sample of systems from the large crop of *Kepler* planet candidates, and we have established the planetary nature of some of them. The work has been divided into two main phases. In the following, we summarize the results of both of them:

Phase 1: high-spatial resolution imaging of *Kepler* candidates

In the first phase, we have obtained high-spatial resolution images of the host candidates, in order to unveil possible close (either projected or bounded) companions. The lucky-imaging technique was applied with the AstraLux instrument at Calar Alto Observatory. In total, we observed 233 *Kepler* Objects of Interest (KOIs). We detected companions closer than 6 arcsec for the 33.5% of them. In particular, companions in the range 3-6 arcsec were found in the 19.7% of the sample, and companions closer than 3 arcsec were detected in the 18.0% of the total sample. The same proportions were found for the active sample of 174 KOIs (currently having at least one planet candidate). The results of this work were published in Lillo-Box et al. (2012, 2014b).

Thanks to the multi-color observations for the sample of closer companions, we were able to characterize them and provide hints for the joint formation (and thus probable physical association) of 11 companions to 10 KOIs. Additionally, the planet properties of the non-isolated KOIs were updated by taking into account the additional flux from the companions. In the case of the isolated sample, we have presented the BSC parameter that quantifies their probability of being actually isolated given the high-resolution image. This parameter can be applied to any

type of high-resolution image and we encourage its use to quantify the quality of this type of observations. The BSC has allowed us to directly compare our results to other similar surveys in the *Kepler* sample, which used other similar but distinct techniques. We can conclude that our survey combines an important improvement of the planet candidacy for isolated KOIs with a large sample of observed targets (reducing the probability of chance-aligned sources by more than 50% for the 62% of our targets), as compared to other large surveys. Additionally, the observations for the sample of isolated KOIs can be used to feed statistical validation tools like BLENDER or PASTIS.

We have discussed the implications of our results in different aspects of the multiplicity rate of planet hosts. We found a close companion at 65 AU to the subsequently validated multi-planetary system Kepler-444 (KOI-3158, Campante et al., 2015) composed by small rocky planets and have preliminary confirmation of the planet revolving in a 33-days orbit around KOI-2481, where we have detected a possible stellar-mass companion in a 193-days orbit. These two systems represent a challenge for the study of multiplicity in planet hosts, both in terms of existence and stability of the orbits. The validated S-type planetary-system Kepler-444 also represents a challenge for the theorized type of planets able to grow in multi-planetary systems, expected to be much more massive than what has been detected in this system. Additionally, we have found no difference in the multiplicity rate of multi-planetary and single-planet systems. But low number statistics and the lack of planet confirmation prevents us from extracting definite conclusions.

Our high-resolution observations were also used in the validation of the the planetary system Kepler-37 (Barclay et al., 2013), hosting the smallest planet known to date, Kepler-37 b. Besides, we provided high-resolution observations for some of the super-Earth-like planet hosts in the work by Marcy et al. (2014), who confirmed and validated a large sample of small planets.

Phase 2: radial velocity characterization of *Kepler* planet candidates

In this second phase, we used the results of Phase 1 to perform an exhaustive radial velocity follow-up of isolated planet candidates in order to confirm their planetary nature and characterize their physical and orbital properties. We used the new spectrograph CAFE at the Calar Alto Observatory. Our project served as a test case to prove the capabilities of the instrument as a planet hunter. We selected a subsample of the isolated targets (32 in total) that were expected to be feasible with this instrument.

In total, we have provide definite confirmation for 5 planets in 4 planetary systems so far, namely Kepler-91 b (Lillo-Box et al., 2014a,c), Kepler-432 b (Ciceri et al., 2015), Kepler-447 b (Lillo-Box et al., 2015b), and the two-planetary system KOI-372 b,c (Mancini et al., 2015, in prep.).

The confirmation of the inflated hot-Jupiter Kepler-91 b has opened a new window in our understanding of the evolution of planetary systems when their hosts evolve off the main-sequence. It has been the **first confirmed planet known to transit a giant star and is the closest planet orbiting such an evolved host**, being the previous stage to a planetary engulfment. Subsequently, with the confirmation of the massive Jupiter-size planet Kepler-432 b we continued increasing the sample of planets orbiting in close-in orbits (< 0.5 AU) to their giant hosts, starting to populate a previously void region in the $R_\star$ vs. a diagram. This paucity was proposed to be due to planet engulfment in the sub-giant phase or due to a lower efficiency of massive stars to form planets. Our results show that massive stars can form planets that could be subsequently engulfed/disrupted by their hosts.

The other two confirmed planets orbit around main-sequence stars. We demonstrated that Kepler-447 b has the largest impact parameter known for a planetary transit. This fact makes this an extremely interesting target for subsequent follow-up to look for additional bodies in the system, since any even small perturber would introduce detectable transit timing/depth/duration variations. The long-cadence observations of *Kepler* (29.4 min), however, prevented this analysis. In the case of the young solar analog KOI-372, we have preliminary confirmed the planetary nature of the transiting giant planet KOI-372 b and we have detected TTVs in its transits, indicating the presence of an outer (less massive) planet. We have modeled these TTVs and provided some plausible solutions for its orbital and physical parameters, which suggest that this second planet lies within the habitable zone of its host star.

Besides, we analyzed the radial velocity data of a sample of false positives and fast rotators, rejecting the planetary nature for 6 KOIs and providing upper-mass limits for 7 KOIs, some of them being in the planetary- and brown dwarf-mass domain. This work was published in Lillo-Box et al. (2015a).

Our recent analysis of the remaining planets under study shows preliminary confirmation of KOI-375.01 (a long-period giant planet in the habitable zone of its host star), KOI-1032.10 (a possible hidden massive planet), KOI-5684 (a possible two-planet system in 3:1 MMR), KOI-2481 (a possible extremely packed S-type planetary system), KOI-684 (a possible super-Neptune planet), and KOI-3919 (a possible "false" false-positive).

This work is another example of the important and powerful synergies between space- and ground-based observatories of any kind, being both key parts of the scientific progress. In particular, we have extensively used the Calar Alto Observatory, whose facilities and personnel are extremely valuable. This shows the need of maintaining the mid-size telescopes (of the class 2-4m), since apart from other capabilities, they allow the execution of long-term intensive follow-up programs such as the one presented in this dissertation.

Future work

The near-future plans in the context of this dissertation are as follows:

- The definitive planet confirmation of the preliminary results presented in section § 6.7. These cases are of key interest because of the reasons presented above, but still require longer baselines and/or a more complete phase coverage in RV.

- A more specific and detailed follow-up is needed for Kepler-91 b in order to unveil the origin of the detected additional dips in the residuals of the light curve. A Spitzer proposal has been prepared and will be submitted for next round with this purpose. Owing to test the possible scenarios, we would need higher-precision radial velocity in a relatively large timespan. This would unveil possible outer planets, provide a more precise measurement of the eccentricity of the orbit, and test the possibility of having a smaller co-orbiting body. A HARPS-N proposal has been submitted with this purpose.

- A higher-cadence ($\sim$ 1-min) precise photometric follow-up of Kepler-447 b is needed to detect possible additional bodies on this system by taking profit of the large impact parameter of its transit. This would require space-based photometric follow-up with the future missions *CHEOPS* and *PLATO*, that will accomplish these two requirements.

- Subsequent follow-up of KOI-372 to definitely uncover the orbital and physical parameters of the second planet in this young extrasolar system. According to the current calculations, its estimated RV semi-amplitude would be 3-8 m/s, for which high-resolution and highly-stabilized spectrograph (like HARPS-N/TNG or HIRES/Keck) would be required.

- We have demonstrated (together with other similar works) the need for high-spatial resolution images in transit searches. The current and forthcoming missions *K2*, *TESS*, *CHEOPS*, and *PLATO* will need an extensive ground-based follow-up in this regard due to their large pixel sizes, aiming at reaching high photometric precisions. Instruments like AstraLux will be of key importance in this regard.

- Together with other few cases, the detection of Kepler-91 b by the detection of the light curve modulations opens the window to perform planet searches with this technique. Interestingly, like RV, it allows the detection of planets at high inclinations. Hence, we plan to look for these modulations in the whole sample of *Kepler* and *K2* targets. This could be extended to the forthcoming high-precision photometric space-based surveys mentioned above.

- In the instrumental plane, a more dedicated pipeline for CAFE should be developed. This process in currently on-going. Added to this, we have also suggested other improvements to be implemented by the observatory, such as the installation of a double-scrambler, an octagonal fiber, or a more precise centering and guiding system.

As for long-term projects related to this thesis, we would like to explore the population of minor bodies in extrasolar systems. In particular, Trojan bodies could be tracers of the planet formation and of the first stages of planet migration, possibly being captured during this process. The size of these systems, at least theoretically, is not restricted so that rocky exo-Trojans could co-orbit with gas giants. Since these bodies are a byproduct of planet formation, we think that they will be of key interest in the forthcoming years. Moreover the above mentioned space-based missions will reach sufficient precision as to detect these kind of objects. During the exciting coming years, we will be performing a comprehensive and exhaustive search for exo-Trojans with the TROY project.

List of Publications

Since I started my PhD in September 2010, I have participated in 23 refereed articles so far, six out of them as first author and another two as second author. In total, these articles amount 351 citations (as of May 2015), with an h-index of 10. Some of these articles are high impact, with tens of citations in few months since their publication. Also, some of them had a high impact in national and international media. The complete list of publications (**first authored marked in bold face**) is presented below in inverse chronological order of acceptance and can be found in this ADS link.[1] Currently, I have three other papers in preparation (all as first author and not listed below).

Refereed publications

[23] *"KOI-372: a young extrasolar system with two giant planets on wide and eccentric orbits"*. L. Mancini, **J. Lillo-Box**, J. Southworth, L. Borsato, D. Gandolfi, S. Ciceri, D. Barrado, R. Brahm, and Th. Henning.
Submitted to A&A. *ArXiv e-prints, 1504.04625*

[22] *"A Detection of the Secondary Eclipse of Qatar-1b in the Ks-band"*. P. Cruz, D. Barrado, **J. Lillo-Box**, M. Diaz, J. Birkby , M. López-Morales , J. J. Fortney.
Submitted to A&A.

[21] *"Spectro-astrometry of LkCa 15 with X-Shooter: Searching for emission from LkCa 15* b*"*. E.T. Whelan, N. Huélamo, J.M. Alcalá, **J. Lillo-Box**, H. Bouy, D. Barrado, J. Bouvier, B. Merín.
2015, A&A*, in press. ArXiv e-prints, 1504.04824*

[20] **"Kepler-447 b: a hot-Jupiter with an extremely grazing transit". J. Lillo-Box**, D. Barrado, N. C. Santos, L. Mancini, P. Figueira, S. Ciceri, Th. Henning.
2015, A&A*, 577, 105. ArXiv e-prints, 1502.03267.*

[19] *"One of the Closest Planet Pairs to the 3:2 Mean Motion Resonance, Confirmed with K2 observations and Transit Timing Variations: EPIC 201505350"*. D. J. Armstrong, D. Veras, S. C. C. Barros, O. Demangeon, J. McCormac, H. P. Osborn, **J. Lillo-Box**, A. Santerne, M. Tsantaki, J. M. Almenara, D. Barrado, I. Boisse, A. S. Bonomo, F. Bouchy, D. J. A. Brown, G, Bruno, J. Rey Cerda, B. Courcol, M. Deleuil, R. F. Díaz, A. P. Doyle, G. Hébrard, J. Kirk, K. W. F. Lam, D. L. Pollacco, A. Rajpurohit, J. Spake, S. R. Walker.
ArXiv e-prints, 1503.00692 , submitted to A&A.

[1] http://adsabs.harvard.edu/cgi-bin/nph-abs_connect?library&libname=Refereed+papers&libid=534b8fbe52

[18] **"Eclipsing binaries and fast rotators in the Kepler sample. Characterization via radial velocity analysis from Calar Alto". J. Lillo-Box**, D. Barrado, L. Mancini, Th. Henning, P. Figueira, S. Ciceri, N. Santos.
2015, A&A*, 576, 88. ArXiv e-prints, 1501.05183.*

[17] *"Detection of the secondary eclipse of WASP-10b in the Ks-band".* P. Cruz, D. Barrado, **J. Lillo-Box**, M. Diaz, J. Birkby, M. López-Morales, S. Hodgkin, J. J. Fortney.
2015, A&A*, 574, 103. ArXiv e-prints, 1412.2996.*

[16] *"Kepler-432 b: a massive planet in a highly eccentric orbit transiting a red giant".* S. Ciceri, **J. Lillo-Box**, J. Southworth, L. Mancini, Th. Henning, D. Barrado.
2015, A&A *Letters, 573L, 5C*

[15] **"Radial velocity confirmation of Kepler-91 b. Additional evidence of its planetary nature using the Calar Alto/CAFE instrument". J. Lillo-Box**, D. Barrado, Th. Henning, L. Mancini, S. Ciceri, P. Figueira, N.C. Santos, J. Aceituno, S. Sánchez.
2014, A&A*, 568L, 1L*; DOI: 10.1051/0004-6361/201424587

[14] **"High-resolution imaging of Kepler planet host candidates. A comprehensive comparison of different techniques". J. Lillo-Box**, D. Barrado, H. Bouy.
2014, A&A*, 566A, 103L*; DOI: 10.1051/0004-6361/201423497

[13] *"Gas and dust in the Beta Pictoris Moving Group as seen by the Herschel Space Observatory.".* P. Riviere-Marichalar, D. Barrado, B.Montesinos, G. Duchene, H. Bouy, C. Pinte, F. Menard, J. Donaldson, C. Eiroa, A. V. Krivov, I. Kamp, I. Mendigutía, W. R. F. Dent, **J. Lillo-Box**.
2014, A&A*, 565A, 68R*; DOI: 10.1051/0004-6361/201322901

[12] *"WTS-2 b: a hot Jupiter orbiting near its tidal destruction radius around a K-dwarf".* J. L. Birkby, M. Cappetta, P. Cruz, J. Koppenhoefer, O. Ivanyuk, A. J. Mustill,S. T. Hodgkin, D. J. Pinfield, B. Sipöcz, G. Kovács, R. Saglia, Y. Pavlenko, D. Barrado, A. Bayo, D. Campbell, S. Catalan, L. Fossati, M.-C. Gálvez-Ortiz, M. Kenworthy, **J. Lillo-Box**, E. L. Martín, D. Mislis, E. J. W. de Mooij, S. V. Nefs, I. A. G. Snellen, H. Stoev, J. Zendejas, C. del Burgo, J. Barnes, N. Goulding, C. A.Haswell, M. Kuznetsov, N. Lodieu, F. Murgas, E. Palle, E. Solano, P. Steele, R. Tata.
2014, MNRAS, 440, 1470B; DOI: 10.1093/mnras/stu343

[11] *"The long-term steady motion of Saturn's Hexagon and the stability of its enclosed jetstream under seasonal changes".* A. Sánchez-Lavega, T. del Río-Gaztelurrutia, R. Hueso, S. Pérez-Hoyos, E. García-Melendo, A. Antuñano, I. Mendikoa, J. F. Rojas, **J. Lillo-Box**, D. Barrado Navascués, J. M. Gomez-Forrellad, C. Go, D. Peach, T. Barry, D. P. Milika, P. Nicholas, A. Wesley and the IOPW-PVOL Team.
2014, GeoRL, 41, 1425S; DOI: 10.1002/2013GL059078

[10] *"CSI 2264: Simultaneous optical and infrared light curves of young disk-bearing stars in NGC 2264 with CoRoT and Spitzer – evidence for multiple origins of variability"*. A. M. Cody, J. Stauffer, A. Baglin, and 42 other coauthors including **J. Lillo-Box**
2014, AJ, 147, 82C; DOI: 10.1088/0004-6256/147/4/82

[9] *"Masses, radii, and orbits of small Kepler planets: the transition from gaseous to rocky planets"*. G. W. Marcy, H. Isaacson, A. W. Howard, and 100 other coauthors including **J. Lillo-Box**
2014, ApJS, 210, 20M; DOI: 10.1088/0067-0049/210/2/20

[8] **"Kepler-91b: a planet at the end of its life. Planet and giant host star properties via light-curve variations". J. Lillo-Box**, D. Barrado, A. Moya, B. Montesinos, J. Montalbán, A. Bayo, M. Barbieri, C. Régulo, L. Mancini, H. Bouy, and Th. Henning.
2014, A&A*, 562A, 109L*; DOI: 10.1051/0004-6361/201219631

[7] *"Gas and dust in the TW Hydrae association as seen by the Herschel Space Observatory"*. P. Riviere-Marichalar, C. Pinte, D. Barrado, W. F. Thi, C. Eiroa, I. Kamp, B. Montesinos, J. Donaldson, J. -C. Augereau, N. Huélamo, A. Roberge, D. Ardila, G. Sandell, J. P. Williams, W. R. F. Dent, F. Menard, **J. Lillo-Box**, G. Duchene
2013 A&A*...555A..67R*; DOI: 10.1051/0004-6361/201321506

[6] *"CAFE: Calar Alto Fiber-fed Echelle spectrograph"*. J. Aceituno, S. F. Sanchez, F. Grupp, **J. Lillo-Box**, M. Hernan-Obispo, D. Benitez, L. M. Montoya, U. Thiele, S. Pedraz, D. Barrado, S. Dreizler, J. Bean
2013, A&A*, 552A, 31A*; DOI: 10.1051/0004-6361/201220361

[5] *"A sub-Mercury-sized exoplanet"*. Thomas Barclay, Jason F. Rowe, Jack J. Lissauer, and 55 other coauthors including **J. Lillo-Box**
2013, Nature, 494, 452B; DOI: 10.1038/nature11914

[4] *"Magnetic activity and accretion on FU Tau A: clues from variability"*. Aleks Scholz, Beate Stelzer, Grainne Costigan, David Barrado, Jochen Eislöffel, **J. Lillo-Box**, Pablo Riviere-Marichalar, Hristo Stoev
2012, MNRAS, 419, 1271S; DOI: 10.1111/j.1365-2966.2011.19781.x

[3] *"Ground-based observations of the long-term evolution and death of Saturns 2010 Great White Spot"*.
International Outer Planet Watch Team IOPW-PVOL Sanchez-Lavega A., del Río-Gaztelurrutia T., Delcroix M., Legarreta J. J., Gomez-Forrellad J. M., Hueso R., García-Melendo E., Perez-Hoyos S., Barrado-Navascues D., **J. Lillo-Box**.
2012, Icarus, 220, 561I; DOI: 10.1016/j.icarus.2012.05.033

[2] **"Multiplicity in transiting planet-host stars. A lucky imaging study of Kepler candidates".**
J. Lillo-Box, D. Barrado, H. Bouy
2012, A&A*, 546A, 10L*; DOI: 10.1051/0004-6361/201219631

[1] *"First T dwarfs in the VISTA Hemisphere Survey"*.
N. Lodieu , B. Burningham, A. Day-Jones, R.-D. Scholz, F. Marocco, S. Koposov, D. Barrado y Navascues, P. W. Lucas, P. Cruz, **J. Lillo-Box**, H. Jones, A. Perez-Garrido, M. T. Ruiz, D. Pinfield, R. Rebolo, V. J. S. Bejar, S. Boudreault, J. P. Emerson, M. Banerji, E. Gonzalez-Solares, S. T. Hodgkin, R. McMahon, J. Canty, C. Contreras
2012, A&A*, 548A, 53L*; DOI: 10.1051/0004-6361/201220182

Non-refereed publications & proceedings

"Multiplicity and properties of Kepler planet candidates: High-spatial imaging and RV studies.".
D. Barrado, **J. Lillo-Box**, H. Bouy, J. Aceituno, S. Sánchez.
European Physical Journal Web of Conferences, 2013EPJWC..4705008B

"E(B-V) determination of peculiar stars with the three-points method.".
C. Morales, A. Cassatella, **J. Lillo-Box**, & R. Hedrosa.
Highlights of Spanish Astrophysics VI, 2011, vol pg. 541-541.

Appendix A

GAbox: a statistically tested fitting algorithm

A.1 Introduction

A correct sampling of the parameter space in models depending on a large number of free parameters would require a huge (unmanageable) grid of models. For instance, in a case where observations could be modeled by six parameters, sampling each parameter with 15 values would end up with 6^{15} different sets of parameters. Depending on the time employed by a computer to calculate each model, the amount of time would last many weeks for a good sampling. Instead, a clever way to select the particular set of parameters to be tested can save a lot of computing time. This is actually the main goal of the so-called genetic algorithms (GA). These are stochastic search procedures inspired by natural selection and genetics (see Goldberg, 1989, Holland, 1975, and references therein). In this Appendix, we provide the details of the implementation of our own GA. Part of this text was presented in Lillo-Box et al. (2014a). Here, we detail the description more in depth.

A.2 The *GAbox* working scheme

We have written a genetic algorithm (IDL-based) to explore the whole parameter space without the need of creating a model grid. Basically, a range (minimum and maximum) for each parameter must be supplied, and optionally a prior (initial guessed) value for each parameter. The symbols used in this section are summarized and explained in Table A.1. The program performs the following steps:

TABLE A.1: Definitions of the symbols and designations used along the paper.

Symbol	Designation	Explanation
SG	SuperGeneration	Also called 'chain' in MCMC analysis
G(t)	Generation	Set of individuals at time t
I	Individual	A concrete set of parameters to build the model.
nSG	number of SG	Number of SG requested by the user.
nG	number of G	Number of G per each SG.
nI	number of I	Number of I per G (fixed by user).
p_{ch}	Chage prob.	Probability that an individual from G(t) is changed in G(t+1).
A_{ch}	Chage par.	Normalized amplitude to generate the child population from parents.
N_1	Req. subtests	Number of generations to increase the counter of tests ($n_2(t) = n_2(t-1) + 1$).
N_2	Req. tests	Number of subtests to consider the current parameters as the final solution.
$n_1(t)$	subtests	Current number of generations accomplishing the tolerance criterion.
$n_2(t)$	tests	Current number of subtests
nINV	Invasors	Random population acroos the whole range introduced when counter= n_1
nF	Foreings	Small population of individuals in the whole range introduced in each generation.
F_p	Prob. foreings	Probability that foreings are included in the generation.
$p_i^{\min}$	Min. value	Minimun allowed value for parameter i.
$p_i^{\max}$	Max. value	Maximun allowed value for parameter i.
Δ_{p_i}	Range ampl.	Amplitude of the allowed parameter range ($\Delta_{p_i} = p_i^{\max} - p_i^{\min}$).

1. Set up of parents for Generation $G(t_i)$. If $t = 0$, then parents are set up from priors. See § A.2.1.

2. Produce nI individuals based on parents that will compose the $G(t_i)$. See § A.2.2.

3. With a certain probability, include nF *foreigns*. See § A.2.3.

4. In specific cases, include $nINV$ *invaders*. See § A.2.3.

5. Generate the models for the whole population of individuals: $N_{tot} = nI + nF + nINV$ and test the optimization function f, which compares the observations with the N_{tot} models. See § A.2.4.

6. Sort the results of the optimization function and select new parents for the next Generation $G(t_{i+1})$. See § A.2.5.

In the next section we explain in detail each of these steps. Also, in Fig. A.1 we summarize the whole *GAbox* process in a flow chart.

GAbox requires an input file with X columns and one row per free parameter to be explored. The columns are: 1st) parameter name (no spaces allowed), 2nd) minimum value allowed for the parameter, 3rd) maximum value allowed for the parameter, 4th) number format of the parameter (float, double, integer, etc.), 5th) prior of the parameter (must be inside the parameter range of columns 2nd and 3rd), 6th) confidence level for the prior, being 0 for no confidence (thus prior will be uniform) and 1 for a high confidence (thus the range will be stretched to the prior value in column 5th).An example for a 6-parameters model is given in Table A.2.

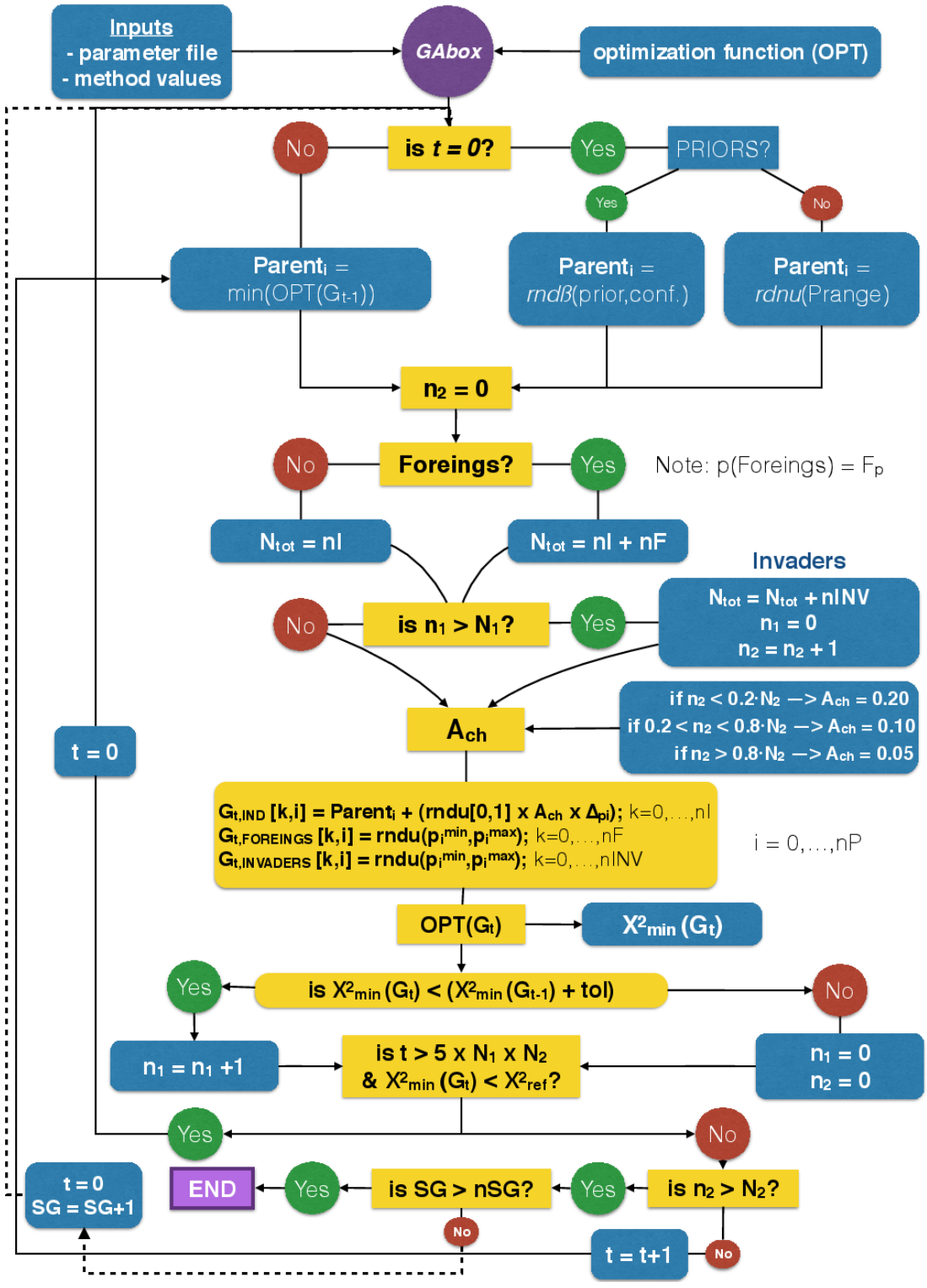

FIGURE A.1: Flow chart of *GAbox*. The notation is explained along the text and summarized in Table A.1. In the figure the uniform and β random distributions are represented as *rdnu* and *rdn*β, respectively. The cost function (usually χ^2) is represented by OPT and its value by χ^2.

TABLE A.2: Example of an input file for a 5-parameters model.

Parameter	minimum	maximum	type	prior	confidence
a0	-25	20	D	3	0.6
a1	-4	4	D	0	0.5
a2	-10	10	D	-4	0.8
a3	-10	10	D	5	0.5
a4	0	3	D	1	0.3

A.2.1 Setting up parents

In the first generation G_0, we do not have (*a priori*) any information about the characteristic hyper-surface of the optimization function. Hence, if no priors are set by the user, a random parent is generated by *GAbox* from a uniform distribution inside the ranges provided in the ranges file (see section § A.2).

If, instead, a rough idea about the best parameter location is guessed and passed by the *prior* column in the ranges file, the parents of G_0 will be restricted to a smaller range. This range depends on the confidence level ($\Psi_{p_i} \in [0, 1]$) for each parameter, which is set by the user and represents an idea about how sure the user is about the prior. Mathematically, this means that the parent will be chosen from a β-distribution like

$$f(x; \alpha, \beta) = Ax^{\alpha-1}(1-x)^{\beta-1}. \tag{A.1}$$

In this equation, A is a normalization constant, and the two parameters α and β are chosen so that

$$\alpha = \frac{1}{1-\Psi_{p_i}} \tag{A.2}$$

and

$$\beta = \frac{\alpha-1}{p_i^0} + (2-\alpha) \tag{A.3}$$

where p_i^0 is the prior value for parameter i. The latter equation is applied to force the distribution to have a mode value equal to the prior. We designed a routine for such purpose (*randombeta.pro*). Figure A.2 shows an example of two β-distributions for parameter p_i and two confidence levels and prior values. For comparison purposes, we have set two different confidence levels for our given prior ($p_i^0 = 7$), which are $\Psi_{p_i} = 0.5$ (red line) and $\Psi_{p_i} = 0.8$ (blue line). We have also set the upper and lower limits for this parameter, $\max_{p_i} = 10$ and $\min_{p_i} = 0$. The larger Ψ_{p_i}, the more restricted is the first generation of parents.

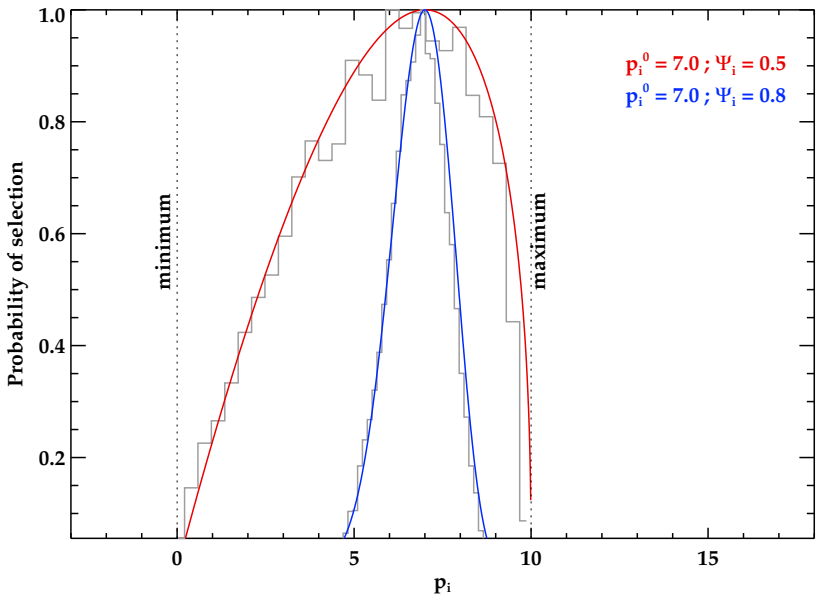

FIGURE A.2: Probability distribution for two different confident levels of parameter p_i: $\Psi_{p_i} = 0.5$ (red line) and $\Psi_{p_i} = 0.8$ (blue line). Dotted vertical lines show the minimum and maximum limits (defined by the user) for this parameter.

Neither foreigns nor invaders are included in generation zero. This generation is tested by computing the models corresponding to the parameters in each individual and evaluating the optimization function for these models. The best individual in G_0 is then selected to be the parent of G_1.

A.2.2 Generating the individuals of G_t

The best individual from G_{t-1} is used to generate the next population of individuals. At this point, two parameters are crucial for the efficiency and convergence of the method. These are the **change probability** ($\mathbf{p_{ch}}$) and the **change amplitude** ($\mathbf{A_{ch}}$). For each parameter conforming an individual, the value coming from the parent will be changed with a probability p_{ch}. This means that some of the parameters of the parent will be changed and others will remain. In the case that the change is accepted, the change amplitude parameter controls the amplitude over which the parameter will be changed. The new parameter is then randomly selected from a **uniform distribution** inside the box centered in the parent value with amplitude A_{ch}. The greater p_{ch}, the more uniformly populated will be the region defined by A_{ch}.

In order to improve the accuracy of the final parameters, the A_{ch} is modified according to the number of tests (n_2) overcame by the parent. The default values for A_{ch} are:

$$A_{ch} = \begin{cases} 0.20\,\Delta_{p_i} & \text{if } n_2(t) < 0.2\,N_2 \\ 0.10\,\Delta_{p_i} & \text{if } 0.2\,N_2 > n_2(t) > 0.8\,N_2 \\ 0.05\,\Delta_{p_i} & \text{if } n_2(t) > 0.8\,N_2 \end{cases} \tag{A.4}$$

but they can be modified by the user. The process is repeated for every parameter. And this is done nI times to complete the population of the current generation.

In Fig. A.3, we have ran a simulation for a two-parameter problem showing the effect of the values of the two variables involved in this step (i.e., p_{ch} and A_{ch}). There we can see that the greater p_{ch}, the more uniformly will be populated the region defined by A_{ch}. And the smaller A_{ch}, the more concentrated will be the new population around the parent in the parameter space.

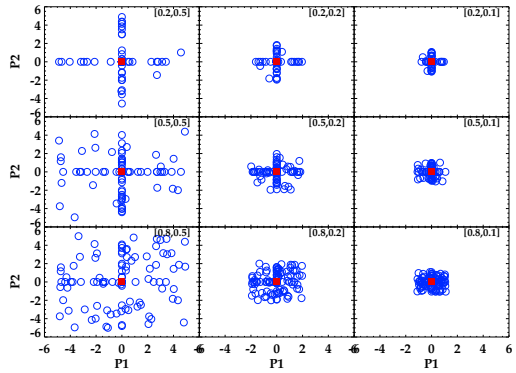

FIGURE A.3: Simulation of the generation of a population of 100 individuals (blue open circles) for a two parameters problem assuming different values of the change probability (p_{ch}) and change amplitude (A_{ch}). The different values are shown in each panel as [p_{ch}, A_{ch}].The parent (fill red square) is assumed to be $P_1 = 0$ and $P_2 = 0$.

As mentioned in section § A.2, a flag can be introduced in the input file defining the type of the parameter (i.e., integer, double, etc.). This is accounted for by the routine that generates the new individuals so that the new population satisfies this criterion.

Also, the number of individuals to be generated in each iteration nI is defined by the user. This number must be set by taking into account several factors:

- The computational time employed in calculating a model for a particular individual. If this calculation is slow, a large nI will last in a very slow process for *GAbox*.
- The size of the parameter space (namely the number of parameters and how constrained they are with the limits set by the user).
- The quality of the observations. If the observations are precise (small uncertainties in the data), the parameter space needs to be well sampled in each generation to reach the best

parameter so that we would need a large nI. If the uncertainties were large, we would expect that the parameters will not be well constrained so that nI can be smaller.

- The values set for the previously defined change probability (p_{ch}) and change amplitude (A_{ch}), which define the real parameter space that will be covered by the individuals.

As a rule of thumb, we have checked that using 10-30 individuals per parameter is a good compromise for problems with less than 6 parameters in which the model is calculated in relatively short time.

A.2.3 Avoiding local minima: Introducing *foreigns* and *invaders*

In order to avoid the GA to get trapped in a local minima, we introduce two classes of new inhabitants in the population of individuals: *foreigns* and *invaders*.

We define *foreigns* as additional individuals that are included in each generation with a probability F_p. This probability can be defined by the user and its default value is $F_p = 0.1$. The number of foreigns (nF) can also be defined by the user but should be set to typical values around $nF = 0.1\,nI$. The parameters of each foreign are generated *from a uniform distribution* in the whole parameter space allowed by the user (i.e., $p_i^{F_j} \epsilon$ [min$_{pi}$,max$_{p_i}$]). The inclusion of this additional population allows a continuous control in every generation that the GA does not get trapped in a local minima. The number of foreigns must be accordingly set depending on the number of free parameters (i.e., on the size of the parameter space) in order to correctly sample the parameter space without loosing efficiency.

The *invaders* are defined as a large number of additional individuals introduced when the parent of the population satisfies the tolerance criterion during N_1 generations (i.e., if $n_1(t) > N_1$). If the criterion is found, it means that a minimum of the hyper-surface of the optimization function has been found. To destabilize such minimum and search for other possible deeper minima, we introduce $nINV$ invaders in the new population. These are taken *from a uniform distribution* the whole parameter space allowed by the user. The typical number of invaders should be around $nINV = 0.01 \times nP^5$ to cover, at least, the 1% of the parameter space, assuming that we divide each parameter range in 5 slices. For instance, for a 6-parameter problem we would set $nINV \sim 80$.

A.2.4 Testing the generation G_t: the optimization function

After the new population with $N_{tot} = nI + nF + nINV$ individuals has been created, the models corresponding to each individual are generated and the optimization function is evaluated. This

TABLE A.3: Critical values for the χ^2 distribution (upper tail).

	Confidence				
# Free Param	0.90	0.95	0.975	0.99	0.999
1	2.706	3.841	5.024	6.635	10.828
2	4.605	5.991	7.378	9.210	13.816
3	6.251	7.815	9.348	11.345	16.266
4	7.779	9.488	11.143	13.277	18.467
5	9.236	11.070	12.833	15.086	20.515
6	10.645	12.592	14.449	16.812	22.458
7	12.017	14.067	16.013	18.475	24.322

function is the one to be minimize/maximize. In usual astronomical problems, this function corresponds to the χ^2 distribution defined as:

$$\chi^2 = \sum_{i=0}^{Ndata} \frac{(O_i - M_i)^2}{\sigma_{O_i}^2} \tag{A.5}$$

where O_i is the $i-th$ observational point and M_i is the correspondent value at the same X-value. The optimization function can, however, be user defined according to each particular problem.

A.2.5 Tolerance criterion

A tolerance criterion for stopping the algorithm must be defined. For maximum likelihood optimization functions, where the χ^2 is used, we use 90% confidence to obtain the p-values corresponding to the number of free parameters to be fitted. Different confidence levels can be used. In Table A.3, we show the corresponding p-values for different number of free parameters and confidence levels.

At a given time t, we evaluate if the best individual having the least value of the optimization function ($\chi^2_{\rm min}$) accomplishes the tolerance criterion, i.e., $\chi^2_{\rm min}(t) < \chi^2_{\rm min}(t-1) + tol$. If such criterion is satisfied during N_1 generations, a population of invaders is included in the next generation of individuals and $n_1(t+1)$ is set to zero while n_2 is set to $n_2(t+1) = n_2(t) + 1$. If this is satisfied N_2 times (i.e., if the population of individuals has survived during $N_1 \times N_2$ generations), the genetic algorithm is stopped and a the current individual with the minimum value of the optimization function is provided as the solution for the current SG. Subsequently, another SG is started repeating the same process explained in the previous sections.

Thus, *GAbox* provides different sets of possible solutions of a given problem, all of them accomplishing this tolerance criterion.

A.3 Post-analysis of the solutions

After the fitting process, *GAbox* will end up with a set of nSG possible solutions corresponding to the different SG analyzed. Thus, a post-processing analysis is needed to extract conclusions about the fitting results. In this section, we describe several packages specifically performed to provide the user with some statistical and useful analysis to interpret the solution.

A.3.1 Elevation Profiles of Fitness (EPF)

An important aspect of the GA process is how the solutions are concentrated in the parameter space allowed by the user. The elevation profiles of fitness (hereafter EPFs) represent, for each parameter, the path that each solution has covered according to the fitness values (i.e., it traces the temporary solutions of each generation for each given SG). We simply plot, the solutions of all generations against their fitness values. These diagrams for each parameter allows the user to check different aspects of the fitting. We illustrate this with a simple example in which we have fitted a straight line to data with different levels of noise (see Fig. A.4).

The shape of the EPF for each parameter reveals how accurate is the solution. It is thus obvious that this shape will depend on the noise of the observational data points. In Fig. A.4, we show the EPFs of the slope and intercept obtained by *GAbox* for three different levels of noise in the observed data. If we focus on the intercept parameter (second column of plots), we can easily see that the noisier are the data, the broader is the EPF of the parameter. It is also important to note the different scales in the fitness value for the different levels of noise. As expected, lower (better) values of the fitness are reached by EPF for less noisy data.

The location of the EPF in the parameter space of a given parameter provides information about how good is the user-defined range for this parameter. For instance, in Fig. A.4, the parameter space of the intercept is relatively well defined since the minimum is located close to the center of the range and it is wide enough to allow the GA to explore a sufficient range of values. In contrast, the EPFs of the slope suggest that the parameter space is too wide for the given dataset so that the computing time would have been smaller if a smaller range had been set for this parameter.

Thus, note that a zero-order (quick) fitting of the data using *GAbox* with a small number of SG (around 100) can provide the user with the approximated EPFs of each parameter and, then, have a first guess of: i) the best χ^2 achievable given the observational data, ii) the goodness of the user-constrained range for each parameter, and iii) the goodness of the data according to the model.

A.3.2 Selecting the *manifold* solutions

The nSG solutions provided by *GAbox* usually have different values of the fitness parameter, different number of needed generations to reach the best solutions, etc. Thus, among the whole solutions, we must provide a criteria to select the best solutions. This process allows us to discard possible solutions trapped in local minima (although given the design of the algorithm we do not expect many local minima in the space of solutions).

For maximum likelihood problems, we use the minimum fitness value (χ^2_{min}) among all solutions as a reference. Then, for a given confidence level (default is $\alpha_{def} = 99\%$, we obtain the p-value ($p_{0.99}$) from Table A.3 and select all solutions with fitness values accomplishing $\chi^2 < \chi^2_{min} + p_{0.99}$. The confidence level is also user-tunable. This process thus ends up with nS statistically acceptable solutions, being nS≤nSG. The ratio rS=nS/nSG provides the effectivity of the algorithm for a given problem.

We will refer to this selection of nS solutions as the manifold solutions.[1]

A.3.3 Parameter error estimation

Due to the controlled randomness of the GA processes, it is difficult to provide an estimation of the error for the given parameters as well as a single solution for the fit. We will end up the fitting process with a set of nS sets of parameters. If the problem has a unique solution, this set of solutions will be all concentrated in a small region of the parameter space and the errors corresponding to each set parameters should contain all possible solutions. Indeed, if the problem is well-defined and well-solved by the GA algorithm, the standard deviation of all solutions for a given parameter (which we call σ_{GA}), must be smaller than the real uncertainty (σ_p, given the observational points) for this parameter. This will not be the case when we have multi-valuated problems.

Thus, for each solution S_j ($j = 0, ..., nS$), we compute the individual errors of each parameter p_i^j ($i = 0, ..., N_{params}$). For simplicity in the notation, we will focus on a single solution and omit the superscript ^{j} denoting the solution S_j. We used these values as a prior for a subsequent MCMC analysis. We have used our own algorithm with the Metropolis-Hating scheme (*MCMCbox*). But there are many other tools and algorithms that perform this calculation.

[1] Because of its similarity to the manifold PDF defined by Bayesian Identification Framework (BIF) analysis.

A.4 Tool testing and examples

A.4.1 A simple case: fitting a straight line

This is a really simple case for which other fitting techniques are more efficient than genetic algorithms, due to the low number of free parameters. However, it is used here as an example of the functioning and data-products of *GAbox*. In this case, we have a model like $y = p_0\, x + p_1$, where p_0 is known as the slope and p_1 as the intercept. We have generated three different datasets by varying the level of noise in the simulated data (see first column of plots in Fig. A.4).

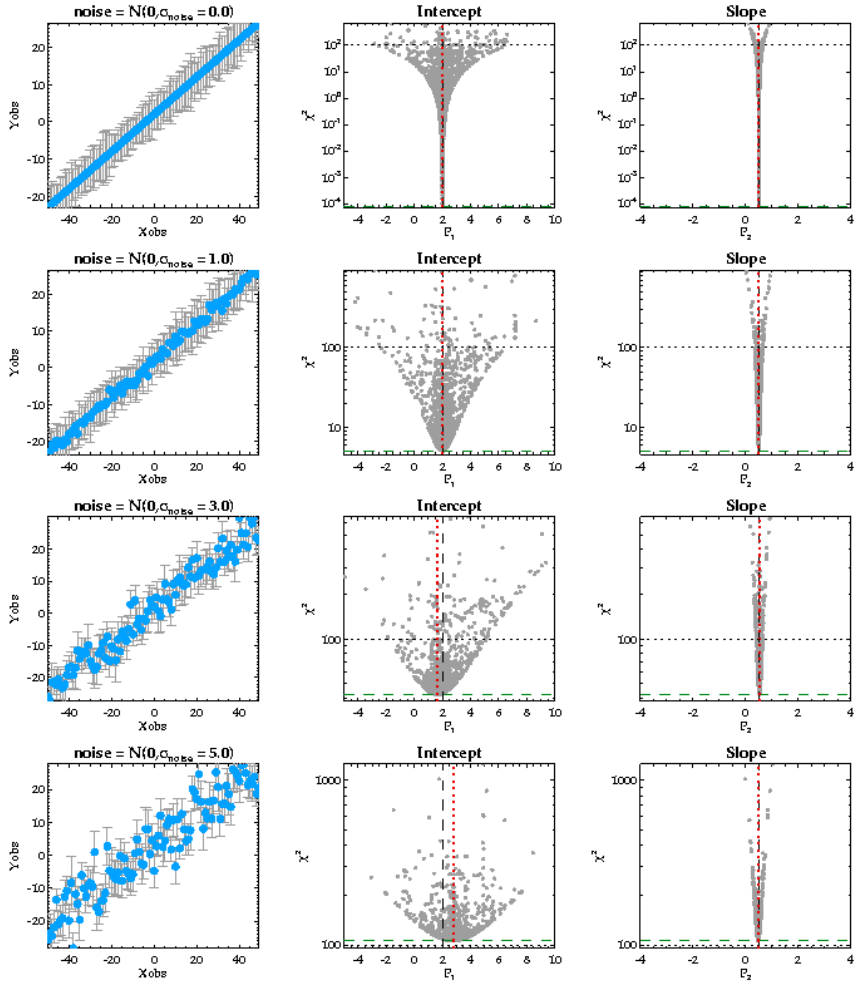

FIGURE A.4: Elevation profiles of fitness achieved by *GAbox* in the fitting of a straight line to simulated observational data with different levels of gaussian noise added. First column is the data used, second column are the EPFs for the intercept, and third column are the EPFs for the slope. In the EPFs diagrams, we have marked the true value with a black vertical dotted line, the best-fitted value with a red vertical dotted line, and the minimum value of the optimization function with a green horizontal dashed line. For comparison purposes between the different levels of noise, the $\chi^2 = 100$ is explicitly marked with a black horizontal dashed line.

A.4.2 Application to real data

GAbox has already been applied to different sets of data with different purposes. In particular, we used it in Lillo-Box et al. (2014a) to fit the lightcurve modulations in Kepler-91 (see section § 6.2). The analytic shape of these modulations and the large number of parameters involved required a more dedicated algorithm to model the different effects and inspired the development of this tool. *GAbox* has been also used in Riviere-Marichalar et al. (2013) and Riviere-Marichalar et al. (2014) as a SED fitter aiming at determining the best black body emission describing the dust temperature and infrared excess in different members with circumstellar disks in the young stars TW Hydrae and β Pictoris.

Additionally it has been used to perform joint fittings with different sets of observations, as we did for Kepler-447 b (see section § 6.4 and Lillo-Box et al., 2015b) where we simultaneously modeled the radial velocity and the transit signal of the planet. We have also test *GAbox* to obtain the astrometric calibration of astronomical images with successful (although preliminary) results.

In summary, *GAbox* is a powerful, user-tunable, easily adaptable to many problems, and user-friendly algorithm whose capabilities have already been demonstrated in different works and with different datasets. It is specially recommended in high-dimensional parameter spaces were MCMC algorithms could get trapped in local minima. In these cases, a first exploration of the parameter space by using *GAbox* could importantly reduce the computing time by providing some priors for the subsequent MCMC analysis (which will additionally provide uncertainty estimations).

Bibliography

Aceituno, J., Sánchez, S. F., Grupp, F., et al. 2013, A&A, 552, A31

Adamów, M., Niedzielski, A., Villaver, E., Nowak, G., & Wolszczan, A. 2012, ApJ Letters, 754, L15

Adams, E. R., Ciardi, D. R., Dupree, A. K., et al. 2012, AJ, 144, 42

Adams, E. R., Dupree, A. K., Kulesa, C., & McCarthy, D. 2013, AJ, 146, 9

Adams, F. C. & Laughlin, G. 2003, Icarus, 163, 290

Aerts, C., Christensen-Dalsgaard, J., & Kurtz, D. W. 2010, Asteroseismology, Astronomy and Astrophysics Library (Springer)

Agol, E., Steffen, J., Sari, R., & Clarkson, W. 2005, MNRAS, 359, 567

Ahlers, J. P., Seubert, S. A., & Barnes, J. W. 2014, ApJ, 786, 131

Aigrain, S., Pont, F., & Zucker, S. 2012, MNRAS, 419, 3147

ALMA Partnership, A., Brogan, C. L., Perez, L. M., et al. 2015, ArXiv e-prints

Amado, P. J., Quirrenbach, A., Caballero, J. A., et al. 2013, in Highlights of Spanish Astrophysics VII, ed. J. C. Guirado, L. M. Lara, V. Quilis, & J. Gorgas, 842–847

Anderson, D. R., Barros, S. C. C., Boisse, I., et al. 2011, PASP, 123, 555

Anderson, E. R., Duvall, Jr., T. L., & Jefferies, S. M. 1990, ApJ, 364, 699

Andrews, S. M. & Williams, J. P. 2005, ApJ, 631, 1134

Andrews, S. M. & Williams, J. P. 2007, ApJ, 671, 1800

Angerhausen, D., DeLarme, E., & Morse, J. A. 2014, ArXiv e-prints, 1404.4348

Anglada-Escudé, G. & Tuomi, M. 2012, A&A, 548, A58

Antoniadou, K. I., Voyatzis, G., & Varvoglis, H. 2014, ArXiv e-prints

Armitage, P. J. & Bonnell, I. A. 2002, MNRAS, 330, L11

Baland, R.-M., van Hoolst, T., Yseboodt, M., & Karatekin, Ö. 2011, A&A, 530, A141

Ballard, S., Fabrycky, D., Fressin, F., et al. 2011, ApJ, 743, 200

Baraffe, I., Chabrier, G., Allard, F., & Hauschildt, P. H. 1998, A&A, 337, 403

Baraffe, I., Chabrier, G., Barman, T. S., Allard, F., & Hauschildt, P. H. 2003, A&A, 402, 701

Baranne, A., Mayor, M., & Poncet, J. L. 1979, Vistas in Astronomy, 23, 279

Barclay, T., Endl, M., Huber, D., et al. 2015, ApJ, 800, 46

Barclay, T., Huber, D., Rowe, J. F., et al. 2012, ApJ, 761, 53

Barclay, T., Rowe, J. F., Lissauer, J. J., et al. 2013, Nature, 494, 452

Barnes, S. A. & Kim, Y.-C. 2010, ApJ, 721, 675

Batalha, N. M. 2014, Proceedings of the National Academy of Sciences, 111, 12647

Batalha, N. M., Rowe, J. F., Bryson, S. T., et al. 2013, ApJ Supplements, 204, 24

Batalha, N. M., Rowe, J. F., Gilliland, R. L., et al. 2010, ApJ Letters, 713, L103

Bayo, A., Barrado, D., Huélamo, N., et al. 2012, A&A, 547, A80

Bayo, A., Barrado, D., Stauffer, J., et al. 2011, A&A, 536, A63

Bayo, A., Rodrigo, C., Barrado, D., et al. 2013, ArXiv e-prints

Bayo, A., Rodrigo, C., Barrado Y Navascués, D., et al. 2008, A&A, 492, 277

Bear, E. & Soker, N. 2011, MNRAS, 414, 1788

Beck, P. G., Bedding, T. R., Mosser, B., et al. 2011, Science, 332, 205

Bedding, T. R., Huber, D., Stello, D., et al. 2010, ApJ Letters, 713, L176

Bedding, T. R., Mosser, B., Huber, D., et al. 2011, Nature, 471, 608

Béky, B., Bakos, G. Á., Hartman, J., et al. 2011, ApJ, 734, 109

Belkacem, K., Goupil, M. J., Dupret, M. A., et al. 2011, A&A, 530, A142

Belkacem, K., Samadi, R., Mosser, B., Goupil, M. J., & Ludwig, H.-G. 2013, ArXiv e-prints, 1307.3132

Birkby, J. L., Cappetta, M., Cruz, P., et al. 2014, MNRAS, 440, 1470

Bloemen, S., Marsh, T. R., Østensen, R. H., et al. 2011, MNRAS, 410, 1787

Bodenheimer, P., Lin, D. N. C., & Mardling, R. A. 2001, ApJ, 548, 466

Boisse, I., Bouchy, F., Chazelas, B., et al. 2010a, in Astronomy of Exoplanets with Precise Radial Velocities, 25P

Boisse, I., Bouchy, F., Hébrard, G., et al. 2011, A&A, 528, A4

Boisse, I., Eggenberger, A., Santos, N. C., et al. 2010b, A&A, 523, A88

Boley, A. C., Hayfield, T., Mayer, L., & Durisen, R. H. 2010, Icarus, 207, 509

Borsato, L., Marzari, F., Nascimbeni, V., et al. 2014, A&A, 571, A38

Borucki, W. J., Koch, D., Basri, G., et al. 2010, Science, 327, 977

Borucki, W. J., Koch, D., Jenkins, J., et al. 2009, Science, 325, 709

Borucki, W. J., Koch, D. G., Basri, G., et al. 2011, ApJ, 736, 19

Borucki, W. J., Koch, D. G., Batalha, N., et al. 2012, ApJ, 745, 120

Borucki, W. J. & Summers, A. L. 1984, Icarus, 58, 121

Boss, A. P. 2006, ApJ, 641, 1148

Bouchy, F., Díaz, R. F., Hébrard, G., et al. 2013, A&A, 549, A49

Bouchy, F., Isambert, J., Lovis, C., et al. 2009, in EAS Publications Series, Vol. 37, EAS Publications Series, ed. P. Kern, 247–253

Bourrier, V., Lecavelier des Etangs, A., & Vidal-Madjar, A. 2015, A&A, 573, A11

Bouy, H., Bertin, E., Moraux, E., et al. 2013, A&A, 554, A101

Brandl, B. R., Feldt, M., Glasse, A., et al. 2014, in Society of Photo-Optical Instrumentation Engineers (SPIE) Conference Series, Vol. 9147, Society of Photo-Optical Instrumentation Engineers (SPIE) Conference Series, 21

Brauer, F., Dullemond, C. P., & Henning, T. 2008, A&A, 480, 859

Briceño, C., Luhman, K. L., Hartmann, L., Stauffer, J. R., & Kirkpatrick, J. D. 2002, ApJ, 580, 317

Broeg, C., Fortier, A., Ehrenreich, D., et al. 2013, in European Physical Journal Web of Conferences, Vol. 47, European Physical Journal Web of Conferences, 3005

Brogi, M., Keller, C. U., de Juan Ovelar, M., et al. 2012, A&A, 545, L5

Brown, B. P., Browning, M. K., Brun, A. S., Miesch, M. S., & Toomre, J. 2010, ApJ, 711, 424

Brown, T. M., Gilliland, R. L., Noyes, R. W., & Ramsey, L. W. 1991, ApJ, 368, 599

Brown, T. M., Latham, D. W., Everett, M. E., & Esquerdo, G. A. 2011, AJ, 142, 112

Burke, C. J., Bryson, S. T., Mullally, F., et al. 2014, ApJ Supplements, 210, 19

Burkert, A. & Ida, S. 2007, ApJ, 660, 845

Cahoy, K. L., Marley, M. S., & Fortney, J. J. 2010, ApJ, 724, 189

Campante, T. L., Barclay, T., Swift, J. J., et al. 2015, ApJ, 799, 170

Campbell, B., Walker, G. A. H., & Yang, S. 1988, ApJ, 331, 902

Carpenter, J. M., Mamajek, E. E., Hillenbrand, L. A., & Meyer, M. R. 2006, ApJ Letters, 651, L49

Casassus, S., van der Plas, G., M, S. P., et al. 2013, Nature, 493, 191

Cenko, S. B., Fox, D. B., Moon, D.-S., et al. 2006, PASP, 118, 1396

Chabrier, G. 2001, ApJ, 554, 1274

Chabrier, G. & Baraffe, I. 2000, A&A Annual Review, 38, 337

Charbonneau, D., Brown, T. M., Latham, D. W., & Mayor, M. 2000, ApJ Letters, 529, L45

Christensen-Dalsgaard, J. 2004, Solar Physics, 220, 137

Christensen-Dalsgaard, J. 2012, Astronomische Nachrichten, 333, 914

Chubak, C., Marcy, G., Fischer, D. A., et al. 2012, ArXiv e-prints

Ciceri, S., Lillo-Box, J., Southworth, J., et al. 2015, A&A, 573, L5

Claret, A. 2000, A&A, 363, 1081

Claret, A. & Bloemen, S. 2011, A&A, 529, A75

Coelho, P., Barbuy, B., Meléndez, J., Schiavon, R. P., & Castilho, B. V. 2005, A&A, 443, 735

Cosentino, R., Lovis, C., Pepe, F., et al. 2014, in Society of Photo-Optical Instrumentation Engineers (SPIE) Conference Series, Vol. 9147, Society of Photo-Optical Instrumentation Engineers (SPIE) Conference Series, 8

Cosentino, R., Lovis, C., Pepe, F., et al. 2012, in Society of Photo-Optical Instrumentation Engineers (SPIE) Conference Series, Vol. 8446, Society of Photo-Optical Instrumentation Engineers (SPIE) Conference Series, 1

Cowan, N. B. & Agol, E. 2011, ApJ, 729, 54

Cunha, D., Santos, N. C., Figueira, P., et al. 2014, A&A, 568, A35

Currie, T. 2009, ApJ Letters, 694, L171

Cutri, R. M., Skrutskie, M. F., van Dyk, S., et al. 2003, VizieR Online Data Catalog, 2246, 0

Daemgen, S., Hormuth, F., Brandner, W., et al. 2009, A&A, 498, 567

Debosscher, J., Sarro, L. M., Aerts, C., et al. 2007, A&A, 475, 1159

Deleuil, M., Almenara, J.-M., Santerne, A., et al. 2014, A&A, 564, A56

Désert, J.-M., Charbonneau, D., Demory, B.-O., et al. 2011, ApJ Supplements, 197, 14

Desidera, S. & Barbieri, M. 2007, A&A, 462, 345

Díaz, R. F., Almenara, J. M., Santerne, A., et al. 2014a, MNRAS, 441, 983

Díaz, R. F., Montagnier, G., Leconte, J., et al. 2014b, A&A, 572, A109

Dohlen, K., Beuzit, J.-L., Feldt, M., et al. 2006, in Society of Photo-Optical Instrumentation Engineers (SPIE) Conference Series, Vol. 6269, Society of Photo-Optical Instrumentation Engineers (SPIE) Conference Series, 0

Dolan, C. J. & Mathieu, R. D. 2002, AJ, 123, 387

Doyle, A. P., Davies, G. R., Smalley, B., Chaplin, W. J., & Elsworth, Y. 2014, MNRAS, 444, 3592

Doyle, L. R., Carter, J. A., Fabrycky, D. C., et al. 2011, Science, 333, 1602

Dressing, C. D., Adams, E. R., Dupree, A. K., Kulesa, C., & McCarthy, D. 2014, arXiv.org

Dumusque, X., Santos, N. C., Udry, S., Lovis, C., & Bonfils, X. 2011, A&A, 527, A82

Dupret, M.-A., Belkacem, K., Samadi, R., et al. 2009, A&A, 506, 57

Dvorak, R., Pilat-Lohinger, E., Schwarz, R., & Freistetter, F. 2004, A&A, 426, L37

Dziembowski, W. A., Gough, D. O., Houdek, G., & Sienkiewicz, R. 2001, MNRAS, 328, 601

Eggenberger, A., Udry, S., & Mayor, M. 2004, A&A, 417, 353

Egner, S. E. 2007, Master's thesis, University of Heidelberg

Esteves, L. J., De Mooij, E. J. W., & Jayawardhana, R. 2013, ApJ, 772, 51

Esteves, L. J., De Mooij, E. J. W., & Jayawardhana, R. 2014, ArXiv e-prints

Everett, M. E., Barclay, T., Ciardi, D. R., et al. 2014, arXiv.org

Everett, M. E., Howell, S. B., & Kinemuchi, K. 2012, PASP, 124, 316

Eyer, L. & Bartholdi, P. 1999, A&A, Supplement, 135, 1

Faigler, S. & Mazeh, T. 2011, MNRAS, 415, 3921

Faigler, S. & Mazeh, T. 2014, ArXiv e-prints, 1407.2361

Figueira, P. 2010, Radial velocities in the IR: new light shed on planets

Figueira, P., Santos, N. C., Pepe, F., Lovis, C., & Nardetto, N. 2013, A&A, 557, A93

Flower, P. J. 1996, ApJ, 469, 355

Fortney, J. J., Marley, M. S., & Barnes, J. W. 2007, ApJ, 659, 1661

Fossati, L., Bagnulo, S., Elmasli, A., et al. 2010, ApJ, 720, 872

Fried, D. L. 1965, Journal of the Optical Society of America (1917-1983), 55, 1427

Fried, D. L. 1978, Journal of the Optical Society of America (1917-1983), 68, 1651

Gandolfi, D., Parviainen, H., Deeg, H. J., et al. 2015, A&A, 576, A11

Gandolfi, D., Parviainen, H., Fridlund, M., et al. 2013, A&A, 557, A74

Gilliland, R. L., Marcy, G. W., Rowe, J. F., et al. 2013, ApJ, 766, 40

Gilliland, R. L., Star, K. M., Adams, E. R., et al. 2014, arXiv.org, 1009

Girardi, L., Bertelli, G., Bressan, A., et al. 2002, A&A, 391, 195

Girardi, L., Groenewegen, M. A. T., Hatziminaoglou, E., & da Costa, L. 2005, A&A, 436, 895

Goldberg, D. 1989, Genetic Algorithms in Search, Optimization, and Machine Learning, Artificial Intelligence (Addison-Wesley)

Goodman, J. 1993, ApJ, 406, 596

Goudfrooij, P., Bohlin, R. C., Maíz-Apellániz, J., & Kimble, R. A. 2006, PASP, 118, 1455

Gough, D. O. 1986, in Hydrodynamic and Magnetodynamic Problems in the Sun and Stars, ed. Y. Osaki, 117

Gray, D. F. & Brown, K. 2001, PASP, 113, 723

Gray, D. F., Scott, H. R., & Postma, J. E. 2002, PASP, 114, 536

Gray, R. O. & Corbally, C. J. 1994, AJ, 107, 742

Grevesse, N. & Sauval, A. J. 1998, Space Science Reviews, 85, 161

Gruberbauer, M., Guenther, D. B., & Kallinger, T. 2012, ApJ, 749, 109

Guillot, T. 2010, A&A, 520, A27

Guillot, T. & Showman, A. P. 2002, A&A, 385, 156

Hart, M. H. 1978, in Bulletin of the American Astronomical Society, Vol. 10, Bulletin of the American Astronomical Society, 554

Harvey, J. 1985, Future Missions in Solar Heliospheric and Space Plasma Physics (E. Rolfe and B. Battrick)

Haswell, C. A. 2010, Transiting Exoplanets, 9780521139380 (Cambridge University Press)

Hatzes, A. P., Cochran, W. D., & Endl, M. 2010, in Astrophysics and Space Science Library, Vol. 366, Astrophysics and Space Science Library, ed. N. Haghighipour, 51

Hayashi, C. 1981, in IAU Symposium, Vol. 93, Fundamental Problems in the Theory of Stellar Evolution, ed. D. Sugimoto, D. Q. Lamb, & D. N. Schramm, 113–126

Haywood, R. D., Collier Cameron, A., Queloz, D., et al. 2014, MNRAS, 443, 2517

Hekker, S., Gilliland, R. L., Elsworth, Y., et al. 2011, MNRAS, 414, 2594

Hekker, S., Kallinger, T., Baudin, F., et al. 2009, A&A, 506, 465

Helled, R. & Vazan, A. 2013, in AAS/Division for Planetary Sciences Meeting Abstracts, Vol. 45, AAS/Division for Planetary Sciences Meeting Abstracts, 415.03

Hellier, C., Anderson, D. R., Collier Cameron, A., et al. 2012, MNRAS, 426, 739

Herrero, E., Lanza, A. F., Ribas, I., Jordi, C., & Morales, J. C. 2013, A&A, 553, A66

Hirano, T., Masuda, K., Sato, B., et al. 2015, ApJ, 799, 9

Hirano, T., Narita, N., Sato, B., et al. 2012a, ApJ Letters, 759, L36

Hirano, T., Sanchis-Ojeda, R., Takeda, Y., et al. 2012b, ApJ, 756, 66

Holland, J. 1975, Adaptation in natural and artificial systems: an introductory analysis with applications to biology, control, and artificial intelligence (University of Michigan Press)

Holman, M. J. & Wiegert, P. A. 1999, AJ, 117, 621

Horch, E. P., Howell, S. B., Everett, M. E., & Ciardi, D. R. 2014, arXiv.org

Hormuth, F. 2007, Master's thesis, University of Heidelberg

Hormuth, F., Brandner, W., Hippler, S., & Henning, T. 2008, Journal of Physics Conference Series, 131, 012051

Houdek, G., Balmforth, N. J., Christensen-Dalsgaard, J., & Gough, D. O. 1999, A&A, 351, 582

Howell, S. B., Everett, M. E., Sherry, W., Horch, E., & Ciardi, D. R. 2011, AJ, 142, 19

Howell, S. B., Rowe, J. F., Bryson, S. T., et al. 2012, ApJ, 746, 123

Huber, D., Bedding, T. R., Stello, D., et al. 2010, ApJ, 723, 1607

Huber, D., Chaplin, W. J., Christensen-Dalsgaard, J., et al. 2013, ApJ, 767, 127

Huber, D., Ireland, M. J., Bedding, T. R., et al. 2012, ApJ, 760, 32

Huber, D., Silva Aguirre, V., Matthews, J. M., et al. 2014, ApJ Supplements, 211, 2

Hunter, T. R. & Ramsey, L. W. 1992, PASP, 104, 1244

Ivezić, Ż., Connolly, A., VanderPlas, J., & Gray, A. 2013, Statistics, Data Mining, and Machine Learning in Astronomy (Princeton University Press)

Jackson, B., Greenberg, R., & Barnes, R. 2008, ApJ, 681, 1631

Jenkins, J. M. 2002, ApJ, 575, 493

Jenkins, J. M., Caldwell, D. A., Chandrasekaran, H., et al. 2010, ApJ Letters, 713, L87

Jewitt, D. & Sheppard, S. 2005, Space Science Reviews, 116, 441

Johnson, J. A., Fischer, D. A., Marcy, G. W., et al. 2007, ApJ, 665, 785

Jones, M. I., Jenkins, J. S., Bluhm, P., Rojo, P., & Melo, C. H. F. 2014, A&A, 566, A113

Jones, M. I., Jenkins, J. S., Rojo, P., & Melo, C. H. F. 2011, A&A, 536, A71

Jones, M. I., Jenkins, J. S., Rojo, P., Melo, C. H. F., & Bluhm, P. 2013, A&A, 556, A78

Kallrath, J. & Milone, E. F. 2009, Eclipsing Binary Stars: Modeling and Analysis (Springer)

Kaltenegger, L. 2000, in ESA Special Publication, Vol. 462, Exploration and Utilisation of the Moon, ed. B. H. Foing & M. Perry, 199

Kane, S. R. & Gelino, D. M. 2010, ApJ, 724, 818

Kane, S. R. & Gelino, D. M. 2012, MNRAS, 424, 779

Kasper, M., Beuzit, J.-L., Verinaud, C., et al. 2010, in Society of Photo-Optical Instrumentation Engineers (SPIE) Conference Series, Vol. 7735, Society of Photo-Optical Instrumentation Engineers (SPIE) Conference Series, 2

Kasting, J. F., Whitmire, D. P., & Reynolds, R. T. 1993, Icarus, 101, 108

Kepler, J. 1609, Astronomia Nova Aitiologētos, Sev Physica Coelestis, tradita commentariis De Motibvs Stellae Martis, Ex observationibus G. V. Tychonis Brahe ... (-)

Kepler, J. 1619, Harmonices mundi libri V

Kipping, D. & Bakos, G. 2011, ApJ, 733, 36

Kipping, D. M. 2009, MNRAS, 392, 181

Kipping, D. M. 2010, MNRAS, 408, 1758

Kipping, D. M., Bakos, G. Á., Buchhave, L., Nesvorný, D., & Schmitt, A. 2012, ApJ, 750, 115

Kjeldsen, H. & Bedding, T. R. 1995, A&A, 293, 87

Kjeldsen, H., Bedding, T. R., & Christensen-Dalsgaard, J. 2008, ApJ Letters, 683, L175

Kley, W. 2010, in EAS Publications Series, Vol. 42, EAS Publications Series, ed. K. Gożdziewski, A. Niedzielski, & J. Schneider, 227–238

Knutson, H. A., Charbonneau, D., Allen, L. E., et al. 2007, Nature, 447, 183

Knutson, H. A., Charbonneau, D., Cowan, N. B., et al. 2009, ApJ, 703, 769

Kopparapu, R. K., Ramirez, R., Kasting, J. F., et al. 2013, ApJ, 765, 131

Kraus, A. L., Ireland, M. J., Hillenbrand, L. A., & Martinache, F. 2012, ApJ, 745, 19

Kumar, P., Ao, C. O., & Quataert, E. J. 1995, ApJ, 449, 294

Kunitomo, M., Ikoma, M., Sato, B., Katsuta, Y., & Ida, S. 2011a, ApJ, 737, 66

Kunitomo, M., Ikoma, M., Sato, B., Katsuta, Y., & Ida, S. 2011b, ApJ, 737, 66

Kurucz, R. L. 1979, ApJ Supplements, 40, 1

Labeyrie, A. 1970, A&A, 6, 85

Lada, C. J., Muench, A. A., Luhman, K. L., et al. 2006, AJ, 131, 1574

Lambert, J. H. 1759, L perspective affranchie de l'embaras du Plan geometral

Latham, D. W., Stefanik, R. P., Mazeh, T., Mayor, M., & Burki, G. 1989, Nature, 339, 38

Laughlin, G. & Chambers, J. E. 2002, Astronomical Journal, 124, 592

Law, N. M., Morton, T., Baranec, C., et al. 2014, ApJ, 791, 35

Leconte, J., Forget, F., Charnay, B., Wordsworth, R., & Pottier, A. 2013, Nature, 504, 268

Lillo-Box, J., Barrado, D., Moya, A., et al. 2014a, A&A, 562, A109

Lillo-Box, J., Barrado, D., & Bouy, H. 2012, A&A, 546, A10

Lillo-Box, J., Barrado, D., & Bouy, H. 2014b, A&A, 566, A103

Lillo-Box, J., Barrado, D., Henning, T., et al. 2014c, A&A, 568, L1

Lillo-Box, J., Barrado, D., Mancini, L., et al. 2015a, ArXiv e-prints, 1501.05183

Lillo-Box, J., Barrado, D., Santos, N. C., et al. 2015b, ArXiv e-prints, 1502.03267

Lillo-Box, J., et, a., & al., e. 2015c, in prep.

Lin, D. N. C., Bodenheimer, P., & Richardson, D. C. 1996, Nature, 380, 606

Lind, K., Asplund, M., & Barklem, P. S. 2009, A&A, 503, 541

Lindegren, L. & Dravins, D. 2003, A&A, 401, 1185

Lissauer, J. J., Fabrycky, D. C., Ford, E. B., et al. 2011, Nature, 470, 53

Lissauer, J. J., Marcy, G. W., Bryson, S. T., et al. 2014, ApJ, 784, 44

Lodieu, N., Perez-Garrido, A., Bejar, V. J. S., et al. 2014, arXiv.org

Loeb, A. & Gaudi, B. S. 2003, ApJ Letters, 588, L117

López-Morales, M. & Seager, S. 2007, ApJ Letters, 667, L191

Lovis, C., Mayor, M., Pepe, F., Queloz, D., & Udry, S. 2008, in Astronomical Society of the Pacific Conference Series, Vol. 398, Extreme Solar Systems, ed. D. Fischer, F. A. Rasio, S. E. Thorsett, & A. Wolszczan, 455

Macintosh, B. A., Anthony, A., Atwood, J., et al. 2014, in Society of Photo-Optical Instrumentation Engineers (SPIE) Conference Series, Vol. 9148, Society of Photo-Optical

Instrumentation Engineers (SPIE) Conference Series, 0

Madhusudhan, N. & Burrows, A. 2012, ApJ, 747, 25

Mancini, L., Lillo-Box, J., Southworth, J., & al., e. 2015, in prep.

Mancini, L., Southworth, J., Ciceri, S., et al. 2014, A&A, 568, A127

Mandel, K. & Agol, E. 2002, ApJ Letters, 580, L171

Marcy, G. W. & Butler, R. P. 1995, in Bulletin of the American Astronomical Society, Vol. 27, American Astronomical Society Meeting Abstracts, 1379

Marcy, G. W., Isaacson, H., Howard, A. W., et al. 2014, ApJ Supplements, 210, 20

Massey, R., Schrabback, T., Cordes, O., et al. 2014, MNRAS, 439, 887

Masuda, K., Hirano, T., Taruya, A., Nagasawa, M., & Suto, Y. 2013, ApJ, 778, 185

Mathur, S., García, R. A., Régulo, C., et al. 2010, A&A, 511, A46

Matijevič, G., Prša, A., Orosz, J. A., et al. 2012, AJ, 143, 123

Mayor, M. & Queloz, D. 1995, Nature, 378, 355

Mazeh, T., Holczer, T., & Shporer, A. 2015, ApJ, 800, 142

Mazeh, T., Nachmani, G., Holczer, T., et al. 2013, ArXiv e-prints

Mazeh, T., Nachmani, G., Sokol, G., Faigler, S., & Zucker, S. 2012, A&A, 541, A56

McQuillan, A., Aigrain, S., & Mazeh, T. 2013a, MNRAS, 432, 1203

McQuillan, A., Mazeh, T., & Aigrain, S. 2013b, ApJ Letters, 775, L11

Miglio, A., Brogaard, K., Stello, D., et al. 2012, MNRAS, 419, 2077

Miglio, A., Chiappini, C., Morel, T., et al. 2013a, in European Physical Journal Web of Conferences, Vol. 43, European Physical Journal Web of Conferences, 3004

Miglio, A., Chiappini, C., Morel, T., et al. 2013b, MNRAS, 429, 423

Miglio, A., Montalbán, J., Baudin, F., et al. 2009, A&A, 503, L21

Mislis, D., Heller, R., Schmitt, J. H. M. M., & Hodgkin, S. 2012, A&A, 538, A4

Montalbán, J., Miglio, A., Noels, A., et al. 2013, ApJ, 766, 118

Montalbán, J., Miglio, A., Noels, A., Scuflaire, R., & Ventura, P. 2010, ApJ Letters, 721, L182

Montet, B. T., Johnson, J. A., Muirhead, P. S., et al. 2014, ArXiv e-prints

Moraux, E., Bouvier, J., Stauffer, J. R., & Cuillandre, J.-C. 2003, A&A, 400, 891

Mordasini, C., Alibert, Y., Georgy, C., et al. 2012, A&A, 547, A112

Mordasini, C., Klahr, H., Alibert, Y., Benz, W., & Dittkrist, K.-M. 2010, ArXiv e-prints

Morel, T. & Miglio, A. 2012, MNRAS, 419, L34

Morris, S. L. & Naftilan, S. A. 1993, ApJ, 419, 344

Morton, T. D. & Johnson, J. A. 2011a, ApJ, 738, 170

Morton, T. D. & Johnson, J. A. 2011b, ApJ, 738, 170

Mosser, B., Barban, C., Montalbán, J., et al. 2011, A&A, 532, A86

Mosser, B., Belkacem, K., Goupil, M.-J., et al. 2010, A&A, 517, A22

Mosser, B., Goupil, M. J., Belkacem, K., et al. 2012, A&A, 540, A143

Mosser, B., Michel, E., Belkacem, K., et al. 2013, A&A, 550, A126

Mouschovias, T. C. 1991, ApJ, 373, 169

Moya, A. 2011, ArXiv e-prints, 1111.2274

Moya, A., Amado, P. J., Barrado, D., et al. 2010, MNRAS, 405, L81

Mugrauer, M., Neuhaeuser, R., Guenther, E., & Mazeh, T. 2005, Astronomische Nachrichten, 326, 629

Mugrauer, M. & Neuhäuser, R. 2009, A&A, 494, 373

Müller, H. M., Huber, K. F., Czesla, S., Wolter, U., & Schmitt, J. H. M. M. 2013, A&A, 560, A112

Muterspaugh, M. W., Lane, B. F., Kulkarni, S. R., et al. 2010, AJ, 140, 1657

Nakagawa, Y., Sekiya, M., & Hayashi, C. 1986, Icarus, 67, 375

Nardetto, N., Mourard, D., Kervella, P., et al. 2006, A&A, 453, 309

Ngo, H., Knuston, H. A., Hinkley, S., et al. 2014, arXiv.org, 13

Nidever, D. L., Marcy, G. W., Butler, R. P., Fischer, D. A., & Vogt, S. S. 2002, ApJ Supplements, 141, 503

Niedzielski, A., Villaver, E., Wolszczan, A., et al. 2015, A&A, 573, A36

O'Donovan, F. T., Charbonneau, D., Torres, G., et al. 2006, ApJ, 644, 1237

Ofek, E. O. 2008, PASP, 120, 1128

Ortiz, M., Gandolfi, D., Reffert, S., et al. 2015, A&A, 573, L6

Papagiannis, M. D. 1992, Journal of the British Interplanetary Society, 45, 227

Pasquini, L., Avila, G., Dekker, H., et al. 2008, in Society of Photo-Optical Instrumentation Engineers (SPIE) Conference Series, Vol. 7014, Society of Photo-Optical Instrumentation Engineers (SPIE) Conference Series, 1

Passy, J.-C., Mac Low, M.-M., & De Marco, O. 2012, ApJ Letters, 759, L30

Pepe, F., Lovis, C., Ségransan, D., et al. 2011, A&A, 534, A58

Pepe, F. A., Cristiani, S., Rebolo Lopez, R., et al. 2010, in Society of Photo-Optical Instrumentation Engineers (SPIE) Conference Series, Vol. 7735, Society of Photo-Optical Instrumentation Engineers (SPIE) Conference Series, 0

Perryman, M. 2014, American Journal of Physics, 82, 552

Perryman, M. A. C., de Boer, K. S., Gilmore, G., et al. 2001, A&A, 369, 339

Pfahl, E., Arras, P., & Paxton, B. 2008, ApJ, 679, 783

Pfeiffer, M., Frank, C., & Baumüller, D. 1992, in Astronomische Gesellschaft Abstract Series, Vol. 7, Astronomische Gesellschaft Abstract Series, ed. G. Klare, 191

Pickles, A. J. 1998, VizieR Online Data Catalog, 611, 863

Pinsonneault, M. H., An, D., Molenda-Żakowicz, J., et al. 2012, ApJ Supplements, 199, 30

Pollack, J. B., Hubickyj, O., Bodenheimer, P., et al. 1996, Icarus, 124, 62

Queloz, D., Henry, G. W., Sivan, J. P., et al. 2001, A&A, 379, 279

Quinn, S. N., White, T. R., Latham, D. W., et al. 2014, ArXiv e-prints

Quintana, E. V., Barclay, T., Raymond, S. N., et al. 2014, Science, 344, 277

Quintana, E. V., Rowe, J. F., Barclay, T., et al. 2013, ApJ, 767, 137

Quirrenbach, A., Amado, P. J., Caballero, J. A., et al. 2014, in Society of Photo-Optical Instrumentation Engineers (SPIE) Conference Series, Vol. 9147, Society of Photo-Optical Instrumentation Engineers (SPIE) Conference Series, 1

Rafikov, R. R. 2004, AJ, 128, 1348

Rafikov, R. R. 2005, ApJ Letters, 621, L69

Raghavan, D., Henry, T. J., Mason, B. D., et al. 2006, ApJ, 646, 523

Raghavan, D., McAlister, H. A., Henry, T. J., et al. 2010, ApJ Supplements, 190, 1

Rauer, H., Catala, C., Aerts, C., et al. 2014, Experimental Astronomy, 38, 249

Ribas, Á., Bouy, H., & Merín, B. 2015, A&A, 576, A52

Ricker, G. R., Winn, J. N., Vanderspek, R., et al. 2014, in Society of Photo-Optical Instrumentation Engineers (SPIE) Conference Series, Vol. 9143, Society of Photo-Optical Instrumentation Engineers (SPIE) Conference Series, 20

Riviere-Marichalar, P., Barrado, D., Montesinos, B., et al. 2014, A&A, 565, A68

Riviere-Marichalar, P., Pinte, C., Barrado, D., et al. 2013, A&A, 555, A67

Roell, T., Neuhäuser, R., Seifahrt, A., & Mugrauer, M. 2012, A&A, 542, A92

Rosenblatt, F. 1971, Icarus, 14, 71

Rowe, J. F., Bryson, S. T., Marcy, G. W., et al. 2014, ApJ, 784, 45

Russell, H. N. 1916, ApJ, 43, 173

Safronov, V. S. & Zvjagina, E. V. 1969, Icarus, 10, 109

Sahlmann, J., Lazorenko, P. F., Segransan, D., et al. 2015a, ArXiv e-prints

Sahlmann, J., Triaud, A. H. M. J., & Martin, D. V. 2015b, MNRAS, 447, 287

Sánchez-Lavega, A., del Río-Gaztelurrutia, T., Delcroix, M., et al. 2012, Icarus, 220, 561

Sánchez-Lavega, A., Río-Gaztelurrutia, T., Hueso, R., et al. 2014, GRL, 41, 1425

Sanchis-Ojeda, R., Rappaport, S., Pallé, E., et al. 2015, ArXiv e-prints

Sanchis-Ojeda, R. & Winn, J. N. 2011, ApJ, 743, 61

Santerne, A., Díaz, R. F., Moutou, C., et al. 2012, A&A, 545, A76

Santerne, A., Moutou, C., Bouchy, F., Hébrard, G., & Deleuil, M. 2009, in SF2A-2009: Proceedings of the Annual meeting of the French Society of Astronomy and Astrophysics, ed. M. Heydari-Malayeri, C. Reyl'E, & R. Samadi, 21

Santos, N. 2010, in Astronomy of Exoplanets with Precise Radial Velocities, 10

Santos, N. C., Mortier, A., Faria, J. P., et al. 2014, A&A, 566, A35

Sato, B., Hirano, T., Omiya, M., et al. 2015, ArXiv e-prints

Schmidt, B. E., Blankenship, D. D., Patterson, G. W., & Schenk, P. M. 2011, Nature, 479, 502

Schneider, J., Auvergne, M., Baglin, A., et al. 1998, in Astronomical Society of the Pacific Conference Series, Vol. 148, Origins, ed. C. E. Woodward, J. M. Shull, & H. A. Thronson, Jr., 298

Schödel, R. & Girard, J. H. 2012, The Messenger, 150, 26

Schwarz, G. 1978, Annals of Statistics, 6, 461

Scuflaire, R., Montalbán, J., Théado, S., et al. 2008, Astrophysics & Space Science, 316, 149

Seager, S. & Mallén-Ornelas, G. 2003, ApJ, 585, 1038

Sestito, P. & Randich, S. 2005, A&A, 442, 615

Showman, A. P. & Guillot, T. 2002, A&A, 385, 166

Shporer, A., Jenkins, J. M., Rowe, J. F., et al. 2011, AJ, 142, 195

Shu, F. H., Adams, F. C., & Lizano, S. 1987, A&A Annual Review, 25, 23

Silva, A. V. R. 2003, ApJ Letters, 585, L147

Silva-Valio, A. & Lanza, A. F. 2011, A&A, 529, A36

Silvotti, R., Schuh, S., Janulis, R., et al. 2007, Nature, 449, 189

Sing, D. K. 2010, A&A, 510, A21

Sliski, D. H. & Kipping, D. M. 2014, ArXiv e-prints, 1401.1207

Smalley, B., Anderson, D. R., Collier Cameron, A., et al. 2011, A&A, 526, A130

Smith, J. A., Tucker, D. L., Kent, S., et al. 2002, AJ, 123, 2121

Smith, R., Churcher, L. J., Wyatt, M. C., Moerchen, M. M., & Telesco, C. M. 2009, A&A, 493, 299

Southworth, J. 2008, MNRAS, 386, 1644

Southworth, J. 2011, MNRAS, 417, 2166

Southworth, J. 2013, A&A, 557, A119

Southworth, J., Hinse, T. C., Jørgensen, U. G., et al. 2009, MNRAS, 396, 1023

Stello, D. & Nissen, P. E. 2001, A&A, 374, 105

Straizys, V. & Kuriliene, G. 1981, Astrophysics & Space Science, 80, 353

Strehl, K. 1902, Astronomische Nachrichten, 158, 89

Sudarsky, D., Burrows, A., Hubeny, I., & Li, A. 2005, ApJ, 627, 520

Takahashi, Y. H., Narita, N., Hirano, T., et al. 2013, ArXiv e-prints

Tassoul, J.-L. 1987, ApJ, 322, 856

Tassoul, M. 1980, ApJ Supplements, 43, 469

Tenenbaum, P., Jenkins, J. M., Seader, S., et al. 2012, ArXiv e-prints, 1212.2915

Thebault, P. 2011, Celestial Mechanics and Dynamical Astronomy, 111, 29

Thébault, P., Marzari, F., & Scholl, H. 2006, Icarus, 183, 193

Thompson, S. E., Everett, M., Mullally, F., et al. 2012, ApJ, 753, 86

Tinney, C. G., Wittenmyer, R. A., Butler, R. P., et al. 2011, ApJ, 732, 31

Toomre, J., Latour, J., & Zahn, J.-P. 1981, in Bulletin of the American Astronomical Society, Vol. 13, Bulletin of the American Astronomical Society, 907

Torres, G. 2010, AJ, 140, 1158

Torres, G., Fressin, F., Batalha, N. M., et al. 2011, ApJ, 727, 24

Tregloan-Reed, J., Southworth, J., Burgdorf, M., et al. 2015, ArXiv e-prints

Tregloan-Reed, J., Southworth, J., & Tappert, C. 2013, MNRAS, 428, 3671

Udry, S., Mayor, M., & Santos, N. C. 2003, A&A, 407, 369

Ulrich, R. K. 1986, ApJ Letters, 306, L37

Vandakurov, Y. V. 1967, AZh, 44, 786

Vanderplas, J., Connolly, A., Ivezić, Ž., & Gray, A. 2012, in Conference on Intelligent Data Understanding (CIDU), 47 –54

Ventura, P., D'Antona, F., & Mazzitelli, I. 2008, Astrophysics & Space Science, 316, 93

Villaver, E. & Livio, M. 2009, ApJ Letters, 705, L81

Villaver, E., Livio, M., Mustill, A. J., & Siess, L. 2014, ApJ, 794, 3

Waite, Jr., J. H., Lewis, W. S., Magee, B. A., et al. 2009, Nature, 460, 487

Walkowicz, L. M. & Basri, G. S. 2013, MNRAS, 436, 1883

Wallenquist, Å. 1950, Arkiv for Astronomi, 1, 59

Wang, J., Fischer, D. A., Xie, J.-W., & Ciardi, D. R. 2014a, ApJ, 791, 111

Wang, J., Xie, J.-W., Barclay, T., & Fischer, D. A. 2014b, ApJ, 783, 4

Wang, Sharon, X., Wright, J. T., Cochran, W., et al. 2012, ApJ, 761, 46

Weidenschilling, S. J. 1977, MNRAS, 180, 57

Welsh, W. F., Orosz, J. A., Aerts, C., et al. 2011, ApJ Supplements, 197, 4

Welsh, W. F., Orosz, J. A., Seager, S., et al. 2010, ApJ Letters, 713, L145

White, T. R., Bedding, T. R., Stello, D., et al. 2011, ApJ, 743, 161

White, T. R., Huber, D., Maestro, V., et al. 2013, MNRAS

Willems, B. & Aerts, C. 2002, A&A, 384, 441

Wolszczan, A. & Frail, D. A. 1992, Nature, 355, 145

Wright, E. L., Eisenhardt, P. R. M., Mainzer, A. K., et al. 2010, AJ, 140, 1868

Wright, J. T. & Howard, A. W. 2009, ApJ Supplements, 182, 205

Yan, Z., Shen, Z.-Q., Yuan, J.-P., et al. 2013, MNRAS, 433, 162

Yanny, B., Guhathakurta, P., Bahcall, J. N., & Schneider, D. P. 1994, AJ, 107, 1745

Yorke, H. W., Bodenheimer, P., & Laughlin, G. 1993, ApJ, 411, 274

Zahn, J. P. 1966, Annales d'Astrophysique, 29, 565

Zhou, G., Bayliss, D., Hartman, J. D., et al. 2014, MNRAS, 437, 2831

Zhou, G. & Huang, C. X. 2013, ApJ Letters, 776, L35

Zucker, S. 2003, MNRAS, 342, 1291